

Mineralogical-Geochemical Characterisation of Cassiterite
and Wolframite Ores for an Analytical Fingerprint:
Focus on Trace Element Analysis by LA-ICP-MS

Von der Naturwissenschaftlichen Fakultät der
Gottfried Wilhelm Leibniz Universität Hannover

zur Erlangung des Grades
Doktor der Naturwissenschaften (Dr. rer. nat.)

genehmigte Dissertation
von

Dipl.-Geow. Simon Goldmann

geboren am 06.01.1982 in Hannover

2016

Referent: Prof. Dr. Francois Holtz

Koreferent: Prof. Dr. Frank Melcher

Tag der Promotion: 15. April 2016

Table of Contents

List of Figures	I
List of Tables	XIV
Acknowledgements	XVI
Abstract	XVII
Zusammenfassung	XVIII
1 Introduction	1
1.1 Socio-economic background	1
1.2 Economic relevance	4
2 Short synopses on the history of tin and tungsten	5
2.1 History of tin	5
2.2 History of tungsten	6
3 Metal and mineral properties	8
3.1 Tin	8
3.2 Tin minerals	9
3.2.1 Cassiterite	11
3.3 Tungsten	14
3.4 Tungsten minerals	15
3.4.1 Wolframite group	16
3.4.2 Ferberite	18
3.4.3 Hübnerite	19
3.4.4 Scheelite	21
4 The tin market	23
4.1 Applications of tin	23
4.2 Mine production and projects	24
4.3 Processing and beneficiation of tin	29
4.4 Pricing	30
4.5 Future trends	33
5 The tungsten market	34
5.1 Applications of tungsten	34
5.2 Mine production and projects	35
5.3 Processing and beneficiation of tungsten	40
5.4 Pricing	41
5.5 Future trends	44
6 Tin and tungsten deposits	45
6.1 Geochemistry and granites	45
6.2 Detailed descriptions of tin-tungsten deposit types	52
6.2.1 Magmatic deposits	53
6.2.2 Transitional magmatic-hydrothermal deposits	57
6.2.3 Hydrothermal deposits	67
6.2.4 Stratiform and stratabound deposits	70
6.2.5 Massive sulphide deposits	73
6.2.6 Placers	75

7	Methodology	76
7.1	Sampling and starting material	76
7.2	Sample preparation	77
7.3	Scanning electron microscopy with Mineral Liberation Analysis (MLA)	77
7.4	Laser ablation inductively coupled plasma mass spectrometry (LA-ICP-MS)	79
7.5	Electron probe microanalysis (EPMA)	82
8	Method development for cassiterite analysis by laser ablation inductively coupled plasma mass spectrometry (LA-ICP-MS)	85
8.1	Parameters	85
8.2	Calibration, standardisation, and data evaluation	87
8.3	Development of analytical procedure for cassiterite	98
8.3.1	Low resolution mode	99
8.3.2	Medium resolution	108
9	Method development for wolframite analysis by laser ablation inductively coupled plasma mass spectrometry (LA-ICP-MS)	124
9.1	Parameters	124
9.2	Calibration, standardisation, and data evaluation	125
9.3	Development of analytical procedure for wolframite	128
9.3.1	Low resolution mode	128
9.3.2	Medium resolution	130
10	Results	136
10.1	Detailed descriptions of investigated deposits	136
10.1.1	Africa	139
10.1.2	Asia	145
10.1.3	Australia	149
10.1.4	Europe	150
10.1.5	North America	152
10.1.6	South America	153
10.2	Mineralogical composition	157
10.3	Trace element composition	161
10.3.1	Electron probe microanalysis	161
10.3.2	LA-ICP-MS analysis	165
10.3.2.1	LA-ICP-MS analysis of cassiterite	167
10.3.2.2	LA-ICP-MS analysis of wolframite	171
11	Discussion	176
11.1	Mineralogical composition	176
11.2	Trace element composition	179
11.2.1	Trace elements in cassiterite	180
11.2.2	Trace elements in wolframite	196
11.3	Geochemistry of granites compared to trace elements in cassiterite and wolframite	204
11.4	Analytical Fingerprint	207
12	Conclusions	223
13	References	227

List of Figures

Figure 1.1: Trading routes of ore concentrates from the eastern provinces of the Democratic Republic of Congo through eastern Africa to the major ports of Mombasa and Dar-es-Salaam (International Alert, 2010).

Figure 1.2: Criticality of different commodities based on the Herfindahl-Hirschman-Index and the country risk rating of the Aggregate Governance Index of the World Bank (BGR, 2010).

Figure 2.1: The Nebra Sky Disc and associated bronze finds (Copyright: State Office for Heritage Management and Archeology Saxony-Anhalt, Germany; photograph taken by J. Lipták)

Figure 3.1: Various crystal habit of cassiterite (Ahlfeld, 1958): a) pegmatitic type, b) greisen type, twinned (Saxony), c) greisen type, d) hydrothermal vein type (Cornwall), epithermal type (needle tin)

Figure 3.2: Euhedral cassiterite crystal from the El Karit hydrothermal vein deposit, Morocco with coin (1 €) for scale. Specimen is taken from the BGR mineral collection.

Figure 3.3: Rutile-type crystal structure of cassiterite. Open circles represent sites of oxygen and filled circles are sites of tin (Kleber, 1998).

Figure 3.4: Micrograph of cassiterite (medium grey) and columbite-tantalite (light grey) embedded in epoxy resin (dark grey) from the Shori Sn-Ta-bearing pegmatite, Rwanda. Note simple twinning of the cassiterite grain. Cassiterite is characterised by grey colour, low reflectance but distinct bireflectance in plane polarised reflected light (left figure). In crossed polarised reflected light (right figure), cassiterite is anisotropic and shows many characteristic yellow-brown internal reflections.

Figure 3.5: Crystal structure of wolframite. Open circles represent sites of oxygen, black-filled circles are sites of tungsten and grey-filled circles are sites of iron or manganese (Kleber, 1998).

Figure 3.6: Wolframite crystals from the Xihuashan hydrothermal vein deposit, China with coin (1 €) for scale. Specimen is taken from the BGR mineral collection.

Figure 3.7: Photomicrographs of wolframite crystals. Left: euhedral ferberite crystal (light grey, left) is replaced by scheelite (medium grey, along rim of ferberite) and euhedral magnetite is formed (almost white). Matrix is composed of quartz (dark grey). This sample was taken from Namaqualand, South Africa and is courtesy of Johann Raith. Right: Simple twinning in large ferberite crystal indicated by bireflectance. This sample originates from the Bugarama tungsten mine, Rwanda.

Figure 3.8: Reinite composed of randomly oriented fibrous ferberite crystals forming a porous aggregate replacing scheelite. Sample originates from the Bugarama tungsten mine, Rwanda.

Figure 3.9: Large scheelite crystals from the tungsten deposit Felbertal, Mittersill, Austria. Picture A was taken at daylight (please note 1 €-coin for scale). Picture B shows the same view as picture A using ultraviolet light. Different generations of scheelite are discernible under ultraviolet radiation: scheelite 2 forms large crystals with yellowish fluorescence in the cores and scheelite 3 is present along the rims with bright blue fluorescence (Raith & Stein, 2006).

Figure 3.10: Crystal structure of scheelite. Open circles represent sites of oxygen, black-filled circles are sites of tungsten and grey-filled circles are sites of calcium (Kleber, 1998)

Figure 4.1: Annual global tin mine production from 1990 to 2013 in metric tons of metal content (BGR database).

Figure 4.2: Global tin mine production in tons metal content for 2013 (total: 298464 tons Sn; BGR database)

Figure 4.3: Reserve estimates (proven + probable) given as tin content in metric tons and grade in percent for selected tin mine projects

Figure 4.4: Resource estimates (indicated + inferred) given as tin content in metric tons and grade in percent for selected tin mine projects

Figure 4.5: Annual global refined tin production of major smelting companies from 2003 to 2012. Data only given for significant output larger than 2700 tons refined tin (ITRI)

Figure 4.6: Price chart for refined tin (99.85% minimum grade) from January 2001 to June 2015 (BGR database & Kuala Lumpur Tin Market)

Figure 5.1: Annual global tungsten mine production from 1990 to 2012 in metric tons of metal content (BGR database). Please note that production from China is displayed on a secondary vertical axis.

Figure 5.2: Global tungsten mine production for 2012 in metric tons of metal content in concentrate (total: 78776 tons W; BGR database)

Figure 5.3: Reserve estimates (proven + probable) given as WO_3 -content in metric tons of and WO_3 -grade in percent for selected tungsten mine projects.

Figure 5.4: Resource estimates (indicated + inferred) given as WO_3 -content in metric tons of and WO_3 -grade in percent for selected tungsten mine projects.

Figure 5.5: Price chart for ammonium paratungstate (APT) and ferrotungsten (FeW) from January 1997 to June 2015 (Metal Bulletin and BGR database)

Figure 6.1: Ore systems and metal associations in relation to redox conditions and the differentiation of the magma indicated by the range from intermediate to felsic intrusions (Pirajno, 2009)

Figure 6.2: Elements grouped by their ionic radii and valence states into high field strength elements (HFSE), large ion lithophile elements (LILE), elements with variable valences and small ionic radii (SIR), and elements falling in between (Transition)

Figure 6.3: Generalised schematic sketch showing the principle tin-tungsten deposits in relation to a granitic intrusion

Figure 6.4: Schematic cross section through a concentrically zoned pegmatite (Fetherston, 2004 modified after Černý, 1993). Vertical lines: aplitic border zone with fine-grained albite and quartz ± muscovite; v-pattern: wall zone with coarse-grained quartz, K-feldspar, albite, and muscovite; dotted pattern: outer intermediate zone with massive cleavelandite, often replaced by sugary albite with minor muscovite and quartz; crosshatched pattern: inner intermediate zone with coarse-grained spodumene, quartz, K-feldspar, and muscovite; black lines: core margin with large tourmaline, beryl, and spodumene.

Figure 6.5: Steeply dipping pegmatite intruded into Kibaran metasedimentary country rocks. Left picture was taken at Remera, Rutsiro, Rwanda. Right picture was taken by Frank Melcher at Nkegete, Gatumba, Rwanda

Figure 6.6: Hub stock greisen deposit near Krásno, Czech Republic. Left picture: former open pit and 'Pinge' (collapse area) of the Hub stock greisen deposit. Right picture: boulder with typical greisen pocket composed of massive quartz and zinnwaldite. Surrounding rock is greisenized granite composed of quartz, zinnwaldite, and topaz.

Figure 6.7: Geologic setting of the Bolivian Tin Belt (dashed outline) and location of major ore deposits (Dietrich et al., 2000)

Figure 6.8: Generalised cross-section through a porphyry tin deposit showing the relation of ore-bearing veins, alteration zones, and porphyry intrusion (Sillitoe et al., 1975)

Figure 6.9: Geological schematic sketch illustrating the mineralogical skarn zonation in the contact zone of the granitic intrusion (right) with the Tamames Limestone Formation (left) at the Los Santos scheelite skarn deposit, Spain (Tornos et al., 2008).

Figure 6.10: Geological map (A) and cross section (B) of the CanTung mine (Rasmussen et al., 2011 and references therein). The section line a-b on the map A indicates the strike of the cross section B. CS=Circular Stock, MS=Mine Stock, QFP Dyke=Quartz feldspar porphyry dyke.

Figure 6.11: Schematic model for the distribution of skarn and carbonate-replacement deposits in relation to a granite intrusion (Lehmann, 1990).

Figure 6.12: Pattern of metal zoning around granite intrusions in the St. Agnes District, Cornwall, south-west England (Bromley & Holl, 1986; Le Boutillier, 2002).

Figure 6.13: Sn-W mineralised vein deposits. Left picture: Reinite-bearing quartz vein crosscutting graphitic phyllites from the Nyakabingo mine, Rwanda. Right picture: Large cassiterite crystals in quartz vein from Krupka, Czech Republic.

Figure 6.14: Classification and distribution of different placer deposit types of a river valley in relation to a nearby outcrop of the primary ore deposit (Pohl, 2011).

Figure 7.1: Heavy mineral pre-concentrate from Rukaragata pegmatite in Rwanda. This pre-concentrate is essentially composed of cassiterite and columbite-tantalite (black grains).

Figure 7.2: The *FEI Quanta 600 FEG* environmental scanning electron microscope with Mineral Liberation Analysis software in operation at BGR, Hannover. The left screen is showing an EDX-spectrum of an analysed mineral grain and the right screen displays the BSE image of the scanned sample surface.

Figure 7.3: Classified MLA image of a mixed cassiterite-coltan pre-concentrate from the Jos Plateau, Nigeria (Coltan-372). Legend is reduced and only minerals with more than 1 area% are included.

Figure 7.4: The LA-ICP-MS system in operation at BGR, Hannover. The *New Wave UP193-FX* laser ablation unit is shown on the right hand side with the *ATLEX-300-SI* excimer laser stored in the cabinet below. The screen displays the ablation pit of the laser on a columbite-tantalite grain. The *Thermo Scientific ELEMENT-XR* mass spectrometer is shown on the left hand side.

Figure 7.5: Arrangement of plasma torch, induction coil and interface with the sampler and skimmer cones (Thermo, 2005).

Figure 7.6: Different detector types in ICP-MS. a) Faraday cup, b) secondary electron multiplier, c) scheme of a secondary electron multiplier (SEM) detector with analogue and counting modes for detection (Wiedenbeck et al., 2012; Thermo, 2005).

Figure 7.7: The *Cameca SX-100* electron microprobe in operation at BGR, Hannover. The right screen displays the BSE image of the scanned sample surface and the next screen to the left is showing optical image of the reflected light microscope. The two screens to the left are for the control computer.

Figure 8.1: Detection limits for LA-ICP-MS analysis of cassiterite.

Figure 8.2: Detection limits for LA-ICP-MS analysis of wolframite.

Figure 8.3: Time-resolved signal of LA-ICP-MS analysis of cassiterite. Green shaded area is integrated for background and blue shaded area is integrated for sample signal.

Figure 8.4: Time-resolved signal of LA-ICP-MS analysis of cassiterite with apatite inclusion indicated by increase in Ca and P. Green shaded area is integrated for background and blue shaded area is integrated for sample signal.

Figure 8.5: Comparison of LA-ICP-MS and EPMA data for titanium. The analyses for both methods were performed on the same grains of cassiterite concentrate AS 8829. The LA-ICP-MS data are calibrated against NIST SRM 610 glass (in blue) and columbite-(Fe) Coltan 139 (in red), respectively. The black line shows the 1:1 trend.

Figure 8.6: Comparison of LA-ICP-MS and EPMA data for iron. The analyses for both methods were performed on the same grains of cassiterite concentrate AS 8829. The LA-ICP-MS data are calibrated against NIST SRM 610 glass (in blue) and columbite-(Fe) Coltan 139 (in red), respectively. The black line shows the 1:1 trend.

Figure 8.7: Comparison of LA-ICP-MS and EPMA data for niobium. The analyses for both methods were performed on the same grains of cassiterite concentrate AS 8829. The LA-ICP-MS data are calibrated against NIST SRM 610 glass (in blue) and columbite-(Fe) Coltan 139 (in red), respectively. The black line shows the 1:1 trend.

Figure 8.8: Comparison of LA-ICP-MS and EPMA data for tantalum. The analyses for both methods were performed on the same grains of cassiterite concentrate AS 8829. The LA-ICP-MS data are calibrated against NIST SRM 610 glass (in blue) and columbite-(Fe) Coltan 139 (in red), respectively. The black line shows the 1:1 trend.

Figure 8.9: Fractionation indices relative to Ca (Fryer et al., 1995). Symbols categorize elements according to the classification of Goldschmidt (1923). Diagram taken from Günther et al. (1999).

Figure 8.10: Diagram of intensity versus mass-charge ratio showing the high resolution spectrum of gallium on the nominal mass of 69 amu. Measurement on cassiterite sample (Coltan 240)

Figure 8.11: Diagram of intensity versus mass-charge ratio showing the high resolution spectrum of gallium on the nominal mass of 71 amu. Note the interference caused by MnO and ArP. Measurement on cassiterite sample (Coltan 240)

Figure 8.12: Diagram of intensity versus mass-charge ratio showing the high resolution spectrum of germanium on the nominal mass of 73 amu. Measurement on cassiterite sample (Coltan 240)

Figure 8.13: Diagram of intensity versus mass-charge ratio showing the high resolution spectrum of germanium on the nominal mass of 74 amu. Note the interference caused by Ar₂ and Cl₂. Measurement on cassiterite sample (Coltan 240)

Figure 8.14: Diagram of intensity versus mass-charge ratio showing the high resolution spectrum of barium on the nominal mass of 137 amu. Note that the SnO interference cannot be resolved in high resolution mode. Measurement on cassiterite sample (Coltan 240)

Figure 8.15: Diagram of intensity versus mass-charge ratio showing the low resolution spectrum for the nominal mass range from 134 to 150 amu including the light REE. Note the high blank values for xenon and barium. Inset shows that SnNa is not generating the high background signals. Measurement on blank sample

Figure 8.16: Diagram of intensity versus mass-charge ratio showing the low resolution spectrum for the nominal mass range from 145 to 166 amu including the REE. Note the interferences of SnNaO and BaO compounds. Measurement on blank sample

Figure 8.17: Diagram of intensity versus mass-charge ratio showing the low resolution spectrum for the nominal mass range from 166 to 182 amu including the heavy REE. Measurement on blank sample

Figure 8.18: Diagram of intensity versus mass-charge ratio showing the high resolution spectrum for lanthanum on the nominal mass of 139 amu. Measurement on cassiterite sample (Coltan 240)

Figure 8.19: Diagram of intensity versus mass-charge ratio showing the medium resolution spectrum for cerium on the nominal mass of 140 amu. Measurement on cassiterite sample (Coltan 240)

Figure 8.20: Diagram of intensity versus mass-charge ratio showing the high resolution spectrum for gadolinium on the nominal mass of 155 amu. Note the strong interference of SnNaO. Measurement on cassiterite sample (Coltan 240)

Figure 8.21: Diagram of intensity versus mass-charge ratio showing the high resolution spectrum for terbium on the nominal mass of 159 amu. Note the strong interference of SnNaO. Measurement on cassiterite sample (Coltan 240)

Figure 8.22: Diagram of intensity versus mass-charge ratio showing the medium resolution spectrum for carbon on the nominal mass of 12 amu. Measurement on cassiterite sample (Coltan 240)

Figure 8.23: Diagram of intensity versus mass-charge ratio showing the medium resolution spectrum for sodium on the nominal mass of 23 amu. Note the interference of Ti^{2+} . Measurement on cassiterite sample (Coltan 240)

Figure 8.24: Diagram of intensity versus mass-charge ratio showing the medium resolution spectrum for magnesium on the nominal mass of 24 amu. Note the interferences of Ti^{2+} and C_2 . Measurement on cassiterite sample (Coltan 240)

Figure 8.25: Diagram of intensity versus mass-charge ratio showing the medium resolution spectrum for aluminum on the nominal mass of 27 amu. Note the interference of CN. Measurement on cassiterite sample (Coltan 240)

Figure 8.26: Diagram of intensity versus mass-charge ratio showing the medium resolution spectrum for silicon on the nominal mass of 29 amu. Note the interferences of CO, N_2 and N_2H compounds. Measurement on cassiterite sample (Coltan 240)

Figure 8.27: Diagram of intensity versus mass-charge ratio showing the medium resolution spectrum for phosphorous on the nominal mass of 31 amu. Note the interferences of NO and NOH compounds. Measurement on cassiterite sample (Coltan 240)

Figure 8.28: Diagram of intensity versus mass-charge ratio showing the medium resolution spectrum for sulfur on the nominal mass of 32 amu. Note the interference of O_2 compound. Measurement on cassiterite sample (Coltan 240)

Figure 8.29: Diagram of intensity versus mass-charge ratio showing the medium resolution spectrum for calcium on the nominal mass of 44 amu. Note the interferences of SiO and CO_2 compounds. Measurement on cassiterite sample (Coltan 240)

Figure 8.30: Diagram of intensity versus mass-charge ratio showing the medium resolution spectrum for scandium on the nominal mass of 45 amu. Note the interferences of SiO compounds and the non-resoluble overlap of Zr^{2+} ion. Measurement on cassiterite sample (Coltan 240)

Figure 8.31: Diagram of intensity versus mass-charge ratio showing the medium resolution spectrum for vanadium on the nominal mass of 51 amu. Measurement on cassiterite sample (Coltan 240)

Figure 8.32: Diagram of intensity versus mass-charge ratio showing the medium resolution spectrum for chromium on the nominal mass of 52 amu. Note the interference of ArC compound. Measurement on cassiterite sample (Coltan 240)

Figure 8.33: Diagram of intensity versus mass-charge ratio showing the medium resolution spectrum on the nominal mass of 59 amu. Note the absence of the cobalt peak and the strong interference of Sn^{2+} . Measurement on cassiterite sample (Coltan 240)

Figure 8.34: Diagram of intensity versus mass-charge ratio showing the medium resolution spectrum for cobalt on the nominal mass of 59 amu. Note the slope of the interference of Sn^{2+} . Measurement on cassiterite sample (Coltan 240)

Figure 8.35: Diagram of intensity versus mass-charge ratio showing the medium resolution spectrum for nickel on the nominal mass of 60 amu. Note the strong interference of Sn^{2+} . Measurement on cassiterite sample (Coltan 240)

Figure 8.36: Diagram of intensity versus mass-charge ratio showing the medium resolution spectrum for nickel on the nominal mass of 60 amu. Note the influence of Sn^{2+} . Measurement on cassiterite sample (Coltan 240)

Figure 8.37: Diagram of intensity versus mass-charge ratio showing the medium resolution spectrum for copper on the nominal mass of 63 amu. Note the interference of ArNa. Measurement on cassiterite sample (Coltan 240)

Figure 8.38: Diagram of intensity versus mass-charge ratio showing the medium resolution spectrum for zinc on the nominal mass of 68 amu. Note the interference of ArSi. Measurement on cassiterite sample (Coltan 240)

Figure 8.39: Diagram of intensity versus mass-charge ratio showing the low resolution spectrum for cadmium on the nominal mass of 111 amu. Note the abundance sensitivity of Sn on the nominal mass of 112 amu. Measurement on cassiterite sample (Coltan 240)

Figure 8.40: Diagram of intensity versus mass-charge ratio showing the medium resolution spectrum for cadmium on the nominal mass of 111 amu. Measurement on cassiterite sample (Coltan 240)

Figure 8.41: Diagram of intensity versus mass-charge ratio showing the low resolution spectrum for indium on the nominal mass of 113 amu. Note the abundance sensitivity of Sn on the nominal masses of 112 and 113 amu. Measurement on cassiterite sample (Coltan 240)

Figure 8.42: Diagram of intensity versus mass-charge ratio showing the medium resolution spectrum for indium on the nominal mass of 113 amu. Note that the abundance sensitivity of Sn is discriminated in medium resolution. Measurement on cassiterite sample (Coltan 240)

Figure 8.43: Diagram of intensity versus mass-charge ratio showing the medium resolution spectrum for tin on the nominal mass of 118 amu. Measurement on cassiterite sample (Coltan 240)

Figure 8.44: Diagram of intensity versus mass-charge ratio showing the low resolution spectrum for antimony on the nominal mass of 121 amu. Note the abundance sensitivity of Sn on the nominal mass of 120 amu. Measurement on cassiterite sample (Coltan 240)

Figure 8.45: Diagram of intensity versus mass-charge ratio showing the medium resolution spectrum for antimony on the nominal mass of 121 amu. Note that the abundance sensitivity of Sn is discriminated in medium resolution. Measurement on cassiterite sample (Coltan 240)

Figure 9.1: Comparison of LA-ICP-MS and EPMA data for manganese. The analyses for both methods were performed on the same wolframite grains of concentrate AS 8829. The black line shows the 1:1 trend.

Figure 9.2: Comparison of LA-ICP-MS and EPMA data for iron. The analyses for both methods were performed on the same wolframite grains of concentrate AS 8829. The black line shows the 1:1 trend.

Figure 9.3: Comparison of LA-ICP-MS and EPMA data for niobium. The analyses for both methods were performed on the same wolframite grains of concentrate AS 8829. Detection limit of niobium for EPMA is approximately 290 ppm, EPMA data below detection limit are set to 0. The black line shows the 1:1 trend.

Figure 9.4: Diagram of intensity versus mass-charge ratio showing the medium resolution spectrum of indium on the nominal mass of 115 amu. Note that the ^{115}Sn interference cannot be resolved in high resolution mode. Measurement on wolframite sample (WOLF)

Figure 9.5: Diagram of intensity versus mass-charge ratio showing the medium resolution spectrum of titanium on the nominal mass of 47 amu. Note the interference caused by NO_2 . Measurement on wolframite sample (WOLF)

Figure 9.6: Diagram of intensity versus mass-charge ratio showing the medium resolution spectrum of iron on the nominal mass of 56 amu. Note the interference caused by ArO . Measurement on wolframite sample (WOLF)

Figure 9.7: Diagram of intensity versus mass-charge ratio showing the medium resolution spectrum of niobium on the nominal mass of 93 amu. Note the interference caused by bivalent ^{186}W ion. Measurement on wolframite sample (WOLF)

Figure 10.1: Geological map of the World (modified after Bouysse, 2009) showing the deposits of ore concentrate samples. Rectangles mark areas of higher sample density which are displayed in separate maps below.

Figure 10.2: Cross-section through the Zaaiploaats tin deposits in South Africa showing the intrusive contact of the granite and the low grade zone of Sn enrichment (Robb, 2005 modified after Coetzee & Twist, 1989).

Figure 10.3: Regional zonation of pegmatites around a parental granite intrusion in the Gatumba area, Rwanda. Barren pegmatites are closer to the parental intrusion, whereas mineralized pegmatites occur in greater distance (Hulsbosch et al., 2013).

Figure 10.4: Geological map of Rwanda showing the location of ore concentrate samples (modified after Theunissen et al., 1991). Rectangles mark concession areas with higher sample density. Detailed maps of the Nyakabingo, Nemba, Rutsiro and Rutongo areas are given in the Discussion chapter.

Figure 10.5: Geological map of the Democratic Republic of the Congo showing the location of ore concentrate samples (modified after Lepersonne, 1974).

Figure 10.6: Geological map (upper image) and cross-section (lower image) of the Abu Dabbab leucogranite stock in the Eastern Desert, Egypt (Küster, 2008).

Figure 10.7: Geological map of the Southeast Asian Tin Belt showing the location of samples (modified after Cobbing et al, 1986).

Figure 10.8: Geological map of the Mongolia showing the location of ore concentrate samples (modified after Kovalenko & Yarmolyuk, 1995).

Figure 10.9: Geological map and cross section of the Greenbushes pegmatite (Fetherston, 2004 modified from Partington et al., 1995).

Figure 10.10: Geological map of the Rondônia Tin Province showing the location of ore concentrate samples (modified after Bettencourt, 1999).

Figure 10.11: Geological map of the Bolivian Tin Belt showing the location of ore concentrate samples (modified after Dietrich et al, 2000).

Figure 10.12: Geological map of the San Rafael deposit showing the relation of mineralised quartz veins to the granitic intrusion (Mlynarczyk et al., 2003).

Figure 10.13: Examples for classified MLA images: A) Mixed wolframite-cassiterite concentrate from Bishasha, DR Congo (AS9829); B) Mixed coltan-cassiterite concentrate from Kirwa, Rwanda (AS7757); C) Cassiterite concentrate from Muana, DR Congo (AS8837).

Figure 10.14: BSE image (A), X-ray element distribution maps of Sn (B), Ta (C), Fe (D), Nb (E), and Zr (F) of cassiterite showing inhomogeneous elemental distribution with correlation of Ta, Nb, and Fe with decreasing Sn. Cathodoluminescence image (G) shows that strong luminescence coincides with low trace element contents of cassiterite. Note columbite-tantalite inclusions in the core.

Figure 10.15: X-ray element distribution maps of Sn (A), Zr (B), Ta (C), and Fe (D) in cassiterite showing distinct growth zoning with correlation of Ta (plus Nb) and Fe with decreasing Sn. Cathodoluminescence image (E) shows that strong luminescence coincides with low trace element contents, especially along the rim of cassiterite at the bottom of the image.

Figure 10.16: BSE image and Mg, Fe, and Mn X-ray element distribution maps of wolframite from Zlatná Baňa, Ochtiná, Slovakia (Ferenc & Uher, 2007).

Figure 10.17: The variability in the trace element composition of cassiterite is displayed by the 10th percentile (dashed lower line), median (solid line), and 90th percentile (stippled upper line) of normalised concentration values for different ore deposit types (selected samples; see Table 10.7): pegmatites in green, hydrothermal veins in blue, disseminated deposits in red, and Bolivian polymetallic deposits in yellow. Robust statistical parameters are used as the trace element data are not normally distributed and to avoid overestimation of outliers.

Figure 10.18: Exemplary photographs of different cassiterite concentrates already prepared as polished sections. The colour of cassiterite is variable ranging from dark black to almost pure white.

Figure 10.19: Comparison of trace element data for black and white cassiterite. Note different scales for trace and minor elements, respectively.

Figure 10.20: Diagram showing the niobium and tantalum contents [in ppm] in wolframite versus its ferberite/hübnerite ratio given as $Fe/(Fe+Mn)$.

Figure 10.21: This diagram shows that trace elements concentration levels (blue: Nb; red: Mo; green: Co) in wolframite are dependent on the ferberite/hübnerite ratio given as $Fe/(Fe+Mn)$.

Figure 10.22: The variability in the trace element composition of wolframite is displayed by the 10th percentile (dashed lower line), median (solid line), and 90th percentile (stippled upper line) of normalised concentration values for different ore deposit types (selected samples; see Table 10.8): high temperature hydrothermal veins in blue, greisen deposits in red, low temperature hydrothermal veins in green, and reinitite deposits in yellow. Robust statistical parameters are used as the trace element data are not normally distributed and to avoid overestimation of outliers.

Figure 10.23: Variability of chondrite-normalised REE patterns of wolframite from each tungsten deposit given as the 10th percentile (lower line with squares) and 90th percentile (upper line with diamonds). Composition of C1 carbonaceous chondrite is taken from McDonough & Sun (1995). Upper left diagram: Rwanda, upper right diagram: DR Congo, lower left diagram: Mongolia, lower right diagram: rest of the world.

Figure 11.1: MLA images of two heavy mineral concentrates from Simba, Rwanda. Different colours represent different mineral phases: e.g., cassiterite (blue), columbite-tantalite (pinkish and red), rutile (yellow), topaz (pale blue), muscovite (pale green), quartz (pale violet) and Fe oxides (apricot). Comparison of these two MLA images reveals the different ore grade of the two concentrates although they originate from the same deposit: 46.7 area% cassiterite (left) versus 12.7 area% cassiterite (right).

Figure 11.2: Binary diagram showing the Zr/Hf versus Ta/Nb ratios from LA-ICP-MS analysis of cassiterite originating from different deposit types, namely pegmatite (red squares), disseminated or greisen (blue diamonds), hydrothermal vein (yellow circles), and polymetallic vein (green triangles) deposits, respectively. Note the distinct cluster (marked by the ellipse) of values for cassiterite from disseminated deposits below the pegmatite field. This cluster is made up by analyses of cassiterite from the Abu Dabbab and Nuweibi rare metal granite deposits.

Figure 11.3: Diagram showing a correlation of the median Pb concentration in cassiterite versus the geological age of the deposit. The Pb value is given as median of the single LA-ICP-MS cassiterite analyses of the individual concentrate in ppm. Corresponding age dates for the respective deposits are taken from the literature (references for each deposit are mentioned in results chapter) as an estimation for the formation age of the cassiterite mineralisation.

Figure 11.4: “Columbite quadrilateral” showing the Ta/(Ta+Na) and Mn/(Mn+Fe) compositions from LA-ICP-MS analysis of cassiterite originating from different deposit types, namely pegmatite (red squares), disseminated (blue diamonds), hydrothermal vein (yellow circles), and polymetallic vein (green triangles) deposits, respectively. Note the distinct cluster (marked by the ellipse) of values for cassiterite from the Abu Dabbab and Nuweibi rare metal granite deposits. Solid arrow indicates the major fractionation path of magmatic cassiterite and the dashed arrow generalises the columbite-tantalite fractionation trend.

Figure 11.5: “Columbite quadrilateral” showing the Ta/(Ta+Na) and Mn/(Mn+Fe) compositions from LA-ICP-MS analysis of cassiterite originating from selected pegmatite deposits.

Figure 11.6: Binary plot showing the Ga versus In concentration of cassiterite from deposits of the Bolivian Tin Belt. The line clearly separates the pluton-related deposits (squares) from the porphyry deposits (diamonds).

Figure 11.7: Binary diagram showing the concentrations of Nb [ppm] versus Ga [ppm] from LA-ICP-MS analysis of cassiterite originating from different deposit types of the Bolivian Tin Belt. The top down arrangement of the deposits in the legend corresponds to their distribution from north to south.

Figure 11.8: Binary diagram showing the concentrations of Fe [ppm] versus In [ppm] from LA-ICP-MS analysis of cassiterite from ore concentrates originating from different deposit types, namely pegmatite (red squares), disseminated or greisen (blue diamonds), hydrothermal vein (yellow circles), and polymetallic vein (green triangles) deposits, respectively. Additionally, results from Geevor samples (purple crosses) are also plotted.

Figure 11.9: Binary diagram showing the concentrations of Nb [ppm] versus Sc [ppm] from LA-ICP-MS analysis of wolframite worldwide.

Figure 11.10: Normalised element distribution patterns of wolframite from worldwide ore concentrates with focus on Central Asian deposits in the lower two diagrams. Variability of the trace element composition is given as the 10th percentile (lower line with diamonds) and 90th percentile (upper line with squares) of the normalised values.

Figure 11.11: Comparison of trace element data (upper left: Ta, upper right: Nb; lower left: Mn, and lower right: Ga) in cassiterite from different Sn deposits with whole rock geochemical data of the respective associated intrusion. Data points are omitted if no corresponding value from whole rock analysis was measured. Please note that data are displayed on logarithmic scale, except for Ga (lower right).

Figure 11.12: Comparison of trace element data (on logarithmic scale) in wolframite (dark) from two W deposits with whole rock geochemical data of the respective associated intrusion (pale).

Figure 11.13: Geological map of the Nyakabingo mine, Rwanda (slightly modified after De Clercq, 2012; De Clercq compiled this map from various sources). The sample locations of the different tunnels are marked by red circles with the corresponding section numbers. The two profiles A and B were investigated by Friso De Clercq during his Ph.D. thesis.

Figure 11.14: Normalised element distribution patterns of ferberite from ore concentrates originating from ten tunnels of the Nyakabingo mine. Variability of the trace element composition is given as the 10th percentile (lower line with diamonds) and 90th percentile (upper line with squares) of the normalised values.

Figure 11.15: Geological map showing the close spatial distribution of hydrothermal quartz veins and pegmatites in the Nemba mine, Rwanda (detail from the map of Brinkmann, 1987).

Figure 11.16: Normalised element distribution patterns of cassiterite from three ore concentrates originating from Nemba in comparison to typical pegmatite (7994, 8042) and hydrothermal vein (9732) patterns.

Figure 11.17: Normalised element distribution patterns of cassiterite from three ore concentrates originating from Bugalula in comparison to typical pegmatite (8868, 9668) and hydrothermal vein (9667) patterns.

Figure 11.18: Geological map of the Rutsiro area, Rwanda. Uwinka Formation: graphitic phyllite, quartz phyllite; Nyungwe Formation: quartzite, phyllite; Butare Complex: gneiss, migmatite, metaquartzite, micaschist, amphibolites, pegmatite (detail from map of Theunissen et al., 1991).

Figure 11.19: Normalised element distribution patterns of cassiterite from ore concentrates originating from eight localities of the Rutsiro concession. Variability of the trace element composition is given as the 10th percentile (lower line with diamonds) and 90th percentile (upper line with squares) of the normalised values.

Figure 11.20: Normalised element distribution patterns of wolframite from ore concentrates originating from five localities of the Rutsiro concession. Variability of the trace element

composition is given as the 10th percentile (lower line with diamonds) and 90th percentile (upper line with squares) of the normalised values.

Figure 11.21: Binary diagram showing the concentrations of Zn [ppm] versus Co [ppm] from LA-ICP-MS analysis of wolframite originating from five localities of the Rutsiro concession.

Figure 11.22: Binary diagram showing the concentrations of Y [ppm] versus V [ppm] from LA-ICP-MS analysis of wolframite originating from five localities of the Rutsiro concession.

Figure 11.23: Geological map of the Rutongo area in Rwanda showing the distribution of the tin mines and their distinct relation to the quartzite units within the anticlinal structure (De Clercq, 2012; modified after Pohl, 1975).

Figure 11.24: Normalised element distribution patterns of cassiterite from ore concentrates originating from six tunnels of the Nyamyumba deposit. Variability of the trace element composition is given as the 10th percentile (lower line with diamonds) and 90th percentile (upper line with squares) of the normalised values.

Figure 11.25: Normalised element distribution patterns of cassiterite from ore concentrates originating from six deposits of the Rutongo area. Variability of the trace element composition is given as the 10th percentile (lower line with diamonds) and 90th percentile (upper line with squares) of the normalised values.

List of Tables

Table 3.1: Compilation of Sn-bearing minerals

Table 3.2: Compilation of W-bearing minerals

Table 6.1: Compilation of whole rock geochemical data for some granitic intrusions (including pegmatites) related to Sn and W deposits (references are listed below the table). Element oxides plus fluorine are given in wt.% and trace elements are given in ppm. Please note that total iron is given as FeO*.

Table 7.1: Maximum resolution (R_{max}) of the three different resolution modes (low, medium and high resolution).

Table 7.2: Parameters including measured lines, measurement time (meas. time) in seconds, used standards, and average detection limits (det. lim.) in ppm at 40 and 120 nA for each element during analysis of cassiterite by EMPA.

Table 7.3: Parameters including measured lines, measurement time (meas. time) in seconds, used standards, and average detection limits (det. lim.) in ppm at 30 kV for each element during analysis of wolframite and scheelite by EMPA.

Table 8.1: Composition of the matrix of NIST SRM 610 in weight percent oxide (Pearce et al., 1997)

Table 8.2: Compositional data for spike elements of NIST SRM 610 in ppm (Pearce et al., 1997)

Table 8.3: Summary of the measured elements for cassiterite analysis by LA-ICP-MS including the selected isotope, its relative abundance, selected resolution mode for the mass spectrometer, and potential interferences

Table 9.1: Summary of the measured elements for wolframite analysis by LA-ICP-MS including the selected isotope, its relative abundance, selected resolution mode for the mass spectrometer, and potential interferences

Table 10.1: Summarising table on metallogenic provinces or single deposit (detailed descriptions are given in the respective section) including county (AU=Australia, BO=Bolivia, BR=Brazil, CD= Democratic Republic of the Congo, CA=Canada, CO=Colombia, CZ=Czech Republic, EG=Egypt, GB=Great Britain, HK=Hong Kong ID=Indonesia, MM=Myanmar, MN=Mongolia, MY=Malaysia, NG=Nigeria, PE=Peru, PT=Portugal, RU= Russia, RW=Rwanda, TH=Thailand, US= United States of America, ZA=South Africa), deposit types (rg=rare metal granite, see 6.2.1; an=anorogenic, see 6.2.1; pe=pegmatite, see 6.2.1, gr=greisen, see 6.2.2; po=porphyry, see 6.2.2; hv=hydrothermal vein, see 6.2.3; pl=placer, primary deposit in brackets, see 6.2.6), dominating ore minerals (cs=cassiterite, wolf=wolframite, coltan=columbite-tantalite, schee=scheelite, sulf=sulphides) in the concentrates, geologic age (in million years), type of associated intrusion and their surrounding host rocks.

Table 10.2: MLA data for worldwide cassiterite concentrates (for country see Table 10.1.) with rel. abundances of mineral phases (in area%)

Table 10.3: MLA data for worldwide wolframite and mixed wolframite-cassiterite concentrates (for country see Table 10.1.) with relative abundances of classified mineral phases (in area%)

Table 10.4: Electron probe microanalysis of cassiterite in wt.% oxide and atoms per formula unit normalised to 2 oxygens (bdl = below detection limit, Table 7.2)

Table 10.5: Electron probe microanalysis of wolframite and scheelite in wt% oxide and atoms per formula unit normalised to 4 oxygens (bdl = below detection limit, Table 7.3)

Table 10.6: Normalisation values for cassiterite and wolframite (values represent ppm and are only given for elements with positive median)

Table 10.7: List of the selected samples which were included in Figure 10.17 to display the variability for the respective tin deposit types

Table 10.8: List of the selected samples which were included in Figure 10.22 to display the variability for the respective wolframite deposit types

Table 11.1: Chemical composition of cassiterite by electron probe microanalysis (EMPA) compiled from the literature. Analyses are given in wt.% element oxide, 0 values are below detection limit. Original data from Möller et al. (1988) and Somarin (2009) were converted from wt.% element into wt.% element oxide for comparability.

Table 11.2: Chemical composition of cassiterite by different analytical methods (ES = Emission spectrography, ICP-MS = inductively coupled plasma mass spectrometry, INAA = instrumental neutron activation analysis, PIXE = particle induced X-ray emission, XRF = X-ray fluorescence) compiled from the literature. Analyses are given in ppm element, 0 values are below detection limit. Original data from Dudykina (1959) were converted from wt.% element into ppm element, wt.% element oxide from Swinden (1983) were converted into ppm element, and wt.% Fe₂O₃ from Gan & Chen (1994) were converted into ppm Fe for comparability.

Table 11.3: Chemical composition of wolframite by different analytical methods (EPMA = electron probe microanalysis, AAS = atomic absorption spectroscopy, XRF = X-ray fluorescence) compiled from the literature. Analyses are given in wt.% element oxide or ppm element, 0 values are below detection limit. Original data from Ferenc & Uher (2007) and Barkov et al. (2008) in wt.% ZnO were converted into ppm Zn and original element ppm for Nb, Ta, Sn, and Sc from Gan & Chen (1992) were converted into wt.% of the respective element oxide for comparability.

Acknowledgements

This study was funded by the Federal Institute for Geosciences and Natural Resources (Bundesanstalt für Geowissenschaften und Rohstoffe, BGR) as “Hochschulvergabeprojekt” (research subcontract to universities) and this project forms the basis of the Ph.D. thesis of the author at Institute for Mineralogy at the Leibniz University of Hannover.

There are a lot of people I wish to thank and who helped to make this thesis possible.

I want to express my biggest thanks to the supervisors of my thesis, Prof. Dr. Frank Melcher (formerly BGR, now University of Leoben) and Prof. Dr. Francois Holtz (Leibniz University of Hannover), for their encouragement and advice throughout the project. I am greatly indebted to Frank for his enthusiasm and valuable discussions about pegmatites and hydrothermal ore deposits. I’m very grateful to Francois for his passion and support, especially in terms of granitic melts as well as honey.

Thanks a lot to Dr. Eike Gäbler (BGR) who let me in on the secrets of mass spectrometry and for his patience during method development in his LA-ICP-MS laboratory.

Dr. Thomas Oberthür (BGR) is kindly thanked for making it possible to do the major work of the thesis in the Ore Deposit Research Department at BGR and for the provision of sample material from Geevor, Zaaiplaats, and Kamativi mines.

I also want to thank Dr. Maria Sitnikova (BGR) for her assistance with the Mineral Liberation Analysis and sample material from the Russian Spokoynoye deposit.

Jerzy Lodziak and Christian Wöhrle (both BGR) are kindly thanked for their support at the electron microprobe.

I am also grateful to Dr. Torsten Graupner (BGR) for the good mood in our office and for sample material from the Rutsiro concession.

The following people are kindly thanked for providing ore concentrates from all over the world: Dr. Philip Schütte (BGR), Thomas Munyambondera and Alexis Kagaba (both Geology and Mines Department, Kigali), Dr. Stijn Dewaele (Royal Museum for Central Africa, Tervuren), Dr. Peter Buchholz (BGR), Dr. Harald Elsner (BGR), Kay Nimmo (International Tin Research Institute, St. Albans), and Dr. Miloš René (Academy of Sciences of the Czech Republic, Prague).

High-quality polished sections from Don Henry and Peter Rendschmidt (both BGR) are very much acknowledged.

I really appreciate the good company of the following BGR staff during sampling campaigns in Central Africa: Dr. Rudolf Mauer, Dr. Philip Schütte, Prof. Dr. Bali Barume, Dr. Uwe Näher, Désirée Ruppen, Dr. Jürgen Vasters, Dr. Gudrun Franken and Einar Roßmann.

Dr. Dieter Huy (BGR) is kindly thanked for provision of global mine production data for tin and tungsten concentrates.

Special thanks go to my fellow Ph.D. students at BGR Anna, Malte and Flo who made the time really enjoyable and offered carefree discussions on very special issues at the round table. Cheers!

Last but most importantly, I also want to take the opportunity to thank my wife Sabine and our lovely daughters Laura & Lena for their patience, especially during the periods of writing. You make my life filled with love and joy!

Abstract

Illegal mining and trading of tantalum, tin, and tungsten ores (also known as 3T minerals) as well as gold fund ongoing violent conflicts in several African countries, especially in the eastern provinces (North Kivu, South Kivu, and Maniema) of the Democratic Republic of the Congo (DRC). On behalf of the German Federal Ministry for Economic Cooperation and Development (BMZ), the Federal Institute for Geosciences and Natural Resources (BGR) started the Analytical Fingerprint (AFP) project to verify the origin of columbite-tantalite ('Coltan') ore concentrates. In this study, the application of AFP to cassiterite and wolframite concentrates based on mineralogical and geochemical parameters using different analytical methods is tested. 1) The mineralogical composition and variability of ore concentrates is determined by an automated scanning electron microscope (SEM) technique with Mineral Liberation Analysis (MLA) software. 2) The major and trace element composition of single ore minerals in the concentrates are measured in a first attempt by electron probe microanalysis (EPMA) and finally by laser ablation inductively coupled plasma-mass spectrometry (LA-ICP-MS).

In the first part of this thesis, the important metal and mineral properties are highlighted. The economics of tin and tungsten are also assessed focussing on exploration/mining projects and the respective marked situation. The second part deals with the major analytical work, especially the method development for the LA-ICP-MS analysis of cassiterite and wolframite, and the treatment of the data. It was demonstrated that the mineralogical composition of ore concentrates and the trace element distribution in cassiterite and wolframite in particular are controlled by specific ore forming processes and the respective geological setting. Especially trace element data can be used to discriminate between different deposit types, metallogenic provinces, and even individual ore deposits on concession scale. The various parameters during ore formation are superimposed on each other and generate a characteristic, unique trace element signature, which is preserved within the ore minerals. Several case studies are presented to test if the application of trace element data serves as a proof of origin in terms of an 'Analytical Fingerprint'.

Keywords: cassiterite, wolframite, trace elements, LA-ICP-MS

Zusammenfassung

Der illegaler Bergbau und Handel mit Tantal-, Zinn- und Wolframerzen (auch bekannt als 3T-Minerales) und Gold finanzieren in einigen afrikanischen Staaten andauernde gewaltsame Konflikte, insbesondere in den Ostprovinzen (Nordkivu, Südkivu und Maniema) der Demokratischen Republik Kongo (DRC). Die Bundesanstalt für Geowissenschaften und Rohstoffe (BGR) hat im Auftrag des Deutschen Bundesministeriums für wirtschaftliche Zusammenarbeit und Entwicklung (BMZ) das Projekt Analytischer Herkunftsnachweis (AFP) initiiert, um die Herkunft von Columbit-Tantalit-Erzkonzentraten ('Coltan') zu verifizieren. In der vorliegenden Studie wird die Anwendbarkeit des AFP auf Kassiterit- und Wolframitkonzentrate anhand von mineralogischen und geochemischen Parametern, die mittels verschiedener Methoden ermittelt werden, getestet. 1) Die mineralogische Zusammensetzung der Erzkonzentrate und deren Variabilität werden durch automatisierte Rasterelektronenmikroskopie mit Mineral Liberation Analysis (MLA)-Software bestimmt. 2) Die Haupt- und Spurenelementzusammensetzung von Einzelkörnern in den Konzentraten wurden in einem ersten Ansatz mittels Elektronenstrahlmikrosonde (EPMA) und schließlich mittels Laserablation-induktiv gekoppeltes Plasma-Massenspektrometrie (LA-ICP-MS) gemessen.

Im ersten Teil der Arbeit werden die wichtigen Metall- und Mineraleigenschaften herausgearbeitet. Außerdem werden die wirtschaftlichen Aspekte der Metalle Zinn und Wolfram mit besonderem Fokus auf Explorations-/Bergbauprojekten und die jeweilige Marktsituation bewertet. Der zweite Teil behandelt die Hauptarbeit zur Analytik, insbesondere die Methodenentwicklung für die Analyse von Kassiterit und Wolframit mittels LA-ICP-MS, und die Datenauswertung. Es hat sich gezeigt, dass die mineralogische Zusammensetzung der Erzkonzentrate und insbesondere die Verteilung der Spurenelemente in Kassiterit und Wolframit durch spezifische erzbildende Prozesse und das jeweilige geologische Umfeld kontrolliert werden. Vor allem die Spurenelementdaten können genutzt werden um zwischen verschiedenen Lagerstättentypen, metallogenetischen Provinzen und sogar Einzellagerstätten auf Konzessionsebene zu unterscheiden. Die unterschiedlichen Parameter überlagern sich während der Erzbildung und generieren somit eine charakteristische, einzigartige Spurenelementsignatur, welche in den Erzmineralen erhalten wird. Einige Fallbeispiele werden angeführt, um zu zeigen, dass die Anwendung von Spurenelementdaten als ein Herkunftsnachweis im Sinne des AFP dienen kann.

Schlagwörter: Kassiterit, Wolframit, Spurenelemente, LA-ICP-MS

1 Introduction

1.1 Socio-economic background

Illegal mining and trading of tantalum, tin, and tungsten ores (also known as 3T minerals) as well as gold fund ongoing violent conflicts in several African countries, especially in the eastern provinces (North Kivu, South Kivu, and Maniema) of the Democratic Republic of the Congo (DRC). Various armed groups, for example the Forces démocratiques de libération du Rwanda (FDLR), the Congolese army Forces Armées de la République Démocratique du Congo (FARDC), Congrès national pour la défense du peuple (CNDP) and various Mayi Mayi militia, compete for access and control of the mines and use the revenue from mineral trade and illegal taxation to finance their troops (Melcher et al., 2008; Melcher et al., 2010). Several Non-Governmental Organisations (e.g., Enough Project, FinnWatch, Global Witness, International Alert, Pole Institute etc.) were dealing with the subject of exploitation and trade of minerals from conflict regions and published a lot of reports on this topic. The mines are almost exclusively operated by artisanal and small-scale miners.

The minerals are then transported from the mine to mineral traders and exporters (also known as ‘comptoirs’) located for example in the provincial capitals, like Bukavu (South Kivu) or Goma (North Kivu). These pre-concentrates are sorted and upgraded in the ‘comptoirs’. The ore concentrates are then either legally exported or smuggled to the neighbouring countries Uganda, Rwanda, and Burundi to avoid taxation. Finally, the mineral concentrates reach the major seaports Mombasa in Kenya or Dar-es-Salaam in Tanzania and are shipped to smelters all over the world (especially in Southeast Asia) for refining into metal (Figure 1.1).

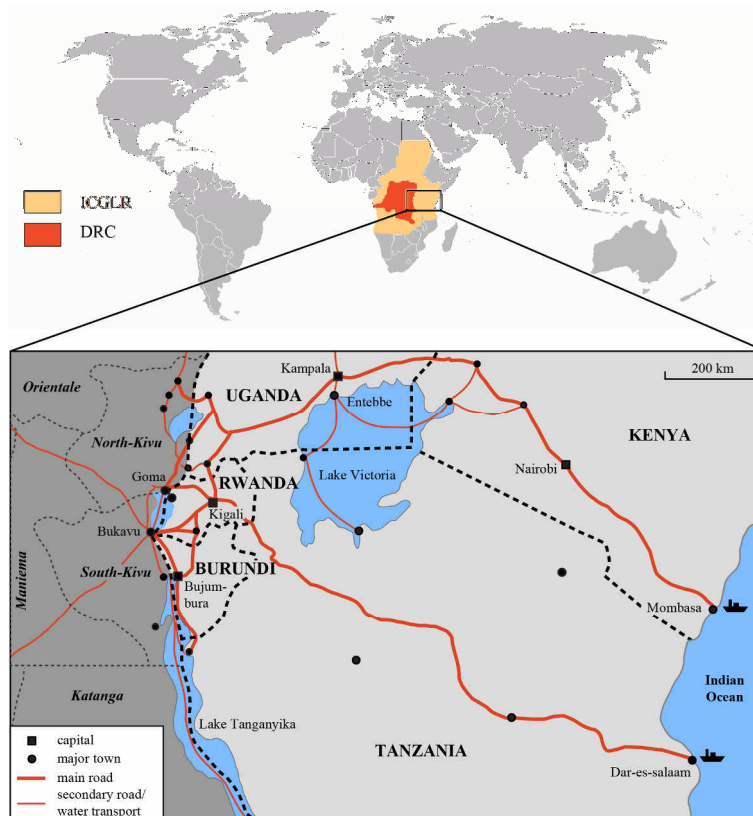


Figure 1.1: Trading routes of ore concentrates from the eastern provinces of the Democratic Republic of Congo through eastern Africa to the major ports of Mombasa and Dar-es-Salaam (International Alert, 2010).

The smelting companies represent the bottleneck in the supply chain because at this point ore concentrates of different origin come together and are mixed for smelting. Finally, the refined metals are further processed into intermediate compounds for their final use in the electronics industry, for example in laptops, mobile phones, home entertainment devices, etc.

The situation became even more complicated for the small-scale miners in Central Africa since the Dodd-Frank Wall Street Reform and Consumer Protection Act of the United States Securities and Exchange Commission (SEC) was implemented. The Dodd-Frank Act (Section 1502: Conflict minerals) insists from US-listed companies to exercise due diligence on the traceability of conflict minerals (cassiterite, columbite-tantalite, gold, wolframite) or their derivatives originating from the Democratic Republic of Congo or neighbouring countries (SEC, 2010). This led to a 'de facto' embargo of cassiterite, columbite-tantalite, gold, and wolframite from Central Africa. On the one hand the Dodd-Frank Act will reduce income from mineral trade for armed groups, but on the other hand this will also have great impact on 'regular' artisanal miners whose livelihood is strongly dependent on mining of these minerals.

The panel of experts of the United Nations Security Council for the DRC recommended the development of a traceability system to proof the origin of mineral commodities from Central Africa. On behalf of the German Federal Ministry for Economic Cooperation and Development (BMZ), the Federal Institute for Geosciences and Natural Resources (BGR) started two pilot projects on the traceability of mineral concentrates (Melcher et al., 2010). The first project was a feasibility study to verify the origin of columbite-tantalite ('Coltan') ores, the so-called Analytical Fingerprint (AFP). The second project developed a mineral certification scheme to implement traceability, transparency, and social, ethical and ecological standards for mineral production and trade in the concept of the Certified Trading Chains (CTC) in the Great Lakes Region. The AFP method is placed as an optional analytical proof of origin within the framework of CTC (Melcher et al., 2010), but AFP may also be used for positive certification of ore shipments from known mining sites (Melcher et al., 2009). It has to be taken into account that the individual fingerprint of the ore concentrate is deleted after refining into metal and proof of origin by AFP is no longer possible from this point.

Hoefs (2010) defined a geochemical fingerprint as "a chemical signal that provides information about the origin, the formation and/or the environment of a geological sample, which does not alter with growth or age". Several applications and methods of fingerprinting are for example summarised by Kamber (2009) and Hoefs (2010). The AFP project developed a proof of origin for 'Coltan' ore concentrates based on mineralogical and geochemical parameters using different analytical methods. The origin of an unknown mineral concentrate is identified by comparing its mineralogical and geochemical characteristic features with samples of known provenance stored in a database (Melcher et al., 2010; Gäbler et al., 2011). A three-stage approach is proposed to measure the following critical parameters: 1) mineralogical composition and variability of ore concentrates measured by an automated scanning electron microscope (SEM) technique with Mineral Liberation Analysis (MLA) software, 2) major and trace element composition of single ore minerals in the concentrates by LA-ICP-MS, and 3) radiometric U-Pb model ages of the ore minerals are also determined by LA-ICP-MS (Melcher et al., 2009; Gäbler et al., 2011). In a first approach, samples from known localities were investigated using a variety of methods.

During the feasibility study on 'Coltan' concentrates, it was recommended to work on the AFP for tin and tungsten ore concentrates, which now forms the starting point of the following study. The extension of 'Coltan' certification scheme by an AFP for

tin and tungsten ores allows control of a significant portion of the minerals exported from the Great Lakes region (Melcher et al., 2010). Traceability and due diligence along the supply chain also supports market access of mineral exports from the Great Lakes region to the world market.

1.2 Economic relevance

Another significant aspect of tin and tungsten is that both metals are regarded as critical metals (Figure 1.2) by the Federal Institute for Geosciences and Natural Resources (BGR, 2010), the British Geological Survey (BGS, 2011), the Institute for Future Studies and Technology Assessment and Adelphi (Erdmann et al., 2011); of these two metals only tungsten is categorised as critical by the European Commission (2010). The various studies used different factors to determine the ranking of a particular commodity, for example supply and demand situation, political and economic stability of the producing countries (Herfindahl-Hirschmann-Index), level of company or country concentration, reserves and resources, technological applications for the future, and possible substitutions.

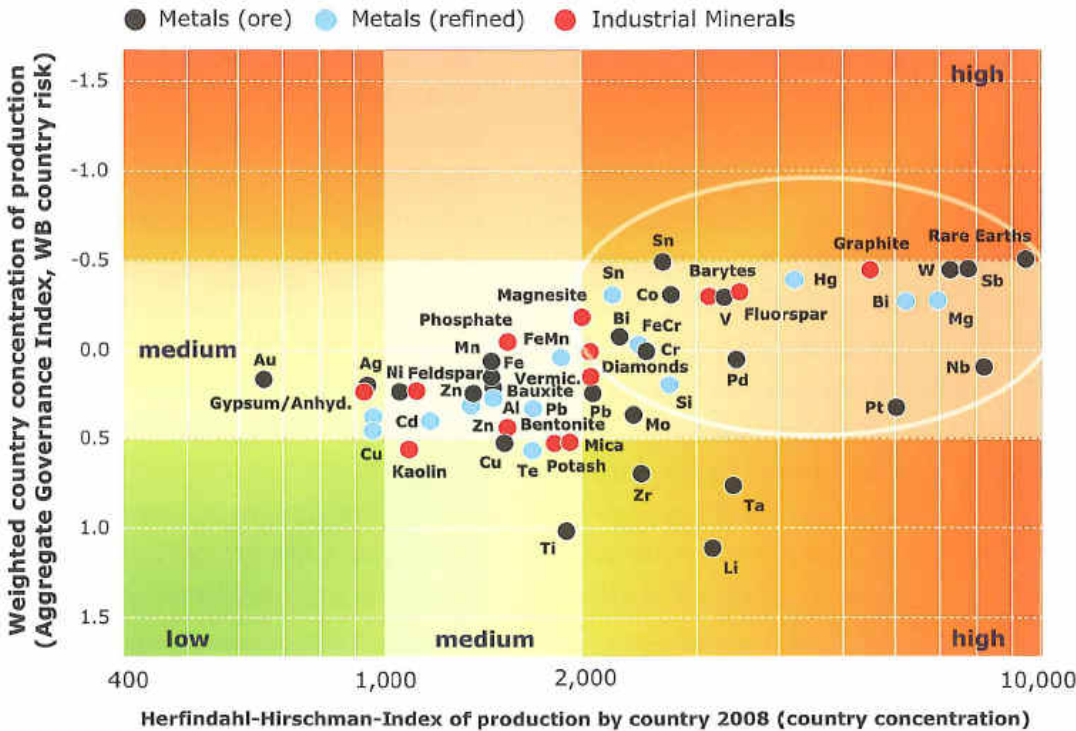


Figure 1.2: Criticality of different commodities based on the Herfindahl-Hirschman-Index and the country risk rating of the Aggregate Governance Index of the World Bank (BGR, 2010).

2 Short synopses on the history of tin and tungsten

2.1 History of tin

Tin is one of the oldest known metals and was used in ancient times as Cu-Sn alloy, also known as bronze. The oldest finds of bronze objects date back to approximately 3500 BC and were discovered in Turkey, Mesopotamia and Egypt (Ahlfeld, 1958). This was beginning of the Bronze Age which lasted until approximately 1000 BC. For example the famous Nebra Sky Disc (Figure 2.1) was manufactured between 2100 to 1700 BC and its bronze plate is made of copper alloy containing 2.6% Sn (Schmiderer, 2008). In the beginning, copper and tin were smelted together accidentally because these two elements are found together in some ore deposits. The ancient smelters discovered that the combination of the two metals was harder and easier to cast than copper on its own. These properties led to the replacement of copper by bronze for the manufacturing of tools and weapons.



Figure 2.1: The Nebra Sky Disc and associated bronze finds (Copyright: State Office for Heritage Management and Archeology Saxony-Anhalt, Germany; photograph taken by J. Lipták)

However, tin deposits were rarer than copper deposits in that time and new sources for tin had to be discovered. Earliest tin mining appeared about 2500 BC in the Erzgebirge area, spread out to Brittany in France, southwest England and the Iberian Peninsula around 2000 BC (Penhallurick, 1986). The Greeks imported tin from the 'Casseterides' (Tin Islands) which are possibly referred to as the British Isles (Ahlfeld, 1958) and the copper derived from Cyprus. At this time tin was referred to as a form of lead. For example, the Romans distinguished between 'plumbum nigrum' (black lead) for lead and

'plumbum album' or 'plumbum candidum' (white lead) for tin (Ahlfeld, 1958). The element tin is named after the Etruscan god called 'Tinia' (Heiserman, 1992) and the chemical symbol Sn derives from the Latin word 'stannum'.

Tin alloys such as bronze were produced earlier than the pure metal. Elemental tin was possibly produced in China by reduction with coal in 1800 BC. In the 17th century metallic tin was used in plates, cups and dining utensils, but generally unalloyed tin is too soft for such applications (Heiserman, 1992). Therefore the most common application for tin was in the coating of plate steel to prevent corrosion.

2.2 History of tungsten

In medieval times, miners in the Saxon-Bohemian Erzgebirge discovered that a certain mineral (the now-known wolframite) associated with cassiterite ores reduced the tin recovery during the smelting process and disturbed the reduction of the cassiterite (Ahlfeld, 1958). The similar densities of wolframite and cassiterite led to considerable complications during the separation and concentration of the ore minerals. The tungsten remained in the slag resulting in a dense phase forming at the bottom of the melting furnace which is difficult to separate from the tin melt during tapping (Lassner & Schubert, 2009). Tin probably remained within the slag as metallic droplets which caused a deficit in the tin yield. During the smelting process appeared foam on the surface of the liquid tin and in this foam much of the valuable tin could stay as droplets (Lassner & Schubert, 2009). These observations led to the description that the unknown mineral "devours the tin like the wolf the sheep" and it was called "Spuma Lupi" by Georgius Agricola in 1546. In 1757, the name for the mineral was modified by Johan Gottschalk Wallerius to "wolfram" which means "wolf's froth" or "wolf's spittle" (King, 2005).

Axel Fredrik Cronstedt mentioned in 1758 a heavy mineral which he called "tung sten" for the Swedish words for "heavy stone" (Ahlfeld, 1958). In the year 1781 Carl Wilhelm Scheele, a German-Swedish chemist and pharmacist, investigated "tung sten" and showed that the mineral contains lime and an unknown component which he called tungstic acid (Lassner & Schubert, 2009). Tobern Olof Bergman, a Swedish chemist and mineralogist at the University of Uppsala, proposed that a new metal can be obtained by reduction of the formerly discovered tungstic acid with charcoal. The calcium tungstate mineral "tung sten" was later named scheelite by the German mineralogist Karl Cäsar von Leonhard in 1821 (Lassner & Schubert, 2009). In the year 1779, the Irish chemist

Peter Woulfe examined that the now-known mineral wolframite forms a yellow dye when treated with hydrochloric acid and concluded that it must contain an undiscovered element; today is known that tungstic acid was formed (Lassner & Schubert, 2009).

The Spanish chemists Juan José Elhúyar, a student of Bergman from 1781 to 1782, and his brother Fausto Elhúyar showed that the mineral wolframite contained iron, manganese and the same tungstic acid (Andrews, 1955; Ahlfeld, 1958). In the year 1783 they discovered the metallic element tungsten by reducing the tungstic acid with charcoal as Bergman recommended. This mineral was given the name “Wolframit” by Friedrich August Breithaupt in the year 1820 (Andrews, 1955; Ahlfeld, 1958; Lassner & Schubert, 2009).

However, another theory for the discovery of the element tungsten has recently been established, which was provoked by the finding of the so-called “Trewiddle Ingot” in 2003 near St. Austell in Cornwall in southwest England (Rehren, 2005). The Natural History Museum discovered that the 19 kg heavy object consists of a large amount of elemental tungsten. This led to speculations that elemental tungsten was produced prior to the discovery of the Elhúyar brothers. However, it is unclear if the object represents a purposeful attempt to produce a tungsten ingot by an unknown process or just dumped waste of tungsten material which accumulated in the tin slag during repeated smelting and processing (King, 2005; Rehren, 2005).

3 Metal and mineral properties

Tin and tungsten are classified as heavy metals, because both elements have a higher atomic number than iron (${}_{26}\text{Fe}$). The nucleosynthesis of elements and isotopes heavier than Fe occurs basically by various neutron capture processes during supernovae (e.g., de Laeter & Jeffery, 1967). Siderophile elements like tungsten likely migrated into the interior of the earth during early core formation, but these elements are surprisingly overabundant in today's Earth's mantle and crust (Willbold et al., 2011). This 'surplus' of siderophile elements was recently interpreted by Willbold et al. (2011) to be the result of influx by meteorites after consolidation of the earth about 3.8 billion years ago. Although tin and tungsten are not situated close to each other in the periodic table, they are often closely associated in nature especially in mineral deposits.

3.1 Tin

Tin (Sn) has the atomic number of 50 with a relative atomic mass of 118.71 (Lide, 2009) and is situated in the fourteenth group of the fifth period in the periodic table. It has the electron configuration of $[\text{Kr}]4d^{10}5s^25p^2$. Tin is a malleable, silvery white metal with a bluish tint. Ten stable isotopes of tin are known; this makes tin the element with the highest number of stable isotopes. The atomic masses and relative abundances of the stable isotopes are: ${}^{112}\text{Sn}$ with 0.97%, ${}^{114}\text{Sn}$ with 0.66%, ${}^{115}\text{Sn}$ with 0.34%, ${}^{116}\text{Sn}$ with 14.35%, ${}^{117}\text{Sn}$ with 7.68%, ${}^{118}\text{Sn}$ with 24.23%, ${}^{119}\text{Sn}$ with 8.59%, ${}^{120}\text{Sn}$ with 32.59%, ${}^{122}\text{Sn}$ with 4.63% and ${}^{124}\text{Sn}$ with 5.79% (Rosman et al., 1984; Lee & Halliday, 1995; Clayton et al., 2002; Lide, 2009).

Tin is a geochemically incompatible element and is enriched during magmatic differentiation. The average Sn contents increase from ultramafic (0.3 ppm), mafic (0.9 ppm), intermediate (1.5 ppm) to felsic (3.5 ppm) rocks (data compiled from different authors by Hamaguchi et al., 1964 and Hamaguchi & Kuroda, 1969 with references therein). This underlines that the geochemical behaviour of tin is predominantly lithophile with the highest concentrations in felsic rocks. The average upper continental crust and the bulk continental crust are estimated to contain 2.1 ppm and 1.7 ppm, respectively (Rudnick & Gao, 2004).

Important properties of tin metal are its low hardness of 1.5 on the Mohs scale ($\text{VHN}_{10} = 7$ to 9 kg/mm^2 on Vickers scale; Criddle & Stanley, 1993), low melting point at $231.93 \text{ }^\circ\text{C}$ and a contrasting high boiling point at $2602 \text{ }^\circ\text{C}$ (Lide, 2009). It also

spontaneously forms an oxidised, non-reactive coating on the surface which inhibits further oxidation. This behaviour in the context of corrosion is called passivation.

Elemental tin occurs in three allotropic forms. The common form is β -tin or so-called white tin which is stable in the temperature range from 13.2 °C and 162 °C with a relatively high density of 7.29 g/cm³ (Lide, 2009). The β -tin has a tetragonal body centred crystal system with the crystal class 4/mmm (Lide, 2009). The structure type is a distorted diamond structure with tetrahedrally coordinated tin atoms. The lattice constants are $a=5.83 \text{ \AA}$ and $c=3.18 \text{ \AA}$ (Strunz & Nickel, 2001; Anthony et al., 2001). It is opaque with metallic lustre. A special phenomenon of white tin is that it shows a characteristic sound when the metal is deformed by bending which is called the 'cry of tin'. This audible cracking is caused by the movement of the single crystals along the grain boundaries and the plastic deformation causes twinning. Below a temperature of 13.2 °C the β -tin transforms into α -tin which is also known as grey tin. This phenomenon was described as the 'tin pest' or 'tin disease', because this phase transition is accompanied by an expansion of the volume of about 27 percent and causes disaggregation of tin-containing items. Grey tin has a cubic diamond-type crystal system and a density of 5.77 g/cm³ (Lide, 2009), which is considerably lower than the density of β -tin. At temperatures above 162 °C, the β -tin transforms into γ -tin or brittle tin which has a density of 6.54 g/cm³ and the crystal lattice changes into orthorhombic (Lide, 2009). The commercial grades of tin (99.85%) resist transformation because of the inhibiting effect of minor impurities (e.g. Sb, Bi, Ag; Lide, 2009).

3.2 Tin minerals

The important valences of tin in natural compounds are Sn²⁺ (stannous) and Sn⁴⁺ (stannic) with ionic radii in sixfold coordination of 0.93 Å and 0.69 Å, respectively (Shannon, 1976; Taylor, 1979), but is extremely rare in its native form (Anthony et al., 2001; Dekov et al., 2009). Native tin is only reported from some unique placers (Krivitskaya et al., 1995), associated with pitchblende at Nesbitt LaBine uranium mine (Silman, 1954), in seafloor spreading zones (Dekov et al., 1996), in the black shale-hosted Sukhoi Log gold deposit (Distler et al., 2004), and from supergene alteration zones of epithermal gold veins near Pukanec, Slovakia (Schmiderer, 2008). Although a large number of different Sn-bearing minerals are known (Table 3.1), cassiterite (SnO₂) is by far the most important tin ore.

Table 3.1: Compilation of Sn-bearing minerals

Name	Chemical Formula	Crystal system	Sn in wt. %
Abramivite	Pb ₂ SnInBiS ₇	triclinic	12.1
Atokite	(Pd,Pt) ₃ Sn	cubic	23.5
Berndtite	SnS ₂	trigonal	64.9
Burtite	CaSn(OH) ₆	cubic	45.5
Cabriite	Pd ₂ SnCu	orthorhombic	30.0
Canfieldite	Ag ₈ SnS ₆	orthorhombic	10.1
Cernyite	Cu ₂ CdSnS ₄	tetragonal	24.4
Chatkalite	Cu ₆ Fe ²⁺ Sn ₂ S ₈	tetragonal	25.5
Cylindrite	Pb ₃ Sn ₄ FeSb ₂ S ₁₄	triclinic	25.7
Foordite	Sn ²⁺ (Nb,Ta) ₂ O ₆	monoclinic	26.7
Franckeite	(Pb,Sn ²⁺) ₆ Sn ⁴⁺² Fe ²⁺ Sb ₂ S ₁₄	triclinic	13.7
Hemusite	Cu ₆ SnMoS ₈	cubic	13.9
Herzenbergite	SnS	orthorhombic	78.7
Ixiolite	(Ta,Nb,Sn,Fe,Mn) ₄ O ₈	orthorhombic	variable
K�esterite	Cu ₂ (Zn,Fe)SnS ₄	tetragonal	32.7
Kiddcreekite	Cu ₆ SnWS ₈	cubic	12.6
Malayaite	CaSnSiO ₅	monoclinic	44.5
Mawsonite	Cu ₆ ¹⁺ Fe ₂ ³⁺ Sn ⁴⁺ S ₈	tetragonal	13.7
Mohite	Cu ₂ SnS ₃	monoclinic	34.7
Niggliite	PtSn	hexagonal	37.8
Ottemannite	Sn ₂ S ₃	orthorhombic	71.2
Paolovite	Pd ₂ Sn	orthorhombic	35.8
Pirquitasite	Ag ₂ ZnSnS ₄	tetragonal	22.5
Romarchite	SnO	tetragonal	88.1
Rustenburgite	(Pt,Pd) ₃ Sn	cubic	18.6
Suredaite	PbSnS ₃	orthorhombic	30.4
Teallite	PbSnS ₂	orthorhombic	30.4
Thoreaulite	Sn ²⁺ Ta ₂ O ₆	monoclinic	20.6
Toyohaite	Ag ₂ FeSn ₃ S ₈	tetragonal	40.3
Varlamoffite	(Sn,Fe)(O,OH) ₂	tetragonal	65.7
Wodginite	(Fe,Mn)(Sn,Ti)(Nb,Ta) ₂ O ₈	monoclinic	variable

However, Sn-bearing sulphosalts such as stannite (Cu₂FeSnS₄) and teallite (PbSnS₂) occur in some sulphide-rich hydrothermal deposits in economically important enrichments (for example in Bolivia). Various tin alloys with platinum group elements are known (Daltry & Wilson, 1997; Cabri, 2002), for example from the Bushveld Complex, South Africa (Melcher & Lodziak, 2007) and Noril'sk, Russia (Barkov et al., 2000). Tin also forms silicates such as malayaite (CaSnSiO₅) and is also incorporated in some rock-forming minerals such as titanite (sphene), ilmenite, epidote, magnetite,

rutile, monazite, xenotime, apatite, garnet (andradite in particular), biotite, muscovite, and hornblende. The incorporation of Sn occurs by substitution of Ti^{4+} or Fe^{3+} under conditions of high oxygen fugacity (Lehmann, 1982). For example, Layne & Spooner (1991) report high Sn concentrations in epidote (up to 1.56 wt.% SnO_2), andradite (up to 0.79 wt.% SnO_2), and amphibole (up to 0.61 wt.% SnO_2) from the JC tin skarn in the Yukon Territory, Canada. Extremely high Sn concentrations in garnet are reported from Namibia (McIver & Mihálik, 1975) and the Lost River skarn deposit in Alaska (Dobson, 1982) with up to 5.8 wt.% SnO_2 and 5.9 wt.% SnO_2 , respectively. Wang et al. (2013) measured Sn in biotite (100 to 200 ppm SnO_2 , on average 125 ppm SnO_2) and late-magmatic titanite (8 to 26 wt.% SnO_2 , on average 14.8 wt.% SnO_2) from the Qitianling granite in the Nanling Range, China.

3.2.1 Cassiterite

Cassiterite is tin oxide with the chemical formula $Sn^{[6]}O_2$ (coordination number in square brackets). Pure cassiterite has a melting point of about 1625 °C (Paparoni et al., 2010). It crystallises in the tetragonal crystal system. Cassiterite occurs commonly as prisms with {110} and {010} or bipyramids with {111} and {011} (Klein & Hurlbut, 1993). Cassiterite is often twinned along (011) which results in elbow-shaped crystals with a characteristic notch (Klein & Hurlbut, 1993). This habit of cassiterite was called 'Visiergrauen' by miners in the Saxonian-Bohemian Erzgebirge (Figure 3.1). Ahlfeld (1958) stated that the various crystal habits of cassiterite represent different mineralisation stages and therefore different conditions of formation, especially temperature. Generally, bipyramidal crystals occur in pegmatites, short prismatic pyramids with twinning present in greisen deposits and hydrothermal veins, and finally long prismatic along {321} so-called 'needle tin' is found in low temperature, epithermal stages (Ahlfeld, 1958; Ramdohr, 1975; Taylor, 1979; Swinden, 1983). A special variety of tin oxide is so-called 'wood tin'. The term is used for botryoidally, concentrically layered and radiating structures of fine-grained cassiterite (Lufkin, 1977; Hosking et al., 1987). The colour of wood tin is very variable depending on the Fe^{3+} content (Lufkin, 1977). Wood tin is formed at late-stage, low-temperature conditions often in association with rhyolitic volcanic rocks, for example in Mexico, Russia, Cornwall and Bolivia.

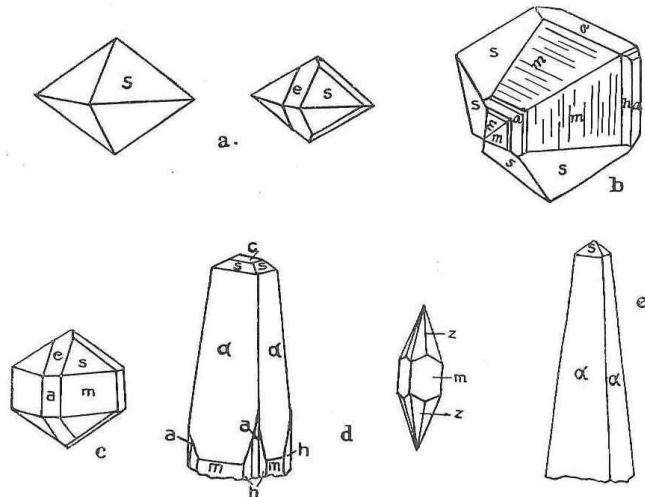


Figure 3.1: Various crystal habit of cassiterite (Ahlfeld, 1958): a) pegmatitic type, b) greisen type, twinned (Saxony), c) greisen type, d) hydrothermal vein type (Cornwall), e) epithermal type (needle tin)

Cassiterite has a high hardness of 6 to 7 on the Mohs scale (VHN₂₀₀ = 1239 to 1467 kg/mm² on Vickers scale; Criddle & Stanley, 1993) and a high density of 6.8 to 7.1 g/cm³ (Klein & Hurlbut, 1993). Its cleavage is imperfect along the {010} plane (Klein & Hurlbut, 1993) and the fracture is brittle with conchoidal shape. The colour of cassiterite varies from colourless, yellowish and reddish brown to brownish black with a yellow to mostly colourless streak. The lustre is greasy on fracture planes and adamantine on crystal planes. Diaphaneity commonly ranges from opaque to translucent and rarely transparent (Figure 3.2).



Figure 3.2: Euhedral cassiterite crystal from the El Karit hydrothermal vein deposit, Morocco with coin (1 €) for scale. Specimen is taken from the BGR mineral collection.

The structure is the rutile type in a room-centred tetragonal elemental cell with cell dimensions of $a=4.738 \text{ \AA}$ and $c=3.188 \text{ \AA}$ (Lide, 2009; Bolzan et al., 1997; Strunz & Nickel, 2001; Anthony et al., 2001). Tin atoms are located at the corners and in the centre of the tetragonal unit cell. Single tin atoms are surrounded by six oxygen atoms in octahedral coordination and each oxygen atom is surrounded by three tin atoms (Figure 3.3). Cassiterite has an ideal tin content of 78.78 wt.% Sn and an oxygen content of 21.22 wt.% O.

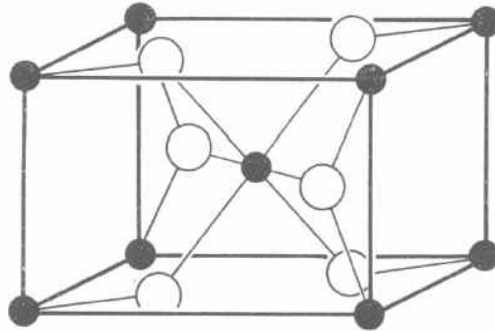


Figure 3.3: Rutile-type crystal structure of cassiterite. Open circles represent sites of oxygen and filled circles are sites of tin (Kleber, 1998).

Cassiterite displays low reflectivity with 10.6 to 12.0% in air and 1.72 to 2.39% in oil at a wavelength of 589 nm in incident light (Criddle & Stanley, 1993). The reflection colour is medium grey and bireflectance is visible in twinned grains; twinning is common (Figure 3.4). With crossed polars in incident light, cassiterite shows strong anisotropy masked by yellowish brown internal reflections (Figure 3.4). In transmitted light, cassiterite may show pleochroism and colour zoning.

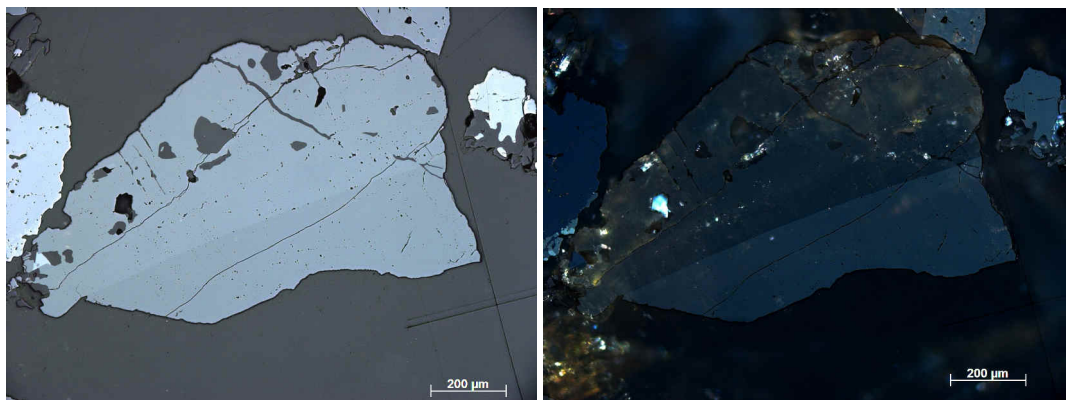


Figure 3.4: Micrograph of cassiterite (medium grey) and columbite-tantalite (light grey) embedded in epoxy resin (dark grey) from the Shori Sn-Ta-bearing pegmatite, Rwanda. Note simple twinning of the cassiterite grain. Cassiterite is characterised by grey colour, low reflectance but distinct bireflectance in plane polarised reflected light (left figure). In crossed polarised reflected light (right figure), cassiterite is anisotropic and shows many characteristic yellow-brown internal reflections.

3.3 Tungsten

Tungsten (W) is a transition metal and has the atomic number of 74 with a relative atomic mass of 183.84 (Lide, 2009). The element tungsten is found in the sixth group of the sixth period in the periodic table. The colour of pure tungsten metal is lustrous white to steel grey. The economic importance of tungsten derives from its extraordinary properties which are its high density of 19.25 g/cm^3 , high hardness of 7.5 on the Mohs scale and low coefficient of thermal expansion. Tungsten also shows good thermal and electrical conductivity. Additionally, tungsten holds the highest melting point at $3422 \text{ }^\circ\text{C}$ (second of all elements after carbon which sublimates at $3642 \text{ }^\circ\text{C}$), the highest tensile strength at temperatures over $1650 \text{ }^\circ\text{C}$ and the lowest vapour pressure of all metals (Lide, 2009). Its boiling point of $5555 \text{ }^\circ\text{C}$ is the second highest of all elements (only surpassed by rhenium with $5596 \text{ }^\circ\text{C}$); this is close to the temperature on the sun's surface (Lide, 2009). Elemental tungsten shows superconductivity at extremely low temperatures. Tungsten is not attacked by air, water or non-oxidising acids. Oxidising acids form an oxide layer on the surface which results in passivation. Tungsten is only attacked by mixtures of fluoric acid and saltpetre acid.

Tungsten has the electron configuration of $[\text{Xe}]4f^{14}5d^46s^2$. Its crystal system is body-centred cubic with a lattice constant of 3.16 \AA and octahedral coordination of the tungsten atoms (Strunz & Nickel, 2001; Mills et al., 2011). Naturally occurring tungsten consists of five isotopes whose half-lives are so long that they can be considered stable. The atomic masses of the isotopes are ^{180}W , ^{182}W , ^{183}W , ^{184}W , and ^{186}W with the relative abundances 0.12%, 26.50%, 14.31%, 30.64%, and 28.43%, respectively (Völkening et al., 1991; Lee & Halliday, 1995; Lide, 2009). However, altogether 33 tungsten isotopes are known (Völkening et al., 1991; Lee & Halliday, 1995).

Tungsten occurs in nature predominantly in the hexavalent state, but the oxidation states may range from 0 to +6. The ionic radii are 0.66 \AA for W^{4+} , 0.62 \AA for W^{5+} , 0.60 \AA for W^{6+} in octahedral coordination, and 0.42 \AA for W^{6+} in tetrahedral coordination (Shannon, 1976). Tungsten minerals occur mainly as tungstates like scheelite and wolframite; sulphides like tungstenite (WS_2) are scarce. The geochemical behaviour of the element tungsten depends on the oxidation state. Metallic tungsten shows siderophile behaviour at reducing conditions and the oxidised hexavalent ion is lithophile in character (Lassner & Schubert, 1999; Arevalo Jr. & McDonough, 2008). Tungsten is enriched during magmatic differentiation and fractionation, because hexavalent tungsten is strongly incompatible and W^{6+} is not incorporated into early

rock-forming minerals. The W contents in igneous rocks range from 0.1 to 0.8 ppm for ultramafic, from 0.5 to 1.2 ppm for mafic, from 1.1 to 2.7 ppm for intermediate, from 1.3 to 3.7 ppm for felsic rocks, and are approximately 1.3 ppm in alkali-rich rocks (Wiendl, 1968; Krauskopf, 1970; Barabanov, 1971; Triller, 1987 and references therein). The average upper continental crust and the bulk continental crust are estimated to contain 1.9 ppm W and 1.0 ppm W, respectively (Rudnick & Gao, 2004). Interestingly, elevated W concentrations are also found in manganese nodules and crusts (38-173 ppm W) from the Pacific seafloor (Kunzendorf & Glasby, 1992; Hein et al., 2013).

3.4 Tungsten minerals

Tungsten occurs extremely rare in its elemental form and was recently approved as a new mineral (Mills et al., 2011) by the International Mineralogical Association (IMA). Native tungsten is reported only from alluvial deposits of the Bol'shaya Pol'ya river in the Ural region (Novgorodova et al., 1995) and from the black shale-hosted Sukhoi Log gold deposit, Russia (Distler et al., 2004). The economically important ore minerals are scheelite (CaWO_4) and the minerals of the isomorphous wolframite solid solution series $(\text{Fe,Mn})\text{WO}_4$ with the iron-rich endmember ferberite (FeWO_4) and the manganese-rich counterpart hübnerite (MnWO_4). These minerals are generally described as ABO_4 compounds with divalent ions (Fe^{2+} , Mn^{2+} , Ca^{2+}) on the A site and hexavalent ions (W^{6+} , plus potentially Mo^{6+}) on the B site. The structure of ABO_4 compounds is crucially controlled by the ionic radius of the A^{2+} cation. Tungstates with the general formula AWO_4 crystallise in the scheelite structure if the radius of the cation on the A site is greater than 0.9 Å; whereas the wolframite structure occurs if the radius of the A^{2+} cation is less than 0.9 Å (Hazen et al., 1985; Macavei & Schulz, 1993). The transition from scheelite to wolframite structure can be stimulated by high pressures of about 1.2 GPa for CaWO_4 (Kuzmin & Purans, 2001).

The scheelite structure is regarded as a cubic close-packed array of A^{2+} cations and $[\text{BO}_4]^{2-}$ groups, whereas the wolframite structure is made up of hexagonally close-packed oxygens with certain octahedral sites filled by A and B cations (Cid-Dresdner & Escobar, 1968; Sleight, 1972; Kuzmin & Purans, 2001). Generally, large cations like Sr^{2+} , Pb^{2+} and Ba^{2+} are incorporated in the scheelite-type structure, whereas small cations such as Mg^{2+} , Zn^{2+} , and Ni^{2+} are found in the wolframite-type structure (Ghaderi et al, 1999; Kuzmin & Purans, 2001). Tungsten minerals show frequent substitution of W by Mo, because of their nearly identical radii of their hexavalent ions. This results in several

isomorphic series such as scheelite - powellite (CaMoO_4), stolzite (PbWO_4) - wulfenite (PbMoO_4) and tungstenite (WS_2) - molybdenite (MoS_2) (Hsu, 1981; Pavlu, 1986; Secco et al., 2008).

In the group of tungsten sulphides such as tungstenite the tungsten ion is tetravalent. Hydrated tungsten oxides (e.g. anthoinite, tungstite etc.) are characteristic weathering products of scheelite and wolframite or products of hydrothermal alteration (Sahama, 1981). Tungsten also occurs as trace element in some rock-forming minerals, especially in micas, rutile, ilmenite, titanite (sphene), and magnetite. Other W-bearing minerals are summarised in the following table (Table 3.2).

Table 3.2: Compilation of W-bearing minerals

Name	Chemical Formula	Crystal system	W content in wt.%
Anthoinite	$\text{AlWO}_3(\text{OH})$	triclinic	59.3
Cuprotungstite	$\text{Cu}_3^{2+}(\text{WO}_4)_2(\text{OH})_2$	tetragonal	51.0
Huanzalaite	MgWO_4	monoclinic	67.6
Hydrotungstite	$\text{WO}_3 \cdot 2\text{H}_2\text{O}$	monoclinic	68.6
Kiddcreekite	Cu_6SnWS_8	cubic	19.6
Krasnoselskite	CoWO_4	monoclinic	59.9
Mpororoite	$\text{Al}(\text{WO}_3)(\text{OH})_3 \cdot 2(\text{H}_2\text{O})$	monoclinic	53.2
Raspite	PbWO_4	monoclinic	40.4
Russelite	Bi_2WO_6	orthorhombic	26.4
Sanmartinite	$(\text{Zn},\text{Fe}^{2+})\text{WO}_4$	monoclinic	59.1
Stolzite	PbWO_4	tetragonal	40.4
Tungstenite	WS_2	hexagonal	74.1
Tungstibite	$\text{Sb}^{3+}_2\text{WO}_6$	orthorhombic	35.1
Tungstite	$\text{WO}_3 \cdot 2\text{H}_2\text{O}$	orthorhombic	73.6
Yttrotungstite	$\text{YW}_2\text{O}_6(\text{OH})_3$	monoclinic	56.8

3.4.1 Wolframite group

Wolframite group minerals are characterised by the general chemical formula $(\text{Fe},\text{Mn})^{[6]}\text{W}^{[6]}\text{O}_4$ (coordination number in square brackets; Kuzmin & Purans, 2001). The wolframite group represents a solid solution series with isomorphous substitution of Fe^{2+} and Mn^{2+} on the A site. The Fe-rich endmember is called ferberite and the Mn-rich endmember is named hübnerite. By definition, minerals with a chemical composition between 20 mol.% and 80 mol.% of either endmember component are termed wolframite. The Zn-bearing mineral sanmartinite $(\text{Zn},\text{Fe}^{2+})\text{WO}_4$ (Angelelli & Gordon, 1948) and the rare Mg-rich member Huanzalaite MgWO_4 (Miyawaki et al., 2010) also belong to the wolframite group. Complete miscibility down to 414°C exists between

ZnWO₄ and the endmembers ferberite and hübnerite, respectively (Hochleitner & Schröcke, 1985). Wolframite group minerals have a monoclinic crystal lattice with the crystal class 2/m. The oxygen ions form a distorted hexagonal close packing of spheres in the wolframite structure and W- and Fe-octahedra form zigzag chains in the direction of the c-axis with each chain containing just one type of cation (Cid-Dresdner & Escobar, 1968; Kleber, 1998; Figure 3.5).

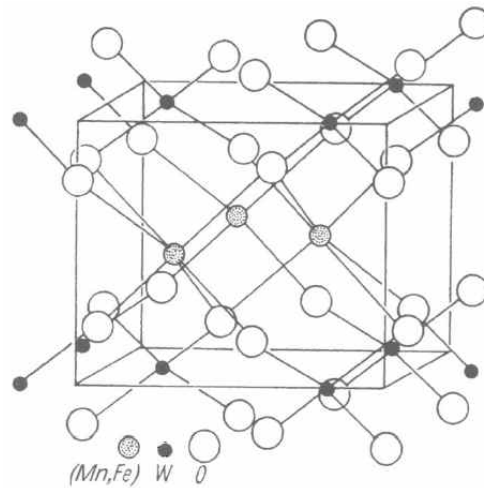


Figure 3.5: Crystal structure of wolframite. Open circles represent sites of oxygen, black-filled circles are sites of tungsten and grey-filled circles are sites of iron or manganese (Kleber, 1998).

Wolframite commonly crystallises as thick tables with {100} or as short prisms with {110} (Figure 3.6). Crystal faces are frequently striated parallel to the c-axis (Klein & Hurlbut, 1993). Individual crystals are often twinned along (100) and cleavage is perfectly parallel to (010) plane and indistinct along (100) (Figure 3.6; Ramdohr, 1975). Wolframite group minerals exhibit hardness similar to scheelite ranging from 4 to 4.5 on the Mohs scale (VHN₁₀₀ = 319 to 390 kg/mm² on Vickers scale; Criddle & Stanley, 1993) and density ranges from 7.18 to 7.51 g/cm³ with increasing with iron content (Pavlu, 1986). The colour varies from densely black for ferberite over brownish black for wolframite and reddish brown for hübnerite. The crystal habit of wolframite is influenced by temperature. Short prismatic crystals are found in pegmatites, whereas tabular crystals occur in hydrothermal veins (Lawrence, 1961).

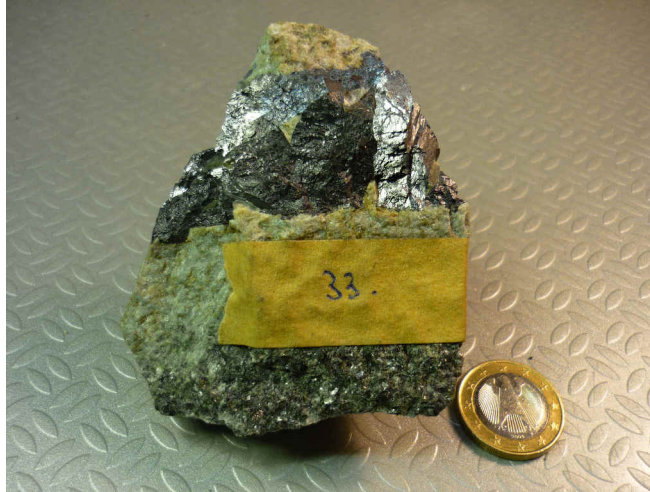


Figure 3.6: Wolframite crystals from the Xihuashan hydrothermal vein deposit, China with coin (1 €) for scale. Specimen is taken from the BGR mineral collection.

Under the reflected light microscope, wolframite is medium grey in colour and shows rather low reflectance with 15.1 to 16.25% in air and 4.07 to 4.73% in oil at a wavelength of 589 nm (Criddle & Stanley, 1993) with weak bireflectance (Figure 3.7). But wolframite displays distinct anisotropy with crossed polars ranging from greenish grey to brown. Some sporadic brownish internal reflections are visible in ferberite and wolframite, whereas the hübnerite shows brilliant reddish brown internal reflections.

3.4.2 Ferberite

Ferberite (named after the German mineralogist Moritz Rudolf Ferber) is monoclinic, but has a pseudo-orthorhombic crystal habit. The lattice constants are $a=4.734 \text{ \AA}$, $b=5.734 \text{ \AA}$ and $c=4.963 \text{ \AA}$ with an angle of $\beta=90^{\circ}12'$ (Cid-Dresdner & Escobar, 1968; Sieber et al., 1983). The ideal composition of ferberite is 76.34 wt.% WO_3 and 23.66 wt.% FeO which is equivalent to a tungsten content of 60.54 wt.% W for FeWO_4 . The colour is black with a submetallic lustre. The streak is brownish black. Ferberite occurs as tabular or bladed crystals commonly flattened along $\{100\}$. Cleavage is perfect along (010) and the fracture is uneven. Twinning on (100) and (023) is common. Ferberite has a melting point of 1266 °C (Schröcke, 1960). Replacement of ferberite by scheelite is not uncommon (Figure 3.7 left; Raith & Prochaska, 1995).

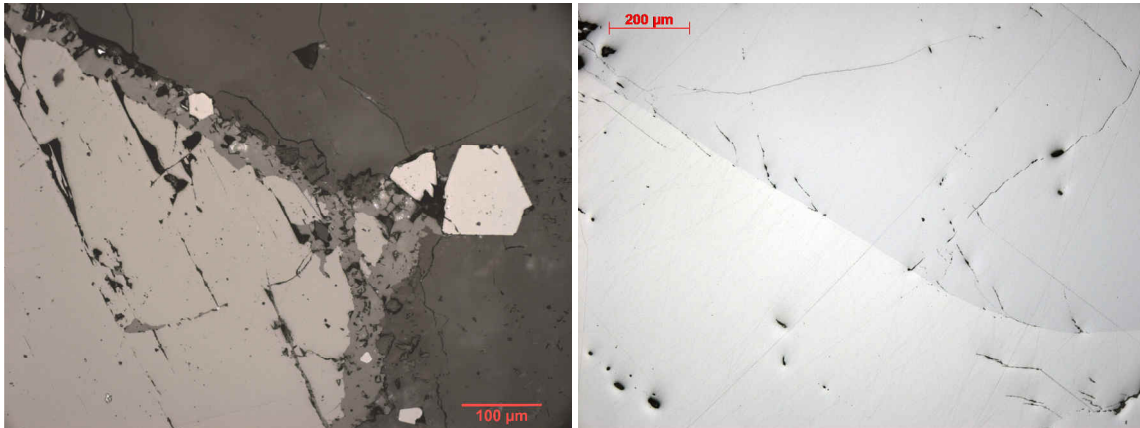


Figure 3.7: Photomicrographs of wolframite crystals. Left: euhedral ferberite crystal (light grey, left) is replaced by scheelite (medium grey, along rim of ferberite) and euhedral magnetite is formed (almost white). Matrix is composed of quartz (dark grey). This sample was taken from Namaqualand, South Africa and is courtesy of Johann Raith. Right: Simple twinning in large ferberite crystal indicated by bireflectance. This sample originates from the Bugarama tungsten mine, Rwanda.

In certain deposits in Uganda, Rwanda, the Democratic Republic Congo and Japan ferberite occurs as polycrystalline pseudomorphs after scheelite, so-called reinite (Figure 3.8; Sahama, 1981; Goldmann et al., 2013). The scheelite was replaced by polycrystalline ferberite through the interaction with iron-rich fluids (Frisch, 1975).

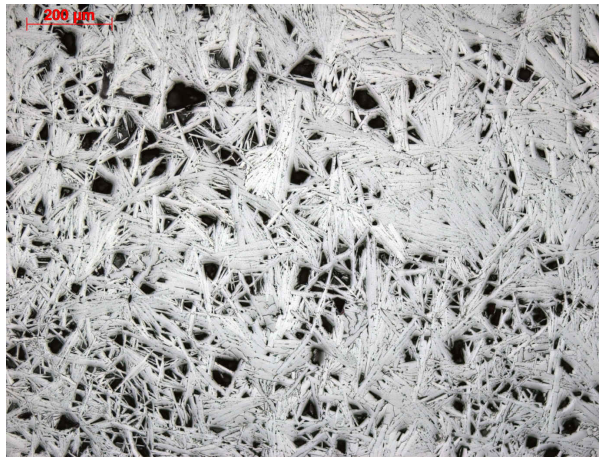


Figure 3.8: Reinite composed of randomly oriented fibrous ferberite crystals forming a porous aggregate replacing scheelite. Sample originates from the Bugarama tungsten mine, Rwanda.

3.4.3 Hübnerite

Hübnerite (named after the German metallurgist Friedrich Adolf Hübner) is monoclinic. The lattice constants are $a=4.829 \text{ \AA}$, $b=5.759 \text{ \AA}$ and $c=4.998 \text{ \AA}$ with an angle of $\beta=91^\circ 18'$ (Dachs et al., 1967; Anthony et al., 2001; Lide, 2009). Hübnerite commonly forms bladed crystals along $\{100\}$ which are striated or furrowed in direction of elongation. Twinning

on (100) is common. It shows perfect cleavage along (010) and the fracture is uneven. The colour is yellowish to reddish brown to brownish black with submetallic to resinous lustre and yellow to reddish brown streak (Pavlu, 1986). Hübnerite ideally contains 76.57 wt.% WO_3 and 23.43 wt.% MnO which is equivalent to a W content of 60.72 wt.% W for $MnWO_4$. At low Fe contents hübnerite can be intensely red and crystals may be transparent or translucent. Hübnerite has a melting point of 1301 °C (Schröcke, 1960).

Excursus on the hübnerite/ferberite ratio:

Some authors suggested, that the hübnerite/ferberite ratio can be used as an indicator for the temperature of formation with hübnerite crystallising at higher temperatures than ferberite (Oelsner, 1952; Leutwein, 1952; Oelsner, 1954; Ahlfeld, 1958; Hollister, 1970), but the reverse case was also observed (Taylor & Hosking, 1970; Higgins, 1985). Therefore, the hübnerite/ferberite ratio in wolframite cannot be used as a geothermometer (Groves & Baker, 1972; Hsu, 1976; Moore & Howie, 1978; Amossé, 1978a, 1978b; Willgallis, 1982; Nakashima et al., 1986; Campbell & Petersen, 1988; Bailly et al., 2002), because wolframite composition varies over the complete series between both endmembers in a similar temperature range (Ivanova & Naumov, 1986, Mignardi et al., 1998) and is controlled mainly by other factors than temperature (e.g., acidity of the fluid). The discussion on the interpretation of the hübnerite/ferberite ratio was reviewed by Kempe & Wolf (1994).

Ferberite forms over a wide temperature range from room temperature at 25 °C up to 400 °C at more acidic pH-values, but hübnerite can only be formed at temperatures above 200 °C at neutral to alkaline environment (Horner, 1979; Shibue, 1982). As indicated by experiments, a complete solid solution series of wolframite exists at temperatures above 400 °C (Schröcke, 1960; Hsu, 1976; Mignardi et al., 1996). These experiments also show that under temperature conditions lower than 370 °C no solid solution exists, but the almost pure endmembers are formed with ferberite and hübnerite coexisting (Schröcke, 1960; Kempe & Wolf, 1994). For example, zoned wolframite crystals from the epithermal Baia Sprie deposit, Romania show a significant change of the chemical composition from almost pure hübnerite in the cores to nearly pure ferberite at the rims (Bailly et al., 2002). However, complete miscibility between both endmembers is possible in nature even at temperatures lower than 400 °C (Willgallis, 1982) and experiments showed complete solid solution down to temperatures of 160 °C under hydrothermal conditions (Hochleitner & Schröcke, 1985). But generally, the ranges of the hübnerite/ferberite ratio are rather narrow on the deposit scale (Kempe & Wolf, 1994; Mignardi et al., 1998) and Kempe & Wolf (1994) also used the hübnerite/ferberite ratio to classify wolframite deposits into Sn-W and Sn-free W deposits. Several authors also demonstrate that the composition of the surrounding wall rocks and the interaction of the W-bearing solution with the country rocks are the major factors controlling the hübnerite/ferberite ratio (Barabanov, 1971; Nakashima et al., 1986).

3.4.4 Scheelite

Scheelite (named after the German-Swedish chemist Carl Wilhelm Scheele) is the mineralogical name for calcium tungstate which has the chemical formula $\text{Ca}^{[8]}\text{W}^{[4]}\text{O}_4$ (coordination number in square brackets; Kuzmin & Purans, 2001) and crystallises in the tetragonal crystal system with the crystal class 4/m. The habit is mostly as bipyramids with octahedral forms with $\{111\}$ and $\{112\}$ or as tabular crystals with diagonal striation. Its cleavage along (101) is distinct, along (112) interrupted and along (001) indistinct (Pavlu, 1986). Fracture is uneven to conchoidal. Twinning on (110) is common (Pavlu, 1986). The hardness ranges from 4.5 to 5 on the Mohs scale ($\text{VHN}_{100} = 383$ to 464 kg/mm^2 on Vickers scale; Criddle & Stanley, 1993) and the density varies between 5.9 and 6.1 g/cm^3 (Strunz & Nickel, 2001). The colour of scheelite is very variable, but commonly greyish white. The streak is white to almost colourless. The lustre is adamantine on crystal planes (Klein & Hurlbut, 1993) and greasy on fracture planes. The edges are translucent and some specimens are transparent. Scheelite shows characteristic whitish-blue fluorescence when exposed to short-wavelength ultraviolet radiation. This property is used as a diagnostic method in ore prospection, exploration, and mining. The colour of the fluorescence is influenced by the molybdenum content (Figure 3.9) and changes from bright blue (less than 0.5 mol.% CaMoO_4), white to pale yellow (0.5 to 2 mol.% CaMoO_4) to bright yellow or orange (more than 2 mol.% CaMoO_4) with increasing molybdenum content (Greenwood, 1943; Hsu & Galli, 1973; Kwak, 1987).

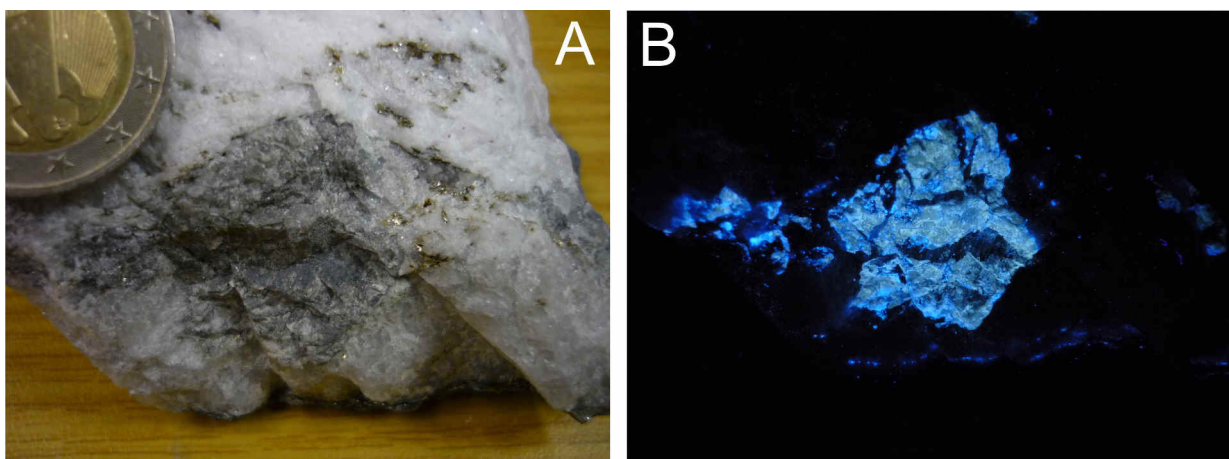


Figure 3.9: Large scheelite crystals from the tungsten deposit Felbertal, Mittersill, Austria. Picture A was taken at daylight (please note 1 €-coin for scale). Picture B shows the same view as picture A using ultraviolet light. Different generations of scheelite are discernible under ultraviolet radiation: scheelite 2 forms large crystals with yellowish fluorescence in the cores and scheelite 3 is present along the rims with bright blue fluorescence (Raith & Stein, 2006).

The crystal structure has a tetragonal body-centred elemental cell with WO_4 tetrahedrons along c-direction. The divalent calcium cation is surrounded by eight oxygen atoms of the tungstate anionic groups $[\text{WO}_4]^{2-}$ and the scheelite structure may be regarded as a cubic close-packed array of Ca^{2+} cations and $[\text{WO}_4]^{2-}$ groups (Figure 3.10; Sleight, 1972; Pavlu, 1986; Kuzmin & Purans, 2001; Okrusch & Matthes, 2009).

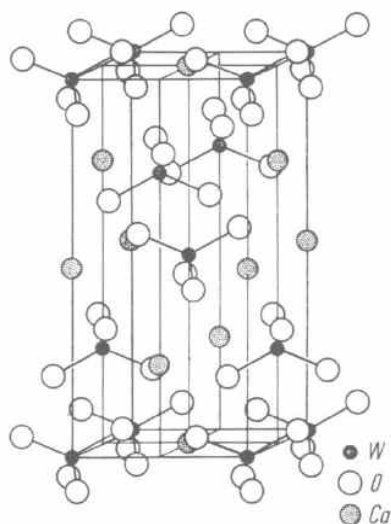


Figure 3.10: Crystal structure of scheelite. Open circles represent sites of oxygen, black-filled circles are sites of tungsten and grey-filled circles are sites of calcium (Kleber, 1998)

Scheelite is ideally composed of 19.48 wt.% CaO and 80.52 wt.% WO_3 which is equivalent to a W content of 63.85 wt.% W for CaWO_4 . The lattice parameters are $a = 5.24 \text{ \AA}$ and $c = 11.37 \text{ \AA}$ (Pavlu, 1986; Anthony et al., 2001) and the W-O bond length is 1.785 \AA (Pavlu, 1986). At temperatures above $600 \text{ }^\circ\text{C}$ scheelite forms a solid solution with wolframite (Grubb, 1967). The mineral stolzite (PbWO_4) is isotypic to scheelite and a complete solid solution series exists at temperatures above $725 \text{ }^\circ\text{C}$ (Hsu, 1981). Scheelite forms a complete solid solution series with powellite (CaMoO_4), but natural scheelite contains only a minor powellite component (Hsu & Galli, 1973).

In reflected light, scheelite shows extremely low reflectance of 9.68 to 10.05% in air and 1.37 to 1.48% in oil at a wavelength of 589 nm (Criddle & Stanley, 1993). Scheelite shows distinct anisotropy with crossed polars, but this feature is masked numerous bright white to yellowish internal reflections.

4 The tin market

4.1 Applications of tin

The major application of tin nowadays is as solder. Solder is a low-melting alloy and is used to attach components onto circuit boards or to join metals, whereby the melting point of the solder is lower than that of the other components. Soft solder with melting points lower than 450 °C is used as mechanic and electric connection in switching networks for electronic devices. There is an increasing demand for tin in recent years because Pb-free solder contains more Sn than the common Pb-based solder. In 2006 the European Union enacted the directive on the restriction of the use of certain hazardous substances in electrical and electronic equipment (European Commission, 2003). This directive restricted the use of Pb-Sn alloys in the manufacture of electric and electronic devices because of environmental and health concerns about lead. Additionally, China and Japan joined this arrangement. Lead-tin solder contained 63% Sn and has a eutectic melting point of 183 °C. New Pb-free solders are based on Sn-Ag-Cu alloys with more than 95% Sn and a melting temperature of 220 °C (Angerer et al., 2009). On a global scale more than 50% are used as solder; especially in Asia up to 65% are consumed as solder due to Asia's dominance in the electronics sector, whereas in Europe and Northern America the share of tin as solder is significantly lower with 25 and 30%, respectively.

In former times, the major use of tin was as tinplate for food and beverage cans, but it became less important over the years and now less than 20% of the tin production is used for tinplate (16%; Elsner 2014). Tinplate is produced by electrolytic coating of steel plate (with thicknesses of 0.1 to 0.5 mm) with a thin tin film between 1 and 6 g Sn per m² (Roos, 2014); the coating process is called hot dip tinning. Tin is most suitable for this application in food and beverage cans because it is non-toxic and non-corrosive.

There is an increasing demand for tin (15% of world's tin consumption; Elsner, 2014) in chemicals and pigments in the plastic and glass industry. But Sn-bearing organic compounds are also used as biocides and as stabilising agent in the production of polyvinyl chloride (PVC).

Tin is also used in different alloys like bronze or red brass (6% of world's tin consumption; Elsner, 2014). Bronze is used by mankind since ancient times for objects of daily use such as tools or weapons, but today bronze and red brass are mainly used as cast alloy in engineering. Additionally, bronze is easier to cast than copper because the addition of tin significantly reduces the melting temperature compared to elemental

copper. Another series of alloys composed of Sn, Sb and Cu is used as bearing metal in antifriction applications; these alloys are also known as Babbitt metals in the United States.

Molten tin is used in the production of so-called 'float glass' (2% of world's tin consumption; Elsner, 2014). The industrially applicable process was invented by Sir Alastair Pilkington whereby molten glass floats on liquid tin and a very plane surface is formed (Pilkington, 1969). Tin is suitable for this process because of its high density, low melting point and its surface tension.

A modern application of tin is as transparent and electrically conducting indium-tin-oxide (ITO), which is typically composed of 25 wt.% Sn and 75 wt.% In (Angerer et al., 2009). The ITO is used as electrically conductive coating on flat glass for screens and displays. This utilisation will have increasing significance on future demand for tin and indium.

4.2 Mine production and projects

Since the early nineties China and Indonesia followed by Peru are the world's leading tin producers. During the last decade China and Indonesia have played the dominating role on the tin market because both together accounted for about 65 to 70% of the global tin concentrate production (Figures 4.1 & 4.2). For example in 2013, the world mine production was about 298500 tons of tin in concentrate, thereof China and Indonesia produced about 30 and 33%, respectively (BGR database; Figure 4.2). The last years Myanmar became an emerging producer of cassiterite concentrates, which are exported in total to China.

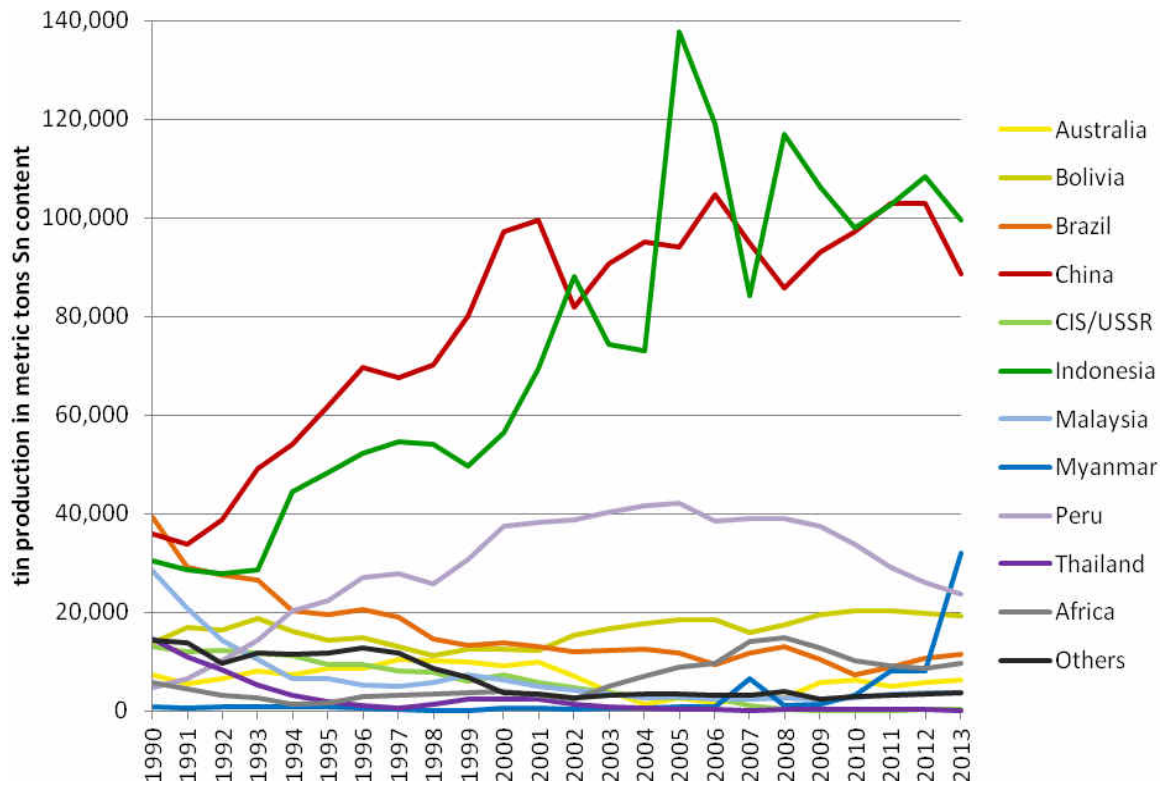


Figure 4.1: Annual global tin mine production from 1990 to 2013 in metric tons of metal content (BGR database).

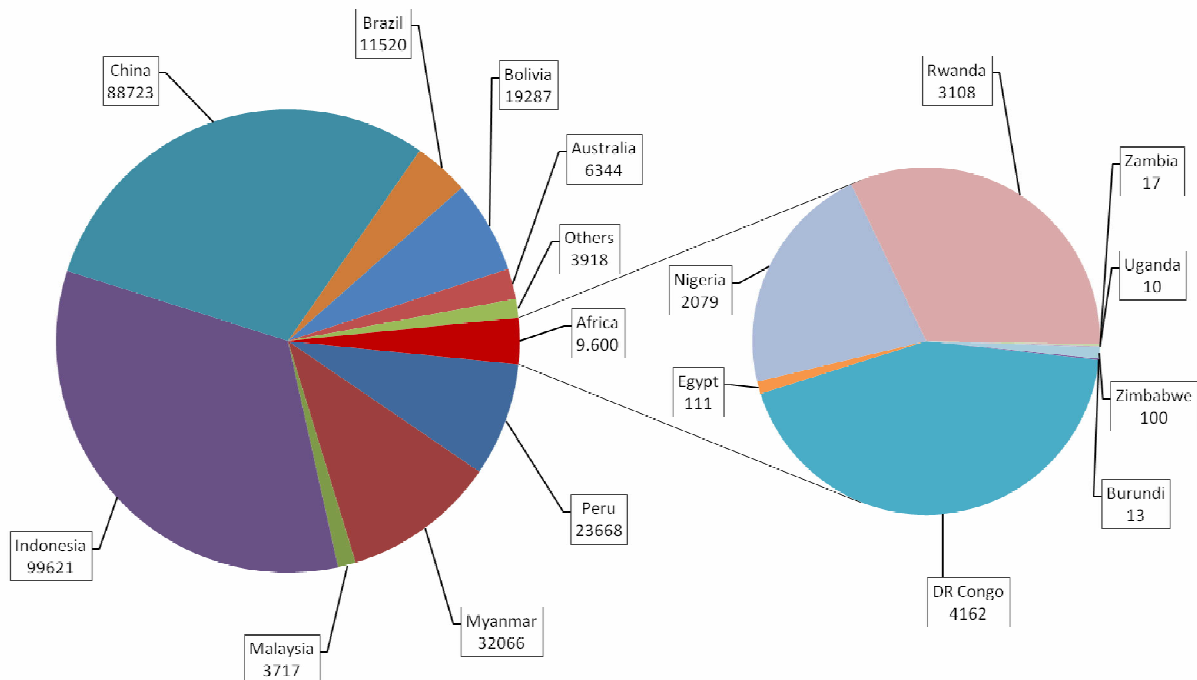


Figure 4.2: Global tin mine production in tons metal content for 2013 (total: 298464 tons Sn; BGR database)

The major tin mining districts in China are located in the Yunnan (Gejiu), Guangxi (Dachang), Hunan, and Jiangxi Provinces of southern China. Hydrothermal vein, stockwork, greisen, skarn, and carbonate replacement deposits are associated with three different magmatic events during the Mesozoic: 1) W-Sn-Nb-Ta mineral deposits are related to Upper Triassic (230-210 Ma) peraluminous granites, 2) Upper Jurassic (160-150 Ma) metaluminous granite intrusions formed W-Sn deposits, and 3) Sn-polymetallic deposits are associated with Cretaceous (120-80 Ma) intrusions of S-type granites (Mao et al., 2013).

In Indonesia the region of the Bangka-Belitung islands accounts for the majority of its tin production. Tin mining is focussed on alluvial placer deposits located in on- and offshore environments (86% according to Elsner, 2014). Primary tin deposits are related to Sn-bearing biotite granite plutons of the Southeast Asian Tin Belt (Schwartz et al., 1995). The majority of the cassiterite mine production in Indonesia is contributed by artisanal and small-scale miners (about 70% according to Elsner, 2014). But total production is declining strongly due to exhausted reserves and unsustainable mining (along with severe environmental damage).

In Peru, the Minsur smelter is supplied with tin ore concentrates from the San Rafael mine, which constitutes the only active Peruvian tin mine. The San Rafael deposit represents one of the world's highest grade tin deposits constituting proven and probable reserves of 4.5 million tons of ore grading 2.24% Sn as stated in the annual report 2013 of Minsur. However, production is declining because reserves are almost exhausted, but there is ongoing exploration and reprocessing of the tailings dumps is considered. In 2008, Minsur acquired Taboca Mineração which is operating the Pitinga mining area situated in the State of Amazonas, Brazil. In former times, cassiterite and columbite-tantalite ore concentrates were exclusively produced by dredging methods from alluvial placers, but now mining activities are focussing on primary hard rock ores.

The Bolivian Huanuni and Colquiri tin mines plus the Vinto smelter were nationalised by President Morales to get higher income from taxes and are these operations are now run by the state-owned Corporación Minera de Bolivia COMIBOL. However, there were several strikes at the Vinto smelter and the Huanuni mine in the past (ITRI). But the Vinto smelter is also supplied with cassiterite concentrates from the Colquiri, Caracoles and Morococala mines.

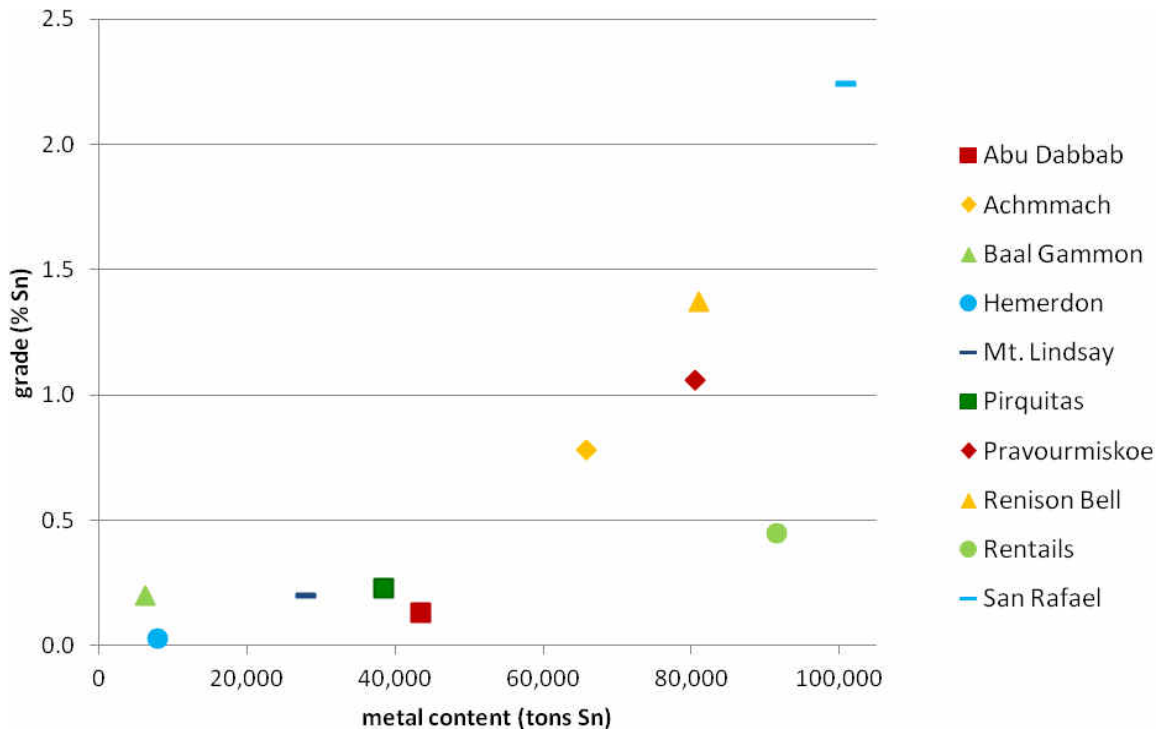


Figure 4.3: Reserve estimates (proven + probable) given as tin content in metric tons and grade in percent for selected tin mine projects

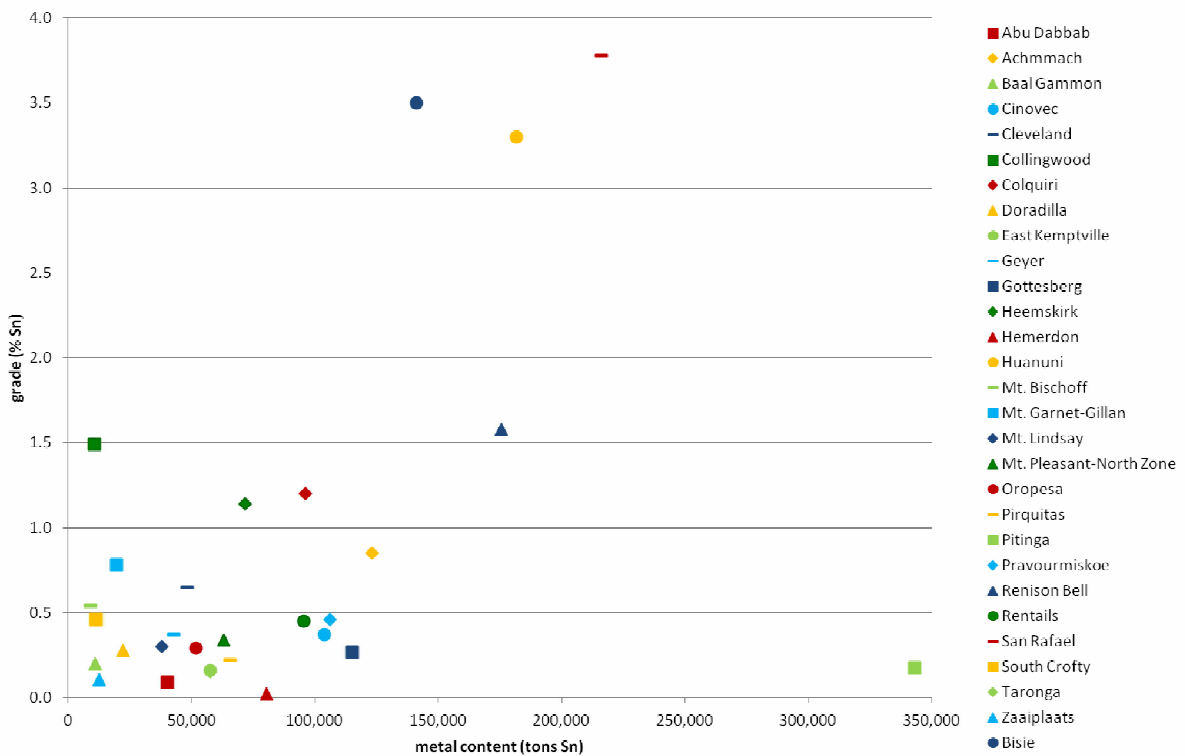


Figure 4.4: Resource estimates (indicated + inferred) given as tin content in metric tons and grade in percent for selected tin mine projects

The Australian Metals X Ltd. restarted its Renison project in Tasmania 2010 as a 50:50-joint venture with the Chinese Yunnan Tin Group. The concentration plant gets ore feeds from the Renison Bell underground mine and initially also from the Mt. Bischoff open pit. The Renison Bell mine has mineral reserves of 5.91 million tons of ore grading 1.37% Sn and a total mineral resource of 11.1 million tons of ore grading 1.58% Sn, as stated in the 2014 annual report. Additionally, the nearby tailings (termed 'Rentails' by Metals X) from former mining activities at Renison Bell mine are estimated to constitute a total reserve of 20.35 million tons of ore at 0.45% Sn.

There is an increasing need to initiate sustainable mining projects outside China and Indonesia. The following details on the projects including resource/reserve estimates (Figures 4.3 & 4.4) are taken from the respective websites of the companies. Kasbah Resources Ltd. is exploring the Achmmach tin deposit in Morocco and reported in its 2014 annual report total mineral resources of 14.6 million tons of ore grading 0.85% Sn and a maiden reserve estimate of 8.45 million tons at 0.78% Sn. Australian Gippsland wants to start the Abu Dabbab tantalum-tin project in Egypt and could become the world's largest tantalum producer with tin as by-product. The deposit contains total mineral resource of 44.5 million tons of ore at 250 ppm Ta and 0.09% Sn. As stated in the annual report 2014, placer mining on alluvial cassiterite surrounding Abu Dabbab was in operation by Gippsland Ltd. from March 2012 to September 2014 and produced about 150 tons of tin in concentrate. The Canadian Adex Mining Inc. wants to start the Mt. Pleasant mine located in New Brunswick, Canada. The North Zone of the Mt. Pleasant mine contains about 12.4 million tons of ore grading 0.38% Sn, 64 ppm In and 0.86% Zn as indicated resource. Venture Minerals Ltd. is exploring the Mt. Lindsay skarn deposit in Tasmania and defined a total (proven + probable) minerals reserve of 14 million tons of ore at a tin grade of 0.2% Sn. Tin International Ltd., a subsidiary of Deutsche Rohstoff AG, is exploring the Gottesberg and Geyer deposits in the Erzgebirge, Germany. Exploration drilling identified a total mineral resource of 42.1 million tons of ore grading 0.27% Sn for Gottesberg and an indicated resource of 11.6 million tons at a grade of 0.37% Sn for Geyer. Stellar Resources Ltd. owns the Heemskirk tin project in Tasmania. The prefeasibility study (completed in July 2013) estimated a total mineral resource (combined from three ore bodies) of 6.28 million tons of ore grading 1.14% Sn. The Mt. Garnet tin project in Queensland is developed by Consolidated Tin Mines Ltd. and the total mineral resource (combined from three deposits) is estimated to 12 million tons at a grade of 0.4% Sn (as stated in the annual report 2013). A joint venture between

Western United Mines Ltd. and Celeste Mining Corp. is in progress to restart mining in the historic South Crofty mine in Cornwall which has been closed in 1998. Current operations include tunnelling, backfill and exploration drilling.

Tin is won as by-product at the Panasqueira tungsten mine in Portugal (about 30 tons of Sn in concentrate per year; Franco et al., 2014) and tin should also be recovered when the Hemerdon Ball tungsten mine in Devon becomes operable (about 450 tons of Sn in concentrate per year). Recycling is also an important factor in tin supply, especially the low-melting solder is suitable for recycling.

4.3 Processing and beneficiation of tin

Tin is mined from placer deposits, particularly in the Southeast Asian Tin Belt (e.g., Indonesia, Malaysia and Thailand), with relatively low minimum grades (about 150 g cassiterite per m³; Elsner, 2014). These deposits represent alluvial, eluvial or residual placers of deeply weathered primary deposits. Cassiterite is concentrated in placer deposits due to its high density and its resistance to mechanical and chemical weathering. The stream and offshore placer deposits are mined by dredges, huge floating processing plants with bucket chains excavating the cassiterite-bearing sediments from the seafloor or from streambeds. The placer deposits on land are either operated by open-pit mining or by hydraulic gravel pump mining. In gravel pump mining, the unconsolidated material is disaggregated by high-pressure water jets and the resulting slurry is flushed down to a low-level pond; the cassiterite-bearing material is then transported to the processing plant by a pump at the bottom of the pond (Evans, 1994). The low-grade ores from placer deposits are processed by washing, screening and concentration by gravity on shaking tables and spirals to separate the cassiterite.

Tin is also recovered from primary tin deposits by underground mining methods, but significantly higher tin grades of minimum 0.5 wt.% Sn are required to operate economically (Elsner, 2014). Tin ores from lode deposits are also upgraded by gravity methods, but the concentrates require roasting and magnetic separation to remove the sulphides (Evans, 1994).

The final marketable cassiterite concentrate contains tin grades ranging from 70 to 75 wt.% Sn and is suitable for smelting in a furnace at temperatures of about 1400 °C. The tin oxide is reduced with carbon to form carbon dioxide and crude tin (1). Limestone and silica are added to form the slag.



The crude tin is then refined in a reverberatory furnace to obtain higher purity. Tin melts at a lower temperature than most other metals and therefore temperature is raised slightly above the melting point of tin that only tin turns liquid and the other metals stay solid (Evans, 1994). This refining process is called liquidation and effectively removes iron, arsenic, copper, and antimony. Electrolytic refining is applied to achieve higher purity grades of to 99.99% Sn. Remaining impurities like bismuth and lead are deposited at the bottom of the furnace.

Tin slags contain recoverable amounts of other metals, for example tantalum. In this case the tin slags are reprocessed after smelting and a certain amount of the world's tantalum production derives from these slags, especially from the Thailand Smelting and Refining Corporation (Thaisarco).

4.4 Pricing

Tin is traded at the London Metal Exchange (LME) in the United Kingdom and at the Kuala Lumpur Tin Market (KLTM) in Malaysia. Both institutions publish the actual tin price quotation. Tin is traded on these exchanges in the form of ingots with a minimum purity of 99.85%. In modern times, the Malayan Peninsula with Indonesia, Malaysia, Thailand and neighbouring People's Republic of China has been the top-producing region for cassiterite concentrates. Additionally, most of the important companies producing refined tin are situated in Southeast Asia (Figure 4.5), for example the Yunnan Tin Group from China, PT Timah from Indonesia, the Malaysia Smelting Corporation (MSC) and the Thailand Smelting and Refining Corporation (Thaisarco).

Other important smelters are located in South America (Figure 4.5), such as the Peruvian Minsur S.A., the Empresa Metalurgica Vinto and Operaciones Metalúrgicas S.A. (OMSA) from Bolivia, and Taboca Mineração S.A. located in Brazil. In 2008, the Brazilian tin operations Taboca Mineração and Mamoré Mineração e Metalurgia were sold by Paranapanema S.A. and became subsidiaries of Minsur S.A. from Peru.

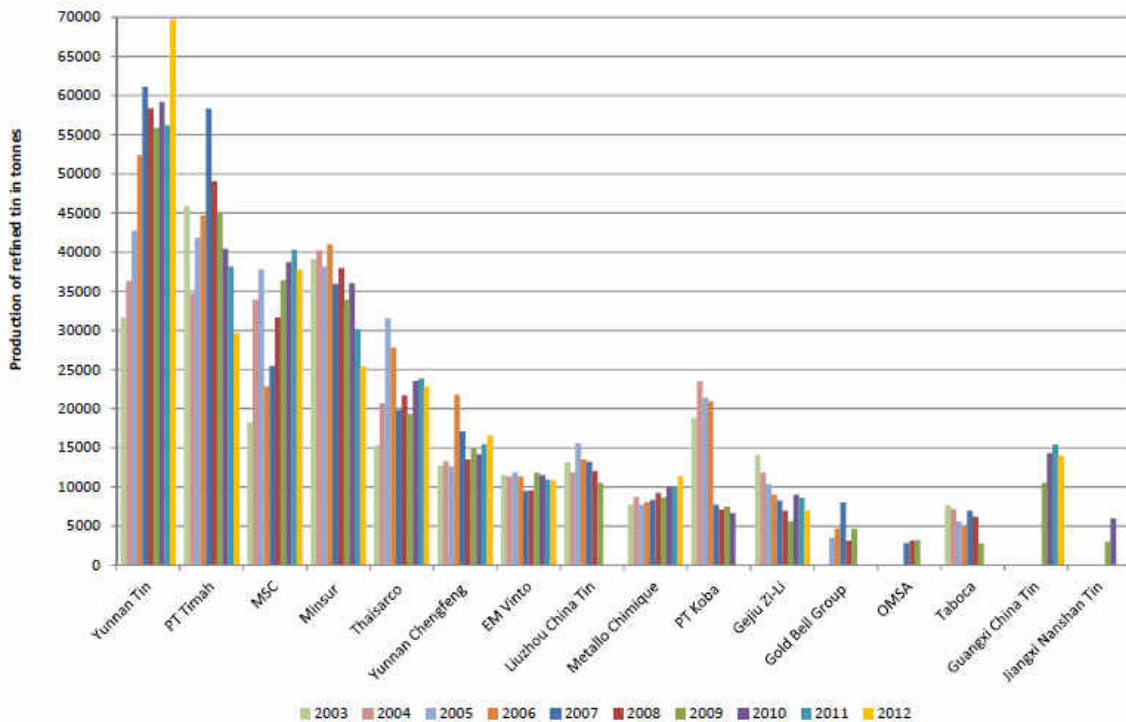


Figure 4.5: Annual global refined tin production of major smelting companies from 2003 to 2012. Data only given for significant output larger than 2700 tons refined tin (ITRI)

In July 2006, the directive on the restriction of hazardous Substances (RoHS-directive 2002/95/EG) became effective in the European Union and the former Sn-Pb solders were replaced by Sn-Ag-Cu solders with significantly higher tin contents. This caused an increasing demand for tin and pushed the price higher (Figure 4.6). Additionally, the crackdown on Indonesian miners and smelters led to sharp disruption in the world's tin supply and this led to increasing tin prices in the year 2007 (Elsner, 2014; Figure 4.6). The tin price continuously increased from about 6000 US\$ per ton since November 2005 and reached the climax at up to 25500 US\$ per ton in May 2008 (Figure 4.6). This has been the highest tin price ever and resulted from low stocks, supply concerns caused by deficits and funds buying. This was strengthened by the growing demand as solders in electronics without any adequate substitute. In the end of 2008, the global economic and financial crisis also influenced the electronics industry and affected the tin prices which dropped to approximately 11000 US\$ per ton (Figure 4.6). Since the global economic and financial crisis in 2008, tin price is continuously rising up to an all-time high of 33600 US\$ per ton in April 2011 (Figure 4.6). This high price for tin metal is driven by a significant supply deficits and the use of Pb-free solders in electronics. Prices are also affected by interventions of governmental institutions, especially in Indonesia mines and tin smelters and on the Bangka-Belitung Islands were shut down in order to prevent

(illegal) small-scale mining activities to protect the environment; similar actions against small-scale mining were also done by the Chinese government. In South America, several strikes during the last years in mines and smelters in Bolivia and also in Peru interrupted tin production in these countries.

Three Chinese companies are situated in the top ten of refined tin production (Figure 4.5), namely the Yunnan Tin Group, Yunnan Chengfeng and Liuzhou China Tin. As a result of the booming economy, the market situation is changing and China has turned into a net importer of tin since September 2007 (ITRI, 22.01.2008). Therefore China established export and production quotas for several commodities to meet the strong domestic demand for raw materials. At the beginning of the year 2008, the Chinese government induced a 10% export tax on refined tin. The Chinese government successively cut the annual export quota for tin and tin products from 33300 tons in 2008 (ITRI, 17.10.2008) down to at least 11900 tons for 2014 (ITRI, 16.12.2013), regardless most of China’s tin production is consumed domestically without touching export quotas.



Figure 4.6: Price chart for refined tin (99.85% minimum grade) from January 2001 to June 2015 (BGR database & Kuala Lumpur Tin Market)

4.5 Future trends

The future consumption of tin is depending on new applications and the resulting supply-demand situation. Generally, consumption of raw materials is directly linked to the global economic growth which had an annually growth rate of approximately 4% the last years. Angerer et al. (2009) developed an indicator for the future demand for commodities/raw materials depending on today's global production in relation to the demand in the year 2030 related to respective applications. This is also a measure for future mine development. The foresight for tin estimates that the demand for tin is going to increase and the indicator is increasing from 0.62 in 2006 to 0.77 in 2030 (Angerer et al., 2009). Increasing demand is coupled to the increasing demand for solder and transparent electrodes (ITO) in electric and electronic devices. A new application for tin is in lithium ion batteries, which are used in mobile phones, laptops, and electric cars. Tin in the form of tin whiskers is replacing graphite as anode material resulting in a significantly higher capacity (Fraser, 2012). Additionally, there is tightness on the supply side, because new large scale projects are not expected to start production in the near future.

5 The tungsten market

5.1 Applications of tungsten

The following descriptions of the major tungsten applications are a general summary of the detailed illustrations given by Andrews (1955) and Lassner & Schubert (2009).

Cemented carbides, also known as hardmetals, are the major application of tungsten nowadays and more than 60% of the tungsten production is consumed for this purpose. In 1927, the German steel-producing company Krupp presented the first hardmetal under the trademark 'Widia' ("wie **D**iamant" which is German for "like diamond") at the Spring Fair in Leipzig. Cemented carbides are made by pressing and sintering tungsten carbide particles into a metallic binder matrix of cobalt or nickel metal powder. Cemented carbides combine the hardness of the carbide with the toughness of the metallic binder and the metallic matrix compensates the brittleness of the carbides. Besides tungsten other metals are used in the form of carbide, such as titanium (TiC), tantalum (TaC) and niobium (NbC). Tungsten carbide (WC) has important properties such as extreme hardness of 9.5 on the Mohs scale, a high melting point (2870 °C), high density (15.6 g/cm³), good thermal conductivity, and high stability. The major uses are in metal cutting, drilling, construction, wear-resisting parts, and military applications. Tungsten is processed to tungsten carbide by heating tungsten powder with carbon between 1400 and 1600 °C. Different grain sizes of the tungsten powder result in different properties of the cemented carbide. Generally, finer grain size and lower binder content results in higher hardness, wear resistance and compressive strength.

About 20% of the tungsten supply is used as alloying compound in the production of high-speed steel (HSS), tool steel, and heat-resistant steel. Tungsten-alloyed steels exhibit remarkable properties like increased hardness, durability, and heat resistance and are used in the production of various tools (e.g., cutting). First tools made of high-speed steel were exhibited in 1900 at the World Exhibition in Paris (Ahlfeld, 1958). Tungsten is added as oxides or as metallic powder, but today usually ferrotungsten (FeW) is used due to its lower melting point of about 2500 °C. Molybdenum is a possible substitute for tungsten in the manufacture of high speed steels.

Tungsten is also used in high temperature alloys based on iron, nickel and cobalt with tungsten contents of up to 25%. These super alloys are used as turbine blades and rocket nozzles in the aerospace industry, in armament as kinetic energy penetrators or

for generators in electric power plants due to the high heat and creep resistance (Lassner & Schubert, 2009).

The story of tungsten mill products started at the beginning of the 20th century with the new application of tungsten as filaments in incandescent light bulbs due to its extremely high melting point and its electrical conductivity. Today this application lost its importance because of substitution by more efficient light sources, but still incandescent light bulbs are in use. Tungsten mill products like rod, wire, and sheets are also produced by powder metallurgy and the tungsten metal powder is produced by reduction of tungsten oxides with hydrogen. Pure metallic tungsten is also used as electrodes in tungsten inert gas (TIG) welding, as cathode material and in thermocouples. Mill products make up about 10% of the total consumption and are used in the electrical and electronic industry as filaments, electrodes and electrical contacts.

Today a small amount of the tungsten production is used in the chemical industry in the form of tungsten oxides, tungstates, tungstic acid or tungsten sulphides in paint, enamel, rubber, plastic and textile industry. Additionally, sodium tungstate is an important fire-proofing agent (Werner et al., 1998).

5.2 Mine production and projects

In 2011, the world mine production was about 73000 tons of tungsten metal in concentrate and is dominated by the People's Republic of China with about 85% market share followed by Russian Federation, Canada, and Bolivia (BGR database; Figures 5.1 & 5.2).

The following details on the projects are taken from the respective web presences of the companies. One of the largest producers of tungsten concentrates outside China is the North American Tungsten Corporation Ltd., which owns the Cantung mine and the Mactung deposit situated in north-western Canada. The Cantung scheelite skarn deposit has probable reserves of 1.82 million tons at a grade of 0.81% WO₃ and an indicated resource of 3.84 million tons at 0.97% WO₃. Production was suspended in October 2009, but restarted in October 2010 and is still ongoing since that time. In its fiscal 2014, North American Tungsten Corporation Ltd. produced about 274000 mtu WO₃ in concentrate from about 393000 tons of ore milled. The largest tungsten producer of Russia is the Primorsky Mining Group which operates the Vostok-2 scheelite mine in the Primorsky krai of the Far Eastern district.

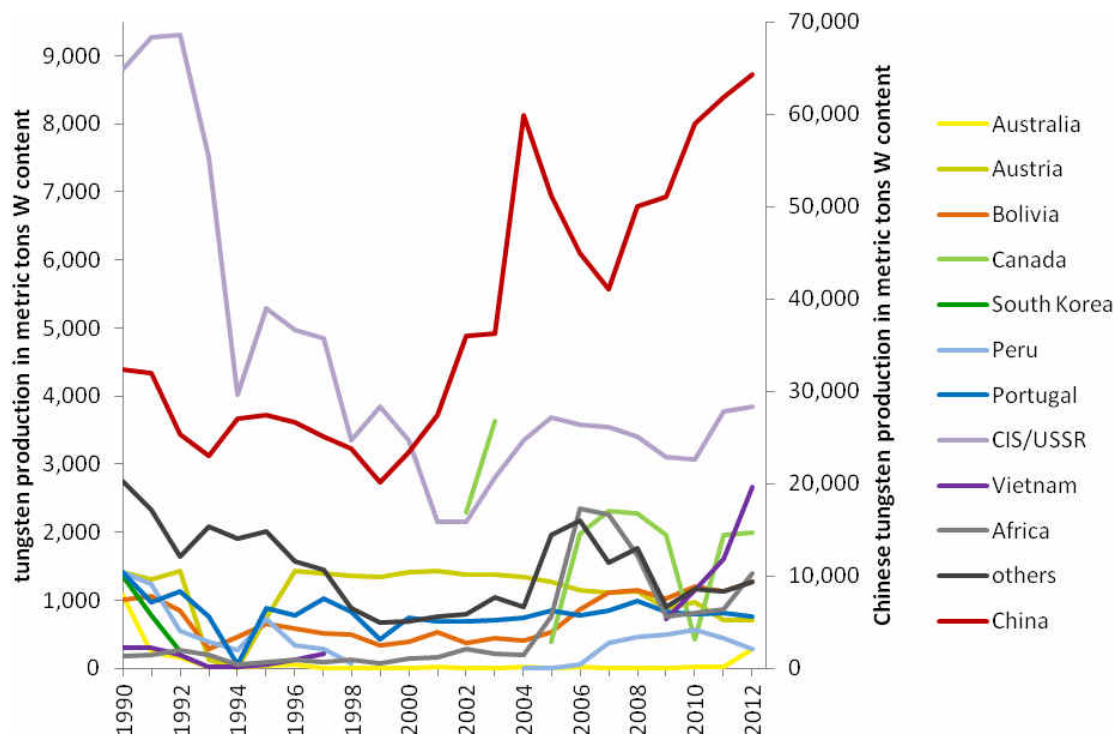


Figure 5.1: Annual global tungsten mine production from 1990 to 2012 in metric tons of metal content (BGR database). Please note that production from China is displayed on a secondary vertical axis.

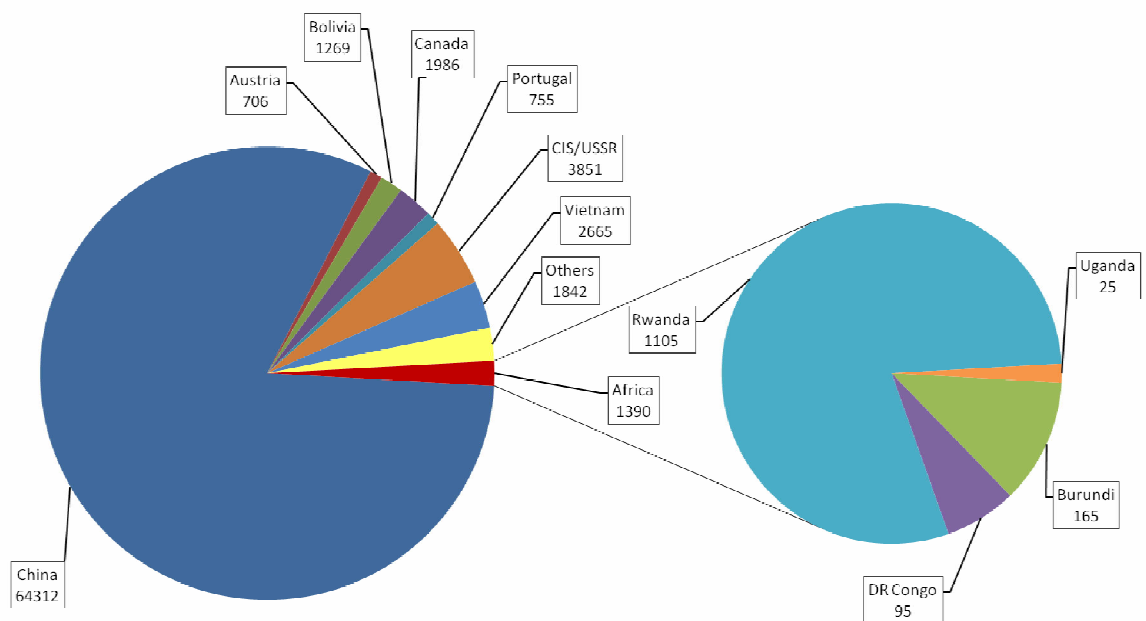


Figure 5.2: Global tungsten mine production for 2012 in metric tons of metal content in concentrate (total: 78,776 tons W; BGR database)

The largest tungsten mines in Europe are the Mittersill scheelite deposit in Austria, the Panasqueira mine in Portugal and the Los Santos deposit in Spain. The Mittersill mine is operated by the Wolfram Bergbau und Hütten AG (WBH) which refine the scheelite concentrates in their processing plant in St. Martin, Styria. WBH was bought in February 2009 by the Swedish mining and tool company Sandvik. The Panasqueira mine is owned by Beralt Tin & Wolfram S.A., a subsidiary of the Japanese Sojitz Tungsten Resources Inc., and currently produces between 85000 to 95000 mtu WO_3 wolframite concentrates per year (Franco et al., 2014). The Los Santos skarn-hosted scheelite deposit was formerly operated by Heemskirk Consolidated Ltd., but was sold to Almonty Industries in 2011. Almonty Industries processed about 460000 tons of ore in its fiscal 2013 producing of about 67500 mtu WO_3 in concentrate. The Los Santos deposit has proven and probable mineral reserves of about 1.88 million tons at a grade of 0.39% WO_3 plus measured and indicated resources of 2.76 million tons at a grade of 0.32% WO_3 . Almonty Industries is operating the Wolfram Camp mine in with indicated and inferred mineral resource of 1.47 million tons of ore at a grade of 0.21% WO_3 (as stated in the technical report from 2014). Wolfram Camp produced 700t of WO_3 in 2013. The Vietnamese Youngsun Industry Co Ltd. produces ferrotungsten from tungsten ores derived from the Thienke and Philieng tungsten mines. Until the end of 2012, another important tungsten producer was the Pasto Bueno mine situated in the Peruvian Andes. The Malaga Inc. of Dynacor was operating the mine from 2005 until end of 2012 and the ore concentrates were completely sold to Global Tungsten & Powders Corporation (formerly Osram Sylvania Inc.). But since 2012 the production is stopped.

The Australian Wolf Minerals Ltd. plans to restart the Hemerdon mine in Cornwall, United Kingdom with about 3500 tons of WO_3 in concentrate per year. Proven and probable reserves are estimated to contain 26.7 million tons of ore grading of 0.19% WO_3 and 0.03% Sn. The Canadian Tiberon Minerals Ltd. explored the polymetallic (tungsten, fluorite, bismuth and copper) Nui Phao deposit in Vietnam with proven and probable reserves of 52.54 million tons of ore grading of 0.21% WO_3 . Masan Resources, part of the Masan Group Corp., acquired the Nui Phao deposit in 2010 and is now developing the mine. Ormonde Mining Ltd. conducted exploration on the Barruecopardo deposit in Spain with proven and probable mineral reserves of 8.7 million tons of ore grading 0.3% WO_3 . Woulfe Mining Corp. (formerly Oriental Minerals Inc.) is assessing resources of the Sangdong scheelite deposit situated in South Korea. Probable reserves of the Sangdong mine are estimated at 13.3 million tons of ore grading 0.42% WO_3 .

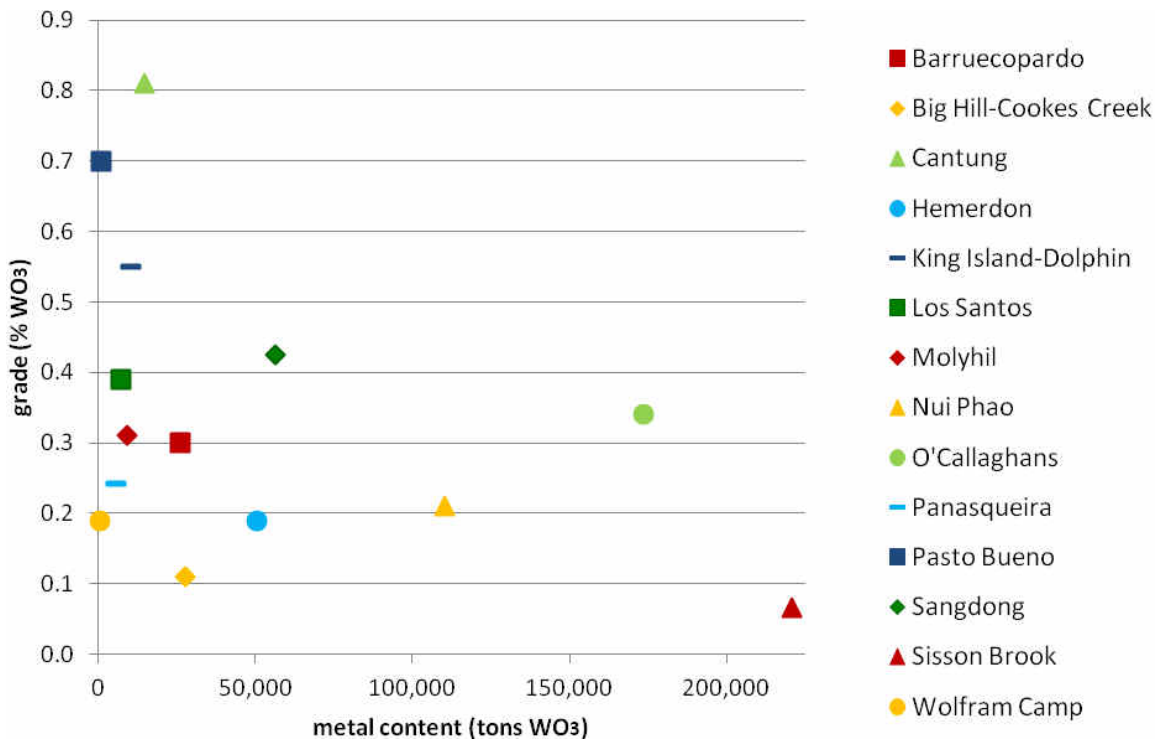


Figure 5.3: Reserve estimates (proven + probable) given as WO₃-content in metric tons of and WO₃-grade in percent for selected tungsten mine projects.

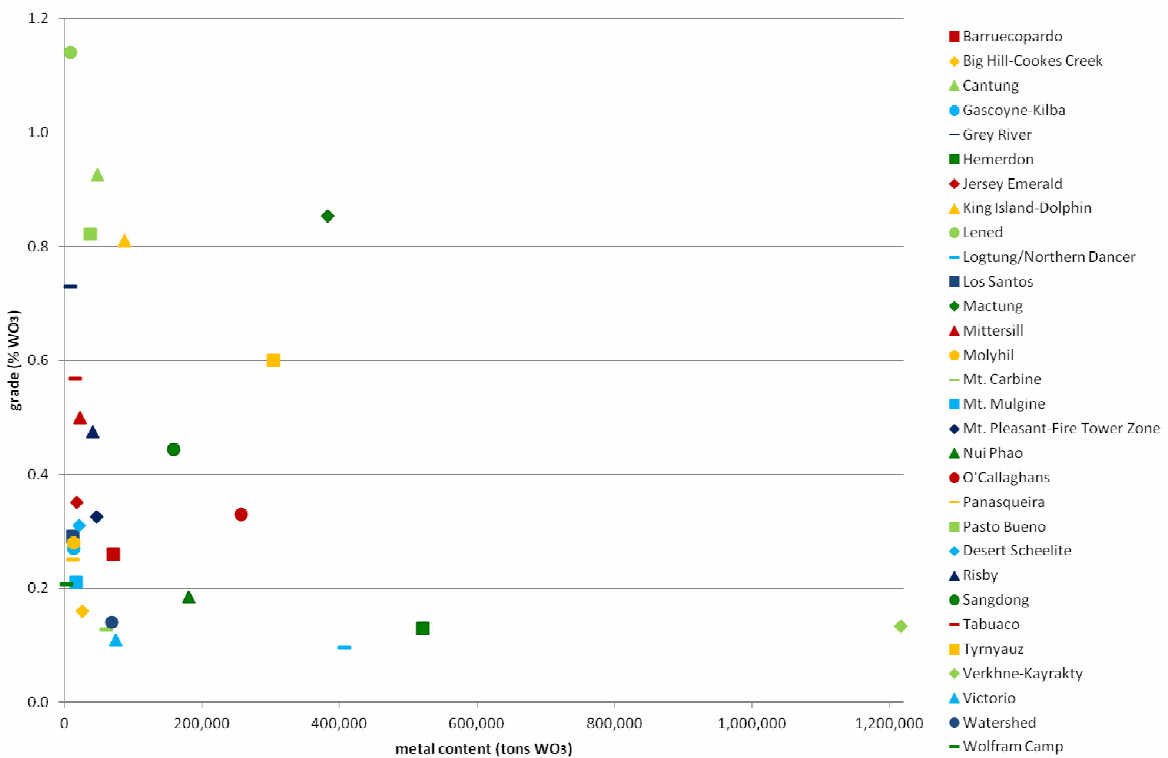


Figure 5.4: Resource estimates (indicated + inferred) given as WO₃-content in metric tons of and WO₃-grade in percent for selected tungsten mine projects.

Assessment and redevelopment of the former scheelite mine on King Island, Australia is performed by King Island Scheelite Ltd. in cooperation with Hunan Nonferrous Metals Corporation Ltd. The indicated resource for Dolphin deposit is estimated at 10.8 million tons at a grade of 0.81% WO_3 with probable reserve of 1.9 million tons at a grade of 0.55% WO_3 . The Canadian Adex Mining Inc. owns the Mt. Pleasant mine located in New Brunswick, Canada. The Fire Tower Zone of the Mt. Pleasant deposit is a W-Mo deposit with indicated and inferred resources of about 14.3 million tons at a grade of 0.33% WO_3 and 0.21% MoS_2 . Northcliff Resources Ltd. owns the Sisson Brook W-Mo porphyry deposit in New Brunswick, Canada. The proven and probable mineral reserves total 334.4 million tons at 0.066% WO_3 and 0.021% Mo. The Molyhil deposit in the Northern Territory, Australia, with probable reserves of 3 million tons at a grade of 0.31% WO_3 and 0.12% Mo is held by Thor Mining PLC.

Black Fire Minerals Ltd., a subsidiary of Thor Mining PLC, is developing the Pilot Mountain project in Nevada, United States, with a resource estimate of indicated and inferred resources of 6.79 million tons of ore at 0.31% WO_3 for the Desert Scheelite deposit. Carbine Tungsten Ltd. (formerly Icon Resources) owns the Mt. Carbine concession and currently produces circa 100 tons WO_3 per month by reprocessing of about 12 million tons of low-grade stockpiles, but also develops the Mt. Carbine mine with an indicated and inferred resource of 47.3 million tons of ore at 0.13% WO_3 . Vital Metals Ltd. develops the Watershed scheelite deposit in Queensland containing an estimated total mineral resource of 49.2 million tons of ore at a grade of 0.14% WO_3 . Playfair Mining Ltd. owns several Canadian tungsten deposits; the Gray River deposit in Newfoundland and the Clea, Risby and Lened scheelite-bearing skarn deposits in the Yukon and Northwest Territories.

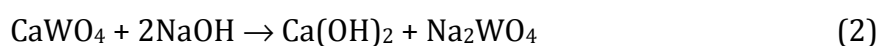
Total global reserves are estimated at 2.76 million tons of tungsten metal with about 45% situated in China with about 1.24 million tons of proven tungsten reserves (Liedtke & Schmidt, 2014).

Another very important source of tungsten is scrap and it is estimated that up to 30 to 40% of tungsten demand is supplied by recycling (Lassner & Schubert, 2009; Liedtke & Schmidt, 2014). Moreover, tungsten scrap is comparatively cheap and also contains very high tungsten grades making it attractive for processors.

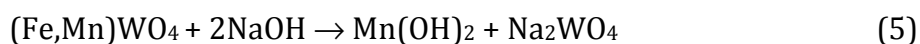
5.3 Processing and beneficiation of tungsten

Tungsten ores are mostly mined by underground methods. The tungsten content generally ranges between 0.1 and 2% WO₃. Exploitable tungsten ores commonly contain 0.7% WO₃ in vein deposits, 0.3% WO₃ in high tonnage underground mines and down to 0.1% WO₃ in open pit operations (Pohl, 2011). Ore dressing usually takes place at the mining site to produce concentrates with marketable grades ranging from 65 to 75% WO₃. The wolframite and scheelite ores are separated mechanically from the gangue minerals by gravity in spirals or on shaking tables due to their high densities. Further on, wolframite is obtained by magnetic separation and scheelite by froth flotation, respectively (Singh Gaur, 2006). Additionally, sulphides are won as a byproduct by flotation or by magnetic separation (Hausen, 1989). Both tungsten raw materials are treated differently in the processing plant.

The major intermediate product in the modern hydrometallurgical processing of tungsten ores (wolframite and scheelite) is ammonium paratungstate (APT). In a first step, the tungsten concentrates (scheelite, wolframite and mixed ore concentrates) are either treated with sodium hydroxide (NaOH) or sodium carbonate (Na₂CO₃) resulting in a solution containing dissolved sodium tungstate and an insoluble residue (Roskill, 1986; Lassner & Schubert, 1999). Scheelite ores are treated either with sodium hydroxide (2) or are roasted with aqueous sodium carbonate (Na₂CO₃) in an autoclave between 190 and 225 °C (3) to produce sodium tungstate (Roskill, 1986; Singh Gaur, 2006).

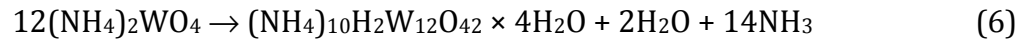


Wolframite ores are processed into sodium tungstate either by an alkali roasting process with sodium carbonate (4) between 800 and 900 °C (Roskill, 1986) or by a leaching process with sodium hydroxide (5) at approximately 120 °C (Singh Gaur, 2006).

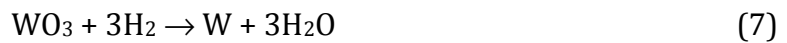


In the following, sodium tungstate is transformed to ammonium tungstate with ammonium hydroxide. In a modern solvent-extraction method, tungsten is extracted from the slightly acidic sodium tungstate solution by aliphatic amines dissolved in an organic solvent (Hausen, 1989; Singh Gaur, 2006). The basic principle is to extract isopolytungstate species from the slightly acidic aqueous solution by the reagent

dissolved in the organic phase, thus separating the tungstate from the sodium ions (Hausen, 1989; Lasser & Schubert, 1999). Finally, ammonium paratungstate $(\text{NH}_4)_{10}\text{H}_2\text{W}_{12}\text{O}_{42} \times 4\text{H}_2\text{O}$ crystallises from this solvent by evaporation (6), whereby ammonia (NH_3) and water are volatilised (Lassner & Schubert, 1999).



Several intermediate tungsten oxide compounds are formed from APT during its thermal decomposition in the temperature range from 300 to 800 °C. The blue oxide ($\text{W}_{20}\text{O}_{58}$) is formed at reducing and the yellow oxide (WO_3) at oxidising conditions during calcination (Hausen, 1989; Lasser & Schubert, 1999). The tungsten trioxide is finished to tungsten metal by reduction with hydrogen (7) at high temperatures of 1000 to 1200 °C.



Changes in the reduction parameters allow the production of tungsten powders with various characteristics such as different grain size, grain size distribution, and powder density (Singh Gaur, 2006). The tungsten metal powders are further processed into mill products such as tungsten rods, wire and sheets. Chemical processing plants producing intermediate tungsten goods like APT usually prefer scheelite concentrates with low molybdenum content. However, scheelite concentrates with relatively high molybdenum contents are processed in the steel industry (in the production of tool steel and high speed steel) by charging these directly into the furnaces (Werner et al., 1998).

Iron-rich wolframite (ferberite) ores are also processed directly by reduction with carbon to produce ferrotungsten (8).



5.4 Pricing

In contrast to other metals, tungsten is not traded on a stock exchange and therefore no official market exists for tungsten goods. However, the price for tungsten is based on information from producers, consumers, traders and users by the present supply and demand situation (DesLauriers, 2005). The actual price quotation is published by the London Metal Bulletin twice a week. In former times, the price was quoted for tungsten raw materials like wolframite or scheelite ore concentrates with a minimum grade of 65% of tungsten trioxide (WO_3). Recently, the traded commodity changed to ammonium paratungstate (APT) because China, the biggest supplier of ore concentrates in the past, renewed its trading strategy and gave preference to the sale of upgraded tungsten

products (Lassner & Schubert, 1999). Tungsten concentrates and APT are sold in U.S. dollars per metric ton unit (US\$/mtu) of WO_3 . This dimension unit represents 1% of a metric ton and is equal to 10 kg of WO_3 . Hence, one metric ton unit of WO_3 contains 7.93 kg of tungsten metal.

Also political influences play an important role due to the strategic importance of the metal (Lassner & Schubert, 1999; Chakhmouradian et al., 2015). A strategic metal can be defined as *“a commodity with no satisfactory substitute which is essential for the national industry or military applications, but is not supplied by domestic producers and has to be imported from other countries”* (Lassner & Schubert, 1999). The strategic importance resulted in stockpiling of large quantities of tungsten material in the United States of America and the Soviet Union during the Cold War. The accumulation of government stockpiles or their release has sometimes acted severely as a disturbance or stabilising effect on the market by avoiding shortages (Lassner & Schubert, 1999; Chakhmouradian et al., 2015). With the end of the Cold War, tungsten materials were released from former Soviet and United States stockpiles.

In 1990 with the end of the Cold War, the global tungsten situation changed dramatically. Chinese and Russian producers became major exporters on the global market and pushed the price down by flooding the market with low-priced tungsten concentrates (DesLauriers, 2005). From 1990 to the early 2000's the availability of tungsten consistently exceeded supply and the prices had fallen below the production costs of most other producers (GBRM, 2008). This resulted in the shutdown of most non-Chinese tungsten mines. Now the global tungsten market is dominated by the China as the world's leading producer and exporter of tungsten ore concentrates. In 2002 the Chinese government restricted export licenses, removed the 13% export tax rebates and forced the processing of the ores to upgraded products. The traded tungsten compounds changed from raw materials to intermediate products such as ammonium paratungstate, tungsten oxides and ferrotungsten. Therefore the processing companies outside China are facing shortages of ore concentrates and urgently seek for alternative sources of raw materials (GBRM, 2008).

As a result of the oversupply situation in the years before 2005 the price for APT ranged at comparatively low levels between 65 and 95 US\$/mtu, but at the beginning of 2005 real shortages became evident and prices started to soar. The price for APT climbed from about 90 US\$/mtu in December 2004 to 290 US\$/mtu in June 2005. The price jumped again up to 469 US\$/mtu in June 2011. The rapid increase of the Chinese

demand for tungsten products, especially in the steel and construction industries, was the result of the great demand of China’s booming economy. This circumstance and the closure of several mines outside China in the years before limited the availability of tungsten products on the global market. Furthermore, China has become a major importer of tungsten goods and additionally reduced its domestic mining activities (GBRM, 2008). Therefore the supply cannot keep up with demand and the supply deficit leads to rising tungsten prices. China actually produces about 85% of the global mine production and uses most of its production domestically. This will further tighten the market and pushes the tungsten price at higher levels. These aspects show that China holds a favourable position to control the tungsten market and in particular the price for tungsten products. The Chinese government restricted the export of tungsten goods and successively reduced the export quota from 16000 tons in 2010 down to 13582 tons for 2014 (ITRI, 16.12.2013; Liedtke & Schmidt, 2014).

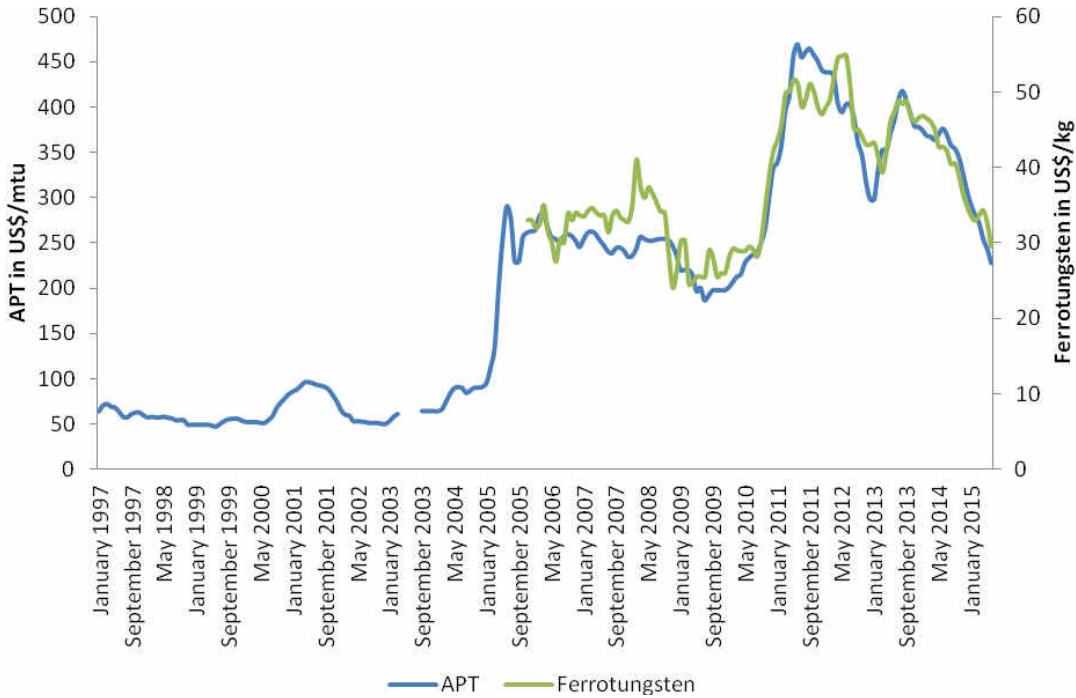


Figure 5.5: Price chart for ammonium paratungstate (APT) and ferrotungsten (FeW) from January 1997 to June 2015 (Metal Bulletin and BGR database)

The global economic and financial crisis in 2008 slightly affected the tungsten price which fell from 250 US\$/mtu APT to about 190 US\$/mtu APT in July 2009. Generally, the tungsten price has been in a more or less steady state over the years and is considerably less fluctuant than other metal prices. The future trend of the tungsten pricing is dependent on the balance between the demand and supply situation, which is

directly linked to Chinese tungsten production and consumption. Nevertheless, the global demand for tungsten is rising especially in China and there is a growing global supply deficit for tungsten since 2004. In 2005, the tungsten demand exceeded 60000 tons for the first time. These facts probably led to rising prices of up to 300 US\$/mtu, caused by Chinese export restrictions and limited supply from non-Chinese producers. Therefore access to producing mines and exploration projects outside China are important for Western industries which desire to become independent from Chinese producers. This leads to increased exploration and mining activities outside China due to rising supply concerns and higher prices. There are only a few producing tungsten mines outside China.

5.5 Future trends

The tungsten market and demand is in steady state at present. There are no adequate substitutes for tungsten in current applications. Possible exceptions may be molybdenum for tungsten as an alloying additive in the production of high-speed steels or ceramics, polycrystalline diamond, and carbides or nitrides of other metals as potential substitutes for sintered tungsten carbide (Werner et al., 1998). However, striking innovative applications for the future are not on the way, except for interesting applications of tungsten in fusion reactors. For example, the ITER research project (International Thermonuclear Experimental Reactor) is currently building fusion reactor plant for production of electric energy. Utilization of tungsten as plasma-facing shielding material on divertors seems promising and about 100 tons of tungsten are needed for the construction of the reactor (Lassner & Schubert, 2009).

6 Tin and tungsten deposits

6.1 Geochemistry and granites

In general, the formation of tin and tungsten deposits is closely linked to late-stage, highly evolved, granitic intrusions (Figures 6.1 & 6.3) with shallow intrusion levels within orogenic belts (e.g. the Variscides of Western Europe and the Kibara belt of Central Africa). Large volumes of granitic magmas are produced during continent-continent collisions, but also in anorogenic continental settings during rifting and crustal thinning (Robb, 2005). However, recent isotopic studies propose that also influx of volatiles from the mantle (e.g., carbon and sulphur) takes part in the formation of melts related to tin deposits (Walshe et al., 2011). Nevertheless, the source of the metals tin and tungsten for the formation of ore deposits is usually assumed to be the continental crust.

As granitic magmatism is a crucial factor in the formation of Sn-W deposits, the most important classification schemes for granites are summarised in the following:

- The well-known aluminium saturation index (ASI) splits the granitic rocks into three groups depending on the alumina content relative to the alkali plus calcium contents: peralkaline ($\text{Al}_2\text{O}_3 < \text{Na}_2\text{O} + \text{K}_2\text{O}$), metaluminous ($\text{Na}_2\text{O} + \text{K}_2\text{O} < \text{Al}_2\text{O}_3 < \text{Na}_2\text{O} + \text{K}_2\text{O} + \text{CaO}$), and peraluminous ($\text{Al}_2\text{O}_3 > \text{Na}_2\text{O} + \text{K}_2\text{O} + \text{CaO}$).
- Ishihara (1977) used the occurrence of specific minerals to separate granitic rocks into magnetite- or ilmenite-series (without magnetite) granites representing either oxidising or reducing conditions. These two rocks series are also associated with distinct ore deposit types; magnetite series magmatism is related to deposits of base metal (Cu, Pb, and Zn) sulphides, Au and Ag, Cu-Mo porphyries and scheelite mineralisation, whereas ilmenite series granitic rocks are characterized by cassiterite, wolframite, beryl, fluorite, and pegmatite deposits (Figure 6.1; Ishihara, 1981).
- Granitic magmas can also be classified regarding their source into three major categories: S-type, I-type (Chappell & White, 1974; White & Chappell, 1977), and A-type granites (Loiselle & Wones, 1979).
 - S-type magmas are generated by partial melting of metasedimentary source rocks and are characterised by peraluminous compositions ranging from granodiorite to granite, high K/Na ratios, high initial strontium isotope ratios ($^{87}\text{Sr}/^{86}\text{Sr}$) indicating a continental crustal source, and relatively reduced system (Clemens, 2003).

- I-type magmas are formed by partial melting of igneous rocks. These melts comprise a wide compositional range from gabbro to granite, are generally metaluminous with low K/Na ratios and formed at relatively oxidised conditions. Generally speaking, magnetite series granites are comparable to I-type and ilmenite series are similar to S-type granites. However, differences between the two classification schemes are given by Takahashi et al. (1980).
- A-type (anorogenic, anhydrous or alkaline) magmas (Whalen et al., 1987; Bonin, 2007) are formed by high-temperature (>830 °C, Clemens et al. 1986) partial melting of granulites which represent the residue remaining from generation of orogenic I-type granite magmas (Collins et al., 1982). The A-type granites are commonly related to extensional rift systems and the melts are generated by decompression melting (Sears et al., 2005) or by mafic underplating, hereby the lower crust is melted by uprising mantle-derived melts (Bridgwater et al., 1974; Clemens et al., 1986). Generally, A-type magmas are weakly alkaline to weakly peraluminous with high Na₂O and low CaO contents, enriched in high field strength elements (HFSE), and high Ga/Al ratios (Collins et al., 1982; Clemens et al, 1986).

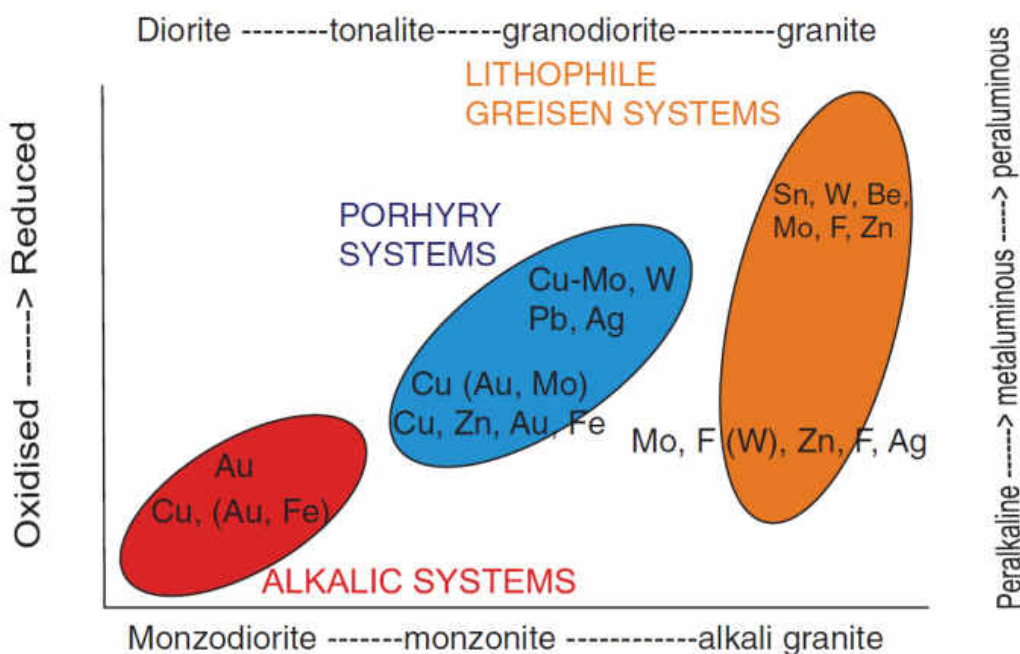


Figure 6.1: Ore systems and metal associations in relation to redox conditions and the differentiation of the magma indicated by the range from intermediate to felsic intrusions (Pirajno, 2009)

Table 6.1: Compilation of whole rock geochemical data for some granitic intrusions (including pegmatites) related to Sn and W deposits (references are listed below the table). Element oxides plus fluorine are given in wt.% and trace elements are given in ppm. Please note that total iron is given as FeO*.

element/oxide	unit	Bobbejaankop	Chorolque	San Rafael	Madeira	Tanco	Greenbushes	Land's End	Krásno	Spokoynoye	Mount Carbine
SiO ₂	wt. %	76.26	68.7	68.66	70.74	76.04	69.14	73.23	74.47	75.55	72.45
TiO ₂	wt. %	0.08	0.57	0.41	0.03	0.01	0.06	0.15	0.04	0.06	0.26
Al ₂ O ₃	wt. %	11.62	14.8	15.57	12.52	13.62	14.67	14.13	14.41	13.60	14.03
FeO*	wt. %	2.27	4.69	4.24	2.75	0.16	1.31	1.24	0.95	1.04	2.15
MnO	wt. %	0.02	0.02	0.07	0.04	0.18	n. a.	0.02	0.07	0.12	0.04
MgO	wt. %	0.00	1.39	1.25	0.07	0.01	0.23	0.22	0.05	0.22	0.49
CaO	wt. %	0.90	0.14	1.11	0.53	0.15	0.97	0.65	0.33	0.45	1.90
Na ₂ O	wt. %	2.40	0.46	2.93	5.06	3.81	4.82	2.69	3.50	3.96	3.04
K ₂ O	wt. %	5.24	2.65	4.90	4.56	2.96	2.07	5.24	4.39	4.00	4.55
P ₂ O ₅	wt. %	0.02	0.11	0.19	0.04	0.86	0.61	0.31	0.33	n. a.	0.10
F	wt. %	0.54	0.07	n. a.	2.44	0.12	n. a.	0.62	0.42	0.41	0.08
Li	ppm	11	n. a.	n. a.	506	3417	2325	450	n. a.	109	n. a.
Be	ppm	n. a.	n. a.	n. a.	25	168	125	2	n. a.	n. a.	n. a.
B	ppm	14	5918	n. a.	n. a.	149	n. a.	910	n. a.	n. a.	n. a.
Sc	ppm	0.5	n. a.	n. a.	n. a.	17	n. a.	3.9	bdl	n. a.	6.9
V	ppm	n. a.	n. a.	48	n. a.	n. a.	n. a.	4	bdl	n. a.	12
Cr	ppm	n. a.	62	45	n. a.	n. a.	n. a.	2.7	bdl	n. a.	3.4
Cu	ppm	56	31	16	n. a.	n. a.	n. a.	6	9	n. a.	3
Zn	ppm	84	30	130	1076	48	n. a.	23	55	n. a.	48
Ga	ppm	n. a.	n. a.	n. a.	61	74	n. a.	25.8	39	n. a.	11.8
As	ppm	n. a.	100	n. a.	25	n. a.	79	3	5	n. a.	n. a.
Rb	ppm	420	161	336	4789	5244	4159	675	1100	385	200
Sr	ppm	6	72	210	22	n. a.	65	29	14	72	103
Y	ppm	151	n. a.	n. a.	155	n. a.	n. a.	13	9	n. a.	56
Zr	ppm	250	135	150	4904	27	27	66	31	n. a.	115
Nb	ppm	53	n. a.	9	1173	56	92	26	40	n. a.	9.5
Mo	ppm	5	2.1	n. a.	n. a.	n. a.	n. a.	0.7	bdl	n. a.	n. a.
Ag	ppm	n. a.	1.2	n. a.	n. a.	n. a.	n. a.	0.1	bdl	n. a.	n. a.
Sn	ppm	164	170	13	1368	128	707	78	87.6	83.5	n. a.
Sb	ppm	1.1	18	n. a.	2	n. a.	n. a.	0.1	bdl	n. a.	n. a.
Cs	ppm	1.5	7	n. a.	41	2649	501	48	105.8	33	9.8
Ba	ppm	96.9	229	721	27	18	n. a.	48	26.2	n. a.	365
Hf	ppm	12.8	3.9	n. a.	293	10	n. a.	2.1	bdl	n. a.	n. a.
Ta	ppm	6.3	1.5	n. a.	189	300	150	8.8	16	24	n. a.
W	ppm	n. a.	24	n. a.	18	0.8	n. a.	18	14	n. a.	n. a.
Pb	ppm	94	29	59	581	39	n. a.	7	12	n. a.	38
Bi	ppm	n. a.	28	n. a.	n. a.	n. a.	n. a.	n. a.	4	n. a.	n. a.
Th	ppm	53	13	n. a.	514	n. a.	11.3	10.9	17	n. a.	20.7
U	ppm	16.5	4	n. a.	337	41	12.6	6.7	8	n. a.	5.4

Mean values for Bobbejaankop granite are calculated from 23 analyses by Pollard et al. (1991)

Mean values for Chorolque porphyry are calculated from 18 analyses by Dietrich et al. (2000)

Mean values for San Rafael fresh granite are calculated from 7 analyses by Kontak et al. (2002)

Mean values for Madeira (apo)granite calculated from mean of analyses (n=7) by Horbe et al. (1991), from mean of analyses (n=5) by Lenharo et al. (2003), and from mean of analyses (n=5) by Costi et al. (2009)

Values for Tanco are from bulk pegmatite analysis by Stilling et al. (2006)

Values for Greenbushes are bulk pegmatite analysis by Partington et al. (1995)

Values for Land's End granite are from whole rock analysis (GPE20) by Chappel & Hine (2006)

Values for Krásno are from whole rock analysis of topaz-albite granite (CZ01; own unpublished data)

Mean values for Spokoynoye granite are calculated from 2 analyses (S-1 & S-2) by Badadina et al. (2006)

Values for Mt Carbine granite are from whole rock analysis (DCC83) by Champion & Bultitude (2013)

In general, tin and tungsten deposits are related to granitic rocks which are characterised by high silica, aluminium and alkali contents and considerable enrichments in incompatible elements (Table 6.1). For example, tin and tungsten are geochemically incompatible elements in granitic melts and are not readily substituted into the main rock-forming minerals because of their ionic radius and/or valence and consequently become enriched during magmatic differentiation (e.g., crystal fractionation). Such elements are concentrated in the residual melts or subsequently in volatile-rich fluids. The incompatible elements are divided into two groups depending either on large ionic size called large ion lithophile elements (LILE: e.g., Cs⁺, Rb⁺, K⁺, Ba²⁺, Pb²⁺, Sr²⁺) or high valence state represented by the high field strength elements (HFSE: e.g., U⁶⁺, Nb⁵⁺, Ta⁵⁺, Ti⁴⁺, Zr⁴⁺, Hf⁴⁺, but also W⁶⁺ and Sn⁴⁺). An additional group can be defined by variably charged cations with small ionic radii (abbreviated as SIR in Figure 6.2) such as Li⁺, Be²⁺, B³⁺ and P⁵⁺.

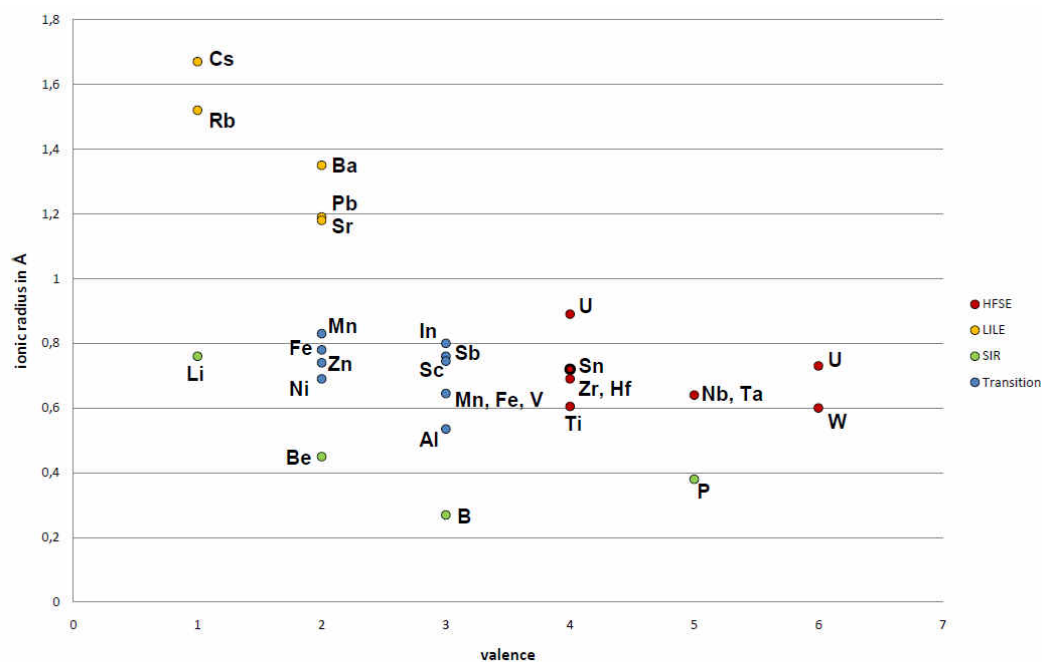


Figure 6.2: Elements grouped by their ionic radii and valence states into high field strength elements (HFSE), large ion lithophile elements (LILE), elements with variable valences and small ionic radii (SIR), and elements falling in between (Transition)

Regarding the origin of the metals, there are two contrasting concepts explaining metal enrichment in melts and formation of ‘specialised’ granites (Lehmann, 1987): magmatic differentiation (Groves & McCarthy, 1978; Lehmann, 1982; Williamson et al., 2010) versus geochemical heritage (Pollard et al., 1983; Eugster, 1984). Generally, all tin and tungsten deposits are formed by magmatic differentiation and subsequent partition into the residual melts or into volatile-rich fluids as outlined above, although there are

several subdivisions of deposit types and both metals are not always found together in a single deposit (for example, hübnerite deposits and scheelite skarn deposits associated with oxidised or I-type granites are commonly devoid of tin). The precipitation of the metals and formation of ore deposits are dependent on temperature, pressure, pH-values, Eh-conditions, behaviour of the fluid (e.g. fluid mixing and fluid-rock interaction) and the surrounding country rock (e.g. Strong, 1988).

Excursus on the geochemistry of Sn and W:

In the course of the formation of granite-related deposits, the enrichment of Sn and W is schematically dependent on two phases. In the first magmatic phase, the enrichment is controlled by the partition coefficient between melt and early crystals. Tin, W and other HFSE are strongly concentrated in residual melts. The magmatic phase is followed by the hydrothermal stage and the concentration of Sn and W in the ore solutions is controlled by element partitioning between final melt and exsolving magmatic fluids (Heinrich, 1990; Pohl, 2011).

Geochemical behaviour of Sn in melts and fluids

Solubility of Sn in melts is mainly dependent on its oxidation state, either as stannous (Sn^{2+}) or stannic (Sn^{4+}) ion, which is mainly controlled by oxygen fugacity and to a lesser extent by composition of the melt; but basically Sn^{2+} is significantly more soluble than Sn^{4+} (Ishihara, 1981; Eadington, 1988; Taylor & Wall, 1992; Linnen et al., 1995; Linnen et al., 1996; Farges et al., 2006). In oxidised melts (I-type or magnetite series magmas) with high oxygen fugacity, Sn^{4+} is present which is readily substituted for Fe^{3+} or Ti^{4+} into the lattice of rock-forming minerals such as biotite, pyroxene, amphibole, ilmenite or titanite and the remaining Sn is insufficient to form an ore deposit (Taylor & Wall, 1992). On the contrary, reduced melts (S-type or ilmenite series magmas) have low oxygen fugacity and Sn^{2+} is not suitable for substitution into early rock-forming minerals (Ishihara, 1981). Consequently, Sn^{2+} is strongly incompatible and accumulates in the residual melts which form highly evolved granites (Linnen et al., 1995). Therefore, reduced ilmenite series or S-type magmas have a higher Sn solubility than oxidised magnetite series or I-type melts. This was also demonstrated by experiments (Parparoni et al., 2010). Addition of volatiles like Cl and F also enhances Sn solubility in peraluminous melts (Bhalla et al., 2005; Keppler, 1993) and Sn is significantly enriched in highly evolved melts with high H_2O , F, and P contents (Thomas & Webster, 2000). Highly evolved, granitic melts may contain large amounts of dissolved Sn (up to 7000 ppm Sn; Thomas & Webster, 2000) which were measured in melt inclusions (Webster et al., 1997; Thomas & Webster, 2000; Borisova et al., 2012), natural rock compositions (up to 2745 ppm Sn in the Qiguling rhyolite; Xie et al., 2013; Cuney et al., 1992), and experimental studies (Bhalla, 2005). Even at low temperatures close to the solidus of the granitic melt, high Sn concentrations up to 0.3 wt.% SnO_2 can be dissolved (Bhalla, 2005) and this indicates that natural, granitic melts are mostly undersaturated in Sn (Štemprok, 1990; Linnen & Cuney, 2005). An increase in oxygen fugacity probably causes precipitation of primary magmatic cassiterite from these melts (Linnen et al., 1995).

In the next stage, it is important to examine under which conditions Sn preferentially partitions into the melt or into the fluid. Partitioning experiments between granitic melts and aqueous fluids show that the fluid-melt partition coefficient

($KD_{\text{fluid/melt}}$) of Sn strongly increases with high Cl content in the solution (Manning & Pichavant, 1988; Keppler & Wyllie, 1991), but changes in the F concentration do not have any significant influence on the fluid-melt partition coefficient (Keppler & Wyllie, 1991). This indicates that at high Cl contents in the fluid, Sn preferentially partitions from the melt into the fluid ($KD_{\text{fluid/melt}} > 1$) and cassiterite subsequently precipitates in hydrothermal quartz veins. On the other hand, low Cl concentrations favour partitioning of Sn into the melt and primary magmatic cassiterite may crystallise from the melt, for example in pegmatites. This is consistent with the observations of Borisova et al. (2012) that precipitation of cassiterite can occur from hydrous peraluminous pegmatitic melts and Cl-rich brines. Nevertheless, Zajacz et al. (2008) demonstrate that partition coefficients of Sn are not only dependent on the Cl content in the fluid, but other physicochemical parameters (e.g. pH value, oxygen fugacity) also play an important role.

Contrasting to its behaviour in melts, Sn forms soluble complexes with Cl⁻, F⁻, and [OH]⁻ in hydrothermal fluids (Patterson et al., 1981; Jackson & Helgeson, 1985; Cigala et al., 2012), but Sn could also be transported in the vapour phase under certain HCl-rich conditions (Migdisov & Williams-Jones, 2005). In general, the role of Cl as complexing agent in natural, hydrothermal fluids (or brine with >26 wt.% NaCl equivalent) is considerably more important for the transport of Sn than the influence of F (Heinrich, 1990; Taylor & Wall, 1993; Wood & Samson, 1998). Divalent Sn is mobilized as various chloride complexes like [SnCl]⁺, SnCl₂, [SnCl₃]⁻ or [SnCl₄]²⁻ over a wide range from reduced to moderately oxidised conditions at concentrations from hundreds up to thousands of ppm (Heinrich, 1990; Taylor & Wall, 1993; Wood & Samson, 1998; Sherman et al., 2000). Other Sn complexes of minor importance are stannous fluoride compounds such as [SnF]⁺, SnF₂ or [SnF₃]⁻ in fluids with high F concentrations (Klintsova et al., 1975; Polya, 1989) and hydroxide complexes such as Sn(OH)₂ and Sn(OH)₄ at higher pH-values (Jackson & Helgeson, 1985).

Basically, the solubility of Sn is significantly higher at acidic, reducing conditions and the dominant Sn species are chloride complexes (Lehmann, 1990; Wood & Samson, 1998; Migdisov & Williams-Jones, 2005). This implies that precipitation of cassiterite is dominantly controlled by increasing oxygen fugacity and decreasing acidity (increasing pH-value) and Cl content in the fluid (Taylor & Wall, 1993; Sherman et al., 2000). Oxidising conditions change the speciation of Sn from Sn²⁺ to Sn⁴⁺ and cassiterite is precipitated because of the lower solubility of Sn⁴⁺ (Linnen et al., 1996; Farges et al., 2006; Paparoni et al., 2010). However, decreasing salinity of the fluid also causes destabilisation of the chloride complexes resulting in precipitation of cassiterite (Heinrich, 1990; De Clercq, 2012). Fluid inclusion studies indicate that cassiterite is mainly precipitated from fluids with temperatures ranging from 200 to 500 °C and pressures below 2000 bars and salinities generally less than 20 wt.% NaCl equivalent (e.g., Kelly & Turneaure, 1970; Haapala & Kinnunen, 1979; Kelly & Rye, 1979; Patterson et al., 1981; Collins, 1981; Haapala & Kinnunen, 1982; Roedder, 1984; Giuliani, 1987; Mangas & Arribas, 1987; Mangas & Arribas, 1988; Jackson et al., 1989; Campbell & Panter, 1990; Layne & Spooner, 1991; Linnen & Williams-Jones, 1994; Ren et al., 1995; Markl & Schumacher, 1996; Polya et al., 2000; Sherman et al., 2000; Müller et al., 2001; Wilkinson, 2001; Somarin & Ashley, 2004; Bettencourt et al., 2005; Macey & Harris, 2006; Wagner et al., 2009; Sushchevskaya & Bychkov, 2010; De Clercq, 2012; Dolníček et al., 2012). Significantly higher salinities of up to about 45 wt.% NaCl equivalent are reported from the Sn deposits of Bolivia (Kelly & Turneaure, 1970; Roedder, 1984; Sugaki et al., 1988) and higher temperatures are reported from skarn deposits (e.g. the JC tin skarn deposit in Yukon Territory, Canada; Layne & Spooner, 1991).

Geochemical behaviour of W in melts and fluids

Experiments show that W is almost exclusively present in its hexavalent state in silicate melts, especially under oxidising conditions (Ertel et al., 1996; Linnen, 1998b; Linnen, 2005; O'Neill et al., 2008; Wade et al., 2013; Che et al., 2013); the only exception is the occurrence of W^{4+} at extremely low oxygen fugacity (O'Neill et al., 2008). The minimum solubility of wolframite (in this case hübnerite) is lowest at an ASI of about 1.0 (about 3000 ppm W at 800 °C and 2 kbar), but wolframite solubility increases strongly with decreasing values for ASI in peralkaline compositions (up to 25000 ppm W at 800 °C and 2 kbar) and increases slightly with increasing ASI in peraluminous melts (Linnen & Cuney, 2005; Che et al., 2013). Some fluxing elements like P increase the wolframite solubility in granitic melts (Che et al., 2013), but Li has no effect (Linnen, 1998b). Tungsten present as W^{6+} is an incompatible element and W is consequently enriched in latest and most evolved melt fractions.

Partition coefficients ($KD_{\text{fluid/melt}}$) indicate that W partitions in favour of the fluid if pure aqueous fluids are present, especially without any chloride and fluoride contents in the fluids (Keppler & Wyllie, 1991; Wood & Samson, 2000), but some studies suggest that $KD_{\text{fluid/melt}}$ of W also increase with increasing chloride content in the fluids (Manning & Henderson, 1984; Zajacz et al., 2008). Zajacz et al. (2008) state that these discrepancies occur because $KD_{\text{fluid/melt}}$ of W is not only dependent on the chlorine content of the fluid but on a combined effect of other additional parameters (e.g., ASI of the melt, pH value, and chlorine content in the fluid).

The dominant W species dissolved in moderately acidic, hydrothermal fluids are H_2WO_4 , $[HWO_4]^-$, and $[WO_4]^{2-}$ (Foster, 1977; Wesolowski et al., 1984; Ivanova, 1986; Seward & Barnes, 1997; Wood & Samson, 1998; Wood & Samson, 2000). The speciation of these W compounds is controlled by the acidity of the solution; H_2WO_4 species is stable at acidic conditions, whereas $[HWO_4]^-$ occurs close to neutral and $[WO_4]^{2-}$ is stable at alkaline pH values (Ivanova & Khodakovskiy, 1968; Wesolowski et al., 1984; Ivanova, 1986; Wood, 1992). These simple tungstate ions are stable at higher temperatures, whereas polymeric species become stable with decreasing temperature (Wesolowski et al., 1984; Seward & Barnes, 1997); but these complexes with Cl^- , F^- , $[CO_3]^{2-}$, $[PO_4]^{3-}$ or alkalies are of minor importance for the transport of W in hydrothermal fluids (Higgins, 1980; Wood & Vlassopoulos, 1989; Keppler & Wyllie, 1991; Wood, 1992; Wood & Samson, 2000). Generally, wolframite is precipitated from acidic fluids with temperatures ranging from 200 to 500 °C, pressures from 200 to 1500 bars, variable CO_2 contents and salinities of mostly less than 15 wt.% NaCl equivalent (e.g., Kelly & Turneure, 1970; Landis & Rye, 1974; Ivanova et al., 1978; Kelly & Rye, 1979; Casadevall & Rye, 1980; Campbell et al., 1984; Roedder, 1984; Ball et al., 1985; Ivanova, 1986; Ivanova & Naumov, 1986; Campbell & Robinson-Cook, 1987; Giuliani et al., 1988; Thorn, 1988; Jackson et al., 1989; Campbell & Panter, 1990; Lüders, 1996; Wood & Samson, 2000; Polya et al., 2000; Wilkinson, 2001; Rios et al., 2003; Zhang et al., 2003; Somarin & Ashley, 2004; Romer & Lüders, 2006; Sushchevskaya & Bychkov, 2010; Liu et al., 2011; Wei et al., 2012; De Clercq, 2012; Moura et al., 2014). Other authors suggest that wolframite may also form under epithermal conditions at temperatures below 250 °C (Bailly et al., 2002) or W may also be transported by high temperature (650 to 750 °C) vapours in the form of H_2WO_4 species (Bernard et al., 1990). Transport and precipitation of W takes place in the same valence state (W^{6+}) and is therefore independent of oxygen fugacity, but the oxygen fugacity probably has strong influence if either ferberite or hübnerite are formed. At increasing oxygen fugacity, Fe^{2+} oxidises to Fe^{3+} and this results in a preferred formation of Mn-rich wolframite or hübnerite (Shibue, 1982; Mignardi et al., 1998; Botto et al., 2000). Dominant parameters controlling the

deposition of wolframite are the activity of the ions (Fe^{2+} , Mn^{2+} , $[\text{WO}_4]^{2-}$) in the ore fluid, pH conditions, composition of the surrounding wall rock, fluid-rock interaction, and fluid mixing (Barabanov, 1971; Groves & Baker, 1972; Horner, 1979; Ivanova & Naumov, 1986; Nakashima et al., 1986, Mignardi et al., 1998; Wei et al., 2012). Loss of CO_2 and increasing pH are the major factors controlling the precipitation of wolframite from CO_2 -rich fluids (Higgins, 1980; Roedder, 1984; Ball et al., 1985; Higgins, 1985).

6.2 Detailed descriptions of tin-tungsten deposit types

Tin and tungsten ores occur in different deposit types which are more or less related to a granitic intrusion (Figure 6.3). In the following the various Sn and W deposit types are described in detail and are put into one of the general groups: primary magmatic, transitional magmatic-hydrothermal, hydrothermal, stratiform-stratabound, massive sulphide (it has to be noted that the latter two may also be added to the hydrothermal group; but these groups occur in different geological settings with specific mineral assemblages and are treated here separately for clarity) or secondary placer deposits. These groups are arranged from broadly higher to lower temperatures of formation and from roughly deeper to shallower levels in the crust.

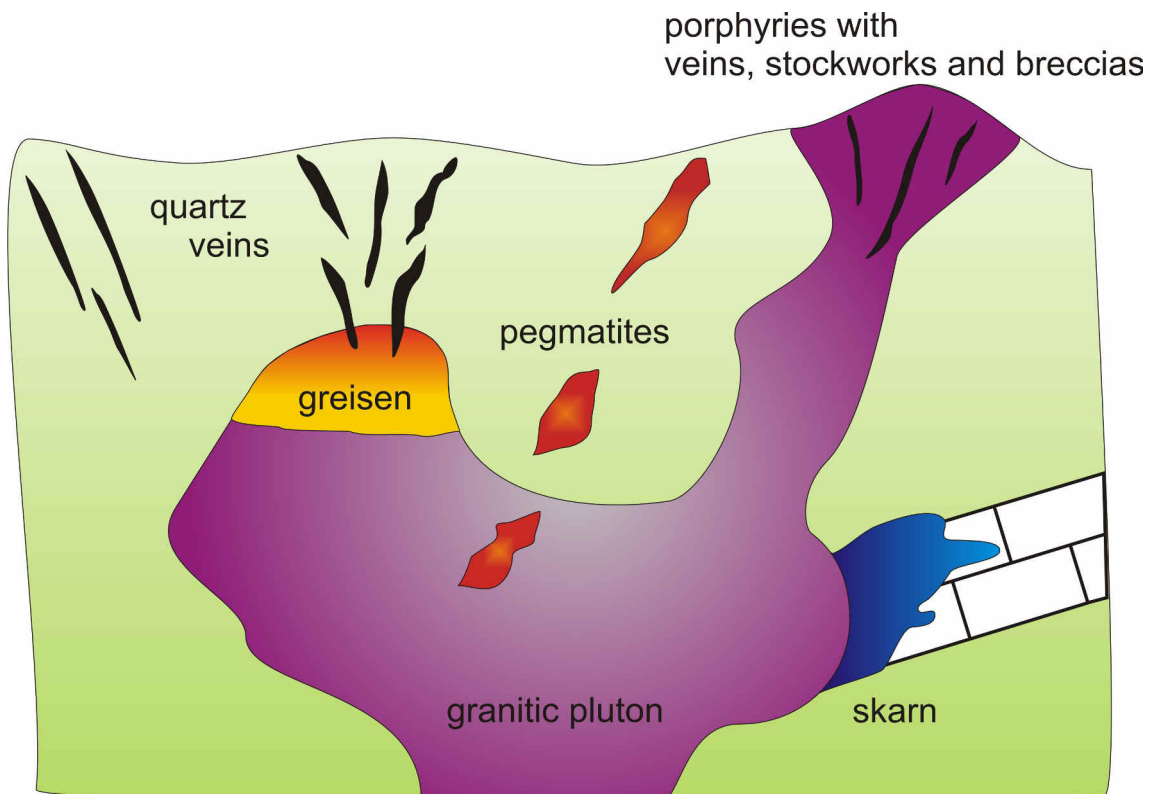


Figure 6.3: Generalised schematic sketch showing the principle tin-tungsten deposits in relation to a granitic intrusion

6.2.1 Magmatic deposits

Orthomagmatic cassiterite deposits are restricted to 'specialized' or rare metal granites with disseminated Sn-Ta mineralisation. These rare metal granites constitute the final and volumetrically smallest melt fractions of multi-stage intrusion systems and are associated with Sn-Ta mineralisation in their cupolas (Groves & McCarthy, 1978; Lehmann, 1990). The initial melts of 'specialised' or rare-metal granites are mostly formed by partial melting of deeply buried metasedimentary rocks during orogenic events of continental collision and are therefore classified either as ilmenite-series or S-type granites, respectively. However, rare metal granites may also be related to anorogenic settings and are consequently classified as A-type granites (detailed description is given below). During fractional crystallisation the evolving melt is successively enriched in fluxing agents such as H₂O, F, B, Li, and P which significantly lower the solidus temperature and viscosity of the melts (Linnen & Cuney, 2005). These volatiles also depolymerise the melt structure and more Sn can be accommodated by the melt (Antipin et al., 1981; Lehmann, 1990). These melts are characterised by low viscosity, shallow level of emplacement (<3-4 km) and probably ascended rapidly (Plimer, 1987b). Cassiterite and columbite-tantalite are primary magmatic accessories disseminated throughout the granite stocks forming low-grade, large-tonnage deposits. However, the cupolas of rare metal granites are invariably affected to a certain degree by greisen alteration (detailed description is given below). Examples for rare metal granites with disseminated cassiterite mineralisation are the leucogranites of the Eastern Desert, Egypt (Mohamed, 1993; Küster, 2008) or the Younger Granites of the Jos Plateau, Nigeria (Olade, 1980).

Tin and minor tungsten mineralisation is also related to granitic magmatism of anorogenic origin. The deposits are either associated with rapakivi granite massifs (A-type granites), ring complexes or, in a special case, with the granites of the Lebowa Granite Suite of the Bushveld Complex. In general, rapakivi granites are restricted to Precambrian shields and are Proterozoic in age ranging from 1.8 to 1.0 billion years (Rämö & Haapala, 1995). There is a distinct bimodal association in rapakivi granite complexes with gabbros and anorthosites together with granites, monzonites and syenites (Rämö & Haapala, 1995). Rapakivi granites are generally porphyritic and show a peculiar texture with ovoid alkali feldspar megacrysts mantled by andesine or oligoclase (Rämö & Haapala, 1995). The rapakivi granite magmas are generated by uprising of mantle-derived magmas (mafic underplating) resulting in partial melting of

both upper mantle and lower continental crust (Rämö & Haapala, 1995). However, the tin-polymetallic (W-Be-Zn-Cu-Pb) mineralisation is related to the latest intrusive phase of the rapakivi granite complex constituted by topaz-bearing microcline-albite granite without rapakivi texture (Haapala, 1995) forming disseminated ore, but also greisen, quartz vein and skarn deposits (see below). Haapala (1995) also suggests that iron oxide-copper-gold deposits (IOCG) are also related to rapakivi granite magmatism, such as the giant Olympic Dam deposit of South Australia.

Disseminated tin deposits associated with ring complexes are for example found in the Jos Plateau in Nigeria (Olade, 1980; Bowden & Kinnaird, 1984; Imeokparia, 1988; Pastor & Turaki, 1985; Ogunbajo 1993; Obaje, 2009). The Jos Plateau is known for its economically important alluvial cassiterite placers. Primary Sn-Ta mineralisation is present in Panafrican pegmatites and Mesozoic ring complexes. Placers may contain mixtures from both sources, but the studied samples mostly revealed the younger mineralization. The ring complexes are formed by peraluminous late-stage biotite granites of the Jurassic Younger Granites series with cassiterite and columbite-tantalite disseminations in the roof zones (Olade, 1980; Imeokparia, 1988; Ogunbajo, 1993). The Younger Granites are generally peralkaline with high amounts of Na₂O and K₂O. These granites are composed of albitic feldspars, perthitic potassium feldspars, alkaline pyroxenes like aegerine, and Na-rich amphiboles like arfvedsonite and riebeckite (Bowden, 1982; Obaje, 2009). The granites are related to mantle plume activity associated with rifting in extensional tectonic settings (Imeokparia, 1988; Kinnaird & Bowden, 1987).

The most important tin mines in the Bushveld Complex, South Africa, were the Rooiberg, Zaaiplaats, and Union Tin mines until mining ceased in 1993. These tin deposits are associated with the 3.5 km thick and about 2050 million years old Lebowa Granite Suite which represents the younger, acid plutonic phase of the Bushveld Complex (Kleeman & Twist, 1989; Walraven et al., 1990; McNaughton et al., 1993). The cassiterite (and minor scheelite) mineralisation occurs as disseminated accessory phases in the most fractionated portions of the host granite, in miarolitic cavities, and in high-grade pipe ore bodies (Leube & Stumpfl, 1963a,b; McNaughton et al., 1993). An extraordinary feature are the pipes (up to 900 m in length and 13 m in diameter) which are characterized by annular structure with sharp contacts to the enclosing granite and are composed of quartz, black tourmaline, fluorite or calcite with cassiterite, pyrite, chalcopyrite, scheelite and minor quantities of rare earth- and base metal-bearing

minerals (Crocker, 1986). The tin mineralization is related to incompatible trace element concentration during crystal fractionation of late-stage granitic melts (Crocker, 1986). Further description is given below in chapter 10.

Pegmatites form from residual melts which derived from anatexis of crustal rocks or crystallisation of parental granitic plutons. Incompatible, rare elements and volatiles are concentrated by fractionation in the residual melts (Simmons & Webber, 2008). Volatiles such as H₂O, F, B, and P also serve as fluxes which lower crystallisation temperatures (down to about 450 °C), decrease nucleation rates, melt polymerisation, and viscosity and increase diffusion rates and solubility of the metals (London, 1987). Undercooling and disequilibrium crystallisation dominate the crystal textures and zoning of the pegmatite body (London, 2005). As indicated by experiments, primary magmatic cassiterite crystallises from pegmatite melts, but this early magmatic cassiterite may also be dissolved by late-stage hydrothermal fluids and subsequently cassiterite-bearing quartz veins are formed in the periphery of Sn-bearing pegmatites (Webster et al., 1997).

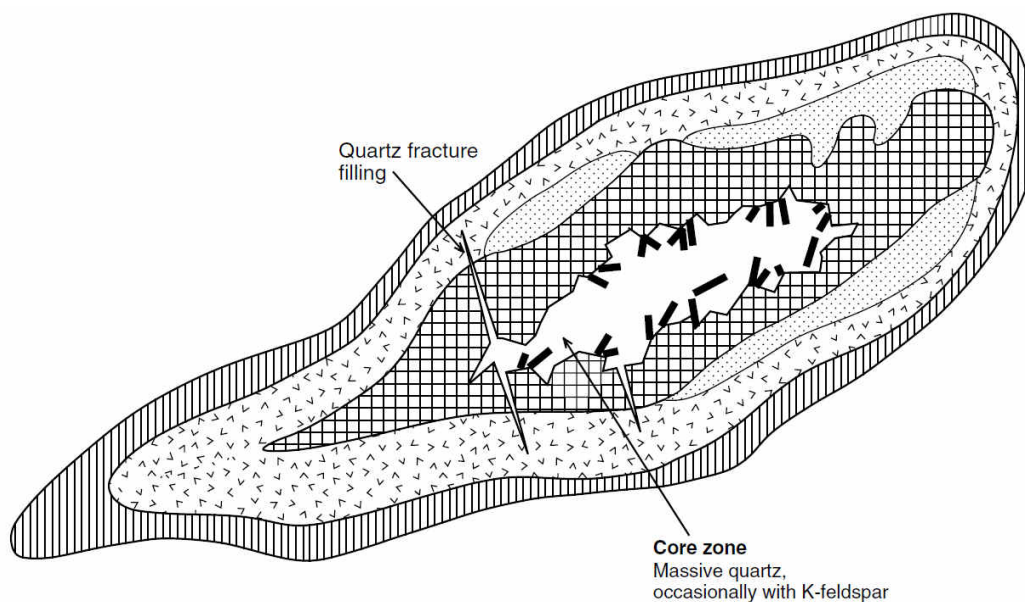


Figure 6.4: Schematic cross section through a concentrically zoned pegmatite (Fetherston, 2004 modified after Černý, 1993). Vertical lines: aplitic border zone with fine-grained albite and quartz ± muscovite; v-pattern: wall zone with coarse-grained quartz, K-feldspar, albite, and muscovite; dotted pattern: outer intermediate zone with massive cleavelandite, often replaced by sugary albite with minor muscovite and quartz; crosshatched pattern: inner intermediate zone with coarse-grained spodumene, quartz, K-feldspar, and muscovite; black lines: core margin with large tourmaline, beryl, and spodumene.

Economical concentrations of tin are related to rare element pegmatites of the LCT-family (lithium, caesium, tantalum); on the contrary, tin is almost absent in pegmatites of the NYF-family (niobium, yttrium, fluorine) (Černý & Ercit, 2005). LCT-family pegmatites are peraluminous and derive mainly from S-type granitic melts, but less commonly from I-type granitic melts (Černý & Ercit, 2005). Tin-bearing pegmatites are mainly composed of quartz, microcline, albite, and muscovite and frequently associated topaz, lepidolite, beryl and tourmaline. Major ore minerals are cassiterite, columbite-tantalite, beryl and spodumene, which are frequently found in the intermediate zones around the quartz core (Figure 6.4). Cassiterite occurs disseminated throughout the pegmatite body, but is frequently found in the albite-dominated intermediate zone (e.g., Wise & Brown, 2011).



Figure 6.5: Steeply dipping pegmatite intruded into Kibaran metasedimentary country rocks. Left picture was taken at Remera, Rutsiro, Rwanda. Right picture was taken by Frank Melcher at Nkegete, Gatumba, Rwanda

Examples for Sn-bearing pegmatites are Greenbushes in Western Australia (Partington et al., 1995), Tanco in Canada (Thomas & Spooner, 1988), the Black Hills in the United States (Walker et al., 1989), eastern Brazil (Heinrich, 1964; Morteani et al., 2000), Pampean Ranges of northwestern Argentina (Galliski et al., 2008), southern Nigeria (Matheis et al., 1982), Kamativi and Bikita in Zimbabwe (Rijks & van der Veen, 1972),

southern Zambia (Legg & Namateba, 1982), western-central Namibia (e.g., Wagener, 1989), and the pegmatites from Central Africa (Varlamoff, 1972; Figure 6.5), especially Manono-Kitotolo in Katanga (Günther & Ngulube, 1992). The largest and economically most important pegmatites are restricted to the Precambrian; but there are also large mineralized pegmatites in the Paleozoic, for example the Altai #3 pegmatite, China in terms of Ta (McCauley & Bradley, 2014).

In general, pegmatites rarely contain tungsten minerals, but accessory wolframite and/or scheelite are reported from several pegmatite deposits. For example, Nb-bearing wolframite from the Nuaparra pegmatite in Mozambique (Saari et al., 1968), wolframite from the Dolní Bory pegmatites in the Czech Republic (Novák & Šrein, 1989), scheelite from the pegmatites of Silver Hill, Washington, USA (Page, 1942), scheelite from Natas pegmatite, Namibia (Diehl, 1991), cassiterite associated with wolframite and scheelite in tourmaline-bearing pegmatite in the Upington area, South Africa (von Knorring & Condliffe, 1987), and hübnerite from pegmatites of the Phuket island, Thailand (Gocht & Pluhar, 1982; Suwimonprecha et al., 1995). Wolframite from the Nong Sua pegmatite in Thailand is related to quartz veins of hydrothermal origin (Linnen et al., 1992; Linnen & Williams-Jones, 1993).

Anomalously elevated tin concentrations are found in the iron oxide-apatite ores of Grängesberg (Sweden) with an average grade of about 100 ppm Sn, but these tin contents are not of economic interest (Björkst edt, 1972). These iron oxide-apatite deposits (also known as Kiruna-type) are interpreted to be of magmatic origin (Jonsson et al., 2013). Tin occurs in the form of cassiterite, but also in magnetite; tungsten in the form of scheelite is also present with an average concentration of 15 ppm W (Björkst edt, 1972).

6.2.2 Transitional magmatic-hydrothermal deposits

Greisen (old German mining term) generally refers to massive quartz-mica rocks accompanied by fluorite, topaz, tourmaline and other F- or B-bearing minerals (Figure 6.6). However, greisen is used primarily to describe a type of alteration rather than a type of deposit (Sinclair, 1996). Greisens are also described as 'disseminated' deposits or their formation was termed 'pneumatolytic' in former times. Greisen alteration is formed by post-magmatic hydrothermal fluids (at temperatures ranging between 250 and 450 °C) in the apical portions (cupolas) of evolved granitic intrusions at depths

ranging from 1.5 to 5 km where boiling of the gas-rich fluids can occur (Halter et al., 1996; BGS, 2011; Dolníček et al., 2012). The associated intrusions are highly fractionated, peraluminous to peralkaline granites of S-type affinity or ilmenite series (Ishihara, 1981), but greisen deposits are also found in the apical parts of A-type granites (Haapala, 1995; Botelho & Moura, 1998; Lenharo et al., 2002; Bettencourt et al., 2005). The following elements are significantly enriched: Sn, W and Mo accompanied by Bi, Li, Be and F. The major ore minerals are cassiterite and wolframite typically associated with various sulphides like pyrite, arsenopyrite, chalcopyrite, bismuthinite, molybdenite, and sphalerite. Micas are characteristically rich in Li, such as zinnwaldite.



Figure 6.6: Hub stock greisen deposit near Krásno, Czech Republic. Left picture: former open pit and 'Pinge' (collapse area) of the Hub stock greisen deposit. Right picture: boulder with typical greisen pocket composed of massive quartz and zinnwaldite. Surrounding rock is greisenized granite composed of quartz, zinnwaldite, and topaz.

During greisenisation the primary rock-forming minerals of the granite are dissolved by acidic supercritical fluids ('pneumatolytic') and are replaced by quartz, topaz and fluorite. The association of cassiterite and F-bearing minerals leads to the assumption that tin is transported as fluorine complex and cassiterite is formed at decreasing temperature and pressure conditions: $\text{SnF}_{4(\text{melt})} + 2\text{H}_2\text{O} \rightarrow \text{SnO}_{2(\text{cassiterite})} + 4\text{HF}$ (e.g., Abdalla et al., 2008). Released hydrofluoric acid causes low pH values resulting in formation of topaz or fluorite in later stages. The breakdown of feldspars and the conversion of biotite to muscovite during greisen alteration are of fundamental importance for the genesis of the Sn-W deposits, because plagioclase and especially biotite are the principal metal carriers in the unaffected granite (Pirajno, 1992). Generally, the greisen is characterised by increased SiO_2 , Li and F contents and losses in K_2O , Na_2O , and Al_2O_3 (e.g., Mohamed, 1993). The hydrothermal fluids are generated during crystallisation of the intrusive granitic magma which is enriched in volatiles such

as F, Cl, Li and H₂O. These fluids cause greisen alteration, but also form quartz vein deposits with wolframite and cassiterite as major ore minerals. Two end-members of greisen formation are defined (Shcherba, 1970a; Shcherba, 1970b; Plimer, 1987b; Pirajno, 1992): one representing a closed system where the fluids are contained within the granitic cupola (endogreisen); and one indicating open system conditions in which the fluids are channelled along fractures and faults from within the parent cupola into country rocks forming mineralised quartz veins (exogreisen). The formation of these two contrasting deposit types is dependent on the predominant occurrence of fluorine or boron; endogreisen formation at $F > B$ and exogreisen formation at $B > F$ (Lehmann et al., 2000). Endo- or exogreisen formation is also controlled by the initial overpressure of the exsolved fluid, the principal minimum shear and the tensile strength of the surrounding country rocks (Plimer, 1987b). For example, low intrusion level of the granitic melt, high tensile strength of the country rocks, low initial fluid pressure, and fluid undersaturation of the melt result in the formation of endogreisen (Plimer, 1987b).

Typical tin-tungsten greisen deposits are found in the European Variscides, e.g. in the Erzgebirge along the German-Czech border (Figure 6.6) or in Cornwall, England. Major greisen deposits related to A-type rapakivi granites are found in Brazil (Dall'Agnol et al., 1999), for example the Rondônia tin province (Bettencourt et al., 1999; Bettencourt et al., 2005), the Pitinga deposit in Amazonas (Lenharo et al., 2002; Lenharo et al., 2003; Bastos Neto et al., 2009; Borges et al., 2009), in the eastern Amazonian craton (Lamarão et al., 2012) and the Goiás tin province (Botelho & Moura, 1998; Lenharo et al., 2002). Minor deposits are situated in southern Finland (Haapala, 1997).

Cassiterite-bearing greisen deposits are also associated with anorogenic ring complexes, for example in the Jos Plateau of Nigeria or in the Silsilah ring complex of Saudi Arabia. In the Silsilah ring complex, cassiterite is found in topaz-quartz greisen zones related to cupolas of highly evolved, zinnwaldite-bearing alkali-feldspar granite. The rest of the Silsilah ring complex is composed of peralkaline granites and alkaline dacites. It is suggested that these intrusive rocks form a single differentiation series from alkaline dacite and peralkaline granite to peraluminous alkali-feldspar granite (du Bray, 1985).

Porphyry deposits form a wide spectrum of metal assemblages including gold, copper, molybdenum, tungsten, and tin. In comparison, porphyry tungsten and porphyry tin have lower oxidation and sulphidation states and lower temperatures (below 500 °C) than the others (Seedorff et al., 2005). Porphyry tin deposits (also known as ‘Bolivian type’) are found in a well-defined metallogenic province called the Bolivian Tin Belt (Figure 6.7; detailed description is given in chapter 10) and are related to apical zones or stocks of subvolcanic, porphyritic, calc-alkaline intrusions in the form of breccias, stockworks, and polymetallic veins.

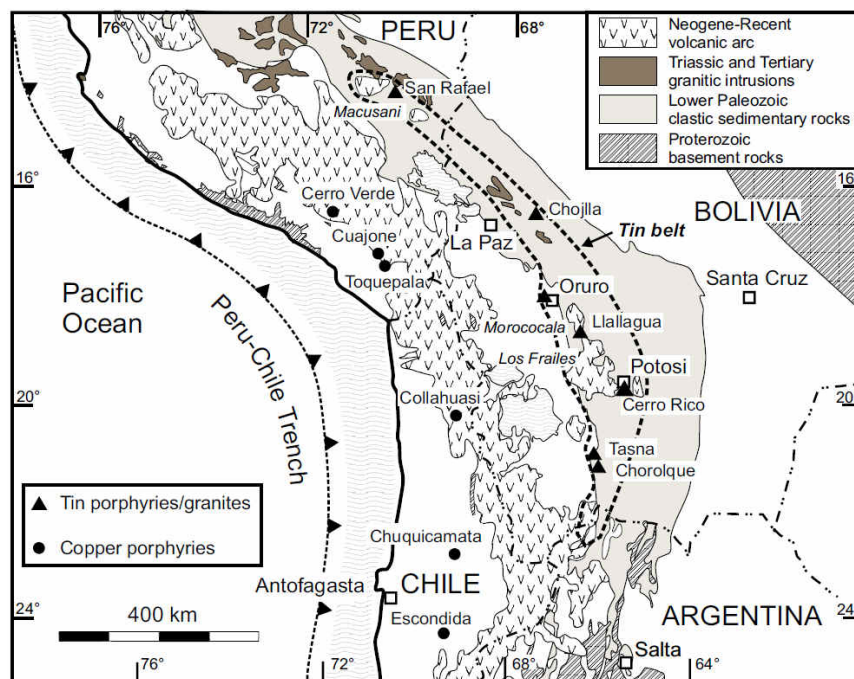


Figure 6.7: Geologic setting of the Bolivian Tin Belt (dashed outline) and location of major ore deposits (Dietrich et al., 2000)

They are called porphyry tin deposits as there are several similarities and analogies to porphyry copper systems, especially the well-defined alteration zoning with argillitisation grading downward into sericitisation and further into tourmalinisation (Figure 6.8; Sillitoe et al., 1975; Grant et al., 1980). But the porphyry tin deposits were emplaced at shallower depths than copper porphyries (Pirajno, 1992).

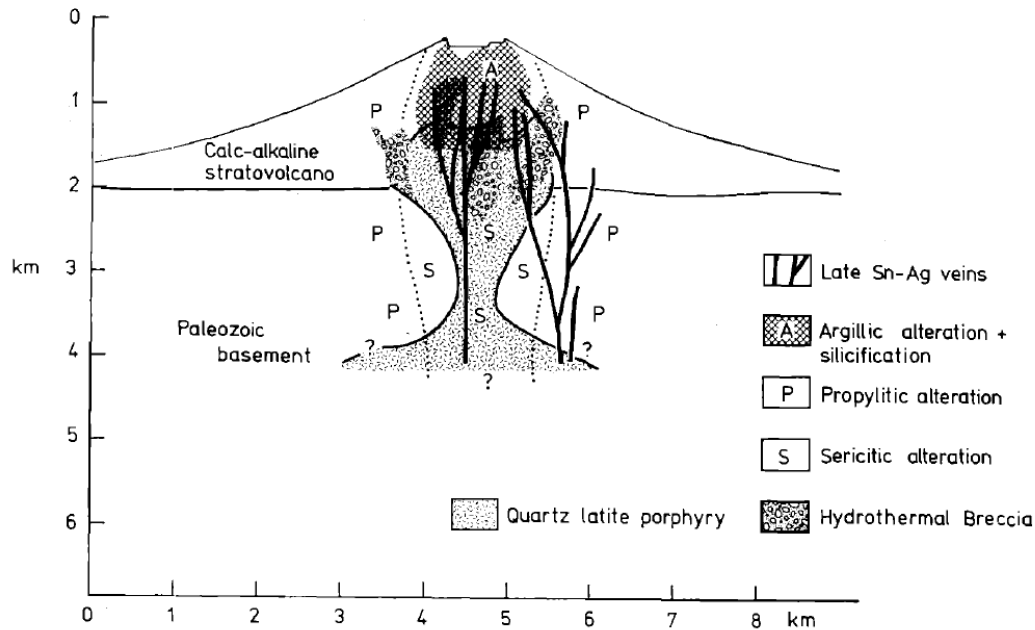


Figure 6.8: Generalised cross-section through a porphyry tin deposit showing the relation of ore-bearing veins, alteration zones, and porphyry intrusion (Sillitoe et al., 1975)

Intrusive and collapse breccias are common in subvolcanic environments and these offer permeability for the mineralising fluids and excellent depositional sites for the ores (Taylor, 1979). The complex polymetallic sulphide-rich ores show a wide mineralogical variety. Tin often occurs as acicular cassiterite crystals, but complex sulphides and sulphosalts like stannite ($\text{Cu}_2\text{FeSnS}_4$), teallite (PbSnS_2), cylindrite ($\text{Pb}_3\text{Sn}_4\text{FeSb}_2\text{S}_{14}$), etc are also common. Base metal sulphides associated with silver are also frequently found. The complexity of the ores is attributed to telescoping as a result of near-surface deposition (Mulligan, 1975) and successive evolution of the mineralising system from early high temperature, magmatic fluids to low temperature fluids mixed with meteoric waters. Telescoping also includes precipitation of metals at different juxtaposing mineralisation stages. Porphyry tin deposits are also found outside Bolivia, e.g. in the Ardlethan tin field in Australia (Ren et al., 1995).

Tungsten also occurs in porphyry deposits and is mostly associated with molybdenum. Tungsten porphyry deposits are usually very large but of low grade, for example the Logtung/Northern Dancer deposit in Canada contains 162 million tons of ore at an average grade of 0.13% WO_3 (Noble et al., 1984). Other major tungsten porphyries are the Mount Pleasant (Davis & Williams-Jones, 1985) and Sisson Brook deposits in New Brunswick, Canada. Due to their large tonnage, porphyry deposits represent a significant tungsten resource for the future (Werner et al., 1998).

However, some typical copper-molybdenum porphyry deposits contain tungsten (wolframite or scheelite) and/or tin (cassiterite) mineralisation which are recovered as by-products (e.g. Climax porphyry deposit, Colorado).

Tin-bearing breccia pipe deposits are generally associated with boron-rich granite-related hydrothermal systems in a subvolcanic environment, for example in Bolivia (Lehmann et al., 2000), Cornwall (Allman-Ward et al., 1982; Williamson et al., 2010), Ardlethan tin field in Australia (Ren et al., 1995), and the Uchkoshkon tin deposit in Kyrgyzstan (Solomovich et al., 2012). Similar to the aforementioned greisen systems, the internal pressure of the magmatic system progressively increases due to fluid release until it is significantly larger than the minimum shear and tensile strength of the overlying country rocks; the hydraulic overpressure is released by explosive expansion (Plimer, 1987b, Ren et al., 1995). Lehmann et al. (2000) stated that the release of mechanical energy is significantly stronger in B-rich systems in contrast to F-rich systems. This causes rapid precipitation of cassiterite in a matrix composed of tourmaline with minor quartz and sericite (Plimer, 1987b). The distinct association of tourmaline with cassiterite is the indicator of high boron concentrations during mineralisation. The high boron contents of these systems are probably leached and remobilised by hydrothermal fluids from the pelitic country rocks (Lehmann et al., 2000).

Skarn (old Swedish mining term) deposits are generally formed by contact metamorphism (also known as tactites) and replacement reactions (e.g. metasomatism) due to intrusion of granitic melts into carbonate-rich rocks (calcitic and dolomitic limestone, marble, marl; see Figure 6.10). Moreover, skarns can also form in any rock type from fluids of different origin and are not solely restricted to nearby igneous plutons (Meinert et al., 2005). Skarns also form in other geological settings, for example along faults and shear zones or geothermal systems (Meinert et al., 2005). Skarns either develop in the igneous, intrusive rock called endoskarn or in the carbonate-bearing country rock called exoskarn. Skarn refers to coarse-grained calc-silicate rocks essentially composed of pyroxene (hedenbergite-diopside) and garnet (grossular-andradite-almandine) (Dawson, 1996; Meinert et al., 2005). Thus skarn is a descriptive term based upon mineralogy in the sense of Meinert et al. (2005). Other typical skarn minerals are wollastonite, vesuvianite (idocrase), epidote, forsterite, fluorite, various

sulphides and boron-bearing minerals. Common sulphides are pyrrhotite, chalcopyrite, pyrite, galena, sphalerite and bismuth sulphides (Einaudi et al., 1981). Most skarn deposits show a mineralogical zoning in their pyroxene and garnet contents (e.g., Figure 6.9; Meinert et al., 2005). In addition, the chemical composition changes with distance from the contact. Highest andradite content in garnet is found closest to the contact and systematically decreases with increasing distance accompanied by a corresponding increase in grossular content (Kwak & Tan, 1981). Pyroxene shows a similar pattern with highest hedenbergite amount at the contact; diopside content in pyroxene is increasing with increasing distance from the contact (Kwak & Tan, 1981). Skarn deposits are economically important hosts for Fe (mostly magnetite), Au, Cu, Zn, Mo, and of course W and Sn.

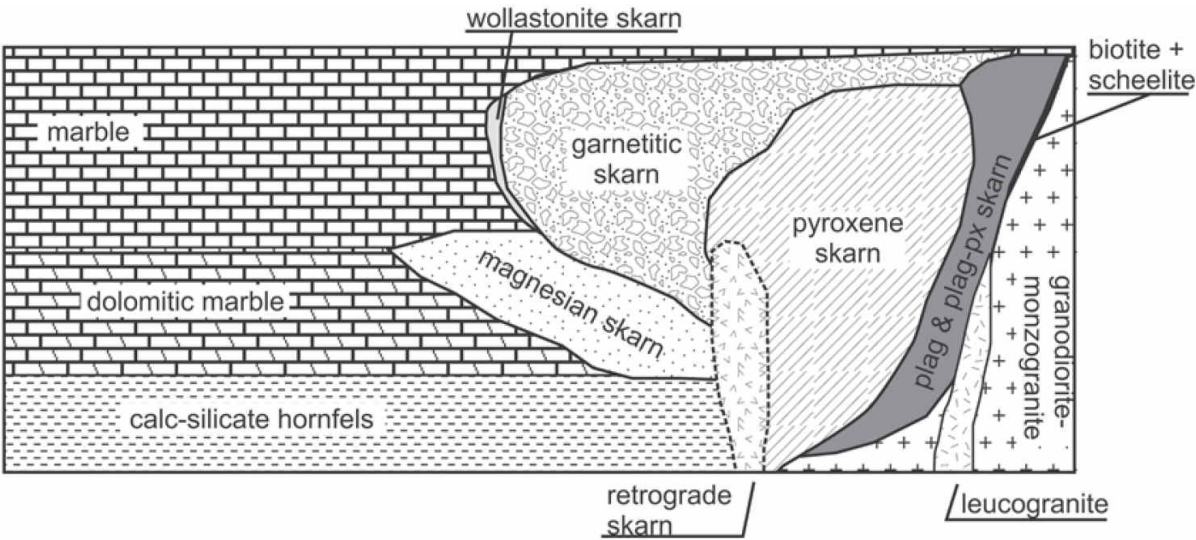


Figure 6.9: Geological schematic sketch illustrating the mineralogical skarn zonation in the contact zone of the granitic intrusion (right) with the Tamames Limestone Formation (left) at the Los Santos scheelite skarn deposit, Spain (Tornos et al., 2008).

Skarn formation basically develops in three phases: initially the country rock is affected by contact metamorphism during intrusion of the magma. Then, hydrothermal fluids are released from the crystallising magma which infiltrate and react with the permeable, carbonate-bearing country rock. During the early stages, the hydrothermal fluids are of magmatic origin and with time these fluids are modified by rock interaction, decreasing temperature and salinity, changes in Eh-pH conditions, and influx of meteoric water. Permeability controls the ability of the fluids to infiltrate the carbonate-rich wall rocks and is therefore an important factor during skarn formation. The replacement of the host rock coincides with an influx of Si, Al, Fe, Mg and removal of CO₂, H₂O, Na. Dissolution of carbonates and dehydration results in increasing porosity and

permeability. These processes, in particular the rapid increase of pH, result in skarn formation and subsequent precipitation of ore minerals, mostly in the form of sulphides. Finally, the skarn paragenesis is overprinted by retrograde alteration accompanied by increasing influence of circulating meteoric waters and crystallisation of hydrous minerals. The retrograde alteration assemblage is composed of hydrous minerals like epidote, biotite, hornblende, actinolite, and chlorite and was formed at lower temperatures (Einaudi et al., 1981).

Tungsten skarns are associated with calc-alkaline plutons in major orogenic belts surrounded by large, high temperature aureoles (Figure 6.10; Meinert et al., 2005). The plutons are typically porphyritic granodiorite to quartz monzonite (Figure 6.10; Einaudi et al., 1981). Tungsten skarns show a characteristic zoning with proximal Fe-rich, generally scheelite-bearing skarn and distal barren, Fe-poor calc-silicate skarn. Generally, scheelite of early stages is fine grained and rich in molybdenum; on the other hand late-stage scheelite is medium to coarse grained with low molybdenum contents (Einaudi et al., 1981; Kwak & Tan, 1981). Molybdenite is often associated with late-stage molybdenum-poor scheelite (Kwak & Tan, 1981). Individual scheelite crystals are zoned with highest molybdenum contents in the core decreasing gradually towards the rim. Additionally, the molybdenum concentrations in scheelite decrease with increasing distance from the contact zone (Plimer, 1983). Tungsten skarns are divided into two general groups: oxidised and reduced types (Newberry & Einaudi, 1981; Plimer, 1983; Ivanova & Naumov, 1986; Newberry & Swanson, 1986; Kwak, 1987; Newberry, 1998; Timón Sánchez et al., 2009). Oxidised (Fe^{3+} -rich) skarns are related to magnetite series I-type granites and are host to W-Mo-Cu ore mineralisation. Pyrite represents the major sulphide and Mo is either present in Mo-rich scheelite or as molybdenite. Oxidised skarns may also contain significant concentrations of gold (Souza Neto et al., 2008). Reduced (Fe^{2+} -rich) skarns are either related to A-type granitoids or ilmenite series S-type granites and show the association of W-Sn-F (Kwak, 1987). Dominant sulphide is pyrrhotite and scheelite has low Mo concentrations. Good examples of major tungsten skarn deposits are Cantung in Canada (Figure 6.10; Rasmussen et al., 2011), Pine Creek in the USA (Newberry, 1982), Tyrnyauz in the Caucasus Mountains, Vostok-2 in Primorsky Krai, Russian Far East, Sangdong in South Korea, Salau in the French Pyrenees, Los Santos in Spain (Tornos et al., 2008), King Island in Australia (Kwak, 1978), and Kara, Tasmania (Zaw & Singoyi, 2000).

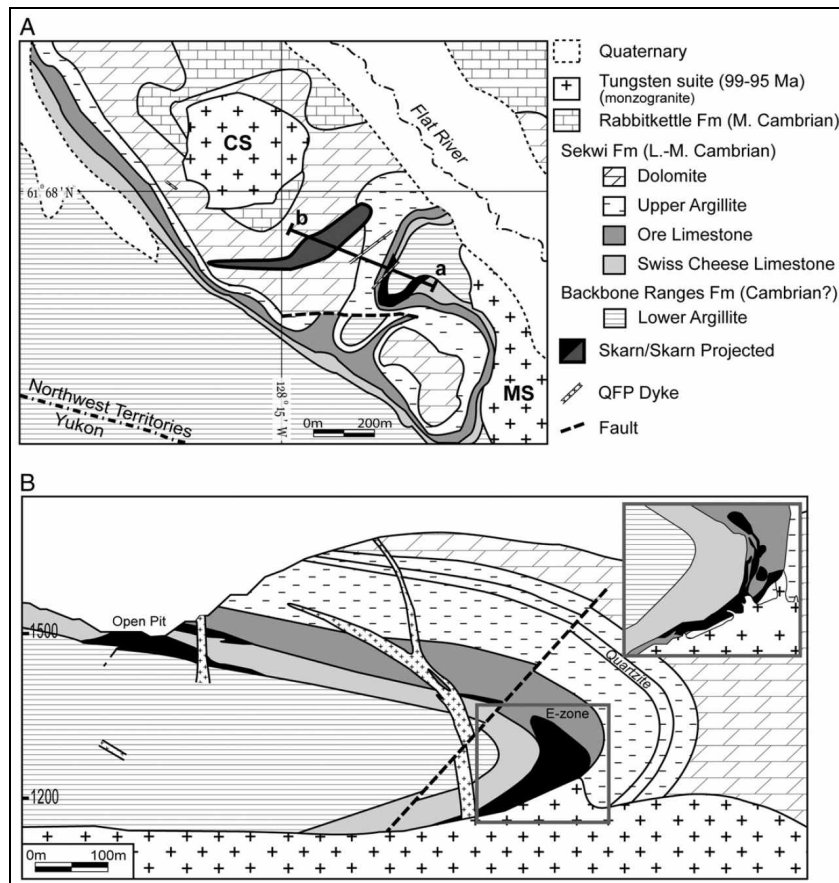


Figure 6.10: Geological map (A) and cross section (B) of the CanTung mine (Rasmussen et al., 2011 and references therein). The section line a-b on the map A indicates the strike of the cross section B. CS=Circular Stock, MS=Mine Stock, QFP Dyke=Quartz feldspar porphyry dyke.

Tin skarns are almost exclusively associated with peraluminous ilmenite series or S-type granites (Einaudi et al., 1981; Chen et al., 1992; Newberry, 1998; Meinert et al., 2005). The granites have high silica and alkali contents. A variety of Sn-bearing minerals besides cassiterite occur, such as Sn-rich titanite (malayaite, CaSnSiO_5), borates (like hulsite, $(\text{Fe}^{2+}, \text{Mg})_2(\text{Fe}^{3+}, \text{Sn})\text{BO}_5$ and Sn-bearing ludwigite, $(\text{Mg}_2\text{Fe}^{3+}\text{BO}_5)$, Sn-bearing aluminosilicates (garnet, epidote, actinolite), Sn-rich magnetite (Mulligan, 1975), and the very rare mineral nordenskiöldine (CaSnB_2O_6 ; Chen et al., 1992) For example, amphibole with up to 2.4 wt.% Sn and Ca-garnet with up to 4.75 wt.% Sn are reported from tin skarns (Laznicka, 2010). In contrast to the other skarn types, tin skarn formation is often accompanied by characteristic greisen alteration (Kwak, 1987). Extensive greisen alteration of Sn-bearing skarn minerals can liberate the tin and oxide or sulphide ore is formed (Meinert et al., 2005). High F and B contents are characteristic for tin skarn deposits and typically minerals like fluorite, topaz and tourmaline occur. Certain tin skarn deposits form rhythmically layered or laminated skarns called

'wrigglite' (Kwak & Askins, 1981). Most tin skarn deposits are uneconomic, because on the one hand cassiterite is not easily processed due to its very fine grain size (for example at Shizhuyuan the grain size of cassiterite is ranging between 2 and 20 μm , Chen et al., 1992), on the other hand tin is often incorporated in silicate minerals (e.g., malayaite) and is not economically recoverable. Examples for Sn-bearing skarn are the Lost River deposit in Alaska (Dobson, 1982), the Mt. Lindsay and Moina deposits in Tasmania (Kwak & Askins, 1981; Kwak, 1983), the JC deposit in Yukon Territory, Canada (Layne & Spooner, 1991), and the major Sn-bearing skarns in southern China, for example Gejiu, Dachang, and Shizhuyuan deposits (Chen et al., 1992). The most important Sn-bearing skarn related to A-type rapakivi granite is the Pitkäranta deposit in Russian Karelia (Haapala, 1995).

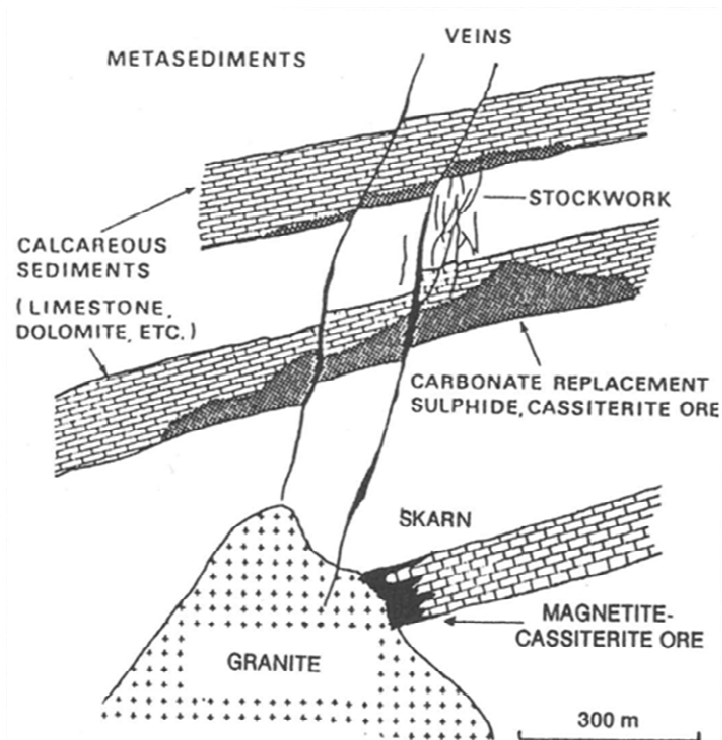


Figure 6.11: Schematic model for the distribution of skarn and carbonate-replacement deposits in relation to a granite intrusion (Lehmann, 1990).

A special group of tin skarns, often referred to as replacement deposits, are accompanied by considerable iron sulphide (pyrrhotite) or oxide (magnetite) mineralisation (Kwak, 1987). Plimer (1983) suggests that basically the assemblage magnetite-cassiterite occurs closer to the contact zone whereas pyrrhotite-cassiterite ore forms at greater distances from the pluton (Figure 6.11). These replacement deposits are of higher economic importance for tin than the above mentioned skarns and are formed further away from the granite intrusion, also known as 'distal tin skarn'

(Kwak, 1987). According to Meinert et al. (2005), large tin skarn systems like for example Renison Bell in Tasmania is spatially zoned from proximal Ca-enriched skarn with minor disseminated cassiterite to distal skarn-absent Mg-rich sulphide-rich replacement deposit with major cassiterite mineralization.

6.2.3 Hydrothermal deposits

Tin- and tungsten-bearing hydrothermal quartz vein, stockwork deposits and sheeted vein systems are found in the roof regions of granitic plutons and in the surrounding country rock, but hydrothermal veins also occur unrelated to parental granites. Hydrothermal veins are tabular bodies of variable thickness, vertical and horizontal extent mostly formed in fractures and fissures (Pohl, 2011). Shallow intrusion levels of the granitic magmas and gradual increasing fluid pressure during crystallisation of the pluton are characteristic for vein deposits (Plimer, 1987b). These veins are often closely associated with greisen deposits and/or are bordered by greisen alteration (e.g., Plimer, 1987b). The density and width of individual veins change with increasing distance from the granite. The shape of the veins changes successively from single, thick veins (up to several meters) at the base to large numbers of thin veins (few centimetres) forming a stockwork or sheeted vein system further away from the pluton (Plimer, 1987b). The formation of the vein system is controlled by mechanical and geochemical factors. Mechanical strain and the internal pressure of the fluid generate fractures and faults which serve as pathways for the migrating ore-bearing fluid; whereas geochemical parameters, such as fluid-rock interaction, Eh-pH conditions, etc. control the precipitation of the ore minerals from the hydrous fluid at favourable sites (e.g., Plimer, 1987b, Jiang et al., 1997; Roberts et al., 1998; Sanderson et al., 2008). The conditions and parameters controlling the precipitation of the ore minerals from hydrothermal fluids is dealt with in the excursus on the geochemistry of Sn and W at the beginning of this chapter. Quartz is the dominant gangue mineral associated with variable amounts of muscovite, feldspar, tourmaline, topaz, and fluorite. The major ore minerals are cassiterite and/or wolframite and/or scheelite commonly accompanied by sulphides like molybdenite, arsenopyrite, pyrrhotite, pyrite and bismuthinite. Cassiterite and wolframite occur in similar hydrothermal veins, but often do not occur together in the same deposit. De Clercq (2012) stated for Sn- and W-vein deposits in Rwanda that the lithology of the host rock is controlling if either cassiterite or wolframite occurs in the hydrothermal veins; wolframite-bearing veins are found in successions of alternating

metapelite and sandstone, whereas cassiterite-bearing veins are hosted by sandstone or quartzite (De Clercq, 2012).

Basically, a temporal succession of metal precipitation can be observed. Ore precipitation begins with an early ‘oxide stage’ (cassiterite, wolframite), followed by a ‘sulphide stage’ (pyrite, chalcopyrite, arsenopyrite, molybdenite, galena, and bismuthinite) and a final carbonate-oxide (calcite, siderite, iron oxides) stage (Pirajno, 1992; Sinclair, 1996; Wood & Samson, 2000; Pirajno, 2009). Spatial metal zoning is also commonly found in many hydrothermal Sn-W deposits; either caused by sequential precipitation of the metals from one parental fluid or by bulk precipitation from compositionally different fluids (Audétat et al., 2000b). The deposits of Cornwall (Sinclair, 1996), the Herberton tinfield (Blake & Smith, 1970; Taylor & Steveson, 1972), and also the deposits related to the Mole granite (Audétat et al., 2000b) serve as examples for distinct zonal distribution around intrusive plutons with Sn-W closest to or within the granite, followed by a Cu zone and finally grading outward into Pb-Zn association (Figure 6.12). A similar distribution with distinct vertical and horizontal zoning is found in the polymetallic deposits of the Gejiu ore district in the Yunnan Province of China (Cheng et al., 2013). The W-Be-Bi-Mo-Sn association occurs in or close to the granite forming either greisen or skarn mineralisation and in the deeper portion of the veins (Cheng et al., 2012; Cheng et al., 2013). Cassiterite mineralisation associated with Cu sulphides is found in the lower central part of the veins, whereas Pb-Zn mineralisation (galena and sphalerite) occurs in the upper portions of the veins (Cheng et al., 2012; Cheng et al., 2013).

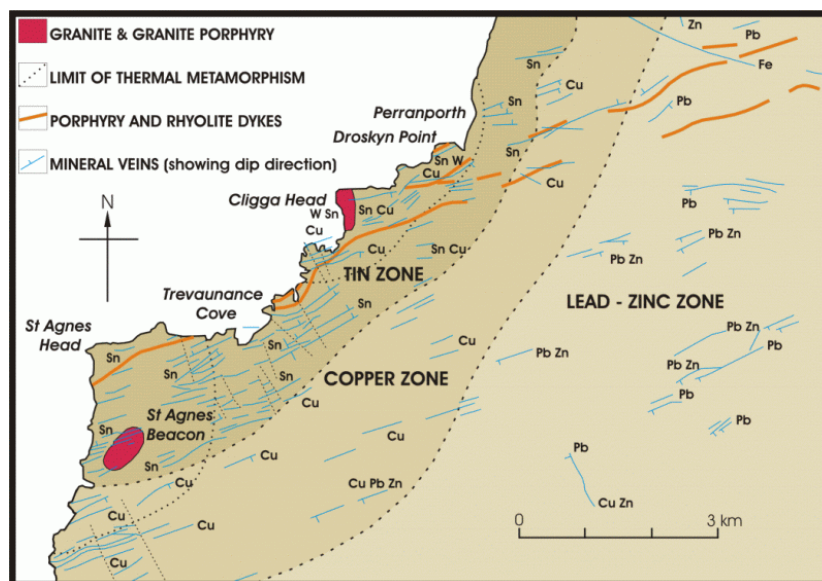


Figure 6.12: Pattern of metal zoning around granite intrusions in the St. Agnes District, Cornwall, south-west England (Bromley & Holl, 1986; LeBoutillier, 2002).

The hydrothermal fluids may derive from different sources. Magmatic fluids are either expelled from granitic melts during solidification and cooling, but hydrothermal fluids are also generated by breakdown of hydrous minerals during metamorphism. Another source of hydrothermal fluids is meteoric water which percolates through fractures and is heated at deeper levels or in the thermal aureole of magmatic intrusions. Two contrasting concepts on the formation of hydrothermal ore deposits exist (Hedenquist & Lowenstern, 1994; Audétat et al., 2008 and references therein). The first model interpreted the intrusion as source of both fluids and metals (e.g. Burnham, 1997). The second model regards the intrusion only as a heat source driving convection of meteoric water and the metals are leached out of the surrounding country rocks (e.g. Cathles, 1981). However, mixing of magmatic-hydrothermal fluids with meteoric waters also causes precipitation of Sn-W ores (Audétat et al., 2008).

Typical hydrothermal vein deposits with associated tin and/or tungsten mineralisation are San Rafael (Sn), Pasto Bueno (W) in Peru and the Rwandan reinite mines Nyakabingo, Gifurwe and Bugarama (Figure 6.13). An example for a vein/stockwork deposit with scheelite and associated cassiterite is the Parrilla W-Sn deposit from Spain (Mangas & Arribas, 1988).



Figure 6.13: Sn-W mineralised vein deposits. Left picture: Reinite-bearing quartz vein crosscutting graphitic phyllites from the Nyakabingo mine, Rwanda. Right picture: Large cassiterite crystals in quartz vein from Krupka, Czech Republic.

Scheelite occurs as a common accessory phase in hydrothermal quartz veins forming orogenic (also known as mesothermal) gold deposits (Kempe & Oberthür, 1997; Ghaderi et al., 1999; Kempe et al., 2000; Graupner et al., 2010). Orogenic gold deposits are found in metamorphic belts typically associated with greenschist facies rocks (Groves et al.,

1998). The Au-bearing veins formed during compressional or transpressional deformation at convergent margins and are related to deep-seated first-order fault zones (Groves et al., 1998; Goldfarb et al., 2005). However, scheelite is also present in intrusion-related gold deposits. Intrusion-related gold deposits are associated with intermediate to felsic intrusions with a composition between magnetite and ilmenite series which are situated in a tectonic setting typical for Sn-W deposits (Thompson et al., 1999; Lang & Baker, 2001). These deposits are characterised by sheeted vein, greisen-like and breccia mineralisation styles, and the gold mineralisation is also commonly accompanied by scheelite (Thompson et al., 1999; Mair et al., 2006).

A special kind of low temperature hydrothermal tin deposit is related to rhyolitic lava flows or shallow seated rhyolite domes (Huspeni et al., 1984; Burt & Sheridan, 1988). This rhyolite-hosted tin mineralisation (also known as 'Mexican type') occurs in erratic veinlets and breccias as deep red cassiterite and in the form of yellowish to dark brown wood tin (Huspeni et al., 1984; Ruiz, 1988). Associated minerals are specular hematite, various forms of silica (e.g. quartz, chalcedony, cristobalite, tridymite, etc.), and F-bearing minerals like topaz and fluorite (Huspeni et al., 1984). Wood tin and silica either precipitated as gels (Herzenberg, 1936) or from highly supersaturated hydrothermal fluids (Lufkin, 1977; Hosking et al., 1987). Transportation of Sn probably occurs in the form of colloids (Knopf, 1916; Wagner, 1926; Newhouse & Buerger, 1928; Herzenberg, 1936; Lehmann, 1990). It is also suggested that Sn is transported at these near surface conditions by vapour exsolved from volatile saturated magmas (Williams-Jones & Heinrich, 2005). The rhyolite-hosted tin deposits form in high level environments at low temperature conditions (Lufkin, 1977; Taylor, 1979) probably at temperatures below 150 °C (Pan & Ypma; 1973). This mineralisation is generally of low grade and is found in Mexico, Russia and Bolivia (Turneure, 1971; Sillitoe et al., 1975; Plimer, 1983; Ruiz, 1988).

6.2.4 Stratiform and stratabound deposits

Cassiterite is also found in various types of stratabound tin deposits. One type of these deposits is hosted by black shales and cassiterite is associated with stratabound polymetallic sulphides, for example the Dachang tin field in China (Tanelli & Lattanzi, 1985; Pašava et al., 2003; Fan et al., 2004). S-type biotite granites intruded into carbonates and calcareous black shales, which contain significant amounts of organic

carbon and constitute the source of sulphur. Pašava et al. (2003) suggest that the organic matter kept the oxygen fugacity of the fluid sufficiently low which facilitated transport and accumulation of reduced Sn^{2+} species in distal sites of metal deposition. The major sulphide mineral is pyrrhotite followed by arsenopyrite and sphalerite with minor stannite, galena, pyrite and chalcopyrite.

Another type of stratabound tin deposits, also known as Manto deposits in South America, is described in the following from Poland and Bolivia. In Poland the tin deposits are hosted by metamorphic schists of the Stara Kamienica chain close to Gierczyn, southwestern Poland (Mochacka et al., 2001). Tin mineralisation is hosted by almandine-bearing quartz-chlorite schist of the Precambrian Izera block which is bounded to the south by the Variscan Karkonosze granite pluton (Wiszniewska et al., 1998). Cassiterite is associated by various sulphides (dominantly pyrrhotite, chalcopyrite, arsenopyrite, and sphalerite) and sulphosalts (Mochacka et al., 1999). The origin of the tin deposit is a matter of debate and several models have been proposed (Speczik & Wiszniewska, 1984; Wiszniewska et al., 1998; Mochacka et al., 1999 and references therein).

In Bolivia the Manto deposits are hosted by the Silurian Catavi Formation composed of quartzites and black shales (Schneider & Lehmann, 1977; Lehmann, 1979, Lehmann, 1985). The tin mineralisation is distributed heterogeneously over the quartzite layers and can be traced over about 20 km along strike. The largest enrichments are found in the Kellhuani and Huallatani mines. The ore paragenesis is quite simple and is composed of fine-grained cassiterite, tourmaline, pyrite and hematite (Schneider & Lehmann, 1977). The stratabound occurrence of the tin deposits is interpreted as sedimentary tin enrichment and probably represents paleo-placers (Schneider & Lehmann, 1977), but this interpretation is controversially discussed (Lehmann, 1979). Sedimentological (e.g., grain size distribution) and paleogeographical conditions necessary for placer formation argue against a paleo-placer and thus a magmatic-hydrothermal origin related to a biotite-muscovite granite porphyry is proposed (Lehmann, 1985). The stratabound character of the Manto deposits is the result of preferred fracturing of the quartzite due to boiling during crystallisation of the granite porphyry (Lehmann, 1985).

A special kind of tungsten deposit was discovered by Maucher (1965), the so-called stratiform deposit type of the W-Sb-Hg formation. The stratiform-synsedimentary scheelite deposits are often accompanied by Sb and Hg mineralisation in the form of

stibnite and cinnabar, respectively (Maucher, 1976; Höll, 1977). Other minerals of this paragenesis are quartz, various carbonates (calcite, dolomite, siderite) and minor sulphides (pyrite, chalcopyrite), but cassiterite is always absent (Kempe & Wolf, 1994). The ore formation has been interpreted to be related to submarine (ultra-)mafic and acid volcanism associated with hydrothermal activity and precipitation of tungsten on the seafloor (Höll, 1977). This model is comparable to syngenetic exhalative (SEDEX) deposits (Plimer, 1980). These deposits are formed from relatively low temperature fluids below 200 °C with low salinities of 3 to 15 wt.% NaCl equivalent (Kempe & Wolf, 1994; Kempe et al., 1994). The three elements of the W-Sb-Hg formation occur in variable shares: in some deposits the W-Sb-Hg formation is represented by just two minerals, especially in the combination of cinnabar-stibnite and scheelite-stibnite, but the occurrence of cinnabar-scheelite is unlikely (Maucher, 1976). However, in other deposits one mineral predominates and the other two only occur as accessories (Maucher, 1976).

There is a lot of debate about the origin of the Mittersill deposit in the Felber valley of the Austrian Alps (Thalhammer et al., 1989) which was once interpreted as the tungsten endmember of the syngenetic W-Sb-Hg formation (Höll, 1975; Höll et al., 1972). Scheelite is the major ore mineral related to interstratified quartzite bands and mineralisation is strongly controlled by the bedding of the metavolcanic host rocks ('hornblendite'). But scheelite is also present in discordant quartz veins which were interpreted as feeder zones of syngenetic mineralization. Several authors now support a primary, epigenetic tungsten mineralisation related to the intrusion of granitic magmas and the discordant quartz veins consequently represent stockwork mineralisation (e.g., Raith & Schmidt, 2010 and references therein). The granitoids, mostly classified as I-type magmas (Finger et al., 1985), intruded during the Variscan orogeny and are now present as orthogneisses (e.g., the K1 gneiss) found in distinct spatial association with the tungsten mineralisation and are also mineralised. The epigenetic, magmatic-hydrothermal origin of the Mittersill deposit is also supported by Re-Os dating of molybdenite resulting in Variscan ages of about 340 Ma which is equivalent to the intrusion age of the K1 gneiss (Raith & Stein, 2006).

Stratiform and stratabound tungsten mineralisation is also found elsewhere, but there is much debate on their genesis (Lahusen, 1972; Skaarup, 1974; Plimer, 1987a; Cheilletz, 1988; Raith, 1991; Appel, 1994; Raith & Prochaska, 1995). Some stratabound tungsten deposits are interpreted as former tungsten enriched evaporates (Ririe, 1989)

as W is also enriched in brines and evaporates, such as the Searles lake deposit situated in proximity to the Death Valley, California, USA (Ririe, 1989). Evaporates and concentrated brines of the Searles lake cover an area of about 90 km² and contain approximately 70 ppm WO₃ leading to a total of estimated 77000 tons WO₃ (Carpenter & Garret, 1959). The total W content is remarkable but tungsten is not recovered at the moment. Tungsten-bearing brines and evaporites are found in arid regions of the former Soviet Union and Western United States.

The tungsten deposits of Rwanda and Uganda were formerly also interpreted as syngenetic precipitation of ferberite and scheelite in black shales followed by remobilisation into vein-type deposits (Cheilletz, 1988). However, there is still debate on the genesis of these tungsten deposits. Today, most authors support a granite-related hydrothermal deposition of the tungsten minerals in quartz veins (Frisch, 1975; Pohl, 1976; Pohl, 1994; de Clercq et al., 2008; De Clercq, 2012; Goldmann et al., 2013); whereby scheelite precipitated early and was subsequently replaced by ferberite forming characteristic pseudomorphs of ferberite after scheelite, so-called reinite.

6.2.5 Massive sulphide deposits

Massive sulphide deposits may host tin mineralisation, but mostly at uneconomic grades. Two general types of massive sulphide deposits occur, namely volcanogenic massive sulphide (VMS) and sedimentary exhalative (SEDEX) deposits. As defined by Robb (2005), VMS deposits are formed from hydrothermal fluids around submarine volcanic centres; SEDEX deposits are also related to similar hydrothermal processes but are formed within rift basins and are hosted by marine clastic sediments without a direct link to volcanism (Robb, 2005). The principal ore forming processes are circulation and convection of seawater and subsequent leaching of metals from the volcanic rocks of the oceanic crust. The metal-rich hydrothermal solutions vent directly into the seawater and mainly sulphides precipitate caused by the rapid changes in temperature and pressure. In VMS deposits the convection is driven by active volcanic centres (e.g. seafloor spreading zones or back-arc settings), whereas SEDEX deposits are formed by rift-related geothermal hydrothermal activity controlled by faults.

Cassiterite is formed syngenetically with the sulphides and is typically fine-grained due to rapid precipitation in contact with seawater. Massive sulphide deposits are major sources for Cu, Zn, Pb, Ag and Au but only a few contain recoverable Sn, e.g. Kidd Creek in Ontario and Sullivan in British Columbia, and Neves Corvo in Portugal.

Cassiterite is also found in massive sphalerite ore from the volcanogenic massive sulphide deposits along the 'Cu-Zn line' in the Murchison greenstone belt (Schwarz-Schampera et al., 2010). The formation of cassiterite ores in tin-bearing massive sulphide deposits is related to polymetallic, low-temperature (~200 °C), highly saline, acidic (pH of 2 – 4), and strongly reduced fluids (Schwarz-Schampera, 2000). There is much debate on the origin of tin in massive sulphide deposits and most authors support leaching from tin-enriched host rocks, but others suggest significant magmatic-hydrothermal contribution (Huston et al., 2011).

In the Kidd Creek VMS deposit, tin mineralization occurs in two different mineral assemblages. Cassiterite is generally related to polymetallic massive sphalerite ores, whereas stannite occurs in the underlying chalcopyrite-rich ores (Hannington et al., 1999). It is assumed that Sn was deposited at relatively low-temperatures together with Zn and Pb (Hennigh & Hutchinson, 1999; Hannington et al., 1999). In the Neves Corvo VMS deposit, cassiterite and various Cu-Sn-bearing sulphosalts are closely associated with the massive chalcopyrite ores (Oliveira et al., 1997; Relvas et al., 2006). Generally, the Cu-rich ores occur at the base of the deposits, overlain by the Zn-rich ores followed by 'barren' massive pyrite ores in the upper part of the deposits (Oliveira et al., 1997; Serranti et al., 2002). The massive cassiterite ores most likely formed by direct venting into seawater during early stages, subsequently followed by generation of massive sulphides (Relvas et al., 2006; Gaspar, 2002). Though both deposits contain significant amounts of tin compared to other massive sulphide deposits, the distribution and mineral assemblages differ significantly. At Neves-Corvo, tin mineralisation is generally linked to Cu ores, whereas cassiterite at Kidd Creek is related to Zn ores (Hannington et al., 1999). A common feature of Sn-rich massive sulphide deposits are high Ag grades accompanied by remarkably low Au levels (Hannington et al., 1999).

The Sullivan SEDEX deposit at Kimberley, British Columbia, was an important producer of Pb, Zn and Ag with Sn as by-product. The ores are composed of alternating layers of galena, Fe-rich sphalerite, and pyrrhotite with minor amounts of pyrite, chalcopyrite and arsenopyrite (Mulligan, 1975). Chalcopyrite is invariably associated with high Sn grades and tourmalinised footwall is indicative for cassiterite mineralisation (Mulligan, 1975). Highest Sn contents in the ore are found around to the central pyrrhotite zone.

6.2.6 Placers

Secondary deposits, also known as placers, are formed by weathering and erosion of the primary ore deposit or mineralized regional rock exposures followed by transport, deposition, and accumulation of the ore minerals due to their high density (much higher than 2.65 g/cm^3 representing the density of the major rock-forming mineral quartz), hardness, and resistance/stability to mechanical and chemical weathering (Garnett & Bassett, 2005). Placers are subdivided into different types, namely eluvial, colluvial, alluvial/fluvial (Figure 6.14), glacial, marine, and aeolian deposits depending on the transporting medium and the distance to the primary deposit (Garnett & Bassett, 2005).

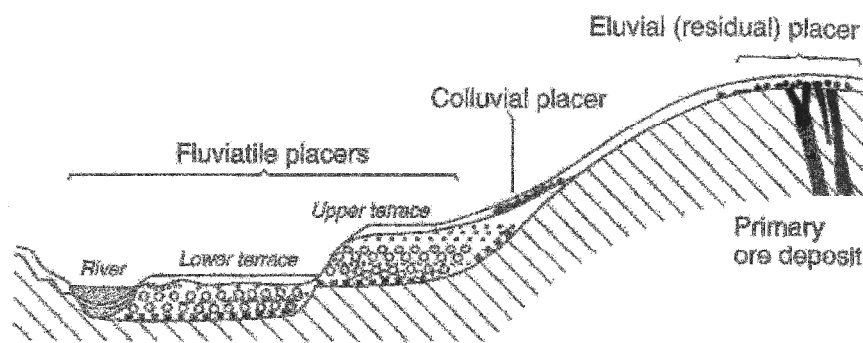


Figure 6.14: Classification and distribution of different placer deposit types of a river valley in relation to a nearby outcrop of the primary ore deposit (Pohl, 2011).

The initiation of placer formation may be generalized to three major events, which are tectonic activity, a change in climate, and a relative change in sea level (Garnett & Bassett, 2005). Flowing water represents the most important medium for transport and sorting of the various detrital minerals, whereby density is controlling separation and settling of the minerals at sites of lower stream velocity (Garnett & Bassett, 2005). Alluvial cassiterite placers are a major source for tin, especially in Southeast Asia (Schwartz et al., 1995). Cassiterite is capable forming a placer deposit as it exhibits high density ($\sim 7 \text{ g/cm}^3$) and hardness (6-7 on Mohs scale) with poor cleavage, thus providing high resistance to mechanical abrasion. Tungsten placers are only found in eluvial or residual deposits. Although wolframite and scheelite have high density (scheelite: $\sim 6 \text{ g/cm}^3$; wolframite: $7.2\text{-}7.5 \text{ g/cm}^3$), both minerals show intermediate hardness (4 to 5 on Mohs scale) with good cleavage and subsequently become fragmented during transport preventing the formation of distal placer deposits.

7 Methodology

7.1 Sampling and starting material

Heavy mineral concentrates are the preferred sample material for AFP because concentrates provide a sufficient number of individual ore minerals for analysis and possibly also contain accessory minerals which may be indicative for individual ore deposits. However, these unwanted minerals are removed during further processing of the ore concentrate. A statistically representative sample for AFP is directly sampled on-site, consists of about 50-200 grams depending on the grain size of the ore concentrate and represents the actual production from the mining site. The quality and mineralogical composition of the ore concentrate is dependent on the mineralogical variability of the ore deposit, the mining method and the beneficiation process (Melcher et al., 2008; Melcher et al., 2009). This indicates that the composition of the representative sample may change with mining progress or processing technique. Artisanal and small-scale mining is common in Central Africa and the heavy mineral concentrates are usually produced by ground sluicing, panning and sieving (Figure 7.1). These pre-concentrates may undergo limited additional processing (e.g., magnetic separation) before they are exported (Melcher et al., 2010). Industrial mechanised mining operations produce almost pure ore concentrates using several beneficiation steps in an ore processing plant (e.g., density separation, magnetic separation, flotation, etc.). These concentrates are also a representative sample, but characteristic accessory minerals are probably removed during the beneficiation process.



Figure 7.1: Heavy mineral pre-concentrate from Rukaragata pegmatite in Rwanda. This pre-concentrate is essentially composed of cassiterite and columbite-tantalite (black grains).

A responsibly taken ore concentrate is characteristic for a single ore deposit and represents an adequate sample of the given population. The reproducibility of variability of various ore concentrates from a single deposit was tested by Melcher et al. (2010). Four 'Coltan' concentrates from the Manono deposit (Democratic Republic of Congo), which were taken at different dates, show matching mineralogical and chemical compositions (Melcher et al., 2010).

7.2 Sample preparation

Samples used for AFP comprise mostly heavy mineral concentrates, but single mineral grains and hard rock samples are also used for this study. Heavy mineral concentrates are the preferred sample type for AFP. Polished sections are prepared by mounting representative grain aliquots into epoxy resin, grinding, and stepwise diamond polishing down to 0.25 μm on cloth laps. These polished sections are suitable for MLA, EPMA and LA-ICP-MS analysis.

7.3 Scanning electron microscopy with Mineral Liberation Analysis (MLA)

An environmental scanning electron microscope (ESEM), the so-called *FEI Quanta 600 FEG ESEM*, is used to identify different mineral phases (Figure 7.2). Characteristic X-ray spectra are used for qualitative and semi-quantitative elemental analysis by an energy dispersive X-ray spectrometer (EDX). The source for the electron beam is a field emission gun in a high-vacuum environment. The emitted electron beam is focused by condenser lenses and is scanning in a raster pattern over a rectangular section of the sample. Secondary and backscattered electrons plus characteristic X-rays are the result of the interaction of the electron beam with the sample. The secondary electrons (SE) are detected to display the surface morphology and the backscattered electrons (BSE) show the mean atomic number of the individual phases.

The Mineral Liberation Analysis (MLA) software uses the EDX system combined with BSE imaging to automatically identify the mineral phases of ore concentrates (Gu, 2003; Fandrich et al., 2007). The characteristic X-ray spectrum of each mineral phase is compared with the X-ray spectra of known standards stored in a database. After comparison each mineral phase on the sample surface is classified and displayed on a MLA image (Figure 7.3). Other parameters which are identified by MLA include relative abundances, grain size distributions, intergrowths of single mineral phases, and the total mineralogical composition of the ore concentrate.



Figure 7.2: The *FEI Quanta 600 FEG* environmental scanning electron microscope with Mineral Liberation Analysis software in operation at BGR, Hannover. The left screen is showing an EDX-spectrum of an analysed mineral grain and the right screen displays the BSE image of the scanned sample surface.

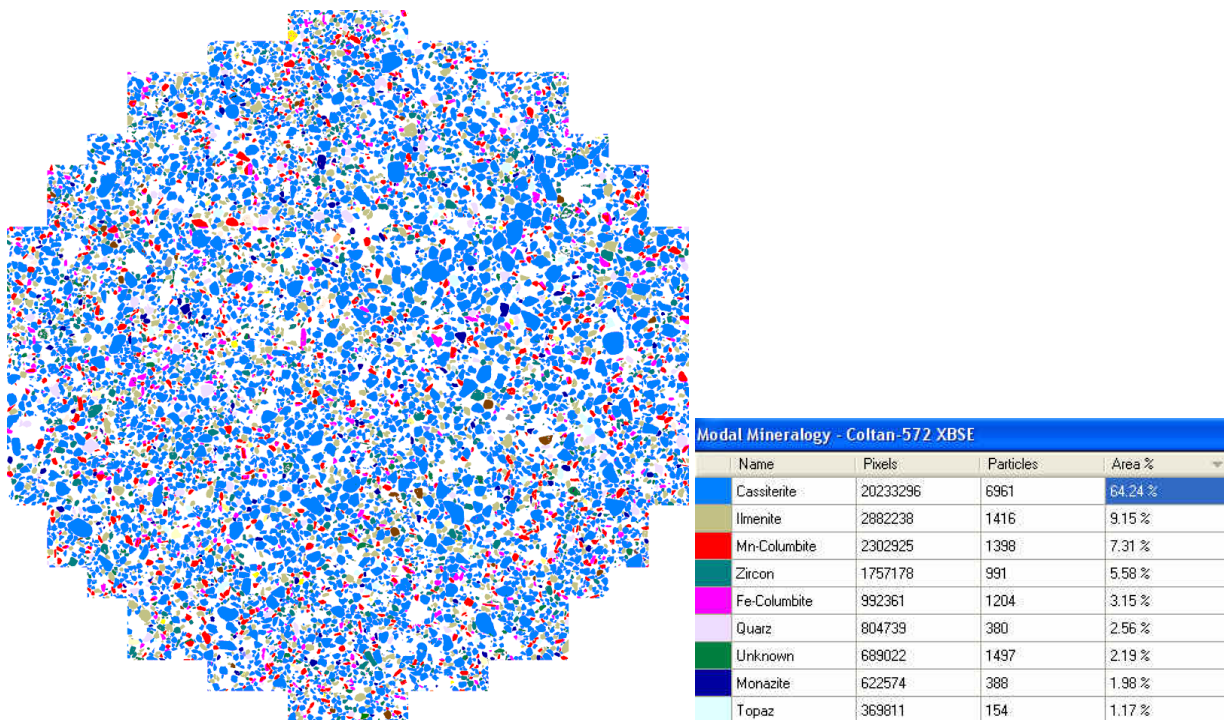


Figure 7.3: Classified MLA image of a mixed cassiterite-coltan pre-concentrate from the Jos Plateau, Nigeria (Coltan-372). Legend is reduced and only minerals with more than 1 area% are included.

7.4 Laser ablation inductively coupled plasma mass spectrometry (LA-ICP-MS)

LA-ICP-MS is used for quantitative in-situ analysis of solid samples and fluid or melt inclusions for determination of trace element concentrations or isotope ratios with a high spatial resolution down to some tens of microns in diameter (Heinrich et al., 2003). The mass spectrometer (MS) is a *Thermo Scientific ELEMENT-XR* high-resolution sector field inductively coupled plasma mass spectrometer coupled to a *New Wave UP193-FX* laser ablation system with an *ATLEX-300-SI* excimer laser (Figure 7.4).



Figure 7.4: The LA-ICP-MS system in operation at BGR, Hannover. The *New Wave UP193-FX* laser ablation unit is shown on the right hand side with the *ATLEX-300-SI* excimer laser stored in the cabinet below. The screen displays the ablation pit of the laser on a columbite-tantalite grain. The *Thermo Scientific ELEMENT-XR* mass spectrometer is shown on the left hand side.

The principle of a laser (acronym for **light amplification by stimulated emission of radiation**) is the emission of coherent, monochromatic light by stimulated excitation of photons in an optical resonator. The amplification results from reflection of the photons in the space between two mirrors. A part of the radiation escapes the optical resonator through a semi-reflective mirror and is passed and focused by laser optics onto the sample surface. The optical path of the laser optics is rinsed with nitrogen. The wavelengths of laser light range from infrared via visible to the ultraviolet spectra depending on the different laser media. Solid state lasers most commonly use crystals as laser medium, such as neodymium-doped yttrium-aluminium-garnet (Nd-YAG). Excimer lasers (acronym for **excited dimer**) use noble gases or mixtures composed of noble gases and halogens (such as argon fluoride) as laser media. In the excited state noble gases either form dimers (for example Ar₂ dimers), or complexes with halogens (for

example ArF). The *ATLEX-300-SI* excimer laser uses ArF gas as laser medium and is emitting ultraviolet laser radiation with a short wavelength of 193 nm.

The specimen is contained in a gastight cell of the laser ablation system (LA). The sample material is ablated by focused pulses of the coherent laser beam and the sample aerosol is transported by a flow of He into the inductively coupled plasma (ICP) of the mass spectrometer (MS). Helium is used as carrier gas because it increases sensitivity and transport efficiency compared to Ar (Günther & Heinrich, 1999; Horn & Günther, 2003). The inductively coupled plasma is generated in a quartz torch which is made up by three tubes with different flow rates of Ar, in particular the auxiliary, cool and sample gases (Figure 7.5). The auxiliary gas is injected for continuous burning of the plasma which in turn is controlled by the cool gas with significantly higher flow rates. Radio frequency alternation current is applied to an induction coil, which is wrapped around the torch (Figure 9.4). The resulting high-frequency alternating electromagnetic field in turn induces an electric current into the Ar gas. The Ar gas is heated to high temperatures and finally forms the plasma of ionised argon atoms ($\text{Ar} \rightarrow \text{Ar}^+ + e^-$). The plasma is initially ignited by a Piezo spark. The sample gas is injected directly into the plasma together with the He carrier gas including the sample aerosol. The sample aerosol is vaporised, atomised and ionised by the high temperatures (>5000 K) of the plasma and monovalent ions ($\text{M} \rightarrow \text{M}^+ + e^-$) are formed.

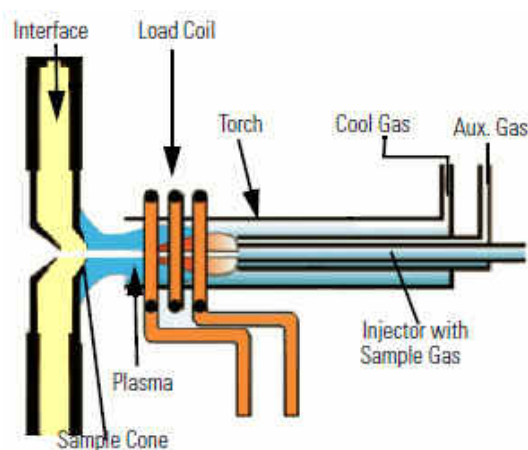


Figure 7.5: Arrangement of plasma torch, induction coil and interface with the sampler and skimmer cones (Thermo, 2005).

The ICP is at atmospheric pressure and at the interface the pressure is reduced stepwise through two nickel orifices, the so-called sampler and skimmer cones, to the high vacuum conditions in the mass spectrometer. The ions are accelerated into the analysing system by applying a high voltage of up to 8 kV. The analyser of the mass spectrometer

separates the ions based upon their mass-charge ratio. The analyser in a sector field mass spectrometer is a double-focusing system in reverse Nier-Johnson geometry composed of a magnetic sector analyser (MSA) followed by an electrostatic analyser (ESA). Both, the MSA and the ESA, focus ions with diverging angles of motion towards the detector. The magnetic field of the MSA is changed by altering the current through the electromagnet to select ions of a specific mass-charge ratio and ion energy. The ESA is dispersive to ion energy only.

The mass spectrometer is able to switch between three fixed resolution modes (low, medium, and high resolution) by changing the geometry of the entrance and exit slits. The mass resolution necessary to separate an interfering signal from the signal of interest is generally defined as $R = m/\Delta m$ (Table 7.1), while Δm is the mass difference necessary to achieve a valley of 10% between the two neighbouring peaks of identical intensity height at mass-charge ratio m and $m \pm \Delta m$. However, some interferences (e.g., $^{90}\text{Zr}^{2+}$ on ^{45}Sc) and isobaric overlaps (e.g., ^{40}Ar on ^{40}Ca) cannot be resolved because they need a higher mass resolution of R greater than 10000.

Table 7.1: Maximum resolution (R_{max}) of the three different resolution modes (low, medium and high resolution).

Mass resolution mode	$R_{\text{max}} = m/\Delta m$
Low	400
Medium	4000
High	10000

Ions are detected by two different detector systems covering a wide measuring range from 5 to 10^{11} counts per second (cps). These are the secondary electron multiplier detector (SEM) for high sensitivity at low count rates and the less sensitive Faraday detector at higher count rates (Figure 9.6). The SEM detector is a dynode system which automatically switches between two detection modes; the analogue and the counting modes depending on the signal intensity. The Faraday cup detects the electric current which is generated by the impact of the charged ions and is suitable for large signal intensities. Therefore, it is possible to detect trace and major elements over a wide concentration range during a single analysis because the system automatically chooses the adequate detection mode (SEM counting, SEM analogue and Faraday cup) depending on the count rate. The counts per second of ions of an isotope are functionally used to quantify the concentration of an element in the sample. In contrast to solution-based analytical techniques which generate a steady state signal, LA-ICP-MS is a dynamic

sampling process. But dissolution of the sample is not needed for laser ablation analyses and therefore dilution errors, contamination, loss of volatiles and interferences from acids and dissolution agents are excluded or at least reduced. Additionally, some minerals including cassiterite are very resistant to dissolution.

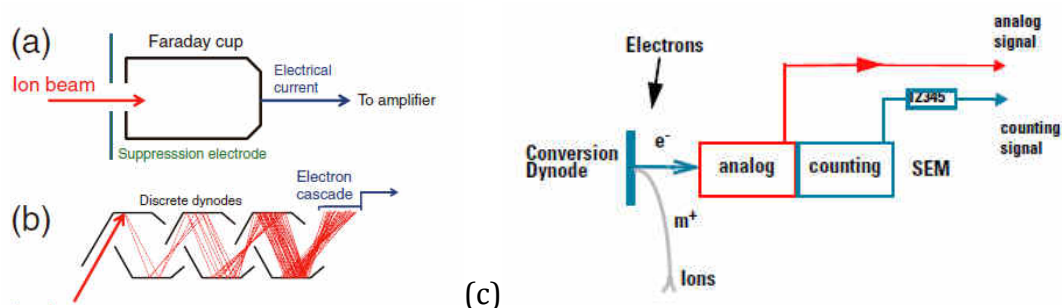


Figure 7.6: Different detector types in ICP-MS. a) Faraday cup, b) secondary electron multiplier, c) scheme of a secondary electron multiplier (SEM) detector with analogue and counting modes for detection (Wiedenbeck et al., 2012; Thermo, 2005).

7.5 Electron probe microanalysis (EPMA)

A *Cameca SX-100* microprobe (Figure 9.7) is used for non-destructive elemental analyses with a high spatial resolution (about 1 μm) of solid samples with polished surfaces. The analyses are carried out either qualitatively or quantitatively for elements ranging from atomic number 5 (boron) to 92 (uranium). Electrons were emitted from a tungsten filament by applying a heating voltage. The electrons were accelerated by high voltage in high vacuum from the cathode to the anode. This high-energy electron beam is focused by condenser lenses onto the sample surface, which needs to be sputtered with a carbon coating to deduct electric charge. The electrons cause physical interactions with the atoms of the sample and different types of radiation are emitted. The secondary X-rays are characteristic for each element. These radiations are analysed qualitatively and semi-quantitatively by energy dispersive X-ray spectrometry (EDX) or quantitatively by wavelength dispersive X-ray spectrometry (WDX). In the WDX spectrometer, the wavelengths of the different X-rays were reflected by specific analyser crystals and are sent to a detector. The spectrometer is adjusted to a specific wavelength for an element of interest and the intensity is equivalent to the concentration in the measured sample. This concentration is calculated by the microprobe with regard to the matrix correction and the former measurements of standards. Besides X-ray radiation, backscattered electrons (BSE) are used to generate images showing the mean atomic number of single phases and cathodoluminescence (CL) of certain minerals is displayed by a CL-detector.

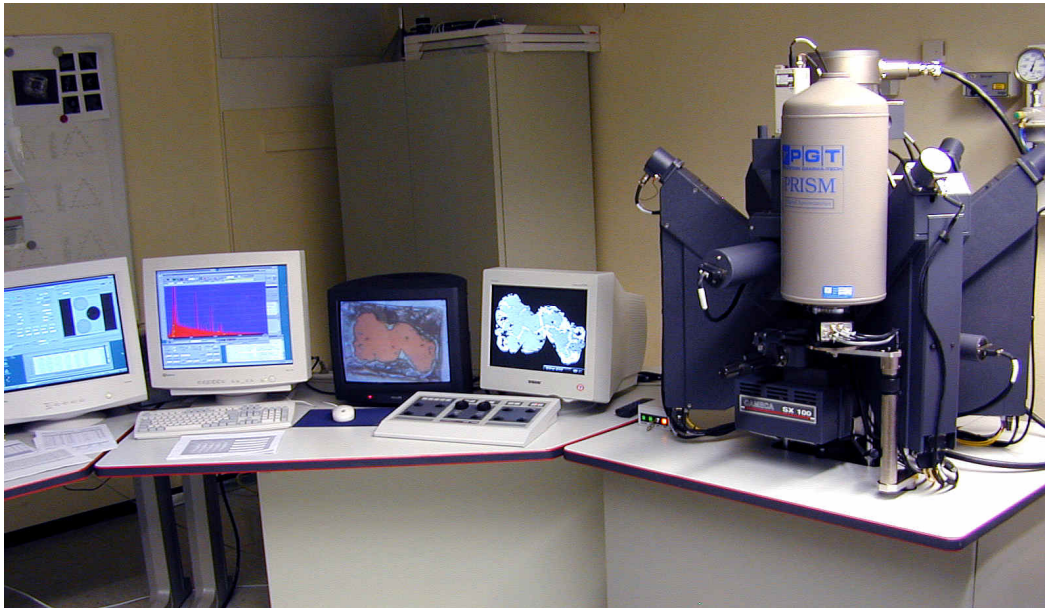


Figure 7.7: The *Cameca SX-100* electron microprobe in operation at BGR, Hannover. The right screen displays the BSE image of the scanned sample surface and the next screen to the left is showing optical image of the reflected light microscope. The two screens to the left are for the control computer.

The measurement conditions for analyses of cassiterite are set to an acceleration voltage of 35 kV at a beam current of 40 or 120 nA (Table 7.2). For wolframite and scheelite analyses, the measurement conditions are set to an acceleration voltage of 30 kV at a beam current of 120 nA (Table 7.3).

Table 7.2: Parameters including measured lines, measurement time (meas. time) in seconds, used standards, and average detection limits (det. lim.) in ppm at 40 and 120 nA for each element during analysis of cassiterite by EPMA.

element	line	meas. time [s]	standard	det. lim. [ppm; 40/120 nA]
Al	K α	20	metal	169/98
Si	K α	20	metal	147/86
Sc	K α	60	metal	78/45
Ti	K α	20	metal	120/69
Mn	K α	20	metal	161/92
Fe	K α	20	metal	152/87
Cu	K α	20	metal	185/108
As	L α	160	GaAs	188/109
Zr	L α	100	metal	307/177
Nb	L α	90	metal	305/182
Sn	L α	10	cassiterite	821/430
Hf	L α	120	metal	195/113
Ta	L α	80	metal	238/139
W	L α	140	metal	179/103
U	M α	120	metal	165/95

Table 7.3: Parameters including measured lines, measurement time (meas. time) in seconds, used standards, and average detection limits (det. lim.) in ppm at 30 kV for each element during analysis of wolframite and scheelite by EPMA.

element	line	meas. time [s]	standard	det. lim. [ppm]
Si	K α	10	rhodonite	153
Ca	K α	10	scheelite	128
Sc	K α	10	metal	138
Ti	K α	10	rutile	208
Mn	K α	10	wolframite	169
Fe	K α	10	wolframite	199
Zr	L α	50	metal	523
Nb	L α	60	columbite	290
Mo	L α	80	metal	289
Sn	L α	20	metal	330
Hf	L α	120	metal	111
Ta	L α	90	tantalite	196
W	L α	10	wolframite	589
U	M α	110	metal	168

8 Method development for cassiterite analysis by laser ablation inductively coupled plasma mass spectrometry (LA-ICP-MS)

Method development for LA-ICP-MS analysis is necessary as this study is the first attempt to determine trace elements in cassiterite by this method. This includes adjustment the setup for the LA-ICP-MS system and selection of the most suitable isotopes for the respective elements to exclude the effect of major interferences.

8.1 Parameters

The laser ablation system and the mass spectrometer are set to conditions, which were developed for cassiterite measurements in particular. An automated cross-calibration procedure (Faraday Cross Calibration) on the ^{36}Ar isotope is run previously to every session to align the signal intensities for the different detector modes of the mass spectrometer. Additionally, a fine-tuning of the gas flows, torch position and transfer lenses of the ion optics is performed before each measurement by optimising the intensities of ^{51}V ($>2.5 \times 10^5$ cps) and ^{119}Sn isotopes ($>2 \times 10^9$ cps) and monitoring of the oxide formation ($<0.001\%$; $^{119}\text{Sn}^{16}\text{O}/^{119}\text{Sn} \times 100$) during ablation of a cassiterite sample (in-house code 'Coltan 240'). The general settings for the Ar flow rates are circa 0.9 L/min for the auxiliary gas, 16.4 L/min for the cool gas and 1.35 L/min for the sample gas. Helium instead of Ar is used as carrier gas at a flow rate of 200 ml/min because He provides high signal intensity, low rate of oxide formation, reduced particle size and reduced particle deposition around the ablation pit (Eggins et al., 1998; Günther & Heinrich, 1999; Horn & Günther, 2003). The plasma power (RF power) for the high-frequency alternation current is set to 1200 W.

Line scan ablation is favoured over static spot ablation resulting in lower detection limits and more constant signal at higher intensity levels (Košler, 2008). The same ablation conditions are used for standard and sample measurements (Kroslakova & Günther, 2007). The positions of the line scans for trace element measurements were placed carefully on 'clean' surfaces to avoid interference from mineral inclusions and exsolution phases or cracks filled with contaminants. Prior to each analysis a pre-ablation scan is run to remove any contamination from the sample surface. The laser adjustment for pre-ablation is set to a spot size of 75 μm in diameter with a scan speed of 15 $\mu\text{m}/\text{s}$ and a frequency of 10 Hz. The washout time after every ablation process takes 80 seconds. The blank is measured for 145 seconds on the Ar sample gas mixed with the He carrier gas from the ablation cell, the so-called 'gas background' (Longerich

et al., 1996). During the background measurement the laser warm-up sequence is run with the shutter being closed. The laser parameters are slightly changed for the ablation scan. The spot size and the scan speed are reduced to 50 μm and 5 $\mu\text{m/s}$, respectively. The frequency is kept at 10 Hz. The laser energy is fixed to 100% of 3 mJ for ablation of cassiterite and NIST 610 glass. The ablation scan takes 210 seconds including 8 passes over the scan line with length of approximately 130 μm .

The mass spectrometer takes 355 seconds in total for the measurement of a single line scan; thereof 145 seconds account for the blank including laser warm-up and 210 seconds for signal measurement with laser ablation. The mass spectrometer performs 30 passes over the whole spectra for the low (LR) and the medium (MR) resolution and is constantly switching between these two resolution modes with a switch delay of 1 second.

The following isotopes have been analyzed: ^{69}Ga , ^{73}Ge , ^{74}Ge , ^{75}As , ^{88}Sr , ^{89}Y , ^{93}Nb , ^{95}Mo , ^{137}Ba , ^{139}La , ^{140}Ce , ^{142}Ce , ^{141}Pr , ^{146}Nd , ^{147}Sm , ^{153}Eu , ^{155}Gd , ^{159}Tb , ^{163}Dy , ^{165}Ho , ^{166}Er , ^{169}Tm , ^{172}Yb , ^{175}Lu , ^{178}Hf , ^{181}Ta , ^{182}W , ^{201}Hg , ^{204}Pb , ^{206}Pb , ^{207}Pb , ^{208}Pb , ^{209}Bi , ^{232}Th , ^{238}U in the low resolution mode and ^{12}C , ^{23}Na , ^{24}Mg , ^{27}Al , ^{29}Si , ^{31}P , ^{32}S , ^{44}Ca , ^{45}Sc , ^{47}Ti , ^{51}V , ^{52}Cr , ^{55}Mn , ^{56}Fe , ^{59}Co , ^{60}Ni , ^{63}Cu , ^{66}Zn , ^{90}Zr , $^{91}\text{Zr}^{2+}$, ^{111}Cd , ^{113}In , ^{118}Sn , ^{121}Sb in the medium resolution mode. For all other elements the system switches between the SEM and Faraday detectors depending on the count rate. Small mass windows of 22% are chosen for most isotopes measured in low resolution. But for some isotopes, which are measured in low resolution mode, wider mass windows of 120% are applied (^{93}Nb , ^{178}Hf , ^{181}Ta , ^{182}W , ^{201}Hg , $^{204-208}\text{Pb}$, ^{209}Bi , ^{232}Th , ^{238}U) to facilitate automated switching to the Faraday detector as these elements possibly occur at higher concentrations. Mass windows of 100% are generally used for isotopes measured in the medium resolution mode. Exceptions are the ^{12}C , ^{29}Si , ^{31}P , ^{32}S and ^{118}Sn isotopes with mass windows of 150% because these elements possibly occur at unexpected high concentrations if inclusions of carbonate, silicate, phosphate, sulphide or sulphate were ablated accidentally; Sn is the major element in cassiterite. A broader mass window is necessary for the automated switching of the detector system.

The search and integration windows for isotopes measured in low resolution are set to 80% and 60%, respectively. For most isotopes measured in medium resolution search and integration windows of 100% and 60% are chosen. Exceptions are isotopes of the transition metals from Fe to Zn. For those isotopes significantly smaller search windows are selected to discriminate interference of the numerous bivalent Sn ions.

8.2 Calibration, standardisation, and data evaluation

The calibration of the ICP-MS is done by analysis of reference material. External calibration using matrix-matched reference materials is the most common calibration strategy in LA-ICP-MS analysis (Longerich et al., 1996; Russo et al., 2002; Heinrich et al., 2003), but matrix-matched mineral standards with adequate certified element concentrations are not available for cassiterite or wolframite. Therefore external calibration strategy using a non-matrix-matched reference material plus internal standardisation has been applied. This procedure has proven to provide sufficiently accurate analyses for many elements in many sample matrices without matrix-matching (Norman et al., 1996; Norman et al., 1998; Heinrich et al., 2003; Jackson, 2008). Možná et al. (2006) reported that in a non-matrix matched calibration strategy with a strong matrix difference between sample and standard material (in this case stainless steel JK27A versus silicate glass NIST 610) the resulting element concentrations may deviate systematically from the accurate values in the range of 13% to 62% for different elements. An ablation yield correction is applied using the internal standardisation to correct for the different ablated masses of different materials, in this case the NIST glass and the natural minerals cassiterite and wolframite (Liu et al., 2008).

External calibration is applied by analysis of the standard reference material NIST 610 glass (from the National Institute of Standards and Technology, Gaithersburg, USA) as reference material. The NIST glasses are generally accepted as calibration materials for micro-analytical trace element measurements, because the concentrations of all trace elements are high enough for precise primary calibration (Perkins et al., 1997; Jochum & Willbold, 2006; Jochum et al., 2011). The preferred values for the chemical composition of the NIST 610 glass were taken from Pearce et al. (1997). However, new data on various reference materials (including NIST 610) are compiled by the GeoReM database (Jochum et al., 2005; Jochum et al., 2011). The NIST 610 standard is a synthetic glass composed mainly of SiO₂, Al₂O₃, CaO and Na₂O (Table 8.1) spiked with a number of trace elements at concentrations of approximately 500 ppm (Table 8.2). The distribution of the spike elements in the NIST 610 glass standard can be regarded as sufficiently homogeneous to be used as reference material in microanalysis (Hinton et al., 1995; Norman et al., 1996, Kane, 1998, Eggins & Shelley, 2002; Luvizotto, 2008; Jochum et al., 2011), although homogeneity tests performed on the NIST 610 glass revealed compositional heterogeneity for some trace elements (Eggins & Shelley, 2002; Jochum et al., 2011). Several authors discussed problems caused by matrix differences

when using NIST glasses for calibration of geological samples (Guillong & Günther, 2002; Danyushevsky et al., 2011). To avoid such difficulties, matrix-matched calibration materials are prepared by synthesis (Ødegård, 1999). As matrix-matched mineral standards are not available for cassiterite or wolframite, a lower accuracy (in the range of up to about 60% according to Možná et al., 2006) has to be taken into account. But at least the application of LA-ICP-MS data for AFP does not necessarily require very accurate data (Gäbler et al., 2013). Comparison of LA-ICP-MS with other analytical methods demonstrates that the results fit well for a wide range of elemental concentrations (Norman et al., 1998).

The NIST 610 reference material is measured repeatedly during a sequence. For internal standardisation an element is chosen which occurs in the standard as well as in the sample in sufficient and known concentration. The concentration of the internal standard element is usually determined independently by alternative analytical methods, for example EPMA. But in this study, Sn was used as internal standard for cassiterite measurements and the concentration of Sn was calculated from the known stoichiometry of pure cassiterite with 78.77 wt.% Sn (787679 ppm Sn). This approach is more time- and cost-effective eliminating the additional measurement of Sn by EPMA prior to the LA-ICP-MS analysis.

Table 8.1: Composition of the matrix of NIST 610 in weight percent oxide (Pearce et al., 1997)

element oxide	wt.%
SiO ₂	69.98
Al ₂ O ₃	2.04
CaO	11.45
Na ₂ O	13.35

Table 8.2: Compositional data for spike elements of NIST 610 in ppm (Pearce et al., 1997)

element	ppm	atomic number
Ag	239	47
As	317	33
Ba	424	56
Be	466	4
Bi	358	83
Cd	259	48
Ce	448	58
Co	405	27

Cr	405	24
Cs	361	55
Cu	430	29
Dy	427	66
Er	426	68
Eu	461	63
Fe	457	26
Ga	438	31
Gd	420	64
Ge	426	32
Hf	418	72
Ho	449	67
In	441	49
K	486	19
La	457	57
Li	485	3
Lu	435	71
Mg	465	12
Mn	433	25
Mo	377	42
Nb	419	41
Nd	431	60
Ni	444	28
P	343	15
Pb	413	82
Pr	430	59
Rb	431	37
Sb	369	51
Sc	441	21
Sm	451	62
Sn	396	50
Sr	497	38
Ta	377	73
Tb	443	65
Th	451	90
Ti	434	22
Tm	420	69
U	457	92
V	442	23
W	445	74
Y	450	39
Yb	462	70
Zn	456	30
Zr	440	40

The concentrations for each element are calculated by the equation (9) given by Longerich et al. (1996):

$$c_{SAM}^{AN} = \frac{cps_{SMP}^{AN}}{\frac{cps_{STD}^{AN}}{c_{STD}^{AN}} \times \left(\frac{cps_{SAM}^{IS}}{cps_{STD}^{IS}} \frac{c_{STD}^{IS}}{c_{SAM}^{IS}} \right)} \quad (9)$$

- c_{SAM}^{AN} : concentration (ppm) of the analyte element in the sample
 cps_{SAM}^{AN} : intensity (cps) of the analyte element in the sample
 c_{STD}^{AN} : concentration (ppm) of the analyte element in the reference material
 cps_{STD}^{AN} : intensity (cps) of the analyte element in the reference material
 c_{SAM}^{IS} : concentration (ppm) of the internal standard element in the sample
 cps_{SAM}^{IS} : intensity (cps) of the internal standard element in the sample
 c_{STD}^{IS} : concentration (ppm) of the internal standard element in the reference material
 cps_{STD}^{IS} : intensity (cps) of the internal standard element in the reference material

Internal standardisation is used for correction of matrix effects, elemental fractionation, sensitivity drift and differences in ablation yield. Ablation yield is the term describing the amount of material which is ablated and transported to the ICP. However, short wavelength lasers (such as the 193 nm ArF-excimer Laser) minimise inter-matrix elemental fractionation differences during ablation (Guillong et al., 2003; Heinrich et al., 2003). Further criteria to reduce the effect of elemental fractionation during LA-ICP-MS analysis besides laser wavelength are laser energy, pulse rate, pit size and depth (Heinrich et al., 2003; Sylvester, 2008; Gaboardi & Humayun, 2009). As stated by Heinrich et al. (2003), elemental fractionation is reduced to a level of typically less than 5% relative standard deviation.

The limits of detection are calculated for each element on the basis of three times the standard deviation of the background measurement (Figures 8.1 & 8.2; Heinrich et al., 2003). The detection limits are dependent on background intensity, signal sensitivity (cps per ppm) and ablation rate (Norman et al., 1996.) In this context it should be mentioned that the detection limit for Ni is quite high, because nickel orifices are utilised in the interface of the mass spectrometer which results in high background signals.

Figure 8.1: Detection limits for LA-ICP-MS analysis of cassiterite.

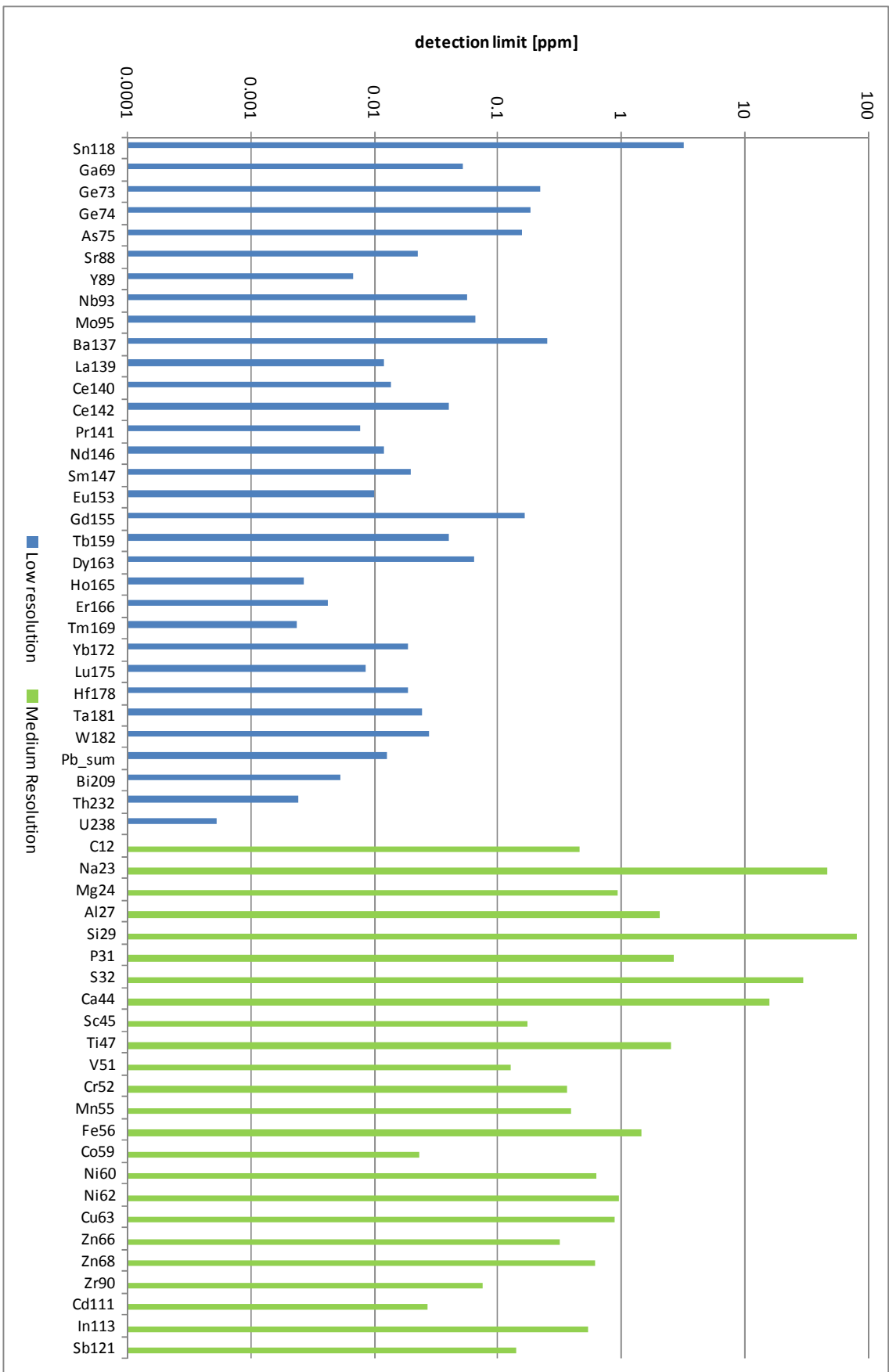
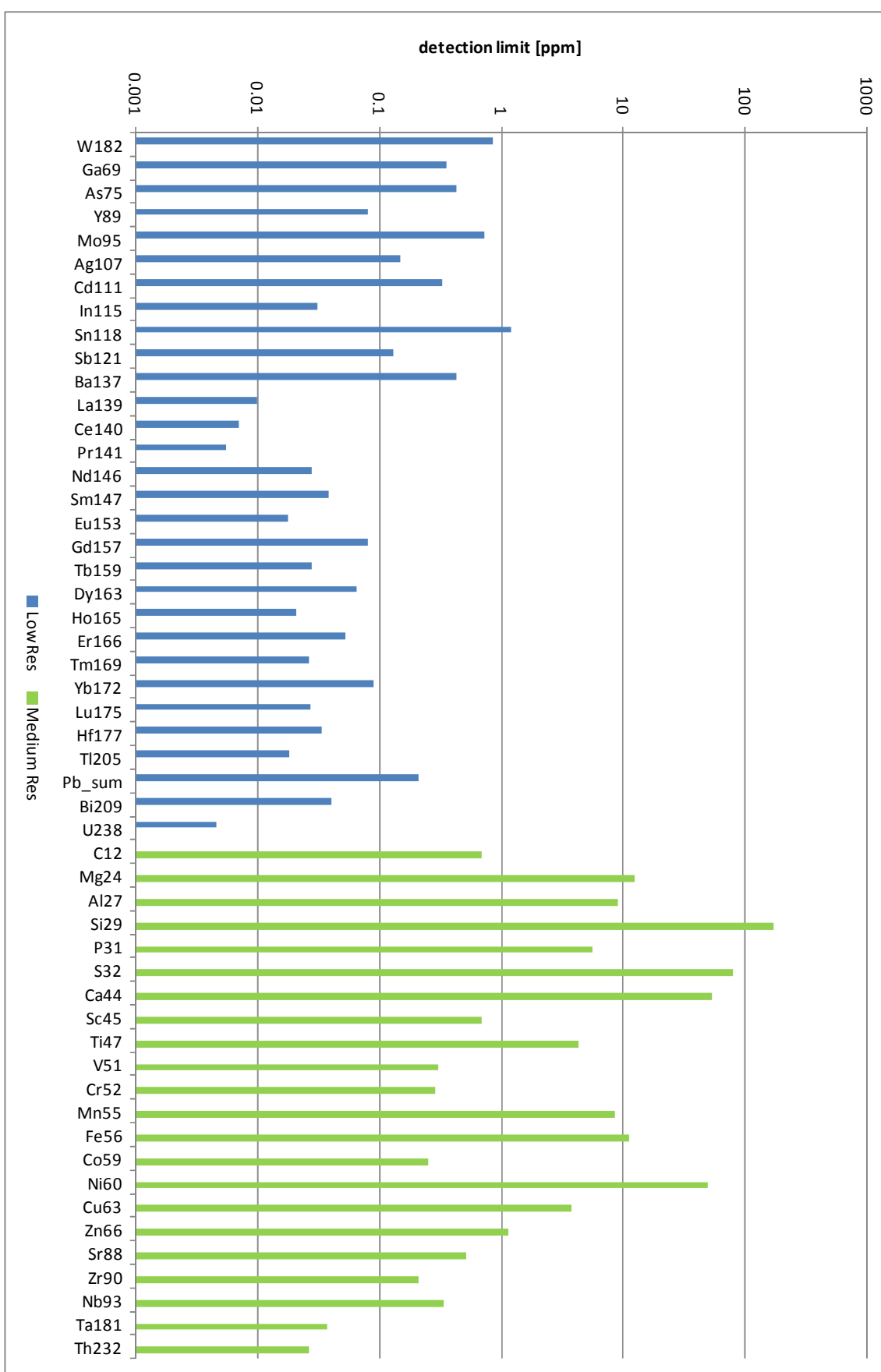


Figure 8.2: Detection limits for LA-ICP-MS analysis of wolframite.



In contrast to solution-based analytical techniques which generate stable and constant signals, laser ablation is a dynamic sampling process generating transient signals and a special data acquisition and reduction has to be applied (Jackson et al., 2008). Therefore the evaluation of the large amount of raw data is handled with an in-house software tool which was implemented in JAVA using the libraries JFreeChart, commons Math and POI (Gäbler et al., 2011). The signals for background and sample measurements are time-resolved and therefore selected time intervals are integrated for the blank and sample signals (Figure 8.3). The net intensities are calculated by subtracting the background from the signal intensity. The median values of the integrated signals are calculated to discriminate outliers. Higher irregular signal intensities caused by mineral inclusions are identified by careful examination of the time-resolved signal and these measurements are discarded (Figure 8.4).

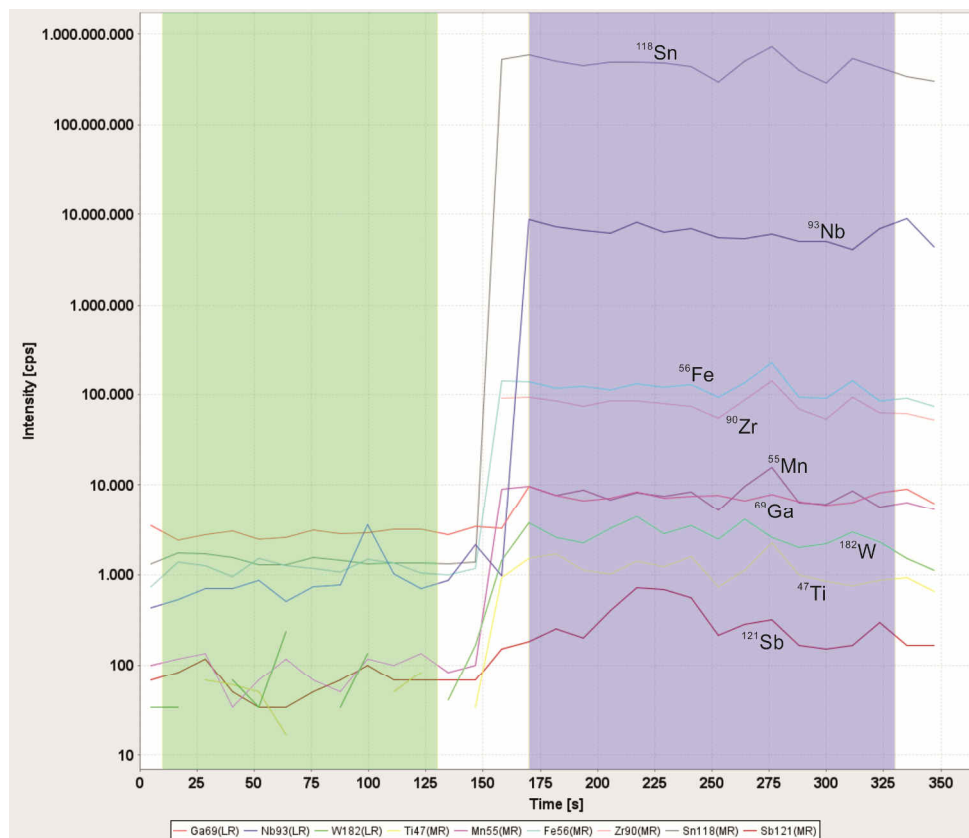


Figure 8.3: Time-resolved signal of LA-ICP-MS analysis of cassiterite. Green shaded area is integrated for background and blue shaded area is integrated for sample signal.

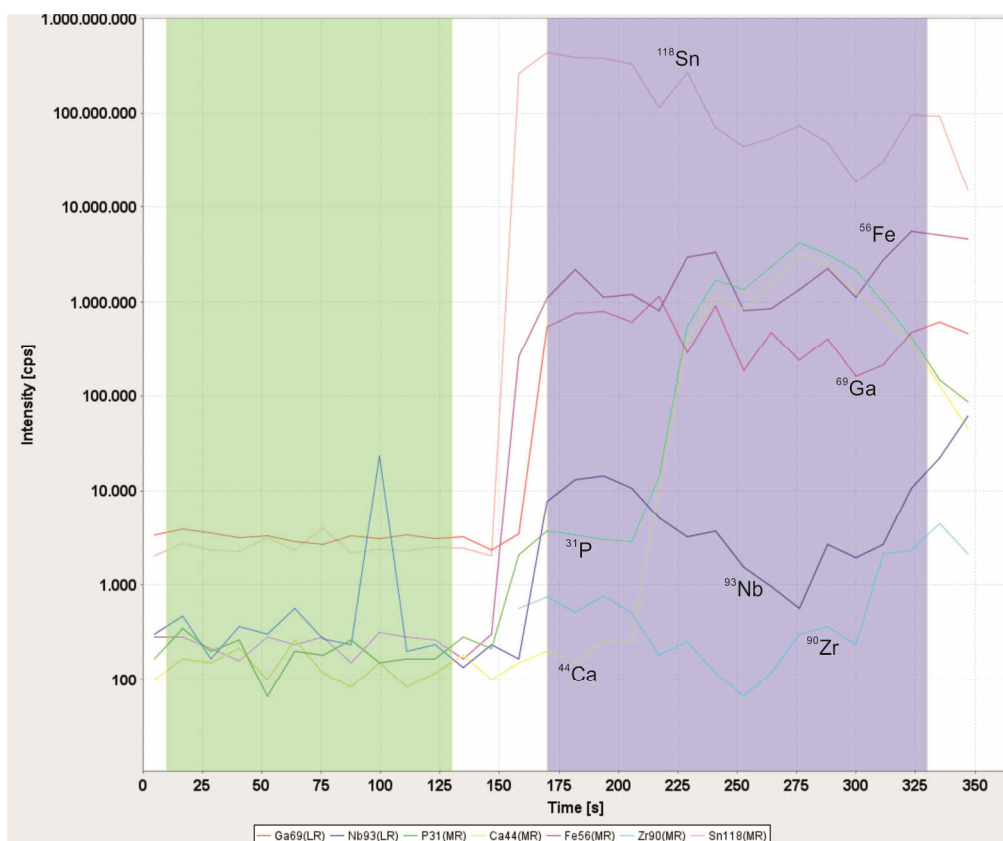


Figure 8.4: Time-resolved signal of LA-ICP-MS analysis of cassiterite with apatite inclusion indicated by increase in Ca and P. Green shaded area is integrated for background and blue shaded area is integrated for sample signal.

The standardisation and calibration strategy is verified by comparison of the LA-ICP-MS data with electron microprobe analyses of a cassiterite concentrate from the Democratic Republic of the Congo (AS 8829). The LA-ICP-MS data were calibrated using the NIST 610 glass and the in-house Coltan 139 sample as reference materials. The in-house Coltan 139 standard is a columbite-(Fe) crystal from Madagascar which was characterized by LA-ICP-MS, electron microprobe, solution ICP-MS methods and X-ray fluorescence analysis (Melcher et al., 2009; Gäbler et al., 2011). Titanium (Figure 8.5), Fe (Figure 8.6), Nb (Figure 8.7), and Ta (Figure 8.8) are chosen for comparison of the methods, because these elements occur in cassiterite at sufficiently high concentrations for detection by electron microprobe. Analyses by both methods were not performed on exactly the same spot of the particular grain because the analytical spot size of both methods differs significantly. For the electron microprobe a defocused electron beam with a spot size of about 10 μm in diameter was used, in contrast to the 50 μm wide and about 130 μm long ablation lines of the LA-ICP-MS. Therefore the data scatter relative to the 1:1 line is partly due to chemical zoning of the heterogeneous cassiterite grains and the different analytical spot sizes and volumes (see Figures 8.5-8.8).

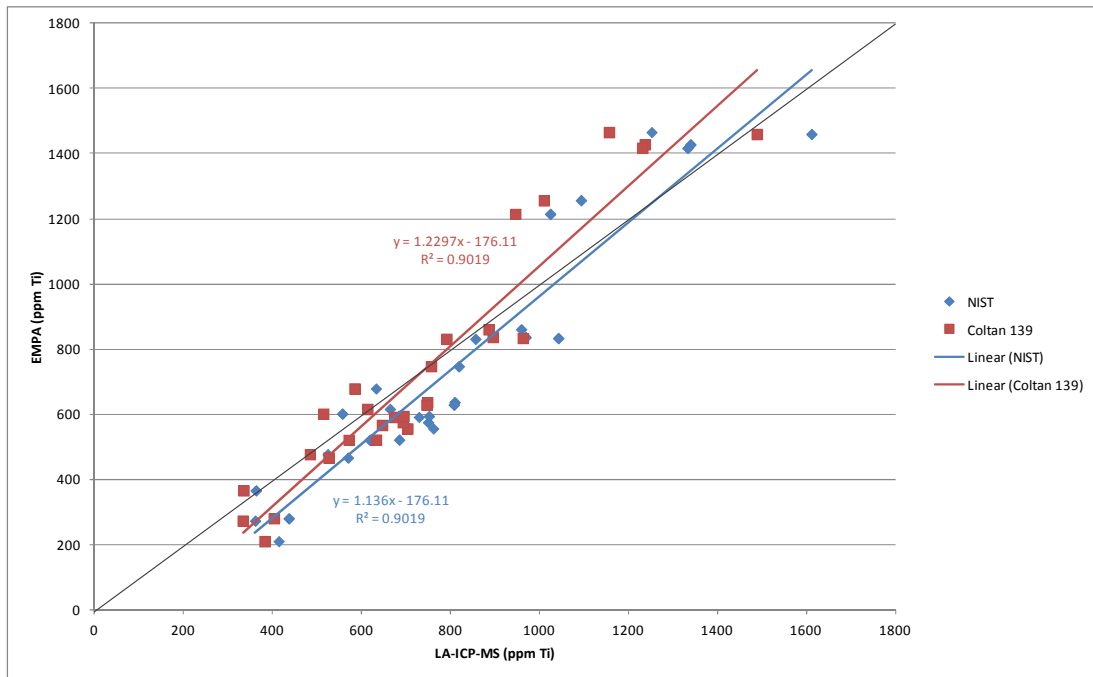


Figure 8.5: Comparison of LA-ICP-MS and EPMA data for titanium. The analyses for both methods were performed on the same grains of cassiterite concentrate AS 8829. The LA-ICP-MS data are calibrated against NIST 610 glass (in blue) and columbite-(Fe) Coltan 139 (in red), respectively. The black line shows the 1:1 trend.

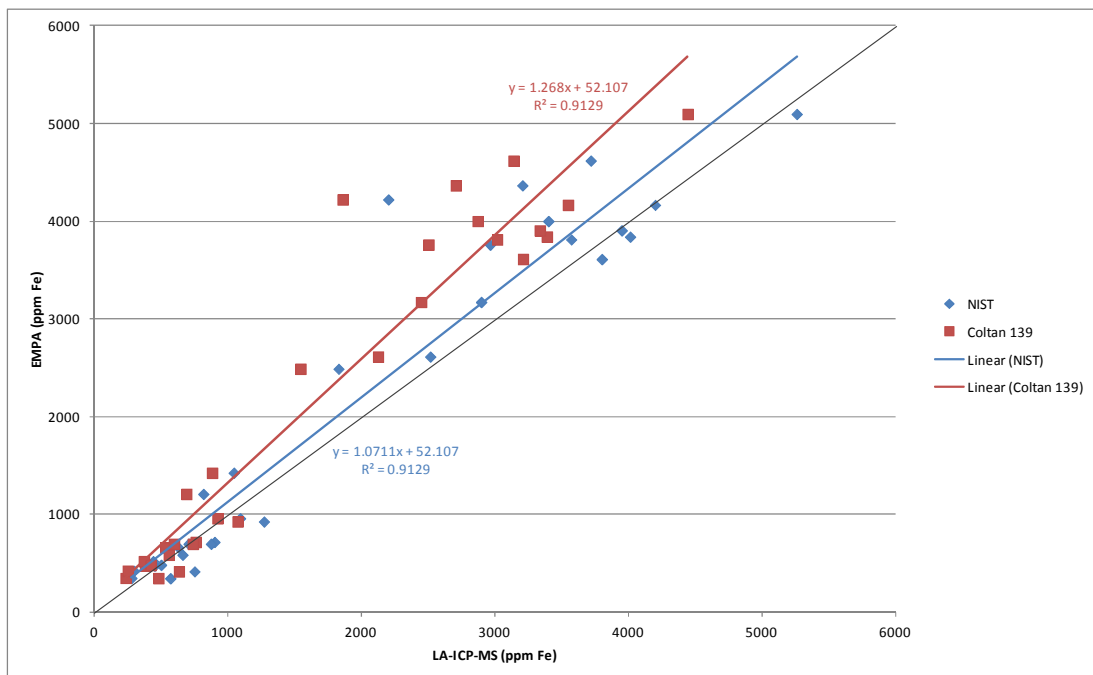


Figure 8.6: Comparison of LA-ICP-MS and EPMA data for iron. The analyses for both methods were performed on the same grains of cassiterite concentrate AS 8829. The LA-ICP-MS data are calibrated against NIST 610 glass (in blue) and columbite-(Fe) Coltan 139 (in red), respectively. The black line shows the 1:1 trend.

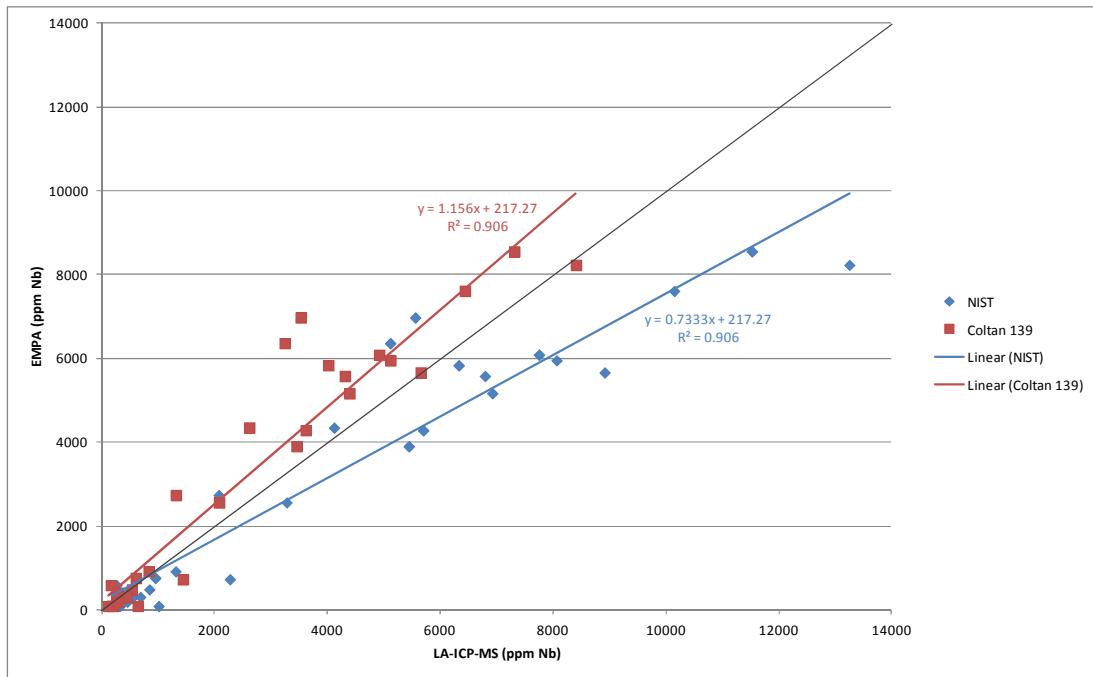


Figure 8.7: Comparison of LA-ICP-MS and EPMA data for niobium. The analyses for both methods were performed on the same grains of cassiterite concentrate AS 8829. The LA-ICP-MS data are calibrated against NIST 610 glass (in blue) and columbite-(Fe) Coltan 139 (in red), respectively. The black line shows the 1:1 trend.

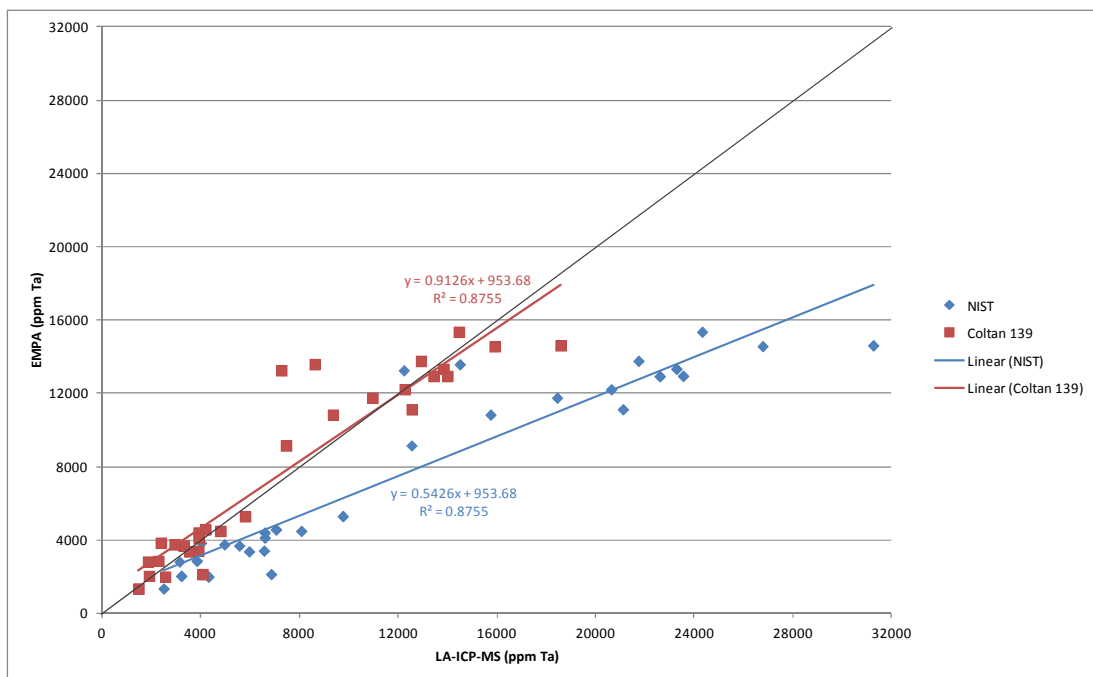


Figure 8.8: Comparison of LA-ICP-MS and EPMA data for tantalum. The analyses for both methods were performed on the same grains of cassiterite concentrate AS 8829. The LA-ICP-MS data are calibrated against NIST 610 glass (in blue) and columbite-(Fe) Coltan 139 (in red), respectively. The black line shows the 1:1 trend.

However, comparison of the analyses for Ti (Figure 8.5) and Fe (Figure 8.6) indicate that both methods produce consistent data and it is shown that the standardisation strategy using the NIST 610 reference material yields reliable results. But the data for Nb (Figure 8.7) and Ta (Figure 8.8) show a discrepancy by standardisation either on NIST 610 or the in-house Coltan 139 reference materials. The strong differences, particularly in the measurements of Ta, are probably the effect of elemental fractionation during ablation of non-matrix-matched reference material. Elemental fractionation in LA-ICP-MS refers to changes in the relative proportions of elements in a sample to its original composition that are produced during analysis (Sylvester, 2008). Refractory elements, like Ta and Nb, show lower signal intensities than volatile elements when using non-matrix-matched calibration (Eggins et al., 1998). This effect is dependent on the elemental temperature of condensation, the volatility of the elements and the transparency of the calibration material (Figure 8.9). Elemental fractionation increases with higher transparency of the reference material resulting in measured concentrations of refractory elements being lower and measured concentrations of volatile elements being higher (Gaborardi & Humayun, 2009). Further processes leading to elemental fractionation are described by Sylvester (2008). On the contrary, non-transparent reference materials show less matrix-dependent elemental fractionation. In this study, the NIST 610 reference material is transparent compared to the opaque columbite-(Fe) crystal. Additionally, the columbite-(Fe) more closely matches the composition of cassiterite because both minerals are oxides. Therefore, data of refractory elements with high elemental temperature of condensation (e.g. Ta, Nb, W, Zr, Hf) certainly provide more reliable results when calibrated against in-house Coltan 139 reference standard.

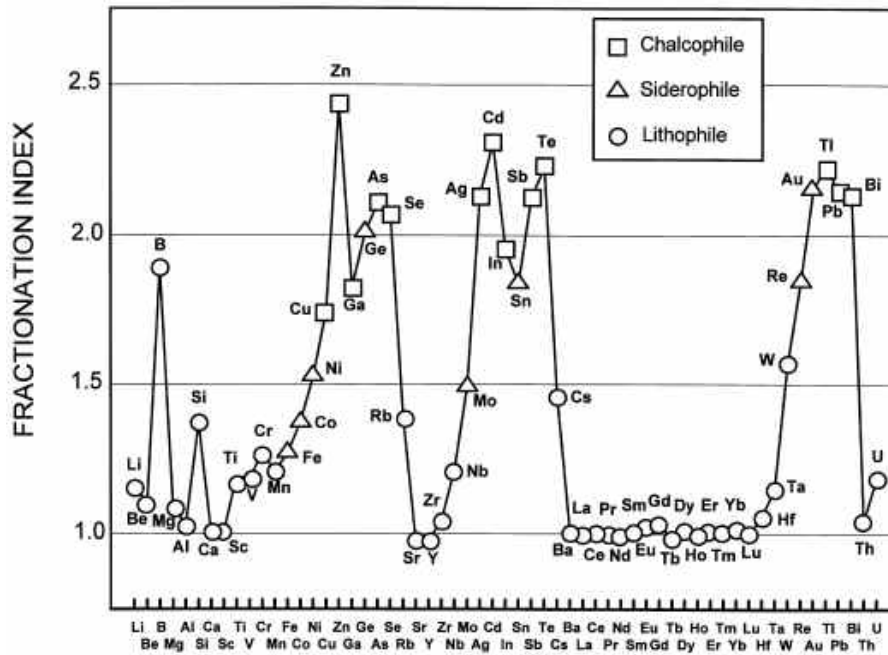


Figure 8.9: Fractionation indices relative to Ca (Fryer et al., 1995). Symbols categorize elements according to the classification of Goldschmidt (1923). Diagram taken from Günther et al. (1999).

8.3 Development of analytical procedure for cassiterite

Method development was performed to verify and optimise measurement conditions of selected isotopes for cassiterite analyses. Therefore measurements were undertaken on blank, NIST 610 reference glass and cassiterite samples (Coltan 240) to verify and optimise the settings for selected individual isotopes. The relative isotopic abundances of the elements are taken from Rosman & Taylor (1998). The result of this work is summarised at the end of this chapter in Table 8.3, where the recommended isotope for each element and possible interferences are listed.

Generally, most isotopes are measured in the low resolution mode for higher signal intensity, because an increase in resolution is coupled to a large reduction in sensitivity. For problematic elements with more than one isotope, the isotopic ratios are checked to exclude interference problems and finally the primary most abundant isotopes are chosen. In some cases the less abundant isotope is measured because of isobaric interferences or interferences caused by oxides and Ar compounds or bivalent ions on the primary isotope. However, some isotopes have to be measured in medium resolution mode to separate interferences. Interferences are caused by isobaric isotopes, multiple charged ions or molecular ions having the same mass-charge ratio as the selected isotope. These interferences result in incorrect higher signal intensity for the

isotope of interest. Interferences of molecular compounds originate from constituents of the various gases, especially Ar from the plasma gas and He from the carrier gas. Influential contaminants of these gases are H, C, O, S, Cl, and Hg. For example, the transition metals from Sc to Zn are measured in medium resolution to discriminate interfering Ar compounds. The major components of the sample matrix also generate significant interferences; in this case the major interfering element is Sn. Other contaminants are Na and Si which are components of the quartz torch. The isotopes ^{12}C , ^{31}P , ^{32}S , ^{23}Na , ^{24}Mg , ^{27}Al , ^{28}Si and ^{44}Ca are used to check if silicates, carbonates, phosphates and sulphides were analyzed accidentally during a scan.

Tuning of the apparatus and monitoring of the oxide formation reduces the generation of molecular oxide species. Thus, not all interferences can be separated even at the maximum resolution level, for example isobaric interferences such as ^{40}Ca and ^{40}Ar . But at least one isotope free from isobaric interferences can be found for each element (except for In), although in many cases this will be a less abundant isotope.

8.3.1 Low resolution mode

Several elements are free from interferences and consequently the most abundant isotope is measured in the low resolution mode. These isotopes are ^{88}Sr (82.6%), ^{95}Mo (15.9%), ^{181}Ta (99.9%), ^{182}W (26.5%), ^{238}U (99.3%) and the lead isotopes ^{206}Pb (24.1%), ^{207}Pb (22.1%) and ^{208}Pb (52.4%). The ^{204}Pb isotope is used for the determination of common lead for U-Pb dating and has to be corrected for the isobaric ^{204}Hg interference. Besides, several selected elements are monoisotopic such as ^{89}Y , ^{93}Nb , ^{209}Bi , and ^{232}Th , but these have no significant interferences and are measured in the low resolution mode.

Gallium is measured on the ^{69}Ga isotope in the low resolution mode because it shows no interferences (Figure 8.10). On the contrary, the signal of the ^{71}Ga isotope is interfered by $^{55}\text{Mn}^{16}\text{O}$ (99.8%), $^{40}\text{Ar}^{31}\text{P}$ (99.6%), and $^{36}\text{Ar}^{35}\text{Cl}$ (0.26%) compounds (Figure 8.11). Furthermore, the ^{69}Ga isotope is preferred due to its higher relative abundance of 60.1% in contrast to the ^{71}Ga isotope with 39.9%.

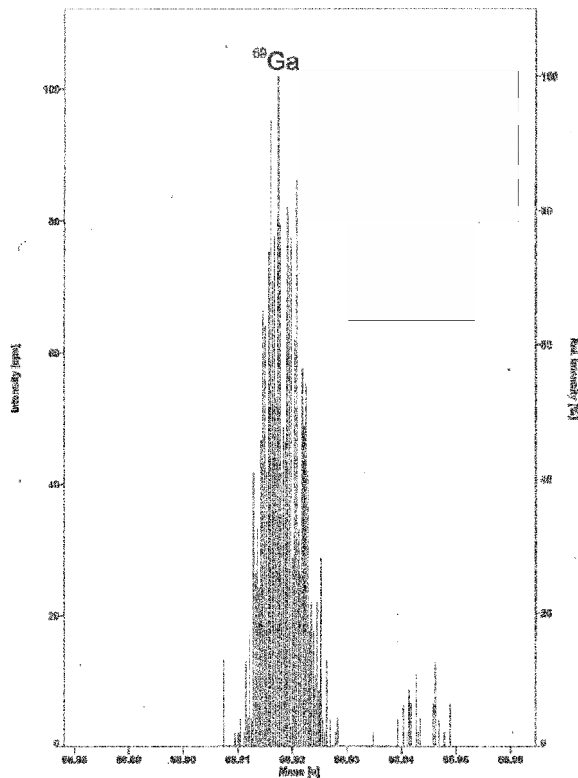


Figure 8.10: Diagram of intensity versus mass-charge ratio showing the high resolution spectrum of gallium on the nominal mass of 69 amu. Measurement on cassiterite sample (Coltan 240)

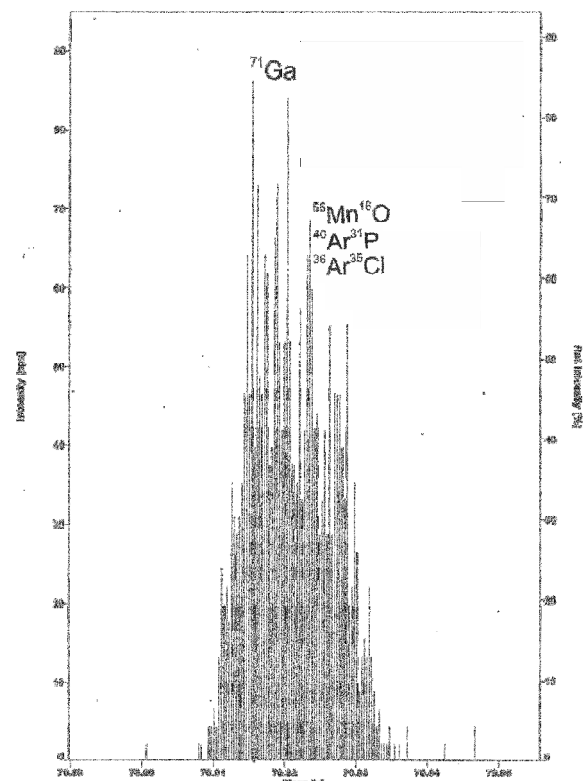


Figure 8.11: Diagram of intensity versus mass-charge ratio showing the high resolution spectrum of gallium on the nominal mass of 71 amu. Note the interference caused by MnO and ArP. Measurement on cassiterite sample (Coltan 240)

Germanium is measured on the most abundant ^{74}Ge (36.3%) isotope despite the interferences caused by an isobaric ^{74}Se (0.9%) isotope plus $^{36}\text{Ar}^{38}\text{Ar}$ (0.04%) and $^{37}\text{Cl}_2$ (5.9%) compounds (Figure 8.13) which likewise influence the blank and the sample signal. ^{72}Ge (27.5%) isotope is discarded because of considerable $^{56}\text{Fe}^{16}\text{O}$ (91.5%), $^{40}\text{Ar}^{32}\text{S}$ (94.6%) and $^{35}\text{Cl}^{37}\text{Cl}$ (36.7%) interferences. The other Ge isotopes are perturbed by isobaric interferences. In addition, Ge could also be measured on the ^{73}Ge isotope with a relative low abundance of 7.7%. No significant interferences are found in immediate proximity to the ^{73}Ge peak (Figure 8.12), but this isotope is affected by the bivalent $^{146}\text{Nd}^{2+}$ ion at elevated Nd contents.

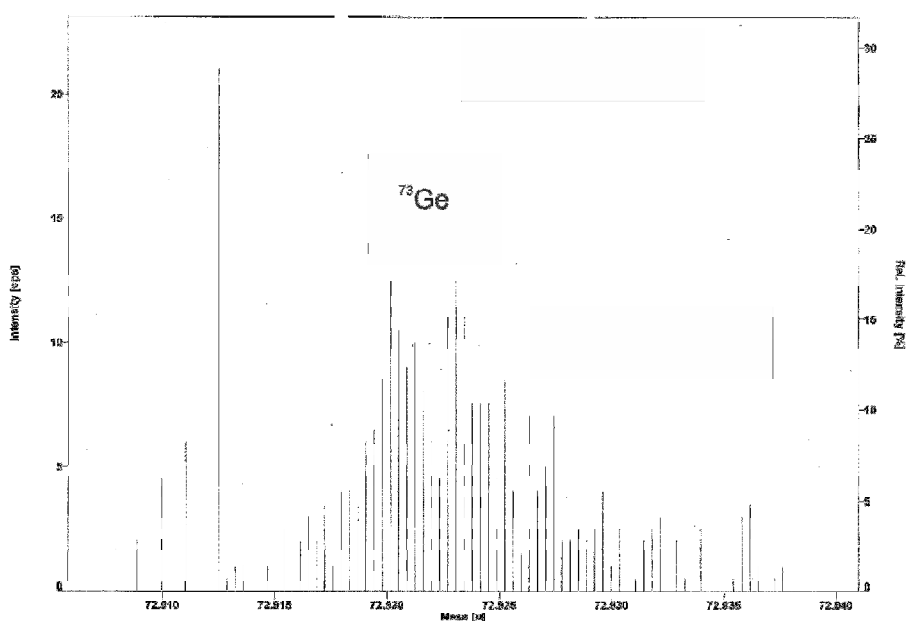


Figure 8.12: Diagram of intensity versus mass-charge ratio showing the high resolution spectrum of germanium on the nominal mass of 73 amu. Measurement on cassiterite sample (Coltan 240)

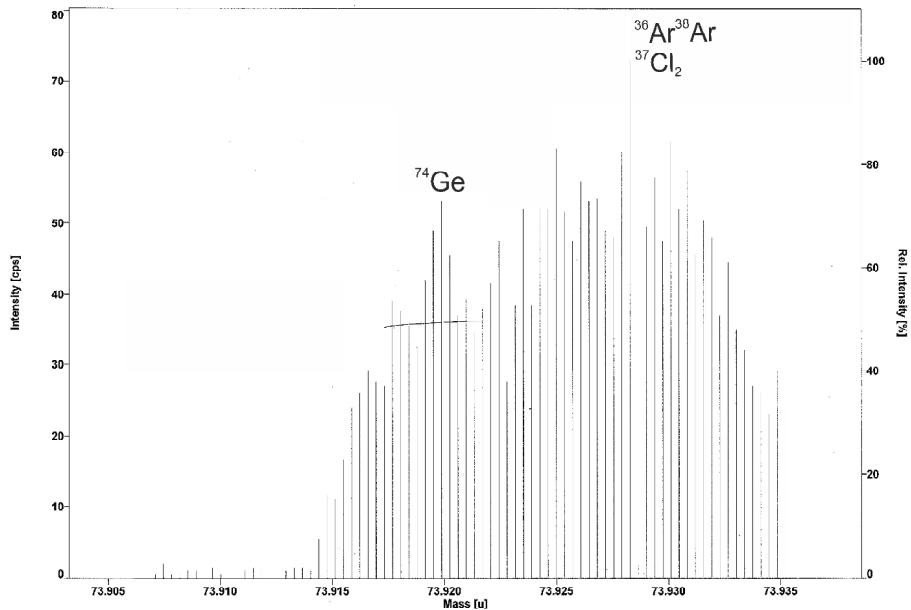


Figure 8.13: Diagram of intensity versus mass-charge ratio showing the high resolution spectrum of germanium on the nominal mass of 74 amu. Note the interference caused by Ar_2 and Cl_2 . Measurement on cassiterite sample (Coltan 240)

Arsenic is a monoisotopic element with the nominal mass of 75 amu. The signal of the ^{75}As isotope is interfered by the $^{40}\text{Ar}^{35}\text{Cl}$ (75.5%) compound. This interference derives from the plasma gas and likewise influences the background and sample signals. Therefore this interference has little influence on the correct signal, but results in increased detection limits.

There are only two *barium* isotopes without isobaric interferences, but both are interfered by Sn oxide ions. The ^{135}Ba isotope (6.6%) is perturbed by relative high $^{117}\text{Sn}^{18}\text{O}$ (8.6%) interference. Therefore, the ^{137}Ba (11.2%) isotope is selected despite a small $^{119}\text{Sn}^{18}\text{O}$ (0.02%) interference (Figure 8.14). These SnO interferences cannot be resolved and need a higher resolution than the maximum resolution mode of the mass spectrometer.

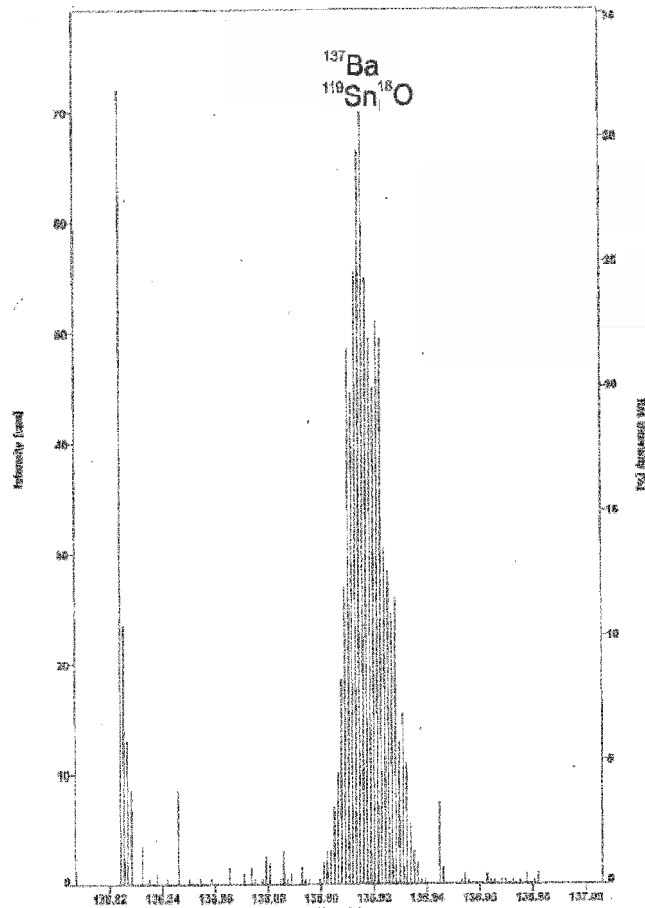


Figure 8.14: Diagram of intensity versus mass-charge ratio showing the high resolution spectrum of barium on the nominal mass of 137 amu. Note that the SnO interference cannot be resolved in high resolution mode. Measurement on cassiterite sample (Coltan 240)

The lanthanides or *rare earth elements* (REE) from La to Lu are measured in low resolution to gain high signal intensities, but several of these elements show elevated background values in blank measurements (Figures 8.15, 8.16, and 8.17). These interferences are caused by Sn and Ba compounds which accumulate on the sampler and skimmer cones (Figures 8.15 and 8.16). *Praseodymium*, *terbium*, *holmium* and *thulium* are monoisotopic elements and are measured on the specific nominal masses although the ^{159}Tb isotope is perturbed by a considerable non-resoluble $^{120}\text{Sn}^{23}\text{Na}^{16}\text{O}$ interference, which leads to an elevated background signal of about 8000 cps (Figure 8.16). The influence of the interference is nearly identical for the blank and the sample signal and therefore Tb is only measurable at high concentrations in the sample.

Lanthanum is measured on the most abundant ^{139}La (99.9%) isotope which shows no significant interferences (Figure 8.18). The isotopes of *cerium* are significantly interfered by Sn compounds. The ^{140}Ce (88.5%) isotope is perturbed by a non-resoluble

$^{124}\text{Sn}^{16}\text{O}$ (5.8%) interference (Figure 8.19). So the ^{142}Ce (11.1%) isotope is preferred for the measurement, although the signal is perturbed by a negligible interference of $^{124}\text{Sn}^{18}\text{O}$ (0.01%) and the considerable isobaric interference of the ^{142}Nd (27.2%) isotope. The isobaric interference is corrected via the measurement of *neodymium* on the ^{146}Nd (17.2%) isotope, which in turn shows no significant interferences. *Samarium* is measured on the ^{147}Sm (15.0%) isotope because it is devoid of any interference. The more frequent ^{152}Sm and ^{154}Sm isotopes are interfered by isobaric Gd isotopes. Both *europium* isotopes are significantly affected by interferences. The ^{153}Eu (52.2%) isotope is chosen for the measurement because it only shows elevated background values of approximately 500 cps caused by the interference of $^{137}\text{Ba}^{16}\text{O}$ (11.3%). On the other hand, the ^{151}Eu (47.8%) isotope is strongly interfered (with blank values of more than 500 cps) by $^{135}\text{Ba}^{16}\text{O}$ (6.6%) and $^{137}\text{Ba}^{14}\text{N}$ (11.3%) compounds (Figure 8.16). Therefore, the blank as well as the sample values are always incorrect, particularly if elevated Ba contents are present in the sample. There are only two *gadolinium* isotopes without isobaric interferences, but both are significantly interfered by SnNaO compounds. Anyhow, the ^{155}Gd (14.8%) isotope is favoured over the ^{157}Gd (15.7%) isotope because the interference of $^{116}\text{Sn}^{23}\text{Na}^{16}\text{O}$ with less than 3000 cps is significantly lower than the $^{118}\text{Sn}^{23}\text{Na}^{16}\text{O}$ interference exceeding 4000 cps for the background value (Figure 8.16, Figure 8.20). There are two *dysprosium* isotopes without isobaric overlap, but both show elevated blank values caused by SnNaO compounds (Figure 8.21). The ^{163}Dy (24.9%) isotope has a slightly higher background value caused by the $^{124}\text{Sn}^{23}\text{Na}^{16}\text{O}$ interference than the ^{161}Dy (18.9%) isotope which is interfered by the $^{122}\text{Sn}^{23}\text{Na}^{16}\text{O}$ compound. But the ^{163}Dy isotope is preferred because of its higher isotopic abundance. *Erbium* is measured on the isotope with the nominal mass of 166 amu, because it has the lowest background signal and the highest relative abundance (33.6%) compared to the other Er isotopes. *Ytterbium* has three isotopes without isobaric interferences, namely ^{171}Yb (14.3%), ^{172}Yb (21.8%) and ^{173}Yb (16.1%) isotopes. The ^{172}Yb isotope is chosen for the measurement because of its higher relative abundance compared to the other two Yb isotopes. *Lutetium* is measured on the dominant ^{175}Lu (97.4%) isotope, although the background is slightly elevated (about 200 cps).

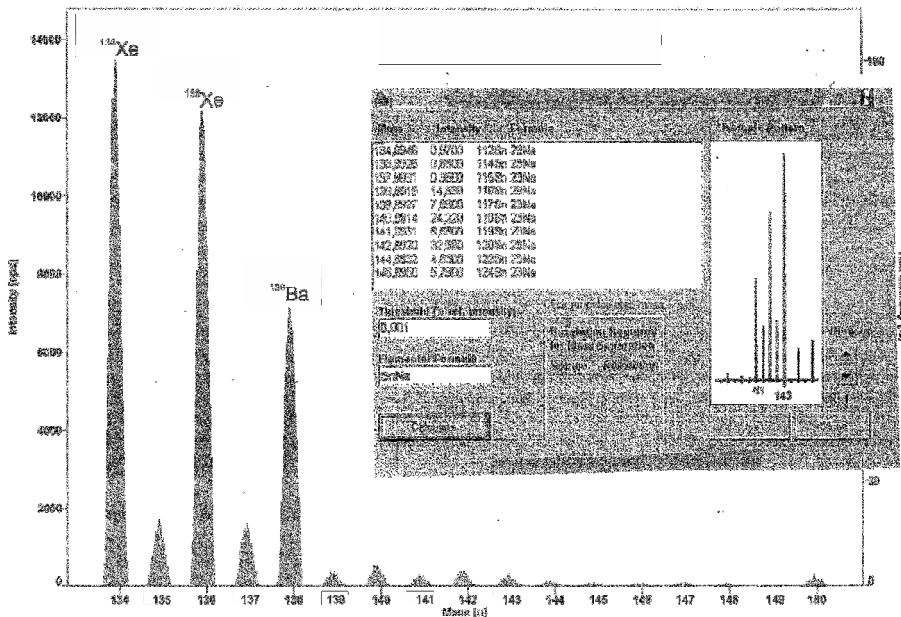


Figure 8.15: Diagram of intensity versus mass-charge ratio showing the low resolution spectrum for the nominal mass range from 134 to 150 amu including the light REE. Note the high blank values for xenon and barium. Inset shows that SnNa is not generating the high background signals. Measurement on blank sample

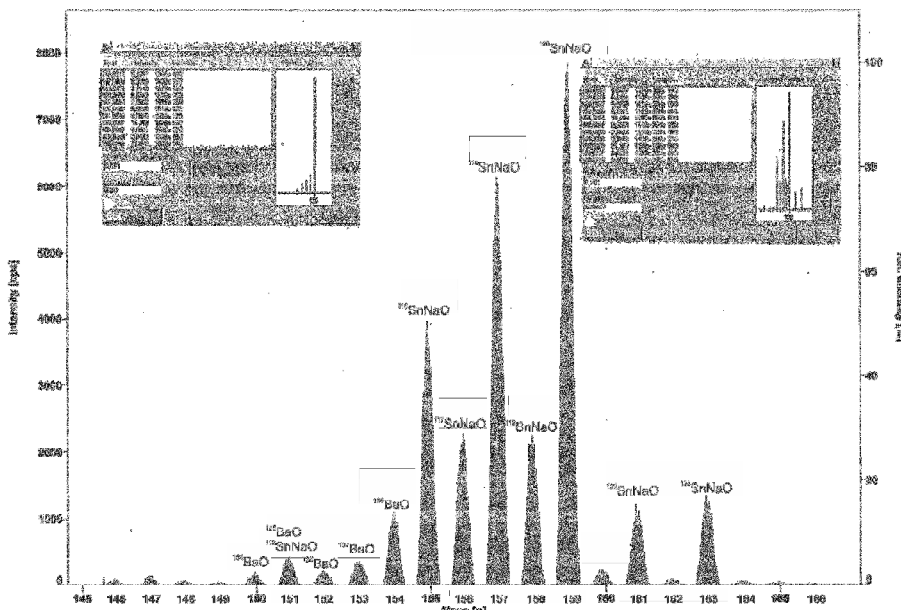


Figure 8.16: Diagram of intensity versus mass-charge ratio showing the low resolution spectrum for the nominal mass range from 145 to 166 amu including the REE. Note the interferences of SnNaO and BaO compounds. Measurement on blank sample

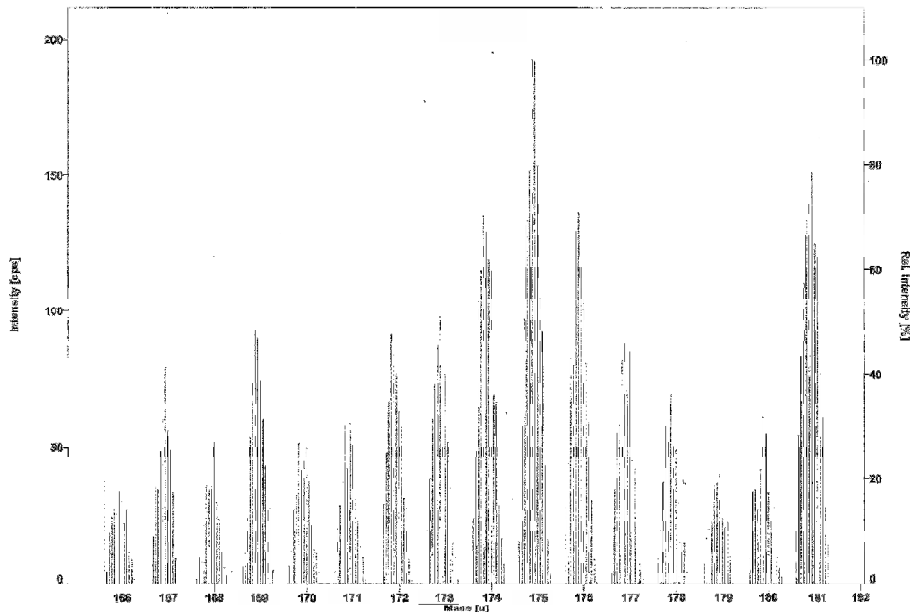


Figure 8.17: Diagram of intensity versus mass-charge ratio showing the low resolution spectrum for the nominal mass range from 166 to 182 amu including the heavy REE. Measurement on blank sample

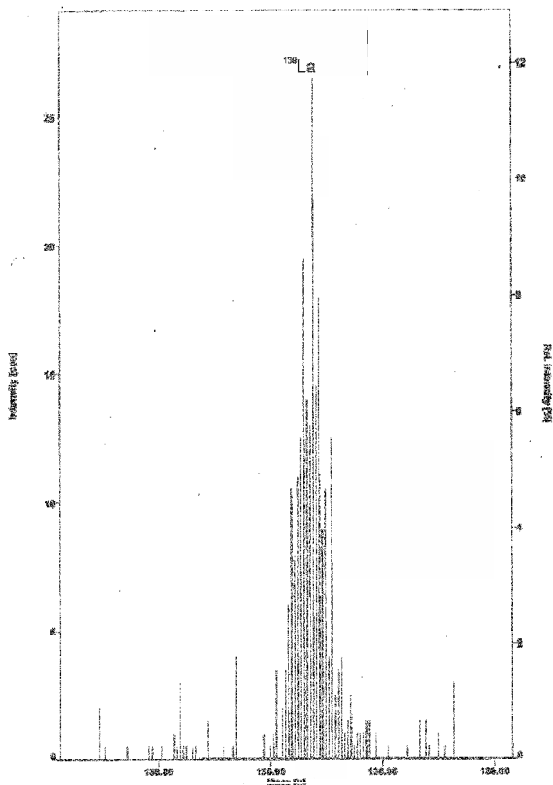


Figure 8.18: Diagram of intensity versus mass-charge ratio showing the high resolution spectrum for lanthanum on the nominal mass of 139 amu. Measurement on cassiterite sample (Coltan 240)

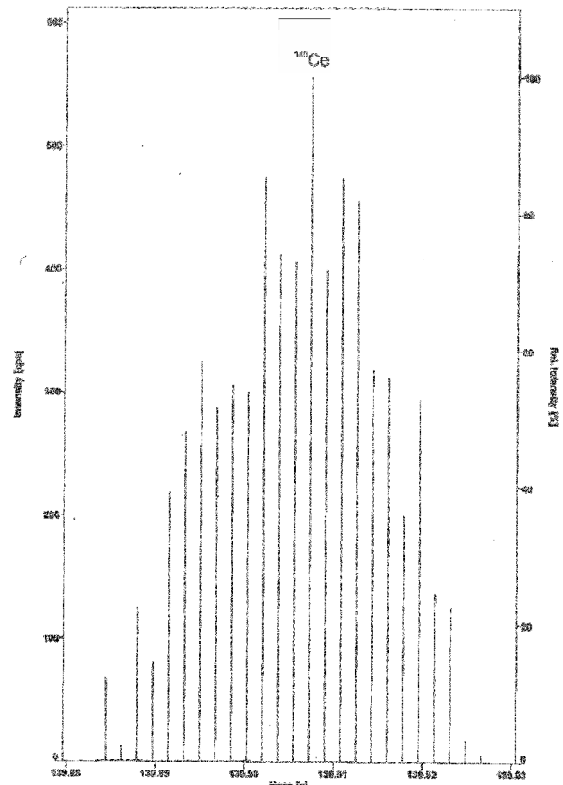


Figure 8.19: Diagram of intensity versus mass-charge ratio showing the medium resolution spectrum for cerium on the nominal mass of 140 amu. Measurement on cassiterite sample (Coltan 240)

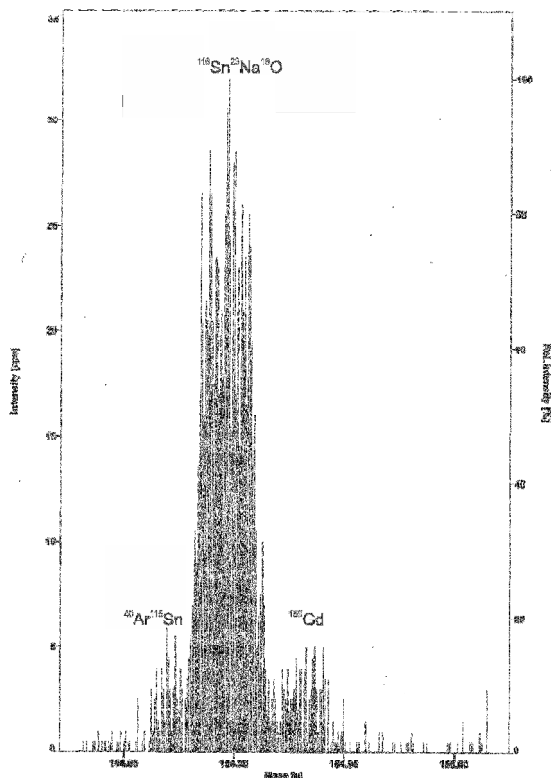


Figure 8.20: Diagram of intensity versus mass-charge ratio showing the high resolution spectrum for gadolinium on the nominal mass of 155 amu. Note the strong interference of SnNaO. Measurement on cassiterite sample (Coltan 240)

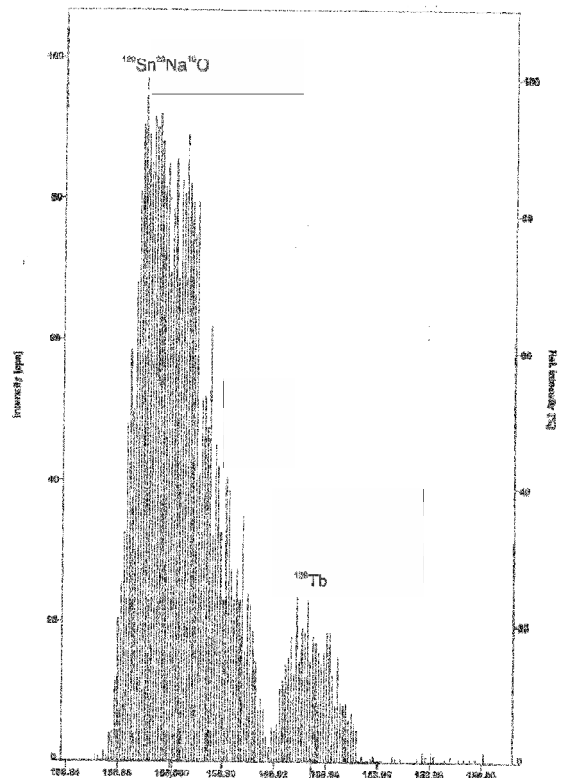


Figure 8.21: Diagram of intensity versus mass-charge ratio showing the high resolution spectrum for terbium on the nominal mass of 159 amu. Note the strong interference of SnNaO. Measurement on cassiterite sample (Coltan 240)

The most abundant *hafnium* isotope ^{180}Hf (35.1%) is interfered by two isobaric interferences caused by ^{180}W (0.12%) and ^{180}Ta (0.01%) isotopes. Therefore the ^{178}Hf (27.3%) isotope is chosen for measurement.

Mercury is measured in low resolution on the ^{201}Hg (13.2%) isotope and is used for correction of the isobaric ^{204}Hg (6.9%) interference on the ^{204}Pb (1.4%) isotope. Mercury derives from the sample gas. The measurement on the ^{204}Pb isotope is necessary to calculate a correct concentration for common lead for U-Pb dating.

8.3.2 Medium resolution

Some elements measured in medium resolution show the same interference patterns during analysis of cassiterite as described later for wolframite. This is the case for the following isotopes: ^{47}Ti and ^{56}Fe . To avoid repetition, please refer to the method development of wolframite (chapter 9.3.2) for detailed description.

The measurement of *carbon* is performed on the most abundant ^{12}C (98.9%) isotope (Figure 8.22). The medium resolution mode is chosen to discriminate the interference of the bivalent ^{24}Mg (78.6%) ion.

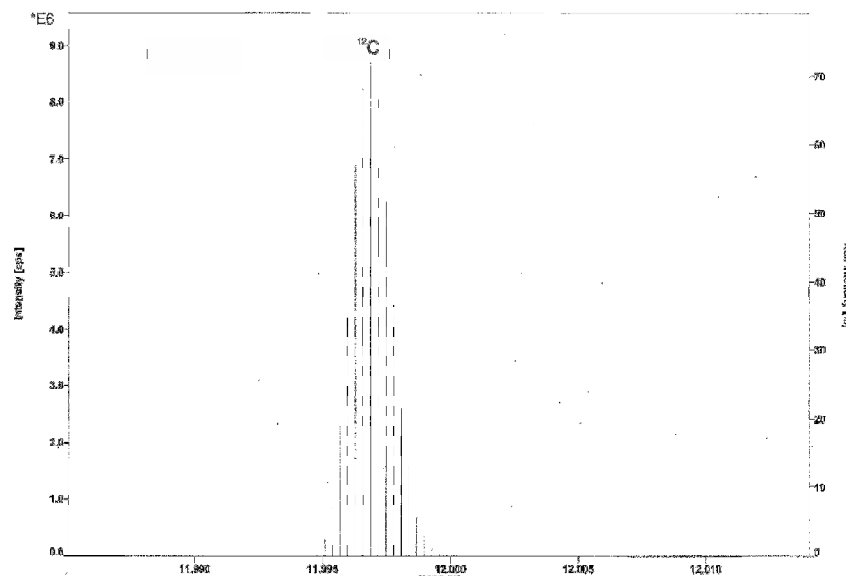


Figure 8.22: Diagram of intensity versus mass-charge ratio showing the medium resolution spectrum for carbon on the nominal mass of 12 amu. Measurement on cassiterite sample (Coltan 240)

Sodium is a monoisotopic element with the nominal mass of 23 amu. The ^{23}Na ion has to be measured in medium resolution to separate the interference of the bivalent Ti ion of the ^{46}Ti (7.9%) isotope (Figure 8.23).

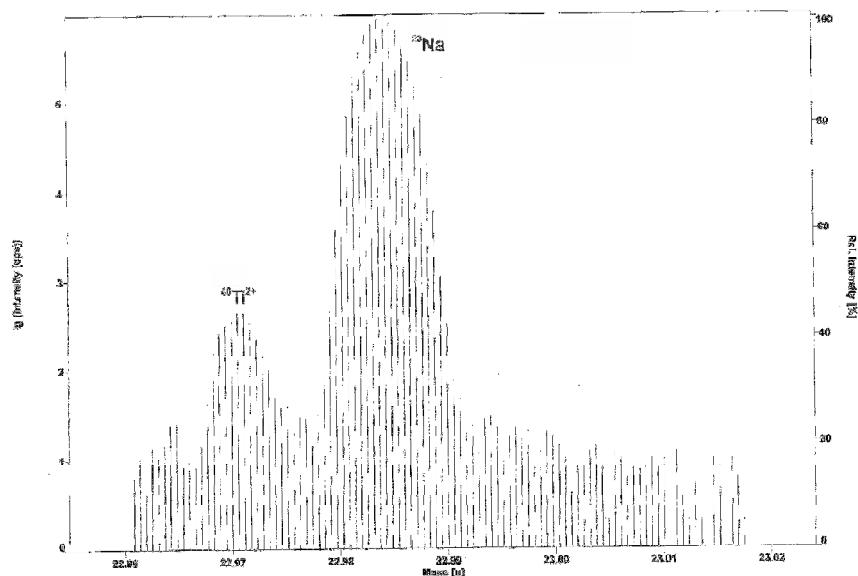


Figure 8.23: Diagram of intensity versus mass-charge ratio showing the medium resolution spectrum for sodium on the nominal mass of 23 amu. Note the interference of Ti^{2+} . Measurement on cassiterite sample (Coltan 240)

Magnesium is measured on the primary isotope ^{24}Mg (79.0%) in medium resolution to discriminate the interferences caused by the bivalent ion of the ^{48}Ti (73.5%) isotope and the $^{12}C_2$ (97.8%) compound (Figure 8.24).

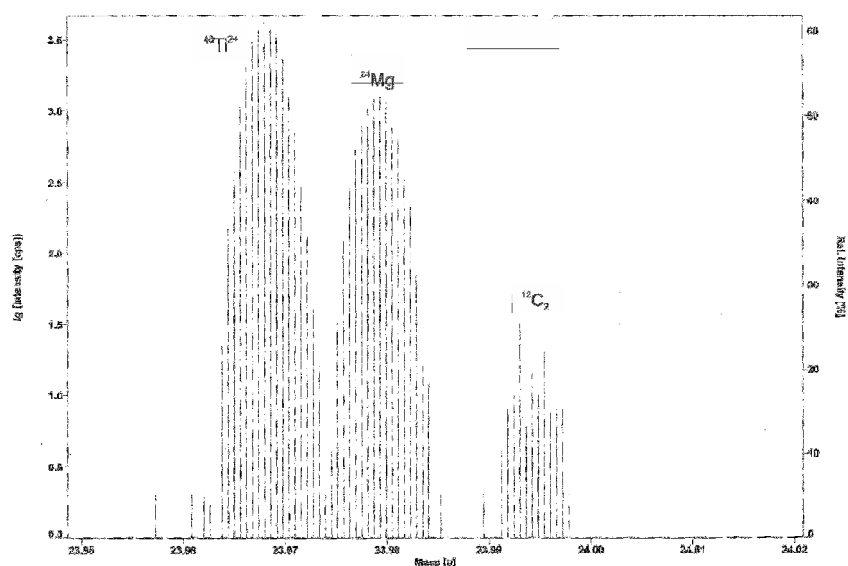


Figure 8.24: Diagram of intensity versus mass-charge ratio showing the medium resolution spectrum for magnesium on the nominal mass of 24 amu. Note the interferences of Ti^{2+} and C_2 . Measurement on cassiterite sample (Coltan 240)

The monoisotopic *aluminium* ion is analyzed on the nominal mass of 27 amu. The medium resolution mode is chosen to separate the small interference caused by a $^{13}\text{C}^{14}\text{N}$ (1.1%) compound (Figure 8.25).

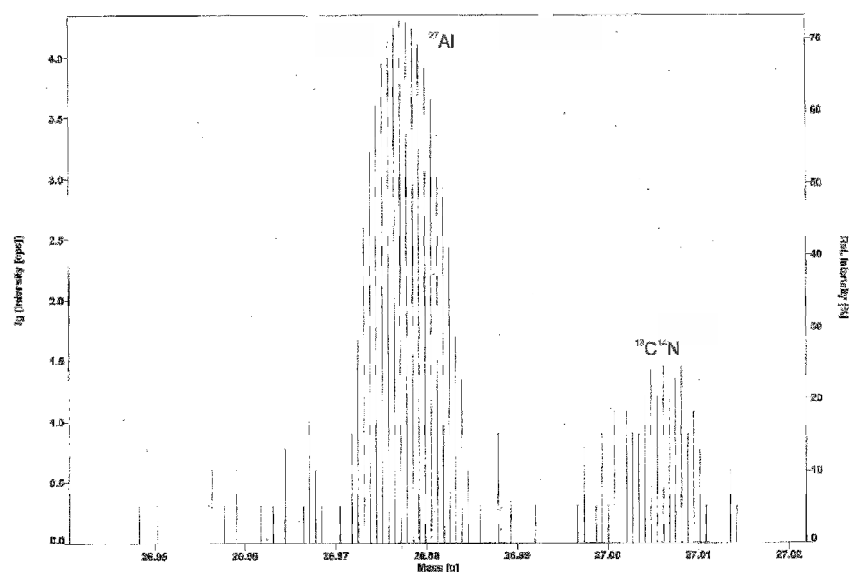


Figure 8.25: Diagram of intensity versus mass-charge ratio showing the medium resolution spectrum for aluminum on the nominal mass of 27 amu. Note the interference of CN. Measurement on cassiterite sample (Coltan 240)

The ^{29}Si (4.7%) isotope is interfered by $^{13}\text{C}^{16}\text{O}$ (1.1%), $^{14}\text{N}^{15}\text{N}$ (0.7%) and $^1\text{H}^{14}\text{N}_2$ (99.3%) compounds which are discriminated in medium resolution (Figure 8.26). The most abundant *silicon* isotope ^{28}Si (92.2%) is neglected to protect the detector from high intensities.

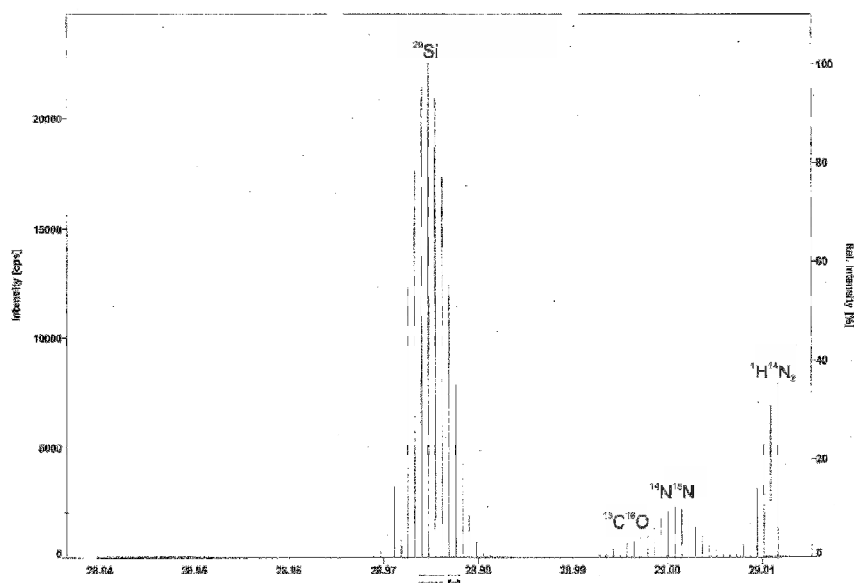


Figure 8.26: Diagram of intensity versus mass-charge ratio showing the medium resolution spectrum for silicon on the nominal mass of 29 amu. Note the interferences of CO, N₂ and N₂H compounds. Measurement on cassiterite sample (Coltan 240)

The monoisotopic element *phosphorous* is measured on the nominal mass 31 in medium resolution to separate interferences caused by $^{15}\text{N}^{16}\text{O}$ (0.4%) and $^1\text{H}^{14}\text{N}^{16}\text{O}$ (99.4%) compounds (Figure 8.27).

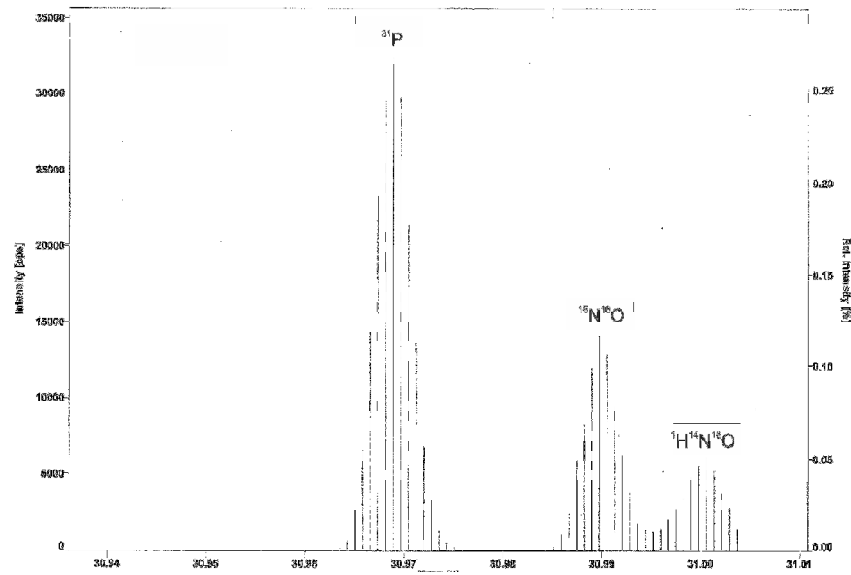


Figure 8.27: Diagram of intensity versus mass-charge ratio showing the medium resolution spectrum for phosphorous on the nominal mass of 31 amu. Note the interferences of NO and NOH compounds. Measurement on cassiterite sample (Coltan 240)

Sulphur is measured on the dominant ^{32}S isotope (94.9%) which is perturbed by a significant interference caused by $^{16}\text{O}_2$ (99.5%) compound which is resolved by using the medium resolution mode (Figure 8.28).

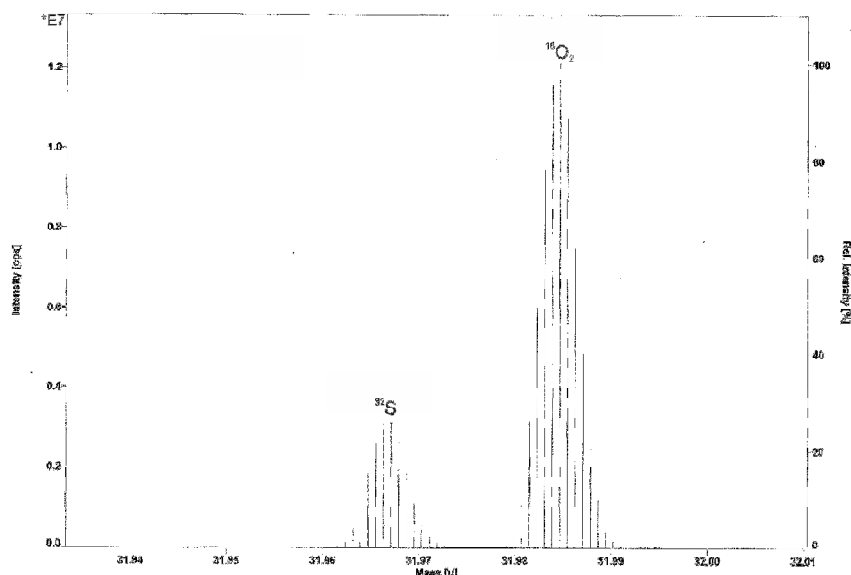


Figure 8.28: Diagram of intensity versus mass-charge ratio showing the medium resolution spectrum for sulfur on the nominal mass of 32 amu. Note the interference of O_2 compound. Measurement on cassiterite sample (Coltan 240)

The most abundant *calcium* isotope on the nominal mass of 40 amu (96.9%) is affected by a strong isobaric ^{40}Ar (99.6%) interference which cannot be resolved. So the ^{44}Ca isotope (2.1%) is selected for the measurement. Medium resolution is chosen to discriminate interferences caused by $^{28}\text{Si}^{16}\text{O}$ (92.0%) and $^{12}\text{C}^{16}\text{O}_2$ (98.4%) compounds (Figure 8.29). However, the interference from the bivalent ^{88}Sr (82.6%) isotope cannot be resolved.

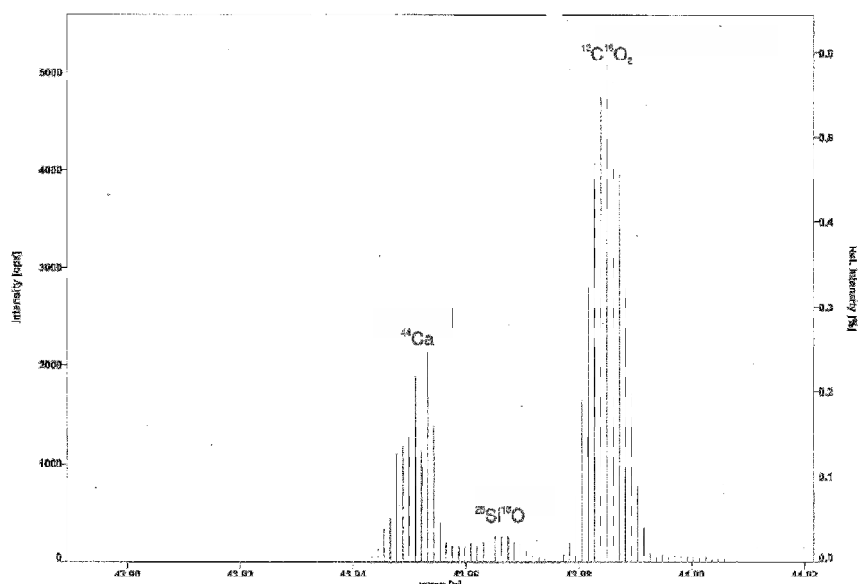


Figure 8.29: Diagram of intensity versus mass-charge ratio showing the medium resolution spectrum for calcium on the nominal mass of 44 amu. Note the interferences of SiO and CO₂ compounds. Measurement on cassiterite sample (Coltan 240)

Scandium is a monoisotopic element with the nominal mass of 45 amu. Medium resolution is chosen for the ^{45}Sc measurement to resolve two Si oxide interferences, namely $^{28}\text{Si}^{17}\text{O}$ (92.0%) and $^{29}\text{Si}^{16}\text{O}$ (98.4%). Additionally, the Sc signal is perturbed by a non-resoluble interference from the bivalent zirconium ion of the ^{90}Zr (51.5%) isotope (Figure 8.30). This interference is corrected by the measurement of the bivalent ^{91}Zr (11.2%) ion on the nominal mass of 45.5 amu.

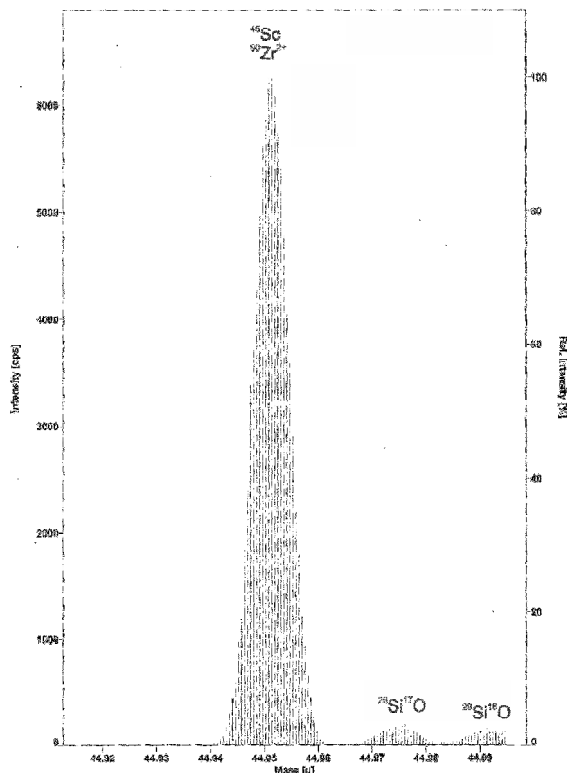


Figure 8.30: Diagram of intensity versus mass-charge ratio showing the medium resolution spectrum for scandium on the nominal mass of 45 amu. Note the interferences of SiO compounds and the non-resoluble overlap of Zr^{2+} ion. Measurement on cassiterite sample (Coltan 240)

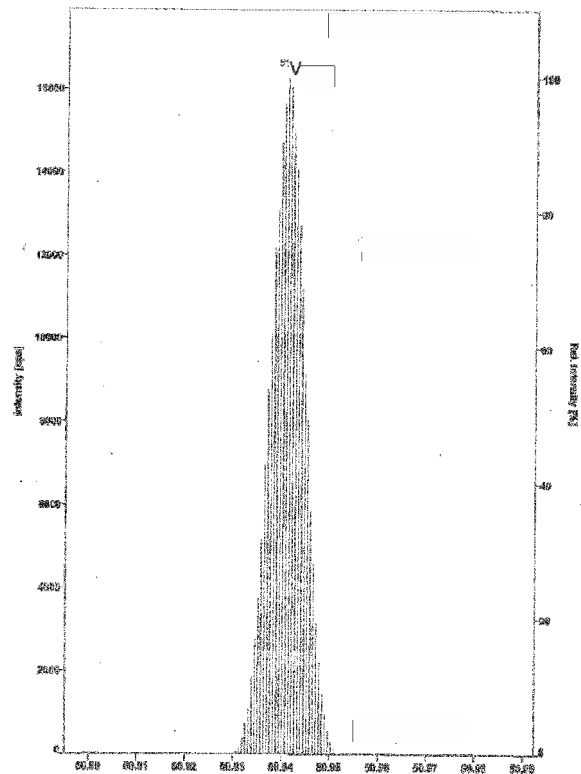


Figure 8.31: Diagram of intensity versus mass-charge ratio showing the medium resolution spectrum for vanadium on the nominal mass of 51 amu. Measurement on cassiterite sample (Coltan 240)

Vanadium is measured on the dominant ^{51}V (99.8%) isotope (Figure 8.31). There are interferences of $^{35}\text{Cl}^{16}\text{O}$ (75.6%) and $^{37}\text{Cl}^{14}\text{N}$ (24.1%) compounds in the proximity of the ^{51}V peak which can be separated by selecting the medium resolution mode.

The major *chromium* (83.8%) isotope is measured on the nominal mass of 52 amu. The signal is interfered by a significant $^{40}\text{Ar}^{12}\text{C}$ (98.5%) compound which is resolved in medium resolution (Figure 8.32).

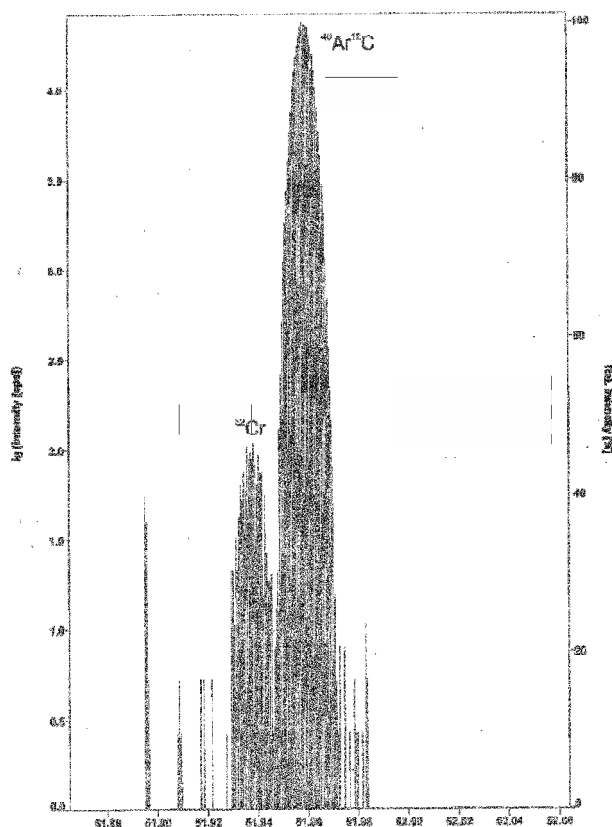


Figure 8.32: Diagram of intensity versus mass-charge ratio showing the medium resolution spectrum for chromium on the nominal mass of 52 amu. Note the interference of ArC compound. Measurement on cassiterite sample (Coltan 240)

There is only one isotope for *manganese* on the nominal mass of 55 amu. Medium resolution is selected to discriminate interferences of $^{39}\text{K}^{16}\text{O}$ (93.0%) and $^{40}\text{Ar}^{14}\text{N}^1\text{H}$ (99.2%) compounds.

Cobalt is a monoisotopic element measured on the nominal mass of 59 amu. The medium resolution mode is chosen for the ^{59}Co ion because of a strong interference of the bivalent ^{118}Sn (24.0%) ion (Figure 8.33) and $\text{Ar}^{40}\text{F}^{19}$ (99.6%) compound. For cassiterite analysis, small search (10%) and integration (30%) windows are set to reduce the effect of the large interference of the bivalent Sn ion (Figure 8.34).

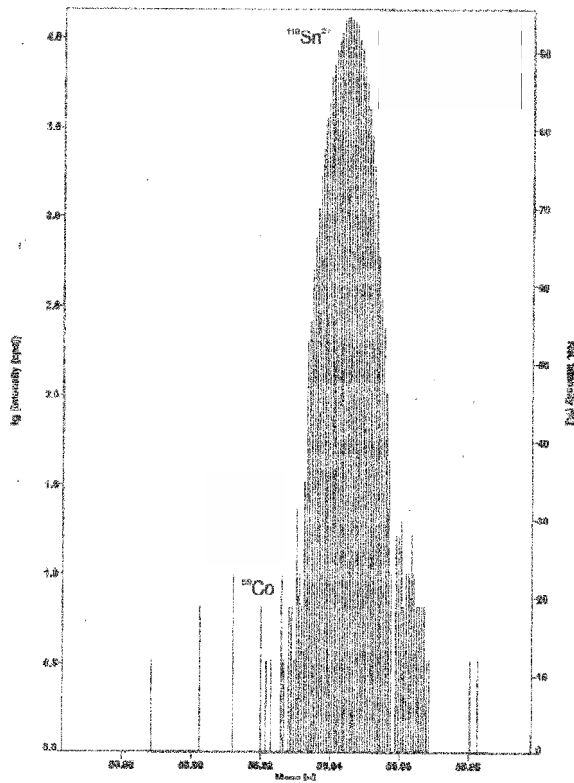


Figure 8.33: Diagram of intensity versus mass-charge ratio showing the medium resolution spectrum on the nominal mass of 59 amu. Note the absence of the cobalt peak and the strong interference of Sn^{2+} . Measurement on cassiterite sample (Coltan 240)

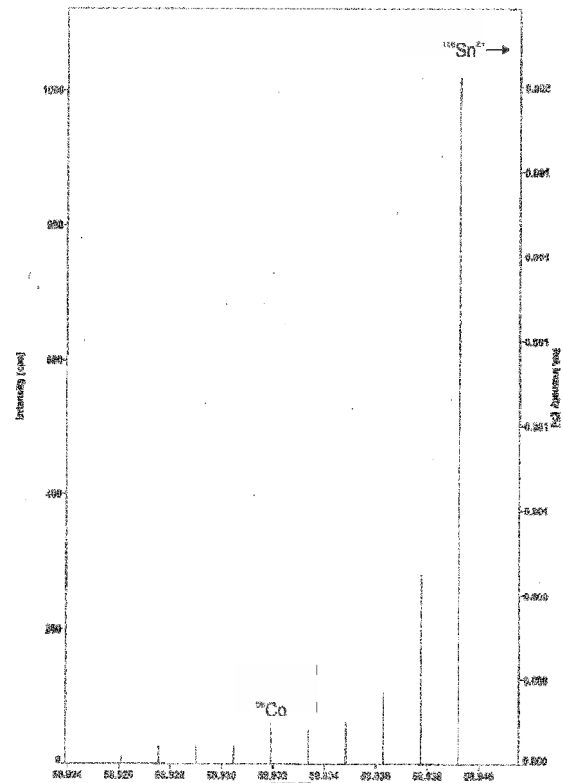


Figure 8.34: Diagram of intensity versus mass-charge ratio showing the medium resolution spectrum for cobalt on the nominal mass of 59 amu. Note the slope of the interference of Sn^{2+} . Measurement on cassiterite sample (Coltan 240)

The most abundant *nickel* isotope ^{58}Ni (68.1%) is perturbed by an isobaric interference of the ^{58}Fe (0.3%) isotope, consequently the ^{60}Ni (26.2%) isotope is measured. The medium resolution mode is chosen for Ni because of a strong interference of a bivalent ^{120}Sn (33.0%) ion (Figure 8.35) and a $\text{Ca}^{44}\text{O}^{16}$ (2.08%) compound. Additionally, a small search (30%) window has to be chosen for cassiterite analysis because of the influence of the strong bivalent Sn interference immediately close to the ^{60}Ni peak (Figure 8.36).

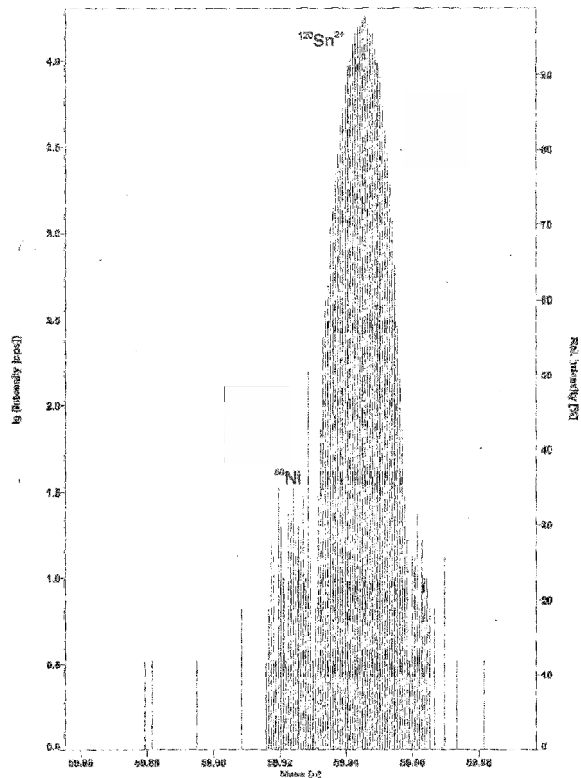


Figure 8.35: Diagram of intensity versus mass-charge ratio showing the medium resolution spectrum for nickel on the nominal mass of 60 amu. Note the strong interference of Sn^{2+} . Measurement on cassiterite sample (Coltan 240)

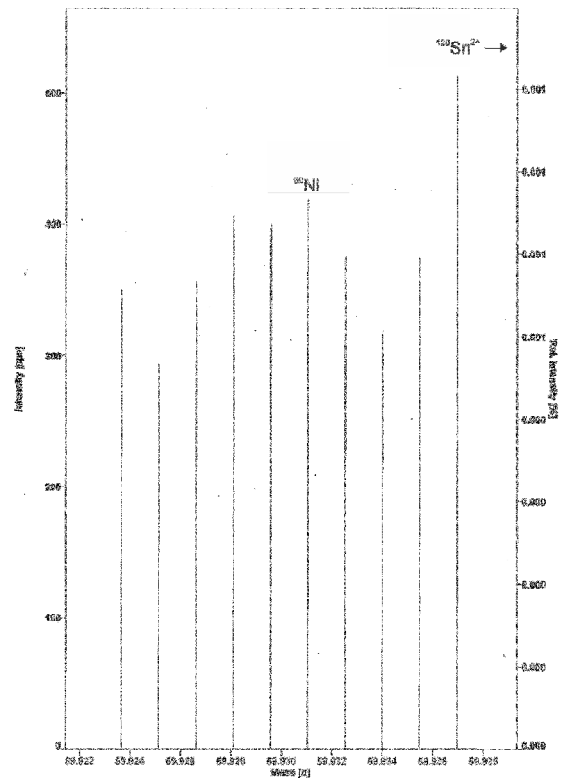


Figure 8.36: Diagram of intensity versus mass-charge ratio showing the medium resolution spectrum for nickel on the nominal mass of 60 amu. Note the influence of Sn^{2+} . Measurement on cassiterite sample (Coltan 240)

Copper is measured on the major ^{63}Cu isotope (69.2%) in medium resolution to discriminate the interference caused by the $^{40}\text{Ar}^{23}\text{Na}$ (99.6%) compound (Figure 8.37). The search window is set to 50%.

The dominant *zinc* isotope ^{64}Zn (48.6%) is interfered by the isobaric ^{64}Ni (0.9%) isotope. Thus, the ^{66}Zn (27.9%) isotope is measured in medium resolution to discriminate the interference caused by the bivalent $^{132}\text{Xe}^{2+}$ (26.9%) ion. The ^{68}Zn (18.8%) isotope is not suitable because of a significant $^{40}\text{Ar}^{28}\text{Si}$ (91.9%) interference for which the high resolution mode necessary (Figure 8.38). The search window is set to 50%.

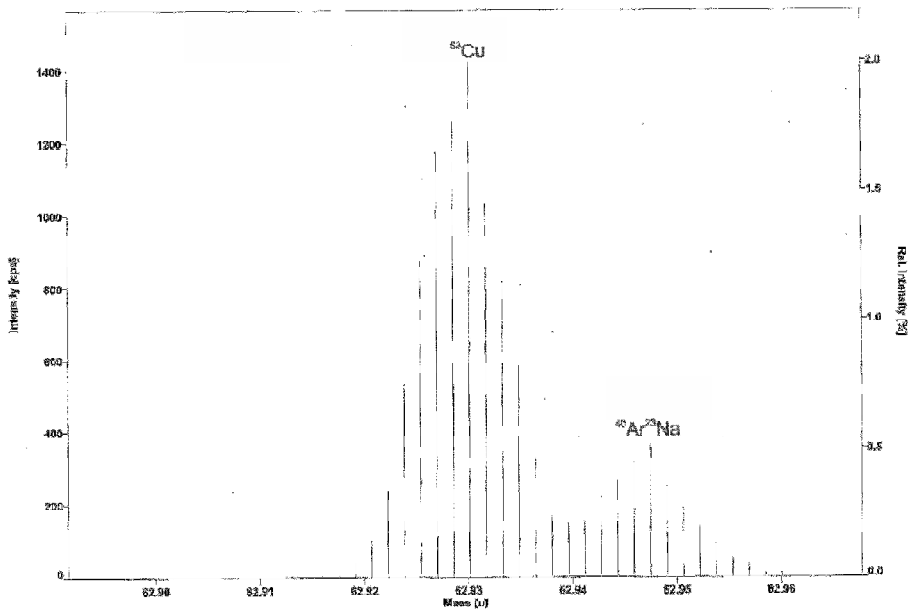


Figure 8.37: Diagram of intensity versus mass-charge ratio showing the medium resolution spectrum for copper on the nominal mass of 63 amu. Note the interference of ArNa. Measurement on cassiterite sample (Coltan 240)

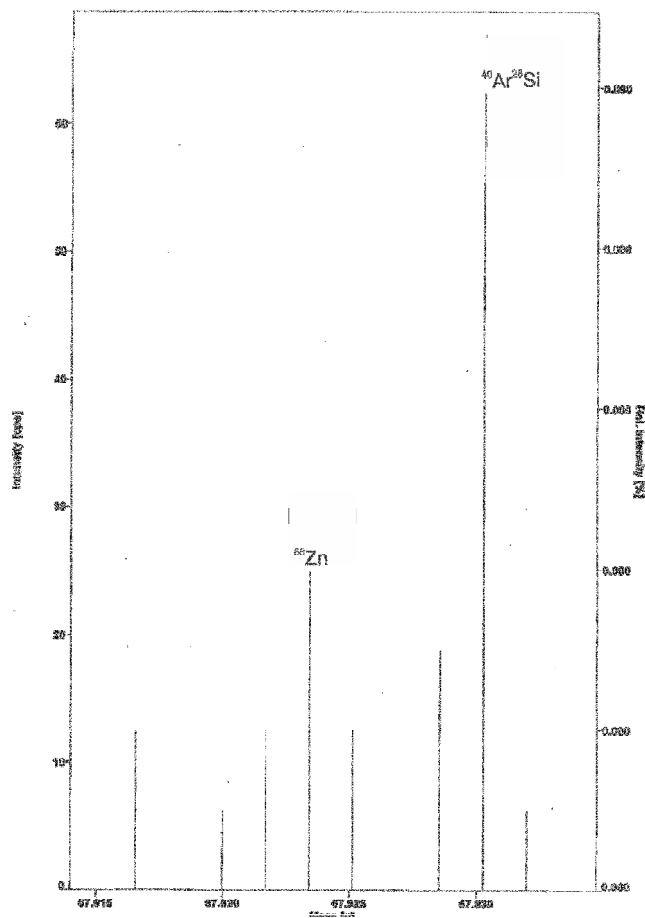


Figure 8.38: Diagram of intensity versus mass-charge ratio showing the medium resolution spectrum for zinc on the nominal mass of 68 amu. Note the interference of ArSi. Measurement on cassiterite sample (Coltan 240)

Zirconium is measured on the dominant ^{90}Zr (51.5%) isotope. The medium resolution is selected in order to discriminate the interference from the bivalent ^{180}W ion (0.1%). For cassiterite analysis, the bivalent ^{91}Zr (11.2%) ion is detected on the nominal mass of 45.5 amu for correction of the ^{45}Sc signal which is interfered by the bivalent ^{90}Zr ion.

Cadmium is measured on the ^{111}Cd (12.8%) isotope because this is the only cadmium isotope without an isobaric interference. The ^{111}Cd isotope is perturbed by interferences of $^{94}\text{Zr}^{17}\text{O}$ (0.01%) $^{93}\text{Nb}^{18}\text{O}$ (0.2%) and $^{95}\text{Mo}^{16}\text{O}$ (14.7%) compounds. These interferences cannot be resolved, but the impact of these interferences is negligible. Medium resolution mode has to be chosen for Cd because of the abundance sensitivity from the dominant peak of the ^{112}Sn (1.0%) isotope (Figure 8.39, Figure 8.40).

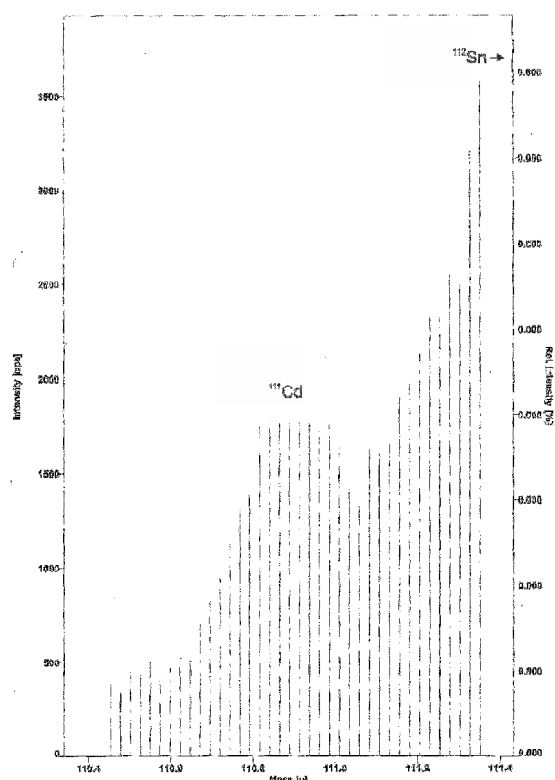


Figure 8.39: Diagram of intensity versus mass-charge ratio showing the low resolution spectrum for cadmium on the nominal mass of 111 amu. Note the abundance sensitivity of Sn on the nominal mass of 112 amu. Measurement on cassiterite sample (Coltan 240)

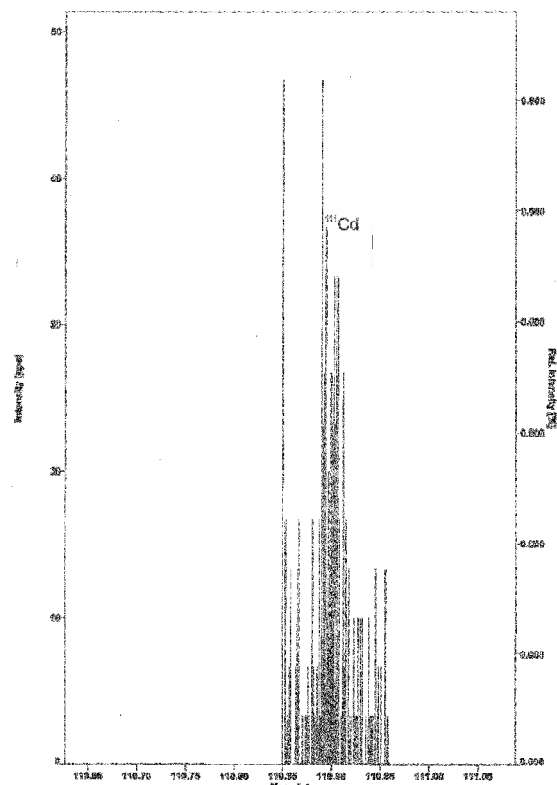


Figure 8.40: Diagram of intensity versus mass-charge ratio showing the medium resolution spectrum for cadmium on the nominal mass of 111 amu. Measurement on cassiterite sample (Coltan 240)

Indium is the only element with isobaric interference on both possible isotopes. The major ^{115}In (95.7%) isotope is significantly interfered by the isobaric ^{115}Sn (0.36%) isotope. Therefore In is measured on the ^{113}In (4.3%) isotope which has to be corrected for the isobaric interference caused by the ^{113}Cd (12.2%) isotope. Due to abundance sensitivity from the ^{112}Sn (1.0%) and ^{114}Sn (0.7%) peaks (Figure 8.41), the medium resolution mode has to be selected for the measurement of indium on the nominal mass of 113 amu (Figure 8.42).

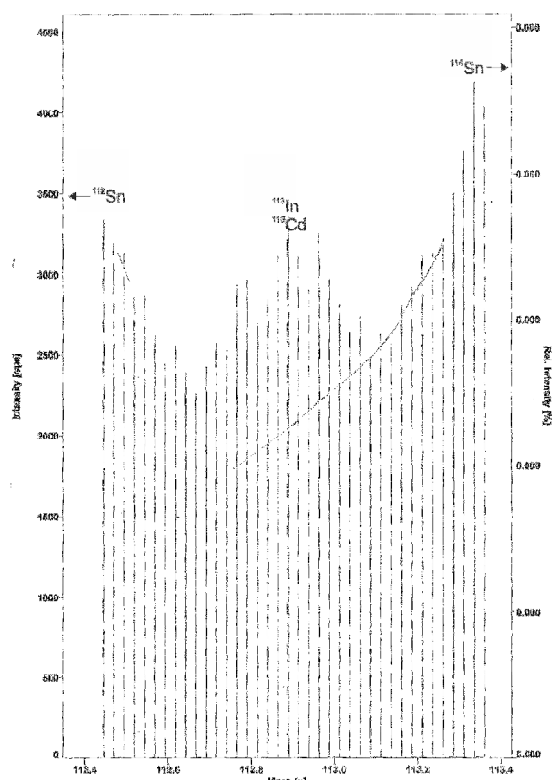


Figure 8.41: Diagram of intensity versus mass-charge ratio showing the low resolution spectrum for indium on the nominal mass of 113 amu. Note the abundance sensitivity of Sn on the nominal masses of 112 and 113 amu. Measurement on cassiterite sample (Coltan 240)

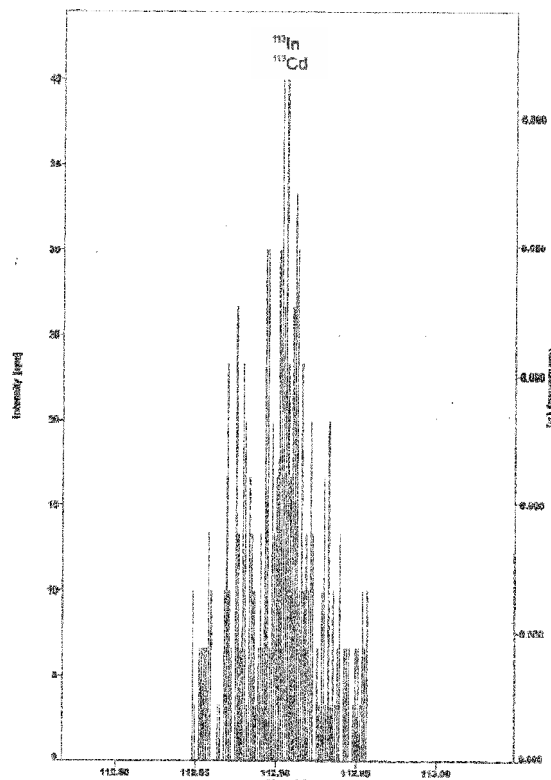


Figure 8.42: Diagram of intensity versus mass-charge ratio showing the medium resolution spectrum for indium on the nominal mass of 113 amu. Note that the abundance sensitivity of Sn is discriminated in medium resolution. Measurement on cassiterite sample (Coltan 240)

Tin is measured on the ^{118}Sn (24.2%) isotope which shows no significant interferences (Figure 8.43). However, the medium resolution mode is chosen to protect the detector from high signal intensities.

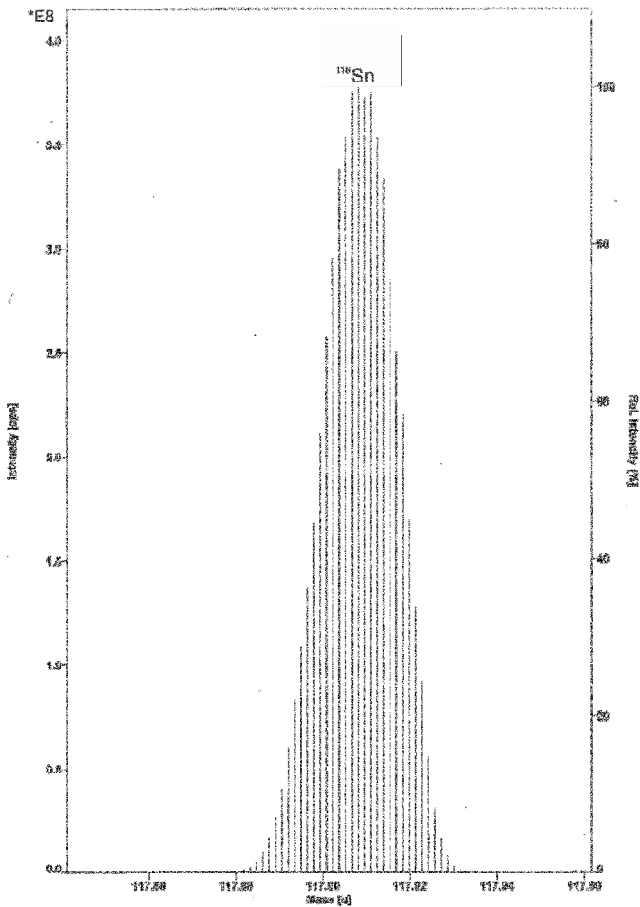


Figure 8.43: Diagram of intensity versus mass-charge ratio showing the medium resolution spectrum for tin on the nominal mass of 118 amu. Measurement on cassiterite sample (Coltan 240)

Antimony is measured on the more abundant ^{121}Sb (57.2%) isotope. There are no significant interferences (Figure 8.44), but medium resolution mode is chosen because of abundance sensitivity from the high peak of the ^{120}Sn (32.6%) isotope (Figure 8.45).

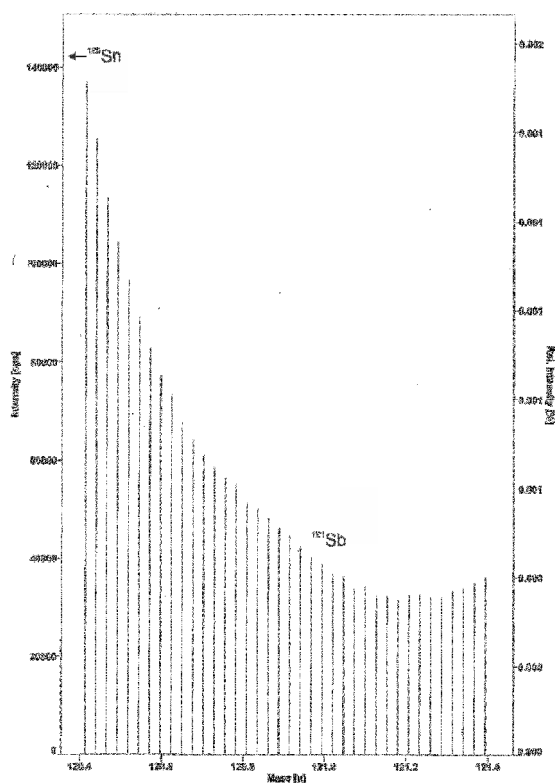


Figure 8.44: Diagram of intensity versus mass-charge ratio showing the low resolution spectrum for antimony on the nominal mass of 121 amu. Note the abundance sensitivity of Sn on the nominal mass of 120 amu. Measurement on cassiterite sample (Coltan 240)

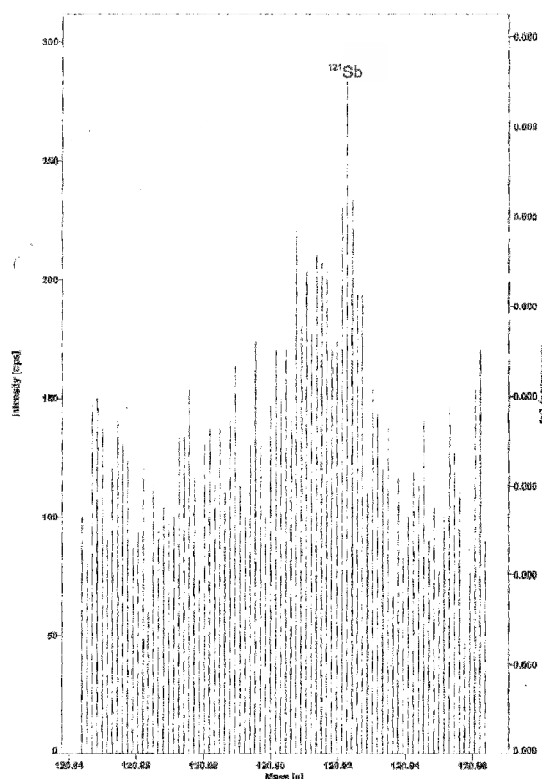


Figure 8.45: Diagram of intensity versus mass-charge ratio showing the medium resolution spectrum for antimony on the nominal mass of 121 amu. Note that the abundance sensitivity of Sn is discriminated in medium resolution. Measurement on cassiterite sample (Coltan 240)

Table 8.3: Summary of the measured elements for cassiterite analysis by LA-ICP-MS including the selected isotope, its relative abundance, selected resolution mode for the mass spectrometer, and potential interferences

element	isotope	rel. abundance (%)	resolution	potential interferences
C	12	98.9	MR	Mg ²⁺
Na	23	100	MR	Ti ²⁺
Mg	24	79.0	MR	C ₂ , Ti ²⁺
Al	27	100	MR	CN
Si	29	4.7	MR	CO, N ₂ , N ₂ H
P	31	100	MR	NO, NOH
S	32	95.0	MR	O ₂
Ca	44	2.1	MR	CO ₂ , SiO, Sr ²⁺
Sc	45	100	MR	SiO, Zr ²⁺
Ti	47	7.4	MR	NO ₂ , Zr ²⁺ , Mo ²⁺
V	51	100	MR	
Cr	52	83.8	MR	ArC
Mn	55	100	MR	ArNH
Fe	56	91.8	MR	ArO, CaO, Sn ²⁺
Co	59	100	MR	
Ni	60	26.2	MR	Sn ²⁺
Cu	63	69.2	MR	ArNa, Xe ²⁺
Zn	68	18.8	MR	Xe ²⁺ , S ₂
Ga	69	60.1	LR	
Ge	74	35.9	LR	Se
As	75	100	LR	ArCl
Sr	88	82.6	LR	
Y	89	100	LR	
Zr	90	51.5	MR	
Nb	93	100	LR	
Mo	95	15.9	LR	
Cd	111	12.8	MR	Abundance Sensitivity ¹¹² Sn
In	113	4.3	MR	Sn
Sn	118	24.2	MR	
Sb	121	57.2	MR	Abundance Sensitivity ¹²⁰ Sn
Ba	137	11.2	LR	SnO
La	139	100	LR	
Ce	142	11.1	LR	Nd, SnO
Pr	141	100	LR	
Nd	146	17.2	LR	
Sm	147	15.0	LR	
Eu	153	52.2	LR	BaO
Gd	155	14.8	LR	SnNaO
Tb	159	100	LR	SnNaO

Dy	163	24.9	LR	SnNaO
Ho	165	100	LR	
Er	166	33.6	LR	
Tm	169	100	LR	
Yb	172	21.8	LR	
Lu	175	97.4	LR	
Hf	178	27.3	LR	
Ta	181	100	LR	
W	182	26.5	LR	
Hg	201	13.2	LR	
Pb			LR	
Bi	209	100	LR	
Th	232	100	LR	
U	238	99.3	LR	

9 Method development for wolframite analysis by laser ablation inductively coupled plasma mass spectrometry (LA-ICP-MS)

As for cassiterite, method development for LA-ICP-MS analysis is necessary as this study is the first attempt to determine trace elements in wolframite by this method. This includes adjustment of the setup for the LA-ICP-MS system and selection of the most suitable isotopes for the respective elements to exclude the effect of major interferences.

9.1 Parameters

The laser and the mass spectrometer are set to conditions which were developed for wolframite measurements in particular. The general setup for the gas flows is the same as for cassiterite analysis (see chapter 8.1). Prior to analysis, fine-tuning by optimising the intensities of ^{24}Mg ($>3 \times 10^6$ cps) and ^{183}W isotopes ($>1 \times 10^9$ cps) and monitoring of the oxide formation ($<0.01\%$; $^{183}\text{W}^{16}\text{O}/^{183}\text{W} \times 100$) during ablation of a wolframite sample (in-house code 'WOLF') is performed (compare with chapter 8.1). Line scan ablation is favoured over static spot ablation resulting in lower detection limits and more constant signal at higher intensity levels. Prior to every analysis a pre-ablation scan is run to remove any contamination from the sample surface. The laser adjustment for pre-ablation is set to a spot size of $75 \mu\text{m}$ in diameter with a scan speed of $15 \mu\text{m/s}$ and a frequency of 10 Hz. The washout time after every ablation process takes 80 seconds. The blank is measured for 140 seconds on the Ar sample gas mixed with the He carrier gas from the ablation cell, the so-called 'gas background' (Longerich et al., 1996). During the background measurement the laser warm-up sequence is run with the shutter being closed. The laser parameters are slightly changed for the ablation scan. The spot size and the scan speed are reduced to $50 \mu\text{m}$ and $5 \mu\text{m/s}$, respectively. The frequency is kept at 10 Hz. The laser energy is fixed to 65% of 4 mJ for ablation of wolframite. Laser energy is changed from 65% to 80% of 4 mJ for the ablation of the NIST 610 glass. The ablation scan takes 210 seconds including 8 passes over the scan line with length of approximately $130 \mu\text{m}$.

The mass spectrometer takes 358 seconds in total for the measurement of a single line scan; thereof 140 seconds account for the blank including laser warm-up and 218 seconds for signal measurement with laser ablation. The mass spectrometer performs 25 passes over the whole spectra for the low (LR) and the medium (MR) resolution and is constantly switching between these two resolution modes with a switch delay of 1 second.

The following isotopes have been analyzed: ^{69}Ga , ^{75}As , ^{89}Y , ^{95}Mo , ^{107}Ag , ^{111}Cd , ^{115}In , ^{118}Sn , ^{121}Sb , ^{137}Ba , ^{139}La , ^{140}Ce , ^{141}Pr , ^{146}Nd , ^{147}Sm , ^{153}Eu , ^{157}Gd , ^{159}Tb , ^{163}Dy , ^{165}Ho , ^{166}Er , ^{169}Tm , ^{172}Yb , ^{175}Lu , ^{177}Hf , ^{201}Hg , ^{204}Pb , ^{205}Tl , ^{206}Pb , ^{207}Pb , ^{208}Pb , ^{209}Bi , ^{238}U in the low resolution mode and ^{12}C , ^{24}Mg , ^{27}Al , ^{29}Si , ^{31}P , ^{32}S , ^{44}Ca , ^{45}Sc , ^{47}Ti , ^{51}V , ^{52}Cr , ^{55}Mn , ^{56}Fe , ^{59}Co , ^{60}Ni , ^{63}Cu , ^{66}Zn , ^{88}Sr , ^{90}Zr , ^{93}Nb , ^{181}Ta , ^{182}W , ^{232}Th in the medium resolution mode. For all elements both SEM and Faraday detectors are used depending on the count rate. Small mass windows of 20% are chosen for most isotopes measured in low resolution. Broader mass windows are applied for ^{69}Ga (100%) and ^{95}Mo (120%). Mass windows of 125% are used for isotopes measured in the medium resolution mode. Exceptions are the ^{44}Ca , ^{55}Mn , ^{56}Fe , and ^{182}W isotopes with mass windows of 150%, because these elements possibly occur at higher concentrations. A broader mass window is necessary for the automated switching of the detector system.

The search and integration windows for isotopes measured in low resolution are set to 20%. A wider search window is chosen for ^{69}Ga and ^{95}Mo with 60% and 150%, respectively. For most isotopes measured in medium resolution search and integration windows are set to 50% and 60%, respectively. Exceptions are ^{24}Mg and ^{52}Cr with search windows of 25%.

9.2 Calibration, standardisation, and data evaluation

Just as for cassiterite, external calibration using a non-matrix-matched reference material plus internal standardisation has been applied (see chapter 8.2). The NIST 610 glass (Tables 8.1 & 8.2) was used as reference material and tungsten was chosen as internal standard for wolframite analyses with the calculated stoichiometric concentration of 60.63 wt.% W (606300 ppm W). Detection limits for wolframite analysis are given in chapter 8.2 (Figure 8.2).

The standardisation and calibration strategy is verified by comparison of the LA-ICP-MS data with electron microprobe analyses of wolframite grains in a concentrate from Kabera, Rwanda (AS9112). The LA-ICP-MS data were calibrated using the NIST 610 glass as reference material. As Mn (Figure 9.1), Fe (Figure 9.2), and Nb (Figure 9.3) occur in concentrations above the detection limit of EPMA, only these elements are considered.

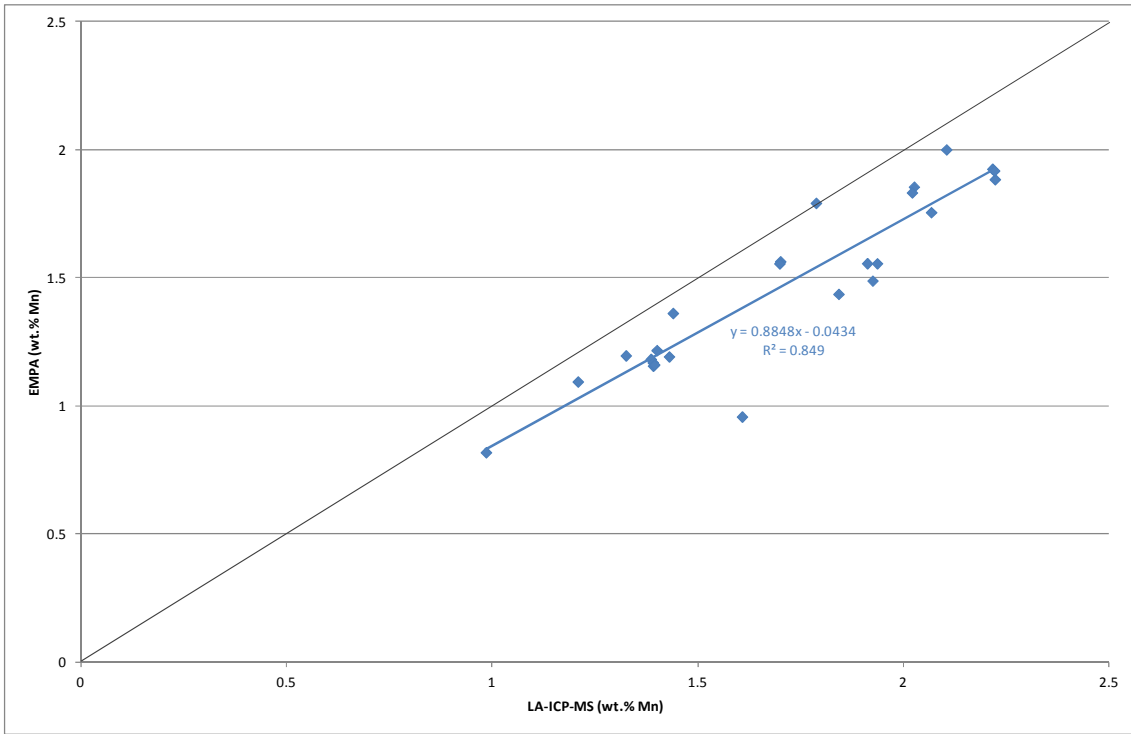


Figure 9.1: Comparison of LA-ICP-MS and EPMA data for manganese. The analyses for both methods were performed on the same wolframite grains of concentrate AS 8829. The black line shows the 1:1 trend.

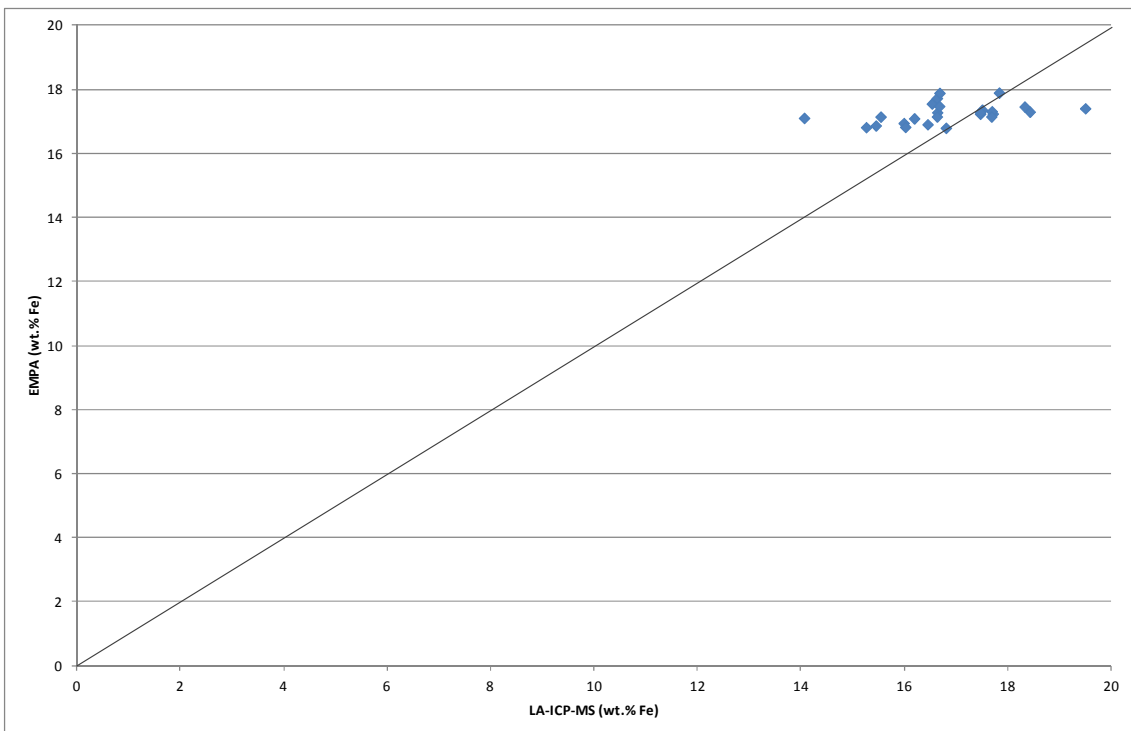


Figure 9.2: Comparison of LA-ICP-MS and EPMA data for iron. The analyses for both methods were performed on the same wolframite grains of concentrate AS 8829. The black line shows the 1:1 trend.

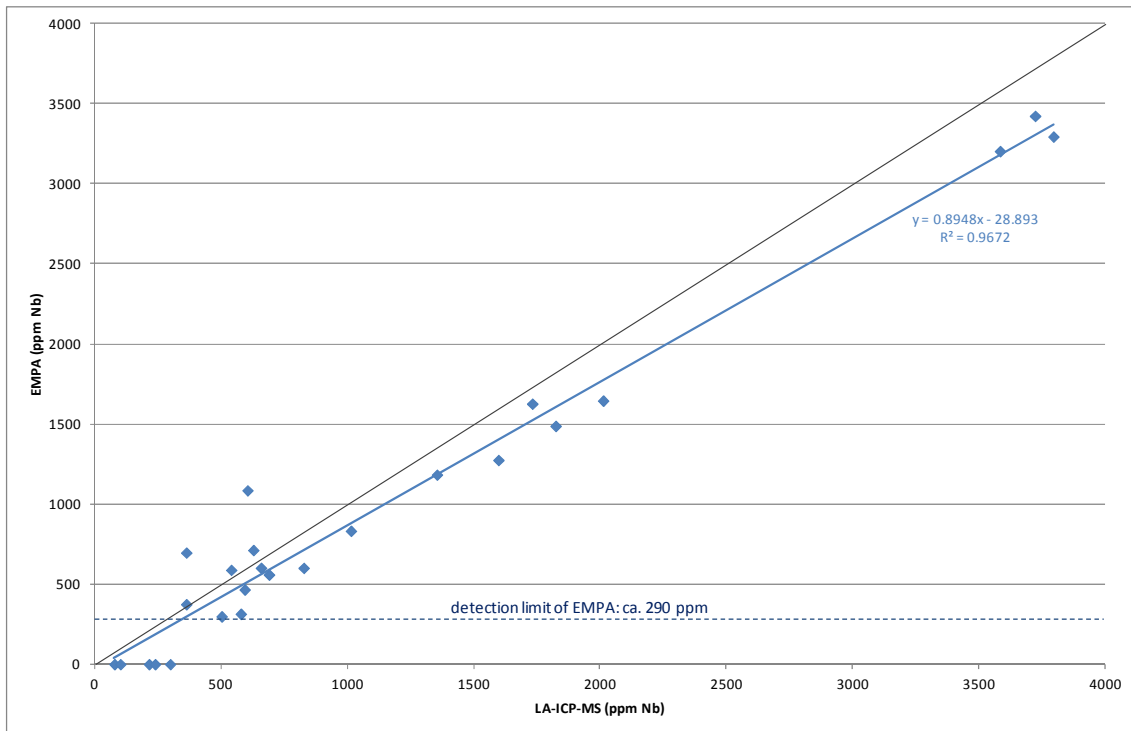


Figure 9.3: Comparison of LA-ICP-MS and EPMA data for niobium. The analyses for both methods were performed on the same wolframite grains of concentrate AS 8829. Detection limit of niobium for EPMA is approximately 290 ppm, EPMA data below detection limit are set to 0. The black line shows the 1:1 trend.

The relative scatter of the data (see Figures 9.1-9.3) is caused by chemical zoning and the different analytical spot sizes and volumes of both methods. However, comparison of the Mn (Figure 9.1) and Nb (Figure 9.3) analyses indicate that both methods produce roughly consistent data and it is shown that the calibration strategy yields comparable results. But the Fe data (Figure 9.2), in fact at higher concentration levels than Mn and Nb, show an obviously larger scatter in the LA-ICP-MS data compared to the EPMA. This is most likely the effect of non-matrix matched calibration of a major element (Fe in wt.%-range for wolframite) against the NIST 610 glass, where the Fe concentration is considerably lower (about 450 ppm; Table 8.2). This effect will presumably also affect the LA-ICP-MS data of other elements (especially Mn) if those are present at higher concentration levels.

9.3 Development of analytical procedure for wolframite

Method development was performed to verify and optimise measurement conditions of selected isotopes for wolframite analyses. Therefore measurements were undertaken on blank, NIST 610 reference glass and wolframite samples (WOLF) to verify and optimise the settings for selected individual isotopes. The relative isotopic abundances of the elements are taken from Rosman & Taylor (1998). The same criteria are considered for the wolframite method as already applied for cassiterite (see chapter 8). The result of this work is summarised at the end of this chapter in Table 9.1, where the recommended isotope for each element and possible interferences are listed.

9.3.1 Low resolution mode

Several elements are free from interferences and consequently the most abundant isotope is measured in the low resolution mode. These isotopes are ^{69}Ga (60.1%), ^{95}Mo (15.9%), ^{107}Ag (51.8%), ^{111}Cd (12.8%), ^{121}Sb (57.2%), ^{205}Tl (70.5%), ^{238}U (99.3%) and the lead isotopes ^{206}Pb (24.1%), ^{207}Pb (22.1%), and ^{208}Pb (52.4%). The ^{204}Pb isotope is used for the determination of common lead for U-Pb dating and has to be corrected for the isobaric ^{204}Hg interference. The monoisotopes ^{89}Y and ^{209}Bi are free from any interference and are also measured in the low resolution mode.

Arsenic is a monoisotopic element with the nominal mass of 75 amu. The signal of the ^{75}As isotope is interfered by the $^{40}\text{Ar}^{35}\text{Cl}$ (75.5%) compound. This interference derives from the plasma gas and likewise influences the background and sample signals. Therefore this interference has little influence on the correct signal for As, but this leads to higher detection limits.

Indium is the only element with isobaric interference on both possible isotopes. The ^{113}In (4.3%) is interfered by ^{113}Cd (12.2%), whereas ^{115}In (95.7%) is perturbed by ^{115}Sn (0.36%). Thus indium is measured on the major isotope which still has to be corrected for the isobaric interference caused by the ^{115}Sn isotope (Figure 9.4). But the ^{115}In isotope can be measured in low resolution because there are no further interferences.

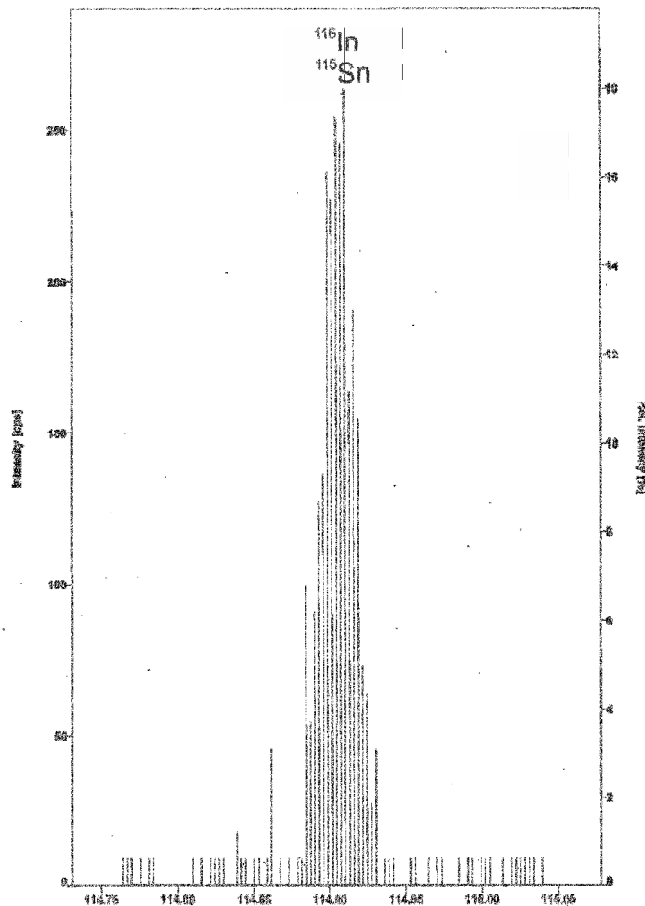


Figure 9.4: Diagram of intensity versus mass-charge ratio showing the medium resolution spectrum of indium on the nominal mass of 115 amu. Note that the ^{115}Sn interference cannot be resolved in high resolution mode. Measurement on wolframite sample (WOLF)

Tin is measured on the ^{118}Sn (24.2%) isotope which shows no significant interferences. But the major isotope ^{120}Sn (32.6%) is interfered by an isobaric overlap with the ^{120}Te (0.1%) isotope.

Barium is measured on the ^{137}Ba (11.2%) isotope because the major isotope ^{138}Ba (71.7%) is interfered by isobaric interferences of the ^{138}La (0.1%) and ^{138}Ce (0.3%) isotopes.

The lanthanides or *rare earth elements* (REE) from La to Lu are measured in low resolution to gain high signal intensities, but several of these elements show elevated background values in blank measurements. *Praseodymium*, *terbium*, *holmium* and *thulium* are monoisotopic elements and are measured on the specific nominal masses. *Lanthanum*, *cerium*, *europium*, *erbium*, and *lutetium* are measured on their most

abundant isotopes ^{139}La (99.9%), ^{140}Ce (88.5%), ^{153}Eu (52.2%), ^{166}Er (33.6%) and ^{175}Lu (97.4%) because these show no significant interferences. *Neodymium* is measured on the ^{146}Nd (17.2%) isotope, because the major isotopes ^{142}Nd (27.2%) and ^{144}Nd (23.8%) are perturbed by isobaric interferences of ^{142}Ce (11.1%) and ^{144}Sm (3.1%), respectively. *Samarium* is measured on the ^{147}Sm (15.0%) isotope because it is devoid of any interference. In contrast, the more frequent ^{152}Sm (26.7%) and ^{154}Sm (22.8%) isotopes are interfered by isobaric Gd isotopes ^{152}Gd (0.2%) and ^{154}Gd (2.2%), respectively. *Gadolinium* is measured on the ^{157}Gd (15.7%) isotope, because the three major isotopes ^{156}Gd (20.5%), ^{158}Gd (24.8%), and ^{160}Gd (21.9%) are perturbed by isobaric interferences of the Dy isotopes ^{156}Dy (0.1%), ^{158}Dy (0.1%), and ^{160}Dy (2.3%), respectively. The ^{163}Dy (24.9%) isotope is used for the measurements of *dysprosium*, because the major isotopes ^{162}Dy (25.5%) and ^{164}Dy (28.2%) are interfered by the isobaric erbium isotopes ^{162}Er (0.1%) and ^{164}Er (1.6%), respectively. *Ytterbium* is measured on the ^{172}Yb (21.8%) isotope, because the most abundant isotope ^{174}Yb (31.8%) is interfered by the isobaric overlap of ^{174}Hf (0.2%).

Hafnium is measured on the ^{177}Hf (18.6%) isotope without any significant interference. The most abundant isotope ^{180}Hf (35.1%) is interfered by two isobaric interferences caused by ^{180}W (0.12%) and ^{180}Ta (0.01%) isotopes.

Mercury is measured in low resolution on the ^{201}Hg (13.2%) isotope and is used for correction of the isobaric ^{204}Hg (6.9%) interference on the ^{204}Pb (1.4%) isotope. Mercury derives from the sample gas. The measurement on the ^{204}Pb isotope is necessary to calculate a correct concentration for common lead for U-Pb dating.

9.3.2 Medium resolution

Several elements measured in medium resolution show the same interference patterns during analysis of wolframite as already described for cassiterite (see chapter 8). This is the case for the following isotopes: ^{12}C , ^{24}Mg , ^{27}Al , ^{29}Si , ^{31}P , ^{32}S , ^{44}Ca , ^{51}V , ^{52}Cr , ^{55}Mn , ^{59}Co , ^{60}Ni , ^{63}Cu , and ^{66}Zn . To avoid repetition, please refer to the method development chapter of cassiterite for detailed description.

During analysis of *scandium* in wolframite, the same interferences occur as already described for cassiterite but the influence of the $^{90}\text{Zr}^{2+}$ ion is not corrected, because the zirconium contents are generally lower in wolframite compared to cassiterite.

Titanium has several possible isotopes for the measurement. The most abundant ^{48}Ti (73.7%) isotope is excluded because of isobaric overlap from the ^{48}Ca (0.2%) isotope. The ^{47}Ti (7.4%) isotope is perturbed by non-resolvable interferences caused by $^{94}\text{Zr}^{2+}$ and $^{94}\text{Mo}^{2+}$ ions, but the influence of both bivalent ions is negligible. The medium resolution mode is necessary for measurement of the ^{47}Ti isotope to discriminate the interference of the $^{15}\text{N}^{16}\text{O}_2$ (0.36%) compound (Figure 9.5).

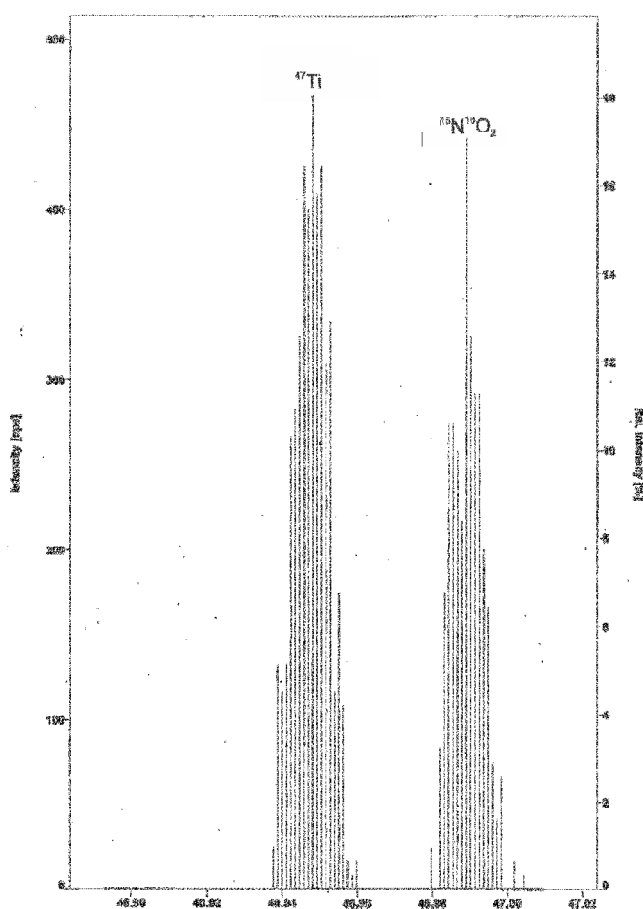


Figure 9.5: Diagram of intensity versus mass-charge ratio showing the medium resolution spectrum of titanium on the nominal mass of 47 amu. Note the interference caused by NO_2 . Measurement on wolframite sample (WOLF)

Iron is measured on the primary ^{56}Fe (91.8%) isotope. The interferences caused by the bivalent ^{112}Sn (1.0%) ion and the $^{40}\text{Ar}^{16}\text{O}$ (99.4%) compound are discriminated by using the medium resolution mode (Figure 9.6). The search window is set to 70%.

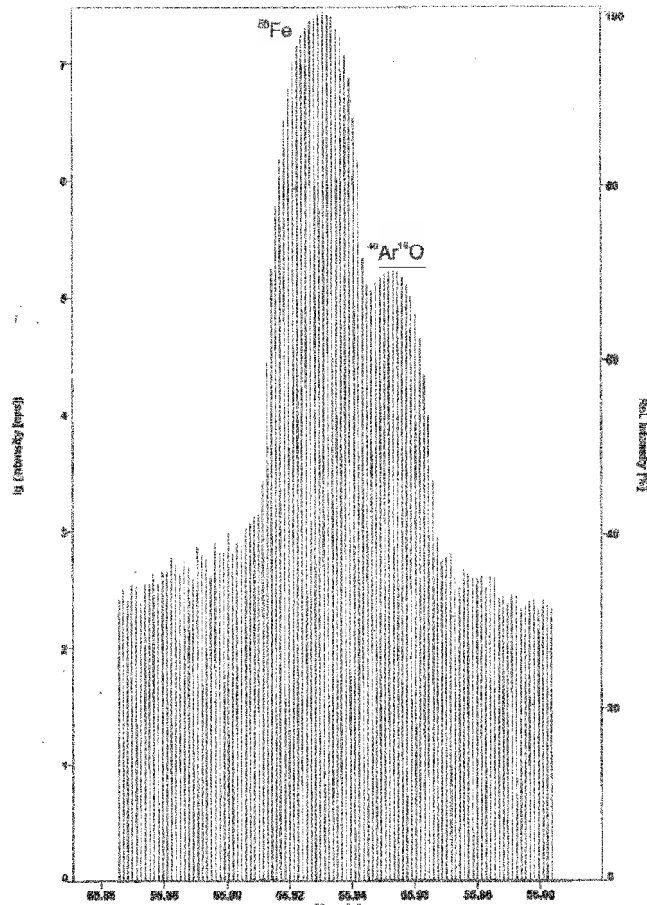


Figure 9.6: Diagram of intensity versus mass-charge ratio showing the medium resolution spectrum of iron on the nominal mass of 56 amu. Note the interference caused by ArO. Measurement on wolframite sample (WOLF)

Strontium is analysed on its major isotope ^{88}Sr (82.6%). The medium resolution mode is chosen for the measurement to discriminate the influence of several bivalent ions, namely ^{176}Hf (5.3%), ^{176}Yb (12.8%), and ^{176}Lu (2.6%).

Niobium is a monoisotopic element with the nominal mass of 93 amu. It is measured in the medium resolution to separate the prominent interference caused by the bivalent ^{186}W (28.4%) ion (Figure 9.7).

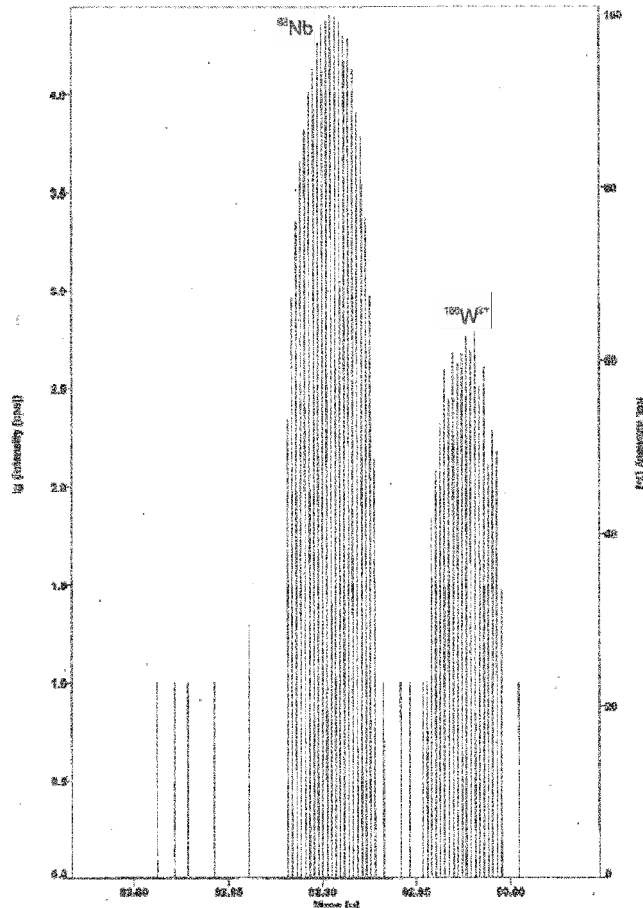


Figure 9.7: Diagram of intensity versus mass-charge ratio showing the medium resolution spectrum of niobium on the nominal mass of 93 amu. Note the interference caused by bivalent ^{186}W ion. Measurement on wolframite sample (WOLF)

Tantalum is measured on the dominant ^{181}Ta (99.9%) isotope, but the medium resolution is chosen to reduce the abundance sensitivity from the significant ^{182}W (26.5%) isotope.

Tungsten is measured on the ^{182}W (26.5%) isotope which shows no significant interferences. However, the medium resolution mode is chosen to protect the detector from high signal intensities.

Thorium is a monoisotope with the nominal mass of 232 amu and is measured in medium resolution because of possible interference from the $^{184}\text{W}^{16}\text{O}_3$ compound.

Table 9.1: Summary of the measured elements for wolframite analysis by LA-ICP-MS including the selected isotope, its relative abundance, selected resolution mode for the mass spectrometer, and potential interferences

element	isotope	rel. abundance (%)	resolution	potential interferences
C	12	98.9	MR	Mg ²⁺
Mg	24	79.0	MR	C ₂ , Ti ²⁺
Al	27	100	MR	CN
Si	29	4.7	MR	Fe ²⁺ , CO, N ₂ , N ₂ H
P	31	100	MR	NO, NOH
S	32	95.0	MR	O ₂
Ca	44	2.1	MR	CO ₂ , SiO, Sr ²⁺
Sc	45	100	MR	SiO, Zr ²⁺
Ti	47	7.4	MR	SiN, Zr ²⁺
V	51	100	MR	
Cr	52	83.8	MR	ArC
Mn	55	100	MR	ArN
Fe	56	91.8	MR	ArO, CaO
Co	59	100	MR	ArF
Ni	60	26.2	MR	CaO, Sn ²⁺
Cu	63	69.2	MR	ArNa, Xe ²⁺
Zn	66	27.9	MR	Xe ²⁺ , S ₂
Ga	69	60.1	LR	
As	75	100	LR	ArCl
Sr	88	82.6	MR	Hf ²⁺ , Yb ²⁺ , Lu ²⁺
Y	89	100	LR	
Zr	90	51.5	MR	W ²⁺
Nb	93	100	MR	W ²⁺
Mo	95	15.9	LR	
Ag	107	51.8	LR	
Cd	111	12.8	LR	
In	115	95.7	LR	Sn
Sn	118	24.2	LR	
Sb	121	57.2	LR	
Ba	137	11.2	LR	
La	139	100	LR	
Ce	140	88.4	LR	
Pr	141	100	LR	
Nd	146	17.2	LR	
Sm	147	15.0	LR	
Eu	153	52.2	LR	
Gd	157	15.7	LR	
Tb	159	100	LR	
Dy	163	24.9	LR	

Ho	165	100	LR	
Er	166	33.6	LR	
Tm	169	100	LR	
Yb	172	21.8	LR	
Lu	175	97.4	LR	
Hf	177	18.6	LR	
Ta	181	100	MR	Abundance Sensitivity ¹⁸² W
W	182	26.5	MR	
Hg	201	13.2	LR	
Tl	205	70.5	LR	
Pb			LR	
Bi	209	100	LR	
Th	232	100	MR	WO ₃
U	238	99.3	LR	

10 Results

Cassiterite and wolframite ore concentrates from various ore deposits and mine sites worldwide (Figure 10.1), but with special emphasis on Central Africa, have been analysed. The mineralogical composition of Sn or W concentrates is determined using MLA (relative mineral proportions in the following descriptions are given in area%), subsequently followed by LA-ICP-MS analysis of major, minor and trace elements of individual cassiterite and wolframite grains in the respective ore concentrates. In a first attempt, it was tested if trace element analysis by EPMA is also feasible.

10.1 Detailed descriptions of investigated deposits

The cassiterite and wolframite concentrates originate from different ore deposit types of various ages ranging from Archaean to Cenozoic (Table 10.1). These deposits are grouped on regional scales (e.g., metallogenic provinces) which are first divided into continents (in alphabetical order) and furthermore subdivided according to their respective age (Table 10.1). Information on geology, mineralogy, and age data are presented in the following.

Table 10.1: Summarising table on metallogenic provinces or single deposit (detailed descriptions are given in the respective section) including county (AU=Australia, BO=Bolivia, BR=Brazil, CD= Democratic Republic of the Congo, CA=Canada, CO=Colombia, CZ=Czech Republic, EG=Egypt, GB=Great Britain, HK=Hong Kong ID=Indonesia, MM=Myanmar, MN=Mongolia, MY=Malaysia, NG=Nigeria, PE=Peru, PT=Portugal, RU= Russia, RW=Rwanda, TH=Thailand, US= United States of America, ZA=South Africa), deposit types (rg=rare metal granite, see 6.2.1; an=anorogenic, see 6.2.1; pe=pegmatite, see 6.2.1, gr=greisen, see 6.2.2; po=porphyry, see 6.2.2; hv=hydrothermal vein, see 6.2.3; pl=placer, primary deposit in brackets, see 6.2.6), dominating ore minerals (cs=cassiterite, wolf=wolframite, coltan=columbite-tantalite, schee=scheelite, sulf=sulphides) in the concentrates, geologic age (in million years), type of associated intrusion and their surrounding host rocks.

Section	Metallogenic province or deposit (examples)	Country	Deposit type	Mineralogy	Age	Intrusion type	Host rocks to mineralization
10.1.1	Bushveld Complex (Zaaiplaats)	ZA	an	cs, schee	2050	A-type granite	granite
10.1.1	Kibara belt (Manono, Rutongo, Nyakabingo)	CD, RW	pe, hv, pl	cs, coltan, wolf	900-1000	S-type granites	metasediments, granites, gneisses
10.1.1	Kamativi	ZW	pe	cs, coltan	1000	pegmatite	paragneiss
10.1.1	Eastern Desert (Abu Dabbab, Nuweibi)	EG	rg	cs, coltan	630	A-type granite	granite
10.1.1	Jos Plateau	NG	pl (an)	cs, coltan	200	A-type granite	granite
10.1.2	Southeast Asian Tin Belt (Bangka-Belitung, Mae Sariang)	ID, MY, TH, MM	pl (gr, hv)	cs, wolf	180-230	S-type minor I-type granites	granite
10.1.2	Central Asia (Yugodzyr, Spokoynoye)	MN, RU	gr, hv	wolf, schee, sulf, cs	140-170	S-type granites	granite, metasediments
10.1.2	Needle Hill	HK	hv	wolf	145	S-type granite	granite
10.1.3	Greenbushes	AU	pe	cs, coltan	2530	pegmatite	gneiss, amphibolite
10.1.3	Mount Carbine	AU	hv	wolf, schee	280	S-type granite	metasediments
10.1.4	Variscan (Hemerdon, Krásno)	GB, CZ, PT	hv, gr, pe	cs, wolf, sulf, coltan	270-300	S-type granites	metasediments
10.1.5	Tanco	CA	pe	cs, coltan	2640	pegmatite	amphibolite, metagabbro
10.1.5	Black Hills	US	pe	cs, coltan	1710	S-type granite	metasediments
10.1.6	São João del Rei	BR	pe	cs, coltan	2120	S-type granite	greenstone belt sequence
10.1.6	Pitinga	BR	an	cs, coltan	1800	A-type granite	granite
10.1.6	Colombia	CO	pl (pe)	cs, coltan	?	?	?
10.1.6	Rondônia (Oriente Novo and Santa Bárbara)	BR	an	cs	980-1075	A-type granite	granite
10.1.6	Araçuaí	BR	pe	cs, coltan	500	S-type granite	metasediments
10.1.6	Bolivian Tin Belt (San Rafael, Huanuni)	BO, PE	po, hv	cs, wolf, sulf	225-10	S-type granite, porphyries	metasediments

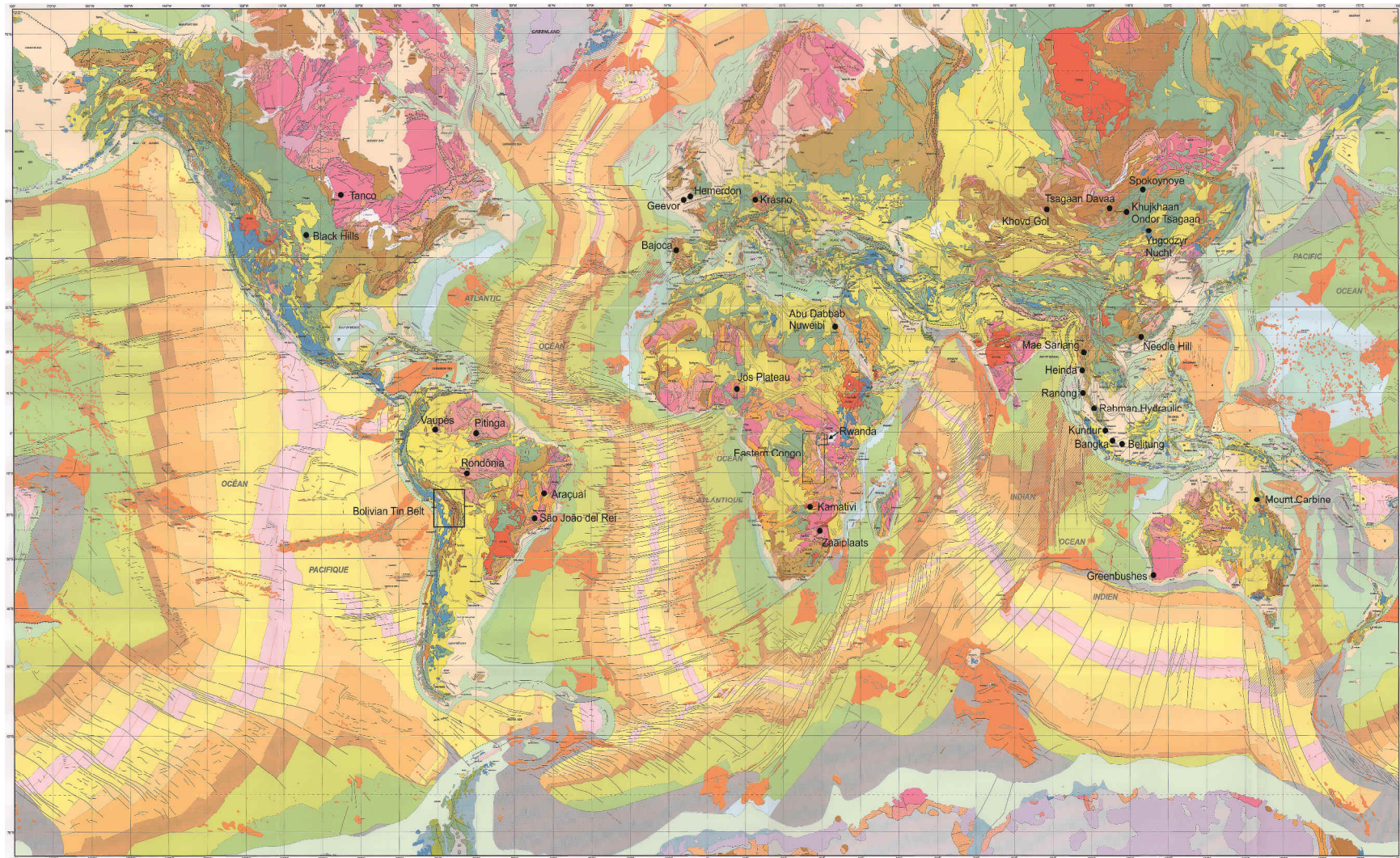


Figure 10.1: Geological map of the World (modified after Bouysse, 2009) showing the deposits of ore concentrate samples. Rectangles mark areas of higher sample density which are displayed in separate maps below.

10.1.1 Africa

The Zaaiplaats tin deposit is situated in the northern lobe of the Bushveld Complex and is associated with the Lebowa Granite Suite (Pollard et al., 1989; Pollard et al., 1991). Tin mineralization is hosted by the coarse-grained Bobbejaankop and the fine-grained Lease granites which represent the upper, fractionated, and altered portion of the Lebowa Granite Suite (Pollard et al., 1989; Pollard et al., 1991; McNaughton et al., 1993). Disseminated cassiterite mineralization in the Bobbejaankop granite forms a low-grade (defined on the basis of >35 ppm Sn) horizon subparallel to the roof (Figure 10.2; McNaughton et al., 1993). The Lease and Bobbejaankop Granites also host a series of shallowly plunging and branching systems of interlinked high-grade pipe ore bodies (McNaughton et al., 1993). The mineralizing event was dated between 2054 and 2050 million years using SHRIMP (sensitive high resolution ion microprobe) age data for cassiterite from the Rooiberg mine (Robb et al., 2000) and at 2099 ± 3 Ma by U-Pb dating of cassiterite from the Zaaiplaats mine (Gulson & Jones, 1992).

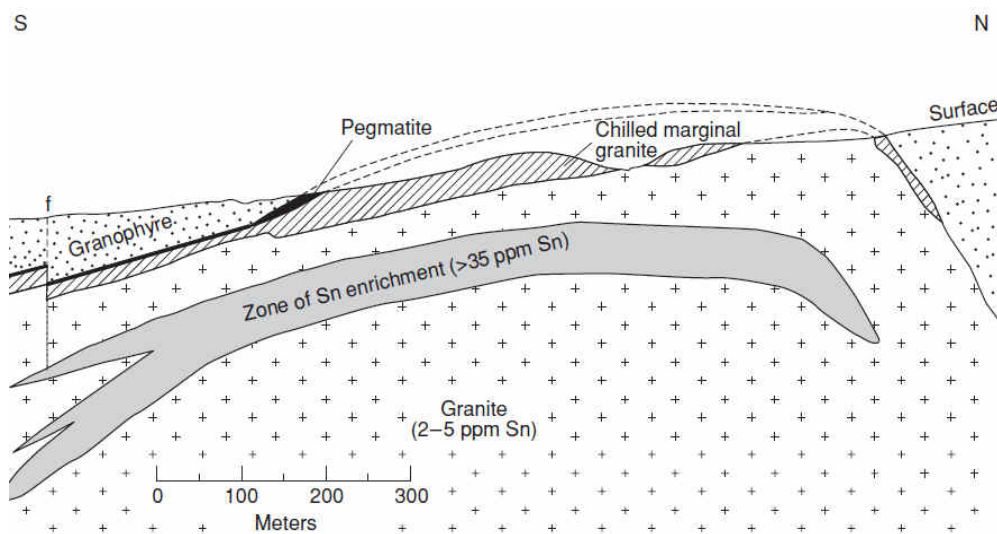


Figure 10.2: Cross-section through the Zaaiplaats tin deposits in South Africa showing the intrusive contact of the granite and the low grade zone of Sn enrichment (Robb, 2005 modified after Coetzee & Twist, 1989).

The Kibara belt of Central Africa is generally portrayed as a single continuous orogenic belt that trends northeast-southwest over approximately 1300 km from the Katanga Province in the Democratic Republic of the Congo up to the Ankole region in southwest Uganda. Recent work by Tack et al. (2010) illustrated that there is a discontinuity in the traditionally defined Kibara belt by the northwest-trending Palaeoproterozoic 'Rusizian' basement which represents the extension of the Palaeoproterozoic Ubende belt of southwest Tanzania. The northern segment or Karagwe-Ankole belt (KAB: Rwanda,

Burundi, and Maniema and Kivu Provinces in the DRC) and southern segment or Kibara belt (KIB: Katanga Province in the DRC) are treated as two separate but coeval belts (Tack et al., 2010; Fernandez-Alonso et al., 2012). The Palaeo- and Mesoproterozoic metasedimentary rocks of the KAB and KIB consist mainly of monotonous pelitic and psammitic sequences, interpreted as shallow-water deposits and were intruded by several generations of S-type granites (Fernandez-Alonso et al., 2012). In the KAB, the main granite generations G1-G3 intruded between 1383 ± 17 Ma and 1371 ± 7 Ma (U-Pb SHRIMP on zircon) followed by the intrusion of the G4-granites (also termed ‘tin granites’) around 986 ± 10 Ma (U-Pb SHRIMP on zircon; Tack et al., 2010; Cahen & Ledent, 1979; Pohl, 1994). Dewaele et al. (2010) state that these G4-granites are parental to the hydrothermal mineralisation or the rare element pegmatites and the metals (Sn, Ta, W, etc) have been mobilised during later hydrothermal events in the succession of the intrusion of the G4-granites.

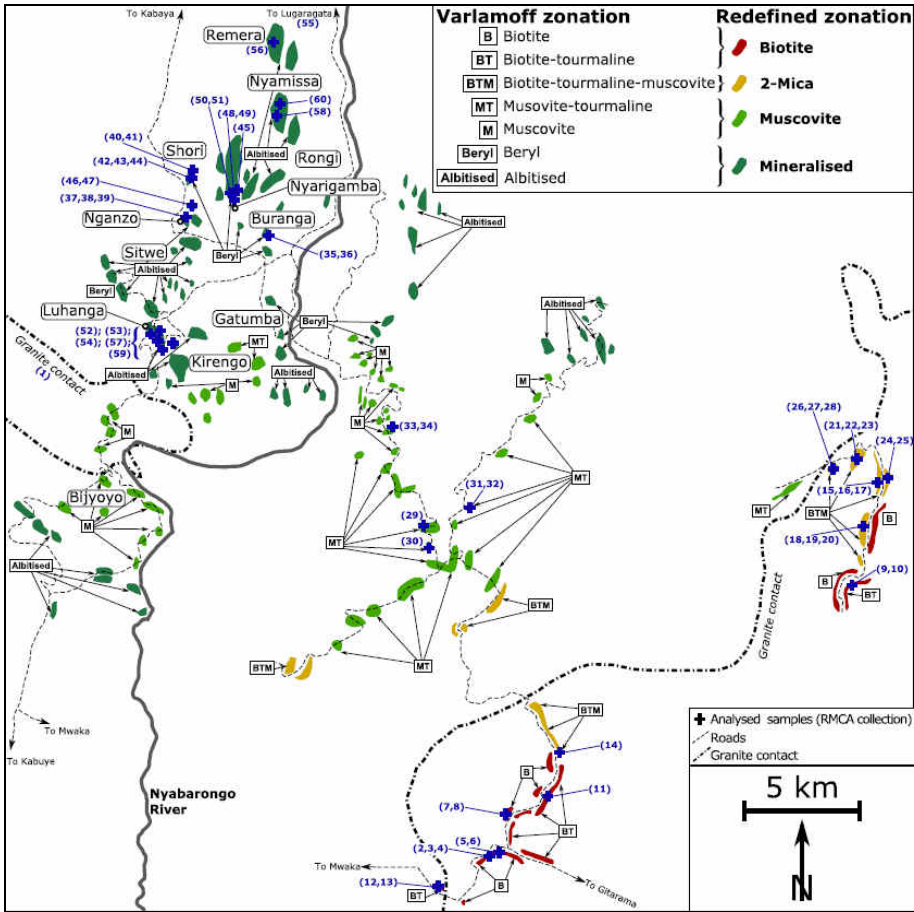


Figure 10.3: Regional zonation of pegmatites around a parental granite intrusion in the Gatumba area, Rwanda. Barren pegmatites are closer to the parental intrusion, whereas mineralized pegmatites occur in greater distance (Hulsbosch et al., 2013).

Cassiterite, columbite-tantalite (coltan), and wolframite deposits related to the G4-granite generation form either Sn-Ta-Nb-bearing LCT-type pegmatites (e.g., Manono-Kitotolo) or hydrothermal quartz veins with Sn (e.g., Rutongo) or W (e.g., Nyakabingo) mineralisation (Figures 10.4 & 10.5; Dewaele et al., 2010; De Clercq, 2012; Melcher et al., 2015). The pegmatites were emplaced after intrusion of the G4-granites along cleavage planes of the Kibaran metasediments and follow their general strike (Dewaele et al., 2011). There is an evident regional zoning of the pegmatites surrounding the granite intrusions, whereby the mineralised pegmatites are furthest from the parental granites (Figure 10.3; Varlamoff, 1972; Hulsbosch et al., 2013). The pegmatites formed from a small residual melt portion after fractionation of these granites (Hulsbosch et al., 2013).

Hydrothermal quartz veins occur close to granitic intrusion, but also isolated with no clear relation to granites or pegmatites (De Clercq, 2012). The veins are principally composed of quartz with minor quantities of muscovite and tourmaline along the contact zones (Dewaele et al., 2010). Major ore minerals are cassiterite or wolframite, but without any columbite-tantalite.

Age estimates of columbite group minerals from the KAB and KIB range from ca. 920 to 1030 Ma with the maximum around 960 to 990 Ma (Romer & Lehmann, 1995; Melcher et al., 2015) indicating a close association with the G4-granites dated at 986 ± 10 Ma (Tack et al., 2010). Some columbite-tantalite and cassiterite concentrates sampled about 50 km east and west of the East African rift yielded younger age estimates ranging from about 500 to 700 Ma; this is interpreted as Pan-African rejuvenation of older mineralised structures (Melcher et al., 2015).

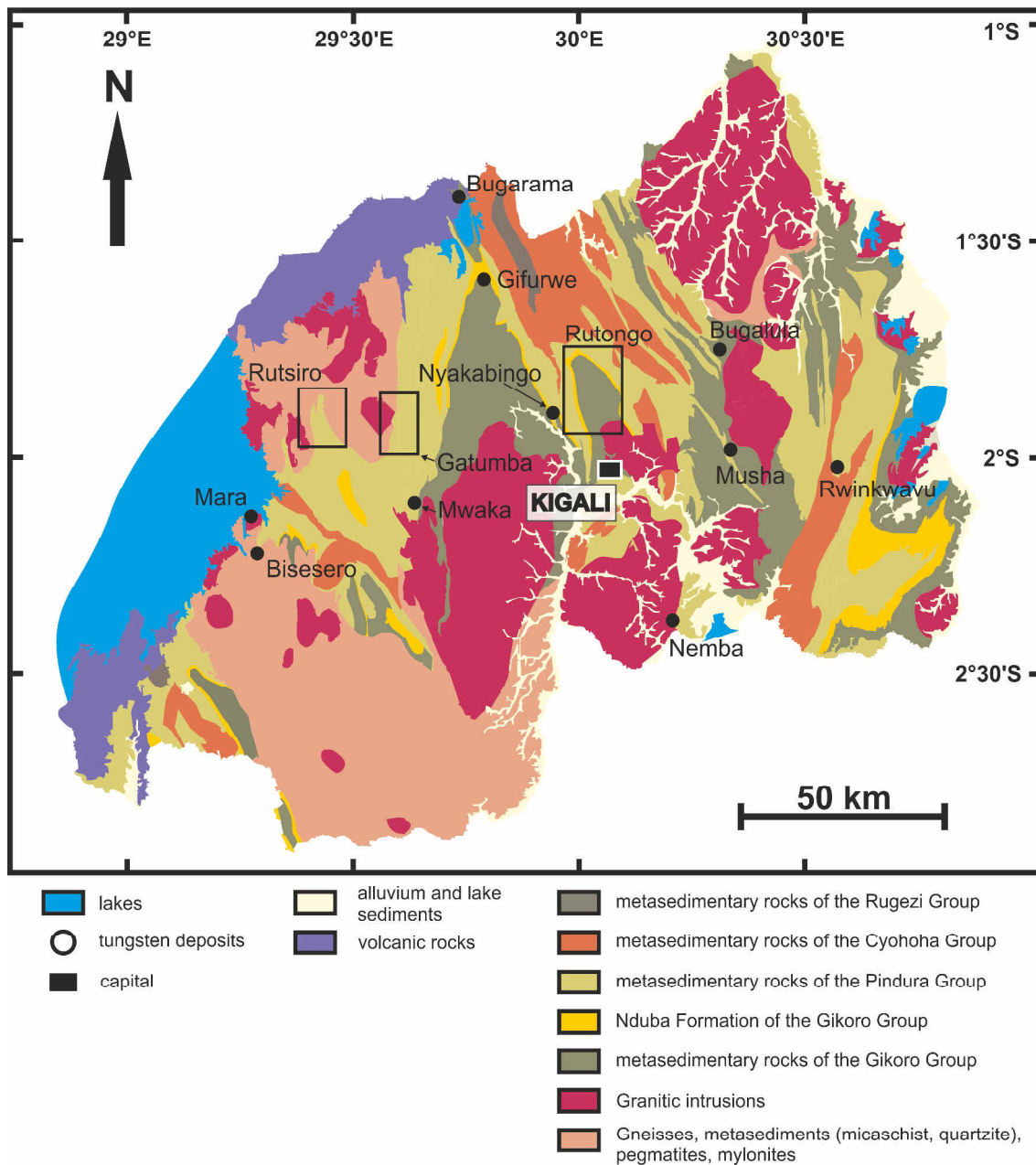


Figure 10.4: Geological map of Rwanda showing the location of ore concentrate samples (modified after Theunissen et al., 1991). Rectangles mark concession areas with higher sample density. Detailed maps of the Nyakabingo, Nemba, Rutsiro and Rutongo areas are given in chapter 11.

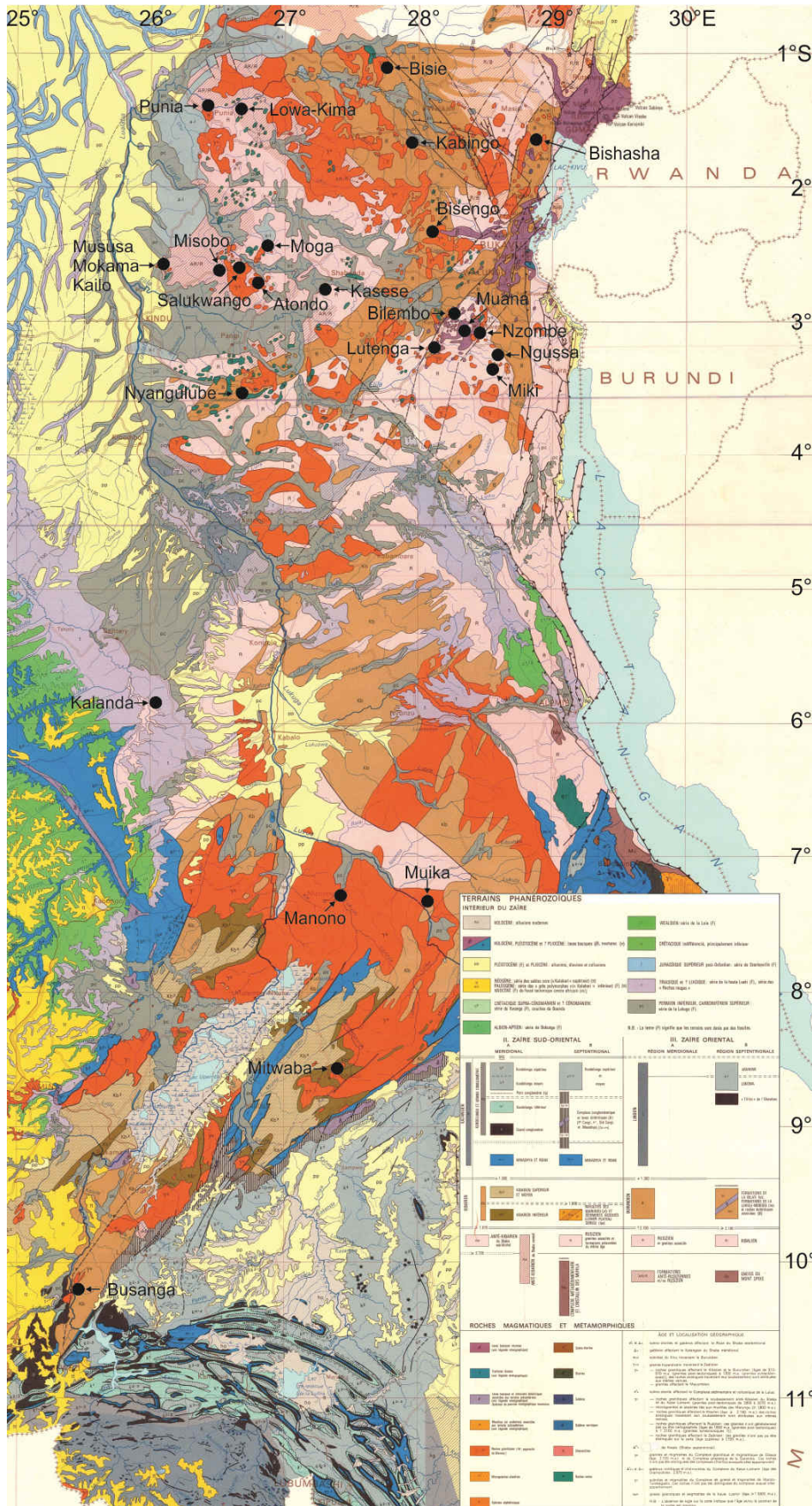


Figure 10.5: Geological map of the Democratic Republic of the Congo showing the location of ore concentrate samples (modified after Lepersonne, 1974).

The Neoproterozoic (990 ± 15 Ma) Kamativi deposit is located in western Zimbabwe. Several flat-dipping pegmatite bodies intruded Palaeoproterozoic paragneisses and schists of the Magondi belt (Rijks & van der Veen, 1972; Melcher et al., 2015). The pegmatite is mineralised in cassiterite, columbite-tantalite, spodumene, amblygonite, and beryl (Rijks & van der Veen, 1972). The very pure tin concentrate from Kamativi contains cassiterite (82%) and minor amounts of columbite-tantalite (5%). Analysis of cassiterite give an U-Pb age estimate of about 1087 Ma and a more precise date of 1031 ± 8 Ma was yielded for selected columbite grains from another ore concentrate from Kamativi (Melcher et al., 2015).

Peraluminous ‘rare-metal’ albite-granite stocks host fine-grained disseminated columbite-tantalite and cassiterite mineralisation in the Abu Dabbab and Nuweibi deposits of the Eastern Desert of Egypt (Helba et al., 1997; Küster, 2008). Quartz veins with cassiterite and minor wolframite crosscutting the country rocks are also present. The Ta-Sn-hosting ‘rare-metal’ granites are highly evolved and represent the most fractionated parts of multiphase granitic intrusion sequences (Figure 10.6; Küster, 2008).

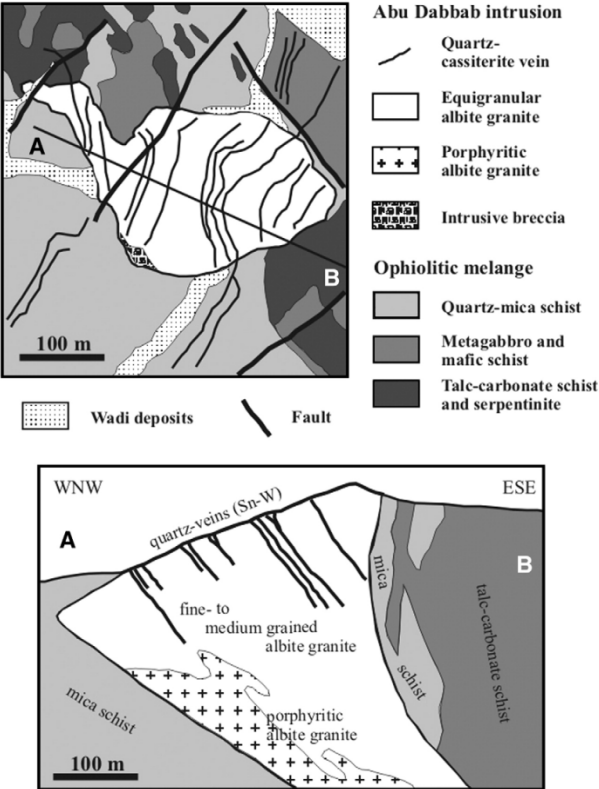


Figure 10.6: Geological map (upper image) and cross-section (lower image) of the Abu Dabbab leucogranite stock in the Eastern Desert, Egypt (Küster, 2008).

Both deposits are quite similar, but Abu Dabbab shows considerably higher Sn contents compared to Nuweibi. Textural and geochemical investigations indicate that columbite-tantalite and cassiterite crystallised under magmatic conditions and rare metal enrichment is caused by high degrees of fractionation (Mohamed, 1993; Helba et al., 1997; Küster, 2008). The tin concentrate from Abu Dabbab was collected from the processing plant and is almost entirely composed of cassiterite (78%) with minor tantalite (5%), wodginite (2%), and tapiolite (1%). The heavy mineral concentrate from Nuweibi placer contains coarse-grained cassiterite (19%) and ilmenite (36%) as the dominant ore minerals. Emplacement ages of the Abu Dabbab and Nuweibi granites are only roughly estimated between 600 and 450 Ma because dating is complicated due to metamict and undersized zircons (Helba et al., 1997; Küster, 2008). Age estimates for cassiterite from Nuweibi yield an age of about 616 Ma.

Peralkaline ring complexes associated with the Jurassic Younger Granites series are found in the Jos Plateau of Nigeria. Primary Sn-Ta deposits occur as disseminations in the roof zones of peraluminous biotite granites which mark the latest intrusion stage of the Younger Granites (Olade, 1980; Bowden & Kinnaird, 1984; Imeokparia, 1988; Pastor & Turaki, 1985; Ogunbajo 1993; Obaje, 2009). However, alluvial heavy mineral placers containing cassiterite and columbite-tantalite are the economically most important deposit type. The single placer concentrate from the Jos Plateau mainly contains cassiterite (64%) with minor columbite (10%), ilmenite (9%), and zircon (6%). Age estimate on columbite from this concentrate yields an age of about 189 Ma.

10.1.2 Asia

The Southeast Asian Tin Belt extends for about 2800 km from Myanmar and Thailand in the north along the Malayan Peninsula to the Indonesian Tin Islands (e.g., Bangka and Belitung) in the south (Figure 10.7; Schwartz et al., 1995). Granitoids are grouped into three elongated provinces from east to west: the Eastern, the Main Range, and the Western Granitoid Provinces (Figure 10.7; Cobbing et al., 1986; Putthapiban & Schwartz, 1994; Schwartz et al., 1995). The granitoids of the Eastern Province (263–79 Ma) range in composition from dominant monzogranite to minor diorite and mainly show I-type characteristics. The Main Range is made up of biotite granite (230–184 Ma) with S-type affinity. In the Western Province (149–22 Ma) S-type biotite granite and hornblende-biotite granite-granodiorite with I-type characteristics occur (Cobbing et al., 1986;

Putthapiban & Schwartz, 1994; Schwartz et al., 1995). A special case are the Tin Islands (193–251 Ma), where Main Range- and Eastern Province-type granitoids occur next to each other (Wikarno et al., 1988; Schwartz et al., 1995). Primary cassiterite deposits are generally related to biotite granite plutons with S-type affinity, but the majority of tin production derives from secondary placer deposits which formed since the Miocene (Putthapiban & Schwartz, 1994; Schwartz et al., 1995).

The Mae Sariang tungsten deposit is located in northwestern Thailand close to the Burmese border (Figure 10.7). Wolframite with minor scheelite and arsenopyrite occurs in steeply dipping hydrothermal quartz veins (the major lode is called Mae Lama) which crosscut granite as well as sandy shales forming the surrounding country rocks (Brown & Jalichandra, 1951; Pitragool & Panupaisal, 1979). Tungsten mineralization is related to the intrusion of the nearby Triassic (247 ± 18 Ma) porphyritic biotite S-type granite (Schwartz et al., 1995).

The Heinda mine is situated on the western coast of southern Myanmar and cassiterite is recovered from alluvial placer deposits which are consolidated to conglomerates (Grundstoffberatung, 1971). Primary mineralisation occurs as cassiterite- and wolframite-bearing greisen bodies and hydrothermal quartz veins along the contact of granites with the metasedimentary country rocks, e.g. quartzite, sandstone, schist, shale, and greywacke (Grundstoffberatung, 1971). Wolframite occurs in the primary mineralisation, but disappeared almost completely during sedimentation and weathering from the conglomerates (Grundstoffberatung, 1971).

The Ranong field consists of alluvial heavy mineral (cassiterite, ilmenite, monazite, xenotime and zircon, but also wolframite) placers along the western coast of Thailand close to the Burmese border (Figure 10.7; Aranyakanon, 1961). Primary Sn-W deposits, such as Haad Som Pan deposit which is especially rich in hübnerite, occur as disseminated greisen zones in the cupolas of Late Cretaceous (78–82 Ma) tourmaline-bearing muscovite granites of the Western Granite Province (Aranyakanon, 1961; Suthakorn, 1992; Schwartz et al., 1995; Imai et al., 2013). At Haad Som Pan, hübnerite occurs besides cassiterite but hübnerite is preferentially concentrated at higher levels compared to cassiterite (Aranyakanon, 1961).

The Rahman Hydraulic tin mine is situated in the Klian Intan district of Malaysia close to the border with Thailand and cassiterite is mined from alluvial/colluvial and primary vein deposits (the primary deposit is also known as Gunung Paku) by open pit methods (Ariffin, 2009). Cassiterite together with sulphides (pyrite, arsenopyrite,

chalcopyrite, and covellite) and tourmaline occurs in generally E-W-striking hydrothermal quartz veins and stockworks (Ariffin, 2009; Malaysian-Thai Working Group, 2009). Primary mineralization is related to Main Range S-type biotite granite of Late Triassic age intruding into Silurian-Devonian metasedimentary (slates with subordinate marble) country rocks (Ariffin, 2009; Malaysian-Thai Working Group, 2009).

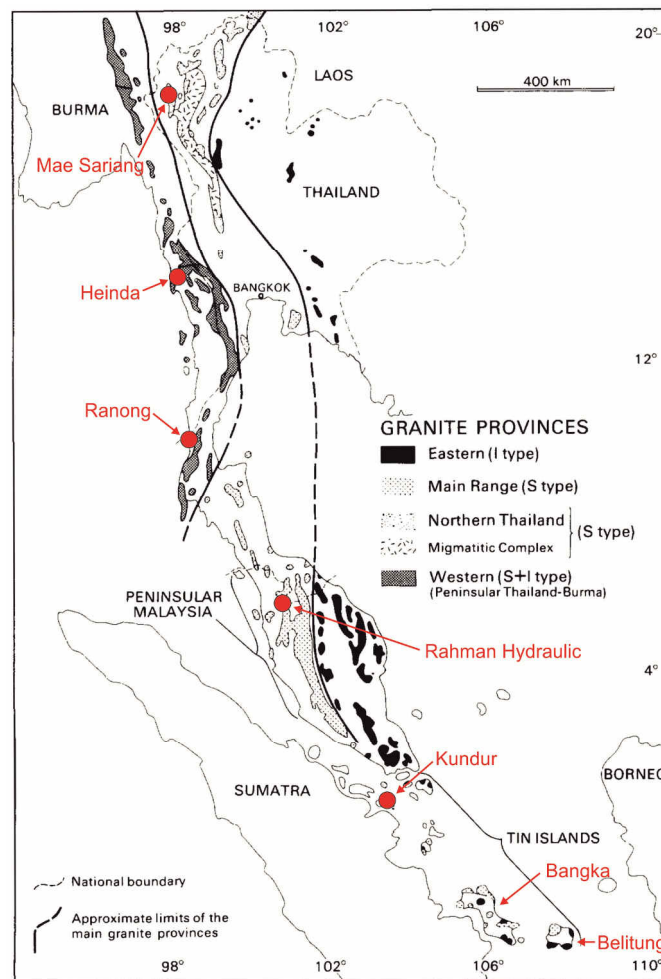


Figure 10.7: Geological map of the Southeast Asian Tin Belt showing the location of samples (modified after Cobbing et al, 1986).

Post-magmatic quartz vein and greisen deposits in Central Asia (here specifically Mongolia and Russia) are related to small massifs or stocks of rare-metal granitic intrusions (Li-F granites) which are mostly Mesozoic in age and formed in a continental collision setting (Figure 10.8; Koval & Yakimov, 1983; Kovalenko & Yarmolyuk, 1995, Gerel, 1998; Kovalenko & Yarmolyuk, 2001). Hydrothermal wolframite-bearing quartz veins occur at the Tsagaan Davaa (with cassiterite as by-product plus minor scheelite and chalcopyrite) and Khovd Gol (with minor stibnite and scheelite; Enchbat, 2007) deposits and in the vicinity of the Khujkhaan placer (United Nations, 1999; Elsner et al.,

2011). The Yugodzyr and Ondor Tsagaan deposits are characterised by wolframite-molybdenite-beryl greisen bodies and quartz veins/stockwork (Ivanova et al., 1978; United Nations, 1999; Elsner et al., 2011); mineralization at Yugodzyr is related to a Ta-bearing Jurassic (wolframite Sm-Nd age 169.3 ± 2.5 Ma; unpublished data by Friedhelm Henjes-Kunst) granite porphyry (Kovalenko & Yarmolyuk, 1995). Polymetallic veins at Nucht contain molybdenite, pyrite, wolframite, cassiterite, and galena (Elsner et al., 2011).

The Spokoynoye tungsten deposit is located in the vicinity of the highly differentiated Orlovka Ta-bearing lithionite-amazonite-albite granite in eastern Transbaikalia, Russia (Badanina et al., 2004). Tungsten mineralisation at Spokoynoye is present as wolframite in quartz veins and greisen bodies in the cupola of a Mesozoic muscovite-albite granite stock, whereas the veins also occur in the surrounding lower Devonian metasediments (Denisenko, 1986; Badanina et al., 2004; Dolgopolova et al., 2005). Both, the Spokoynoye and Orlovka granites, have a common source in the Jurassic (143.8 ± 4.2 Ma) Khangilay granite pluton (Dolgopolova et al., 2005).

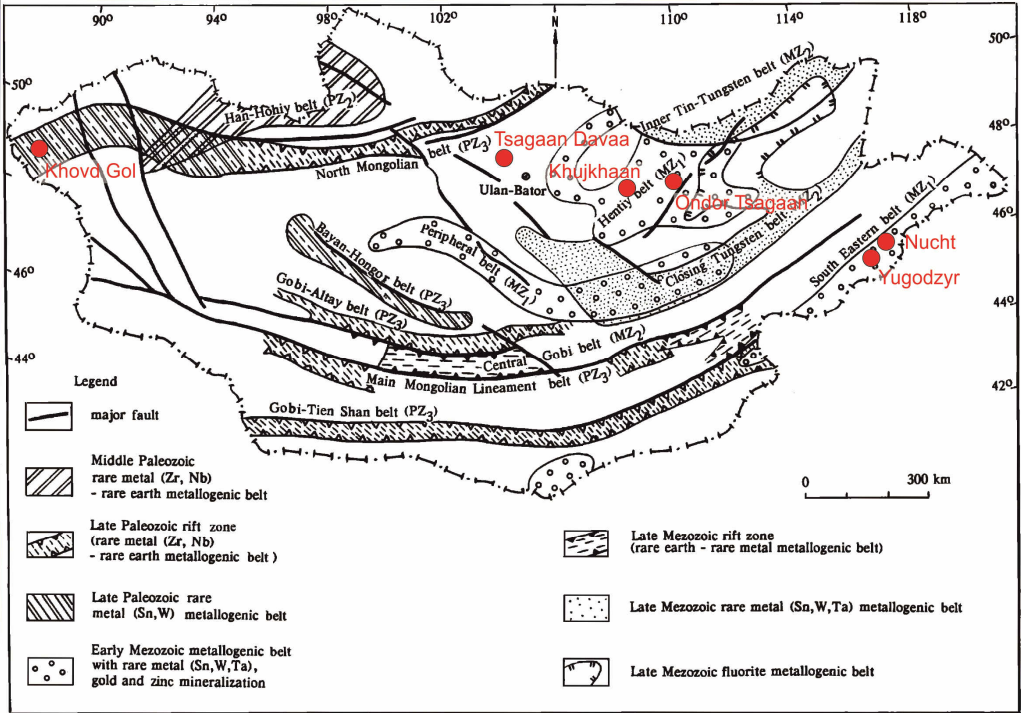


Figure 10.8: Geological map of the Mongolia showing the location of ore concentrate samples (modified after Kovalenko & Yarmolyuk, 1995).

The Needle Hill tungsten deposit is located in the New Territories of Hong Kong. Wolframite-bearing hydrothermal quartz veins with minor molybdenite occur within Upper Jurassic granites (146.4 ± 0.2 Ma U–Pb zircon age; Davis et al., 1997) of the Sha Tin pluton (Davis, 1961; Roberts & Strange, 1991). The tungsten concentrate from Needle Hill essentially contains wolframite (about 83%) with only Fe hydroxides (ca. 10%) and quartz (ca. 2%) as further minor phases.

10.1.3 Australia

The Greenbushes pegmatite is located in Western Australia and intruded as a swarm of linear dykes (~7 km in length and ~1 km width) into the Archaean Balingup metamorphic belt which is composed of gneisses and amphibolites (Figure 10.9; Partington et al., 1995; Fetherston, 2004).

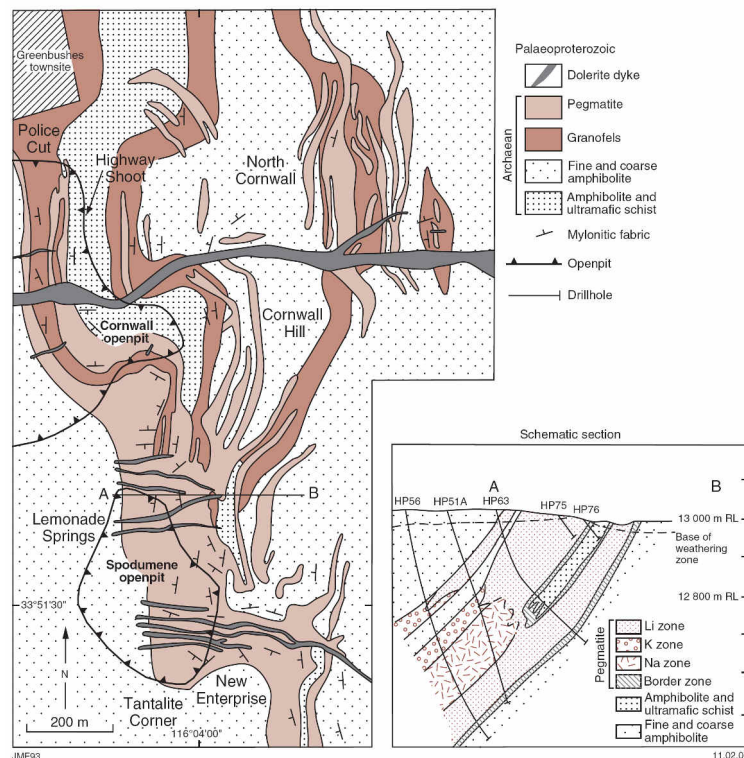


Figure 10.9: Geological map and cross section of the Greenbushes pegmatite (Fetherston, 2004 modified from Partington et al., 1995).

It represents albite-rich pegmatite of the LCT-family with economic Ta-Li-Sn mineralisation. The tantalum ore is composed of columbite-tantalite and other Ta-bearing minerals like stibiotantalite, wodginite, tapiolite, and microlite; cassiterite is won as by-product (Fetherston, 2004; Melcher et al., 2015). Major Li-bearing mineral is spodumene. Dating on zircons yielded an emplacement age of 2527 ± 2 Ma for the

Greenbushes pegmatite (Partington et al., 1995) which is in accordance with various age estimates derived from columbite-group minerals that range from 2423 to 2587 Ma (Melcher et al., 2015). A mixed Ta-Sn concentrate from the processing plant was provided by Talison Minerals Pty Ltd. which contains about 17% cassiterite and about 7% columbite-tantalite according to SEM-MLA plus 1.1% stibiotantalite.

The Mount Carbine deposit is situated west of Cairns in north Queensland and is related to Permian granite plutons intruding Devonian sedimentary rocks and basic volcanics of the Hodgkinson formation (Kwak et al., 1986; De Roo, 1988; Forsythe & Higgins, 1990). Tungsten mineralisation occurs as wolframite and scheelite (80:20 ratio) with minor cassiterite in subvertical sheeted veins and stockworks related to the Permian (278 ± 3 Ma, K-Ar biotite age; Forsythe & Higgins, 1990) Mossman granite (De Roo, 1988; Forsythe & Higgins, 1990).

10.1.4 Europe

The Variscan belt in Western Europe formed from Late Devonian to Permian by continental collision of Laurasia and Gondwana (the so-called Variscan orogeny). This orogenic belt (3000 km long and 700 to 800 km wide) extends more or less continuously from Morocco over western Iberia and southern England towards Northern Bohemia (Matte, 1991). Tin and/or tungsten deposits are associated with late- to post-orogenic granitic plutons and major batholiths.

Polymetallic ore deposits of southwest England are associated with S-type ilmenite series granitic plutons (ranging from 295 to 270 Ma) which are interpreted to be linked at depth forming the Cornubian batholith (Willis-Richards & Jackson, 1989; Jackson et al., 1989; LeBoutillier, 2002; Chappell & Hine, 2006). The former Geevor mine (closed in 1991) is located in the far western end of Cornwall. Cassiterite-bearing quartz veins (locally known as lodes) constitute the major ore bodies which are related to the Permian (274.8 ± 0.5 Ma; Chesley et al., 1993) coarse-grained Land's End granite pluton (Swinden, 1983). These lodes occur in the outer zone of the granite and crosscut the surrounding Devonian metasediments (locally known as killas) and intercalated volcanic country rocks (Swinden, 1983; LeBoutillier, 2002). Lode mineralisation is composed of cassiterite, pyrite, chalcopyrite, and arsenopyrite with fluorite and carbonates (Swinden, 1983; Jackson et al., 1989). Radiometric age dating studies

(including U-Pb, K-Ar, and Rb-Sr dating methods) indicate that mineralisation is directly related to the late-stage intrusions of the granites (Willis-Richards & Jackson, 1989; Chesley et al., 1993; LeBoutillier, 2002). Eight polished sections of ore from different levels of the Geevor mine were analysed.

The Hemerdon W-Sn endogreisen deposit is related to the intrusion of the Permian Hemerdon Ball granite (minimum age of about 290 Ma) which is most likely connected to the much larger Dartmoor granite to the north (Chesley et al., 1993). Wolframite with associated minor molybdenite, cassiterite, and arsenopyrite mineralisation occurs in sheeted quartz veins bordered by greisen alteration within the granite (endogreisen) but also less frequently in the surrounding Devonian killas (Pirajno, 2009).

The Krásno Sn-W greisen deposit is situated in the Slavkovský les in western Czech Republic and is related to a peraluminous topaz-albite granite of the Krudum massif which forms part of the of the younger intrusive complex of the Erzgebirge/Krušné Hory batholith (Breiter et al., 1991; René, 1995; René, 1998; Beran & Sejkora, 2006). The disseminated cassiterite with subordinate wolframite mineralisation (with grades of 0.2 to 0.3% Sn; René, 1998) is restricted to massive greisen in the cupola of a topaz-albite granite stock, the so-called Hub stock, but Sn-W mineralisation also occurs in quartz veins extending from the greisen into the surrounding metamorphic country rocks, mostly composed of biotite paragneisses (René, 1995; René, 1998; Beran & Sejkora, 2006).

The Bajoca pegmatite is one of several bodies in the Fregeneda-Almendra pegmatitic field located in the Central Iberian Zone of Portugal which intruded Precambrian to Upper Cambrian low-grade metasediments. The main pegmatite body extends for almost 700 m with a variable thickness up to 35 m (Vieira & Lima, 2007) and is mined for ceramic feldspar, but was also exploited for cassiterite and columbite-tantalite in former times. Just a few cassiterite grains from Bajoca were analysed.

10.1.5 North America

Close to the Bernic Lake in southeast Manitoba, the Tanco pegmatite intruded into amphibolite and metagabbro of the Archaean Bird River greenstone belt (Crouse & Černý, 1972; Černý, 1982). It is classified as highly fractionated LCT-type pegmatite with Ta-Li-Cs-Sn mineralisation (Stilling et al., 2006). Significant Ta mineralization is present in the form of various partly rare Ta-bearing minerals such as columbite-tantalite, microlite, uranmicrolite, wodginite-group minerals, tantite, simpsonite, stibiotantalite, cesstibtantite, calciotantite, and rankamaite-sosedkoite (Crouse & Černý, 1972; Thomas & Spooner, 1988). Tin occurs in the form of cassiterite plus wodginite and recovered as by-product. Several Li-bearing minerals are present such as lepidolite, petalite, spodumene, and amblygonite and the major Cs-bearing mineral is pollucite (Crouse & Černý, 1972). Crystallisation age of the Tanco pegmatite was dated by several authors at 2640 ± 7 (Baadsgaard & Černý, 1993) and 2641 ± 3 Ma (Camacho et al., 2012). These dates reasonably fit with own age estimates on cassiterite yielding 2654 Ma.

The analysed sample represents a very high-grade cassiterite (93%) concentrate from the processing plant with little arsenopyrite (1.5%), ilmenite (1.5%), apatite (1%), and columbite (0.5%).

The Black Hills pegmatite province is located in South Dakota, USA. Numerous (approximately 24000) pegmatite bodies are associated with the circa 1.7 Ga peraluminous S-type Harney Peak granite pluton (Norton & Redden, 1990), which is famous for the Mt. Rushmore National Monument. Complex zoned pegmatites constitute only a small population (about 2%) in this province, but these are enriched in rare elements like Li, Be, Nb, Ta, Sn, and Cs (Norton and Redden, 1990). Radiometric ages for the pegmatites are approximately 1702 to 1718 Ma (Tkachev, 2010). Tin pegmatites occur as tabular quartz-rich bodies and form an isolated cluster north of the Harney Peak granite close to Hill City.

Two concentrates from this cluster (probably from the Cowboy pegmatite) consist predominantly of cassiterite (more than 40%) with subordinate scheelite (about 3%), ilmenite (3%), Ti-bearing columbite (about 2%), and tapiolite (1.5%).

10.1.6 South America

The São João del Rei pegmatite province is situated in southern Minas Gerais and comprises economically important Sn-Ta-bearing pegmatites like the Volta Grande pegmatite (Lagache & Quéméneur, 1997; Pereira et al., 2004). The spodumene-type pegmatites are associated with the Palaeoproterozoic Ritápolis S-type monzogranite intrusion and intruded into Archaean greenstone belt (ultra-)mafic rocks and (2121 ± 7 Ma; Quemeneur & Noce, 2000; Pereira et al., 2004; Tkachev, 2011). The cassiterite concentrate from São João del Rei predominately contains cassiterite (ca. 60%) and microlite (ca. 20%). Own age estimate based on U-Pb isotopes in cassiterite yields about 2115 Ma.

The economically important Pitinga mine is located in northern Amazonas State of Brazil. Rare metal (Sn, Nb, Ta, Zr, Y, REE) mineralisation and associated cryolite are hosted by Palaeoproterozoic (ranging from 1824 to 1794 Ma; Bastos Neto et al., 2014) Madeira and Água Boa A-type granites (Horbe et al., 1991; Costi et al., 2000; Lenharo et al., 2002; Lenharo et al., 2003; Bastos Neto et al., 2009; Borges et al., 2009). Primary mineralization is restricted to the apogranite facies and occurs as (1) disseminated cassiterite, cryolite, pyrochlore, zircon, columbite-tantalite, xenotime, and thorite in the albite granite facies of the Madeira pluton; (2) hydrothermal cassiterite with associated zircon and columbite-tantalite is related to greisen and episyenites in the Água Boa pluton (Horbe et al. 1991, Costi et al. 2000, Lenharo et al., 2002; Bastos Neto et al., 2009; Borges et al., 2009). A fine-grained tin concentrate from the Pitinga mine contains predominately cassiterite (ca. 70%) with moderate quantities of columbite (ca. 6%) and zircon (ca. 18%).

A very pure tin concentrate from Colombia predominantly contains cassiterite (99%) with little columbite (0.5%). This concentrate is labelled “Vaupés” and possibly derives from placers in eastern Colombia at the border with Brazil. Obviously rounded cassiterite grains also indicate alluvial transport. Primary sources are presumably Ta-Nb-Sn mineralised pegmatites in the Colombian area of the Precambrian Guayana Shield (Cramer et al., 2010). Own age estimates on cassiterite point to an age of about 1411 Ma.

The Rondônia Tin Province is composed of Palaeo- to Mesoproterozoic metamorphic rocks which were intruded by several events of Rapakivi magmatism between 1600 Ma

and 970 Ma (Figure 10.10; Bettencourt et al., 1999; Bettencourt et al., 2005). The Oriente Novo and Santa Bárbara Sn-(W-Ta-Nb) deposits are closely associated with late-stage peraluminous, partly porphyritic alkali-feldspar granites (Figure 10.10; Bettencourt et al., 1999; Bettencourt et al., 2005). The primary mineralisation at Oriente Novo predominantly occurs as stockworks of quartz veins/veinlets with cassiterite and minor wolframite as well as subordinate endogreisen with disseminated cassiterite and columbite–tantalite (Bettencourt et al., 2005). Both mineralization styles are associated with late stage alkali-feldspar granite intrusions of the Santa Clara massif (1074±8 Ma; Bettencourt et al., 1999). At Santa Bárbara, the major mineralisation style is represented by cassiterite-bearing greisens bodies and minor vein-stockwork with cassiterite and wolframite within porphyritic alkali-feldspar granite (978 ± 13 Ma) of the Younger Granites of Rondônia suite (Bettencourt et al., 2005). In comparison, the Oriente Novo deposit is characterised by frequent stockworks and veins whereas greisen mineralisation is common in the Santa Bárbara deposit (Bettencourt et al., 2005). Similar to Santa Bárbara, the São Domingo greisen deposit is also related to a granite intrusion of Younger Granites of Rondônia suite and forms a granite stock in the southern part of the Massangana massif complex (Figure 10.10; 991 ± 14 Ma; Bettencourt et al., 1999; Souza et al., 2003).

Several ore concentrate originate from different tin deposits in the Rondônia Tin Province, namely two from Oriente Novo, one concentrate Santa Bárbara, and one from São Domingo.

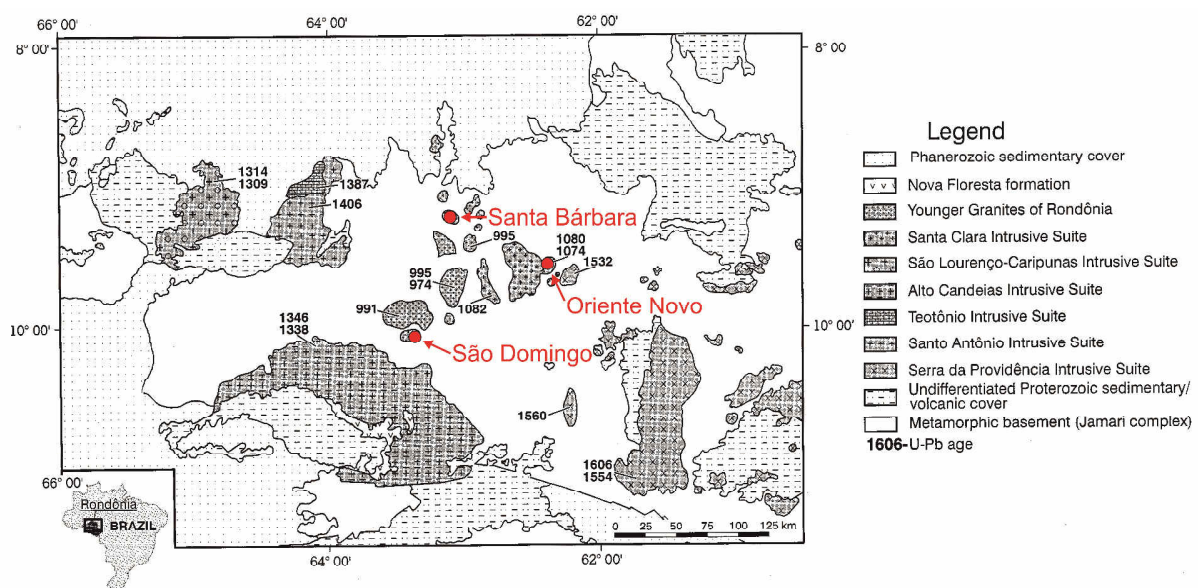


Figure 10.10: Geological map of the Rondônia Tin Province showing the location of ore concentrate samples (modified after Bettencourt, 1999).

The Araçuaí district is located in northern Minas Gerais and belongs to the 800 km long and 150 km wide Eastern Brazilian Pegmatite Province (Morteani et al., 2000; Pedrosa-Soares et al. 2009). Most pegmatites of the Araçuaí district are complex zoned bodies enriched in Li (spodumene, petalite, lepidolite, amblygonite-montebrazite), B (tourmaline), Be (beryl), Ta (columbite-tantalite), Sn (cassiterite), and Cs (pollucite); some also contain tourmalines, beryl, and quartz varieties in gem quality (Pedrosa-Soares et al. 2009). The ore concentrate from Araçuaí is predominantly composed of columbite (up to 25%), wodginite (up to 15%), and cassiterite (about 12%). The formation of the pegmatites is related to a second generation of S-type granite intrusions (535-500 Ma) of the G4 Supersuite (Morteani et al., 2000; Tkachev, 2010) as indicated by U-Pb age estimate for cassiterite yielding about 485 Ma.

The Bolivian Tin Belt forms part of the Eastern Cordillera of the Andes and stretches from southern Peru through Bolivia to northern Argentina (Figure 10.11; Ahlfeld & Schneider-Scherbina, 1964; Kelly & Turneure, 1970; Turneure, 1971; Sillitoe et al., 1975; Grant et al., 1980; Urquidi-Barrau, 1989; Arce-Burgoa & Goldfarb, 2009).

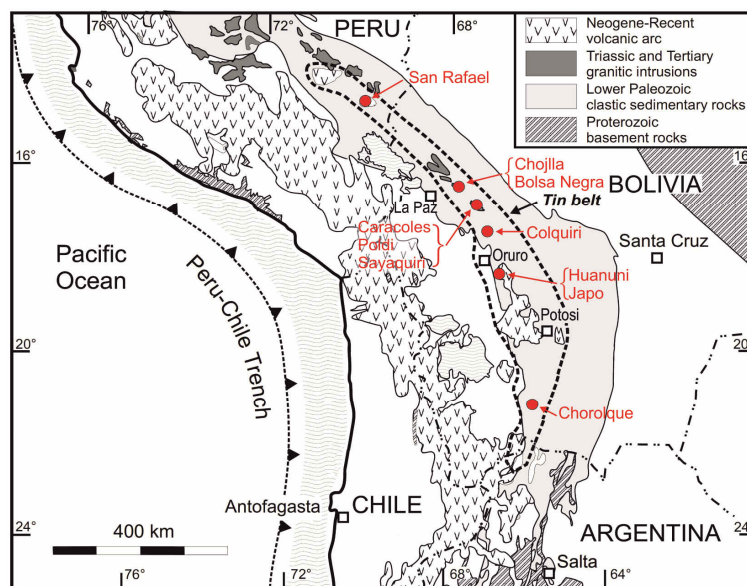


Figure 10.11: Geological map of the Bolivian Tin Belt showing the location of ore concentrate samples (modified after Dietrich et al, 2000).

In the northern part of the Bolivian Tin Belt, Ordovician-Silurian marine metasedimentary rocks are intruded by granodioritic to granitic S-type plutons of Triassic-Jurassic age (225–150 Ma, except for San Rafael at the northernmost portion with 25 Ma) with associated batholithic Sn-W vein-type mineralisation (Ahlfeld & Schneider-Scherbina, 1964; Ishihara et al. 2011). Samples from Caracoles, Poldi,

Sayaquiri, Chojlla, and Bolsa Negra represent this Mesozoic plutonic-related mineralisation. San Rafael deposit is also clearly plutonic-related, but significantly younger in age. The central and southern sectors of the Bolivian Tin Belt are less deeply eroded than the northern sector. In the central part, Sn-W deposits developed within and around Tertiary (46–12 Ma) granitic intrusions (represented by a sample from Colquiri mine), whereas Sn-polymetallic porphyry deposits are closely related to subvolcanic rhyodacitic porphyry stocks of Miocene age (20–12 Ma) in the southern part (Ahlfeld & Schneider-Scherbina, 1964; Grant et al., 1979; McBride et al., 1983; Sugaki et al., 2003). The subvolcanic mineralisation is represented by samples from Huanuni, Japo, and Chorolque.

The San Rafael tin mine serves as an example for the deposits of the Bolivian Tin Belt. San Rafael is located in southern Peru and forms the northernmost edge of the Bolivian Tin Belt (Figure 10.12). It is a high-grade lode deposit with subparallel hydrothermal quartz veins genetically related to a Late Oligocene (25 Ma) peraluminous monzogranite stock which intruded into Lower Palaeozoic marine clastic metasedimentary rocks (Kontak & Clark, 2002; Mlynarczyk et al., 2003; Wagner et al., 2009). The mineralised veins occur within the granite but they also cut the intrusive contact and pass into the surrounding metasediments (Mlynarczyk et al., 2003). The fine-grained high-grade tin concentrates from the beneficiation plant at San Rafael mine contain almost entirely cassiterite. U-Pb model age estimates on cassiterite range between 33 and 23 Ma (mean 25 Ma, n = 8).

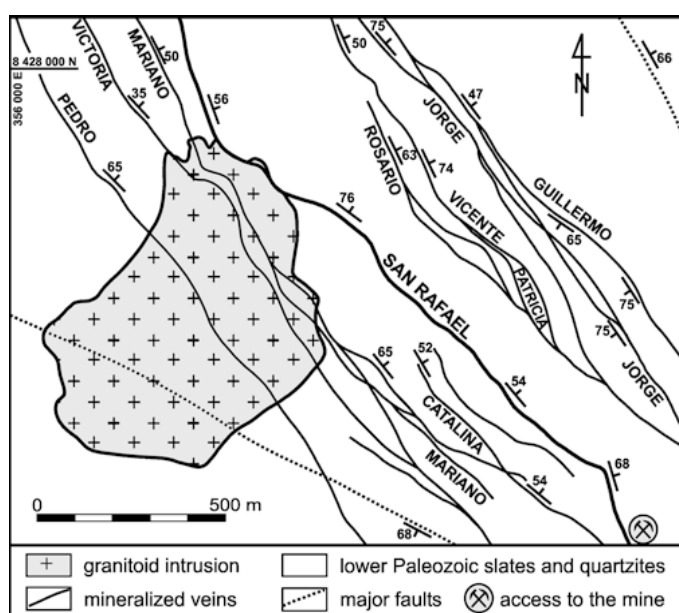


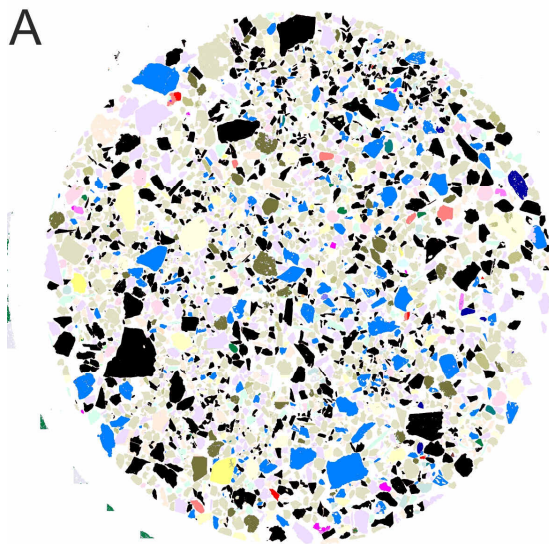
Figure 10.12: Geological map of the San Rafael deposit showing the relation of mineralised quartz veins to the granitic intrusion (Mlynarczyk et al., 2003).

10.2 Mineralogical composition

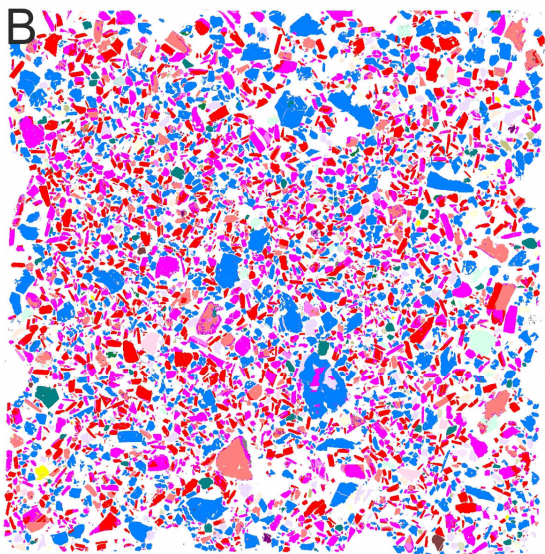
The mineralogical composition of ore concentrates obtained by MLA is given as relative abundances of classified mineral phases (in area%) on the sample surface of polished sections (Tables 10.2 & 10.3). The major phases in the analysed ore concentrates are heavy minerals: besides cassiterite and wolframite, Ta-bearing minerals (like columbite-tantalite, tapiolite, microlite, and wodginite), scheelite, zircon, ilmenite, and rutile occur. Apart from these ore minerals, rock-forming minerals like quartz, feldspars, muscovite, biotite, garnet (mostly almandine), tourmaline, topaz, beryl, and apatite are also common; these derive from the host and surrounding country rocks (Figures 7.3, 10.13 & 11.1).

Tin concentrates from pegmatite deposits are generally characterised by the presence of Ta-bearing minerals, which in turn are absent in concentrates from hydrothermal deposits. Scheelite is common in several wolframite concentrates, but scheelite is also typical for cassiterite concentrates from the Black Hills, South Dakota (Table 10.2). The uncommon tungsten mineral anthoinite $\text{AlWO}_3(\text{OH})$ is characteristically present in tungsten concentrates from reinite deposits in Rwanda (Table 10.2). Non-differentiated Fe oxides (like hematite, goethite or lepidocrocite) are common weathering products and ubiquitously found in tin and tungsten concentrates.

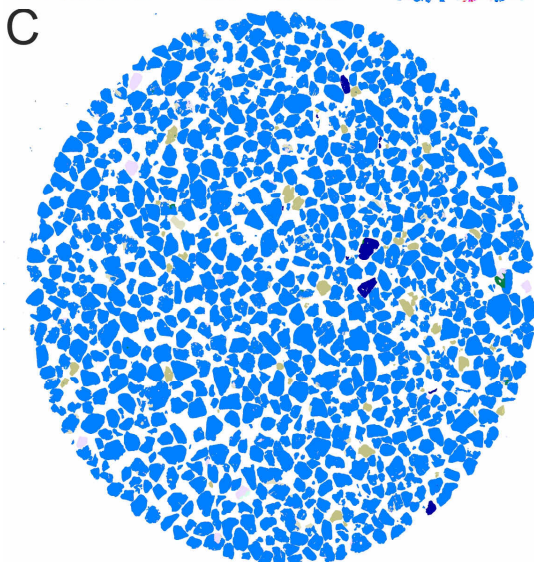
The classified MLA image is also used to identify the position of the essential phases (in this study cassiterite and wolframite) on the sample surface and appropriate target grains of these ore minerals are selected for subsequent trace element analysis using LA-ICP-MS. The number of target grains is strongly dependent on the beneficiation skills of the miner (Figures 10.13 & 11.1).



Name	Pixels	Particles	Area %
Ferberite	7539367	1611	27.13 %
Schoerl	6715815	1534	24.17 %
Quarz	3631045	957	13.07 %
Cassiterite	3040304	390	10.94 %
Goethite	1468493	883	5.28 %
Staurolite	997924	102	3.59 %
Titanomagnetite	947328	116	3.41 %
Pyrite	592687	88	2.13 %
Almandine	495096	244	1.78 %
Muscovite	384211	467	1.38 %
Ilmenite	360781	142	1.30 %
Hornblende	306155	84	1.10 %
Rutile	204592	52	0.74 %
Alumosilicate	152898	84	0.55 %
Mn-Tantalite	138349	20	0.50 %
Monazite	126975	20	0.46 %
Albite	97708	123	0.35 %



Name	Pixels	Particles	Area %
Cassiterite	15464113	2493	30.79 %
Mn-Columbite	11671900	2793	23.24 %
Fe-Columbite	11429447	4008	22.76 %
Mn-Tantalite	4556167	1696	9.07 %
Quarz	1933411	918	3.85 %
Zircon	977051	304	1.95 %
Muscovite	913513	935	1.82 %
Albite	670061	763	1.33 %
Fe-Tantalite	554817	644	1.10 %
Goethite	393709	244	0.78 %
Almandine	337971	140	0.67 %
Schoerl	194433	159	0.39 %



Name	Pixels	Particles	Area %
Cassiterite	27552215	2015	94.77 %
Ilmenite	548314	101	1.89 %
Quarz	311890	291	1.07 %
Schoerl	287667	267	0.99 %
Monazite	169703	22	0.58 %
Chlorite	56717	96	0.20 %
Muscovite	49291	135	0.17 %

Figure 10.13: Examples for classified MLA images: A) Mixed wolframite-cassiterite concentrate from Bishasha, DR Congo (AS9829); B) Mixed coltan-cassiterite concentrate from Kirwa, Rwanda (AS7757); C) Cassiterite concentrate from Muana, DR Congo (AS8837).

Table 10.2: MLA data for worldwide cassiterite concentrates (for country see Table 10.1.) with rel. abundances of mineral phases (in area%)

locality, country	section	cassiterite	wolframite	scheelite	coltan	quartz	Fe oxide	zircon	ilmenite	rutile	microlite	wodginite	tapiolite	feldspars	hornblende	garnet	staurolite	anthoinite	muscovite	biotite	tourmaline	topaz	beryl	apatite	monazite	fluorite	pyrite	arsenopyrite	galena	bismuth	
Araçuaí, BR	Araçuaí, 10.1.6	12.8			25.9	5.1			1.7	7.6	1.3	11.2		5.1		1.9			20.8												
Lutenga, CD	Kibara belt, 10.1.1	45.4	0.6		36.5	0.9	1.8		0.9							1.3			2.8												
Bisengo, CD	Kibara belt, 10.1.1	38.9			41.6				1.4			0.5	8.0	1.3								2.1									
Shori, RW	Kibara belt, 10.1.1	33.8			49.0	4.3			1.2	6.5									1.6												
Kirwa-Gasovu, RW	Kibara belt, 10.1.1	31.3			54.2	4.2			1.8					2.9																	
Nemba, RW	Kibara belt, 10.1.1	40.6			45.3	2.0	3.4	1.0											5.2												
Rutsiro, RW	Kibara belt, 10.1.1	45.8			32.0			1.0	1.1					2.8									7.1								
Ruhanga, RW	Kibara belt, 10.1.1	80.8			3.3	2.7	4.1												1.0		2.2										
Nemba, RW	Kibara belt, 10.1.1	23.4			54.1	2.6	4.7		0.9				1.0						9.0												
Bijoyojo, RW	Kibara belt, 10.1.1	16.5			29.5	17.6	28.0	1.0	1.7										1.5												
Nyamyumba, RW	Kibara belt, 10.1.1	97.2					1.0																								
Manono, CD	Kibara belt, 10.1.1	90.6				2.2				1.2				1.9																	
São João del Rei, BR	São João del Rei, 10.1.6	60.0			1.9	2.2		1.4			21.5	1.1													2.1		1.9				
Greenbushes, AU	Greenbushes, 10.1.3	16.8			6.7	4.3	15.5		5.0		0.9	1.2		3.2	1.3	1.3	24.8		2.8	3.1	3.8	1.6			1.3	3.3					
Lowá-Kima, CD	Kibara belt, 10.1.1	98.4																													
Mususa, CD	Kibara belt, 10.1.1	75.6	23.6																												
Kailo, CD	Kibara belt, 10.1.1	97.0					2.7																								
Kabingo, CD	Kibara belt, 10.1.1	99.8																													
Punia, CD	Kibara belt, 10.1.1	99.2																													
Kasese, CD	Kibara belt, 10.1.1	99.7																													
Nyangulube, CD	Kibara belt, 10.1.1	91.0				1.4	4.3													1.5	3.0										
Muana, CD	Kibara belt, 10.1.1	94.8				1.1			1.9												1.0										
Nzombe, CD	Kibara belt, 10.1.1	87.5																	1.0		6.4										
Ngussa, CD	Kibara belt, 10.1.1	63.9					33.6													1.2											
Bilembo, CD	Kibara belt, 10.1.1	99.7																													
Miki, CD	Kibara belt, 10.1.1	100.0																													
Misobo, CD	Kibara belt, 10.1.1	96.3				3.1																									
Atondo, CD	Kibara belt, 10.1.1	97.3																	1.2			1.2									
Salukwango, CD	Kibara belt, 10.1.1	66.7				3.0	7.0							1.1					15.2		3.4										
Moga, CD	Kibara belt, 10.1.1	99.1																													
Moga, CD	Kibara belt, 10.1.1	66.5				19.6			11.7														1.2								
Mitwaba, CD	Kibara belt, 10.1.1	99.8																													
Muika, CD	Kibara belt, 10.1.1	98.2				1.4																									
Bugalula, RW	Kibara belt, 10.1.1	96.0				1.6													1.4												
Ruhanga, RW	Kibara belt, 10.1.1	11.5			29.6	4.2	17.0	2.4	1.5	2.8		1.0		3.6					1.4				1.4								
Black Hills, US	Black Hills, 10.1.5	71.4		2.5	4.2		8.8		0.8						3.9	2.6															
Tanco, CA	Black Hills, 10.1.5	93.0				0.5			1.4															1.3				1.6			
Black Hills, US	Black Hills, 10.1.5	44.0		4.5	3.9		19.9		4.7				1.4		7.9	2.5				1.4											
Huanuni, BO	Bolivian Tin Belt, 10.1.6	53.6				26.0	4.6														2.9						5.1				
San Rafael, PE	Bolivian Tin Belt, 10.1.6	65.4				16.0									8.7												4.4				
Caracoles, BO	Bolivian Tin Belt, 10.1.6	75.0				7.5																11.0									
Pitinga, BR	Pitinga, 10.1.6	69.2			6.0		1.7	18.3																							
Remera 1, RW	Kibara belt, 10.1.1	11.4			7.5	31.1	2.8		3.4						1.4	24.5			3.1		7.9				1.1						
Gahapfu 2, RW	Kibara belt, 10.1.1	24.8			10.9	44.1										2.2			5.6		6.9										
Gahapfu 1, RW	Kibara belt, 10.1.1	11.2			23.1	44.3								1.3		2.6			9.2		2.8										
Remera 3, RW	Kibara belt, 10.1.1	37.7			1.6	33.1	6.7							2.9		1.1			7.8		1.0	4.7									
Kiyanja 1, RW	Kibara belt, 10.1.1	19.0			29.3	36.1	2.4							1.6					5.4		2.9										
Manihira 1, RW	Kibara belt, 10.1.1	30.9			9.9	1.7										8.6			2.0			43.0									
Kabere, RW	Kibara belt, 10.1.1	41.8				32.7	5.8															5.8									
Nganzo, RW	Kibara belt, 10.1.1	14.5					1.2	38.2																	45.5						
Rwezamenyo, RW	Kibara belt, 10.1.1	99.5																													
Kamativi, ZW	Kamativi, 10.1.1	81.8				5.2																									
Gatumba South, RW	Kibara belt, 10.1.1	58.8			3.4	3.2								21.2									3.9								
Bugalula, RW	Kibara belt, 10.1.1	98.8																													
Nemba, RW	Kibara belt, 10.1.1	55.5					5.0		1.4							4.3			4.1		24.8										
Vampés, CO	Colombia, 10.1.6	99.0				0.5																									
Abu Dabbab, EG	Eastern Desert, 10.1.1	78.3			5.5	1.0		1.2				1.6	0.8	1.3							2.2										
Nuweibi, EG	Eastern Desert, 10.1.1	18.5				3.7	1.3		36.4						23.0				10.5		1.9										
Jos Plateau, NG	Jos Plateau, 10.1.1	64.2			10.5	2.6		5.6	9.2													1.2			2.0						

10.3 Trace element composition

In a first approach, EPMA was used to measure trace elements in cassiterite and wolframite, but low concentration levels of most elements limited the use of the EPMA due to its comparatively high detection limits. Therefore trace element analysis is performed by LA-ICP-MS which provides considerably lower detection limits.

10.3.1 Electron probe microanalysis

Electron probe microanalysis was the first attempt to detect trace elements in cassiterite and wolframite, but it turned out that this method is not capable to detect relevant trace elements at existing concentration levels and just a few elements are above the detection limit of this method. Therefore only a limited number of samples (8 localities for cassiterite and 3 localities for wolframite; see Tables 10.4 & 10.5) were analysed by electron microprobe until this effort was abandoned (Tables 10.4 & 10.5). The respective detection limits for EPMA of cassiterite and wolframite (plus scheelite) are given in the methodology chapter (Tables 7.2 & 7.3).

Electron microprobe analysis of cassiterite (Table 10.4) shows that just a few elements besides Sn are present in sufficient amounts. These are Fe (up to 1.23 wt.% FeO), Ti (up to 1.14 wt.% TiO₂), and W (up to 0.44 wt.% WO₃) plus occasionally Ta (up to 3.2 wt.% Ta₂O₅), Nb (up to 2.37 wt.% Nb₂O₅), Zr (up to 0.11 wt.% ZrO₂), Mn (up to 0.09 wt.% MnO), and Al (up to 0.22 wt.% Al₂O₃) in minor concentrations.

Apart from the major elements Fe, Mn, and W, electron microprobe analyses of wolframite (Table 10.5) detected Nb (up to 0.76 wt.% Nb₂O₅), Mo (up to 0.22 wt.% MoO₃), Ta (up to 0.07 wt.% Ta₂O₅), Sn (up to 0.07 wt.% SnO₂), Sc (up to 0.05 wt.% Sc₂O₃), and Ti (up to 0.04 wt.% TiO₂) as minor elements plus sporadic Ca (up to 0.11 wt.% CaO) due to scheelite replacement of wolframite. Additionally, scheelite was also measured which is characterised (apart from Ca and W as major elements) by minor amounts of Fe (up to 0.52 wt.% FeO), Mo (up to 0.22 wt.% MoO₃), Nb (up to 0.09 wt.% Nb₂O₅), Mn (up to 0.04 wt.% MnO), and Ta (up to 0.03 wt.% Ta₂O₅).

Although just a few elements are above the detection limit, this restricted information already shows certain variability in the elemental composition of cassiterite and wolframite from individual deposits.

Table 10.4: Electron probe microanalysis of cassiterite in wt.% oxide and atoms per formula unit normalised to 2 oxygens (bdl = below detection limit, Table 7.2)

sample	AS8823a		AS8823b		AS8823c		AS8825		AS8826		AS8827		AS8828		AS8829		AS8830		AS8831	
locality	Bisie, DR Congo		Bisie, DR Congo		Bisie, DR Congo		Lowa-Kima, DR Congo		Mususa, DR Congo		Mokama, DR Congo		Kailo, DR Congo		Kabingo, DR Congo		Kisheke, DR Congo		Sasa, DR Congo	
n	21		24		20		99		60		39		100		100		81		9	
	mean	range	mean	range	mean	range	mean	range	mean	range	mean	range	mean	range	mean	range	mean	range	mean	range
Al ₂ O ₃	0.018	bdl-0.156	0.011	bdl-0.224	0.002	bdl-0.035	bdl	bdl	bdl	bdl	0.002	bdl-0.038	0.012	bdl-0.071	0.014	bdl-0.060	bdl	bdl	bdl	bdl
SiO ₂	bdl	bdl	0.007	bdl-0.167	bdl	bdl	bdl	bdl	bdl	bdl	bdl	bdl	bdl	bdl	bdl	bdl	bdl	bdl	bdl	bdl
Sc ₂ O ₃	0.004	bdl-0.022	0.007	bdl-0.043	0.004	bdl-0.025	0.001	bdl-0.017	bdl	bdl	bdl	bdl	0.001	bdl-0.015	bdl	bdl	bdl	bdl	bdl	bdl
TiO ₂	0.094	bdl-0.260	bdl	bdl	0.006	bdl-0.056	0.648	bdl-1.143	0.080	bdl-0.411	0.119	bdl-0.619	0.304	bdl-1.032	0.127	0.030-0.418	0.441	bdl-1.024	0.823	0.560-1.023
MnO	bdl	bdl	0.001	bdl-0.022	bdl	bdl	0.000	bdl-0.021	bdl	bdl	bdl	bdl	0.001	bdl-0.031	0.020	bdl-0.085	bdl	bdl	bdl	bdl
FeO	0.255	bdl-1.014	0.240	bdl-1.234	0.110	bdl-0.632	0.010	bdl-0.060	0.122	0.023-0.459	0.177	bdl-0.709	0.220	bdl-1.035	0.297	0.018-1.012	0.011	bdl-0.025	0.008	bdl-0.047
CuO	0.005	bdl-0.097	bdl	bdl	bdl	bdl	bdl	bdl	bdl	bdl	bdl	bdl	0.000	bdl-0.028	bdl	bdl	bdl	bdl	bdl	bdl
As ₂ O ₃	bdl	bdl	bdl	bdl	bdl	bdl	bdl	bdl	bdl	bdl	bdl	bdl	bdl	bdl	bdl	bdl	bdl	bdl	bdl	bdl
ZrO ₂	bdl	bdl	bdl	bdl	bdl	bdl	0.002	bdl-0.065	0.001	bdl-0.041	0.010	bdl-0.066	0.021	bdl-0.073	0.052	bdl-0.113	bdl	bdl	bdl	bdl
Nb ₂ O ₅	0.002	bdl-0.047	bdl	bdl	bdl	bdl	0.015	bdl-0.175	0.161	bdl-0.892	0.251	bdl-1.221	0.390	bdl-1.663	0.518	bdl-2.368	bdl	bdl	0.011	bdl-0.038
SnO ₂	99.696	96.44-100.78	100.093	97.82-101.21	100.451	98.96-101.31	98.671	96.40-99.98	99.278	97.91-100.62	99.677	97.68-101.92	99.397	94.53-101.03	98.365	94.77-100.45	99.688	98.82-100.84	99.839	99.04-101.37
HfO ₂	bdl	bdl	bdl	bdl	bdl	bdl	bdl	bdl	bdl	bdl	bdl	bdl	0.001	bdl-0.017	0.014	bdl-0.035	bdl	bdl	bdl	bdl
Ta ₂ O ₅	bdl	bdl	bdl	bdl	bdl	bdl	0.002	bdl-0.037	0.051	bdl-0.481	0.098	bdl-0.970	0.185	bdl-3.203	0.972	0.123-2.753	bdl	bdl	bdl	bdl
WO ₃	0.065	bdl-0.307	0.073	bdl-0.367	0.031	bdl-0.271	0.002	bdl-0.046	0.049	bdl-0.441	0.033	bdl-0.333	0.017	bdl-0.358	bdl	bdl	0.001	bdl-0.053	0.047	bdl-0.108
UO ₂	bdl	bdl	bdl	bdl	bdl	bdl	bdl	bdl	bdl	bdl	bdl	bdl	bdl	bdl	bdl	bdl	bdl	bdl	bdl	bdl
Total	100.14		100.43		100.60		99.35		99.74		100.37		100.55		100.38		100.14		100.73	
normalised on the basis of 2 oxygens																				
Al	0.001		0.000		0.000		0.000		0.000		0.000		0.000		0.000		0.000		0.000	
Si	0.000		0.000		0.000		0.000		0.000		0.000		0.000		0.000		0.000		0.000	
Sc	0.000		0.000		0.000		0.000		0.000		0.000		0.000		0.000		0.000		0.000	
Ti	0.002		0.000		0.000		0.012		0.002		0.002		0.006		0.002		0.008		0.015	
Mn	0.000		0.000		0.000		0.000		0.000		0.000		0.000		0.000		0.000		0.000	
Fe	0.005		0.005		0.002		0.000		0.003		0.004		0.005		0.006		0.000		0.000	
Cu	0.000		0.000		0.000		0.000		0.000		0.000		0.000		0.000		0.000		0.000	
As	0.000		0.000		0.000		0.000		0.000		0.000		0.000		0.000		0.000		0.000	
Zr	0.000		0.000		0.000		0.000		0.000		0.000		0.000		0.001		0.000		0.000	
Nb	0.000		0.000		0.000		0.000		0.002		0.003		0.004		0.006		0.000		0.000	
Sn	0.994		0.996		0.998		0.987		0.994		0.991		0.984		0.978		0.992		0.984	
Hf	0.000		0.000		0.000		0.000		0.000		0.000		0.000		0.000		0.000		0.000	
Ta	0.000		0.000		0.000		0.000		0.000		0.001		0.001		0.007		0.000		0.000	
W	0.000		0.000		0.000		0.000		0.000		0.000		0.000		0.000		0.000		0.000	
U	0.000		0.000		0.000		0.000		0.000		0.000		0.000		0.000		0.000		0.000	
Total	1.003		1.002		1.001		1.000		1.001		1.001		1.001		1.000		1.000		1.000	

Table 10.5: Electron probe microanalysis of wolframite and scheelite in wt% oxide and atoms per formula unit normalised to 4 oxygens (bdl = below detection limit, Table 7.3)

sample	AS8737		AS9112		AS9114		AS8737		AS9112
locality	Caracoles, Bolivia		Kabera, Rwanda		Nyakabingo, Rwanda		Caracoles, Bolivia		Kabera, Rwanda
mineral	wolframite		wolframite		wolframite		scheelite		scheelite
n	85		93		34		35		1
	mean	range	mean	range	mean	range	mean	range	
SiO ₂	0.001	bdl-0.046	0.001	bdl-0.062	bdl	bdl	bdl	bdl	bdl
CaO	0.002	bdl-0.064	0.014	bdl-0.107	0.030	bdl-0.078	19.327	18.85-19.61	19.496
Sc ₂ O ₃	0.001	bdl-0.045	bdl	bdl	bdl	bdl	bdl	bdl	bdl
TiO ₂	0.000	bdl-0.036	bdl	bdl	bdl	bdl	bdl	bdl	bdl
MnO	2.767	0.34-20.11	1.474	bdl-2.66	0.965	0.60-2.48	0.002	bdl-0.029	0.042
FeO	21.255	3.08-24.36	22.845	21.52-25.22	23.964	22.52-24.44	0.091	bdl-0.482	0.520
ZrO ₂	bdl	bdl	bdl	bdl	bdl	bdl	bdl	bdl	bdl
Nb ₂ O ₅	0.013	bdl-0.364	0.093	bdl-0.758	bdl	bdl	0.005	bdl-0.070	0.094
MoO ₃	0.017	bdl-0.217	bdl	bdl	bdl	bdl	0.031	bdl-0.215	bdl
SnO ₂	0.003	bdl-0.067	bdl	bdl	bdl	bdl	bdl	bdl	bdl
HfO ₂	bdl	bdl	bdl	bdl	bdl	bdl	bdl	bdl	bdl
Ta ₂ O ₅	0.004	bdl-0.032	0.009	bdl-0.074	0.005	bdl-0.035	0.002	bdl-0.026	bdl
WO ₃	75.798	73.98-76.74	75.518	72.12-76.62	75.446	74.40-76.11	79.739	79.06-80.61	80.037
UO ₂	bdl	bdl	bdl	bdl	bdl	bdl	bdl	bdl	bdl
Total	99.86		99.95		100.41		99.20		100.19
normalised on the basis of 4 oxygens									
Si	0.000		0.000		0.000		0.000		0.000
Ca	0.000		0.001		0.002		1.000		0.998
Sc	0.000		0.000		0.000		0.000		0.000
Ti	0.000		0.000		0.000		0.000		0.000
Mn	0.118		0.063		0.041		0.000		0.002
Fe	0.899		0.965		1.008		0.004		0.021
Zr	0.000		0.000		0.000		0.000		0.000
Nb	0.000		0.002		0.000		0.000		0.002
Mo	0.000		0.000		0.000		0.001		0.000
Sn	0.000		0.000		0.000		0.000		0.000
Hf	0.000		0.000		0.000		0.000		0.000
Ta	0.000		0.000		0.000		0.000		0.000
W	0.993		0.989		0.983		0.998		0.991
U	0.000		0.000		0.000		0.000		0.000
Total	2.012		2.020		2.034		2.002		2.014

The electron microprobe is the method of choice for high resolution X-ray mapping in order to visualize elemental distribution in minerals. The element maps nicely show that cassiterite crystals are often inhomogeneous (Figures 10.14 & 10.15) and distinct growth zoning in cassiterite is also displayed (Figure 10.15). Lower Sn concentrations in cassiterite are accompanied by higher Fe, Ta, Nb, and Zr concentrations (Figures 10.14 & 10.15), which directly implies substitution of these elements for Sn. Despite the inhomogeneous element distribution, it is a striking feature that refractory elements like Ta and Nb are concentrated in the cores of cassiterite crystals (Figure 10.14). Even mineral inclusions may be identified by X-ray element mapping, e.g. columbite-tantalite inclusions, which are characterized by extremely high Ta, Nb, and Fe (Mn as well, but not chosen for X-ray mapping) values, are common in cassiterite from pegmatite deposits (Figure 10.14). The microprobe is also equipped with a cathodoluminescence (CL) detector which displays the luminescence in grey values. CL imagery shows that luminescence decreases with increasing trace element content in total. Especially, Nb, Ta and Fe significantly weaken the intensity of the luminescence.

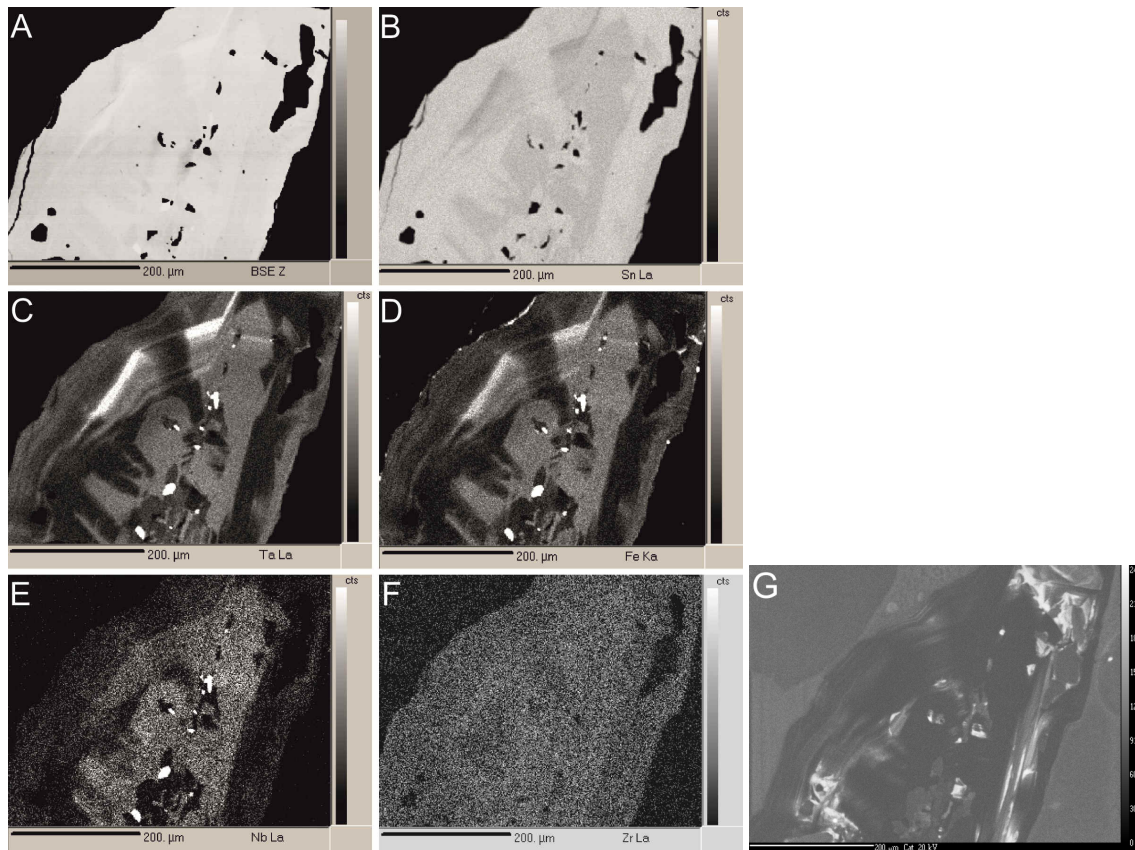


Figure 10.14: BSE image (A), X-ray element distribution maps of Sn (B), Ta (C), Fe (D), Nb (E), and Zr (F) of cassiterite showing inhomogeneous elemental distribution with correlation of Ta, Nb, and Fe with decreasing Sn. Cathodoluminescence image (G) shows that strong luminescence coincides with low trace element contents of cassiterite. Note columbite-tantalite inclusions in the core.

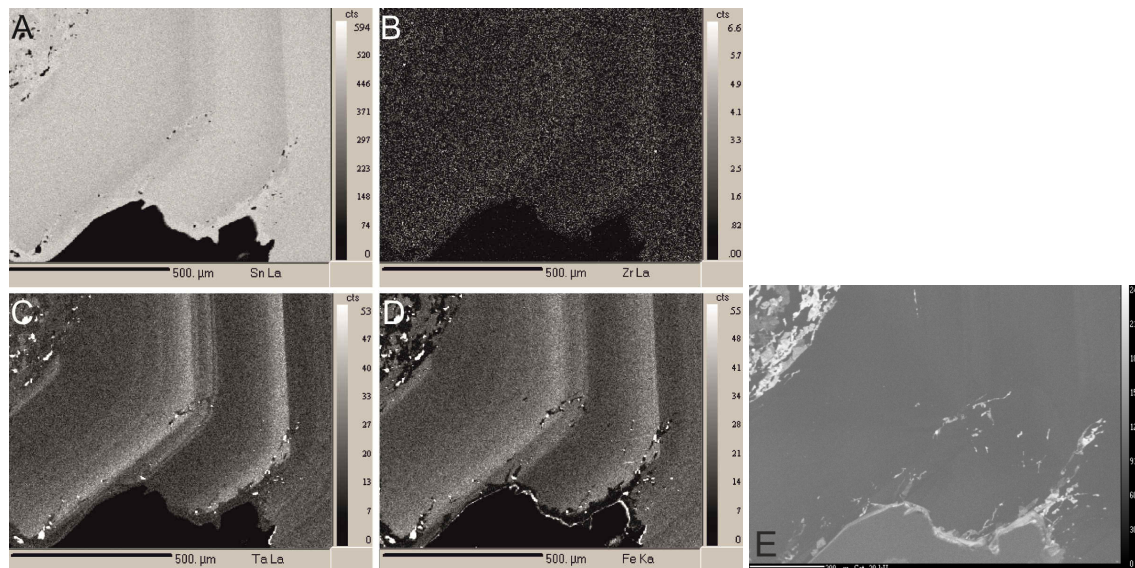


Figure 10.15: X-ray element distribution maps of Sn (A), Zr (B), Ta (C), and Fe (D) in cassiterite showing distinct growth zoning with correlation of Ta (plus Nb) and Fe with decreasing Sn. Cathodoluminescence image (E) shows that strong luminescence coincides with low trace element contents, especially along the rim of cassiterite at the bottom of the image.

Single wolframite crystals may also show inhomogeneous element distribution. As an example, this is confirmed by the investigations of Ferenc & Uher (2007), who carried out X-ray element mapping on wolframite from the Zlatná Baňa occurrence near Ochtiná, Slovakia (Figure 10.16), or Bailly et al. (2002) working on wolframite from Baia Sprie, Romania.

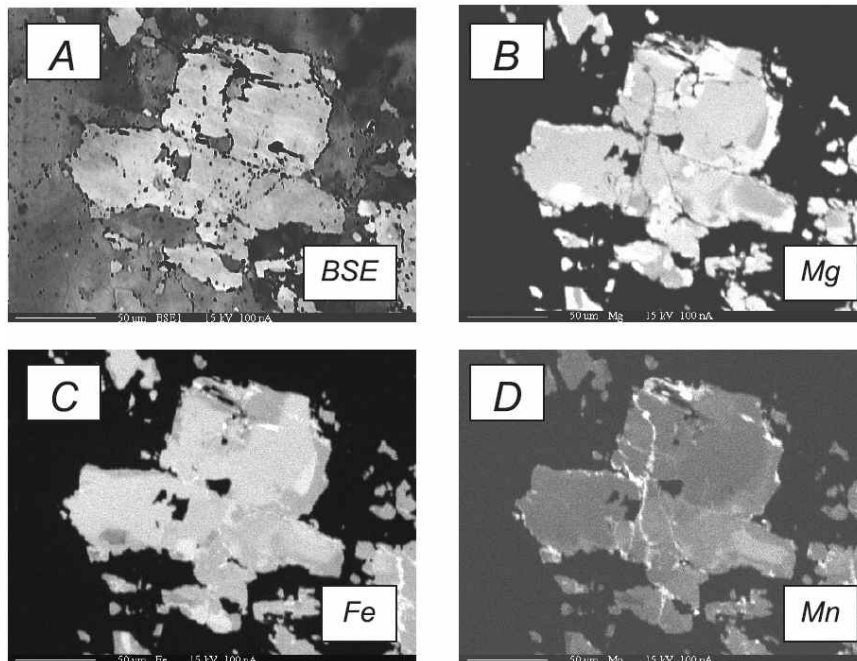


Figure 10.16: BSE image and Mg, Fe, and Mn X-ray element distribution maps of wolframite from Zlatná Baňa, Ochtiná, Slovakia (Ferenc & Uher, 2007).

10.3.2 LA-ICP-MS analysis

The focus for trace element analysis was set on LA-ICP-MS due to its considerably lower detection limits compared to EPMA. The concentration levels of substituting elements are highly variable in cassiterite and wolframite ranging from below the detection limit up to several wt.%, but most trace elements are in the range of tens to several hundreds or thousands of ppm. Generally, the concentrations of major and trace elements in ore minerals (e.g., cassiterite, wolframite, columbite-tantalite, etc.) vary systematically within a single ore deposit (Melcher et al., 2008).

In order to cover the broad spread of data for single elements within an ore concentrate (partly making up several orders of magnitude), a statistically representative number of individual target grains needs to be analysed by LA-ICP-MS. As a practical compromise between sufficient number of analyses and time-consuming analytical capacity, a reasonable effort of about 40 to 50 measurements of single grains per concentrate is chosen.

Due to the high variability of trace elements at various concentration levels over several orders of magnitude (see analytical data for each sample in the appendix), the crystal chemistry of cassiterite and wolframite is illustrated by normalisation to a global average composition for cassiterite and wolframite, respectively. The global average composition is represented by the median calculated from the median values for each individual deposit (Table 10.6; see Appendix A); similar to the approach for coltan given by Melcher et al. (2015). But other normalisation approaches may be also feasible, for example Dare et al. (2014) used bulk continental crust for magnetite normalisation.

Table 10.6: Normalisation values for cassiterite and wolframite (values represent ppm and are only given for elements with positive median)

element	cassiterite	wolframite
Mg		178.6
Al	87.0	
Si	427.5	331.2
Sc	6.67	30.6
Ti	1176	56.3
V	3.25	1.64
Mn	12.8	46697
Fe	1601	143950
Co		2.09
Zn	1.10	81.8
Ga	2.39	
Ge	0.14	
As	0.30	
Sr	0.01	
Y	0.02	39.2
Zr	470.4	8.76
Nb	1467	1186
Mo	0.01	1.57
In	0.10	1.06
Sn		11.4
Sb	0.30	
Hf	63.4	0.28
Ta	997.3	51.7
W	15.4	
Pb	0.36	0.11
Th	0.01	0.04
U	1.55	0.90

10.3.2.1 LA-ICP-MS analysis of cassiterite

About 4900 LA-ICP-MS measurements of cassiterite were carried out on 113 ore concentrates from 80 localities (including single deposits and concessions) and on 18 single grain or ore samples from 5 deposits. Analytical data and specific information for each deposit are given in the appendix of this thesis (Appendix B).

Tin may be substituted by different elements at variable portions up to 14 wt.% in total (Černý et al., 1985; Murciego et al., 1997). Major substituting elements in cassiterite are Ti, Fe, Nb, Ta, and W in the wt.% range (as already identified by EPMA). Other common minor and trace elements are Mn, Zr, Hf, Sc, Sb, V, As, In, Ga, Ge, Zn, Pb, and U at concentration levels up to several hundred ppm. Following elements are generally below the detection limit: Na, Mg, Ca, Cr, Co, Ni, Cu, Sr, Y, Mo, Cd, Ba, REE, Bi, and Th (see analytical data for each sample in the appendix). Although several authors report the occurrence of rare earth elements in cassiterite (Plimer et al., 1991; Pan & Amstutz, 1993; Gan & Chen, 1994; Jiang et al., 2004), these observations cannot be confirmed by our data as REE concentrations are generally below the detection limit.

Different deposit types can be distinguished by the variable trace element signatures of cassiterite (Figure 10.17). Cassiterite from magmatic deposits (pegmatites and rare metal granites) is significantly enriched in Nb, Ta, Zr, Hf, Mn, and Zn, whereas W, Sc, V, In, Sb, Ge, and As concentrations are generally low. Cassiterite from pegmatite deposits also shows a distinct preference of Ta over Nb (Černý & Ercit, 1985). On the contrary, trace elements in cassiterite from hydrothermal vein deposits show high concentrations in Ti, Sc, and V, but low Nb, Ta, Zr, Hf, Mn, Zn, U, Ga, Ge, and As contents. Cassiterite from greisen deposits is characterised by a rather intermediate elemental composition compared to cassiterite from magmatic or hydrothermal deposits with typical additional enrichments in In, W, and Sc. A unique trace element composition with elevated In, Sb, Ga, Ge, As, W, V, Sc, and U concentrations is displayed by cassiterite from the polymetallic vein deposits of the Bolivian Tin Belt.

Detailed examination and discussion of the trace element results in cassiterite are given in the following chapter 11.2.1 and are kept rather short in this part to avoid repetition.

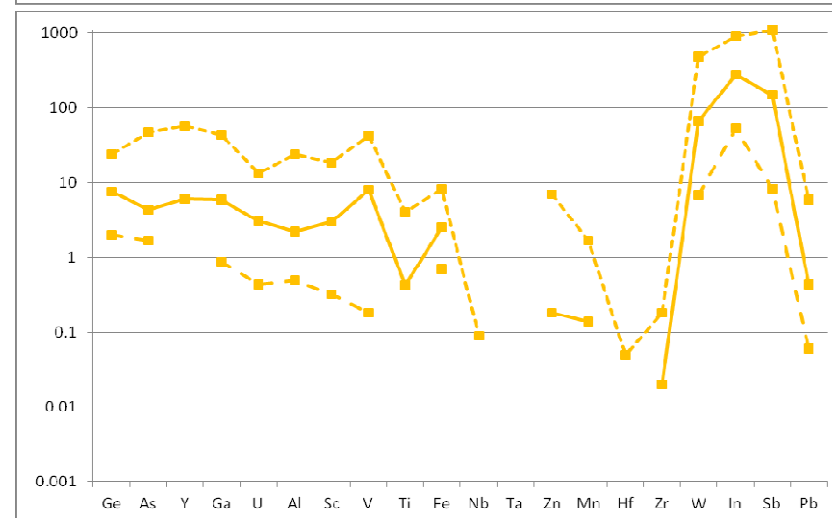
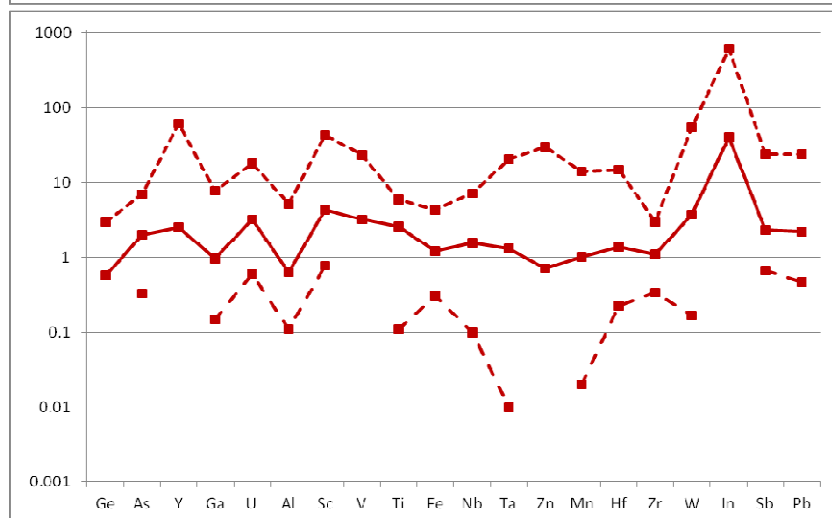
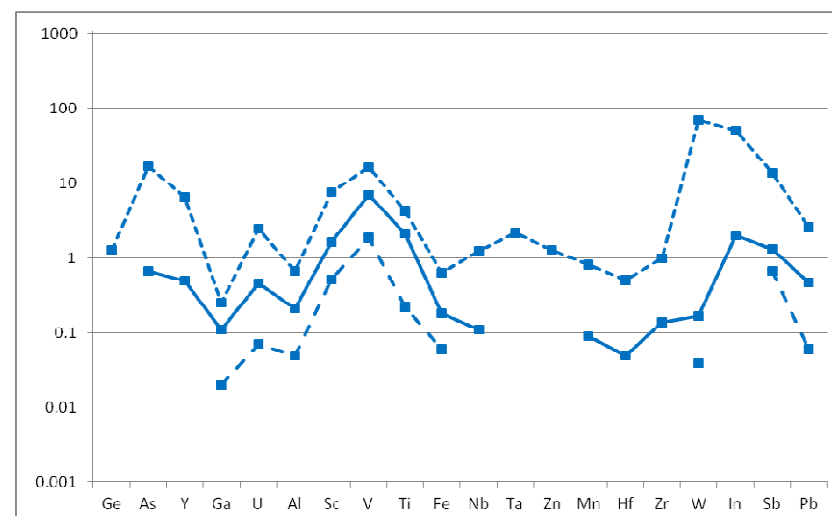
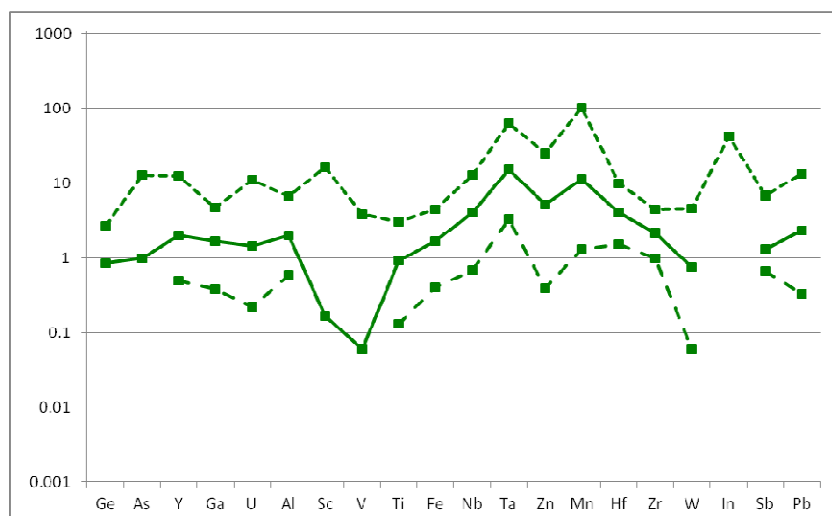


Figure 10.17: The variability in the trace element composition of cassiterite is displayed by the 10th percentile (dashed lower line), median (solid line), and 90th percentile (stippled upper line) of normalised concentration values for different ore deposit types (selected samples; see Table 10.7): pegmatites in green, hydrothermal veins in blue, disseminated deposits in red, and Bolivian polymetallic deposits in yellow. Robust statistical parameters are used as the trace element data are not normally distributed and to avoid overestimation of outliers.

Table 10.7: List of the selected samples which were included in Figure 10.17 to display the variability for the respective tin deposit types

pegmatite	locality	vein	locality	disseminated	locality	polymetallic	locality
7419	Araçuaí	8074	Nyamyumba	Coltan572	Jos Plateau	9312	Caracoles
8027d	Ruhanga	8842	Misobo	8790	Zaaiplaats	9314	Huanuni
8042	Nemba	8861	Rwinkwavu	8843	Atondo	9316	Colquiri
8064	Bijyojyo	8863	Musha	8844	Salukwango	9324	San Rafael
8158	Manono	9328	Rahman Hydraulic	9341	Bangka-Belitung	9325	San Rafael
8419a	São João del Rei	9475	Gitebe	9344	Kundur	9330	Caracoles
8473b1	Greenbushes	9481	Rwezamenyo	9353	Santa Bárbara	9333	Chorolque
9118	Rukaragata	9543	Nyamyumba	9354	Oriente Novo-Barranco	9335	Huanuni
9188	Black Hills	9667	Bugalula	9355	Oriente Novo-Pajura	9338	Japo
9189	Tanco	8823	Bisie	9356	São Domingo	9339	Poldi
9569b	Kamativi			9886	Abu Dabbab	9340	Sayaquiri
9739	Vaupés			9912	Nuweibi		



Figure 10.18: Exemplary photographs of different cassiterite concentrates already prepared as polished sections. The colour of cassiterite is variable ranging from dark black to almost pure white.

The colour of cassiterite ranges from colourless, white, yellowish, pinkish, red, brown to deep black (Figure 10.18) and strongly depends on incorporation of trace elements (Oen et al., 1982; Swinden, 1983; Ollila, 1986; Neiva, 1996). Comparison of selected dark with white to colourless cassiterite grains shows that the black ones have very high trace element concentrations, whereas colourless or white cassiterite is almost chemically pure SnO_2 with only V and Ti in higher concentrations (Figure 10.19).

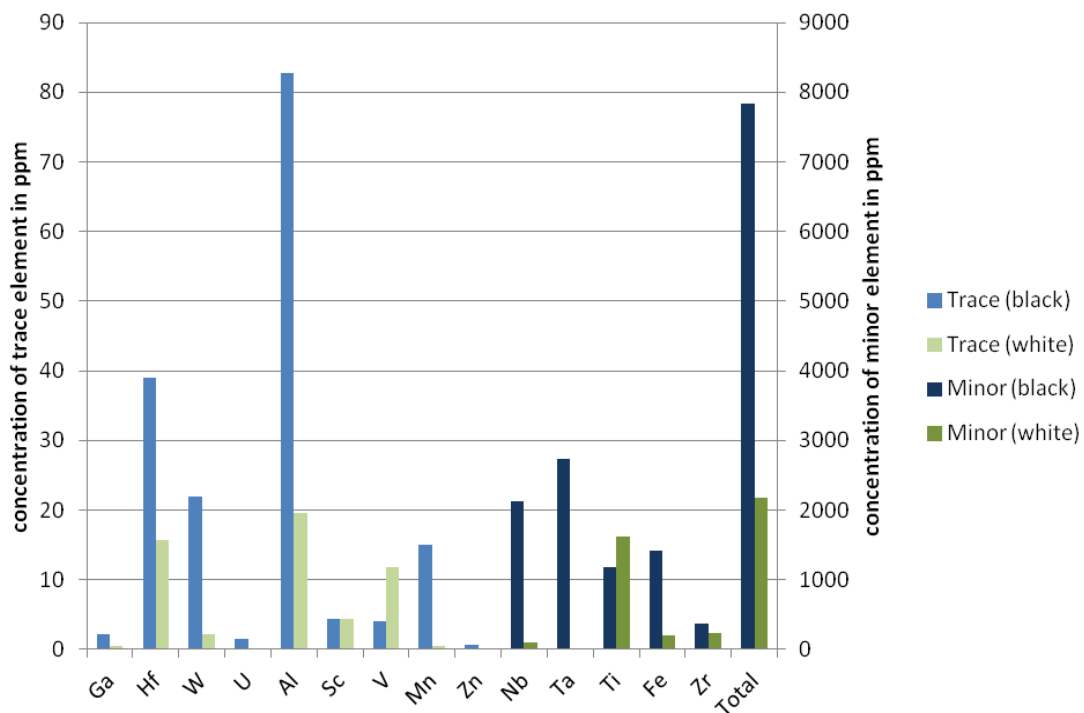


Figure 10.19: Comparison of trace element data for black and white cassiterite. Note the different scales for trace and minor elements, respectively.

10.3.2.2 LA-ICP-MS analysis of wolframite

1650 wolframite grains in 40 ore concentrates and in 1 ore sample from 28 localities (including single deposits or concessions) were analysed by LA-ICP-MS. Analytical data and specific information for each deposit are given in the appendix of this thesis (Appendix C).

Major substituting elements in wolframite are Nb, Mg, Zn, Ti, Ta, Y, Sc, Sn, and Zr. Common minor and trace elements are Co, V, Mo, In, REE (especially HREE), U, Hf, Pb, Th, and Ca in the range up to 100 ppm. Following elements are generally below the detection limit: Al, Cr, Ni, Cu, Ga, As, Sr, Ag, Cd, Sb, Ba, Tl, and Bi. Highest trace element concentrations (Nb as example in Figure 10.20) are commonly found in wolframite with intermediate major element composition, whereas the two endmembers show distinctly lower trace element concentrations (Figure 10.20).

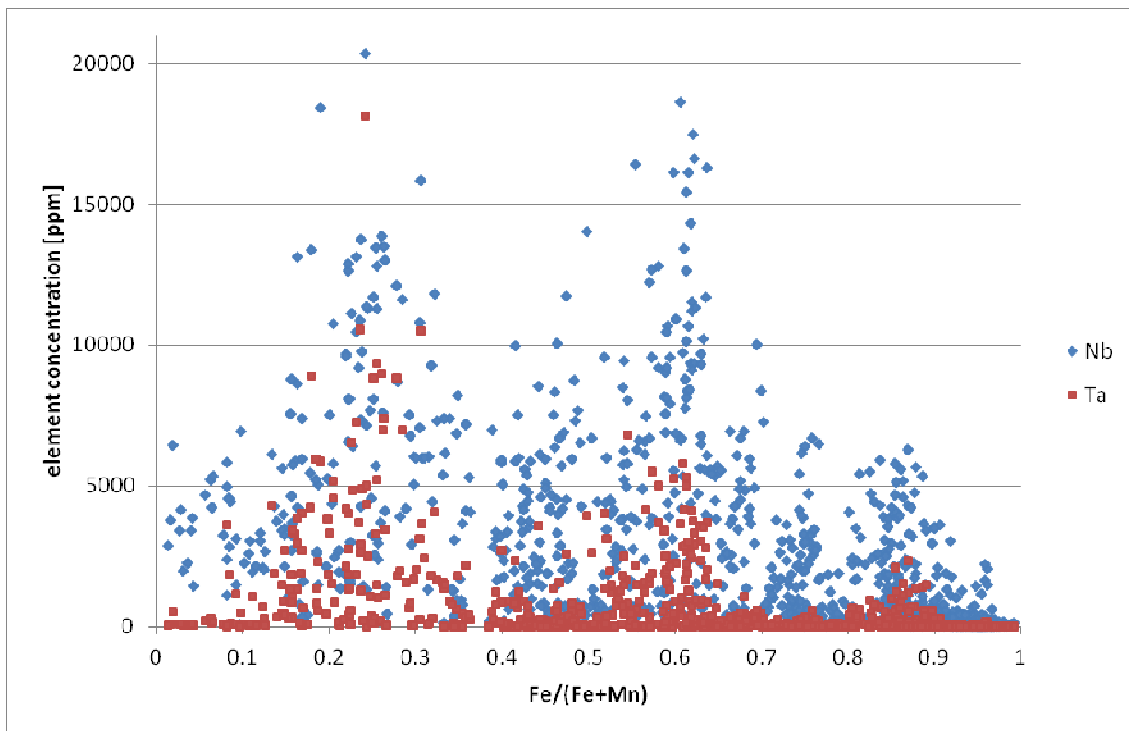


Figure 10.20: Diagram showing the niobium and tantalum contents [in ppm] in wolframite versus its ferberite/hübnerite ratio given as $Fe/(Fe+Mn)$.

Two different trace element groups can be distinguished depending on the ferberite/hübnerite ratio. The first group is composed of elements with generally high valence states like Sn^{4+} , Zr^{4+} , Hf^{4+} , Nb^{5+} , Ta^{5+} , U^{4+} , Th^{4+} plus Cd^{2+} , Y^{3+} , and In^{3+} with rather low valency; this element suite shows positive correlation with Mn content in wolframite (represented by Nb and Ta in Figure 10.21). On the contrary, the other element group is characterised by basically low valence states like Mg^{2+} , Co^{2+} , Sr^{2+} , and

Pb^{2+} and correlates positively with increasing ferberite component in wolframite (represented by Co in Figure 10.21). Another element group is characterised by a more or less homogenous distribution over the whole solid solution series and it seems to be independent of the hübnerite/ferberite ratio like Ti^{4+} , Sc^{3+} , Mo^{6+} , Ca^{2+} , Zn^{2+} (represented by Mo in Figure 10.21).

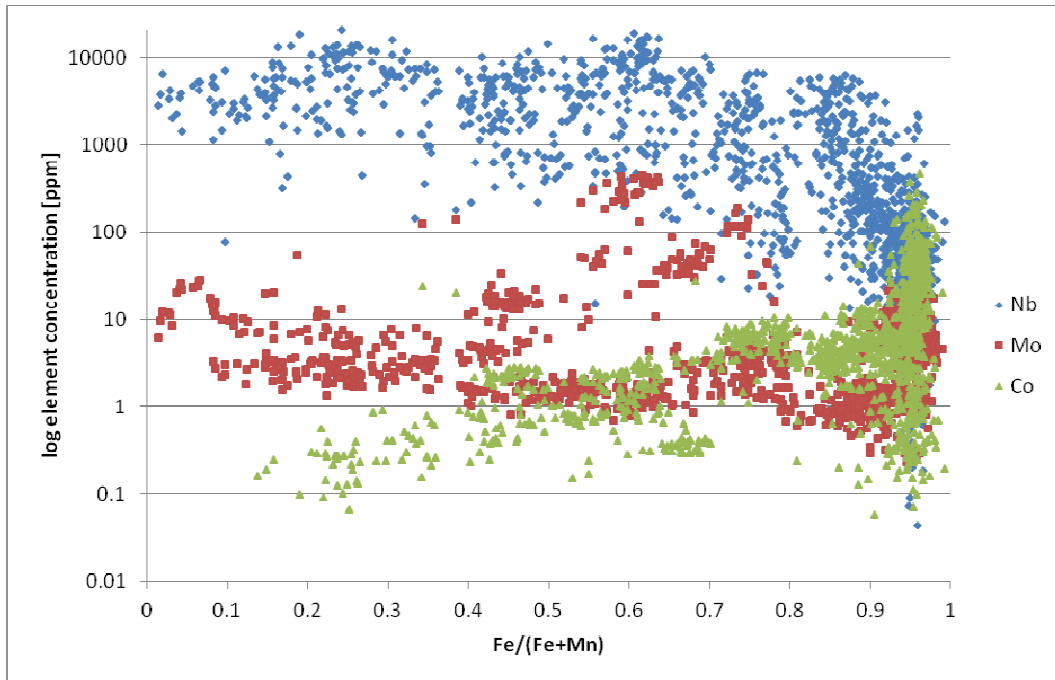


Figure 10.21: This diagram shows that trace elements concentration levels (blue: Nb; red: Mo; green: Co) in wolframite are dependent on the ferberite/hübnerite ratio given as $Fe/(Fe+Mn)$.

Different tungsten deposit types can be characterised by variable trace element compositions of wolframite (Figure 10.22). Wolframite from deposits with strong magmatic influence (high temperature hydrothermal veins and greisen deposits) is significantly enriched in HFSE like Nb, Ta, Zr, Hf, Sn, U, and Th, whereas V, Mg, Co, and Pb concentrations are low. Comparing these two deposit types, it is evident that wolframite from greisen deposits generally contains much higher trace element contents than wolframite from high temperature hydrothermal veins. Wolframite from greisen deposits also characterised by higher Ta/Nb and lower Zr/Hf ratios (Figure 10.22), which already indicate a magmatic influence comparable to cassiterite from pegmatites (see above). Wolframite from low temperature hydrothermal veins has rather low trace element contents especially in HFSE, but is enriched in Mg, V, and Co.

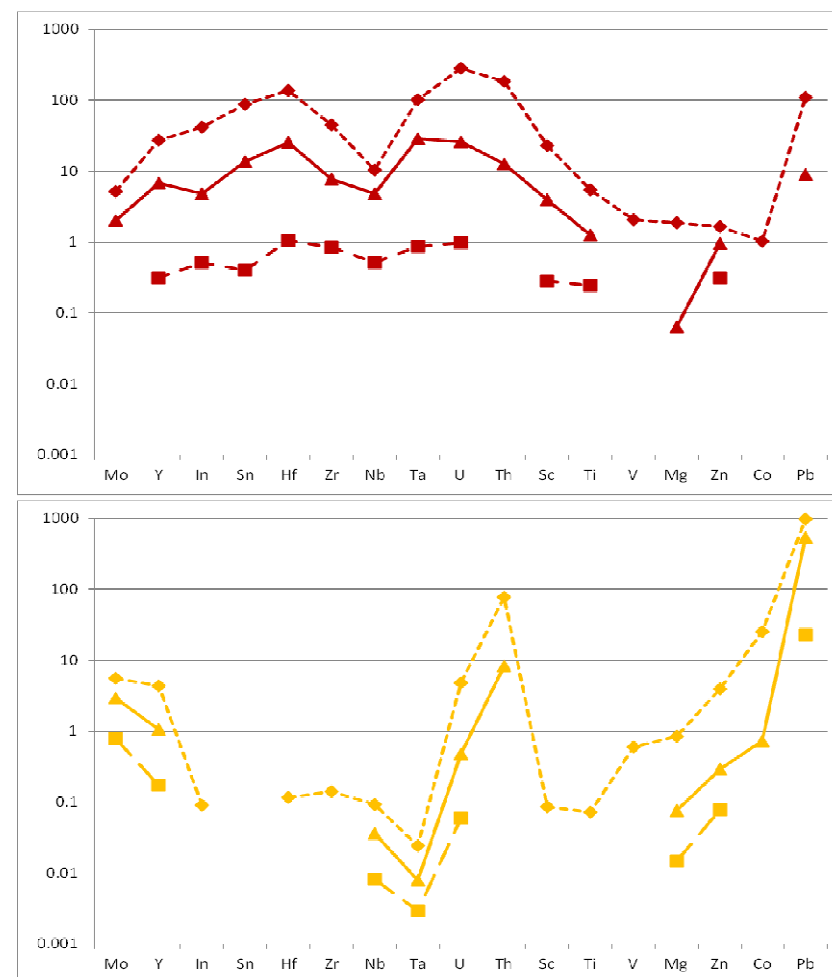
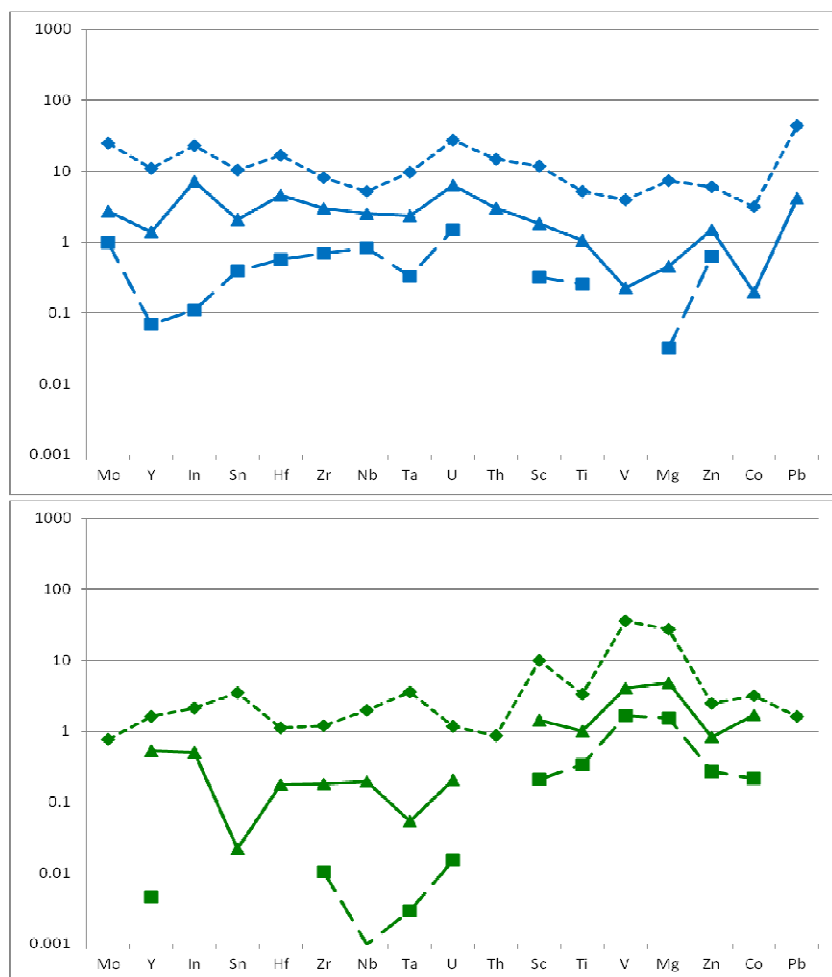


Figure 10.22: The variability in the trace element composition of wolframite is displayed by the 10th percentile (dashed lower line), median (solid line), and 90th percentile (stippled upper line) of normalised concentration values for different ore deposit types (selected samples; see Table 10.8): high temperature hydrothermal veins in blue, greisen deposits in red, low temperature hydrothermal veins in green, and reinite deposits in yellow. Robust statistical parameters are used as the trace element data are not normally distributed and to avoid overestimation of outliers.

Table 10.8: List of the selected samples which were included in Figure 10.22 to display the variability for the respective wolframite deposit types

vein (high-T)	locality	vein (low-T)	locality	greisen	locality	reinite	locality
9212	Tsagaan Davaa	8737	Caracoles	9208	Yugodzyr	9487	Mucaca
9221	Mae Sariang	9493	Rutsiro	9218	Ranong	9639	Gifurwe
9640	Chojlla	9774	Khovd Gol	9776	Hemerdon	9720	Nyakabingo
9642	Needle Hill	9829	Bishasha	K0058	Spokoynoye		
9775	Mount Carbine						

The distinction between the two hydrothermal vein types is made according to the geological setting. High temperature hydrothermal veins occur either in immediate proximity to or within a granitic pluton, whereas low temperature hydrothermal veins are found in the surrounding country rock further away from the intrusion. Almost pure ferberite from Rwandan reinite (ferberite pseudomorphous after scheelite) deposits shows a unique trace element composition with enrichments in Ga, As, Ba, Co, Ni, Sr, Pb, Ca, and Th, but low HFSE contents.

The rare earth elements (REE) readily substitute for Fe and Mn. Chondrite-normalised patterns are used to characterise the distribution of the REE in wolframite (Figure 10.23). Generally, wolframite is characterised by heavy REE (HREE) predominating over light REE (LREE). The inclining REE patterns display a distinct negative Eu anomaly and a weak negative Y anomaly may be present. Manganese-rich wolframite is characterised by steeper patterns with higher HREE concentrations and the negative Eu and Y anomalies are more pronounced. In general, the total REE concentration correlates positively with increasing Mn content. Contrasting, ferberite pseudomorphs after scheelite (reinite) display rather flat REE patterns with just slight increase towards the HREE. A weak positive Eu anomaly is present and the Y anomaly is missing. The LREE (La, Ce, Pr, Nd, and Eu) are significantly enriched in reinite compared to other wolframite compositions (Figure 10.23). Please note that the REE patterns of Mucaca deposit (Figure 10.22, red lines in upper left diagram) show a wide distribution covering both flat 'reinite' patterns and inclining patterns typical for primary wolframite; this indicates that both types of wolframite coexist in this deposit.

Detailed examination and discussion of the trace element results in wolframite are given in the following chapter 11.2.2 and are kept short in this part to avoid repetition.

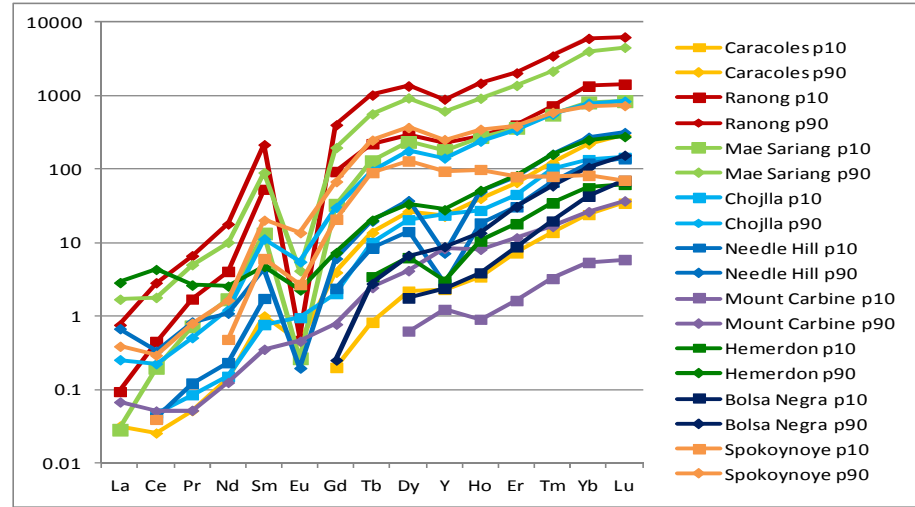
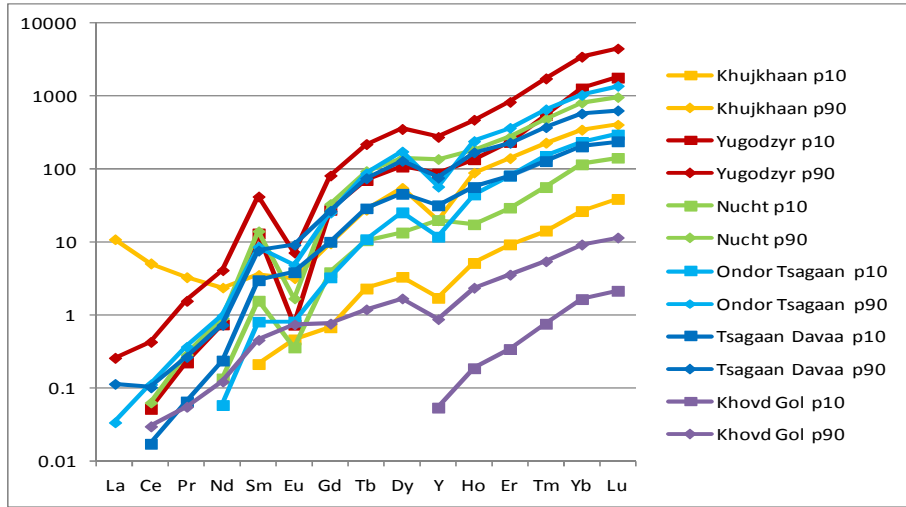
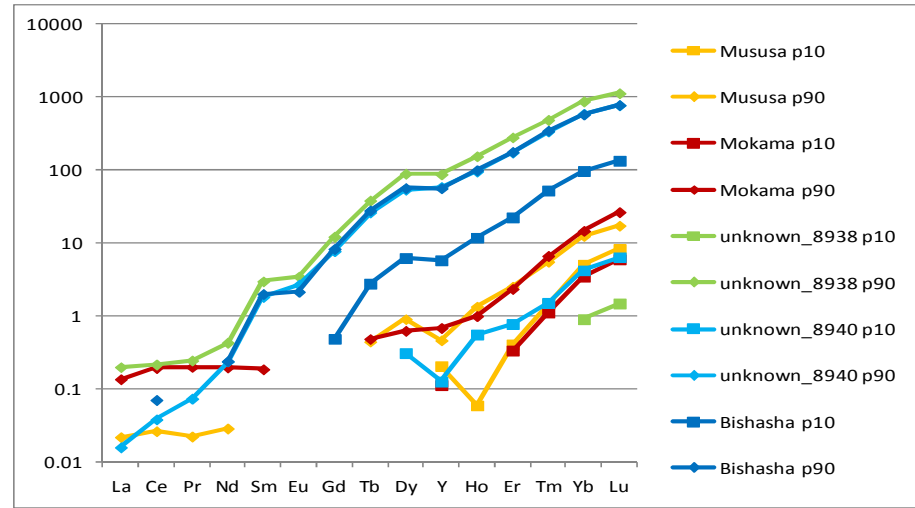
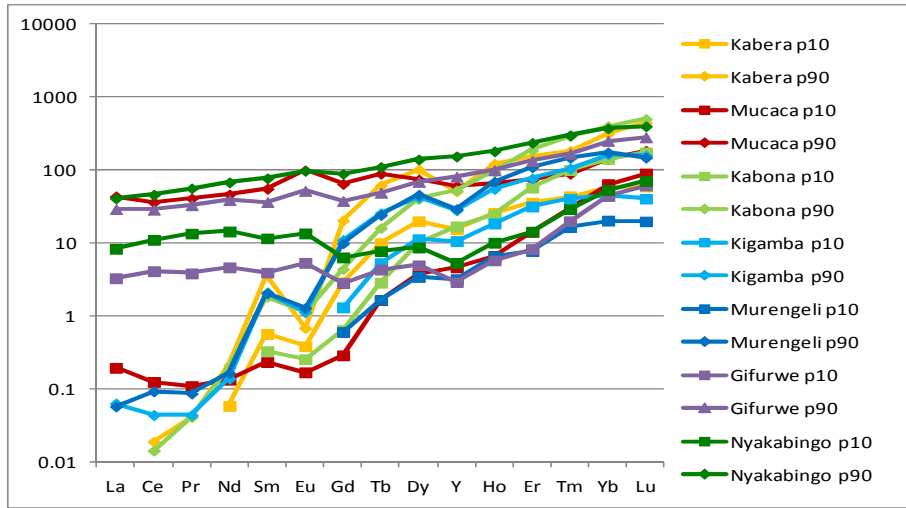


Figure 10.23: Variability of chondrite-normalised REE patterns of wolframite from each tungsten deposit given as the 10th percentile (lower line with squares) and 90th percentile (upper line with diamonds). Composition of C1 carbonaceous chondrite is taken from McDonough & Sun (1995). Upper left diagram: Rwanda, upper right diagram: DR Congo, lower left diagram: Mongolia, lower right diagram: rest of the world.

11 Discussion

The following discussion focuses on the mineralogical composition of Sn and W concentrates and trace element chemistry of cassiterite and wolframite. Parameters and conditions controlling mineral precipitation and trace element incorporation are also discussed.

11.1 Mineralogical composition

The mineralogical composition of ore concentrates is measured by MLA. First, these results permit assessment of the quality of an ore concentrate. As already mentioned, it has to be noted that the grade of the relevant ore minerals in concentrates is strongly dependent on the beneficiation process. Especially in artisanal and small-scale mining, the panning skills of the miners have a significant influence and the mineralogical composition might be easily modified (Figure 11.1). As a consequence, the trace element composition of the relevant ore minerals forms the crucial parameter for the AFP as it cannot be modified by external influences. Alternatively, the MLA step can be skipped by a 'quick LA-ICP-MS' method in order to identify the relevant ore mineral grains as suggested by Gäbler et al. (2013). Please refer to Gäbler et al. (2013) for further details.



Figure 11.1: MLA images of two heavy mineral concentrates from Simba, Rwanda. Different colours represent different mineral phases: e.g., cassiterite (blue), columbite-tantalite (pinkish and red), rutile (yellow), topaz (pale blue), muscovite (pale green), quartz (pale violet) and Fe oxides (apricot). Comparison of these two MLA images reveals the different ore grade of the two concentrates although they originate from the same deposit: 46.7 area% cassiterite (left) versus 12.7 area% cassiterite (right).

The mineralogical composition of an ore concentrate may give first indications on its provenance such as the type of ore deposit from which it was mined. For example, the occurrence or absence of Ta-bearing mineral phases often indicates if an ore concentrate derives from a magmatic or hydrothermal deposit, respectively. Tantalum mineralisation is generally magmatic in origin (rare-element granite or pegmatite body), whereas hydrothermal deposits are devoid of Ta-bearing minerals, because Ta is not transported in hydrothermal fluids due to very low fluid-melt partition coefficients (Linnen & Cuney, 2005). Cassiterite may be found in both deposit types, whereas wolframite occurs almost exclusively in hydrothermal deposits (some known exceptions are listed in the pegmatites paragraph of chapter 6). This observation also reflects the different geochemical behaviour and precipitation mechanisms of Sn and W (see excursus on the geochemistry of Sn and W in chapter 6).

Several accessory or rare mineral phases may be distinctive for some particular ore deposits (Melcher et al., 2008). For example, the Mumba pegmatite in North Kivu displays an exceptional mineral assemblage composed of simpsonite $\text{Al}_4(\text{Ta},\text{Nb})_3\text{O}_{13}(\text{OH})$, lithiowodginite LiTa_3O_8 , and Ba-rich microlite (Melcher et al., 2015). Simpsonite is a rare mineral which occurs only in a very few localities all over the world (Černý & Ercit, 1989; Melcher et al., 2015). The rare Sn-bearing minerals foordite $\text{Sn}^{2+}\text{Nb}_2\text{O}_6$ and thoreaulite $\text{Sn}^{2+}\text{Ta}_2\text{O}_6$ are only found in a couple of occurrences worldwide, e.g. Rutsiro area in Rwanda, Kubitaka in Maniema, and Manono in Katanga (Černý et al., 1988; Melcher et al., 2015). Foordite and thoreaulite are characterised by the presence of divalent Sn and are only found in pegmatites with local low oxygen fugacity conditions (Uher et al., 2008). Anthoinite $\text{AlWO}_3(\text{OH})$ is found in W concentrates from the Rwandan reinitite deposits (e.g., Nyakabingo) and represents a weathering product of the reinitite mineralisation. But anthoinite is also known from other Central African tungsten deposits (Varlamoff, 1947; Sahama et al., 1970; Sahama, 1981).

Other rock-forming minerals in the ore concentrates derive from the host or surrounding country rocks. Zircon, topaz, beryl, and apatite are typical for magmatic (granitic or pegmatitic) host rocks. Quartz, muscovite, and tourmaline are characteristic for hydrothermal veins as well as granitic or pegmatitic rocks. Topaz and fluorite are common in greisen deposits. Other minerals like ilmenite, staurolite, and amphiboles may originate from the surrounding country rocks. Some cassiterite deposits (for example Caracoles, Bolivia) are associated with distinct tourmalinisation and this characteristic feature may also be indicated by the presence of tourmaline in the ore

concentrate. For example in Mongolia, Bi-minerals are common in ores from the Yugodzyr and Ondor Tsagaan deposits.

Various mineral inclusions and exsolutions are frequently hosted by cassiterite crystals. Exsolutions are generally related to cassiterite from high temperature deposits such as pegmatites. The most common minerals occurring either as inclusion or exsolution within cassiterite are columbite-tantalite (Figure 10.14), wolframite, tapiolite, microlite, ixiolite, rutile, zircon, wodginite, ilmenite, magnetite, and thoreaulite (Stevenson & Taylor, 1973; Ramdohr, 1975; Černý et al., 1985; Binde, 1986; Hennigh, 1993; Neiva, 1996; Mausau et al., 2000; Pereira et al., 2004; Klementová & Rieder, 2005; Dill et al., 2006; Beurlen et al., 2008; Neiva, 2008; Rao et al., 2009; Wise & Brown, 2011). When cassiterite contains exsolution of another phase, it shows a concentration gradient indicated by depletion of certain elements close to the exsolved phase. For example, cassiterite is locally depleted in Ta and Fe around an exsolution of tantalite-(Fe) (Gocht & Pluhar, 1982; Neiva, 1996; Klementová & Rieder, 2005; Rao et al., 2009; Wise & Brown, 2011). Cassiterite from massive sulphide deposits is generally devoid of mineral inclusions (Neiva, 1996), but if inclusions are present they are commonly formed by sulphides, especially sphalerite. In this case, sphalerite grains often form the nucleus for the precipitation of cassiterite (Hennigh, 1993). This close association indicates that Sn and Zn are transported together in the hydrothermal fluid of massive sulphide systems (Hennigh, 1993).

Wolframite generally shows less mineral inclusions or exsolutions than cassiterite, but replacement by scheelite (Figure 3.7 left) or weathering to Fe-hydroxides along the rims and cracks are common (Higgins, 1985; Tindle & Webb, 1989; Ferenc & Uher, 2007).

11.2 Trace element composition

Trace element data of single mineral (in this case cassiterite and wolframite) grains from ore concentrates are obtained by LA-ICP-MS analysis. These data are used to understand the factors controlling trace element incorporation and substitution mechanisms. However, submicroscopic mineral inclusions of other mineral phases may also affect the concentration levels of certain elements. Yet, it is difficult to resolve the site of particular trace elements, but crystal chemistry of the host mineral, the presence or absence of other minerals that contain elements of interest in major concentrations, and experimental studies on element solubility are used in this discussion to find evidence for the features of trace element incorporation (Huston et al., 1995).

In order to identify the specific crystal chemistry, the ablation spots for analysis are placed carefully without any surficial inclusions or exsolutions, but contamination from visually undetected inclusions/exsolutions cannot be generally excluded because of the penetration depth of the laser.

Substitution is the ability of ions to occupy preferred sites in the crystal lattice of a mineral and is strongly dependent on charge and size of the substituting ions according to the basic rules of Goldschmidt (1926). As a rule of thumb, substitution is possible if the radii of the two substituting ions differ by less than 15% (Goldschmidt, 1926). Ions differing in the charge by one unit substitute readily if charge neutrality in the crystal is given by coupled substitution. On the one hand, if two ions with same charge and different ionic radii compete for a site in the crystal lattice, the ion with smaller radius is preferred. On the other hand, if two ions have similar ionic radii but different charge, the ion with the higher charge is favoured (Goldschmidt, 1926). Another factor controlling substitution is electronegativity (Ringwood, 1955; White, 2009). Several authors already suggested that trace element composition of minerals may be dependent on further parameters than those mentioned above, for example composition of the melt or fluid, contemporaneous precipitation with other minerals, temperature, oxygen fugacity, etc (Huston et al., 1995; Dupuis & Beaudoin, 2011; Nadoll et al., 2014, Dare et al., 2014; Melcher et al., 2015).

Under certain circumstances, metals might be suitable for substitution in terms of their ionic radii (all effective ionic radii in this study are taken from Shannon, 1976) or valence states, but are not incorporated into the crystal lattice of a given mineral (e.g., cassiterite or wolframite). This is particularly dependent on the different behaviour of the metals either in silicate melts or in hydrothermal fluids. Transport and deposition of

the metals are strongly controlled by the physicochemical conditions of the melt or fluid. For example, the base metal Cu in its divalent state (0.73 Å) has a similar ionic radius compared to Sn⁴⁺ (0.69 Å) in cassiterite or Fe²⁺ (0.78 Å) and Mn²⁺ (0.83 Å) in wolframite. In addition, divalent Cu also has the same valence state as Fe and Mn in wolframite. Nevertheless, Cu is almost exclusively below detection limit in cassiterite and wolframite, respectively. On the one hand, Cu does not precipitate contemporaneously with Sn and W, but rather remains in solution at the conditions of cassiterite and wolframite formation. This is also underpinned by the temporal and spatial succession of metal precipitation commonly found in Sn-W deposits (e.g. Cornwall, Figure 6.12). First Sn and W are deposited during an early oxide stage, subsequently followed by a sulphide stage with precipitation of Cu in the form of chalcopyrite and other Cu-bearing sulphides. On the other hand, metals show significantly different geochemical behaviour. In this case, Sn and W preferentially form oxides, whereas Cu is a chalcophile element which mostly occurs as sulphide minerals. Copper can be considered as representative for other elements commonly forming sulphides, such as Zn (sphalerite/wurtzite, ZnS), Pb (galena, PbS), Bi (bismuthinite, Bi₂S₃), Sb (stibnite, Sb₂S₃), and Cd (greenockite, CdS).

11.2.1 Trace elements in cassiterite

Several workers studied the chemical composition of cassiterite (Dudykina, 1959; Fesser, 1968; Wolf & Espozo, 1972 and references therein; Steveson, & Taylor, 1973; Dunn et al., 1978; Schneider et al., 1978; Moore & Howie, 1979; Taylor, 1979; Dulski, 1980; Gocht & Pluhar, 1982; Oen et al., 1982; Swinden, 1983; Černý et al., 1985; Izoret et al., 1985; Binde, 1986; Ollila, 1986; Giuliani, 1987; Möller et al., 1988; Peng et al. 1988; Ruck et al., 1989; Plimer et al., 1991; Cuney et al., 1992; Hennigh, 1993; Ogunbajo, 1993; Pan & Amstutz, 1993; Yim, 1994; Gan & Chen, 1994; Seifert, 1994; Suwimonprecha et al., 1995; Neiva, 1996; Murciego et al., 1997; Tindle & Breaks, 1998; Hennigh & Hutchison, 1999; Raimbault et al., 1999; Belkasmi et al., 2000; Costi et al., 2000; Serranti et al., 2002; Huang et al., 2002; Breiter & Škoda, 2004; Pereira et al., 2004; Zhao et al., 2005; Pieczka et al., 2007; Abdalla et al., 2008; Galliski et al., 2008; Neiva, 2008; Somarin, 2009; Huston et al., 2011; Martins et al., 2011; Wise & Brown, 2011; Llorens & Moro, 2012a; Llorens & Moro, 2012b; Huang et al., 2014; Chicharro et al., 2015). Despite the huge number of studies dealing with the chemical compositions of cassiterite, almost all only analysed major and at least some minor elements mostly by EPMA. However, these studies already indicate the variability in element concentrations (Tables 11.1 & 11.2).

Table 11.1: Chemical composition of cassiterite by electron probe microanalysis (EPMA) compiled from the literature. Analyses are given in wt.% element oxide, 0 values are below detection limit. Original data from Möller et al. (1988) and Somarin (2009) were converted from wt.% element into wt.% element oxide for comparability.

Reference	Sample locality	Method	n	data	Nb ₂ O ₅	Ta ₂ O ₅	TiO ₂	ZrO ₂	WO ₃	MnO	FeO	Fe ₂ O ₃	V ₂ O ₃	Sc ₂ O ₃	In ₂ O ₃
Moore & Howie (1979)	St. Michael's Mount	EPMA	8	range	0-0.1	0.01-0.09	0.01-0.08		0.01-0.08		0.02-0.29				0.04-0.08
Moore & Howie (1979)	Cligga Head	EPMA	8	range	0.01-0.26	0.01-0.03	0.01-0.06		0.01-1.61		0.05-0.63				0.04-0.08
Cerny et al. (1985)	Peerless pegmatite	EPMA	6	range	0-0.7	0.6-11.7	0-0.1			0-0.3	0-1.4				
Ollila (1985)	Rooiberg	EPMA	8	range	0-0.24	0.1-0.17	0		0-1.09		0.31-2.27				
Ollila (1985)	Union Tin	EPMA	8	range	0-0.08	0.1-0.28	0		0.01-0.28		0.41-1.64				
Ollila (1985)	Zaaiplaats	EPMA	14	range	0-0.55	0.1-0.18	0		0-0.94		0.31-1.47				
Ollila (1985)	Leeuwpoot	EPMA	16	range	0-0.19	0-0.16	0-0.6		0-1.09		0.21-1.55				
Giuliani (1987)	Zaer	EPMA	21	range	0-0.2	0-0.13	0.09-1.0			0-0.07		0-0.4			
Möller et al. (1988)	worldwide	EPMA	4	range	0.57-1.43	0.01-1.22			0.76-1.77	0.01-0.15	0.77-1.8				
Ruck et al. (1989)	Ille-et-Vilaine	EPMA	1		0.1	0	0.4					0.03			
Ruck et al. (1989)	Paredes	EPMA	1		0.43	0	0.43					0.15			
Ruck et al. (1989)	Elmeki	EPMA	1		0.79	0	0.03					0.88			
Ruck et al. (1989)	Matamala	EPMA	1		1.43	0.54	3.75					1			
Ogunbajo (1993)	Barkin Ladi	EPMA	15	range	0-8.14	0-4.44	0-0.87	0-2.26	0-0.35	0-0.35	0.12-5.84				
Ogunbajo (1993)	Gurum	EPMA	15	range	0-4.31	0-1.14	0-1.46	0-0.89	0-1.36	0-0.19	0.43-3.62				
Ogunbajo (1993)	Dorowa	EPMA	15	range	0-1.24	0-1.42	0-0.96	0-12.36	0-0.14	0-0.06	0.21-2.29				
Ogunbajo (1993)	Jarawa	EPMA	15	range	0-1.24	0-0.4	0-1.43	0-0.45	0-0.06	0-0.18	0.12-1.86				
Suwimonprecha et al. (1995)	Phuket	EPMA	8	range	0.04-1.58	0-4.34	0-1.11		0.03-0.13	0-0.6	0.05-1.01				
Neiva (1996)	quartz vein (Sn>W) from Iberian Peninsula	EPMA	10	range	0.1-1.22	0.04-3.19	0.09-0.31		0-0.05	0-0.08	0.13-0.98				
Neiva (1996)	pegmatites from Iberian Peninsula	EPMA	19	range	0-1.84	0-11.89	0.1-0.97		0-0.25	0-0.09	0-2.58				
Neiva (1996)	quartz vein (W>Sn) from Iberian Peninsula	EPMA	17	range	0.01-0.36	0.01-0.39	0.28-0.92		0-0.23	0-0.03	0.02-0.19				
Neiva (1996)	Neves Corvo	EPMA	3	range	0-0.03	0.05-0.4	0-0.04		0-0.95	0-0.02	0.18-1.93				
Tindle & Breaks (1998)	Separation Rapids pegmatites	EPMA	12	range	0-1.19	0.37-8.68				0.03-0.2	0.06-1.73				
Belkasmı et al. (2000)	Yichun	EPMA	12	range	0.08-2.81	0.91-7.79	0-0.89		0	0.11-0.77	0.22-1.13				
Costi et al. (2000)	Pitinga - Madeira pluton	EPMA	22	range	0-2.35	0-0.41	0-0.1				0-1.81				
Costi et al. (2000)	Pitinga - Agua Boa pluton	EPMA	24	range	0-0.62	0-0.2	0.01-1.16				0.01-1.27				
Serranti et al. (2002)	Neves Corvo	EPMA	88	range			0-4.06		0-1.5		0.45-2.19				
Huang et al. (2002)	Yichun	EPMA	9	range	0.32-0.85	0.72-4.04	0.12-0.42		0-0.44	0.07-0.38	0.12-0.39				
Zhao et al. (2005)	Furong	EPMA	6	range	0-0.03		0-2.87			0-0.2	0.04-1				0.08-0.6
Pieczka et al. (2007)	Redziny	EPMA	432	range	0-0.16	0-0.23	0-2.52		0-0.66	0-0.13		0-1.69			
Abdalla et al. (2008)	Abu Dabbab	EPMA	3	range	0.28-0.82	0.51-1.3	0.45-1.4		0.11-0.14		0.75-1.3				
Galliski et al. (2008)	La Viquita	EPMA	11	range	0-1.83		0-0.28	0-0.23	0-0.8	0-0.29	0-2.3				
Neiva (2008)	quartz vein (Sn>W) from Iberian Peninsula	EPMA	5	range	0.05-1.12	0.23-2.37	0.23-0.45		0	0-0.08	0.11-0.89				
Neiva (2008)	quartz vein (W>Sn) from Iberian Peninsula	EPMA	6	range	0-0.07	0-0.28	0.52-0.76		0-0.34	0-0.08	0-0.09				
Somarin (2009)	Glen Eden	EPMA	20	range	0-0.33	0.34-1.31	0-2.9		0.35-1.35	0-0.5	0-3.28				
Martins et al. (2011)	Barroso-Alvao pegmatites	EPMA	7	range	0.03-0.44	0.16-1.99	0.03-0.21		0-0.11	0.03-0.19	0.18-0.41				
Wise & Brown (2011)	Black Mountain pegmatite	EPMA	7	range	0.57-0.96	0.98-2.01	0.01-0.04			0.05-0.1	0.04-0.47	0-0.43			
Llorens & Moro (2012a)	Jálama Batholith pegmatites	EPMA	7	range	0.14-2.26	0-5.39	0.09-0.41	0	0	0-0.51	0.13-0.92		0-0.04		
Llorens & Moro (2012b)	Jálama Batholith quartz veins	EPMA	4	range	0-0.42	0	0.03-0.73	0	0-0.07	0-0.04	0-0.18		0		
Huang et al. (2014)	Xianghualing - cass in ongonite	EPMA	20	mean	0.14	0.34	0.22		0.22	0.03	0.2				0.01
Huang et al. (2014)	Xianghualing - disseminated cass in topazite	EPMA	41	mean	1.26	3.04	0.31		0.88	0.24	1.42				0.03
Chicharro et al. (2015)	Logrosán	EPMA	13	range	0-1.73	0-3.68	0.07-0.93		0-0.12	0-0.42	0.03-1.04				

Table 11.2: Chemical composition of cassiterite by different analytical methods (ES = Emission spectrography, ICP-MS = inductively coupled plasma mass spectrometry, INAA = instrumental neutron activation analysis, PIXE = particle induced X-ray emission, XRF = X-ray fluorescence) compiled from the literature. Analyses are given in ppm element, 0 values are below detection limit. Original data from Dudykina (1959) were converted from wt.% element into ppm element, wt.% element oxide from Swinden (1983) were converted into ppm element, and wt.% Fe₂O₃ from Gan & Chen (1994) were converted into ppm Fe for comparability.

Reference	Sample locality	Method	n	data	Nb	Ta	Ti	Zr	W	Mn	Fe	Zn	V	Sc	In	Ga	Ge	As	Mo	Sb	Pb	Cu	Ni	Ag	Tl	Bi	Be	
Dudykina (1959)	pegmatites	ES	37	mean	6000	5300	4100	2400	730			0	5	650	0	20	0	5	20	0	30			0	0	4	10	
Dudykina (1959)	quartz vein	ES	129	mean	600	150	3500	150	2140			0	20	400	0	4	0	120	0	0	40			10	0	20	10	
Dudykina (1959)	sulphide-cassiterite	ES	43	mean	20	0	1700	30	5600			1210	10	4	210	20	3	1600	30	1600	6000			660	10	160	10	
Plimer et al. (1991)	Mole granite	ICP-MS	10	range				0-5						0-8	0-4.8			0-950		0-2						0-1.2	0-17	
Yim (1994)	NE Tasmania	XRF	19	range	530-4265	5-2920		85-1500	605-1570																			
Gan & Chen (1994)	Dupangling	?	10	range	14.3-351	0-99.9			47.6-517	10.1-280	371-5267			2.4-27	0-37.8			0-43.2		0-95.4								
Stevenson & Taylor (1973)	pegmatites	ES	6	mean	>10000	>10000	1200	458	283		6000			0	13						42			0.4				
Stevenson & Taylor (1973)	greisen	ES	3	mean	>10000	600	970	200	200		3670			47	158						9			0.7				
Stevenson & Taylor (1973)	quartz-cassiterite	ES	13	mean	255	100	1370	65	1110		5200			61	52						23			0.2				
Stevenson & Taylor (1973)	sulphide-cassiterite	ES	4	mean	20	100	1150	40	1520		3600			66	80						131			0.3				
Wolf & Espozo (1972)	Bolivia	ES	61	range	0-3800	0-2000	15- >2500	0-250	0-6000				0-145		0-600	0-800								0-950		0-230	0-250	0-40
Pieczka et al. (2007)	Redziny	INAA/ICP-MS	4	range	1.5-6.2	0.7-1.7		7-53	286-710				0-23	0.4-1.5			3-6		19-77		38-99							
Binde (1986)	Erzgebirge	?	8	mean	80		890	40	>690	19			25	25	25	0	0					2					4	
Binde (1986)	Bolivia (Mesozoic)	?	27	mean	120		>980	35	280	30			6	0	0	0	0					6					0	
Binde (1986)	Bolivia (Tertiary)	?	20	mean	70		250	0	>2100	7			0	65	0	120	2					25					1	
Swinden (1983)	Geevor	XRF	88	range			81-6136	55-27821	860-2188		1568-61953																	
Hennigh (1993)	Kidd Creek	PIXE	21	range	0-41	0-82		10-88	0-140	0	34-1283	0-5930				0-235	0-44	0-15	0-10		0-1764	0-78	0-67					
Hennigh (1993)	Neves Corvo	PIXE	9	range	0	0-105		7-40	41-9737	0	2863-9642	0-77				0-29	0	0-177	0-8		0-31	9-767	0-11					
Hennigh (1993)	Sullivan	PIXE	6	range	0-132	35-50		8-72	0-109	0-403	47-728	0-591				0	0	0-100	0		0-302	0-15	0-55					
Hennigh (1993)	East Kemptville	PIXE	3	range	0-334	30-79		13-107	0-1596	0	36-561	6-13				6	0	6	0-29			0-19	9					
Hennigh (1993)	Panasqueira	PIXE	2	range	11-51	0-58		156-193	0-1424		89-152					0	0	5-6			0	0-8	0					
Hennigh (1993)	Kamativi	PIXE	2	range	3626-12244	9586-12910		481-957	248-449	54-73	2450-5090	48-79				0		24-34	0			98-128	0-27					
Hennigh (1993)	Tanco	PIXE	1	range	1134	18758		485	635	94	2784	107				0	0	36				188	36					
Serranti et al. (2002)	Neves Corvo	PIXE	88	range		0-98						0-136			180-394			0-41		0-243	0-18	10-919						

Tin occurs in the cassiterite structure as Sn^{4+} in sixfold coordination with an ionic radius of 0.69 Å. Tetravalent cations with similar ionic radii fit well for Sn into the cassiterite lattice, for example Ti^{4+} (0.61 Å), Hf^{4+} (0.71 Å), Zr^{4+} (0.72 Å), and U^{4+} (0.73 Å). Despite its comparatively small ionic radius, Ge is most likely also substituted for Sn in its tetravalent state (0.53 Å) and is characteristic in deposits from the Bolivian Tin Belt. Titanium readily substitutes for Sn at high temperatures and cooling probably leads to exsolution of rutile. Experiments show that complete isomorphous solid solution between SnO_2 and TiO_2 exists at temperatures above 1350 °C (Padurow, 1956), but Ti concentrations in cassiterite of generally less than 1 wt.% Ti indicate limited miscibility of SnO_2 and TiO_2 under natural conditions (Dulski, 1980). Zirconium and Hf are regarded as geochemical twins and are substituted into the cassiterite lattice in a similar way. However, Zr and Hf show fractionation depending on the geochemical conditions and the Zr/Hf ratio can be used as geochemical indicator for different deposit types (Dulski, 1980; Dulski et al., 1982; Möller & Dulski, 1983).

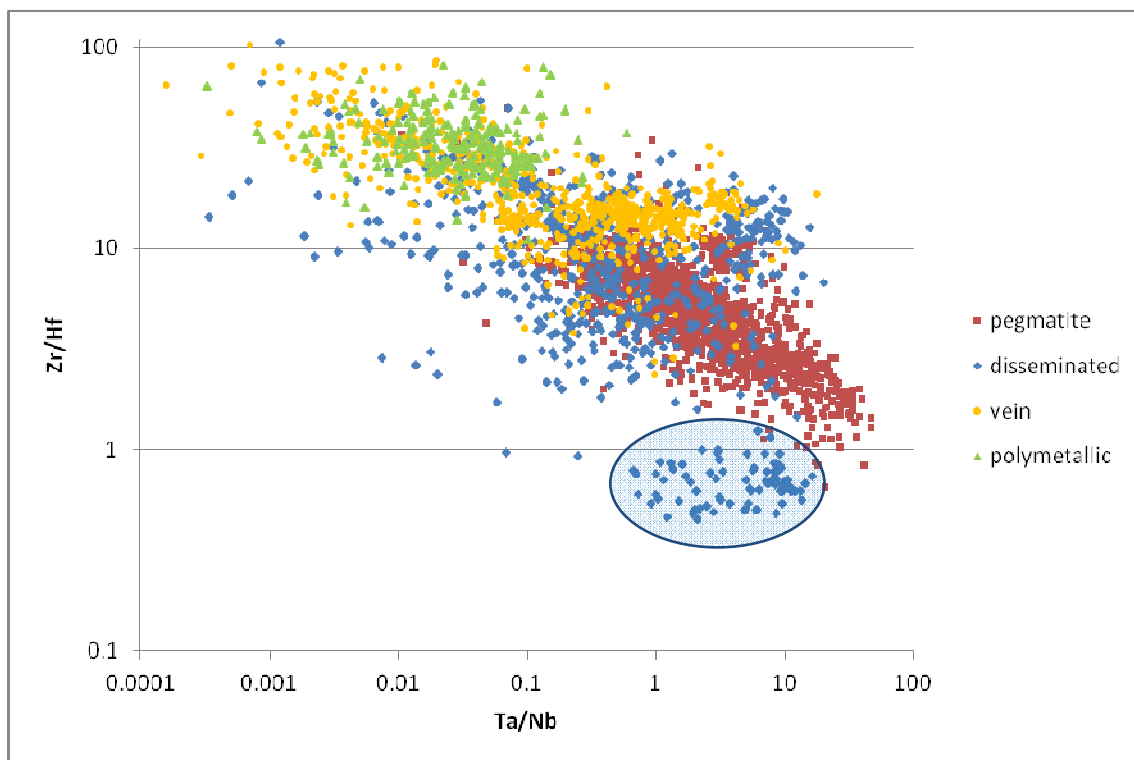


Figure 11.2: Binary diagram showing the Zr/Hf versus Ta/Nb ratios from LA-ICP-MS analysis of cassiterite originating from different deposit types, namely pegmatite (red squares), disseminated or greisen (blue diamonds), hydrothermal vein (yellow circles), and polymetallic vein (green triangles) deposits, respectively. Note the distinct cluster (marked by the ellipse) of values for cassiterite from disseminated deposits below the pegmatite field. This cluster is made up by analyses of cassiterite from the Abu Dabbab and Nuweibi rare metal granite deposits.

Hafnium becomes relatively enriched compared to Zr during magmatic differentiation and the latest fractions of crystallisation have low Zr/Hf ratios (Möller & Dulski, 1983). Consequently, cassiterite from pegmatite deposits has low Zr/Hf ratios ranging from 1 to 10 (about 5 as stated by Möller & Dulski, 1983) with also highest total amounts of Zr and Hf. On the contrary, hydrothermal cassiterite (from quartz veins or from the polymetallic vein deposits of the Bolivian Tin Belt) is characterised by Zr/Hf ratios larger than 10 (approximately 30 as reported by Möller & Dulski, 1983) with lower Zr and Hf contents in total (Figure 11.2). The Zr/Hf ratios of disseminated greisen deposits are situated somehow in-between but more closely linked to the hydrothermal fraction of the trend. As shown in Figure 11.2, the Zr/Hf ratio can be used to discriminate different deposit types and reveal the respective conditions of formation for cassiterite (hydrothermal versus magmatic). For example, the cassiterite grains from the Abu Dabbab and Nuweibi deposits were classified as disseminated type, but the data form a distinct cluster in the Zr/Hf versus Ta/Nb diagram with Zr/Hf ratios below 1 (Figure 11.2). This reflects the true magmatic formation of disseminated cassiterite in the cupola of these rare-metal granite deposits.

Iron occurs in two oxidation states either as Fe²⁺ (ferrous) or Fe³⁺ (ferric). The Fe³⁺ ion (0.65 Å) more readily substitutes for Sn⁴⁺ in the cassiterite lattice than Fe²⁺ (0.78 Å) because of the smaller charge difference. However, both Fe species enter the cassiterite lattice depending on the genetic environment. Cassiterite precipitating from oxidised fluids has higher Fe³⁺ contents than cassiterite depositing from reduced fluids in the presence of the Fe²⁺ (Hennigh, 1993). Besides oxygen fugacity, Murciego et al., (1997) stated that Fe²⁺ preferentially occurs at high temperature conditions above 300 °C whereas Fe³⁺ is present at lower temperatures. High Fe amounts of up to 7.8 wt.% are observed in wood tin (Lufkin, 1977); it is assumed that most of the Fe is present in the form of Fe³⁺ as wood tin forms under oxidising conditions. Excess of Fe³⁺ at oxidising conditions is probably compensated by the presence of OH⁻ groups in the cassiterite lattice (Dusausooy et al., 1988; Ruck et al., 1989; Costi et al., 2000; Losos & Beran, 2004).



The concentrations of the base metals Cu, Zn, and Pb are generally low in cassiterite from any Sn deposit types, even in massive sulphide deposits which are significantly enriched in base metals as stated by Hennigh (1993). The base metal cations Cu⁺ (0.77 Å), Cu²⁺ (0.73 Å), Zn²⁺ (0.74 Å), Pb²⁺ (1.19 Å), and Pb⁴⁺ (0.78 Å) do not

enter the cassiterite lattice because of their significantly differing behaviour in hydrothermal fluids compared to Sn (see above). However, some pegmatite deposits are characterised by elevated Zn contents (Figure 10.17). This indicates that Sn and Zn may be transported and precipitated cogenetically under magmatic conditions. Interestingly, some cassiterite analyses show Pb in significant amounts, but these concentrations most likely represent radiogenic Pb from the radioactive decay of U. This assumption is underpinned by the observation that Pb positively correlates with age and no 'excess Pb' (values for Pb considerably above the drawn line in Figure 11.3) is present in cassiterite of younger ages (Figure 11.3). As a consequence, this means that a minimum formation age can be roughly estimated for an unknown sample using the Pb concentration.

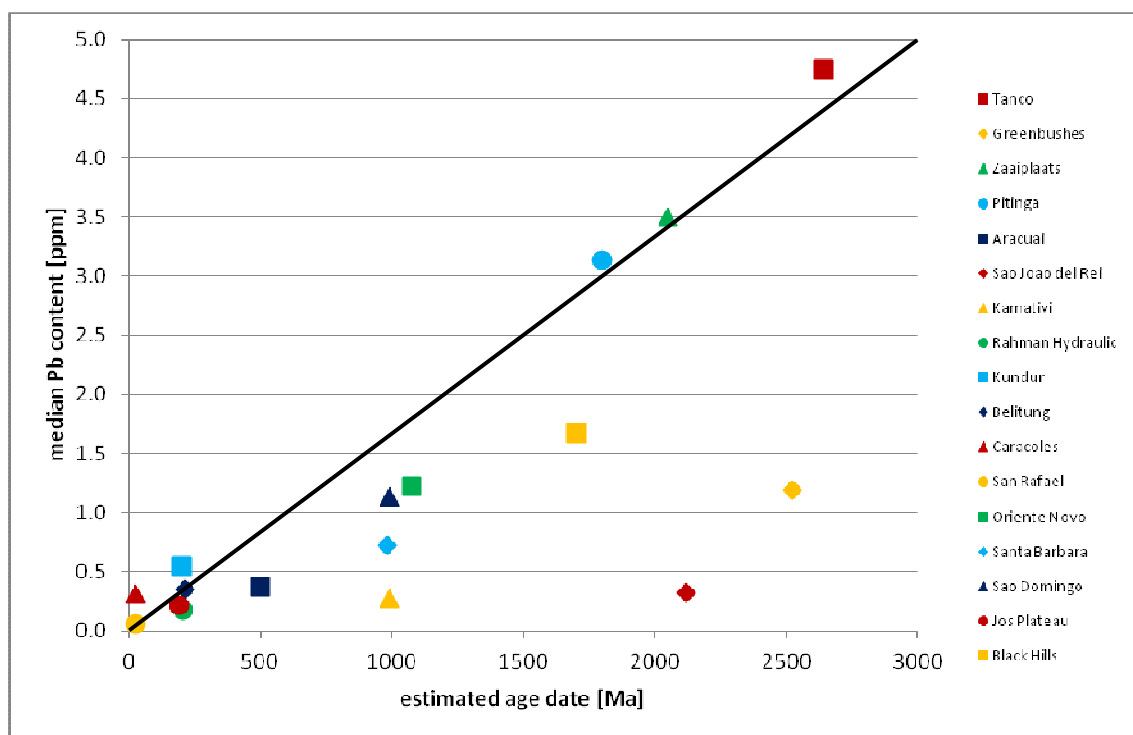


Figure 11.3: Diagram showing a correlation of the median Pb concentration in cassiterite versus the geological age of the deposit. The Pb value is given as median of the single LA-ICP-MS cassiterite analyses of the individual concentrate in ppm. Corresponding age data for the respective deposits are taken from the literature (references for each deposit are mentioned in results chapter) as an estimation for the formation age of the cassiterite mineralisation.

Tungsten occurs in the cassiterite lattice in its hexavalent state with an ionic radius of 0.6 Å. High W contents in cassiterite are interpreted to be indicative for an origin from a magmatic source (Seifert et al. 1997, Hennigh & Hutchinson 1999), but this suggestion cannot be confirmed as high W contents are also encountered in hydrothermal deposits (e.g. Figure 10.17). Wolframite and cassiterite coexist in some deposits, e.g. greisen and

quartz vein deposits, but both may precipitate at different stages of ore formation. Cassiterite is W-poor if it forms at low temperatures after precipitation of wolframite, whereas cassiterite precipitating at higher temperatures shows higher W concentrations (Hennigh, 1993; Taylor, 1979).

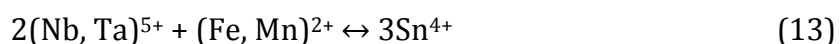
The correlation of W and Fe indicates coupled substitution of both metals for Sn after the two following mechanisms (Möller et al., 1988) as Fe may occur in two oxidation states. Trivalent iron and W^{6+} are probably incorporated by coupled substitution following solid solution of cassiterite and Fe_2WO_6 (Formula 11, Möller et al., 1988). In contrast, coupled substitution of W^{6+} with Fe^{2+} indicates solid solution of ferberite ($FeWO_4$) in cassiterite (Formula 12, Möller et al., 1988; Neiva, 1996). Manganese may be incorporated into cassiterite in a similar way (12). The coupled substitution of W^{6+} and Mn^{2+} (0.83 Å) represents the solid solution of hübnerite ($MnWO_4$) in cassiterite (Gan & Chen, 1994).



Generally, the concentration of Fe is higher than Mn and the very rare occurrences of cassiterite with Mn dominating over Fe are restricted to lepidolite-rich pegmatites (Černý et al., 2004; Masau et al., 2000). Highest Mn concentrations are measured in cassiterite from highly evolved pegmatite deposits and this probably indicates that Mn is preferentially incorporated under magmatic conditions by coupled substitution with Nb^{5+} and Ta^{5+} (see below).

Niobium and Ta behave geochemically very similar; both generally occur in the pentavalent oxidation state and have the same ionic radius of 0.64 Å. Niobium and Ta occur most likely in the pentavalent state at oxidising conditions during cassiterite formation, but the occurrence of tetravalent Nb and Ta (both 0.68 Å) is also proposed (Möller et al., 1988; Murciego et al., 1997). Highest Nb and Ta concentrations are found in cassiterite from high temperature deposits associated with granitic pegmatites which confirms the observations of Dudykina (1959) and Steveson & Taylor (1973). As revealed by X-ray element maps (Figure 10.14), Ta and Nb are especially concentrated in the cores of magmatic cassiterite crystals which are interpreted to be in equilibrium with the initial melt composition from which this early core-forming cassiterite precipitates. The rim of these cassiterite crystals is commonly depleted in Ta and Nb as the melt composition changes due to crystallisation of Ta-Nb phases like columbite-tantalite or incorporation of these elements into early magmatic phases like cassiterite.

Cassiterite from pegmatite deposits is also characterised by a predominance of Ta over Nb (Ta/Nb of about 1 or higher), but Nb generally occurs in higher amounts than Ta in other deposit types (Figures 11.2 & 11.4). This may be the result of the greater natural abundance of Nb in the earth's crust compared to Ta (Möller et al., 1988). Möller et al. (1988) also suggested preferential incorporation of Nb in its tetravalent state into the cassiterite lattice, whereas Ta prefers the pentavalent form. Coupled substitution of Nb⁵⁺ and Ta⁵⁺ with Fe²⁺ and Mn²⁺ for Sn⁴⁺ represents the isomorphous solid solution series of tapiolite (FeTa₂O₆) and cassiterite as both crystallise in the tetragonal crystal system (Dunn et al., 1978; Černý & Ercit, 1985; Möller et al., 1988; Neiva, 1996; Wise & Černý, 1996). High tapiolite contents may be present in natural cassiterite (Černý & Ercit, 1985; Groat et al., 1994) and high Sn concentrations of about 4 mol-% SnO₂ are found in tapiolite (Wise & Černý, 1996). Submicroscopic intergrowth of cassiterite and tapiolite is termed 'staringite' which represents exsolution of a high temperature solid solution phase (Groat et al., 1994). High Mn concentrations in cassiterite with Mn > Fe is only found in highly evolved pegmatites of the lepidolite subtype (Černý et al., 2004).



Fractionation of magmatic cassiterite is also indicated by compositional trends in the 'columbite quadrilateral' (Figures 11.4 & 11.5). The general fractionation trend of cassiterite from pegmatites and rare metal granites is characterised by a two-step evolution with initial Ta enrichment compared to Nb followed by increasing Mn/(Mn+Fe) values (Figures 11.4 & 11.5), but much less fractionated compositions with significantly lower Ta/(Ta+Nb) values are also evident (e.g., Gahapfu in Figure 11.5). This general cassiterite evolution path is oppositional to the common fractionation trend of columbite-tantalite minerals which compositionally starts with enrichments in Mn from columbite-(Fe) towards columbite-(Mn) and then turns to tantalite-(Mn) at higher Ta/(Ta+Nb) ratios (Figure 11.4; Černý, 1992; Melcher et al., 2015).

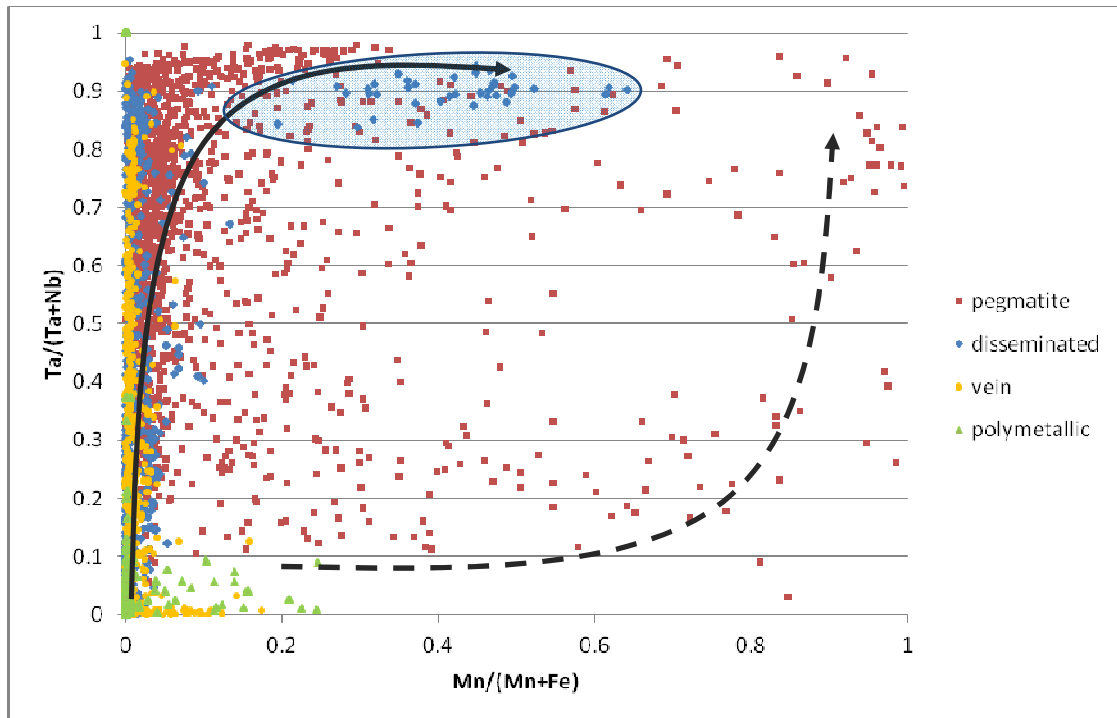


Figure 11.4: 'Columbite quadrilateral' showing the $Ta/(Ta+Na)$ and $Mn/(Mn+Fe)$ compositions from LA-ICP-MS analysis of cassiterite originating from different deposit types, namely pegmatite (red squares), disseminated (blue diamonds), hydrothermal vein (yellow circles), and polymetallic vein (green triangles) deposits, respectively. Note the distinct cluster (marked by the ellipse) of values for cassiterite from the Abu Dabbab and Nuweibi rare metal granite deposits. Solid arrow indicates the major fractionation path of magmatic cassiterite and the dashed arrow generalises the fractionation trend of columbite-tantalite.

Similar evolutionary trends were also observed by Černý et al. (2004) in cassiterite and columbite-tantalite from Varuträsk pegmatite, Sweden. The contrasting cassiterite and columbite-tantalite fractionation trends are controlled by the different crystal structures. Tetragonal rutile-type minerals like cassiterite and tapiolite preferentially incorporate Fe and Ta, whereas orthorhombic columbite-type minerals more readily concentrate Mn and Nb (Černý & Ercit, 1985; Černý & Ercit, 1989; Černý et al., 2004). Figure 11.4 also shows that cassiterite from deposits with hydrothermal influence just scatter in their $Ta/(Ta+Na)$ ratios, but remain at rather low $Mn/(Mn+Fe)$ values because Fe is a major element in cassiterite from these deposits at constantly low Mn concentrations.

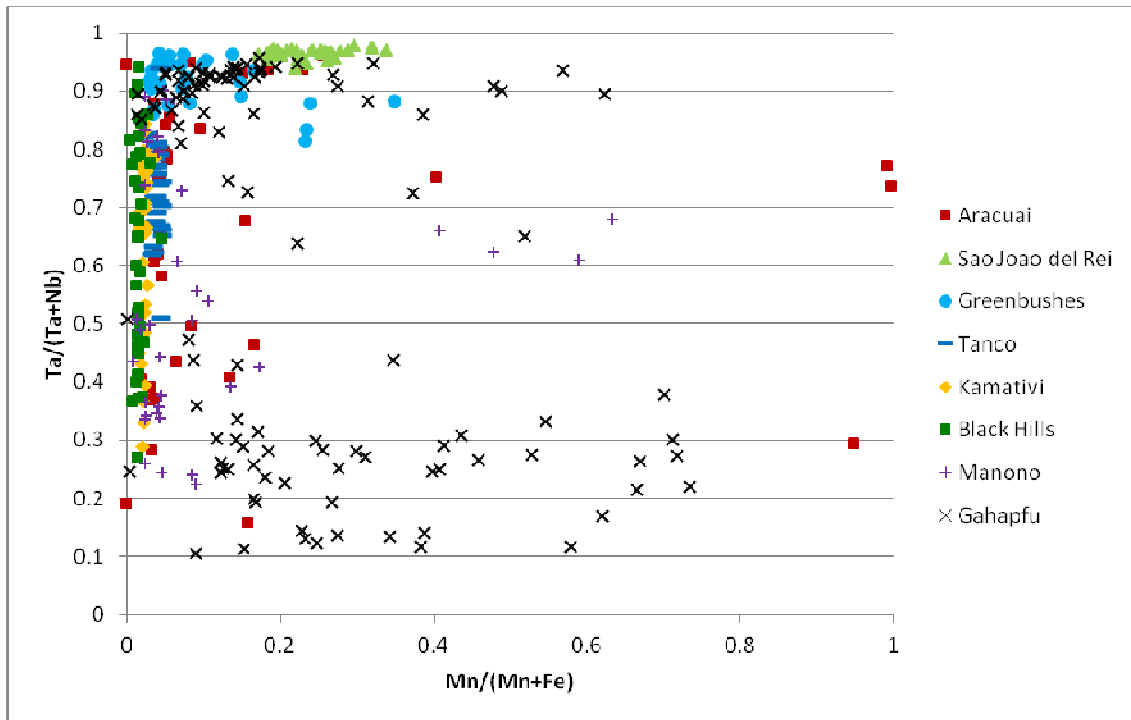


Figure 11.5: 'Columbite quadrilateral' showing the Ta/(Ta+Na) and Mn/(Mn+Fe) compositions from LA-ICP-MS analysis of cassiterite originating from selected pegmatite deposits.

However, coupled substitution of pentavalent niobium and tantalum with trivalent iron for tin is also suggested by some authors (Ramdohr, 1975; Izoret et al., 1985; Dusausoy et al., 1988; Möller et al., 1988; Ruck et al., 1989; Murciego, 1997).



Highest Sc concentrations are generally found in cassiterite from greisen deposits (Borisenko & Lizunov, 1959; Binde, 1986). Scandium concentrations in cassiterite from pegmatite deposits are generally low, which is contrary to the observations of Dudykina (1959). However, some pegmatite deposits also show significant Sc enrichments in cassiterite such as the Greenbushes pegmatite, Western Australia and the Tanco pegmatite, Canada. Scandium is enriched in pyroxenes and other mafic minerals (Melcher et al., 2015) and therefore Sc seems to be mobilised from surrounding mafic igneous country rocks hosting the pegmatite bodies. This is in agreement with the geological settings of the Greenbushes and Tanco pegmatites which intruded into amphibolites and metagabbro, respectively. Wood & Samson (2006) state that Sc is transported in the form of hydroxide complexes in most hydrothermal fluids, but fluoride complexes are important in environments with high F activities like greisen formation. This corresponds to the observations that highest Sc concentrations are found in cassiterite from greisen deposits. Several authors observed positive correlation

of Nb with Sc (0.75 Å for Sc³⁺) indicating coupled substitution of both metals for Sn at high temperatures (Borisenko & Lizunov, 1959; Möller et al., 1988; Kempe & Wolf, 2006).



Some authors discuss the isomorphous substitution of Sn by tetravalent niobium and tantalum which represents the solid solution of (Nb, Ta)⁴⁺O₂ and SnO₂ (Möller et al., 1988; Murciego et al., 1997). Nevertheless, this substitution reaction is unlikely because strongly reducing conditions are required for the existence of tetravalent niobium and tantalum, which are contrary to the oxidising conditions generally present during cassiterite formation.

Gallium (0.62 Å for Ga³⁺) occurs in concentrations of up to several tens of ppm and is a very characteristic element for the Bolivian Tin Belt. The Ga content in cassiterite from the Bolivian Tin Belt was used to discriminate the Mesozoic deposits with low Ga concentrations from the Miocene deposits which are significantly enriched in Ga (Fesser, 1968; Binde, 1986). The different Ga concentrations reflect different degrees of alteration associated with the two contrasting deposit types. Binde (1986) states that Ga is mobilised by the breakdown of feldspars (substitution of Al³⁺ ↔ Ga³⁺ in the feldspar structure); and Ga is transported as hydroxide and fluoride complexes in hydrothermal fluids (Wood & Samson, 2006). Therefore, the higher Ga contents in cassiterite from the porphyry deposits are most likely controlled by the much stronger hydrothermal alteration of the porphyritic host rocks (compared to the pluton-related deposits) causing liberation of Ga by the breakdown of feldspars and subsequent incorporation into cassiterite which precipitates from the hydrothermal fluids (Figure 11.6).

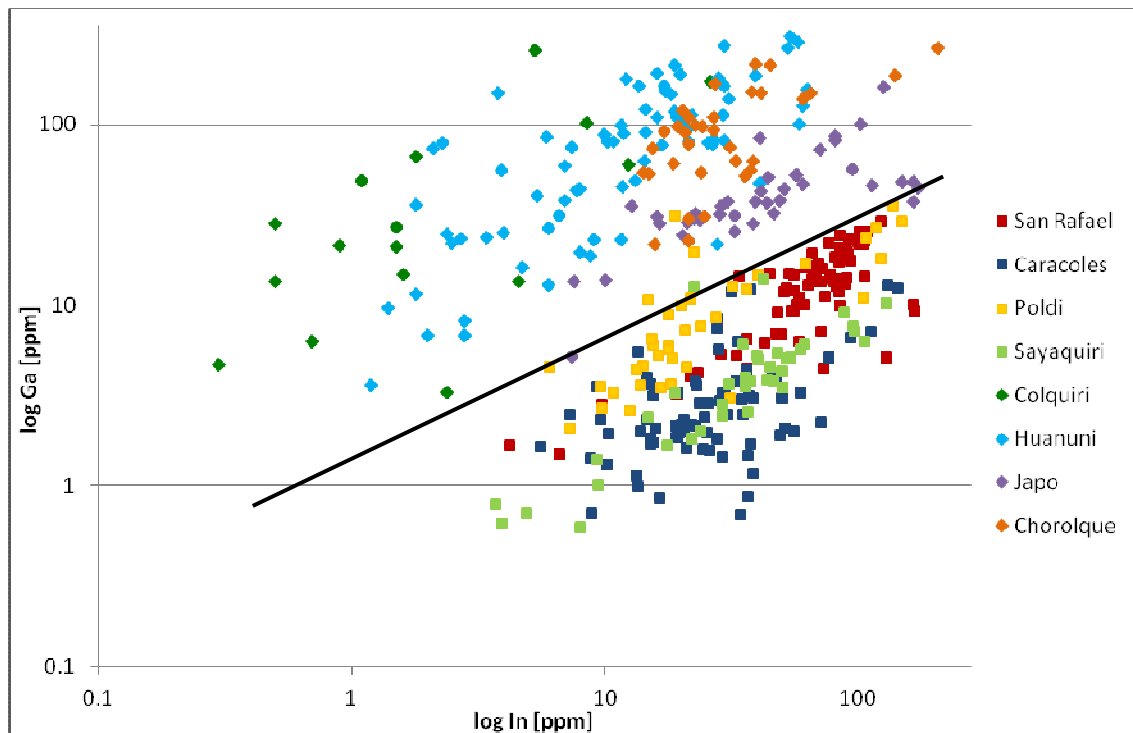


Figure 11.6: Binary plot showing the Ga versus In concentration of cassiterite from deposits of the Bolivian Tin Belt. The line clearly separates the pluton-related deposits (squares) from the porphyry deposits (diamonds).

Raimbault et al. (1999) reported In and Ga concentrations from hydrothermal cassiterite ranging from 0.03 to 300 ppm In and 0.4 to 200 ppm Ga, respectively. High In and Ga contents are found in cassiterite related to high-P fractionated rare-metal granites like Echassières and Montebras from the French Massif Central (Raimbault et al., 1999). The In/Ga ratio may vary over more than three orders of magnitude, but is relatively constant for single deposits and this observation makes the In/Ga ratio a promising parameter to discriminate individual deposits.

Fesser (1968) also mentioned a remarkable distribution of Nb and Ga in cassiterite of the Bolivian Tin Belt with a systematic decrease of Nb from north to south and Ga showing an oppositional trend. These observations are not confirmed by the data of this study with San Rafael as the northernmost and Chorolque as the southernmost deposit (Figure 11.7).

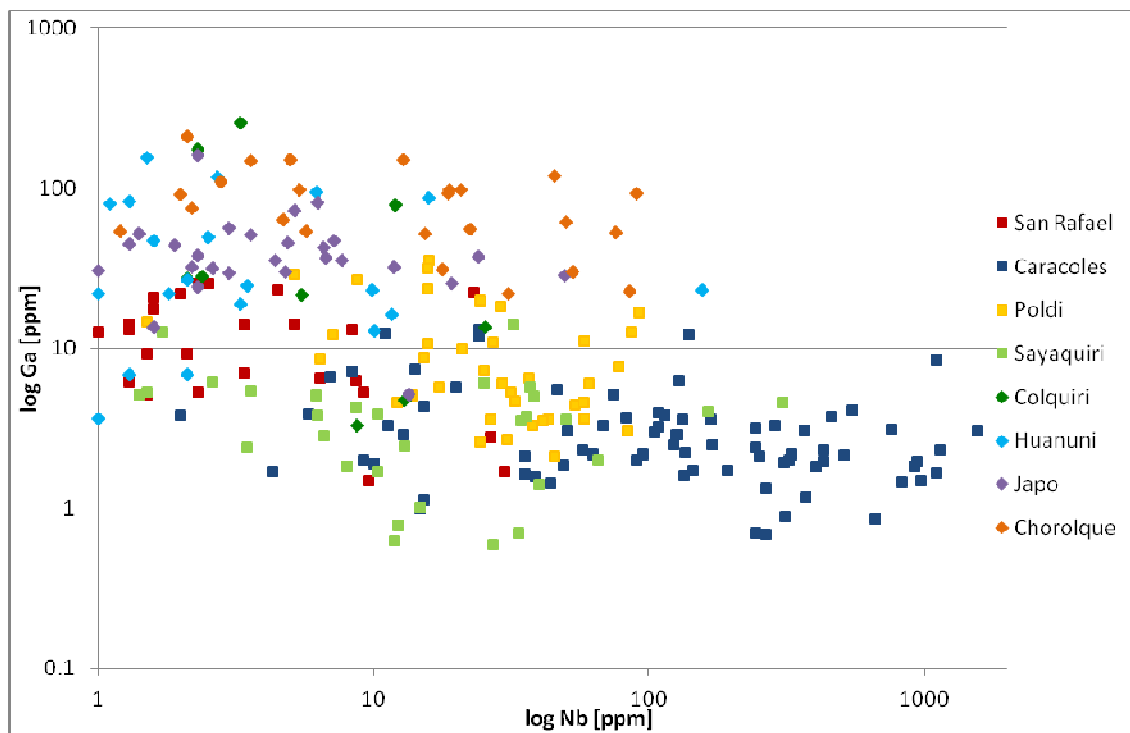


Figure 11.7: Binary diagram showing the concentrations of Nb [ppm] versus Ga [ppm] from LA-ICP-MS analysis of cassiterite originating from different deposit types of the Bolivian Tin Belt. The top down arrangement of the deposits in the legend corresponds to their distribution from north to south.

Indium occurs in the trivalent state with an ionic radius of 0.8 \AA and substitution is most likely coupled to incorporation of pentavalent cations like Nb and Ta. But there is a strong correlation of Fe and In in cassiterite (Figure 11.8), which indicates coupled substitution of these two for Sn (Ivanov & Rozbianskaya, 1961). Two distinct trends are identified which indicates coupled substitution of In and Fe at two different proportions. The high In trend, which is markedly present in cassiterite from Geovor mine, may be interpreted by a possible coupled substitution of Sn by In and divalent Fe according to (16). However, it has to be kept in mind that Fe occurs in concentration levels of more than 1 order of magnitude higher than In; consequently Fe is also incorporated by additional mechanisms.



The other trends can be explained by coupled substitution of In with Fe^{3+} present according to previous reactions (10), (11), and (14) where available In is concurrently incorporated with Fe.

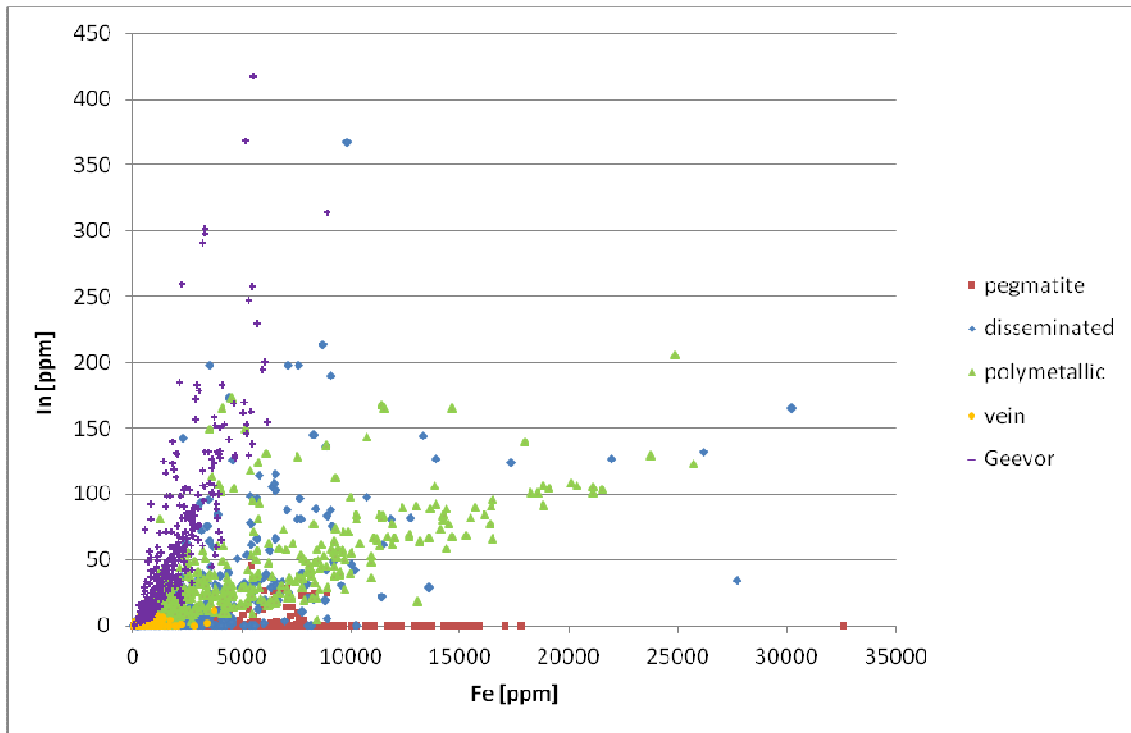


Figure 11.8: Binary diagram showing the concentrations of Fe [ppm] versus In [ppm] from LA-ICP-MS analysis of cassiterite from ore concentrates originating from different deposit types, namely pegmatite (red squares), disseminated or greisen (blue diamonds), hydrothermal vein (yellow circles), and polymetallic vein (green triangles) deposits, respectively. Additionally, results from Geevor samples (purple crosses) are also plotted.

Elevated In concentrations in cassiterite from massive sulphide deposits are interpreted to derive from minute sphalerite inclusions (Hennigh & Hutchinson 1999; Schwarz-Schampera, 2000). Steveson & Taylor (1973) state that cassiterite with high In concentrations are found in deposits with low sulphide contents, whereas Dudykina (1959) reported the opposite with highest In concentrations in cassiterite from cassiterite-sulphide deposits. Our data support the observations of Dudykina (1959), because highest In concentrations are analysed in cassiterite from the sulphide-rich deposits of the Bolivian Tin Belt, which also contain elevated In contents in sphalerite (Ishihara et al., 2011). However, it cannot be excluded that these elevated In concentrations in cassiterite are caused by submicroscopic sphalerite inclusions. High In concentrations (up to 2.0 wt.%) are also found in wood tin (Fesser, 1968; Taylor, 1979 and references therein; Botelho & Moura, 1998), but In is absent in wood tin from Cornwall (Hosking et al., 1987). Indium-rich cassiterite ranging between 0.2 and 0.4 wt.% In is also found in greisen mineralisation associated with A-type granitic magmatism in central Brazil (Botelho & Moura, 1998). Further analytical data on In

concentrations in cassiterite from various localities worldwide (with special emphasis on the Erzgebirge) are compiled by Seifert & Sandmann (2006). Indium concentrations in cassiterite from pegmatites are generally low (Figure 11.8). According to Wood & Samson (2006), In may be transported as hydroxide, fluoride, chloride and bisulphide complexes in hydrothermal fluids. This also underlines low In concentrations in magmatic systems like pegmatites.

The semi-metals antimony (0.76 Å for Sb^{3+} , 0.6 Å for Sb^{5+}) and arsenic (0.58 Å for As^{3+} , 0.46 Å for As^{5+}) are very characteristic for some tin deposits. Both metals are most likely present in their trivalent state in cassiterite. Highest Sb and As concentrations are found in cassiterite from the polymetallic vein deposits from Bolivia and correlate positively with Fe, which indicates a similar substitution mechanism as In according to (16). Antimony and As are generally below the detection limit in cassiterite from pegmatites, but there are a few exceptions such as the pegmatites from Greenbushes, Western Australia and Manono, Katanga Province, Democratic Republic of Congo. Cassiterite from the Greenbushes pegmatite exhibits anomalously high Sb and As concentrations. The unique mineral paragenesis of the Greenbushes pegmatite is underlined by the occurrence of other rare Sb-bearing minerals such as stibiotantalite ($\text{Sb}^{3+}\text{TaO}_4$).

Tin is most likely substituted by U and V in their tetravalent states, although these are redox-sensitive elements occurring in several valence states. For example, V^{4+} was detected in V-doped SnO_2 by electron paramagnetic resonance (EPR) analysis (Ningthoujam et al., 2007). Although the ionic radius of V^{3+} (0.64 Å) is closer to that of Sn^{4+} , V^{4+} (0.58 Å) seems to be the dominating species under oxidising conditions of cassiterite formation (Toplis & Corgne, 2002). In this case, substitution is dominated by valence state rather than ionic radius. Highest V contents are found in cassiterite from hydrothermal vein deposits and this implies that V is probably mobilised from the surrounding country rocks (in particular shales or mafic rocks). The same seems to be applicable for U, where the most common valences states are U^{4+} (0.89 Å) and U^{6+} (0.73 Å) in minerals (Burns, 1999). As the ionic radius of the U^{4+} cation is significantly too large, incorporation into the cassiterite lattice is probably only feasible under high temperature conditions of cassiterite formation. However, natural radiation will cause defects in the crystal structure of the hosting cassiterite and U^{4+} will at least partially oxidise (Burns, 1999). In terms of ionic radius, the U^{6+} may easily substitute for Sn at highly oxidising conditions provided that the charge difference is balanced by coupled

substitution (e.g., with divalent cations). Manganese may also replace Sn in cassiterite in its tetravalent state (0.53 Å), because the most abundant Mn oxide pyrolusite (MnO₂) and cassiterite crystallise in the same rutile-type crystal structure. However, the highest Mn contents are found together with the highest Nb and Ta concentrations in cassiterite from pegmatite deposits and this supports the coupled substitution of pentavalent cations (Nb⁵⁺, Ta⁵⁺) with Mn and Fe in their divalent valence states according to (13).

Substitution of Sn by several elements causes a change in the cell parameters of cassiterite and may, as a consequence, favour the further incorporation of other trace elements. Some substituting elements like Fe, Ti, and Zr lead to an increase in cell size. For example, substitution of Sn by Zr causes a slight increase of the cell parameters of cassiterite to $a = 4.76 \text{ \AA}$ and $c = 3.20 \text{ \AA}$ (compared to $a=4.738 \text{ \AA}$ and $c=3.188 \text{ \AA}$; Lide, 2009) for SnO₂ containing 20% ZrO₂ (Stöcker & Collongues, 1957). Otherwise another suite of elements like Nb and Ta induce decreasing cell parameters (Stöcker & Collongues, 1957; Walia 1971; Clark et al., 1976).

Summarising, cassiterite from quartz vein deposits generally shows high concentrations in V, Sc, In, and Ti. Magmatic cassiterite from pegmatite deposits and rare element granites has generally higher trace element contents in total and is particularly enriched in Ta, Nb, Zr, Hf, Mn, and Zn. Trace element composition of cassiterite from greisen deposits is somehow in-between hydrothermal and magmatic cassiterite but with high additional In and W contents, which also reflects the transitional setting of this deposit type. The higher total concentration of trace elements in cassiterite from magmatic deposits is probably due to the higher temperature of formation. At high temperatures the crystal lattice is disordered and trace elements enter the cassiterite structure more easily.

The analysis of trace elements in cassiterite from different ore deposit types permits classification of cassiterite of unknown origin into a particular type of ore deposit. Consequently, the trace element characteristics can be also used in mineral exploration. For example, the trace element composition of cassiterite from alluvial placers can give indication for a specific type of primary tin deposit in the drainage area (Yim, 1994). But it needs to be kept in mind that placer deposits may represent an accumulation of minerals originating from different deposits (even deposit types) scattered over a large area. Samples from alluvial placers therefore might represent mixed samples from various deposits or mine sites situated in the drainage area, whereas eluvial deposits most likely represent one single deposit.

Colour of cassiterite is controlled by the incorporation of trace elements. The higher the total trace element concentration, the darker the colour of cassiterite (Figure 10.19). As stated by several authors, the colour of cassiterite from massive sulphide deposits exhibits low trace element contents and is commonly colourless, whereas cassiterite from other deposit types (e.g., pegmatite or greisen deposits) is variable ranging from dark black, reddish brown to yellow (e.g., Ollila, 1986; Hennigh, 1993; Neiva, 1996; Murciego et al., 1997). Deep red cassiterite contains Fe and is significantly enriched in Ta compared to Nb (Neiva, 1996; Chicharro et al., 2015). Strong pleochroism of cassiterite is usually associated with high amounts of Fe, Ta, and Nb (Ollila, 1986; Neiva, 1996; Chicharro et al., 2015). Additional parameters influencing the colour of cassiterite are the oxidation state of iron (Fe^{2+} or Fe^{3+}) as the colour of cassiterite also lightens with increasing $\text{Fe}^{3+}/\text{Fe}^{2+}$ ratio (Grubb & Hannaford, 1966; Murciego et al., 1997) and Frenkel defects which cause anisotropic deformation of the cassiterite lattice and generation of colour centres (Goncharov & Filatov, 1971; Hennigh, 1993).

11.2.2 Trace elements in wolframite

The chemical composition of wolframite was also studied by other authors (Table 11.3; Saari et al., 1968; Groves & Baker, 1972; Voyevodin, 1981; Oen et al., 1982; Gu & Schröcke, 1986; Nakashima et al., 1986; Aïssa et al., 1987; Polya, 1988; Novák & Šrein, 1989; Tindle & Webb, 1989; Zhang et al., 1990; Cuney et al., 1992; Gan & Chen, 1992; Kempe & Belyatsky, 1994; Kempe & Wolf, 1994; Seifert, 1994; Mignardi et al., 1998; Belkasmi et al., 2000; Breiter & Škoda, 2004; Ferenc & Uher, 2007; Barkov et al., 2008; Neiva, 2008; Somarin, 2009; Llorens & Moro, 2012b). Again, although several studies worked on the chemical composition of wolframite, only major or at least minor elements were analysed.

Table 11.3: Chemical composition of wolframite by different analytical methods (EPMA = electron probe microanalysis, AAS = atomic absorption spectroscopy, XRF = X-ray fluorescence) compiled from the literature. Analyses are given in wt.% element oxide or ppm element, 0 values are below detection limit. Original data from Ferenc & Uher (2007) and Barkov et al. (2008) in wt.% ZnO were converted into ppm Zn and original element ppm for Nb, Ta, Sn, and Sc from Gan & Chen (1992) were converted into wt.% of the respective element oxide for comparability.

Reference	Sample locality	Method	n	data	WO ₃ (wt.%)	MnO (wt.%)	FeO (wt.%)	Fe ₂ O ₃ (wt.%)	CaO (wt.%)	MgO (wt.%)	Nb ₂ O ₅ (wt.%)	Ta ₂ O ₅ (wt.%)	TiO ₂ (wt.%)	SnO ₂ (wt.%)	ZrO ₂ (wt.%)	Sc ₂ O ₃ (wt.%)	Zn (ppm)	Cu (ppm)	Pb (ppm)	Cd (ppm)	Co (ppm)	Ni (ppm)	
Saari et al. (1968)	Nuaparra	XRF	1		45.1	7.76	7.43	8.43			20.25	5.35	2.68	1.52									
Moore & Howie (1978)	St. Michal's Mount	EPMA	8	range	75.3-75.92	7.31-15.19	8.84-16.27		0.01-0.02		0.13-0.29												
Moore & Howie (1978)	Cligga Head	EPMA	8	range	75.59-76.12	4.74-12.98	10.56-18.46		0-0.01		0.06-0.56												
Moore & Howie (1978)	Chasewater	EPMA	8	range	75.41-75.91	5.36-15.73	7.42-18.51		0.01		0.16-0.41												
Moore & Howie (1978)	South Crofty	EPMA	8	range	75.63-76.65	5.13-16.39	6.60-18.32		0.01		0.16-0.46												
Ivanova et al. (1985)	Yugodzyr	?	18	mean	31.39	9.61						0.060			0.041								
Ivanova et al. (1985)	Kyzyl Tau	?	10	mean	25.27	7.73						0.033			0.027								
Ivanova et al. (1985)	Tsagaan Davaa	?	12	mean	27.56	8.44						0.013			0.010								
Ivanova et al. (1985)	Modoto	?	10	mean	34.46	10.54						0.006			0.004								
Nakashima et al. (1986)	Kaneuchi	EPMA	14	range	73.89-76.67	9.07-18.52	4.96-14.2		0.02-0.08	0.09-0.28	0.43-0.82	0-0.51											
Aïssa et al. (1987)	Echassières	EPMA	12	range	62.19-76.73	1.22-8.08	15.13-21.83				0.02-5.77	0-0.16											
Tindle & Webb (1989)	Glen Gairn (low Nb)	EPMA	8	range	72.18-74.96	17.34-23.42	0.73-5.91		0-0.13		0.21-3.43	0-1.02		0.04-0.29	0.1-0.32								
Tindle & Webb (1989)	Glen Gairn (high Nb)	EPMA	8	range	31.09-68.69	4.81-16.84	3.7-16.23		0.2-3.76		3.61-7.93	0.5-6.95		0.3-1.01	0.32-0.87								
Gan & Chen (1992)	Dupangling	?	8	range	74.13-75.08	11.82-13.72	9.99-12.34				0.023-0.09	0.008-0.058		0.048-0.19	0.006-0.025								
Mignardi et al. (1998)	Panasqueira	EPMA/AAS	182	range	73.6-76.86	1.86-6.23	16.16-21.79										150-457	63-706	34-150	10-34	30-91	102-328	
Belkasmí et al. (2000)	Yichun	EPMA	6	range	72.13-75.2	9.02-20.97	0.31-11.96	1.52-4.5			0.52-1.68	0-0.37		0-0.1									
Ferenc & Uher (2007)	Ochtiná	EPMA	6	range	77.57-79.72	1.64-3.83	8.45-14.32	0-0.13	0-0.03	3.33-7.75	0-0.05	0-0.07	0	0-0.08	0	0-0.05	0						
Barkov et al. (2008)	Canadian Creek	EPMA	15	range	75.75-77.01	0.46-21.93	1.36-23.0		0-0.06	0.01-1.65	0-0.15		0-0.11				0-884						
Neiva (2008)	quartz vein (W>Sn)	EPMA	18	range	72.19-76.22	3.13-22.62	0.9-21.9				0-1.88	0-0.05	0-0.11	0-0.08									
Neiva (2008)	quartz vein (Sn>W)	EPMA	4	range	73.57-74.95	7.86-16.24	8.15-16.54				0.3-0.94	0.07-0.21	0-0.03	0-0.06									
Somarin (2009)	Glen Eden	EPMA	27	range	75.98-79.22	2.96-20.1	3.38-18.45		0-0.5														
Llorens & Moro (2012b)	Jálama Batholith	EPMA	6	range	74.6-76.36	1.98-16.09	6.78-21.5		0-0.03		0.17-0.47	0-0.07	0-0.08	0-0.06	0.7-0.9								
Llorens & Moro (2012b)	Vale das Gatas	EPMA/AAS	82	range	74.36-75.82	19.71-22.18	1.68-3.41										216-231	36-135	40-88	23-50	23-58	91-141	

Wolframite forms a solid solution series between the two endmembers ferberite ($\text{Fe}^{2+}\text{WO}_4$) and hübnerite ($\text{Mn}^{2+}\text{WO}_4$) by diadochous substitution of Fe and Mn. Generally, the major element composition of wolframite in terms of Fe and Mn is relatively homogenous within a single deposit (Kempe & Wolf, 1994; Mignardi et al, 1998) and also in individual quartz veins over rather large distances (Neiva, 2008). This is also demonstrated in the case study on Nyakabingo below. Substitution is strongly dependent on the crystal structure and available space on specific sites. For example, tungstates with the general formula AWO_4 (like wolframite and scheelite) crystallise in the scheelite structure if the radius of the cation on the A site is greater than 0.9 Å, whereas the wolframite structure is preferred if the radius of the A^{2+} cation is less than 0.9 Å (Hazen et al., 1985; Macavei & Schulz, 1993). Generally, large cations like Sr^{2+} , Pb^{2+} and Ba^{2+} are found in the scheelite-type structure, whereas small cations such as Mg^{2+} , Zn^{2+} and Ni^{2+} are preferentially incorporated into the wolframite-type structure (Hazen et al., 1985; Ghaderi et al, 1999; Kuzmin & Purans, 2001).

Iron and Mn are present in sixfold coordination in the wolframite lattice with ionic radii of 0.78 Å for Fe^{2+} and 0.83 Å for Mn^{2+} , respectively. Divalent cations with suitable ionic radii, for example Mg^{2+} (0.72 Å), Zn^{2+} (0.74 Å), Co^{2+} (0.75 Å), and Cd^{2+} (0.95 Å) are readily substituted for Fe^{2+} and Mn^{2+} into the wolframite lattice by simple substitution (Co is shown exemplary for divalent elements in Figure 10.21). No crystallochemical constraints exist for the incorporation of Mg and Zn into the wolframite structure, because huanzalaite (MgWO_4) and sanmartinite (ZnWO_4) are isostructural with wolframite and solid solution series exist between wolframite group minerals (e.g., Hochleitner & Schröcke, 1985; Buhl & Willgallis, 1986; Ferenc & Uher, 2007; Barkov et al., 2008; Miyawaki et al., 2010). For example, extremely high Mg concentrations of up to 7.8 wt.% are reported for wolframite from the Zlatná Baňa occurrence, Slovakia (Figure 10.16; Ferenc & Uher, 2007) and up to 1.65 wt.% for wolframite from the Canadian Creek placer, Canada (Barkov et al., 2008). Elevated Mg concentrations are mobilised by hydrothermal fluids from the surrounding host rocks and are not directly related to the primary source of the fluids (Seifert, 1994; Ferenc & Uher, 2007).

However, incorporation of Ca^{2+} (1.0 Å), Eu^{2+} (1.17 Å), Sr^{2+} (1.18 Å), Pb^{2+} (1.19 Å), and Ba^{2+} (1.35 Å) seems unlikely because of the large differences in ionic radii compared to Fe and Mn. For example, the substitution of Ca for Fe and Mn is also limited because solid solution between wolframite and scheelite only occurs at very high temperatures

(above 600 °C; Grubb, 1967). Excess Ca is exsolved in the form of scheelite at lower temperatures (Grubb, 1967). Another limiting factor in the wolframite-scheelite solid solution series are the two contrasting crystal structure types. By far the highest Ca concentrations are found in ferberite from the Rwandan reinite (ferberite pseudomorphous after scheelite) deposits (e.g., Nyakabino, Gifurwe, Mucaca). Ferberite from these reinite deposits also shows highest concentrations in LILE such as Pb, Sr, Ba, and LREE but extremely low Zr, Hf, Nb, Ta, Sn, Ti, and Sc contents. This unusual chemical composition of the ferberite is most likely inherited from the former scheelite (Goldmann et al., 2013), because these cations (Pb, Sr, Ba, and LREE) have large ionic radii ($>0.9 \text{ \AA}$) and are preferentially incorporated into the scheelite structure (Hazen et al., 1985; Ghaderi et al., 1999; Kuzmin & Purans, 2001).

Tungsten occurs in the hexavalent state and is octahedrally coordinated in wolframite with an ionic radius of 0.6 \AA . Tungsten is frequently substituted by HFSE such as Nb, Ta, Sn, and to a lesser extent Mo. Although Mo should readily substitute for W as both exhibit nearly identical ionic radii (0.59 \AA for Mo^{6+}) and the same valence state, the Mo concentration is interestingly rather low considering these optimal substitution conditions (Figure 10.21). This is probably due to the different geochemical behaviour as Mo preferentially forms sulphides and formation of cogenetic molybdenite in tungsten deposits is common, for example in Yugodzyr (Ivanova et al., 1978) Wolfram Camp (Plimer, 1974; Kwak et al., 1986) or Mount Pleasant (Davis & Williams-Jones, 1985). However, wolframite with elevated Mo concentrations also occurs together with molybdenite in the ore paragenesis. This is for example the case in Yugodzyr (Ivanova et al., 1978), Ondor Tsagaan (Elsner et al., 2011), and Needle Hill (Davis, 1961).

Pentavalent cations like Nb and Ta (both 0.64 \AA) are commonly incorporated into the wolframite lattice because wolframite and columbite-tantalite have similar crystal structures. Incorporation of V^{5+} (0.54 \AA) seems feasible under highly oxidising conditions. Niobium is generally more abundant in wolframite than Ta and high Nb (Figure 10.20) concentrations of up to 8.0 wt.% Nb_2O_5 are reported by Tindle & Webb (1989). High Nb concentrations in wolframite are also interpreted as a solid solution series between columbite(-Fe) and ferberite (Aïssa et al., 1987). Extremely high Nb concentrations of up to 20.25 wt.% Nb_2O_5 are reported for a mineral from the Nuaparra pegmatite in Mozambique, but this possibly represents a mineralogical curiosity termed 'wolframoixiolite' (Saari et al., 1968; Tindle & Webb, 1989). 'Wolframoixiolite' was also reported from a pegmatite at Dolní Bory-Hatě, Czech Republic (Novák et al., 2008). Poly

(1988) found highest Nb concentrations in close spatial association with major faults which served as pathways for the ore-forming fluids. Seifert (1994) observed that Nb concentrations in wolframite decrease with increasing distance from the intrusion. High Ta/Nb ratios are observed in wolframite from greisen deposits in contrast to wolframite from hydrothermal veins (Gan & Chen, 1992). Higher Ta concentrations in wolframite possibly reflect the strong magmatic influence and precipitation from hydrothermal fluids of magmatic origin. In contrast, wolframite from hydrothermal deposits contains very limited amounts of Ta and Nb substituted into the crystal lattice. Breiter & Škoda (2004) stated that magmatic wolframite is enriched in Nb and Ta, but hydrothermal wolframite is characterised by Sc. Niobium, Ta and possibly V⁵⁺ are substituted for W into the wolframite lattice by coupled substitution of trivalent cations (e.g., Fe³⁺, Sc³⁺, In³⁺, Y³⁺, REE³⁺) for Fe²⁺ and Mn²⁺ (Pavlu, 1986; Polya, 1988; Tindle & Webb, 1989; Kempe & Wolf, 2006; Neiva, 2008). For example, the coupled substitution of Sc and Nb is also indicated by strong correlation of both elements (Figure 11.9).

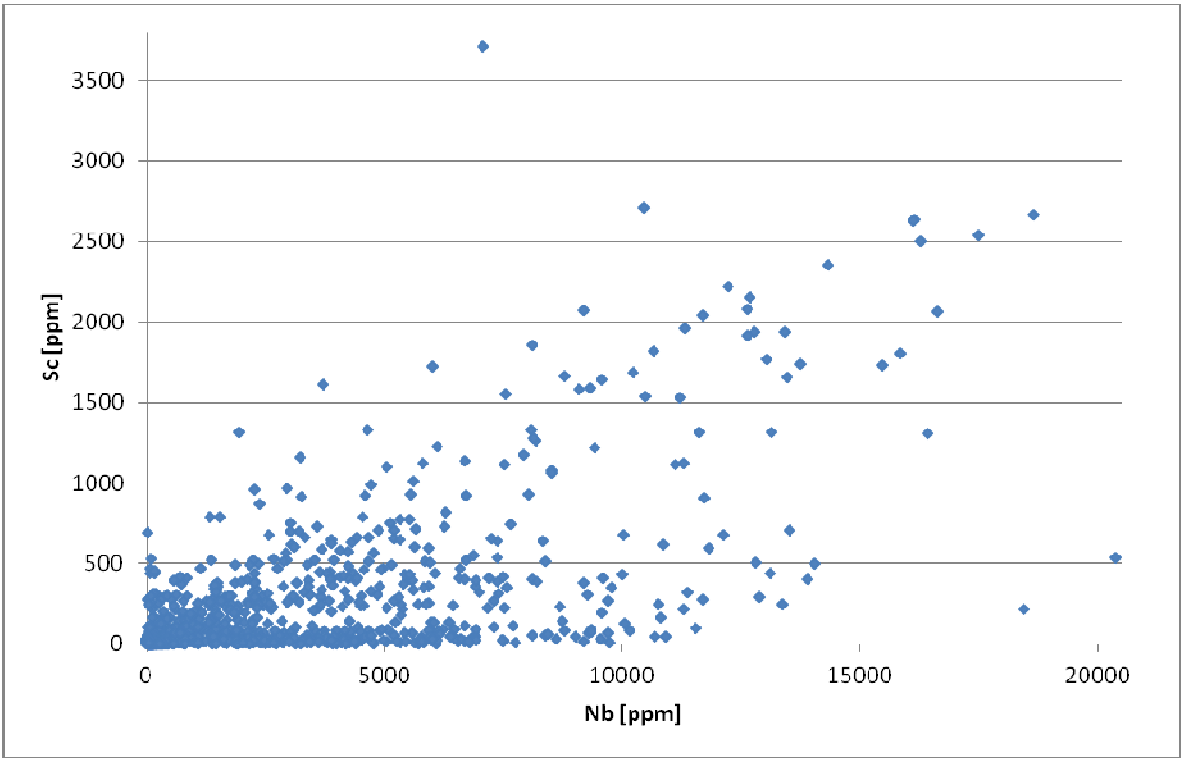
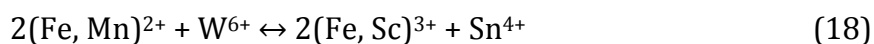


Figure 11.9: Binary diagram showing the concentrations of Nb [ppm] versus Sc [ppm] from LA-ICP-MS analysis of wolframite worldwide.

Tetravalent cations with small ionic radii like Sn⁴⁺ (0.69 Å), Ti⁴⁺ (0.605 Å), and V⁴⁺ (0.58 Å) are substituted for W into wolframite by coupled substitution with trivalent cations like Sc, ferric Fe, Y, In or REE (Tindle & Webb, 1989). Highest Sn concentrations in wolframite are characteristic for Sn-W deposits, where cassiterite is present in the ore paragenesis, for example in the Ranong (Aranyakanon, 1961) or Yugozyr (Taylor, 1979) greisen deposits.



Other tetravalent cations with larger ionic radii like U⁴⁺ (0.89 Å), Zr⁴⁺ (0.72 Å), and Hf⁴⁺ (0.71 Å) substitute for Fe²⁺ and Mn²⁺ generating a vacancy on the A site in the wolframite structure. Similar to cassiterite, wolframite from greisen shows lower Zr/Hf ratios of about 10 or less indicating magmatic fractionation.



Wolframite with high trace element concentrations commonly shows intermediate major element composition and is characterised by a hübnerite/ferberite ratio of about 1 (Kempe & Wolf, 1994). On the contrary, the endmembers ferberite or hübnerite usually exhibit rather low trace element concentrations (Figure 10.20). In general, highest trace element concentrations are related to wolframite which formed at high temperature conditions (Gan & Chen, 1992; Kempe & Wolf, 1994). High temperatures cause disorder of the crystal lattice and favour the incorporation of trace elements into the wolframite structure. As a consequence, this observation also indicates that wolframite with intermediate major element composition forms at higher temperatures than pure ferberite or hübnerite and incorporation of trace elements into the wolframite lattice is significantly controlled by temperature. This is also underlined by comparison of homogenisation temperatures of primary fluid inclusions in wolframite with their hübnerite/ferberite ratio (Enchbat, 2007).

In general, trace element composition is controlled by element availability and as a consequence from the geological setting. For example, wolframite from deposits with distinct magmatic influence is characteristically enriched in Ta, Nb, Zr, and Hf which derived from the nearby granitic intrusion. Wolframite from hydrothermal quartz veins crosscutting the surrounding country rocks are characterised by V, Mg, which are probably mobilized from these rocks. Looking at the normalised trace element patterns in wolframite from different deposits worldwide, it is evident that each deposit displays its individual characteristic trace element distribution with its particular variability for each element (Figure 11.10).

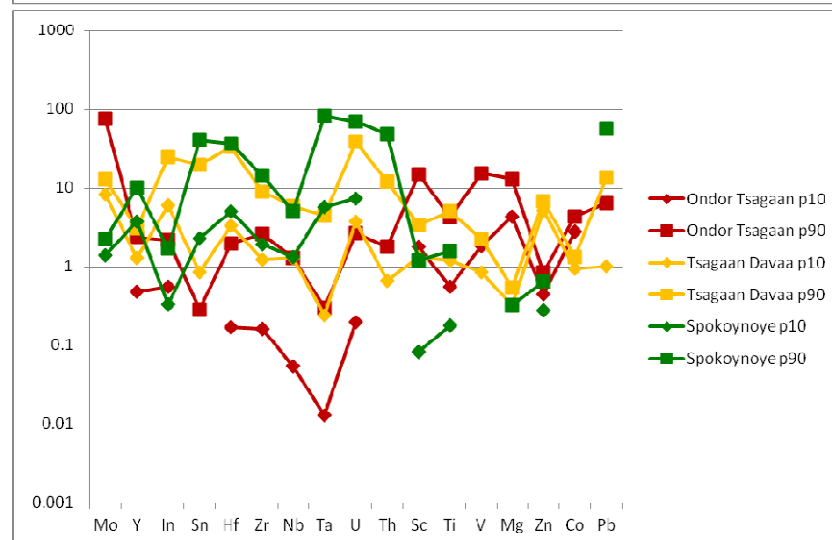
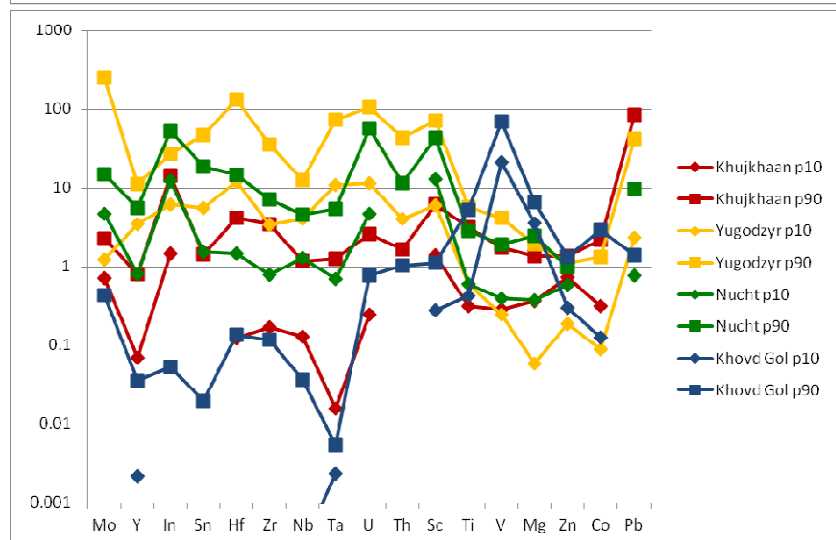
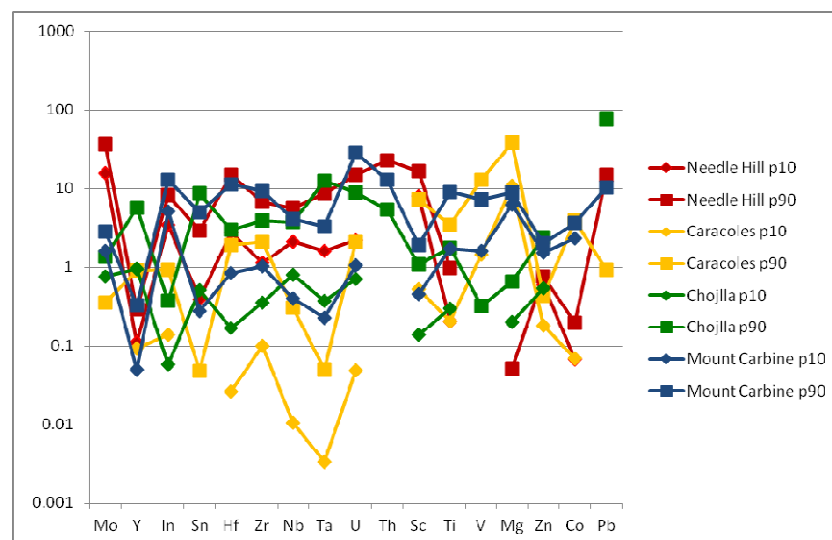
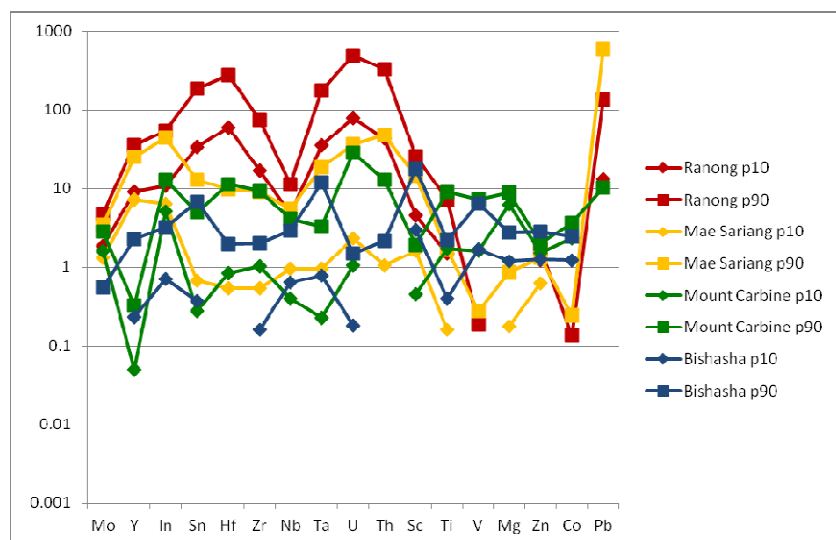


Figure 11.10: Normalised element distribution patterns of wolframite from ore concentrates worldwide with focus on Central Asian deposits in the lower two diagrams. Variability of the trace element composition is given as the 10th percentile (lower line with diamonds) and 90th percentile (upper line with squares) of the normalised values.

Chondrite-normalised REE diagrams generally show inclining patterns from LREE towards HREE (Figure 10.22). The ionic radii of the REE become successively smaller with increasing atomic number ranging from 1.03 Å for La³⁺ to 0.86 Å for Lu³⁺. Therefore the inclining REE patterns are in coherence with the substitution mechanisms, as HREE have smaller ionic radii and are more similar to Fe and Mn compared to LREE. Manganese-rich wolframite generally shows higher HREE and total REE concentrations compared to Fe-rich wolframite (Figure 10.22). This is explained by the slight difference in the ionic radius between Fe²⁺ (0.78 Å) and Mn²⁺ (0.83 Å), hence REE content correlates with Mn as their ionic radii are closer to that of Mn than Fe. Some REE patterns of wolframite are characterised by the presence of more or less pronounced negative Y anomalies. It is conspicuous that especially wolframite from deposits with clear link to granitic intrusions show these Y anomalies. This is caused by the crystallisation of magmatic Y-bearing phosphates (principally xenotime and monazite) from the related granites which fractionated Y from the system; the final hydrothermal fluids from which wolframite precipitated were primarily magmatic in origin and already depleted in Y compared to the other REE. This interpretation is emphasised for example at the Hemerdon endogreisen deposit where wolframite shows a distinct negative Y anomaly in its REE patterns (Figure 10.22) and accessory xenotime is present in the associated Dartmoor granite (Ward et al., 1992).

On the contrary, the distinctive REE pattern of reinite is the result of pseudomorphism and ferberite retains the trace element characteristics of the former scheelite. Rare earth element compositions of scheelite are given by several authors (Uspensky et al., 1998; Ghaderi et al, 1999; Brugger et al., 2000, Dostal et al., 2009). As mentioned before the scheelite structure favours large cations with ionic radii greater than 0.9 Å (Hazen et al., 1985; Ghaderi et al, 1999; Kuzmin & Purans, 2001). The positive Eu anomaly is caused by combined incorporation of Eu²⁺ (1.17 Å) and Eu³⁺ (0.95 Å) into the scheelite structure (Brugger et al., 2008).

11.3 Geochemistry of granites compared to trace elements in cassiterite and wolframite

Unfortunately, comprehensive studies on ore deposits regarding petrology and geochemistry of mineralized host plus surrounding country rocks do not exist (to my knowledge) for Sn-W deposits. But at least whole rock geochemical data are available for some granitic intrusions related to Sn-W deposits (Table 6.1) and this information is used to test if the trace element distributions of cassiterite and wolframite are significantly influenced by the chemical composition of the associated granitic intrusive rocks. Although the datasets for whole rock geochemistry are patchy and incomplete (especially for several trace elements), it turns out that at least some elements apparently have been mobilised from the associated intrusions.

Comparison of whole rock geochemical data of the intrusions with the trace element composition of cassiterite shows that incorporation of HFSE like Ta, Nb, and Hf into cassiterite is significantly controlled by their initial enrichment in the parental intrusion (Figure 11.11). This correlation is particularly evident for cassiterite from pegmatite and greisen deposits. Especially cassiterite from Pitinga mine shows high concentrations in these HFSE plus Th and Zn which strongly correlates with prominent enrichments in these elements in the associated Madeira granite. There are other interesting element correlations in the chemical composition of cassiterite and the related intrusion such as As and Bi for Chorolque.

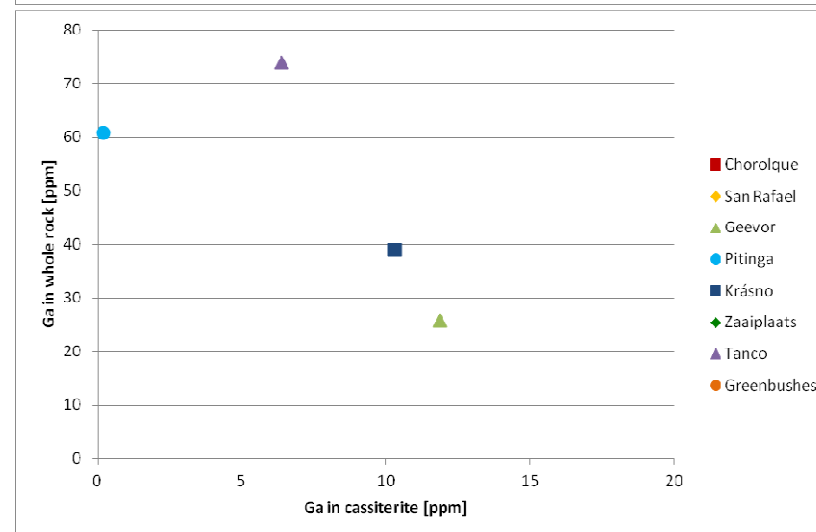
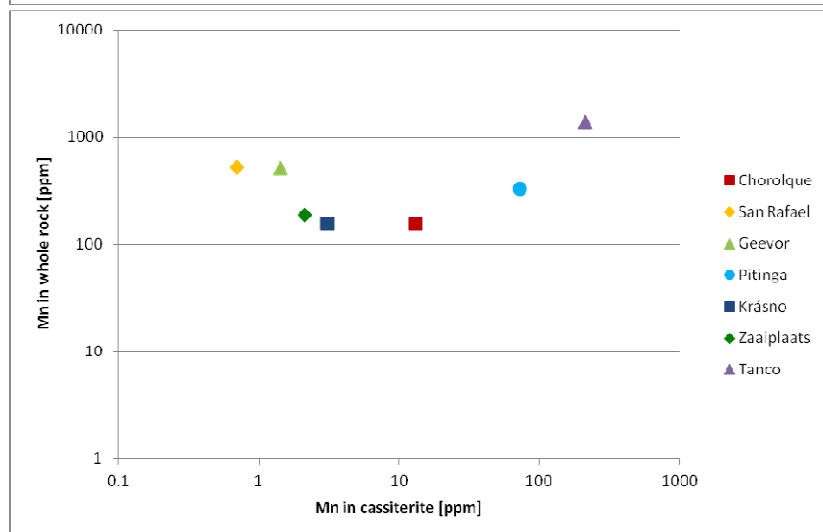
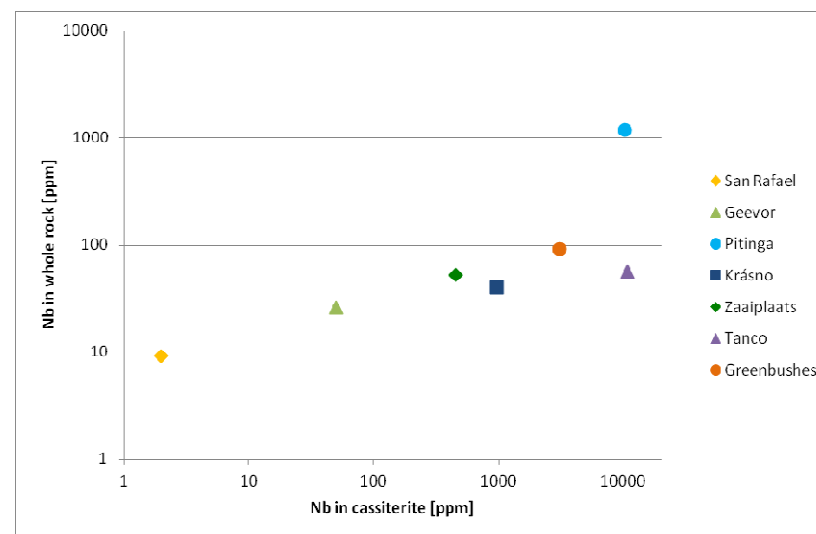
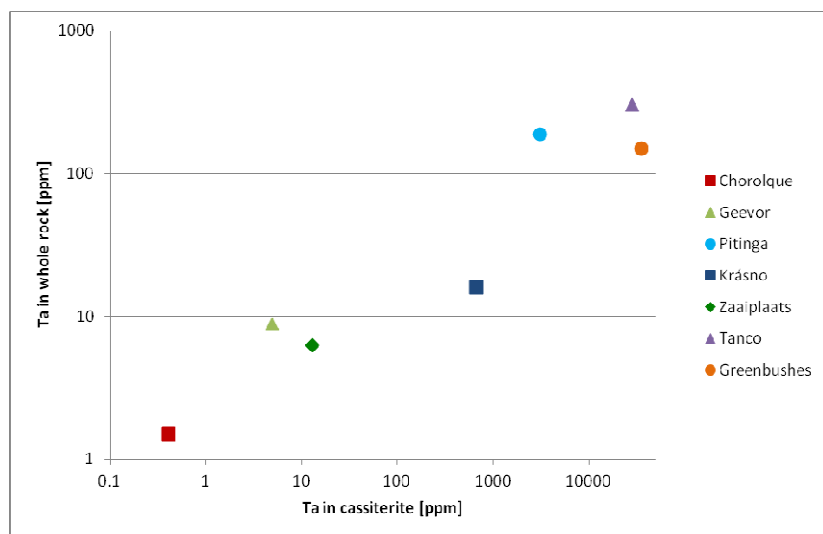


Figure 11.11: Comparison of trace element data (upper left: Ta, upper right: Nb; lower left: Mn, and lower right: Ga) in cassiterite from different Sn deposits with whole rock geochemical data of the respective associated intrusion. Data points are omitted if no corresponding value from whole rock analysis was measured. Please note that data are displayed on logarithmic scale, except for Ga (lower right).

Major elements like Mn, Fe, and Ti do not show any significant correlation between granitic intrusion and cassiterite (Figure 11.11), but this is not surprising as these elements are incorporated into other major rock-forming minerals. But also trace elements like Ga, Sc, Sb, and V do not correlate between granitic intrusion and cassiterite because they are probably mobilised from the surrounding country rocks (Figure 11.11). Unfortunately, this assumption cannot be underpinned as geochemical data of both host and country rocks surrounding tin deposits are not published.

Unfortunately, only two whole rock geochemical datasets for granites (Table 6.1), which are associated with any of the wolframite deposits from our sample list, are found in the literature. Moreover these datasets are far from being complete for most elements and no meaningful conclusions can be drawn. For the sake of completeness, comparison of the whole rock composition of the Spokoynoye and Mount Carbine granites with the trace element composition of the respective wolframite is shown in diagram Figure 11.12.

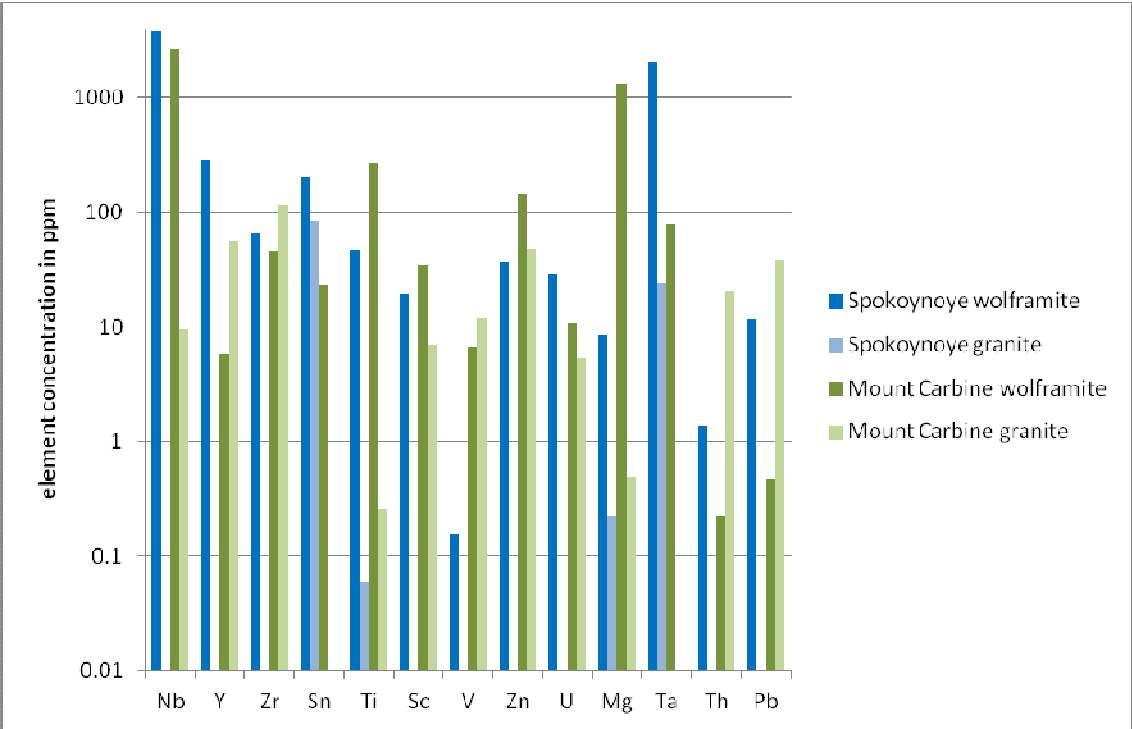


Figure 11.12: Comparison of trace element data (on logarithmic scale) in wolframite (dark) from two W deposits with whole rock geochemical data of the respective associated intrusion (pale).

11.4 Analytical Fingerprint

On a global scale, individual Sn and W ore deposits can be differentiated by the trace element composition of cassiterite and wolframite, respectively. Ore provinces or districts are primarily characterised by the age of the mineralising event and some show exceptional mineral and metal assemblages or the ore minerals show common trace element compositions. This is for example demonstrated for the Bolivian Tin Belt which is characterised by polymetallic tin deposits with distinct metal associations including W, Ag, Sb, Pb, Zn, and/or Bi (Arce-Burgoa & Goldfarb, 2009). In turn, these deposits can be subdivided by their radiometric estimate (see below) into the Triassic-Jurassic (199 to 180 Ma) or Miocene (19 to 8 Ma) age group (Pirajno, 1992; Arce-Burgoa & Goldfarb, 2009). Additionally, cassiterite from the Bolivian Tin Belt is distinctly enriched in In, Sb, Ga, and Ge compared to cassiterite from other deposits worldwide.

An additional parameter for AFP is an U-Pb age estimate of individual cassiterite grains in an ore concentrate (Gäbler et al., 2011). Dating of cassiterite using the U-Pb method is possible, because U^{4+} (0.73 Å) readily substitutes for Sn^{4+} (0.69 Å), whereas Pb does not fit into the cassiterite lattice due to its significantly too large ionic radius (Pb^{2+} , 1.21 Å). Besides major and trace element concentrations, information on U and Pb isotopes is provided by LA-ICP-MS which can be used to estimate a model age to evaluate the timing of mineralisation in individual deposits as described by Gäbler et al. (2011). This approach was already applied to Coltan grains from African pegmatites and rare metal granites (Melcher et al. 2015).

The following case studies are selected to demonstrate feasibility of trace elements in cassiterite and wolframite for AFP and to indicate possible limitations or complications. In a first case study, the trace element variability within an ore deposit is presented by the example of Nyakabingo tungsten mine in Rwanda, where ore concentrates from ten different tunnels were examined. Variability within single grains was demonstrated on the example of columbite-tantalite by Melcher et al. (2015), but similar inhomogenities are expected for cassiterite and wolframite as indicated by X-ray element distribution maps (Figures 10.14, 10.14 & 10.16). The second case study demonstrates the identification of two mineralisation styles which may occur close to each other within a single mine. Nemba and Bugalula mines are chosen as representative examples. Furthermore, the case studies focussing on the Rutsiro and Rutongo areas illustrate the difficulties in the discrimination of individual deposits on concession scale due to the apparent similarity in their trace element composition.

Case study: Nyakabingo

The Nyakabingo mine is located about 15 km northwest of Kigali, the capital of the Republic of Rwanda, and is one of three major tungsten mines besides Bugarama and Gifurwe along the NNW- to SSE-trending “tungsten belt” (Figure 10.4; Frisch, 1975; Pohl, 1976; De Clercq et al., 2008; De Clercq, 2012; Goldmann et al., 2013). Tungsten-bearing hydrothermal quartz veins are hosted by Kibaran metasedimentary rocks composed of alternating sandstones, quartzites, and carbonaceous black shales of the Bumbogo and Shyorongi Formations followed by the prominent Nduba quartzite (Figure 11.13). The major tungsten ore mineral is ferberite, which occurs in the particular form of reinite (ferberite pseudomorphous after scheelite). Precipitation of tungsten minerals was caused by the interaction of hydrothermal fluids of magmatic origin with the carbonaceous shale (De Clercq, 2012; Goldmann et al., 2013).

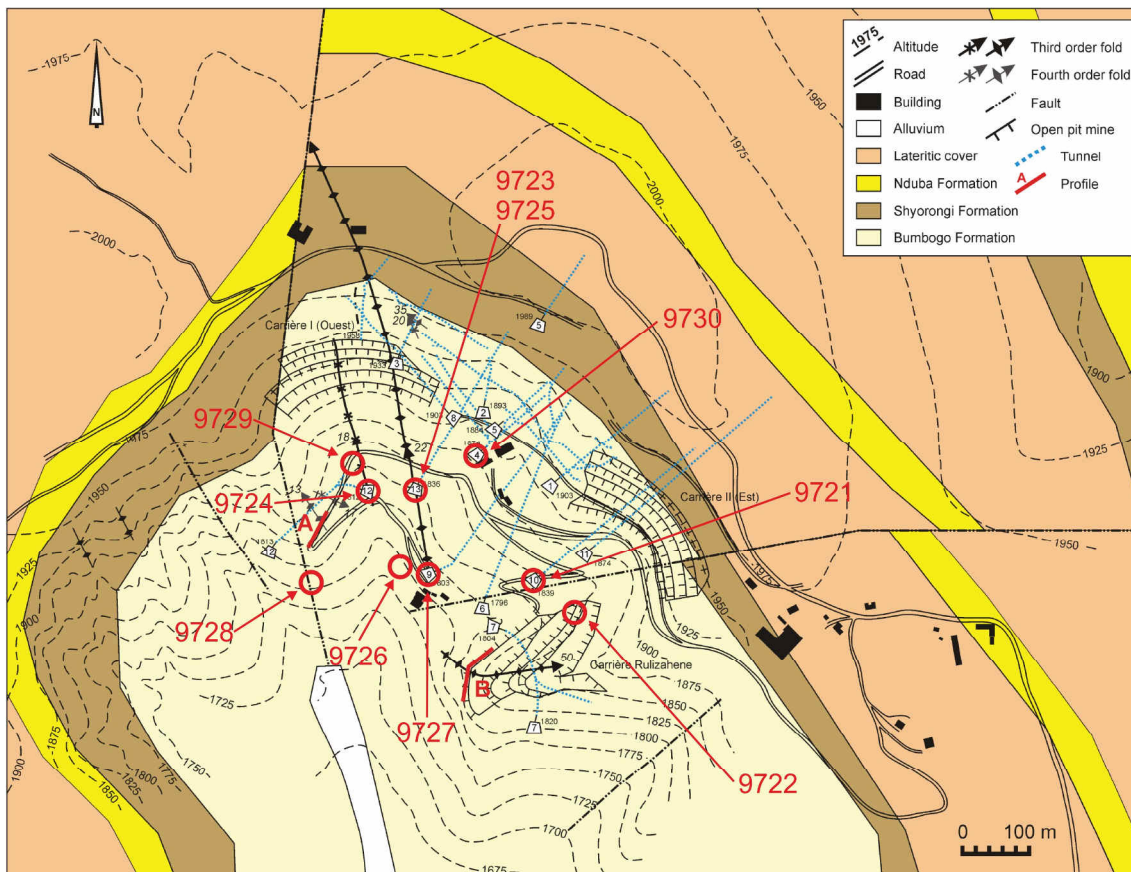


Figure 11.13: Geological map of the Nyakabingo mine, Rwanda (slightly modified after De Clercq, 2012; De Clercq compiled this map from various sources). The sample locations of the different tunnels are marked by red circles with the corresponding section numbers. The two profiles A and B were investigated by Friso De Clercq during his Ph.D. work.

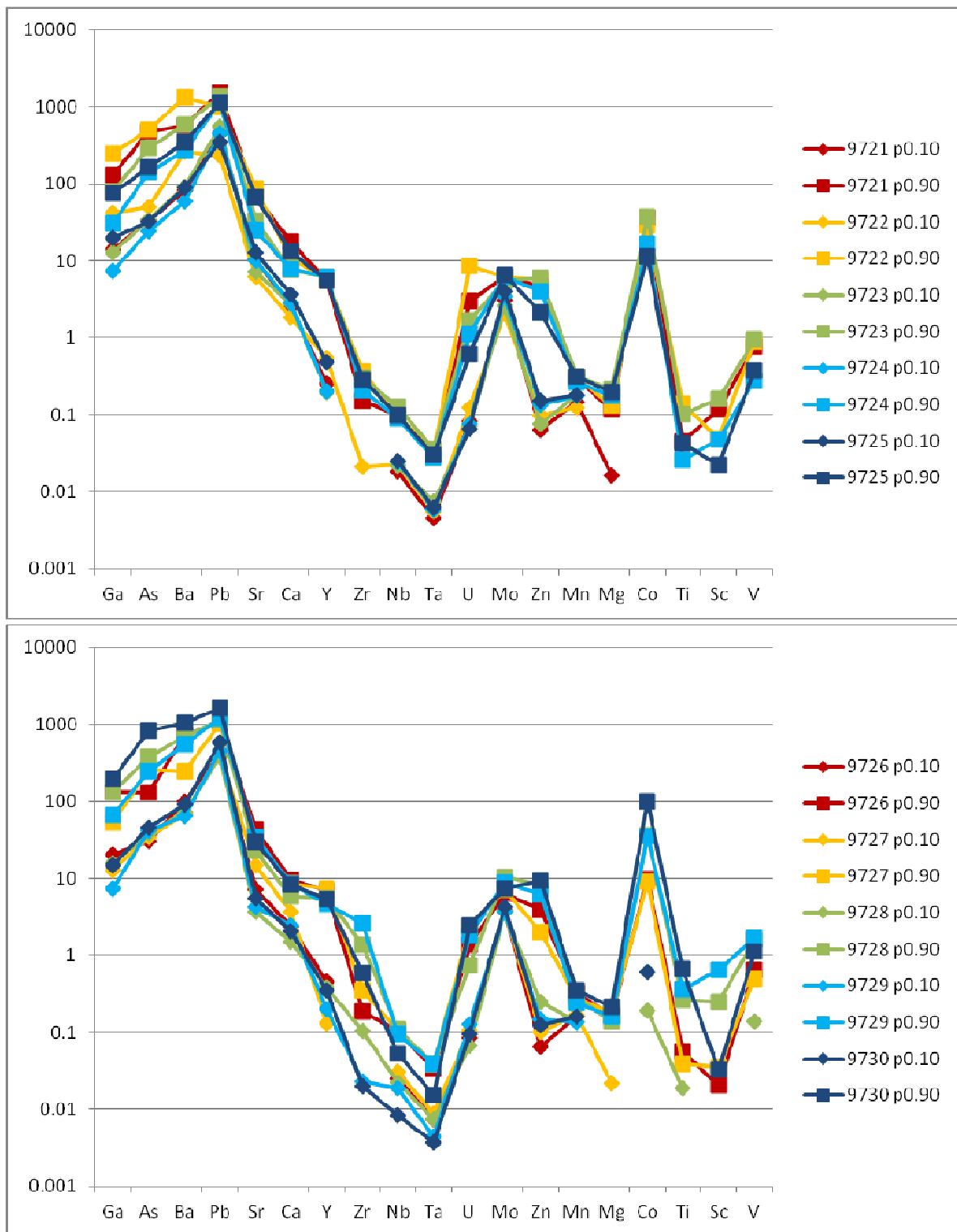


Figure 11.14: Normalised element distribution patterns of ferberite from ore concentrates originating from ten tunnels of the Nyakabingo mine. Variability of the trace element composition is given as the 10th percentile (lower line with diamonds) and 90th percentile (upper line with squares) of the normalised values.

In total ten ore concentrates were sampled from different tunnels of the Nyakabingo mine (Figure 11.13). Reinite of Nyakabingo is characterised by an uncommon trace element composition containing high Ca, Pb, Sr, Ba, As, Ga, and LREE contents, but comparatively low concentration levels in Zr, Hf, Nb, Ta, Sn, In, Ti, and Sc (Figure 11.14; compare with Mucaca from the Rutsiro case study below). This specific trace element signature was probably inherited from the former scheelite (Goldmann et al., 2013).

Comparing the trace element variability in the concentrates from the different tunnels, it is evident that the concentration ranges strongly overlap for most elements as the patterns are very similar in narrow ranges (Figure 11.14). Only exceptions are Zr, Sc, and Ti concentrations, which show a larger scatter among the different concentrates. Nevertheless, this indicates that the trace element composition of wolframite is rather constant within a vein type deposit. As a consequence for the application of APF, at least one sample from a vein type deposit may already contain the relevant information and not each tunnel of a vein deposit has to be necessarily sampled.

Case studies: Nemba & Bugalula

The Nemba mine is situated about 50 km south of Kigali city close to the Burundian border (Figure 10.4). Hydrothermal quartz veins as well as pegmatites are mineralised with cassiterite and both deposit types occur next to each other (Figure 11.15).

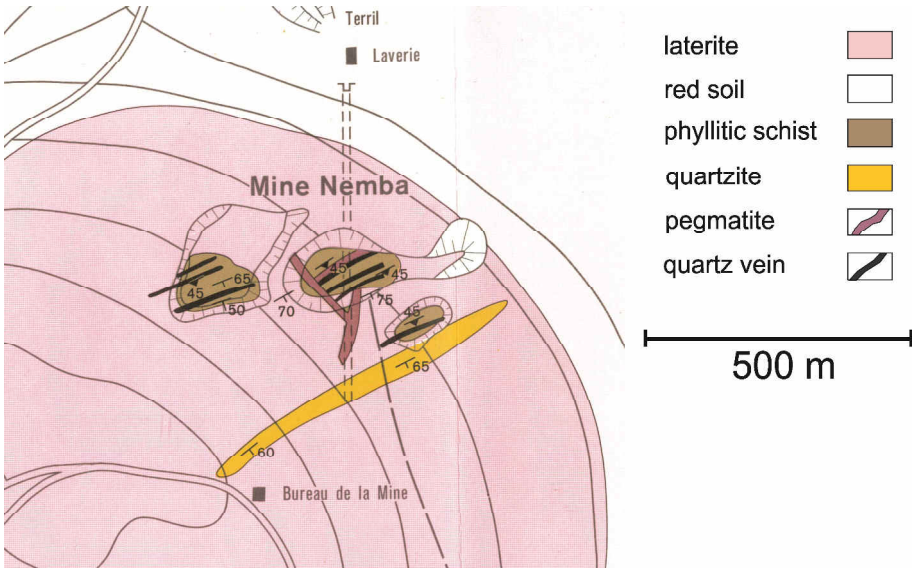


Figure 11.15: Geological map showing the close spatial distribution of hydrothermal quartz veins and pegmatites in the Nemba mine, Rwanda (detail from the map of Brinkmann, 1987).

In addition to cassiterite, columbite-tantalite makes up a significant proportion in the ore concentrates from the pegmatites. The two different mineralisation styles are also evident in the trace element composition of cassiterite either originating from the hydrothermal veins or the magmatic pegmatites. Cassiterite from pegmatites is characterised by relatively high Mn, Ta, Zn, Nb, Hf, Zr, and Ga concentrations, but comparatively low Sc, V, and Ti; on the contrary, hydrothermal cassiterite shows opposing concentration levels in these elements (Figure 11.16). Interestingly, there is no significant difference in the Ta, Nb, and Zr concentrations between these two types (Figure 11.16); the hydrothermal cassiterite from Nemba is exceptionally enriched in these metals indicating precipitation from high-temperature fluids which exsolved from a magmatic source (possibly the pegmatites).

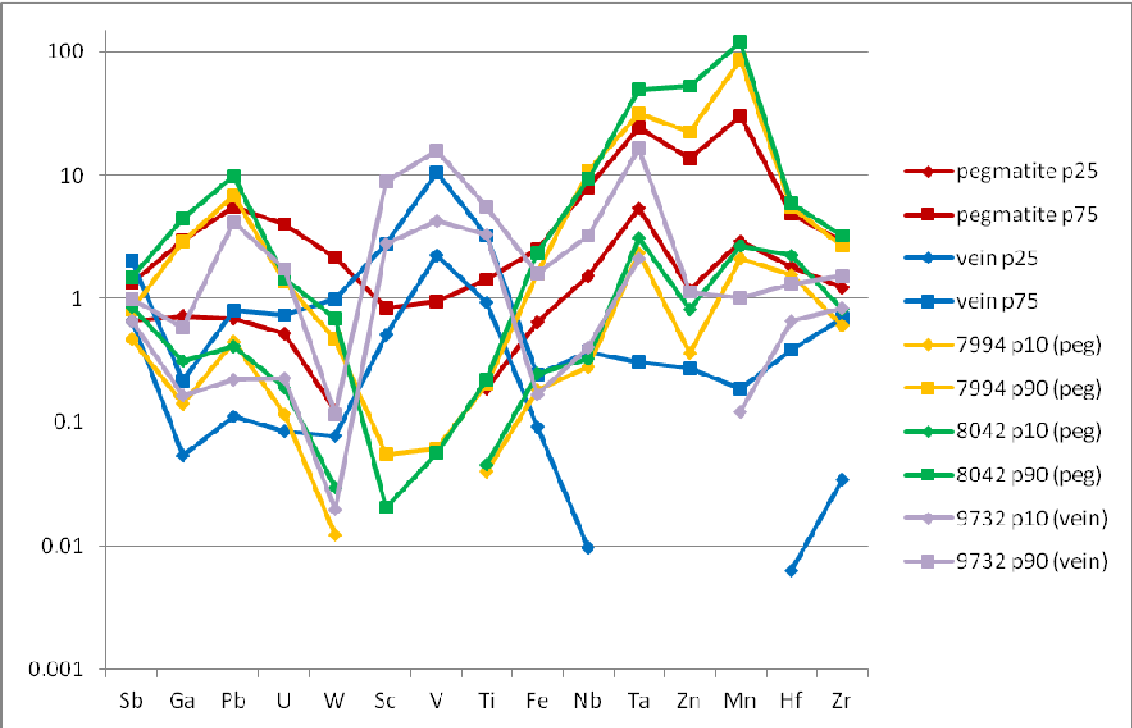


Figure 11.16: Normalised element distribution patterns of cassiterite from three ore concentrates originating from Nemba in comparison to typical pegmatite (7994, 8042) and hydrothermal vein (9732) patterns.

A similar spatial association of hydrothermal quartz veins and pegmatites is also found in the Bugalula mining area about 50 km northeast of Kigali (Figure 10.4). The trace element compositions of magmatic and hydrothermal cassiterite show comparable enrichments and depletions in specific elements analogous to Nemba. Higher Mn, Ta, Nb, Zn, Zr, Hf, Fe, and U concentrations with low V, Sc, and Ti are related to cassiterite from pegmatites, whereas hydrothermal cassiterite displays oppositional distribution

patterns (Figure 11.17). In contrast to Nemba, the two types at Bugalula clearly show contrasting trace element distributions. In particular the Ta, Nb, and Zr concentrations in hydrothermal cassiterite from Bugalula are clearly lower compared to hydrothermal cassiterite from Nemba. Contrasting, the magmatic cassiterite from Bugalula can be discriminated from magmatic cassiterite from Nemba by higher concentration levels of Zn, Ta, Nb, W, and U in cassiterite from Bugalula pegmatites. These observations show that the trace element composition of cassiterite can be used to assign a specific ore deposit type (magmatic versus hydrothermal genesis of tin mineralization). This comparison also demonstrates that cassiterite from different localities with the same genesis can be differentiated from each other by their respective characteristic trace element composition; even though the general trace element trends are similar in terms of the respective deposit type.

Additionally, it has to be taken into account that the cassiterite from Nemba and Bugalula is represented by two different trace element signatures (hydrothermal and magmatic) and both cassiterite types may even be found in a single ore concentrate from the respective mine. This is particularly relevant with regard to AFP.

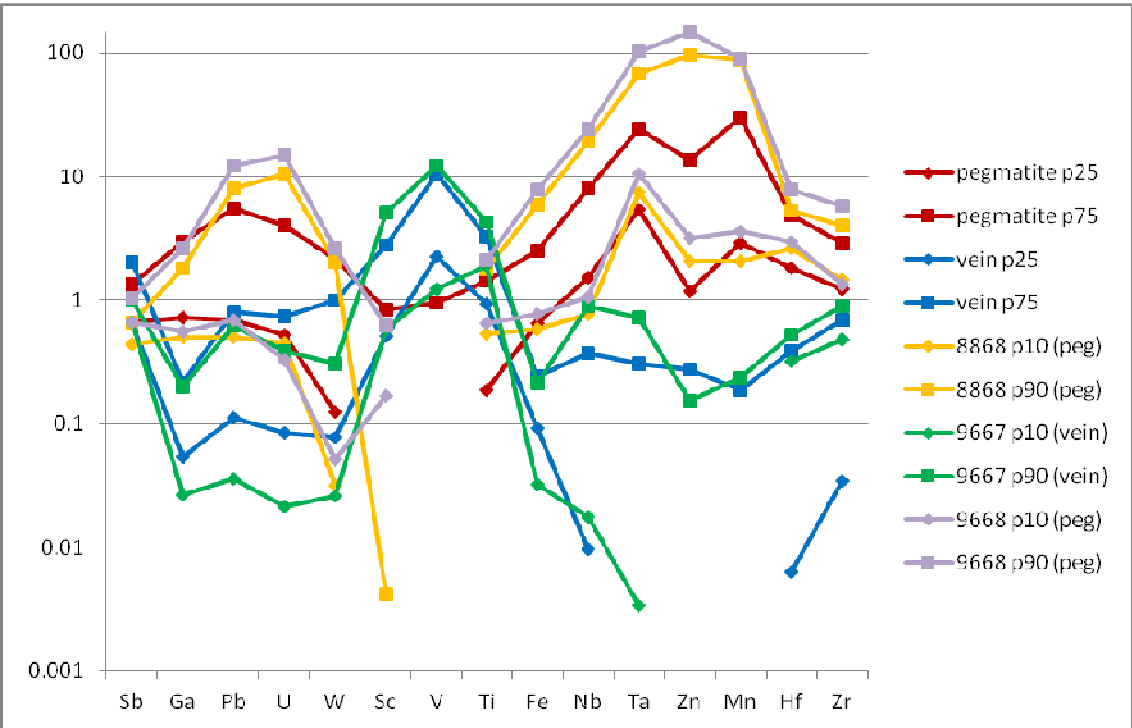


Figure 11.17: Normalised element distribution patterns of cassiterite from three ore concentrates originating from Bugalula in comparison to typical pegmatite (8868, 9668) and hydrothermal vein (9667) patterns.

Case study: Rutsiro

The Rutsiro area is located about 100 km west of Kigali in the Western Province of Rwanda (Figure 10.4). A peculiarity of the Rutsiro mining concession is the close spatial association of W, Sn, and Ta-Nb mineralisations occurring in different deposit types. The geology is composed of Kibaran metasedimentary rocks of the Nyungwe and Uwinka Formations which are underlain by gneisses and migmatites of the metamorphic basement of the Butare Complex (Figure 11.18). This succession is intruded by different generations of granite. Cassiterite is either present in rare metal pegmatites associated with columbite-tantalite or in E-W-striking hydrothermal quartz veins without Ta-Nb mineralisation like the Gitebe deposit. Tungsten in the form of ferberite occurs in hydrothermal quartz veins crosscutting the graphitic phyllites and following an almost NNW-SSE-striking mineralised zone.

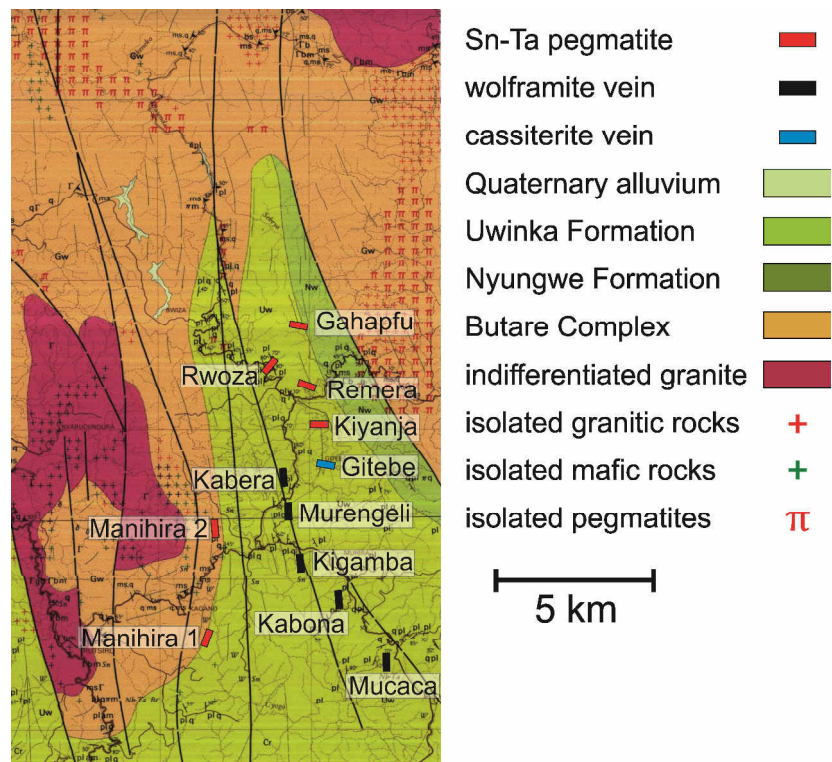


Figure 11.18: Geological map of the Rutsiro area, Rwanda. Uwinka Formation: graphitic phyllite, quartz phyllite; Nyungwe Formation: quartzite, phyllite; Butare Complex: gneiss, migmatite, metaquartzite, micaschist, amphibolites, pegmatite (detail from map of Theunissen et al., 1991).

Comparing the trace element data of cassiterite from the various pegmatites of the Rutsiro concession (namely Remera, Gahapfu, Rwoza, Kiyanja, and Manihira), it is evident that the distribution patterns are in fact typical for magmatic cassiterite, but there is also a strong similarity among each other (Figure 11.19). A notable exception is the trace element composition of cassiterite from Kiyanja1 deposit. The trace element data show a considerably greater variability to lower concentration levels compared to the other deposits, especially in the typical magmatic elements Nb, Ta, Zn, Mn, Hf, and Zr. This concentrate was panned from an alluvial placer deposit in the valley and the large concentration range represents a mixture of various magmatic as well as hydrothermal primary sources. However, the strong similarity of the other pegmatite deposits is obviously caused by similar conditions of formation as the pegmatites are in close spatial relation and are possibly related to a common parental granite. Additionally, the surrounding pegmatite-hosting country rocks belong to the same lithology of the Uwinka Formation (except for the Manihira pegmatites which intruded along the boundary between the Uwinka Formation and the Butare Complex). These factors complicate the discrimination of the individual deposits on the concession scale and at first sight cassiterite from the pegmatite deposits are indistinguishable.

But having a closer look at the data, there are at least some slight differences between the deposits. For example, cassiterite from the northern pegmatites (Gahapfu, Remera, and Kiyanja) occasionally contains Sc and V which are seemingly declining in concentration from north to south. Cassiterite from the two Manihira pegmatites is devoid of Sc and V, but is characterised by comparatively high Mn contents with low Ti and Fe. Cassiterite from Rwoza displays a rather narrow distribution pattern which is unfortunately overlapped by the others, but shows relatively high Zr, Nb, and Hf levels. Generally, the strong overlap in the element distribution makes it challenging to discriminate cassiterite from individual deposits on concession scale. However, statistical treatment of the trace element data by for example Kolmogorov-Smirnov statistics (see excursus below or Gäbler et al., 2013) seems promising to differentiate individual deposits because concentrates from the same locality are more similar in their trace element distributions than concentrates from different localities (Gäbler et al., 2013). On the contrary, cassiterite from the Gitebe quartz vein deposit is significantly different in the trace element distribution compared to the pegmatite deposits and shows a typical hydrothermal pattern (Figure 11.19). On the concession scale, Gitebe is easily distinguished from the other cassiterite deposits.

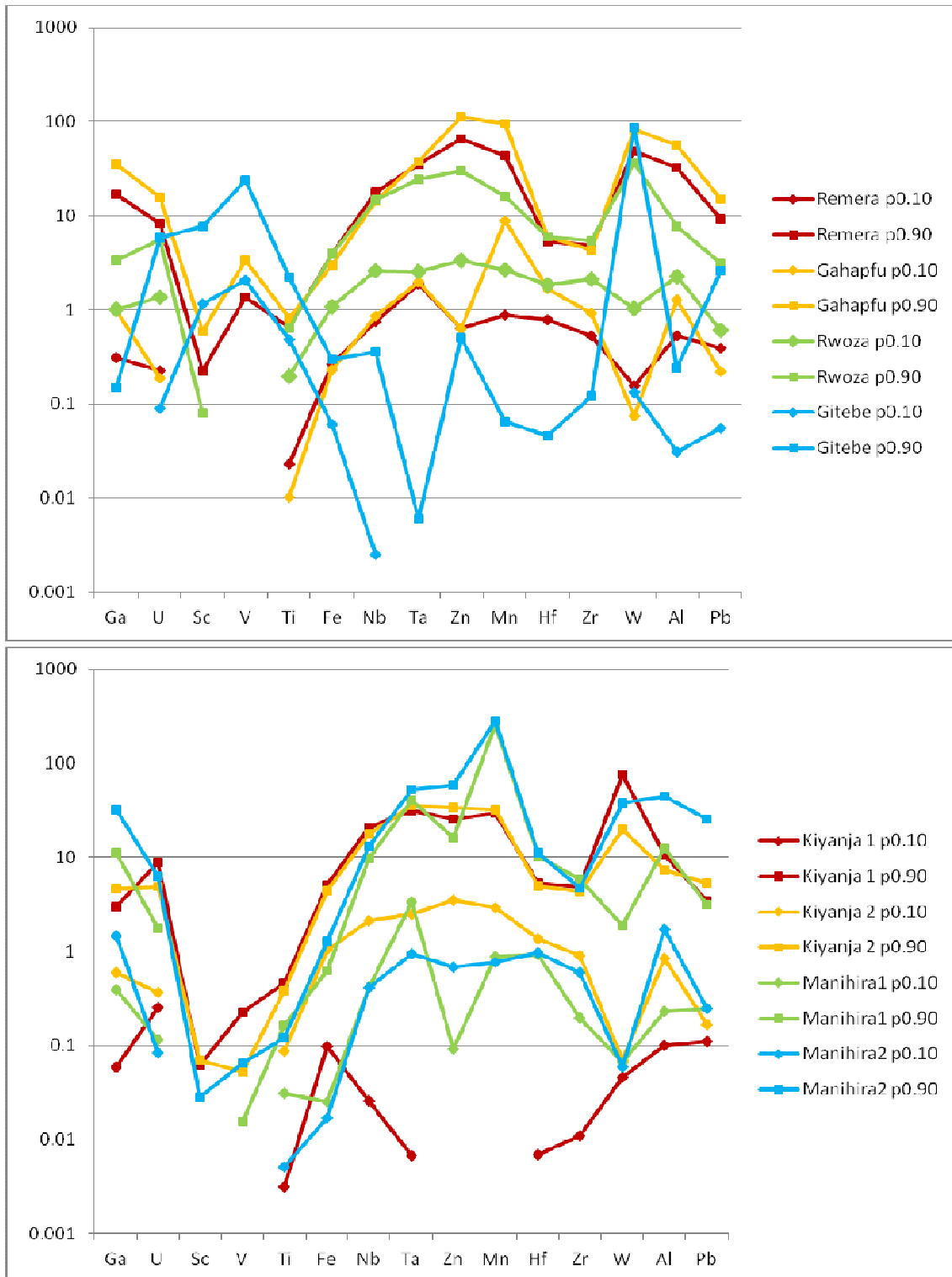


Figure 11.19: Normalised element distribution patterns of cassiterite from ore concentrates originating from eight localities of the Rutsiro concession. Variability of the trace element composition is given as the 10th percentile (lower line with diamonds) and 90th percentile (upper line with squares) of the normalised values.

Excursus on the Kolmogorov-Smirnov statistics:

Kamber (2009) and Hoefs (2010) give examples for application of fingerprint methods but the mentioned materials like glass or steel show much more homogeneous element distributions than natural material like minerals which are characterised by non-parametric element distributions with distinctly larger ranges. Therefore, non-parametric statistics need to be used like the Kolmogorov-Smirnov statistics (Gäbler et al., 2013). The Kolmogorov-Smirnov statistic describes maximum distance between two empirical cumulative distribution functions and was used to compare two samples for a given element as it can be considered as a measure for the similarity of samples. As stated by Gäbler et al. (2013), the empirical distribution function of the brother comparisons (two samples from the same deposit) for a given element should be very close to the theoretical curve, while the distribution function of the non-brother comparisons (two samples from the different deposits) should differ significantly from the other two curves. This approach seems promising to assign if a sample derives from the declared origin or not.

The trace element composition of ferberite from the various W deposits of the Rutsiro concession appears to be quite similar, except for the most southerly locality Mucaca (Figure 11.20). Ferberite from Mucaca displays a totally different element distribution pattern which is typical for reinite (see case study on reinite from Nyakabingo above) with uncommon enrichments in LILE and particularly low concentrations in HFSE (Goldmann et al., 2013). The trace element distributions from the other deposits differ only slightly among each other (Figure 11.20).

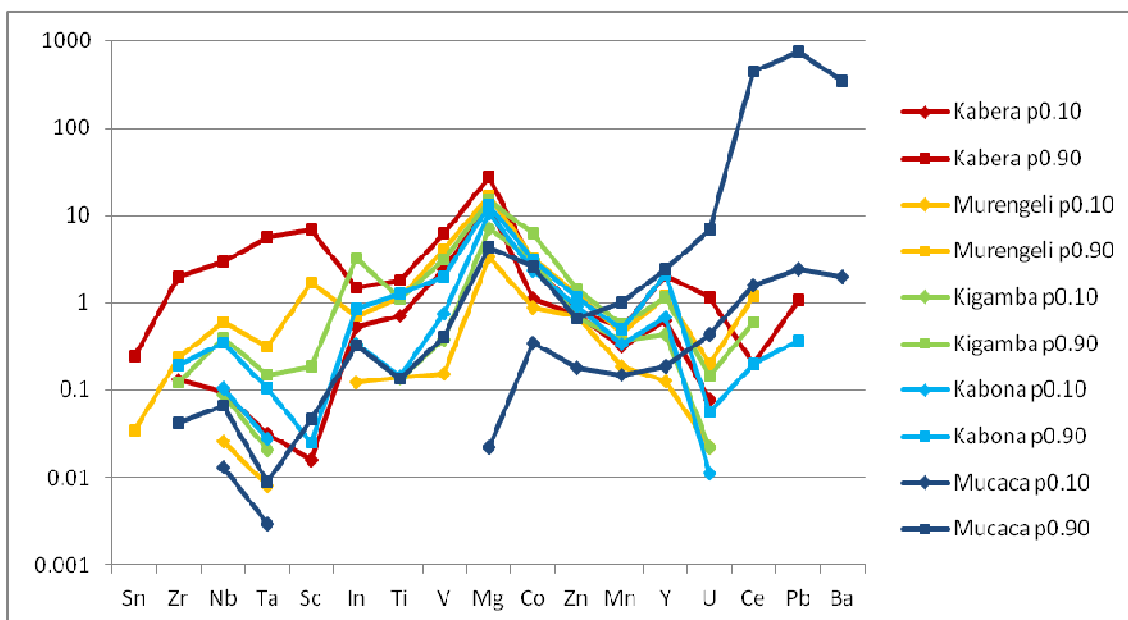


Figure 11.20: Normalised element distribution patterns of wolframite from ore concentrates originating from five localities of the Rutsiro concession. Variability of the trace element composition is given as the 10th percentile (lower line with diamonds) and 90th percentile (upper line with squares) of the normalised values (normalising value for Ba is set to 0.1 which is equivalent to the detection limit).

Ferberite from the Kabera deposit is characterised by highest concentrations in HFSE (Nb, Ta, Zr, Sn, and U) plus Sc. Interestingly, the concentrations of these elements apparently decrease successively from north to south; this may be interpreted as increasing distance of the deposits from a common parental pluton (if this assumption is correct, the pluton could be expected northwards of Kabera). Although the trace element distributions of ferberite from the other deposits seem to be indistinguishable, there are at least some elements which occur in various concentration ranges at different levels and can be used in this case to differentiate individual deposits from each other even on concession scale. Looking at the binary plots of Zn versus Co and Y versus V, it is evident that ferberite from each deposit covers a specific field. In this case, ferberite from Kigamba differs from the other deposits by its comparatively high Co contents (Figure 11.21), whereas ferberites from Murengeli and Kabona cover a similar range in their Zn and Co composition and cannot be distinguished from each other. But ferberite from these two deposits can be differentiated by its Y and V composition and the two deposits plot in two almost separate fields (Figure 11.22).

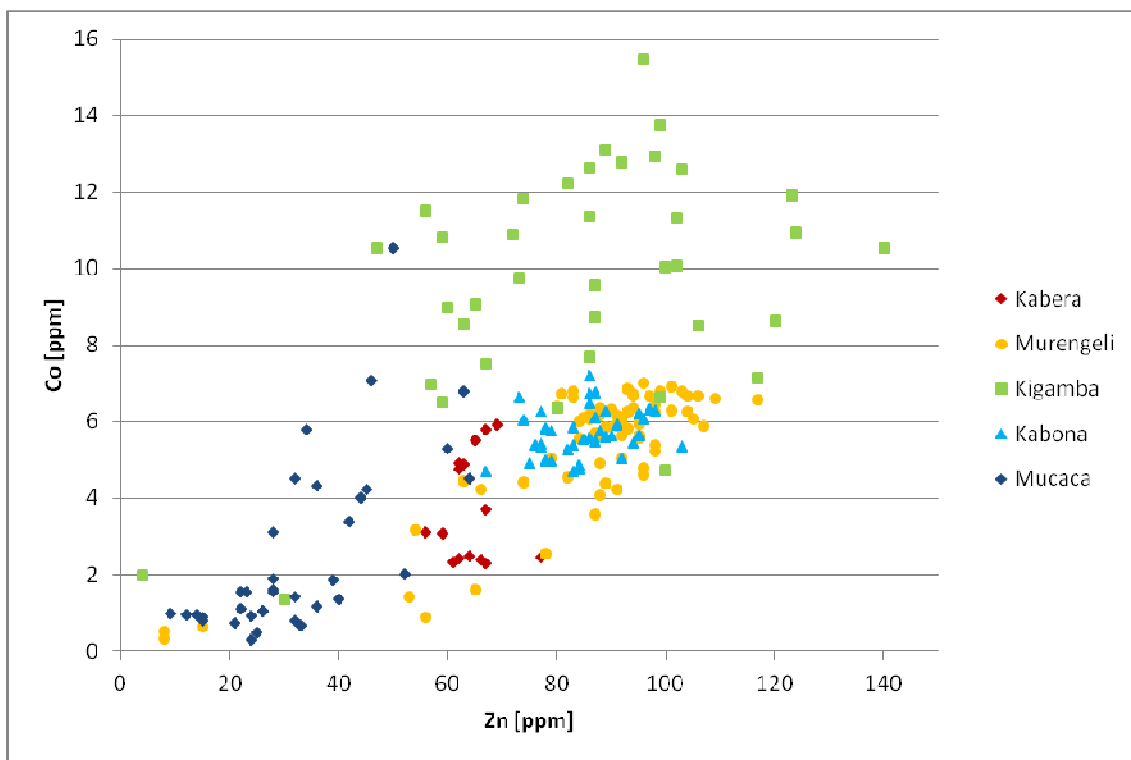


Figure 11.21: Binary diagram showing the concentrations of Zn [ppm] versus Co [ppm] from LA-ICP-MS analysis of wolframite originating from five localities of the Rutsiro concession.

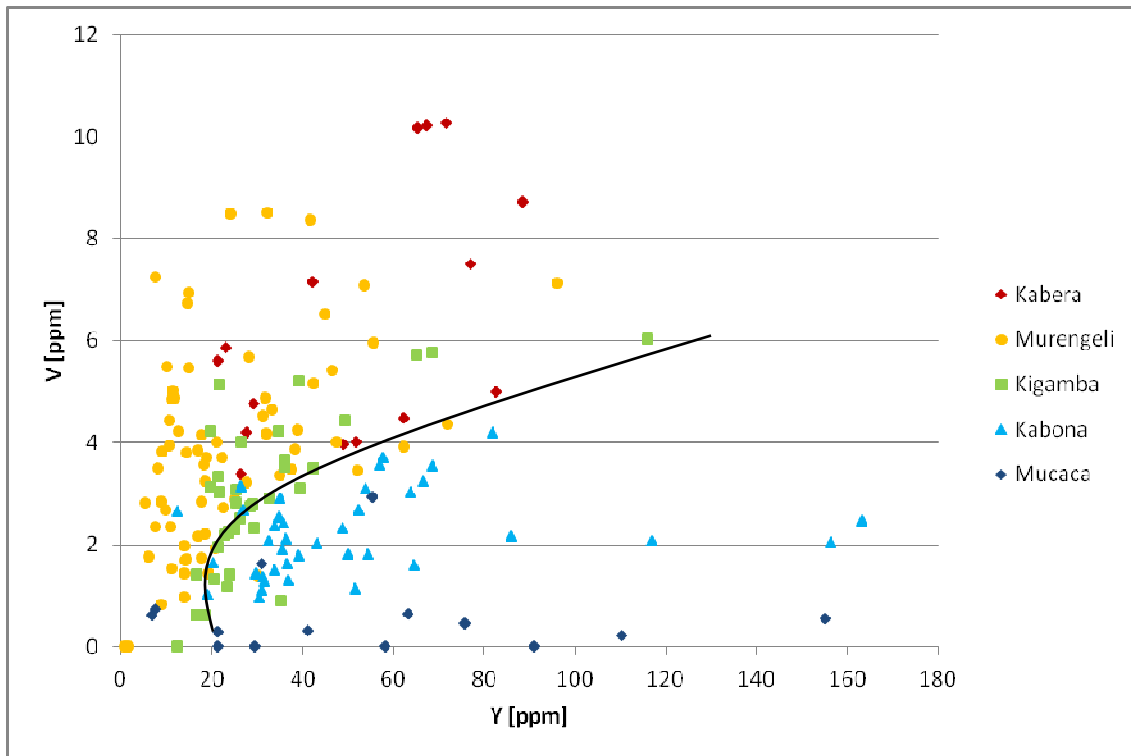


Figure 11.22: Binary diagram showing the concentrations of Y [ppm] versus V [ppm] from LA-ICP-MS analysis of wolframite originating from five localities of the Rutsiro concession.

Case study: Rutongo

Rutongo is the major tin mining area in Rwanda located approximately 15 km north of the capital Kigali (Figure 10.4). The tin mines exploit either primary quartz veins or secondary eluvial/alluvial placers and are situated within a large NNW-plunging anticline (Figure 11.23; Pohl, 1975). The anticline is composed of alternating successions of quartzites, metapelites and sandstones (Pohl, 1975; Dewaele et al., 2010). In the southern portion of the Rutongo area, these Kibaran metasedimentary rocks are intruded by two-mica granite of the Kigali pluton (Figure 10.4; Bertossa et al., 1964), which belongs to the youngest G4-granite generation of the Kibaran belt (Pohl, 1975).

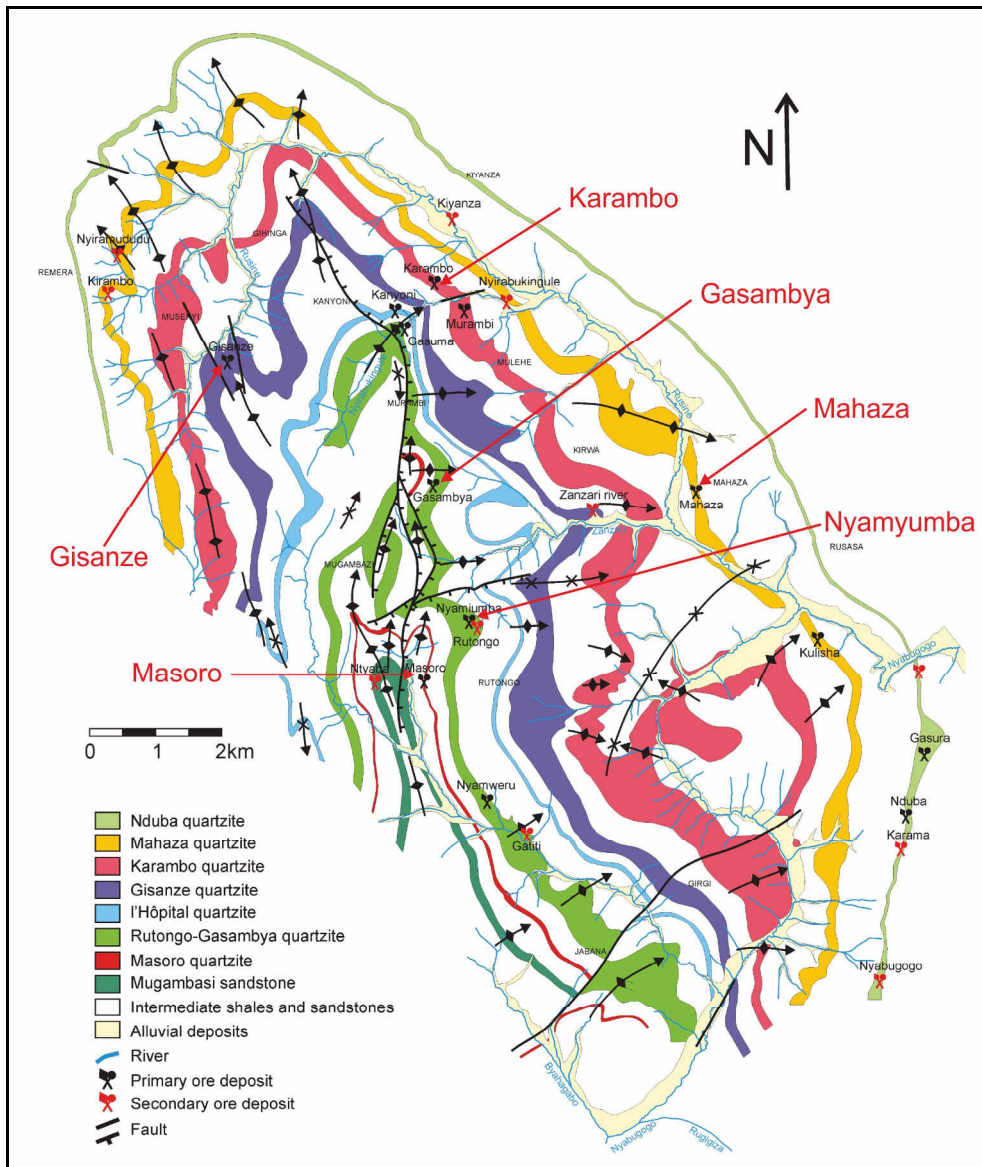


Figure 11.23: Geological map of the Rutongo area in Rwanda showing the distribution of the tin mines and their distinct relation to the quartzite units within the anticlinal structure (De Clercq, 2012; modified after Pohl, 1975).

The primary deposits are composed of swarms of up to several hundred sub-parallel cassiterite-bearing hydrothermal quartz veins and are typically restricted to one of the prominent quartzite horizons, which are separated by units of barren metapelites and sandstones (Figure 11.23; Pohl, 1975; Dewaele et al., 2010; De Clercq, 2012). The cassiterite-mineralised veins are principally composed of quartz with minor muscovite and rare sulphides like arsenopyrite, pyrite, chalcopyrite, and galena (Dewaele et al., 2010; De Clercq, 2012), but the veins are devoid of tungsten minerals (Pohl, 1975). Generally, the mineralised hydrothermal quartz veins have a common N-S strike with 60° dip to the west and are found in the eastern flank of the Rutongo anticline (Pohl, 1975). The only exception from this general distribution is the Gisanze deposit; here the

quartz veins are located on the western flank of the Rutongo anticline and are striking in approximately E-W direction dipping south with 70-80° (Pohl, 1975). Detailed descriptions of the regional geology and the tin deposits of the Rutongo area are given by Pohl (1975), Dewaele et al. (2010), and De Clercq (2012).

Cassiterite concentrate samples were collected from the following deposits of the Rutongo area; in some mines different tunnels were sampled (Figure 11.23): Nyamyumba (n=6), Gasambya (n=3), Masoro (n=2), Gisanze (n=3), Karambo (n=1), and Mahaza (n=1). Variability within a deposit is demonstrated by the trace element compositions of cassiterite from six different tunnels on different mine levels (represented by six respective ore concentrates) of the Nyamyumba mine. Comparison of the trace element composition shows that the six samples are very similar to each other and strongly overlap in narrow ranges (Figure 11.24), although a systematic shift in the Ta concentration levels is evident which correlates with mining level (sample 10019 highest at 1845 m to sample 10024 lowest at 1660 m). This result conclusively indicates that the trace element composition of cassiterite from hydrothermal vein deposits is quite constant over lateral and vertical extend of the veins (compare with case study on Nyakabingo).

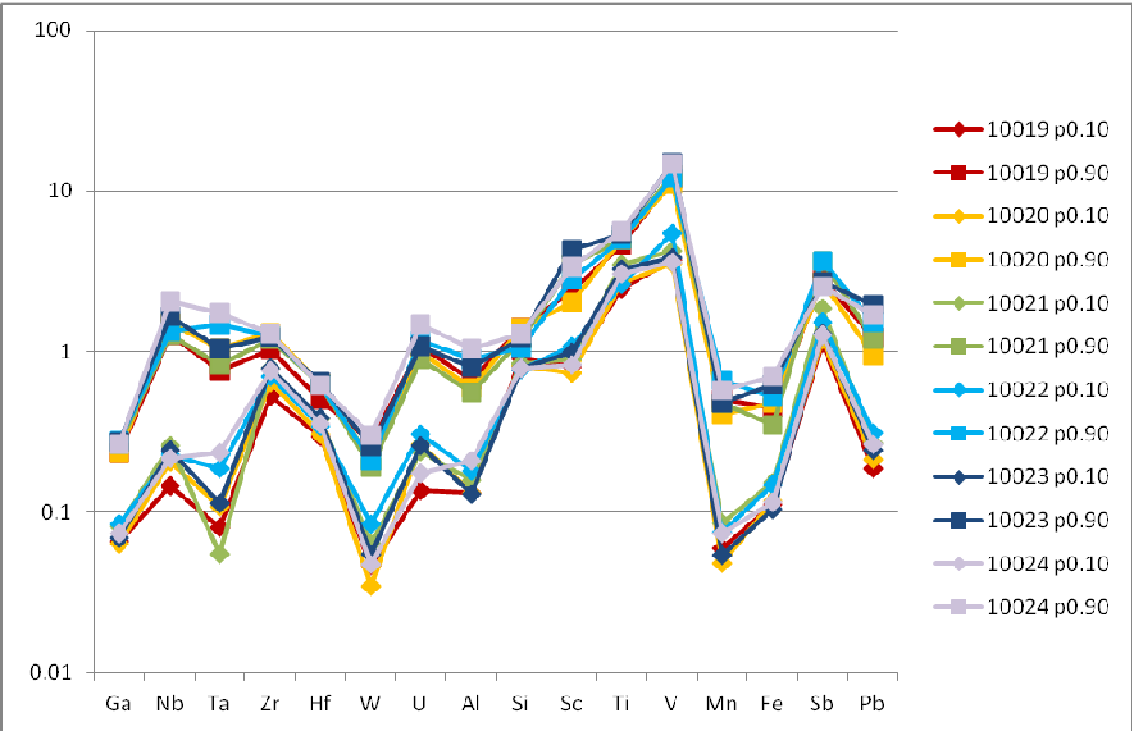


Figure 11.24: Normalised element distribution patterns of cassiterite from ore concentrates originating from six tunnels of the Nyamyumba deposit. Variability of the trace element composition is given as the 10th percentile (lower line with diamonds) and 90th percentile (upper line with squares) of the normalised values.

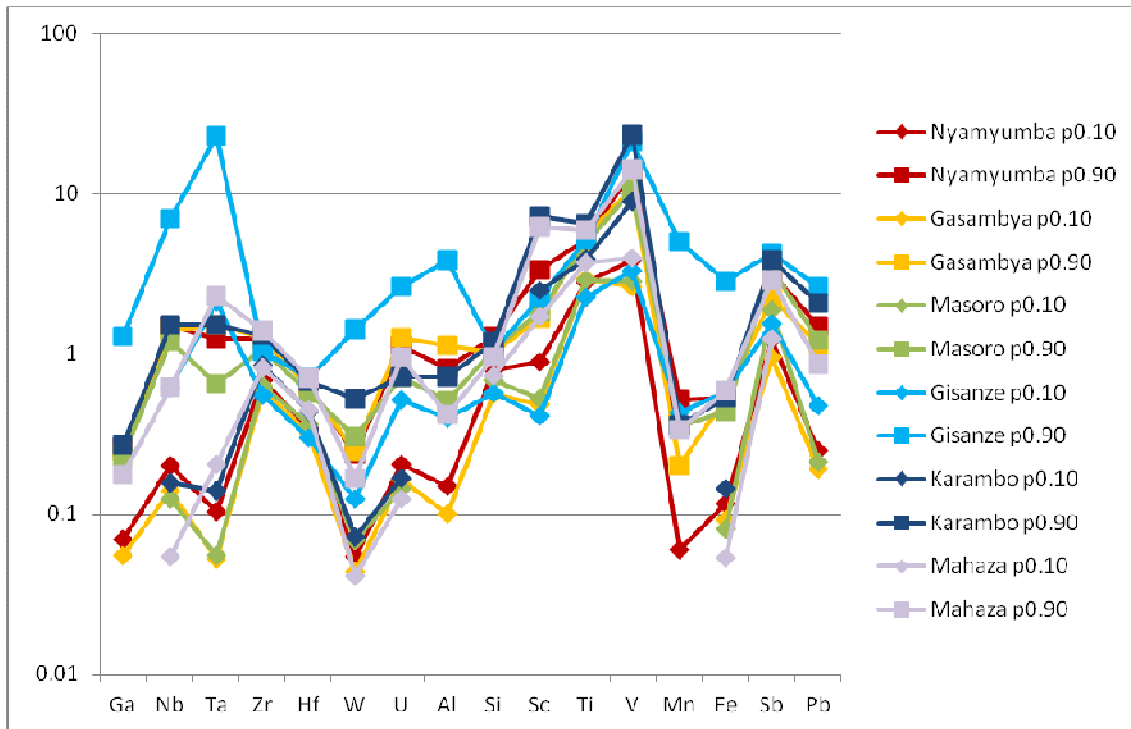


Figure 11.25: Normalised element distribution patterns of cassiterite from ore concentrates originating from six deposits of the Rutongo area. Variability of the trace element composition is given as the 10th percentile (lower line with diamonds) and 90th percentile (upper line with squares) of the normalised values.

Comparison of the cassiterite trace element compositions from the six different deposits (where the respective samples of a single deposit are handled as one) shows that the Gisanze deposit is considerably different from the other deposits of the Rutongo area as it is characterised by higher Ta, Mn, Fe, W, and U contents (Figure 11.25). This markedly different composition reflects the clearly different geological setting of this deposit as outlined above.

However, the cassiterite compositions of the other deposits are rather similar (Figure 11.25). Especially, cassiterite from the Nyamyumba and Gasambya deposits are very similar with only slight differences in Sc and Mn; this strong similarity is reasonable as both deposits occur in close spatial relationship within the same quartzite unit (Rutongo-Gasambya quartzite). Even the cassiterite from the Masoro deposit only shows faintly lower Ta, U, and Al contents compared to Nyamyumba and Gasambya deposits. Although the Masoro deposit is located in immediate vicinity, it is already situated in a separate quartzite unit (Masoro quartzite). The Karambo and Mahaza deposits are characterised by highest Sc and Ta contents of this group, but in turn both samples are somewhat different in their Nb, V, and W contents. Again, these two deposits occur in two separate quartzite units (Figure 11.23).

The slight differences between the various deposits may be attributed to their respective setting within the Rutongo anticline as the individual vein systems occur in different stratigraphic quartzite units. Minor variations in cassiterite chemistry are perhaps influenced by the host rock, even though the quartzites are very pure and almost exclusively composed of quartz with only minor accessories (Dewaele et al., 2010; De Clercq, 2012). Nevertheless, the deposits from the Rutongo mining area are very similar (except for Gisanze) in their cassiterite compositions as they by a single mineralizing event in very similar host rock lithologies. This means for AFP that deposits in close proximity (e.g., on a concession), which formed contemporaneously by the same precipitation mechanism in very similar host rocks, can hardly be discriminated by the chemical composition of cassiterite.

12 Summary and conclusions

For the first time, minor and trace element data by LA-ICP-MS are presented for cassiterite and wolframite single grains in ore concentrates from different ore deposit types worldwide of various geological ages. It turned out that LA-ICP-MS is the method of choice for trace element analysis of cassiterite and wolframite, because considerably lower detection limits are necessary compared to EPMA as concentration levels of most elements are relatively low in these minerals. As a prerequisite, an important part of work was the development and implementation of LA-ICP-MS methods for analysis of cassiterite and wolframite, respectively. This included setup of the LA-ICP-MS system and selection of the most suitable isotopes to avoid interferences (see Chapters 8 & 9).

Individual deposits are characterised by unique mineralogical, geochemical, and geochronological parameters which are recorded during formation of each ore deposit. These are represented by the mineral paragenesis, the crystal chemistry of the single mineral phases, and the U-Pb model age of formation; these parameters can be utilised to perform the AFP. However, the mineral assemblage of the ore concentrate does not represent a robust parameter for AFP as it is strongly dependent on the beneficiation process and could be easily modified. Nevertheless, the occurrence of characteristic or rare mineral phases in the ore concentrate may still serve as an important indicator for a single ore deposit (e.g., rare minerals like simpsonite, lithiowodginite, foordite, thoreaulite, stibiotantalite or anthoinite) or is at least indicative for an ore deposit type (presence or absence of Ta-bearing minerals are indicative for magmatic or hydrothermal deposits, respectively). But as a consequence, the determination of the mineralogical composition of an ore concentrate is not necessarily needed for AFP as the chemical composition of individual ore minerals represents a much more robust parameter and is resistant to external manipulation.

Trace element data of single mineral grains obtained by LA-ICP-MS analysis are the crucial parameter for AFP. The results of trace element analysis of cassiterite and wolframite from a multitude of localities including different ore deposit types indicate that the chemical variability of cassiterite or wolframite is huge and encompasses several orders of magnitude, occasionally even within a single ore concentrate or ore body. Trace element variability is evident on grain scale (chemical zoning in single grains, see Figures 10.8-10.10) as well as on deposit scale (see case studies in Chapter 11). The elemental compositions of single mineral grains represent distinct conditions during formation and also different zones within an ore body. This points out that a

representative number of ore minerals from all zones of the ore body needs to be analysed for AFP to cover the entire variability within the ore body. This may also include additional sampling, especially in zoned pegmatites. However, in this context it was also demonstrated that the trace element variability in hydrothermal vein deposits is rather constant over strike length and depth (see case studies on Nyakabingo and Rutongo) and extensive sampling is not necessary for AFP.

Precipitation of cassiterite and wolframite is controlled by several factors during formation of the ore deposit such as composition of the magma and/or the fluid, depth of emplacement of the magma, origin of the fluids, and interaction with the host or country rocks. Generally, trace element incorporation into the crystal structure of cassiterite or wolframite and the concentration levels of respective trace elements are dependent on:

- 1) Crystallographic constraints according to ionic radius and charge balance
- 2) Element availability influenced by the composition of various possible reservoirs like melt, fluid, host rocks or country rocks and basically by the natural elemental abundance
- 3) Co-precipitation of other minerals competing for a certain element
- 4) Physicochemical parameters like temperature (as trace element incorporation is enabled by higher temperatures), oxygen fugacity (which controls speciation of certain elements) and partition coefficients (which can vary up to several orders of magnitude with melt and fluid compositions)

For example, the Zr/Hf and Ta/Nb ratios in both cassiterite and wolframite serve as an indicator for fractionation and can be already used to discriminate between different ore deposit types in terms of either more magmatic (high Ta/Nb, low Zr/Hf) or hydrothermal (low Ta/Nb, high Zr/Hf) conditions during ore formation. The presence (but also the absence) of trace elements can be interpreted in terms of ore precipitation mechanisms and geological setting. Some trace elements represent magmatic influence and derive from the parental granitic intrusion (e.g., Ta, Nb, Hf, Zr in cassiterite and wolframite), while others indicate pervasive hydrothermal alteration and are mobilised from the surrounding country rocks (e.g., V in hydrothermal cassiterite and wolframite, Sc in cassiterite from the Greenbushes and Tanco pegmatites, Mg in wolframite) or from the magmatic host rock (e.g., Ga in cassiterite from the Bolivian Tin Belt). Several substitution mechanisms for cassiterite and wolframite are proposed, but it is evident

that incorporation of major and minor elements is not solely controlled by one single substitution mechanism (e.g., Fe in cassiterite).

As the above mentioned parameters influence the trace element composition of ore minerals and are superimposed on each other, different ore districts, deposit types and even individual ore deposits can be differentiated. Minerals which form under similar physiochemical conditions in the same environment result in characteristic, unique trace element signatures including similar concentration levels, variability of major, minor, and trace element contents, and inter-elemental ratios and may be used to determine their origin. Though the variability of single elements may be large for cassiterite or wolframite from individual deposits and may overlap with element distribution patterns of these minerals from other deposits, each deposit is characterised by its unique element distribution in the respective mineral taking the variability of all relevant elements into account.

Using the variability and the range of the trace element distribution in ore minerals, it is feasible to discriminate individual deposits even on concession scale as demonstrated by case studies. Nevertheless, it must be admitted that the discrimination on concession scale is challenging due to related geological conditions like similar composition of the host and country rocks, identical parental intrusion and similar intrusion levels, and the same formation age. However, the application of statistical tests like Kolmogorov-Smirnov statistics as stated by Gäbler et al. (2013) seem to be promising to assign if a sample derives from the declared origin or not.

In the course of analysis of numerous cassiterite and wolframite grains from different ore deposits it turns out that several elements generally occur below or close to the detection limit of the method and may be removed from the element list in order to reduce the required time per measurement for future studies (e.g., Sr, Y, Mo, REE, Bi, Na, Ca in cassiterite or Ag, Cd, Tl, Sb, Al, Cr, Ni, Cu, Sr in wolframite). Otherwise, certain elements are generally below the detection limit but may be characteristic for single ore deposits, for example Sr in cassiterite from Abu Dabbab, Japo and Poldi, Y in cassiterite from Pitinga, Sb in wolframite from Khovd Gol, Cu in wolframite from Mucaca, Cd in wolframite from Ranong and Tsagaan Davaa, and the uncommon elements (Ga, Ba, LREE, Sr) in reinte.

Comprehensive studies on mineralogy, petrology, and geochemistry of ore deposits and their associated rocks are a potential field of work for the future to confirm the statements on the relationship between trace elements in ore minerals and

composition of the associated granites as well as surrounding country rocks. Especially the influence of the surrounding country rocks should definitely also be taken into account in these future studies.

13 References

- Abdalla, H.M., Matsueda, H., Obeid, M.A. & Takahashi, R. (2008) – Chemistry of cassiterite in rare metal granitoids and the associated rocks in the Eastern Desert, Egypt; *Journal of Mineralogical and Petrological Sciences*, Vol. 103, pp. 318-326
- Ahlfeld, F. (1958) – Zinn und Wolfram; Die metallischen Rohstoffe ihre Lagerungsverhältnisse und ihre wirtschaftliche Bedeutung, Vol. 11, Enke Publishing, Stuttgart, 212 p.
- Ahlfeld, F. & Schneider-Scherbina, A. (1964) – Los yacimientos minerales y de hidrocarburos de Bolivia; Departamento Nacional de Geología del Ministerio de Minas y Petróleo, Boletín No 5 (especial), 388 p.
- Aïssa, M., Marignac, C. & Weisbrod, A. (1987) – Le stockwerk à ferberite d'Echassières: évolution spatiale et temporelle, cristallographie des ferberites; *Géologie de la France*, No 2-3, pp. 311-333
- Allman-Ward, P., Halls, C., Rankin, A. & Bristow, C.M. (1982) – An intrusive hydrothermal breccia body at Wheal Remfry in the western part of the St Austell granite pluton, Cornwall, England; in: Evans, A.M. (Ed.) – *Metallization Associated with Acid Magmatism*; Vol. 6, John Wiley & Sons, Chichester, pp. 1-28
- Amossé, J. (1978a) – Variation in wolframite composition according to temperature, at Borralha, Portugal, and Enguayales, France; *Economic Geology*, Vol. 73, pp. 1170-1175
- Amossé, J. (1978b) – Physicochemical study of the hübnerite-ferberite ($MnWO_4$ – $FeWO_4$) zonal distribution in wolframite ($Mn_xFe_{(1-x)}WO_4$) deposits: application to the Borralha mine (Portugal); *Physics and Chemistry of Minerals*, Vol. 3, pp. 331-341
- Andrews, M.G. (1955) – Tungsten: the story of an indispensable metal; The Tungsten Institute, Washington, D.C., 27 p.
- Angelelli, V & Gordon, S.G. (1948) – Sanmartinite; *American Mineralogist*, Vol. 33, p. 653
- Angerer, G., Erdmann, L., Handke, V., Lüllmann, A., Marscheider-Weidemann, F., Marwede, M. & Scharp, M. (2009) – Rohstoffe für Zukunftstechnologien: Einfluss des branchenspezifischen Rohstoffbedarfs in rohstoffintensiven Zukunftstechnologien auf die zukünftige Rohstoffnachfrage; Institut für Zukunftsstudien und Technologiebewertung (IZT) & Fraunhofer Institut für System- und Innovationsforschung (ISI), Fraunhofer IRB Verlag, Stuttgart, 383 p.
- Anthony, J.W., Bideaux, R.A., Bladh, K.W. & Nichols, M.C. (Eds.) (2001) – *Handbook of Mineralogy*; Mineralogical Society of America, Chantilly, <http://www.handbookofmineralogy.org/>
- Antipin, V.S, Kovalenko, V.I., Kuznetsova, A.I. & Persikova, L.A. (1981) – Distribution coefficients for tin and tungsten in ore-bearing acid igneous rocks; *Geochemistry International*, Vol. 18, pp. 92-106
- Appel, P.W.U. (1994) – Stratabound scheelite in altered Archaean komatiites, West Greenland; *Mineralium Deposita*, Vol. 29, pp. 341-352
- Aranyakanon, P. (1961) – The cassiterite deposit of Haad Som Pan, Ranong Province, Thailand; Royal Department of Mines, Report of Investigation, Vol. 4., 182 p.
- Arce-Burgoa, O.R & Goldfarb, R.J. (2009) – Metallogeny of Bolivia; *SEG Newsletter*, Society of Economic Geologists, Vol. 79, pp. 1, 8-15
- Arevalo Jr., R. & McDonough, W.F. (2008) – Tungsten geochemistry and implications for understanding the Earth's interior; *Earth and Planetary Science Letters*, Vol. 272, pp. 656-665
- Ariffin, K.S. (2009) – Sediment Hosted Primary Tin Deposit Associated with Biotite Granite and Fault Zone at Gunung Paku, Klian Intan, Upper Perak, Malaysia; *Resource Geology*, Vol. 59, pp. 282-294

- Audétat, A., Günther, D. & Heinrich, C.A. (2000a) – Magmatic-hydrothermal evolution in a fractionating granite: a microchemical study of the Sn-W-F-mineralized Mole Granite (Australia); *Geochimica et Cosmochimica Acta*, Vol. 64, pp. 3373-3393
- Audétat, A., Günther, D. & Heinrich, C.A. (2000b) – Causes for large-scale metal zonation around mineralized plutons: fluid inclusion LA-ICP-MS evidence from the Mole granite, Australia; *Economic Geology*, Vol. 95, pp. 1563-1581
- Audétat, A., Pettke, T., Heinrich, C.A. & Bodnar, R.J. (2008) – The composition of magmatic-hydrothermal fluids in barren and mineralized intrusions; *Economic Geology*, Vol. 103, pp. 877-908
- Baadsgaard, H. & Černý, P. (1993) – Winnipeg River pegmatite populations, southeastern Manitoba; Geological Association of Canada-Mineralogical Association of Canada (GAC-MAC) joint annual meeting, Edmonton, Program with Abstracts, Vol. 18, p. A5
- Badanina, E.V., Veksler, I.V., Thomas, R., Syritso, L.F. & Trumbull, R.B. (2004) – Magmatic evolution of Li-F, rare-metal granites: a case study of melt inclusions in the Khangilay complex, Eastern Transbaikalia (Russia); *Chemical Geology*, Vol. 210, pp. 113-133
- Bailly, L., Grancea, L. & Kouzmanov, K. (2002) – Infrared microthermometry and chemistry of wolframite from the Baia Sprie epithermal deposit, Romania; *Economic Geology*, Vol. 97, pp. 415-423
- Ball, T.K., Fortey, N.J. & Shepherd, T.J. (1985) – Mineralisation at the Carrock Fell tungsten mine, N. England: paragenetic, fluid inclusion and geochemical study; *Mineralium Deposita*, Vol. 20, pp. 57-65
- Barabanov, V.F. (1971) – Geochemistry of tungsten; *International Geology Review*, Vol. 13, pp. 332-344
- Barkov, A.Y., Martin, R.F., Poirier, G. & Yakovlev, Y.N. (2000) – The taimyrite-tatyanite series and zoning in intermetallic compounds of Pt, Pd, Cu, and Sn from Noril'sk, Siberia, Russia; *Canadian Mineralogist*, Vol. 38, pp. 599-609
- Barkov, A.Y., Martin, R.F., Shi, L., LeBarge, W. & Fedortchouk, Y. (2008) – Oscillatory zoning in stanniferous hematite and associated W- and Bi-rich minerals from Canadian Creek, Yukon, Canada; *Canadian Mineralogist*, Vol. 46, pp. 59-72
- Bastos Neto, A.C., Pereira, V.P., Ronchi, L.H., de Lima, E.F. & Frantz, J.C. (2009) – The world-class Sn, Nb, Ta, F (Y, REE, Li) deposit and the massive cryolite associated with the albite-enriched facies of the Madeira A-type granite, Pitinga mining district, Amazonas state, Brazil; *Canadian Mineralogist*, Vol. 47, pp. 1329-1357
- Bastos Neto, A.C., Ferron, J.T.M.M., Chauvet, A., Chemale Jr, F., de Lima, E.F., Barbanson, L. & Costa, C.F.M. (2014) – U-Pb dating of the Madeira Suite and structural control of the albite-enriched granite at Pitinga (Amazonia, Brazil): evolution of the A-type magmatism and implications for the genesis of the Madeira Sn-Ta-Nb (REE, cryolite) world-class deposit; *Precambrian Research*, Vol. 243, pp. 181-196
- Belkasmı, M., Cuney, M., Pollard, P.J. & Bastoul, A. (2000) – Chemistry of the Ta-Nb-Sn-W oxide minerals from the Yichun rare metal granite (SE China): genetic implications and comparison with Moroccan and French Hercynian examples; *Mineralogical Magazine*, Vol. 64, pp. 507-523
- Bernard, A., Symonds, R.B. & Rose, W.I. (1990) – Volatile transport and deposition of Mo, W and Re in high temperature magmatic fluids; *Applied Geochemistry*, Vol. 5, pp. 317-326
- Bettencourt, J.S., Tosdal, R.M., Leite Jr., W.B. & Payolla, B.L. (1999) – Mesoproterozoic rapakivi granites of the Rondônia Tin Province, southwestern border of the

- Amazonian craton, Brazil: I. Reconnaissance U-Pb geochronology and regional implications; *Precambrian Research*, Vol. 95, pp. 41-67
- Bettencourt, J.S., Leite Jr., W.B., Goraieb, C.L., Sparrenberger, I., Bello, R.M.S. & Payolla, B.L. (2005) – Sn-polymetallic greisen-type deposits associated with late-stage rapakivi granites, Brazil: fluid inclusion and stable isotope characteristics; *Lithos*, Vol. 80, pp. 363-386
- Beran, P. & Sejkora, J. (2006) – The Krásno Sn-W ore district near Horní Slavkov: mining history, geological and mineralogical characteristics; *Journal of the Czech Geological Society*, Vol. 51, pp. 3-42
- Bertossa, A., Gérards, J. & Perticec, V. (1964) – Géologie de la région de Kigali; *Bulletin du Service Géologique de Rwanda*, Vol. 1, pp. 3-12
- Beurlen, H., da Silva, M.R.R., Thomas, R., Soares, D.R. & Olivier, P. (2008) – Nb-Ta-(Ti-Sn) oxide mineral chemistry as tracer of rare-element granitic pegmatite fractionation in the Borborema Province, Northeastern Brazil; *Mineralium Deposita*, Vol. 43, pp. 207-228
- BGR (2010) – Bundesrepublik Deutschland: Rohstoffsituation 2009; *Rohstoffwirtschaftliche Länderstudien*, Vol. 39, Federal Institute for Geosciences and Natural Resources (BGR), Hannover, 205 p.
- BGS (2011) – Tungsten; *Commodity Profiles*, MineralsUK, British Geological Survey, Keyworth, United Kingdom, 33p.
- Bhalla, P. (2005) – Solubilities and diffusivities of metals (platinum, tin) and metal-oxide (cassiterite) in silicate melts: the effect of halogens (Cl, F); Ph.D. thesis, Leibniz University of Hannover, 167 p.
- Bhalla, P., Holtz, F., Linnen, R.L. & Behrens, H. (2005) – Solubility of cassiterite in evolved granitic melts: effect of T, fO₂, and additional volatiles; *Lithos*, Vol. 80, pp. 387-400
- Binde, G. (1986) – Beitrag zur Mineralogie, Geochemie und Genese des Kassiterits; *Freiberger Forschungshefte*, Vol. C411, 60 p.
- Björkstedt, K.-A. (1972) – Investigation to determine the content of tin and other trace elements in Grängesberg ore; *Geologiska Föreningens i Stockholm Förhandlingar*, Vol. 94, pp. 165-192
- Blake, D.H. & Smith J.W. (1970) – Mineralogical zoning in the Herberton tinfield, north Queensland, Australia; *Economic Geology*, Vol. 65, pp. 993-997
- Blevin, P.L. & Chappell, B.W. (1995) – Chemistry, origin, and evolution of mineralized granites in the Lachlan Fold Belt, Australia: The metallogeny of I- and S-type granites; *Economic Geology*, Vol. 90, pp. 1604-1619
- Bolzan, A.A., Fong, C., Kennedy, B.J. & Howard, C.J. (1997) – Structural studies of rutile-type metal dioxides; *Acta Crystallographica*, Vol. B53, pp. 373-380
- Bonin, B. (2007) – A-type granites and related rocks: Evolution of a concept, problems and prospects; *Lithos*, Vol. 97, pp. 1-29
- Borges, R.M.K., Villas, R.N.N., Fuzikawa, K., Dall’Agnol, R. & Pimenta, M.A. (2009) – Phase separation, fluid mixing, and origin of the greisens and potassic episyenite associated with the Água Boa pluton, Pitinga tin province, Amazonian Craton, Brazil; *Journal of South American Earth Sciences*, Vol. 27, pp. 161-183
- Borisenko, L.F. & Lizunov, N.V. (1959) – The occurrence of scandium and some other rare elements in cassiterite; *Geokhimiya*, Vol. 1, pp. 64-68
- Borisova, A.Y., Thomas, R., Salvi, S., Vandaudap, F., Lanzanova, A. & Chmeleff, J. (2012) – Tin and associated metal and metalloid geochemistry by femtosecond LA-ICP-QMS microanalysis of pegmatite-leucogranite melt and fluid inclusions: new evidence for melt-melt-fluid immiscibility; *Mineralogical Magazine*, Vol. 76, pp. 91-113

- Botelho, N.F. & Moura, M.A. (1998) – Granite-ore deposit relationships in Central Brazil; *Journal of South American Earth Sciences*, Vol. 11, pp. 527-438
- Botto, I.L., Barone, V.L., Sanchez, M.A. & Schalamuk, I.B. (2000) – Correlation between reducibility and composition of natural wolframite in Argentinian ore deposits; *Mineralogical Magazine*, Vol. 64, pp. 497-505
- LeBoutillier, N.G. (2002) – Tectonics of Variscan magmatism and mineralisation in South West England; Ph.D. thesis, University of Exeter, 639 p.
- Bouysse, P. (2009) – Geological map of the World; Sheet 2: geology and structure, 3rd edition, Commission for the geological map of the World (CGMW), Paris, 1:50000000
- Bowden, P. (1982) – Magmatic evolution and mineralization in the Nigerian Younger Granite Province; in: Evans, A.M. (Ed.) – *Metallization Associated with Acid Magmatism*; Vol. 6, John Wiley & Sons, Chichester, pp. 51-61
- Bowden, P. & Kinnaird, J.A. (1984) – Geology and mineralization of the Nigerian anorogenic ring complexes; *Geologisches Jahrbuch*, Vol. B56, 65 p.
- Breiter, K., Förster, H.-J. & Seltmann, R. (1991) – Geochemical specialization of the tin-bearing granitoid massifs of NW Bohemia; *Mineralium Deposita*, Vol. 26, pp. 298-306
- Breiter, K. & Škoda, R. (2004) – Differences in chemistry of magmatic and hydrothermal cassiterite and wolframite from western Krušné hory Mts.; *Zprávy o geologických výzkumech v roce 2004*, pp. 94-96 (in Czech)
- Bridgwater, D., Sutton, J. & Watterson, J. (1974) – Crustal downfolding associated with igneous activity; *Tectonophysics*, Vol. 21, pp. 57-77
- Brinkmann, J. (1987) – Deutsche Geologische Arbeitsgruppe Burundi: Exploration auf Zinn/Wolfram und Seltene Erden; Federal Institute for Geosciences and Natural Resources (BGR), Technical Cooperation Project 81.2026.3, Final Report, , Hannover, 91 p.
- Bromley, A.V. & Holl, J. (1986) – Tin mineralisation in southwest England; in: Willis, B.A. & Barley, R.W. (Eds.) – *Mineral processing at crossroads*; ASI Serial Number 119, Martinus Nijhoff, Dordrecht, pp. 159-262
- Brown, G.F. & Jalichandra, N. (1951) – Mae Sariang tungsten district, Mae Hong Son; in: Brown, G.F., Buravas, S., Charaljavanaphet, J., Jalichandra, N., Johnston Jr., W.D., Sresthaputra, V. & Taylor Jr., G.C. (authors) – *Geologic Reconnaissance of the Mineral Deposits of Thailand*; Geological Survey Bulletin, Vol. 984, pp. 99-105
- Brugger, J., Lahaye, Y., Costa, S., Lambert, D. & Bateman, R. (2000) – Inhomogeneous distribution of REE in scheelite and dynamics of Archaean hydrothermal systems (Mt. Charlotte and Drysdale gold deposits, Western Australia); *Contributions to Mineralogy and Petrology*, Vol. 139, pp. 251-264
- Brugger, J., Etschmann, B., Pownceby, M., Liu, W., Grundler, P. & Brewe, D. (2008) – Oxidation state of europium in scheelite: tracking fluid-rock interaction in gold deposits; *Chemical Geology*, Vol. 257, pp. 26-33
- Buhl, J.-C. & Willgallis, A. (1986) – The low-temperature crystallization of (Fe,Mn)WO₄ (wolframite), (Zn,Fe)WO₄ (sanmartinite) and (Zn,Mn)WO₄ solid solutions under hydrothermal conditions; *Chemical Geology*, Vol. 56, pp. 271-279
- Burnham, C.W. (1997) – Magmas and hydrothermal fluids; in: Barnes, H.L. (Ed.) – *Geochemistry of hydrothermal ore deposits*; 3rd edition, John Wiley & Sons, New York, pp. 63-123
- Burns, P.C. (1999) – The crystal chemistry of uranium; in: Burns, P.C. & Finch, R. (Eds.) – *Uranium: mineralogy, geochemistry, and the environment*; *Reviews in Mineralogy*, Mineralogical Society of America, Vol. 38, pp. 23-90
- Burt, D.M. & Sheridan, M.F. (1988) – Mineralization associated with topaz rhyolites and related rocks in Mexico; in: Taylor, R.P. & Strong, D.F. (Eds.) – *Recent advances in the*

- geology of granite-related mineral deposits; The Canadian Institute of Mining and Metallurgy, Special Volume 39, Montreal, pp. 303-306
- Cabri, L.J. (2002) – The platinum-group minerals; in: Cabri, L. J. (Ed.) – The geology, geochemistry, mineralogy and mineral beneficiation of platinum-group elements; Canadian Institute of Mining, Metallurgy and Petroleum, Special Volume, Vol. 54, pp. 13-129
- Cahen, L. & Ledent, D. (1979) – Précisions sur l'âge, la pétrogenèse et la position stratigraphique des "granites à étain" de l'est de l'Afrique centrale; Bulletin Société Belge de Géologie, Vol. 88, pp. 33-49
- Camacho, A., Baadsgaard, H., Davis, D.W. & Černý, P. (2012) – Radiogenic isotope systematic of the Tanco and Silverleaf granitic pegmatites, Winnipeg River pegmatite district, Manitoba; Canadian Mineralogist, Vol. 50, pp. 1775-1792
- Campbell, A., Rye, D. & Petersen, U. (1984) – A hydrogen and oxygen isotope study of the San Cristobal mine, Peru: Implications of the role of water to rock ratio for the genesis of wolframite deposits; Economic Geology, Vol. 79, pp. 1818-1832
- Campbell, A.R. & Robinson-Cook, S. (1987) – Infrared fluid inclusion microthermometry on coexisting wolframite and quartz; Economic Geology, Vol. 82, pp. 1640-1645
- Campbell, A. & Petersen, U. (1988) – Chemical zoning in wolframite from San Cristobal, Peru; Mineralium Deposita, Vol. 23, pp. 132-137
- Campbell, A.R. & Panter, K.S. (1990) – Comparison of fluid inclusions in coexisting (cogenetic?) wolframite, cassiterite, and quartz from St. Michael's Mount and Cligga Head, Cornwall, England; Geochimica et Cosmochimica Acta, Vol. 54, pp. 673-681
- Carpenter, L.G. & Garret D.E. (1959) – Tungsten in Searles Lake; American Institute of Mining Engineers Transactions, Vol. 11, pp. 301-303
- Casadevall, T. & Rye, R.O. (1980) – The Tungsten Queen deposit, Hamme district, Vance County, North Carolina: A stable isotope study of a metamorphosed quartz-hübnerite vein; Economic Geology, Vol. 75, pp. 523-537
- Cathles, L.M. (1981) – Fluid flow and genesis of hydrothermal ore deposits; in: Skinner, B.J. (Ed.) – Economic Geology: 75th Anniversary Volume; Society of Economic Geologists, The Economic Geology Publishing Company, pp. 424-457
- Černý, P. (1982) – The Tanco pegmatite at Bernic Lake, Southeastern Manitoba; in: Černý, P. (Ed.) – Granitic pegmatites in science and industry; Short Course Handbook, Mineralogical Association of Canada, Winnipeg, Vol. 8, 527-543.
- Černý, P. & Ercit, T.S. (1985) – Some recent advances in the mineralogy and geochemistry of Nb and Ta in rare-element granitic pegmatites; Bulletin de Minéralogie, Vol. 108, pp. 499-532
- Černý, P., Roberts, W.L., Ercit, T.S. & Chapman, R. (1985) – Wodginite and associated oxide minerals from the Peerless pegmatite, Pennington County, South Dakota; American Mineralogist, Vol. 70, pp. 1044-1049
- Černý, P., Fransolet, A.-M., Ercit, T.S. & Chapman, R. (1988) – Foordite SnNb_2O_6 , a new mineral species, and the foordite-thoreaulite series; Canadian Mineralogist, Vol. 26, pp. 889-898
- Černý, P. & Ercit, T.S. (1989) – Mineralogy of niobium and tantalum: crystal chemical relationships, paragenetic aspects and their economic implications; in: Möller, P. (Ed.) – Lanthanides, tantalum and Niobium; Springer Verlag, Berlin, pp. 27-79
- Černý, P. (1992) – Geochemical and petrogenetic features of mineralization in rare-element granitic pegmatites in the light of current research; Applied Geochemistry, Vol. 7, pp. 393-416
- Černý, P. (1993) – Rare-element granitic pegmatites. Part I: Anatomy and internal evolution of pegmatite deposits; Geoscience Canada, Vol. 18/2, pp.49-67

- Černý, P., Chapman, R., Ferreira, K. & Smeds, S.-A. (2004) – Geochemistry of oxide minerals of Nb, Ta, Sn, and Sb in the Varuträsk granitic pegmatite, Sweden: The case of an “anomalous” columbite-tantalite trend; *American Mineralogist*, Vol. 89, pp. 505-518
- Černý, P. & Ercit, T.S. (2005) – The classification of granitic pegmatites revisited; *Canadian Mineralogist*, Vol. 43, pp. 2005-2026
- Chakhmouradian, A.R., Smith, M.P. & Kynicky, J. (2015) – From “strategic” tungsten to “green” neodymium: a century of critical metals at a glance; *Ore Geology Reviews*, Vol. 64, pp. 455-458
- Chappell, B.W. & White, A.J.R. (1974) – Two contrasting granite types; *Pacific Geology*, Vol. 8, pp. 173-174
- Chappell, B.W. & Hine, R. (2006) – The Cornubian Batholith: an example of magmatic fractionation on a crustal scale; *Resource Geology*, Vol. 56, pp. 203-244
- Che, X.D., Linnen, R.L., Wang, R.C., Aseri, A. & Thibault, Y. (2013) – Tungsten solubility in evolved granitic melts: an evaluation of magmatic wolframite; *Geochimica et Cosmochimica Acta*, Vol. 106, pp. 84-98
- Cheilletz, A. (1988) – Stratiform tungsten deposits: a review; *Geologie en Mijnbouw*, Vol. 67, pp. 293-311
- Chen, J., Halls, C. & Stanley, C.J. (1992) – Tin-bearing skarns of South China: geological setting and mineralogy; *Ore Geology Reviews*, Vol. 7, pp. 225-248
- Cheng, Y., Mao, J. & Yang, Z. (2012) – Geology and vein tin mineralization in the Dadoushan deposit, Gejiu district, SW China; *Mineralium Deposita*, Vol. 47, pp. 701-712
- Cheng, Y., Mao, J., Chang, Z. & Pirajno, F. (2013) – The origin of the world class tin-polymetallic deposits in the Gejiu district, SW China: constraints from metal zoning characteristics and ^{40}Ar - ^{39}Ar geochronology; *Ore Geology Reviews*, Vol. 53, pp. 50-62
- Chesley, J.T., Halliday, A.N., Snee, L.W., Mezger, K., Shepherd, T.J. & Scrivener, R.C. (1993) – Thermochronology of the Cornubian batholith in southwest England: implications for pluton emplacement and protracted hydrothermal mineralization. *Geochimica et Cosmochimica Acta*, Vol. 57, pp. 1817-1835.
- Chicharro, E., Martín-Crespo, T., Gómez-Ortiz, D., López-García J.A., Oyarzun R. & Villaseca, C. (2015) – Geology and gravity modeling of the Logrosán Sn-(W) ore deposits (Central Iberian Zone, Spain); *Ore Geology Reviews*, Vol. 65, pp. 294-307
- Cid-Dresdner, H. & Escobar, C. (1968) – The crystal structure of ferberite, FeWO_4 ; *Zeitschrift für Kristallographie*, Vol. 127, pp. 61-72
- Cigala, R.M., Crea, F., de Stefano, C., Lando, G., Milea, D. & Sammartano, S. (2012) – The inorganic speciation of tin(II) in aqueous solution; *Geochimica et Cosmochimica Acta*, Vol. 87, pp. 1-20
- Clark, A.M., Fejer, E.E., Donaldson, J.D. & Silver, J. (1976) – The ^{119}Sn Mössbauer spectra, cell dimensions, and minor element contents of some cassiterites; *Mineralogical Magazine*, Vol. 40, pp. 895-898
- Clayton, R., Andersson, P., Gale, N.H., Gillis, C. & Whitehouse, M.J. (2002) – Precise determination of the isotopic composition of Sn using MC-ICP-MS; *Journal of Analytical Atomic Spectrometry*, Vol. 17, pp. 1248-1256
- Clemens, J.D., Holloway, J.R. & White, A.J.R. (1986) – Origin of an A-type granite: Experimental constraints; *American Mineralogist*, Vol. 71, pp. 317-324
- Clemens, J.D. (2003) – S-type granitic magmas-petrogenetic issues, models and evidence; *Earth-Science Reviews*, Vol. 61, pp. 1-18
- Cobbing, E.J., Mallick, D.I.J., Pitfield, P.E.J. & Teoh, L.H. (1986) – The granites of the Southeast Asian Tin Belt; *Journal of the Geological Society*; Vol. 143, pp. 537-550

- Coetzee, J. and Twist, D. (1989) Disseminated tin mineralization in the roof of the Bushveld granite pluton at the Zaaiploats Mine, with implications for the genesis of magmatic-hydrothermal tin systems; *Economic Geology*, Vol. 84, pp. 85-102
- Collins, P.L.F. (1981) – The geology and genesis of the Cleveland tin deposit, western Tasmania: fluid inclusion and stable isotope studies; *Economic Geology*, Vol. 76, pp. 365-392
- Collins, W.J., Beams, S.D., White, A.J.R. & Chappell, B.W. (1982) – Nature and origin of A-type granites with particular reference to southeastern Australia, *Contributions to Mineralogy and Petrology*, Vol. 80, pp. 189-200
- Costi, H.T, Horbe, A.M.C., Borges, R.M.K., Dall’Agnol, R., Rossi, A. & Sighnolfi, G. (2000) – Mineral chemistry of cassiterites from Pitinga province, Amazonian craton, Brazil; *Revista Brasileira de Geociencias*, Vol. 30, pp. 775-782
- Cramer, T., Bonilla Pérez, A., Amaya Perea, Z., Franco Victoria, J.A. & Iregui Ramirez, I., (2010) – Mineralizations of Tantalum and Niobium in Vichada and Guainía, eastern part of Colombia (Abstract); *Acta Mineralogica-Petrographica, Abstract Series*, Vol. 6, p. 223
- Criddle, A.J. & Stanley, C.J. (1993) – Quantitative data file for ore minerals; 3rd edition, Chapman & Hall, London, United Kingdom, 635 p.
- Crocker, I.T. (1986) – The Zaaiploats Tinfield, Potgietersrus District; Anhaeusser, C.R. & Maske, S. (Eds.) (1986) – Mineral deposits of Southern Africa, pp. 1287-1299
- Crouse, R.A. & Černý, P. (1972) – The Tanco pegmatite at Bernic Lake, Manitoba. I. Geology and paragenesis; *Canadian Mineralogist*, Vol. 11, pp. 591-608
- Cuney, M., Marignac, C. & Weisbrod, A. (1992) – The Beauvoir topaz-lepidolite albite granite (Massif Central, France): The disseminated magmatic Sn-Li-Ta-Nb-Be mineralization; *Economic Geology*, Vol. 87, pp. 1766-1794
- Dachs, H., Stoll, E. & Weitzel, H. (1967) – Kristallstruktur und magnetische Ordnung des Hübnerits, MnWO₄; *Zeitschrift für Kristallographie*, Vol. 125, pp. 120-129
- Dall’Agnol, R., Costi, H.T., Leite, A.A.S., de Magalhães, M.S. & Teixeira, N.P. (1999) – Rapakivi granites from Brazil and adjacent areas; *Precambrian Research*, Vol. 95, pp. 9-39
- Daltry, V.S.C. & Wilson, A.H. (1997) – Review of platinum-group mineralogy: compositions and elemental associations of the PG-minerals and unidentified PGE-phases; *Mineralogy and Petrology*, Vol. 60, pp. 185-229
- Danyushevsky, L., Robinson, P., Gilbert, S., Norman, M., Large, R., McGoldrick, P. & Shelley, M. (2011) – Routine quantitative multi-element analysis of sulphide minerals by laser ablation ICP-MS: Standard development and consideration of matrix effects; *Geochemistry: Exploration, Environment, Analysis*, Vol. 11, pp. 51-60
- Dare, S.A.S., Barnes, S.-J., Beaudoin, G., Méric, J., Boutroy, E. & Potvin-Doucet, C. (2014) – Trace elements in magnetite as petrogenetic indicators; *Mineralium Deposita*, Vol. 49; pp. 785-796
- Davis, D.W., Sewell, R.J. & Campbell, S.D.G. (1997) – U-Pb dating of Mesozoic igneous rocks from Hong Kong; *Journal of the Geological Society*, Vol. 154, pp. 1067-1076
- Davis, S.G. (1961) – Mineralogy and genesis of the wolframite ore deposit, Needle Hill mine, New Territories, Hong Kong; *Economic Geology*, Vol. 56, pp. 1238-1249
- Davis, W.J. & Williams-Jones, A.E. (1985) – A fluid inclusion study of the porphyry-greisen, tungsten-molybdenum deposit at Mount Pleasant, New Brunswick, Canada; *Mineralium Deposita*, Vol. 20, pp. 94-101
- Dawson, K.M. (1996) – Skarn tungsten; in: Eckstrand, O.R., Sinclair, W.D. & Thorpe, T.I. (Eds.) – *Geology of Canadian mineral deposit types*; *Geology of Canada Number 8*, Geological Survey of Canada, Ottawa, pp. 495-502

- Dekov, V.M., Damyanov, Z.K. & Mandova, E.D. (1996) – Native tin and tin alloys from axial metalliferous sediments of an ultra-fast spreading centre: East Pacific Rise, 21° S survey area; *Neues Jahrbuch für Mineralogie – Monatshefte*, No. 9, pp. 385-405
- Dekov, V.M., Hålenius, U., Billström, K., Kamenov, G. D., Munnik, F., Eriksson L., Dyer, A., Schmidt, M. & Botz, R. (2009) Native Sn–Pb droplets in a zeolitic amygdale (Isle of Mull, Inner Hebrides); *Geochimica et Cosmochimica Acta*, Vol. 73, pp. 2907-2919
- De Clercq, F., Muchez, P., Dewaele, S. & Boyce, A. (2008) – The tungsten mineralisation at Nyakabingo and Gifurwe (Rwanda): preliminary results; *Geologica Belgica*; Vol. 11, pp. 251-258
- De Clercq, F. (2012) – Metallogenesis of Sn and W vein-type deposits in the Karagwe-Ankole belt (Rwanda); Ph.D. thesis, KU Leuven, 270 p.
- De Laeter, J.R. & Jeffery, P.M. (1967) –Tin: its isotopic and elemental abundance; *Geochimica et Cosmochimica Acta*, Vol. 31, pp. 969-985
- Denisenko, V.K. (1986) – Tungsten-bearing provinces of the USSR; in: Beus, A.A. (Ed.) – *Geology of tungsten; International Geological Correlation Programme, Project 26 'mineralization associated with acid magmatism' (MAWAM)*, pp. 127-156
- De Roo, J.A. (1988) – Structural control on the emplacement of the vein-type tungsten-tin ore at Mount Carbine, Queensland, Australia; *Economic Geology*, Vol. 83, pp. 1170-1180
- DesLauriers, D. (2005) – Tungsten price goes parabolic; <http://www.resourceinvestor.com/News/2005/5/Pages/Tungsten-Price-Goes-Parabolic.aspx>
- Dewaele, S., De Clercq, F., Muchez, P., Schneider, J., Burgess, R., Boyce, A. & Fernandez Alonso, M. (2010) – Geology of the cassiterite mineralisation in the Rutongo area, Rwanda (Central Africa): current state of knowledge; *Geologica Belgica*, Vol. 13, pp. 91-112
- Dewaele, S., Henjes-Kunst, F., Melcher, F., Sitnikova, M., Burgess, R., Gerdes, A., Fernandez Alonso, M., De Clercq, F., Muchez, P., & Lehmann, B. (2011) – Late Neoproterozoic overprinting of the cassiterite and columbite-tantalite bearing pegmatites of the Gatumba area, Rwanda (Central Africa); *Journal of African Earth Sciences*; Vol. 61, pp. 10-26
- Diehl, B.J.M. (1991) – Tungsten; Mineral Resources Series, Open File Report MRS 20, Ministry of Mines and Energy, Geological Survey of Namibia, 35 p.
- Dietrich, A., Lehmann, B. & Willianos, A. (2000) – Bulk rock and melt inclusion geochemistry of Bolivian tin porphyry systems; *Economic Geology*, Vol. 95, pp. 313-326
- Dill, H.G., Melcher, F., Füll, M. & Weber, B. (2006) – Accessory minerals in cassiterite: a tool for provenance and environmental analyses of colluvial-fluvial placer deposits (NE Bavaria, Germany); *Sedimentary Geology*, Vol. 191, pp.171-189
- Dingwell, D.B. (1988) – The structures and properties of fluorine-rich magmas: a review of experimental studies; in: Taylor, R.P. & Strong, D.F. (Eds.) – *Recent advances in the geology of granite-related mineral deposits; The Canadian Institute of Mining and Metallurgy, Special Volume 39, Montreal*, pp. 1-12
- Distler, V.V., Yudovskaya, M.A., Mitrofanov, G.L., Prokofev, V.Y. & Lishnevskii, E.N. (2004) – Geology, composition, and genesis of the Sukhoi Log noble metals deposit, Russia; *Ore Geology Reviews*, Vol. 24, pp. 7-44
- Dobson, D.C. (1982) – Geology and alteration of the Lost River tin-tungsten-fluorine deposit, Alaska; *Economic Geology*, Vol. 77, pp. 1033-1052
- Dolgoplova, A., Seltmann, R., Stanley, C., Weiss, D., Kober, B. & Siebel, W. (2005) – Isotope systematics of ore-bearing granites and host rocks of the Orlovka-Spokoinoe mining district, eastern Transbaikalia, Russia; in: Mao, J. & Bierlein, F.P. (Eds.) –

- Mineral Deposit Research: Meeting the Global Challenge; Proceedings of the eight biennial meeting of the Society for Geology applied to Mineral deposits (SGA), Beijing, China, pp. 747-750
- Dolníček, Z., René, M., Prochaska, W. & Kovář, M. (2012) – Fluid evolution of the Hub Stock, Horní Slavkov–Krásno Sn–W ore district, Bohemian Massif, Czech Republic, *Mineralium Deposita*, Vol. 47, pp. 821-833
- Dostal, J., Kontak, D.J. & Chatterjee, A.K. (2009) – Trace element geochemistry of scheelite and rutile from metatubidite-hosted quartz vein gold deposits, Meguma Terrane, Nova Scotia, Canada: Genetic implications; *Mineralogy and Petrology*, Vol. 97, pp. 95–109
- du Bray, E.A. (1985) – Jabal Silsilah tin prospect, Najd region, Kingdom of Saudi Arabia; *Journal of African Earth Sciences*, Vol. 4, pp. 237-247
- du Bray, E.A. (1986) – Geology of the Silsilah ring complex and associated tin mineralization, Kingdom of Saudi Arabia - a synopsis; *American Mineralogist*, Vol. 70, pp. 1075-1086
- Dudykina, A.S. (1959) – Paragenetic associations of element admixtures in cassiterites of different genetic types of tin ore deposits; *Akademiya Nauk SSSR, Trudy Instituta Geologii, Rudnykh Mestorozhdenii, Petrografii, Mineralogii i Geokhimii*; Vol. 21, pp. 111-121 (in Russian)
- Dulski, P. (1980) – Spurenanalyse als Hilfsmittel bei der geochemischen Untersuchung der Genese bolivianischer Sn-Lagerstätten; *Berliner geowissenschaftliche Abhandlungen*, Vol. A/28, Dietrich Reimer Publishing, Berlin, 79 p.
- Dulski, P., Möller, P., Villalpando, A. & Schneider, H.-J. (1982) – Correlation of trace element fractionation in cassiterites with the genesis of the Bolivian metallotect; in: Evans, A.M. (Ed.) – *Metallization Associated with Acid Magmatism*; Vol. 6, John Wiley & Sons, Chichester, pp. 71-83
- Dunn, P.J., Gaines, R.V., Wroe Wolfe, C. & Barbosa, C. (1978) – Epitaxial wadginite and cassiterite from Lavra Jabuti, Baixio, Galilea, Minas Gerais, Brazil; *Mineralogical Record*, Vol. 9, pp. 14-18
- Dupuis, C. & Beaudoin, G. (2011) – Discriminant diagrams for iron oxide trace element fingerprinting of mineral deposit types; *Mineralium Deposita*, Vol. 46, pp. 319-335
- Dusausoy, Y., Ruck, R. & Gaite, J.M. (1988) – Study of the symmetry of Fe³⁺ sites in SnO₂ by Electron Paramagnetic Resonance; *Physics and Chemistry of Minerals*, Vol. 15, pp. 300-303
- Eadington, P.J. (1988) – The solubility of cassiterite in hydrothermal solutions in relation to some lithological and mineral associations of tin ores; in: Taylor, R.P. & Strong, D.F. (Eds.) – *Recent advances in the geology of granite-related mineral deposits*; The Canadian Institute of Mining and Metallurgy, Special Volume 39, Montreal, pp. 25-32
- Eggins, S.M., Kinsley, L.P.J. & Shelley, J.M.G. (1998) – Deposition and element fractionation processes during atmospheric pressure laser sampling for analysis by ICP-MS; *Applied Surface Science*, Vol. 129, pp. 278–286
- Eggins, S.M. & Shelley, J.M.G. (2002) – Compositional heterogeneity in NIST SRM 610-617 glasses; *Geostandards Newsletter*, Vol. 26, pp. 269-286
- Einaudi, M.T., Meinert, L.D. & Newberry, R.J. (1981) – Skarn deposits; in: Skinner, B.J. (Ed.) – *Economic Geology: 75th Anniversary Volume*; Society of Economic Geologists, The Economic Geology Publishing Company, pp. 317-391
- Elsner, H., Buchholz, P., Schmitz, M. & Altangerel, T. (2011) – Industrial minerals and selected rare metals in Mongolia: an investors' guide; *Mineral Resources Authority of Mongolia, Ulaanbaatar*, 322 p.

- Elsner, H. (2014) – Zinn: Angebot und Nachfrage bis 2020; DERA Rohstoffinformationen, Vol. 20, German Mineral Resources Agency (DERA) in the Federal Institute for Geosciences and Natural Resources (BGR), 256 p.
- Enchbat, D. (2007) – Die erzbildenden Fluide in den Au-W-Mineralisationen des mongolischen Altai: Untersuchungen zu Fluideinschlüssen und Spurenelementchemismus von Erz- und Gangmineralen; Freiburger Forschungshefte, Vol. C520, 101 p.
- Erdmann, L., Behrendt, S. & Feil, M. (2011) – Kritische Rohstoffe für Deutschland: Identifikation aus Sicht deutscher Unternehmen wirtschaftlich bedeutsamer mineralischer Rohstoffe, deren Versorgungslage sich mittel- bis langfristig als kritisch erweisen könnte; Institut für Zukunftsstudien und Technologiebewertung (IZT) & adelphi, Berlin, 134 p.
- Ertel, W., O'Neill, H.S.C., Dingwell, D.B. & Spettel, B. (1996) – Solubility of tungsten in a haplogranitic melt as a function of temperature and oxygen fugacity; *Geochimica et Cosmochimica Acta*, Vol. 60, pp. 1171-1180
- Eugster, H.P. (1984) – Granites and hydrothermal ore deposits: a geochemical framework; *Mineralogical Magazine*, Vol. 49, pp. 7-23
- European Commission (2003) – Directive 2002/95/EG of the European Parliament and of the Council of 27 January 2003 on the restriction of the use of certain hazardous substances in electrical and electronic equipment, *Official Journal of the European Union*, Vol. L 37, pp. 19-23
- European Commission (2010) – Critical raw materials for the EU: report of the ad-hoc working group on defining raw materials; European Commission-Enterprise and Industry, 84 p.
- Evans, C.J. (1994) – Tin handbook; 3rd edition, Hüthig, Heidelberg, 248 p.
- Fan, D., Zhang, T., Ye, J., Pašava, J., Křibek, B., Dobeš, P., Vavřín, I. & Žák, K. (2004) – Geochemistry and origin of tin-polymetallic sulfide deposits hosted by the Devonian black shale series near Dachang, Guangxi, China; *Ore Geology Reviews*, Vol. 24, pp. 103-120
- Fandrich, R., Gu, Y., Burrows, D. & Moeller, K. (2007) – Modern SEM-based mineral liberation analysis; *International Journal of Mineral Processing*, Vol. 84, pp. 310-320
- Farges, F., Linnen, R.L. & Brown Jr., G.E. (2006) – Redox and speciation of tin in hydrous silicate glasses: a comparison with Nb, Ta, Mo and W; *Canadian Mineralogist*, Vol. 44, pp. 795-810
- Ferenc, Š & Uher, P. (2007) – Magnesian wolframite from hydrothermal quartz veins in the Rochovce granite exocontact, Ochtiná, Western Carpathians, Slovakia; *Neues Jahrbuch für Mineralogie – Abhandlungen*, Vol. 183, pp. 165-172
- Fernandez Alonso, M., Cutten, H., De Waele, B., Tack, L., Tahon, A., Baudet, D., Barritt, S.D. (2012) – The Mesoproterozoic Karagwe-Ankole Belt (formerly the NE Kibara Belt): the result of prolonged extensional intracratonic basin development punctuated by two short-lived far-field compressional events; *Precambrian Research*, Vol. 216-219, pp. 63-86
- Fesser, H. (1968) – Spurenelemente in bolivianischen Zinnsteinen; *Geologisches Jahrbuch*, Vol. 85, pp. 605-610
- Fetherston, J.M. (2004) – Tantalum in Western Australia; *Geological Survey of Western Australia, Mineral Research Bulletin*, Vol. 22, 153 p.
- Finger, F., Kraiger, H. & Streyrer, H.P. (1985) – Zur Geochemie des K1-Gneises der Scheelitlagerstätte Felbertal (Pinzgau/Salzburg)-ein Vorbericht; *Karinthin*, Vol. 92, pp. 225-235

- Fogliata, A.S., Báez, M.A., Hagemann, S.G., Santos, J.O. & Sardi, F. (2012) – Post-orogenic, Carboniferous granite-hosted Sn–W mineralization in the Sierras Pampeanas Orogen, Northwestern Argentina; *Ore Geology Reviews*, Vol. 45, pp. 16-32
- Forsythe, D.L. & Higgins, N.C. (1990) – Mount Carbine tungsten deposit; in: Hughes, F.E. (Ed.) – *Geology of the Mineral Deposits of Australia and Papua New Guinea*; The Australian Institute of Mining and Metallurgy, Melbourne, pp. 1557-1560
- Foster, R.P. (1977) – Solubility of scheelite in hydrothermal chloride solutions; *Chemical Geology*, Vol. 20, pp. 27-43
- Franco, A., Vieira, R. & Bunting, R. (2014) – The Panasqueira mine at a glance; *International Tungsten Industry Association (ITIA) Newsletter*, June 2014, London, United Kingdom, pp. 1-12
- Fraser, C. (2012) – How tin could revolutionize smartphone batteries; *Tin Investing News*, tin articles, 07.06.2012, <http://tininvestingnews.com/1971-how-tin-could-revolutionize-smartphone-batteries-lithium-ion-electric-vehicles-demand.html>
- Frisch, W. (1975) – Die Wolfram-Lagerstätte Gifurwe (Rwanda) und die Genese der zentralafrikanischen Reinit-Lagerstätten; *Jahrbuch der Geologischen Bundesanstalt Wien*, Vol. 118, pp. 119-191
- Frost, B.R., Barnes, C.G., Collins, W.J., Arculus, R.J., Ellis, D.J. & Frost, C.D. (2001) – A geochemical classification for granitic rocks; *Journal of Petrology*, Vol. 42, pp. 2033-2048
- Fryer, B.J., Jackson, S.E. & Longerich, H.P. (1995) – The design, operation and role of the laser-ablation microprobe coupled with an inductively coupled plasma-mass spectrometer (LAM-ICP-MS) in the Earth Sciences; *Canadian Mineralogist*, Vol. 33, pp. 303-312
- Gäbler, H.-E., Melcher, F., Graupner, T., Bahr, A., Sitnikova, M. A., Henjes-Kunst, F., Oberthür, T., Brätz, H. & Gerdes, A. (2011) – Speeding up the analytical workflow for Coltan fingerprinting by an integrated Mineral Liberation Analysis/LA-ICP-MS approach; *Geostandards and Geoanalytical Research*, Vol. 35, pp. 431-448
- Gäbler, H.-E., Rehder, S., Bahr, A., Melcher, F. & Goldmann, S. (2013) – Cassiterite fingerprinting by LA-ICP-MS; *Journal of Analytical Atomic Spectrometry*, Vol. 28, pp. 1247-1255
- Gaboardi, M. & Humayun, M. (2009) – Elemental fractionation during LA-ICP-MS analysis of silicate glasses: implications for matrix-independent standardization; *Journal of Analytical Atomic Spectrometry*; Vol. 24, pp. 1188-1197
- Galliski, M.A., Marquez-Zavala, M.F., Černý, P., Martínez, V.A. & Chapman, R. (2008) – The Ta–Nb–Sn–Ti oxide-mineral paragenesis from La Viquita, a spodumene-bearing rare-element granitic pegmatite, San Luis, Argentina; *Canadian Mineralogist*, Vol. 46, pp. 379-393
- Gan, G. & Chen, Z. (1992) – Compositional characteristics of wolframite in tin deposits, Dupangling, Guangxi; *Chinese Journal of Geochemistry*, Vol. 11, pp. 156-167
- Gan, G. & Chen, Z. (1994) – Compositional characteristics and existing forms of major, trace and rare earth elements in cassiterite, Dupangling tin ore field, Guangxi; *Chinese Journal of Geochemistry*, Vol. 13, pp. 85-95
- Garnett, R.H.T. & Bassett, N.C. (2005) – Placer deposits; in: Hedenquist, J.W., Thompson, J.F.H., Goldfarb, R.J. & Richards, J.P. (Eds.) – *Economic Geology: 100th Anniversary Volume*; Society of Economic Geologists, pp. 813-843
- Gaspar, O.C. (2002) – Mineralogy and sulfide mineral chemistry of the Neves-Corvo ores, Portugal: insight into their genesis; *Canadian Mineralogist*, Vol. 40, pp. 611-636
- GBRM (2008) – Goodall Business and Resource Management: A preliminary market review of tungsten; <http://www.vitalmetals.com.au/images/vitalmetals-13--ezeed.pdf>

- Gerel, O. (1998) – Phanerozoic felsic magmatism and related mineralization in Mongolia; Bulletin of the Geological Survey of Japan; Vol. 49, pp. 239-248
- Ghaderi, M., Palin, J.M., Campbell, I.H. & Sylvester, P.J. (1999) – Rare earth element systematics in scheelite from hydrothermal gold deposits in the Kalgoorlie-Norseman region, Western Australia; Economic Geology, Vol. 94, pp. 423-438
- Giuliani, G. (1987) – La cassitérite zonée du gisement de Sokhret Allal (Granite des Zaër; Maroc Central): composition chimique et phases fluides associées; Mineralium Deposita, Vol. 22, pp. 253-261
- Giuliani, G., Cheilletz, A. & Mechiche, M. (1987) – Behaviour of REE during thermal metamorphism and hydrothermal infiltration associated with skarn and vein-type tungsten ore bodies in central Morocco; Chemical Geology, Vol. 64, pp. 279-294
- Giuliani, G., Li, Y.D. & Sheng, T.F. (1988) – Fluid inclusion study of Xihuashan tungsten deposit in the southern Jiangxi province, China; Mineralium Deposita, Vol. 23, pp. 24-33
- Gocht, W. & Pluhar, E. (1982) – Types of tin-bearing pegmatites in Phuket, Thailand, with special reference to tantalum-rich ores; in: Evans, A.M. (Ed.) – Metallization Associated with Acid Magmatism; Vol. 6, John Wiley & Sons, Chichester, pp. 91-99
- Goldfarb, R.J., Baker, T., Dubé, B., Groves, D.I., Hart, C.J.R. & Goasselin, P. (2005) – Distribution, character, and genesis of gold deposits in metamorphic terranes; in: Hedenquist, J.W., Thompson, J.F.H., Goldfarb, R.J. & Richards, J.P. (Eds.) – Economic Geology: 100th Anniversary Volume; Society of Economic Geologists, pp. 407-450
- Goldmann, S., Melcher, F., Gäbler, H.-E., Dewaele, S., De Clercq, F. & Muchez, P. (2013) – Mineralogy and trace element chemistry of ferberite/reinite from tungsten deposits in Central Rwanda; Minerals, Vol. 3, 121-144
- Goldschmidt, V.M. (1926) – Geochemische Verteilungsgesetze der Elemente Vol. VII: Gesetze der Krystallochemie; Skrifter utgitt av det Norske Videnskaps Akademi i Oslo, 1: Matematisk - naturvidenskapelig klasse, University of Oslo, 117 p.
- Goncharov, G.N. & Filatov, S.K. (1971) – The typical structural features of cassiterite from Sherlovaya Gora; Geochemistry International, Vol. 8, pp. 268-275
- Grant, J.N., Halls, C., Avila, W. & Snelling, N.J. (1979) – K-Ar ages of igneous rocks and mineralization in part of the Bolivian tin belt; Economic Geology, Vol. 74, pp. 838-851
- Grant, J.N., Halls, C., Sheppard, S.M.F. & Avila, W. (1980) – Evolution of the porphyry tin deposits of Bolivia; in: Ishihara, S. & Takenouchi, S. (Eds.) – Granite magmatism and related mineralization; Society of Mining Geologist of Japan, Mining Geology Special Issue No. 8, pp. 151-173
- Graupner, T., Kempe, U., Enchbat, D., Pätzold, O., Leeder, O. & Spooner, E.T.C. (1999) – Fluid regime and ore formation in the tungsten(-yttrium) deposits of Kyzyltau (Mongolian Altai): evidence for fluid variability in tungsten-tin ore systems; Chemical Geology, Vol. 154, pp. 21-58
- Graupner, T., Niedermann, S., Rhede, D., Kempe, U., Seltmann, R., Williams, C.T. & Klemd, R. (2010) – Multiple sources for mineralizing fluids in the Charmitan gold(-tungsten) mineralization (Uzbekistan); Mineralium Deposita, Vol. 45, pp. 667-682
- Greenwood, R. (1943) – Effect of chemical impurities on scheelite fluorescence; Economic Geology, Vol. 38, pp. 56-64
- Groat, L.A., Putnis, A., Kissin, S.A., Ercit, T.S., Hawthorne, F.C. & Gaines, R.V. (1994) – Staringite discredited; Mineralogical Magazine, Vol. 58, pp. 271-277
- Groves, D.I. & Baker, W.E. (1972) – The regional variation in compositions of wolframites from Tasmania; Economic Geology, Vol. 67, pp. 362-368
- Groves, D.I. & McCarthy, T.S. (1978) – Fractional crystallization and the origin of tin deposits in granitoids; Mineralium Deposita, Vol. 13, pp. 11-26

- Groves, D.I., Goldfarb, R.J., Gebre-Mariam, M., Hagemann, S.G. & Robert, F. (1998) – Orogenic gold deposits: A proposed classification in the context of their crustal distribution and relationship to other gold deposit types; *Ore Geology Reviews*, Vol. 13, pp. 7-27
- Grubb, P.L.C. & Hannaford, P. (1966) – Magnetism in cassiterite; *Mineralium Deposita*, Vol. 2, pp. 148-171
- Grubb, P.L.C. (1967) – Solid solution relationships between wolframite and scheelite; *American Mineralogist*, Vol. 52, pp. 418-426
- Grundstoffberatung (1971) – Zinnerzgrube Heinda; Technical-economic evaluation, Project FE3032, Volume 1 Text, Essen, Germany, 112 p. (in German)
- Gu, Q.G. & Schröcke, H. (1986) – Die Neben- und Spurenelemente in Wolframit und ihre kristall-chemischen Beziehungen zu diesen; *Chemie der Erde*, Vol. 45, pp. 113-127
- Gu, Y. (2003) – Automated scanning electron microscope based mineral liberation analysis; an introduction to JKMR/FEI Mineral Liberation Analyzer; *Journal of Minerals and Materials Characterization and Engineering*, Vol. 2, pp. 33-41
- Guillong, M. & Günther, D. (2002) – Effect of particle size distribution on ICP-induced elemental fractionation in laser ablation-inductively coupled plasma-mass spectrometry; *Journal of Analytical Atomic Spectrometry*; Vol. 17, pp. 831-837
- Guillong, M., Horn, I. & Günther, D. (2003) – A comparison of 266 nm, 213 nm and 193 nm produced from a single solid state Nd:YAG laser for laser ablation ICP-MS; *Journal of Analytical Atomic Spectrometry*, Vol. 18, pp. 1224-1230
- Gulson, B.L. & Jones, M.T. (1992) – Cassiterite: potential for direct dating of mineral deposits and a precise age for the Bushveld Complex granites; *Geology*, Vol. 20, pp. 355-358
- Günther, D. & Heinrich, C.A. (1999) – Enhanced sensitivity in laser ablation-ICP mass spectrometry using helium-argon mixtures as aerosol carrier; *Journal of Analytical Atomic Spectrometry*, Vol. 14, pp. 1363-1368
- Günther, D., Jackson, S.E. & Longerich, H.P. (1999) – Laser ablation and arc/spark solid sample introduction into inductively coupled plasma mass spectrometers; *Spectrochimica Acta, Part B*, Vol. 54, pp. 381-409
- Günther, M. & Ngulube, A. (1992) – The lithium pegmatite at Manono, Zaire; *International Geological Correlation Programme, Project 255: Metallogeny of the Kibara belt, Central Africa, Bulletin – Newsletter*, Vol. 4, pp. 91-99
- Haapala, I. & Kinnunen, K. (1979) – Fluid inclusions in cassiterite and beryl in greisen veins in the Eurajoki stock, Southwestern Finland; *Economic Geology*, Vol. 74, pp. 1231-1238
- Haapala, I. & Kinnunen, K. (1982) – Fluid inclusion evidence on the genesis of tin deposits; in: Evans, A.M. (Ed.) – *Metallization Associated with Acid Magmatism*; Vol. 6, John Wiley & Sons, Chichester, pp. 101-111
- Haapala, I. (1995) – Metallogeny of the rapakivi granites; *Mineralogy and Petrology*, Vol. 54, pp. 149-160
- Haapala, I. (1997) – Magmatic and postmagmatic processes in tin-mineralized granites: topaz-bearing leucogranite in the Eurajoki rapakivi granite stock, Finland; *Journal of Petrology*, Vol. 38, pp. 1645-1659
- Halter, W.E., Williams-Jones, A.E. & Kontak, D.J. (1996) – The role of greisenization in cassiterite precipitation at the East Kemptonville tin deposit, Nova Scotia; *Economic Geology*, Vol. 91, pp. 368-385
- Hamaguchi, H., Kuroda, R., Onuma, N., Kawabuchi, K., Mitsubayashi, T. & Hosohara, K. (1964) – The geochemistry of tin; *Geochimica et Cosmochimica Acta*, Vol. 28, p. 1039-1053

- Hamaguchi, H. & Kuroda, R. (1969) – Abundance in common igneous rocks; in: Wedepohl (Ed.) – Handbook of Geochemistry; Vol. II/4, Springer, Berlin, pp. 50E1-50E5
- Hannington, M.D., Bleeker, W. & Kjarsgaard (1999) – Sulfide mineralogy, geochemistry, and ore genesis of the Kidd Creek deposit: Part I. North, Central, and South orebodies; in: Hannington, M.D. & Barrie, C.T. (Eds.) – The giant Kidd Creek volcanogenic massive sulfide deposit, Western Abitibi Subprovince, Canada; Economic Geology Monograph 10, Society of Economic Geologists, The Economic Geology Publishing Company, pp. 163-224
- Hausen, D.M. (1989) – Process mineralogy applied to exploration, development and exploitation of select tungsten ores; Ore Geology Reviews, Vol. 4, pp. 201-230
- Hazen, R.M., Finger, L.W. & Mariathasan, J.W.E. (1985) – High-pressure crystal chemistry of scheelite-type tungstates and molybdates; Journal of the Physics and Chemistry of Solids, Vol. 46, pp. 253-263
- Hedenquist, J.W. & Lowenstern, J.B. (1994) – The role of magms in the formation of hydrothermal ore deposits; Nature, Vol. 370, pp. 519- 527
- Hein, J.R., Mizell, K., Koschinsky, A. & Conrad, T.A. (2013) – Deep-ocean mineral deposits as a sources of critical metals for high- and green-technology applications: comparison with land-based resources; Ore Geology Reviews, Vol. 51, pp. 1-14
- Heinrich, C.A. (1990) – The chemistry of hydrothermal tin(-tungsten) ore deposition; Economic Geology, Vol.85, pp. 457-481
- Heinrich, C.A., Pettke, T., Halter, W.E., Aigner-Torres, M., Audétat, A., Günther, D., Hattendorf, B., Bleiner, D., Guillong, M. & Horn, I. (2003) – Quantitative multi-element analysis of minerals, fluid and melt inclusions by laser-ablation inductively-coupled-plasma mass-spectrometry; Geochimica et Cosmochimica Acta, Vol. 67, pp. 3473-3496
- Heinrich, E.W.M. (1964) – Tin-tantalum-lithium pegmatites of the São João del Rei district, Minas Gerais, Brazil; Economic Geology, Vol. 59, pp. 982-1002
- Heiserman, D.L. (1992) – Exploring Chemical Elements and their Compounds; TAB Books, New York, 376 p.
- Helba, H., Trumbull, R.B., Morteani, G., Khalil, S.O. & Arslan, A., (1997) – Geochemical and petrographic studies of Ta mineralization in the Nuweibi albite granite complex, Eastern Desert, Egypt; Mineralium Deposita, Vol. 32, pp. 164–179
- Hennigh Q. (1993) – Cassiterite in synsedimentary, massive sulfide deposits: A comparison to cassiterite in “granite-affiliated” tin deposits including pegmatites; M.Sc. thesis, Colorado School of Mines, 129 p.
- Hennigh, Q. & Hutchison, R.W. (1999) – Cassiterite at Kidd Creek: an example of volcanogenic massive sulfide-hosted tin mineralization; in: Hannington, M.D. & Barrie, C.T. (Eds.) – The giant Kidd Creek volcanogenic massive sulfide deposit, Western Abitibi Subprovince, Canada; Economic Geology Monograph 10, Society of Economic Geologists, The Economic Geology Publishing Company, pp. 431-440
- Herzenberg, R. (1936) – Colloidal tin ore deposits; Economic Geology, Vol. 31, pp. 761-766
- Higgins, N.C. (1980) – Fluid inclusion evidence for the transport of tungsten by carbonate complexes in hydrothermal solutions; Canadian Journal of Earth Sciences, Vol. 17, pp. 823-830
- Higgins, N.C. (1985) – Wolframite deposition in a hydrothermal vein system: the Grey River tungsten prospect, Newfoundland, Canada; Economic Geology, Vol. 80, pp. 1297-1327

- Hinton, R.W., Harte, B. & Witt-Eickschen, G. (1995) – Ion probe measurements of National Institute of Standards and Technology Standard Reference Material SRM 610 glass, trace elements; *The Analyst*, Vol. 120, pp. 1315-1319.
- Hochleitner, R. & Schröcke, H. (1985) – Heterogene Gleichgewichte in der Wolframitgruppe; *Tschermaks Mineralogische und Petrologische Mitteilungen*, Vol. 34, pp. 35-47
- Hoefs, J (2010) – Geochemical fingerprints: a critical appraisal; *European Journal of Mineralogy*, Vol. 22, pp. 3-15
- Höll, R. (1975) – Die Scheelitlagerstätte Felbertal und der Vergleich mit anderen Scheelitvorkommen in den Ostalpen; *Habilitationsschrift, Bayerische Akademie der Wissenschaften, Abhandlungen der mathematisch-naturwissenschaftlichen Klasse*, Vol. 157A, pp. 1-114.
- Höll, R. (1977) – Early Paleozoic ore deposits of the Sb-W-Hg formation in the Eastern Alps and their genetic interpretation; in: Klemm, D.D. & Schneider, H.-J. (Eds.) – *Time- and Strata-Bound Ore Deposits*; Springer, Berlin, pp. 169-198
- Höll, R., Maucher, A. & Westenberger, H. (1972) – Synsedimentary-diagenetic ore fabrics in the strata- and time-bound scheelite deposits of Kleinarltal and Felbertal in the Eastern Alps; *Mineralium Deposita*, Vol. 7, pp. 217-226
- Hollister, V.F. (1970) – Manganese-iron ratios in wolframite, South Crofty mine, Cornwall; *Economic Geology*, Vol. 65, p. 592
- Horbe, M.A., Horbe, A.C., Costi, H.T. & Teixeira, J.T. (1991) – Geochemical characteristics of cryolite-tin-bearing granites from the Pitinga Mine, northwestern Brazil-A review; *Journal of Geochemical Exploration*; Vol. 40, pp. 227-249
- Horn, I. & Günther, D. (2003) – The influence of ablation carrier gasses Ar, He and Ne on the particle size distribution and transport efficiencies of laser ablation-induced aerosols: implications for LA-ICP-MS; *Applied Surface Science*, Vol. 207, pp. 144-157
- Horner, C. (1979) – Solubility and hydrolysis of FeWO_4 and MnWO_4 in the 25°-300°C range, and the zonation of wolframite; *Chemical Geology*, Vol. 27, pp. 85-97
- Hosking, K.F.G., Stanley, G.J. & Camm, G.S. (1987) – The occurrence, nature and genesis of wood tin in south-west England; *Transactions of the Royal Geological Society of Cornwall*, Vol. 21, pp. 153-212
- Hsu, L.C. & Galli, P.E. (1973) – Origin of the scheelite-powellite series of minerals; *Economic Geology*, Vol. 68, pp. 681-696
- Hsu, L.C. (1976) – The stability relations of the wolframite series; *American Mineralogist*, Vol. 61, pp. 944-955
- Hsu, L.C. (1981) – Phase relations of some tungstate minerals under hydrothermal conditions; *American Mineralogist*, Vol. 66, pp. 298-308
- Hu, X., Bi, X., Hu, R., Shang, L. & Fan, W. (2008) – Experimental study on tin partition between granitic silicate melt and coexisting aqueous fluid; *Geochemical Journal*, Vol. 42, pp. 141-150
- Huang, F.-F., Wang, R.-C., Xie, L., Zhu, J.-C., Erdmann, S., Che, X.-D. & Zhang, R.-Q. (2014) – Differentiated rare-element mineralization in an ongonite-topazite composite dike at Xianghualing tin district, Southern China: an electron-microprobe study on the evolution from niobium-tantalum-oxides to cassiterite; *Ore Geology Reviews*, Vol. 65, pp. 761-778
- Huang, X.L., Wang, R.C., Chen, X.M., Hu, H. & Liu, C.S. (2002) – Vertical variations in the mineralogy of the Yichun topaz-lepidolite granite, Jiangxi Province, Southern China; *Canadian Mineralogist*, Vol. 40, pp. 1047-1068
- Hulsbosch, N., Hertogen, J., Dewaele, S., Andre, L. & Muchez, P. (2013) – Petrographic and mineralogical characterisation of fractionated pegmatites culminating in the Nb-Ta-

- Sn pegmatites of the Gatumba area (western Rwanda); *Geologica Belgica*, Vol. 16, pp. 105-117
- Huspeni, J.R., Kesler, S.E., Ruiz, J., Tuta, Z., Sutter, J.F. & Jones, L.M. (1984) – Petrology and geochemistry of rhyolites associated with tin mineralization in northern Mexico; *Economic Geology*, Vol. 79, pp. 87-105
- Huston, D.L., Sie, S.H., Suter, G.F., Cooke, D.R. & Both, R.A. (1995) – Trace elements in sulfide minerals from eastern Australian volcanic-hosted massive sulfide deposits: Part I. proton microprobe analyses of pyrite, chalcopyrite, and sphalerite, and Part II. selenium levels in pyrite: comparison with $\delta^{34}\text{S}$ values and implications for the source of sulfur in volcanogenic hydrothermal system; *Economic Geology*, Vol. 90, pp. 1167-1196
- Huston, D.L., Relvas, J.M.R.S., Gemmell, J.B. & Driberg, S. (2011) – The role of granites in volcanic-hosted massive sulphide ore-forming systems: an assessment of magmatic-hydrothermal contributions; *Mineralium Deposita*, Vol. 46, 473-507
- Imai, A., Yonezu, K., Sanematsu, K., Ikuno, T., Ishida, S., Watanabe, K., Pisutha-Arnond, V., Nakapadungrat, S. & Boosayasak, J. (2013) – Rare earth elements in hydrothermally altered granitic rocks in the Ranong and Takua Pa Tin-Field, Southern Thailand; *Resource Geology*, Vol. 63, pp. 84-98
- Imeokparia, E.G. (1988) – Mesozoic granite magmatism and tin mineralization in Nigeria; in: Taylor, R.P. & Strong, D.F. (Eds.) – Recent advances in the geology of granite-related mineral deposits; *The Canadian Institute of Mining and Metallurgy, Special Volume 39*, Montreal, pp. 133-139
- International Alert (2010) – The role of the exploitation of natural resources in fuelling and prolonging crises in the eastern DRC; *International Alert paper*, 87 p.,
- Ishihara, S. (1977) – The magnetite-series and ilmenite-series granitic rocks; *Mining Geology*, Vol. 27, pp. 293-305
- Ishihara, S. (1981) – The granitoid series and mineralization; in: Skinner, B. J. (Ed.) – *Economic Geology: 75th Anniversary Volume*; Society of Economic Geologists, The Economic Geology Publishing Company, pp. 458-484
- Ishihara, S., Murakami, H. & Marquez-Zavalía, M.F. (2011) – Inferred indium resources of the Bolivian tin-polymetallic deposits; *Resource Geology*, Vol. 61, pp. 174-191
- ITRI – News on tin market analysis published online at various dates on <https://www.itri.co.uk/>; International Tin Research Institute (ITRI), St. Albans, United Kingdom
- Ivanov, V.V. & Rozbianskaya A.A. (1961) – Geochemistry of indium in cassiterite-sulfide ores; *Geokhimiya*, Vol. 1, pp. 71-83
- Ivanova, G.F. & Khodakovskiy, I.L. (1968) – Forms of tungsten migration in hydrothermal solutions; *Geokhimiya*, Vol. 8, pp. 930-940
- Ivanova, G.F., Motorina, Z.M. & Naumov, V.B. (1978) – Formation features of the mineral associations of the Yugodzyr molybdenum-tungsten deposit (Mongolia); *International Geology Review*, Vol. 20, pp. 855-863
- Ivanova, G.F., Maksimyak, I.E. & Naumov, V.B. (1985) – Geochemical features of the granitoids and wolframite mineralization in the Kyzyl Tau deposit, West Mongolia; *Geokhimiya*, Vol. 6, pp. 858-868
- Ivanova, G.F. (1986) – Geochemistry of tungsten; in: Beus, A.A. (Ed.) – *Geology of tungsten; International Geological Correlation Programme, Project 26 'mineralization associated with acid magmatism' (MAWAM)*, pp. 11-43
- Ivanova, G.F. & Naumov, V.B. (1986) – Genesis of tungsten deposits; in: Beus, A.A. (Ed.) – *Geology of tungsten; International Geological Correlation Programme, Project 26 'mineralization associated with acid magmatism' (MAWAM)*, pp. 245-270

- Ivanova, G.F., Naumov, V.B. & Kopneva, L.A. (1987) – Fluid inclusion data on the physicochemical parameters for scheelite formation in various types of deposits; *Geochemistry International*, Vol. 24, pp. 48-59
- Izoret, L., Marnier, G. & Dusausoy, Y. (1985) – Caractérisation cristallographique de la cassitérite des gisements d'étain et de tungstène de Galice, Espagne; *Canadian Mineralogist*, Vol. 23, pp. 221-231
- Jackson, K.J. & Helgeson, H.C. (1985) – Chemical and thermodynamic constraints on the hydrothermal transport and deposition of tin: I. Calculation of the solubility of cassiterite at high pressures and temperatures; *Geochimica et Cosmochimica Acta*, Vol. 49, pp. 1-22
- Jackson N.J., Willis-Richards J., Manning, D.A.C. & Sams, M.S. (1989) – Evolution of the Cornubian ore field, southwest England: Part II. Mineral deposits and ore-forming processes; *Economic Geology*, Vol. 84, pp. 1101-1133
- Jackson, S.S. (2008) – Calibration strategies for elemental analysis by LA-ICP-MS; in: Sylvester, P. (Ed.) – *Laser Ablation ICP-MS in the Earth Sciences: current practices and outstanding issues*; Short Course Series, Vol. 40, Mineralogical Association of Canada, Vancouver, pp. 169-188
- Jiang, Z., Oliver, N.H.S., Barr, T.B., Power, W.L. & Ord, A. (1997) – Numerical modelling of fault-controlled fluid flow in the genesis of tin deposits of the Malage ore field, Gejiu mining district, China; *Economic Geology*, Vol. 92, pp. 228-247
- Jiang, S.-Y., Yu, J.-M. & Lu, J.-J. (2004) – Trace and rare-earth element geochemistry in tourmaline and cassiterite from the Yunlong tin deposit, Yunnan, China: implication for migmatitic-hydrothermal fluid evolution and ore genesis; *Chemical Geology*, Vol. 209, pp. 193-213
- Jochum, K.P., Nohl, U., Herwig, K., Lammel, E., Stoll, B. & Hofmann, A.W. (2005) – GeoReM: A new geochemical database for reference materials and isotopic standards; *Geostandards and Geoanalytical Research*, Vol. 29, pp. 333-338
- Jochum, K.P. & Willbold, M. (2006) – Reference Materials in Geoanalytical Research-Review for 2004 and 2005; *Geostandards and Geoanalytical Research*, Vol. 30, pp. 143-156
- Jochum, K.P., Weis, U., Stoll, B., Kuzmin, D., Yang, Q., Raczek, I., Jacob, D.E., Stracke, A., Bribaum, K., Frick, D.A., Günther, D. & Enzweiler, J. (2011) – Determination of reference values for NIST SRM 610-617 glasses following ISO guidelines; *Geostandards and Geoanalytical Research*, Vol. 35, pp. 397-429
- Jonsson, E., Troll, V.R., Högdahl, K., Harris, C., Weis, F., Nilsson, K.P. & Skelton A. (2013) – Magmatic origin of 'Kiruna-type' apatite-iron-oxide ores in Central Sweden; *Scientific Reports*, Vol. 3, No. 1644
- Kamber, B.S. (2009) – Geochemical fingerprinting: 40 years of analytical development and real world applications; *Applied Geochemistry*, Vol. 24, pp. 1074-1086
- Kane, J. (1998) – An assessment of the suitability of NIST glass SRM literature data for the derivation of reference values; *Geostandards Newsletter*, Vol. 22, pp. 15-33
- Kelly, W.C. & Turneure, F.S. (1970) – Mineralogy, paragenesis and geothermometry of the tin and tungsten deposits of the Eastern Andes, Bolivia; *Economic Geology*, Vol. 65, pp. 609-680
- Kelly, W.C. & Rye, R.O. (1979) – Geologic, fluid inclusion, and stable isotope studies of the tin-tungsten deposits of Panasqueira, Portugal; *Economic Geology*, Vol. 74, pp. 1721-1822
- Kempe, U. & Belyatsky, B.V. (1994) – Sm-Nb ages of wolframites from the western Erzgebirge-Vogtland region: possible genetic implications; in: Seltmann, R., Kämpf, H.

- & Möller, P. (Eds.) – Metallogeny of collisional orogens; International association on the genesis of ore deposits (IAGOD), Czech Geological Survey, Prague, pp. 142-149
- Kempe, U., Dandar, S., Getmanskaya, T.I. & Wolf, D. (1994) – The tungsten-antimony mineralization (focused on new occurrences in the Mongolian Altai); in: Seltmann, R., Kämpf, H. & Möller, P. (Eds.) – Metallogeny of collisional orogens; International association on the genesis of ore deposits (IAGOD), Czech Geological Survey, Prague, pp. 301-308
- Kempe, U. & Wolf, D. (1994) – Die Interpretation des H/F-Koeffizienten – immer noch offen; Freiburger Forschungshefte, Vol. C451, pp. 53-87
- Kempe, U. & Oberthür, T. (1997) – Physical and geochemical characteristics of scheelite from gold deposits: a reconnaissance study; in: Papunen, H. (Ed.) – Mineral deposits: research and exploration. Where do they meet? A.A. Balkema, Rotterdam, Netherlands, pp. 209-212
- Kempe, U., Belyatsky, B.V., Krymsky, R.S., Kremenetsky, A.A. & Ivanov, P.A. (2000) – Sm-Nd and Sr isotope systematics of scheelite from the giant Au(-W) deposit Muruntau (Uzbekistan): implications for the age and sources of Au mineralization; Mineralium Deposita, Vol. 36, pp. 379-392
- Kempe, U. & Wolf, D. (2006) – Anomalously high Sc contents in ore minerals from Sn-W deposits: possible economic significance and genetic implications; Ore Geology Reviews, Vol. 28, pp. 103-122
- Keppler, H. & Wyllie, P.J. (1991) – Partitioning of Cu, Sn, Mo, W, U, and Th between melt and aqueous fluid in the systems haplogranite-H₂O-HCl and haplogranite-H₂O-HF; Contributions to Mineralogy and Petrology, Vol. 109, pp.139–150.
- Keppler, H. (1993) – Influence of fluorine on the enrichment of high field strength trace elements in granitic rocks; Contributions to Mineralogy and Petrology, Vol. 114, pp. 479-488
- Kilias, S.P. & Konnerup-Madsen, J. (1997) – Fluid inclusion and stable isotope evidence for the genesis of quartz-scheelite veins, Metaggitsi area, central Chalkidiki Peninsula, N. Greece; Mineralium Deposita, Vol. 32, pp. 581-595
- King, R.J. (2005) – The wolframite series; Minerals explained, Vol. 41
- Kinnaird, J. & Bowden, P. (1987) – African anorogenic alkaline magmatism and mineralization - a discussion with reference to the Niger-Nigerian province; Geological Journal, Vol. 22, pp. 297-340
- Kleber, W. (1998) – Einführung in die Kristallographie; 18th edition revised by Bausch, H.J. & Bohm, J., Verlag Technik, Berlin, 416 p.
- Kleemann, G.J. & Twist, D. (1989) – The compositionally-zoned sheet-like granite pluton of the Bushveld Complex: evidence bearing on the nature of A-type magmatism; Journal of Petrology, Vol. 30, pp. 1383-1414
- Klein, C. & Hurlbut jr., C.S. (1993) – Manual of Mineralogy (after J.D. Dana); 21st edition, John Wiley & Sons Inc., New York, 681 p.
- Klementová, M. & Rieder, M. (2005) – Tantaloniobates in cassiterite: inclusions or exsolutions; Materials Structure, Vol. 12, pp. 104-108
- Klintsova, A.I., Barsukov, L., Shemarykina, T.P. & Khodakovsky, I.L. (1975) – Experimental determination of the stability constants of tetravalent tin hydroxylfluoride complexes; Geochemistry International, Vol. 12, pp. 207-215
- Knopf, A. (1916) – Wood tin in the tertiary rhyolites of northern Nevada; Economic Geology, Vol. 11, pp. 652-661
- Kontak, D.J. & Clark, A.H. (2002) – Genesis of the giant Bonanza San Rafael lode tin deposit, Peru: origin and significance of pervasive alteration; Economic Geology, Vol. 97, pp. 1741-1777

- Košler, J. (2008) – Laser ablation sampling strategies for concentration and isotope ratio analyses by ICP-MS; in: Sylvester, P. (Ed.) – Laser Ablation ICP-MS in the Earth Sciences: current practices and outstanding issues; Short Course Series, Vol. 40, Mineralogical Association of Canada, Vancouver, pp. 79-92
- Koval, P.V. & Yakimov, V.M. (1983) – Tungsten and tin mineralization of Mongolia and its relationship to igneous activity; *International Geology Review*, Vol. 26, pp. 227-237
- Kovalenko, V.I. & Yarmolyuk, V.V. (1995) – Endogenous rare metal ore formations and rare metal metallogeny of Mongolia; *Economic Geology*, Vol. 90, pp. 520-529
- Kovalenko, V.I. & Yarmolyuk, V.V. (2001) – Ore deposits and metallogeny of Mongolia; in: Dergunov, A.B. (ed.) – Tectonics, magmatism, and metallogeny of Mongolia; Routledge, London, pp. 245-266
- Krauskopf, K.B. (1970) – Abundance in common igneous rock types; in: Wedepohl (Ed.) – Handbook of Geochemistry; Vol. II/5, Springer, Berlin, pp. 74E1-74E4
- Krivitskaya, N.N., Sakharova, M.S., Ryabov A.N. & Tsepina A.I. (1995) – New data on the intermetallic compounds of tin; *Moscow University Geology Bulletin*, Vol. 50, pp. 65-70
- Krosiakova, I. & Günther, D. (2007) – Elemental fractionation in laser ablation-inductively coupled plasma-mass spectrometry: evidence for mass load induced matrix effects in the ICP during the ablation of a silicate glass; *Journal of Analytical Atomic Spectrometry*, Vol. 22, pp. 51-62
- Kunzendorf, H. & Glasby, G.P. (1992) – Tungsten accumulations in Pacific ferromanganese deposits; *Mineralium Deposita*, Vol. 27, pp. 147-152
- Küster, D. (2008) – Granitoid-hosted Ta mineralization in the Arabian-Nubian Shield: Ore deposit types, tectono-metallogenetic setting and petrogenetic framework; *Ore Geology Reviews*, Vol. 35, pp. 68-86
- Kuzmin, A. & Purans, J. (2001) – Local atomic and electronic structure of tungsten ions in AWO_4 crystals of scheelite and wolframite types; *Radiation Measurements*, Vol. 33, pp. 583-586
- Kwak, T.A.P. (1978) – The conditions of formation of the King Island scheelite contact skarn, King Island, Tasmania, Australia; *American Journal of Science*, Vol. 278, pp. 969-999
- Kwak, T.A.P. & Askins, P.W. (1981) – Geology and genesis of the F-Sn-W(-Be-Zn) skarn (wrigglite) at Moina, Tasmania; *Economic Geology*, Vol. 76, pp. 439-467
- Kwak, T.A.P. & Tan, T.H. (1981) – The geochemistry of zoning in skarn minerals at the King Island (Dolphin) mine; *Economic Geology*, Vol. 76, pp. 468-497
- Kwak, T.A.P. (1983) – The geology and geochemistry of the zoned Sn-W-F-Be skarns at Mt. Lindsay, Tasmania, Australia; *Economic Geology*, Vol. 78, pp. 1440-1465
- Kwak, T.A.P., Taylor, R.G. & Plimer, I.R. (1986) – Occurrence and genesis of primary tungsten deposits in Australia; in: Beus, A.A. (Ed.) – Geology of tungsten; International Geological Correlation Programme, Project 26 'mineralization associated with acid magmatism' (MAWAM), pp. 217-244
- Kwak, T.A.P. (1987) – W-Sn skarn deposits and related metamorphic skarns and granitoids; *Developments in Economic Geology*, Vol. 24, Elsevier, Amsterdam, 451 p.
- Lagache, M. & Quéméneur, J. (1997) – The Volta Grande pegmatites, Minas Gerais, Brazil: an example of rare-element granitic pegmatites exceptionally enriched in lithium and rubidium; *Canadian Mineralogist*, Vol. 35, pp. 153-165
- Lamarão, C.N., Pinho, S.C.C., de Paiva Júnior, A.L. & Galarza, M.A. (2012) – Mineralogy and geochemistry of the Paleoproterozoic, tin-mineralized Bom Jardim granite of the Velho Guilherme Suite, eastern Amazonian craton; *Journal of South American Earth Sciences*, Vol. 38, pp. 159-173

- Landis, G.P. & Rye, R.O. (1974) – Geologic, fluid inclusion, and stable isotope studies of the Pasto Bueno tungsten-base metal ore deposit, Northern Peru; *Economic Geology*, Vol. 69, pp. 1025-1059
- Lang, J.R. & Baker, T. (2001) – Intrusion-related gold systems: the present level of understanding; *Mineralium Deposita*, Vol. 36, pp. 477-489
- Lahusen, L. (1972) – Schicht- und zeitgebundene Antimonit-Scheelit-Vorkommen und Zinnober-Vererzungen in Kärnten und Osttirol/Österreich; *Mineralium Deposita*, Vol. 7, pp. 31-60
- Lassner, E. & Schubert, W.-D. (1999) – Tungsten: properties, chemistry, technology of the element, alloys, and chemical compounds; Kluwer Academic / Plenum Publishers, New York, 416 p.
- Lassner, E. & Schubert, W.-D. (2009) – Tungsten; International Tungsten Industry Association (ITIA), ISBN 0-95300086-2-2, 134 p.
- Lawrence, L.J. (1961) – Crystal habit of wolframite as an indication of relative temperature of formation; *Neues Jahrbuch für Mineralogie – Monatshefte*, pp.241-247
- Layne, G.D. & Spooner, E.T.C. (1991) – The JC tin skarn deposit, Southern Yukon Territory: I. geology, paragenesis, and fluid inclusion microthermometry; *Economic Geology*, Vol. 86, pp. 29-41
- Laznicka, P. (2010) – Giant metallic deposits: future sources of industrial metals; 2nd edition, Springer, Berlin, 949 p.
- LeBoutillier, N. (2002) – The tectonics of Variscan magmatism and mineralisation in Southwest England; Ph.D. thesis, University of Exeter, Camborne School of Mines, 639 p.
- Lee, D.-C. & Halliday, A.N. (1995) – Precise determinations of the isotopic compositions and atomic weights of molybdenum, tellurium, tin and tungsten using ICP magnetic sector multiple collector mass spectrometry; *International Journal of Mass Spectrometry and Ion Processes*, Vol. 146/147, pp. 35-46
- Legg, C.A. & Namateba, C. (1982) – Regional zoning of tin-tantalum-niobium pegmatites in the Masuku area, Southern Province, Zambia; in: Evans, A.M. (Ed.) – *Metallization Associated with Acid Magmatism*; Vol. 6, John Wiley & Sons, Chichester, pp. 181-190
- Lehmann, B. (1979) – Schichtgebundene Sn-Lagerstätten in der Cordillera Real/Bolivien; *Berliner geowissenschaftliche Abhandlungen*, Vol. A/14, Dietrich Reimer Publishing, Berlin, 135 p.
- Lehmann, B. (1982) – Metallogeny of tin: magmatic differentiation versus geochemical heritage; *Economic Geology*, Vol. 77, pp. 50-59
- Lehmann, B. (1985) – Formation of the strata-bound Kellhuani tin deposits, Bolivia; *Mineralium Deposita*, Vol. 20, pp. 169-176
- Lehmann, B. (1987) – Tin granites, geochemical heritage, magmatic differentiation; *Geologische Rundschau*, Vol. 76, pp. 177-185
- Lehmann, B., Ishihara, S., Michel, H., Miller, J., Rapela, C., Sanchez, A., Tistl, M. & Winkelmann, L. (1990) – The Bolivian Tin Province and regional tin distribution in the Central Andes: a reassessment; *Economic Geology*, Vol. 85, pp. 1044-1058
- Lehmann, B. (1990) – Metallogeny of tin; *Lecture Notes in Earth Sciences*, Vol. 32, Springer, Berlin, 211 p.
- Lehmann, B., Dietrich, A., Heinhorst, J., Métrich, N., Mosbah, M., Palacios, C., Schneider, H.-J., Wallianos, A., Webster, J. & Winkelmann, L. (2000) – Boron in the Bolivian tin belt; *Mineralium Deposita*, Vol. 35, pp. 223-232

- Lenharo, S.L.R., Moura, M.A. & Botelho, N.F. (2002) – Petrogenetic and mineralization processes in Paleo- to Mesoproterozoic rapakivi granites, examples from Pitinga and Goiás, Brazil; *Precambrian Research*, Vol. 119, pp. 277-299
- Lenharo, S.L.R., Pollard, P.J. & Born, H. (2003) – Petrology and textural evolution of granites associated with tin and rare-metals mineralization at the Pitinga mine, Amazonas, Brazil; *Lithos*, Vol. 66, pp. 37-61
- Lepersonne, J. (1974) – Carte Géologique du Zaïre; République du Zaïre, Département des Mines, Service Géologique, 1:2000000
- Leube, A. & Stumpfl, E.F. (1963a) – The Rooiberg and Leeuwpoort tin mines, Transvaal, South Africa, Part 1: General and structural geology; *Economic Geology*, Vol. 58, No. 3, pp. 391-418
- Leube, A. & Stumpfl, E.F. (1963b) – The Rooiberg and Leeuwpoort tin mines, Transvaal, South Africa, Part 2: Petrology, mineralogy and geochemistry; *Economic Geology*, Vol. 58, No. 4, pp. 527-557
- Leutwein, F. (1952) – Die chemische Zusammensetzung der Wolframite und ihre lagerstättenkundliche Bedeutung; *Acta Geologica Academiae Scientiarum*, Vol. 1, pp. 133-141
- Lide, D.R. (Ed.) (2009) – *Handbook of Chemistry and Physics: A Ready-Reference Book of Chemical and Physical Data*; 90th edition, CRC Press, 2804 p.
- Liedtke, M. & Schmidt, M. (2014) – Risikobewertung Wolfram; DERA Rohstoffinformationen, Vol. 19, German Mineral Resources Agency (DERA) in the Federal Institute for Geosciences and Natural Resources (BGR), 106 p.
- Linnen, R.L., Williams-Jones, A.E. & Martin, R.F. (1992) – Evidence of magmatic cassiterite mineralization at the Nong Sua aplite-pegmatite complex, Thailand; *Canadian Mineralogist*, Vol. 30, pp. 739-761
- Linnen, R.L. & Williams-Jones, A.E. (1993) – Mineralogical constraints on magmatic and hydrothermal Sn-W-Ta-Nb mineralization at the Nong Sua aplite-pegmatite, Thailand; *European Journal of Mineralogy*, Vol. 5, pp. 721-736
- Linnen, R.L. & Williams-Jones, A.E. (1994) – The evolution of pegmatite-hosted Sn-W mineralization at Nong Sua, Thailand: Evidence from fluid inclusions and stable isotopes; *Geochimica et Cosmochimica Acta*, Vol. 58, pp. 735-747
- Linnen, R.L., Pichavant, M., Holtz, F. & Burgess, S. (1995) – The effect of fO_2 on the solubility, diffusion, and speciation of tin in haplogranitic melt at 850 °C and 2 kbar; *Geochimica et Cosmochimica Acta*; Vol. 59, pp. 1579-1588
- Linnen, R.L., Pichavant, M. & Holtz, F. (1996) – The combined effects of fO_2 and melt composition on SnO₂ solubility and tin diffusivity in haplogranitic melts; *Geochimica et Cosmochimica Acta*; Vol. 60, pp. 4965-4976
- Linnen, R.L. (1998a) – Depth of emplacement, fluid provenance and metallogeny in granitic terranes; a comparison of western Thailand with other tin belts; *Mineralium Deposita*; Vol. 33, pp. 461-476
- Linnen, R.L. (1998b) – The solubility of Nb-Ta-Zr-Hf-W in granitic melts with Li and Li+F: constraints for mineralization in rare metal granites and pegmatites; *Economic Geology*, Vol. 93, pp. 1013-1025
- Linnen, R.L. (2005) – The effect of water on accessory phase solubility in subaluminous and peralkaline granitic melts; *Lithos*, Vol. 80, pp. 267-280
- Linnen, R.L. & Cuney, M. (2005) – Granite-related rare-element deposits and experimental constraints on Ta-Nb-W-Sn-Zr-Hf mineralization; in: Linnen, R.L. & Samson, I.M. (Eds.) – Rare-element geochemistry and mineral deposits; Geological Association of Canada (GAC), Short Course Notes, Vol. 17, pp. 45-68

- Liu, J., Mao, J., Ye, H. & Zhang, W. (2011) – Geology, geochemistry and age of the Hukeng tungsten deposit, Southern China; *Ore Geology Reviews*, Vol. 43, pp. 50-61
- Liu, Y., Hu, Z., Gao, S., Günther, D., Xu, J., Gao, C. & Chen, H. (2008) – *In situ* analysis of major and trace elements of anhydrous minerals by LA-ICP-MS without applying an internal standard; *Chemical Geology*, Vol. 257, pp. 34-43
- Llorens, T. & Moro, M.C. (2012a) – Oxide minerals in the granitic cupola of the Jálama Batholith, Salamanca, Spain. Part I: accessory Sn, Nb, Ta and Ti minerals in leucogranites, aplites and pegmatites; *Journal of Geosciences*, Vol. 57, pp. 25-43
- Llorens, T. & Moro, M.C. (2012b) – Oxide minerals in the granitic cupola of the Jálama Batholith, Salamanca, Spain. Part II: Sn, W and Ti minerals in intra-granitic quartz veins; *Journal of Geosciences*, Vol. 57, pp. 25-43
- Loiselle, M.C. & Wones, D.R. (1979) – Characteristics and origin of anorogenic granites; *Geological Society of America: Abstracts with Programs*, Vol. 14, p. 468
- London, D. (1987) – Internal differentiation of rare-element pegmatites: Effects of boron, phosphorus, and fluorine; *Geochimica et Cosmochimica Acta*, Vol. 51, pp. 403-420
- London, D. (2005) – Granitic pegmatites: an assessment of current concepts and directions for the future; *Lithos*, Vol. 80, pp. 281-303
- Longerich, H.P., Jackson, S.E. & Günther, D. (1996) – Laser ablation inductively coupled plasma mass spectrometric transient signal data acquisition and analyte concentration calculation; *Journal of Analytical Atomic Spectrometry*, Vol. 11, pp. 899-904
- Losos, Z. & Beran, A. (2004) – OH defects in cassiterite; *Mineralogy and Petrology*, Vol. 81, pp. 219-234
- Lüders, V. (1996) – Contribution of infrared microscopy to fluid inclusion studies in some opaque minerals (wolframite, stibnite, bournonite): metallogenic implications; *Economic Geology*, Vol. 91, pp. 1462-1468
- Lufkin, J.L. (1977) – Chemistry and mineralogy of wood-tin, Black Range, New Mexico; *American Mineralogist*, Vol. 62, pp. 100-106
- Luvizotto, G.L. (2008) – Trace element signatures in rutile: characterization of standards and applications to accessory mineral behaviour in metamorphic rocks; Ph.D. thesis, Heidelberg University, 258 p.
- Macavei, J. & Schulz, H. (1993) – The crystal structure of wolframite type tungstates at high pressure; *Zeitschrift für Kristallographie*, Vol. 207, pp. 193-208
- Macey, P. & Harris, C. (2006) – Stable isotope and fluid inclusion evidence for the origin of the Brandberg West area Sn-W vein deposits, NW Namibia; *Mineralium Deposita*, Vol. 51, pp. 671-690
- Mair, J.L., Goldfarb, R.J., Johnson, C.A., Hart, C.J.R. & Marsh, E.E. (2006) – Geochemical constraints on the genesis of the scheelite dome intrusion-related gold deposit, Tombstone gold belt, Yukon, Canada; *Economic Geology*, Vol. 101, pp. 523-553
- Malaysian-Thai Working Group (2009) – Geology of the Pengkalan Hulu-Betong transect area along the Malaysia-Thailand border; *The Malaysia-Thailand Joint Geological Survey Committee, Geological Papers* Vol. 7, 79 p.
- Mangas, J. & Arribas, A. (1987) – Fluid inclusion study in different types of tin deposits associated with the Hercynian granites of Western Spain; *Chemical Geology*, Vol. 61, pp. 193-208
- Mangas, J. & Arribas, A. (1988) – Hydrothermal fluid evolution of the Sn-W mineralization in the Parrilla ore deposit (Caceres, Spain); *Journal of the Geological Society*, Vol. 145, pp. 144-155

- Manning, D.A.C. (1982) – An experimental study of the effects of fluorine on the crystallization of granitic melts; in: Evans, A.M. (Ed.) – Metallization Associated with Acid Magmatism; Vol. 6, John Wiley & Sons, Chichester, pp. 191-203
- Manning, D.A.C. & Henderson, P. (1984) – The behaviour of tungsten in granitic melt-vapour systems; Contributions to Mineralogy and Petrology; Vol. 86, pp. 286-293
- Manning, D.A.C. & Pichavant, M. (1988) – Volatiles and their bearing on the behaviour of metals in granitic systems; in: Taylor, R.P. & Strong, D.F. (Eds.) – Recent advances in the geology of granite-related mineral deposits; The Canadian Institute of Mining and Metallurgy, Special Volume 39, Montreal, pp. 13-24
- Mao, J., Cheng, Y., Chen, M. & Pirajno, F. (2013) – Major types and time-space distribution of Mesozoic ore deposits in South China and their geodynamic settings; Mineralium Deposita, Vol. 48, pp. 267-294
- Markl, G. & Schumacher, J.C. (1996) – Spatial variations in temperature and composition of greisen-forming fluids: an example from the Variscan Triberg granite complex, Germany; Economic Geology, Vol. 91, pp. 576-589
- Martins, T., Lima, A., Simmons, W.B., Falster, A.U. & Noronha, F. (2011) – Geochemical fractionation of Nb-Ta oxides in Li-bearing pegmatites from the Barroso-Alvão pegmatite field, northern Portugal; Canadian Mineralogist, Vol. 49, pp. 77-791
- Masau, M., Černý, P. & Chapman, R. (2000) – Exsolution of zirconian-hafnian wodginite from manganoan-tantalian cassiterite, Annie Claim #3 granitic pegmatite, Southeastern Manitoba, Canada; Canadian Mineralogist, Vol. 38, pp. 685-694
- Matheis, G., Emofurieta, W.O. & Ohiwerei, S.F. (1982) – Trace element distribution in tin-bearing pegmatites of southwestern Nigeria; in: Evans, A.M. (Ed.) – Metallization Associated with Acid Magmatism; Vol. 6, John Wiley & Sons, Chichester, pp. 205-220
- Matte, P. (1991) – Accretionary history and crustal evolution of the Variscan belt in Western Europe; Tectonophysics, Vol. 196, pp. 309-337
- Maucher, A. (1965) – Die Antimon-Wolfram-Quecksilber-Formation und ihre Beziehung zu Magmatismus und Geotektonik; Freiburger Forschungshefte, Vol. C186, pp. 173-188
- Maucher, A. (1976) – The strata-bound cinnabar-stibnite-scheelite deposits; in: Wolf, K.H. (Ed.) – Handbook of strata-bound and stratiform ore deposits; Vol. 7, Elsevier Scientific Publishing Company, Amsterdam, pp. 477-503
- McBride, S.L., Robertson, C.R., Clark, A.H. & Farrar, E. (1983) – Magmatic and metallogenetic episodes in the northern tin belt, Cordillera Real, Bolivia; Geologische Rundschau, Vol. 72, pp. 685-713
- McCauley, A. & Bradley, D.C. (2014) – The global age distribution of granitic pegmatites; Canadian Mineralogist, Vol. 52, pp. 183-190
- McDonough, W. & Sun, S.S. (1995) – The composition of the earth; Chemical Geology, Vol. 120, 223-253
- McIver, J.R. & Mihálik, P. (1975) – Stannian andradite from “Davib Ost”, South West Africa; Canadian Mineralogist, Vol. 13, pp. 217-221
- McNaughton, N.J., Rosman, K.J.R. (1991) – Tin isotope fractionation in terrestrial cassiterites; Geochimica et Cosmochimica Acta, Vol. 55, pp. 499-504
- McNaughton, M.J., Pollard, P.J., Groves, D.I. & Taylor, R.G. (1993) – A Long-Lived Hydrothermal System in Bushveld Granites at the Zaaipplaats Tin Mine: Lead Isotope Evidence; Economic Geology, Vol. 88, pp. 27-43
- Meinert, L.D., Dipple, G.M. & Nicolescu, S. (2005) – World skarn deposits; in: Hedenquist, J.W., Thompson, J.F.H., Goldfarb, R.J. & Richards, J.P. (Eds.) – Economic Geology: 100th Anniversary Volume; Society of Economic Geologists, pp. 299-336

- Melcher, F. & Lodziak, J. (2007) – Platinum-group minerals of concentrates from the Driekop platinum pipe, Eastern Bushveld Complex - Tribute to Eugen F. Stumpfl; *Neues Jahrbuch für Mineralogie – Abhandlungen*; Vol. 183, pp. 173-195
- Melcher, F., Sitnikova, M.A., Graupner, T., Martin, N., Oberthür, T., Henjes-Kunst, F., Gäbler, H.-E., Gerdes, A., Brätz, H., Davis, D.W. & Dewaele, S. (2008) – Fingerprinting of conflict minerals: columbite-tantalite (“coltan”) ores; *Society for geology applied to mineral deposits, SGA News*, Vol. 23, 20 p.
- Melcher, F., Graupner, T., Sitnikova, M.A., Oberthür, T., Gäbler, H.-E., Bahr, A. & Henjes-Kunst, F. (2009) – Herkunftsnachweis von Columbit-Tantalit-Erzen: Status-quo-Bericht; Federal Institute for Geosciences and Natural Resources (BGR), Internal Report, 11082/09, Hannover, 107 p.
- Melcher, F., Dorner, U., Franken, G., Gäbler, H.-E., Graupner, T., Goldmann, S., Henjes-Kunst, F., Küster, D., Oberthür, T., Sitnikova, M.A., & Vasters, J. (2010) – Geochemical fingerprinting methods identify the origin of raw materials in conflict regions: the example of TTT (Ta, Sn, W) ores in Central Africa; *PANGEO 2010 Extended Abstracts, Journal of Alpine Geology*, Vol. 52, pp. 26-31
- Melcher, F., Graupner, T., Gäbler, H.-E., Sitnikova, M.A., Henjes-Kunst, F., Oberthür, T., Gerdes, A. & Dewaele, S. (2015) – Tantalum-(niobium-tin) mineralisation in African pegmatites and rare metal granites: Constraints from Ta–Nb oxide mineralogy, geochemistry and U-Pb geochronology; *Ore Geology Reviews*, Vol. 64, pp. 667-719
- Migdisov, A.A. & Williams-Jones, A.E. (2005) – An experimental study of cassiterite solubility in HCl-bearing water vapour at temperatures up to 350 °C. Implications for tin ore formation; *Chemical Geology*, Vol. 217, pp. 29-40
- Mignardi, S., Pizzoferrato, M.C. & Ferrini, V (1996) – Hydrothermal synthesis and geochemistry of wolframite; in: *Terra Abstracts*, Vol. 8, Sixth International Symposium on Experimental Mineralogy, Petrology and Geochemistry, Bayreuth, Germany, April 10-13, 1996, Blackwell Science, p. 44
- Mignardi, S., Ferrini, V., Masi, U., Nabais, L.C. & de Sousa Bernardo, M. (1998) – Significance of the major- and trace-element contents of wolframite from the deposits of Panasqueira and Vale de Gatas, Portugal; in: Hagni, R.D. (Ed.) – *Proceedings of the Ninth Quadrennial IAGOD Symposium*, Beijing, China, August 12-18, 1994; *Schweizerbart*, Stuttgart, pp. 475-484
- Mills, S.J., Kartashov, P.M., Kampf, A.R., Rumsey, M.S., Ma, C., Spratt, J., Rossman, G.R. & Novgorodova, M.I. (2011) – Tungsten, IMA 2011-004; *Mineralogical Magazine*, Vol. 75, p. 2539
- Miyawaki, R., Yokoyama, K., Matsubara, S., Furuta, H., Gomi, A. & Murakami, R. (2010) – Huanzalaite, MgWO₄, a new mineral species from the Huanzala mine, Peru; *Canadian Mineralogist*, Vol. 48, pp. 105-112
- Mlynarczyk, M.S.J., Sherlock, R.S. & Williams-Jones, A.E. (2003) – San Rafael, Peru: geology and structure of the world’s richest tin lode; *Mineralium Deposita*, Vol. 38, pp. 555-567
- Mochnacka, K., Mayer, W., Piestrzynski, A. & Kucha, H. (1999) – Petrology of cassiterite aggregates from Gierczyn area, SW Poland; in: Stanley, C.J. et al. (Eds.) – *Mineral Deposits: Processes to Processing*; A.A. Balkema, Rotterdam, Netherlands, pp. 397-400
- Mochnacka, K., Pieczka, A., Gołębiowska, B. & Kozłowski, A. (2001) – Cassiterite from Rędziny and its relationship to the tin-bearing schist of Izera area (SW Poland); in: Piestrzynski, A., et al. (Eds.) – *Mineral Deposits at the Beginning of the 21st Century*; Swets & Zeitlinger B.V. Publishers, Lisse, Netherlands, pp. 457-460

- Mohamed, F.H. (1993) – Rare metal-bearing and barren granites, Eastern Desert of Egypt: geochemical characterization and metallogenetic aspects; *Journal of African Earth Sciences*, Vol. 17, pp. 525-539
- Möller, P. & Dulski, P. (1983) – Fractionation of Zr and Hf in cassiterite; *Chemical Geology*, Vol. 40, pp. 1-12
- Möller, P., Dulski, P., Szacki, W., Malow, G. & Riedel, E. (1988) – Substitution of tin in cassiterite by tantalum, niobium, tungsten, iron and manganese; *Geochimica et Cosmochimica Acta*, Vol. 52, pp. 1497-1503
- Moore, F. & Howie, R.A. (1978) – On the application of the hübnerite:ferberite ratio as a geothermometer; *Mineralium Deposita*, Vol. 13, 391-397
- Moore, F. & Howie, R.A. (1979) – Geochemistry of some Cornubian cassiterites; *Mineralium Deposita*, Vol. 14, 103-107
- Morteani, G., Preinfalk, C. & Horn, A.H. (2000) – Classification and mineralization potential of the pegmatites of the Eastern Brazilian Pegmatite Province; *Mineralium Deposita*, Vol. 35, pp. 638-655
- Moura, A., Dória, A., Neiva, A.M.R., Leal Gomes, C. & Creaser, R.A. (2014) – Metallogenesis at the Carris W–Mo–Sn deposit (Gerês, Portugal): constraints from fluid inclusions, mineral geochemistry, Re–Os and He–Ar isotopes; *Ore Geology Reviews*, Vol. 56, pp. 73-93
- Možná, V., Pisonero, J., Holá, M., Kanický, V. & Günther, D. (2006) – Quantitative analysis of Fe-based samples using ultraviolet nanosecond and femtosecond laser ablation-ICP-MS; *Journal of Analytical Atomic Spectrometry*, Vol. 21, pp. 1194-1201
- Müller, B., Frischknecht, R., Seward, T.M., Heinrich, C.A. & Gallegos, W.C. (2001) – A fluid inclusion reconnaissance study of the Hunanuni tin deposit (Bolivia), using LA-ICP-MS micro-analysis; *Mineralium Deposita*, Vol. 36, pp. 680-688
- Mulligan, R. (1975) – Geology of Canadian tin occurrences; *Economic Geology Report No 28*, Geological Survey of Canada, Department of Energy, Mines and Resources, Ottawa, 155 p.
- Murciego, A., Garcia Sanchez, A., Dusauroy, Y., Martin Pozas, J.M. & Ruck, R. (1997) – Geochemistry and EPR of cassiterites from the Iberian Hercynian Massif; *Mineralogical Magazine*, Vol. 61, pp. 357-365
- Nadoll, P., Angerer, T., Mauk, J.L., French, D. & Walshe, J. (2014) – The chemistry of hydrothermal magnetite: a review; *Ore Geology Reviews*, Vol. 61, pp. 1-32
- Nakashima, K., Watanabe, M. & Soeda, A. (1986) – Regional and local variations in the composition of the wolframite series from SW Japan and possible factors controlling compositional variations; *Mineralium Deposita*, Vol. 21, pp. 200-206
- Naski, G.C. & Hess, P.C. (1985) – SnO₂ solubility: Experimental results in peraluminous and peralkaline high silica glasses; *EOS*, Vol. 66, p. 412
- Neiva, A.M.R. (1996) – Geochemistry of cassiterite and its inclusions and exsolution products from tin and tungsten deposits in Portugal; *Canadian Mineralogist*, Vol. 34, pp. 745-768
- Neiva, A.M.R. (2008) – Geochemistry of cassiterite and wolframite from tin and tungsten quartz veins in Portugal; *Ore Geology Reviews*, Vol. 33, pp. 221-238
- Newberry, R.J. & Einaudi, M.T. (1981) – Tectonic and geochemical setting of tungsten skarn mineralization in the Cordillera; *Arizona Geological Society Digest*, Vol. 14, pp. 99-111
- Newberry, R.J. (1982) – Tungsten-bearing skarns of the Sierra Nevada. I. The Pine Creek Mine, California; *Economic Geology*, Vol. 77, pp. 823-844
- Newberry, R.J. & Swanson, S.E. (1986) – Scheelite skarn granitoids: an evaluation of the roles of magmatic source and progress; *Ore Geology Reviews*, Vol. 1, pp. 57-81

- Newberry, R.J. (1998) – W- and Sn-skarn deposits: a 1998 status report; in: Lentz, D.R. (Ed.) – Mineralized intrusion-related skarn systems; Short Course Series, Vol. 26, Mineralogical Association of Canada, Québec, pp. 289-335
- Newhouse, W.H. & Buerger, M.J. (1928) – Observations on wood tin nodules; *Economic Geology*, Vol. 23, pp. 185-192
- Ningthoujam, R.S., Lahiri, D., Sudarsan, V., Poswal, H.K., Kulshreshtha, S.K., Sharma, S.M., Bhushan, B. & Sastry, M.D. (2007) – Nature of V^{n+} ions in SnO_2 : EPR and photoluminescence studies; *Material Research Bulletin*, Vol. 42, pp. 1293-1300
- Noble, S.R., Spooner, E.T.C. & Harris, F.R. (1984) – The Logtung large tonnage, low-grade W (Scheelite)-Mo porphyry deposit, South-Central Yukon Territory; *Economic Geology*, Vol. 79, pp. 848-868
- Norman, M.D., Pearson, N.J., Sharma, A. & Griffin, W.L. (1996) – Quantitative analysis of trace elements in geological materials by Laser Ablation ICPMS: instrumental operating conditions and calibration values of NIST glasses; *Geostandards Newsletter*, Vol. 20, pp. 247-261
- Norman, M.D., Griffin, W.L., Pearson, N.J., Gracia, M.O. & O'Reilly, S.Y. (1998) – Quantitative analysis of trace element abundances in glasses and minerals: a comparison of laser ablation inductively coupled plasma mass spectrometry, solution inductively coupled plasma mass spectrometry, proton microprobe and electron microprobe data; *Journal of Analytical Atomic Spectrometry*, Vol. 13, pp. 477-482
- Norton, J.J. & Redden, J.A. (1990) – Relations of zoned pegmatites to other pegmatites, granite, and metamorphic rocks in the southern Black Hills, South Dakota; *American Mineralogist*, Vol. 75, pp. 631-655
- Novák, M., Johan, Z., Škoda, R., Černý, P., Šrein, V. & Veselovský, F. (2008) – Primary oxide minerals in the system WO_3 - Nb_2O_5 - TiO_2 - Fe_2O_3 - FeO and their breakdown products from the pegmatite No. 3 at Dolní Bory-Hatě, Czech Republic; *European Journal of Mineralogy*, Vol. 20, pp. 487-499
- Novák, M. & Šrein, V. (1989) – Chemical composition and paragenesis of wolframite from the Dolní Bory pegmatites, western Moravia, Czechoslovakia; *Acta Universitatis Carolinae – Geologica*, Vol. 4, pp. 495-500
- Novgorodova, M.I., Nedashkovskaya, N.N., Rasskazov, A.V., Trubkin, N.V., Semenov, Y.I. & Koshelev, B.L. (1995) – Native tungsten with yttrium oxide inclusions from alluvium of the Bol'shaya Pol'ya River, Subpolar Urals; *Doklady Akademiia Nauk*, Vol. 340, pp. 681-684 (in Russian)
- Obaje, N.G. (2009) – *Geology and mineral resources of Nigeria*; Lecture Notes in Earth Sciences, Vol. 120, Springer, Berlin, 221 p.
- Ødegård, M. (1999) – Preparation of synthetic calibration materials for use in the microanalysis of oxide minerals by direct fusion in high-purity graphite electrodes: preliminary results for quartz and rutile; *Geostandards Newsletter*, Vol. 23, pp. 173-186
- Oelsner, W.O. (1952) – Die pegmatitisch-pneumatolytischen Lagerstätten des Erzgebirges mit Ausnahme der Kontaktlagerstätten; *Freiberger Forschungshefte*, Vol. C9, pp. 16-80
- Oelsner, W.O. (1954) – Bemerkungen über die Anwendbarkeit des H/F-Koeffizienten zur Deutung der Genese von Wolframitlagerstätten; *Freiberger Forschungshefte*, Vol. C10, pp. 62-67
- Oen, I.S., Korpershoek, H.R., Kieft, C. & Lustenhouwer, W.J. (1982) – A microprobe study of rutile, cassiterite, wolframite and sulfides in the Morro Potosí greisen, Rondônia, Brazil; *Neues Jahrbuch für Mineralogie – Monatshefte*; No. 4, pp. 175-191

- Ogunbajo, M.I. (1993) – The mineralogy and geochemistry of some cassiterite from the Younger Granite province of the Jos Plateau, Nigeria; *Journal of African Earth Sciences*; Vol. 16, 465-472
- Okrusch, M. & Matthes, S. (2009) – *Mineralogie: eine Einführung in die spezielle Mineralogie, Petrologie und Lagerstättenkunde*; 8th edition, Springer, Berlin, 658 p.
- Olade, M.A. (1980) – Geochemical characteristics of tin-bearing and tin-barren granites, Northern Nigeria; *Economic Geology*, Vol. 75, pp. 71-82
- Oliveira, J.T., Pacheco, N., Carvalho, P. & Ferreira, A. (1997) – The Neves Corvo mine and the Paleozoic geology of Southwest Portugal; in: Barriga, F.J.A.S. & Carvalho, D. (Eds.) – *Geology and VMS deposits of the Iberian Pyrite Belt*; SEG Neves Corvo Field Conference 1997, Guidebook Series, Vol. 27, pp. 21-71
- Ollila, J.T. (1986) – Origin of colour zoning in cassiterites from tin deposits within the Bushveld complex, South Africa; *Bulletin of the Geological Survey of Finland*; Vol. 58, Part 2, pp. 3-11
- O'Neill, H.S.C., Berry, A.J. & Eggins, S.M. (2008) – The solubility and oxidation state of tungsten in silicate melts: implications for the comparative chemistry of W and Mo in planetary differentiation processes; *Chemical Geology*, Vol. 255, pp. 346-359
- O'Reilly, C., Gallagher, V. & Feely, M. (1997) – Fluid inclusion study of the Ballinglen W-Sn-sulphide mineralization, SE Ireland; *Mineralium Deposita*, Vol. 32, pp. 569-580
- Pabalan, R.T. (1986) – Solubility of cassiterite (SnO₂) in NaCl solutions from 200 °C-350 °C, with geologic applications; Ph.D. thesis, Pennsylvania State University, 140 p.
- Padurow, N.N. (1956) – Mischbarkeit im System Rutil-Zinnstein; *Naturwissenschaften*, Vol. 43, pp. 395-396
- Page, L.R. (1942) – Tin and tungsten deposits at Silver Hill, Spokane County, Washington; United States Department of the Interior, Geological Survey, Strategic Minerals Investigation, Bulletin 931-H, pp. 177-203
- Pan, Y.-S. & Ypma, P.J.M. (1973) – The Mexican type tin deposits-its occurrence, chemistry and physical conditions of deposition; *Abstracts with Programs, Geological Society of America*, Vol. 5, Issue 7, p. 762
- Pan, J. & Amstutz, G.C. (1993) – A geochemical study of rare earth and trace elements in cassiterite from Dachang Sn-polymetallic ore field, Guangxi Province; *Journal of China University of Geosciences*; Vol. 4, pp. 52-58
- Paparoni, G., Walker, D. & Webster, J.D. (2010) – Cassiterite-saturated minimum melting behaviour within Sn-SnO₂-SiO₂ at 1 atm and 10 kbar; *American Mineralogist*, Vol. 95, pp. 784-798
- Partington, G.A., McNaughton, N.J. & Williams, I.S. (1995) – A review of the geology, mineralization, and geochronology of Greenbushes pegmatite, Western Australia; *Economic Geology*, Vol. 90, pp. 616-635
- Pašava, J., Kříbek, B., Dobeš, P., Vavříň, I., Žák, K., Fan, D., Zhang, T. & Boiron, M. (2003) – Tin-polymetallic sulfide deposits in the eastern part of the Dachang tin field (South China) and the role of black shales in their origin; *Mineralium Deposita*, Vol. 38, pp. 39-66
- Pastor, J. & Turaki, U.M. (1985) – Primary mineralization in Nigerian ring complexes and its economic significance; *Journal of African Earth Sciences*, Vol. 3, pp. 223-227
- Patterson, D.J., Ohmoto, H. & Solomon, M. (1981) – Geologic setting and genesis of cassiterite-sulfide mineralization at Renison Bell, western Tasmania; *Economic Geology*, Vol. 76, pp. 393-438
- Pavlu, D. (1986) – The tungsten minerals; in: Beus, A.A. (Ed.) – *Geology of tungsten, International Geological Correlation Programme, Project 26 'mineralization associated with acid magmatism' (MAWAM)*, pp. 45-57

- Peacock, M.A. (1931) – Classification of igneous rock series; *Journal of Geology*, Vol. 39, pp. 54-67
- Pearce, N.J.G., Perkins, W.T., Westgate, J.A., Gorton, M.P., Jackson, S.E., Neal, C.R. & Chenerly, S.P. (1997) – A compilation of new and published major and trace element data for NIST SRM 610 and NIST SRM 612 glass reference materials; *Geostandards Newsletter*, Vol. 21, pp. 115-144
- Pedrosa-Soares, A, Chaves, M. & Scholz, R. (2009) – Eastern Brazilian Pegmatite Province; *Field Trip Guide, PEG2009-4th International Symposium on Granitic Pegmatites*, Recife, 28 p.
- Peng, M., Lu, W. & Zou, Z. (1988) – Spectroscopic analysis and genesis of cassiterite; in: Hutchison, C.S. (Ed.) – *Geology of tin deposits in Asia and the Pacific: selected papers from the International Symposium on the Geology of Tin Deposits*, Nanning, China, October 26-30, 1984; Springer, Berlin, pp. 319-327
- Penhallurick, R.D. (1986) – Tin in antiquity: its mining and trade throughout the ancient world with particular reference to Cornwall; *The Institute of Metals*, Carleton House Terrace, London, United Kingdom, 271 p.
- Pereira, R., Ávila, C.A. & Neumann, R. (2004) – Estudo mineralógico e químico da cassiterita e de suas inclusões sólidas: implicação com a paragênese das mineralizações da província pegmatítica de São João del Rei, Minas Gerais, Brasil; *Arquivos do Museu Nacional*, Rio de Janeiro, Vol. 62, pp. 321-336
- Perkins, W.T., Pearce, N.J.G. & Westgate, J.A. (1997) – The development of Laser Ablation ICP-MS and calibration strategies: examples from the analysis of trace elements in volcanic glass shards and sulfide minerals; *Geostandards Newsletter*, Vol. 21, pp. 175-190
- Pieczka, A., Gołębiowska, B. & Parafiniuk, J. (2007) – Geochemistry and origin of the cassiterite from Rędziny, Lower Silesia, Poland; *Mineralogia Polonica*, Vol. 38, pp. 219-229
- Pilkington, L.A.B. (1969) – The float glass process; *Proceedings of the Royal Society of London*, A 314, pp. 1-25
- Pirajno, F. (1992) – *Hydrothermal Mineral Deposits: principles and fundamental concepts for the exploration geologist*; Springer, Berlin, 709 p.
- Pirajno, F. (2009) – *Hydrothermal Processes and Mineral Systems*; Springer Science+Business Media, 1250 p.
- Pitragool, S. & Panupaisal, S. (1979) – Tin and tungsten mineralization of the Mae Lama mining district, N-W Thailand; *Bulletin of the Geological Society of Malaysia*, Vol. 11, pp. 267-281
- Plimer, I.R. (1974) – Pipe-like molybdenite-wolframite-bismuth deposits of Wolfram, Camp, North Queensland, Australia; *Mineralium Deposita*, Vol. 9, pp. 95-104
- Plimer, I.R. (1980) – Exhalative Sn and W deposits associated with mafic volcanism as precursors to Sn and W deposits associated with granites; *Mineralium Deposita*, Vol. 15, pp. 275-289
- Plimer, I.R. (1983) – The geology of tin and tungsten deposits; *Course Handbook*, Institute of Mineralogy and Petrology, Mining University Leoben, Austria, 212 p.
- Plimer, I.R. (1987a) – The association of tourmalinite with stratiform scheelite deposits; *Mineralium Deposita*, Vol. 22, pp. 282-291
- Plimer, I.R. (1987b) – Fundamental parameters for the formation of granite-related tin deposits; *Geologische Rundschau*, Vol. 76, pp. 23-40
- Plimer, I.R., Lu, J. & Kleeman, J.D. (1991) – Trace and rare earth elements in cassiterite - sources of components for the tin deposits of the Mole Granite, Australia; *Mineralium Deposita*, Vol. 26, pp. 267-274

- Pohl, W. (1975) – Die tektonische Kontrolle der Zinngänge von Rutongo, Rwanda (Afrika); *Mitteilungen der Österreichischen Geologischen Gesellschaft*, Vol. 68, pp. 89-107
- Pohl, W. (1976) – Zur Geologie der Wolframlagerstätte Bugarama, Rwanda, Afrika; *Jahrbuch der Geologischen Bundesanstalt Wien*, Vol. 119, pp. 129-149
- Pohl, W. (1994) – Metallogeny of the northeastern Kibara belt, Central Africa-recent perspectives; *Ore Geology Reviews*, Vol. 9, pp. 105-130
- Pohl, W.L. (2011) – *Economic Geology: Principles and Practice*; John Wiley & Sons Ltd., Chichester, 663 p.
- Pollard, P.J., Taylor, R.G. & Cuff, C. (1983) – Metallogeny of tin: magmatic differentiation versus geochemical heritage—a discussion; *Economic Geology*, Vol. 78, pp. 543-545
- Pollard, P.J., Taylor, R.G. & Tate, N.M. (1989) – Textural evidence for quartz and feldspar dissolution as a mechanism of formation of the Maggs pipe, Zaaiplaats tin mine, South Africa; *Mineralium Deposita*, Vol. 24, pp. 210-218
- Pollard, P.J., Taylor, R.G., Taylor, R.P. & Groves, D.I. (1991) – Petrographic and geochemical evolution of pervasively altered Bushveld granites at the Zaaiplaats tin mine; *Economic Geology*, Vol. 86, pp. 1401-1433
- Polya, D.A. (1988) – Compositional variation in wolframites from the Barroca Grande mine, Portugal: evidence for fault-controlled ore formation; *Mineralogical Magazine*, Vol. 52, pp. 497-503
- Polya, D.A. (1989) – Chemistry of the main-stage ore-forming fluids of the Panasqueira W-Cu(Ag)-Sn deposit, Portugal: Implications for models of ore genesis; *Economic Geology*, Vol. 84, pp. 1134-1152
- Polya, D.A., Foxford, K.A., Stuart, F., Boyce, A. & Fallick, A.E. (2000) – Evolution and paragenetic context of low δD hydrothermal fluids from the Panasqueira W-Sn deposit, Portugal: New evidence from microthermometric, stable isotope, noble gas and halogen analyses of primary fluid inclusions; *Geochimica et Cosmochimica Acta*, Vol. 64, pp. 3357-3371
- Putthapiban, P. & Schwartz, M.O. (1994) – Geochronology of the Southeast Asian Tin Belt granitoids; in: Seltmann, R., Kämpf, H. & Möller, P. (Eds.) – *Metallogeny of collisional orogens*; International association on the genesis of ore deposits (IAGOD), Czech Geological Survey, Prague, pp. 391-398
- Quemeneur, J.J.G. & Noce, C.M. (2000) – Geochemistry and petrology of felsic and mafic suites related to the Paleoproterozoic Transamazonian orogeny in Minas Gerais, Brazil; *Revista Brasileira de Geociências*; Vol. 30, pp. 97-90
- Raimbault, L., Alexandrov, P. & Nong, L.X. (1999) – Behaviour of indium and gallium in hydrothermal cassiterites; in: Stanley, C.J. et al. (Eds.) – *Mineral Deposits: Processes to Processing*; A.A. Balkema, Rotterdam, Netherlands, pp. 421-424
- Raith, J.G. (1991) – Stratabound tungsten mineralization in regional metamorphic calc-silicate rocks from the Austroalpine Crystalline Complex, Austria; *Mineralium Deposita*, Vol. 26, pp. 72-80
- Raith, J.G. & Prochaska, W. (1995) – Tungsten deposits in the Wolfram Schist, Namaqualand, South Africa: Strata-bound versus granite-related genetic concepts; *Economic Geology*, Vol. 90, pp. 1934-1954
- Raith, J.G. & Stein, H.J. (2006) – Variscan ore formation and metamorphism at the Felbertal scheelite deposit (Austria): constraining tungsten mineralisation from Re-Os dating of molybdenite; *Contributions to Mineralogy and Petrology*, Vol. 152, pp. 505-521
- Raith, J.G. & Schmidt, S. (2010) – Tungsten deposit Felbertal, Salzburg, Austria; *Acta Mineralogica-Petrographica, Field Guide Series*, Vol. 3, pp. 1-24

- Ramdohr, P. (1975) – Die Erzminerale und ihre Verwachsungen; 4th edition, Akademie-Verlag, Berlin, 1277 p.
- Rämö, O.T. & Haapala, I. (1995) – One hundred years of Rapakivi Granite; *Mineralogy and Petrology*, Vol. 52, pp. 129-185
- Rao, C., Wang, R.C., Hu, H. & Zhang, W.L. (2009) – Complex internal textures in oxide minerals from the Nanping No. 31 dyke of granitic pegmatite, Fujian Province, southeastern China; *Canadian Mineralogist*, Vol. 47, pp. 1195-1212
- Rasmussen, K.L., Lentz, D.R., Falck, H. & Pattison, D.R.M. (2011) – Felsic magmatic phases and the role of late-stage aplitic dykes in the formation of the world-class Cantung Tungsten skarn deposit, Northwest Territories, Canada; *Ore Geology Reviews*, Vol. 41, pp. 75-111
- Rehren, T. (2005) – The Trehiddle tungsten bloom - an initial report; *International Tungsten Industry Association (ITIA) Newsletter*, June 2005, London, United Kingdom, pp. 2-5
- Relvas, J.M.R.S., Barriga, F.J.A.S., Ferreira, A., Noiva, P.C., Pacheco, N. & Barriga, G. (2006) – Hydrothermal alteration and mineralization in the Neves-Corvo volcanic-hosted massive sulfide Deposit, Portugal: I. Geology, Mineralogy, and Geochemistry; *Economic Geology*, Vol. 101, pp. 753-790
- Ren, S.K., Walshe, J.L., Paterson, R.G., Both, R.A. & Andrew, A. (1995) – Magmatic and hydrothermal history of the porphyry-style deposits of the Ardlethan tin field, New South Wales, Australia; *Economic Geology*, Vol. 90, pp. 1620-1645
- René, M. (1995) – Development of greisenization at the Horní Slavkov Sn-W deposit (Bohemian massif); *Mitteilungen der Österreichischen Mineralogischen Gesellschaft*, Vol. 140, pp. 412-414
- René, M. (1998) – Development of topaz-bearing granites of the Krudum massif (Karlovy Vary pluton); *Acta Universitatis Carolinae – Geologica*, Vol. 42, pp. 103-109
- Rijks, H.R. & van der Veen, A.H. (1972) – The geology of the tin-bearing pegmatites in the eastern part of the Kamativi district, Rhodesia; *Mineralium Deposita*, Vol. 7, pp. 383-395
- Ringwood, A.E. (1955) – The principles governing trace element distribution during magmatic crystallisation, Part I: the influence of electronegativity; *Geochimica et Cosmochimica Acta*, Vol. 7, pp. 189-202
- Rios, F.J., Villas, R.N. & Fuzikawa, K. (2003) – Fluid evolution in the Pedra Preta wolframite ore deposit, Paleoproterozoic Musa granite, eastern Amazon craton, Brazil; *Journal of South American Earth Sciences*, Vol. 15, pp. 787-802
- Ririe, G.T. (1989) – Evaporites and strata-bound tungsten mineralization; *Geology*, Vol. 17, pp. 139-143
- Robb, L.J., Freeman, L.A. & Armstrong, R.A. (2000) – Nature and longevity of hydrothermal fluid flow and mineralisation in granites of the Bushveld Complex, South Africa; in: Barbarin, B., Stephens, W.E., Bonin, B., Vouvhez, J.-L., Clarke, D.B., Cuney, M. & Martin, H. (Eds.) – *Fourth Hutton Symposium: The origin of granites and related rocks*; *Transactions of the Royal Society of Edinburgh: Earth Sciences*, Vol. 91, pp. 269-281
- Robb, L. (2005) – *Introduction to ore-forming processes*; Blackwell Publishing, Malden, USA, 373 p.
- Roberts, K.J. & Strange P.J. (1991) – The geology and exploitation of the Needle Hill wolframite deposit; *Geological Society of Hong Kong, Newsletter*, Vol. 9, pp. 29-40
- Roberts, S., Sanderson, D.J., & Gumiel, P. (1998) – Fractal analysis of Sn-W mineralization from Central Iberia: insights into the role of fracture connectivity in the formation of an ore deposit; *Economic Geology*, Vol. 93, pp. 360-365

- Roedder, E. (1984) – Fluid inclusions; *Reviews in Mineralogy*, Mineralogical Society of America, Vol. 12, 644 p.
- Romer, R.L. & Lehmann, B. (1995) – U–Pb columbite age of Neoproterozoic Ta–Nb mineralization in Burundi; *Economic Geology*, Vol. 90, 2303–2309
- Romer, R.L. & Lüders, V. (2006) – Direct dating of hydrothermal W mineralization: U–Pb age for hübnerite (MnWO₄), Sweet Home Mine, Colorado; *Geochimica et Cosmochimica Acta*, Vol. 70, pp. 4725–4733
- Roos, K. (2014) – Zinn in der Weißblechherstellung; Presentation of ThyssenKrupp Rasselstein at the DERA workshop on tin, Berlin, 28.01.2014, http://www.deutsche-rohstoffagentur.de/DERA/DE/Downloads/zinn_thyssen-krupp.pdf?blob=publicationFile&v=4 (site visited on 14.02.2014)
- Rosman, K.J.R., Loss, R.D. & de Laeter, J.R. (1984) – The isotopic composition of tin; *International Journal of Mass Spectrometry and Ion Processes*; Vol. 56, pp. 281–291
- Rosman, K.J.R. & Taylor, P.D.P. (1998) – Isotopic compositions of the elements 1997 (technical report); *Pure and Applied Chemistry*, Vol. 70, pp. 217–235
- Roskill Information Services Ltd. (1986) – *The economics of tungsten*; 5th edition, London, 264 p.
- Ruck, R., Dusausoy, Y., Nguyen Trung, C., Gaité, J.-M. & Murciego, A. (1989) – Powder EPR study of natural cassiterites and synthetic SnO₂ doped with Fe, Ti, Na and Nb; *European Journal of Mineralogy*, Vol. 1, pp. 343–352
- Rudnick, R.L. & Gao, S. (2004) – Composition of the Continental Crust; in: Rudnick, R.L. (Ed.) – *The Crust; Treatise on Geochemistry* (Eds. Holland, H.D. & Turekian, K.K.), Vol. 3, Elsevier Ltd., Oxford, pp. 1–64
- Ruiz, J. (1988) – Petrology, distribution and origin of rhyolites associated with tin mineralization in the Sierra Madre Occidental, Mexico; in: Taylor, R.P. & Strong, D.F. (Eds.) – *Recent advances in the geology of granite-related mineral deposits*; The Canadian Institute of Mining and Metallurgy, Special Volume 39, Montreal, pp. 322–330
- Russo, R.E., Mao, X., Liu, H., Gonzalez, J. & Mao, S.S. (2002) – Laser ablation in analytical chemistry - a review; *Talanta*, Vol. 57, pp. 425–451
- Saari, E., von Knorring, O. & Sahama, T.G. (1968) – Niobian wolframite from the Nuaparra pegmatite, Zambesia, Mozambique; *Lithos*, Vol. 1, pp. 164–168
- Sahama, T.G., von Knorring, O. & Lehtinen, M. (1970) – New data for anthoinite; *Bulletin of the Geological Society of Finland*, Vol. 42, pp. 95–99
- Sahama, T.G. (1981) – The secondary tungsten minerals, a review; *The Mineralogical Record*, March–April, pp. 81–87
- Sanderson, D.J., Roberts, S., Gumiel, P. & Greenfield, C. (2008) – Quantitative analysis of tin- and tungsten-bearing sheeted vein systems; *Economic Geology*, Vol. 103, pp. 1043–1056
- Schenk, P., Höll, R., Ivanova, G.F., Naumov, V.B. & Kopneva, L.A. (1990) – Fluid inclusion studies of the Felber scheelite deposits; *Geologische Rundschau*, Vol. 79, pp. 451–466
- Schmiderer, A. (2008) – *Geochemische Charakterisierung von Goldvorkommen in Europa*; Ph.D. thesis, Martin Luther University of Halle-Wittenberg, 145 p.
- Schneider, H.-J. & Lehmann, B. (1977) – Contribution to a new genetical concept on the Bolivian Tin Province; in: Klemm, D.D. & Schneider, H.-J. (Eds.) – *Time- and Strata-Bound Ore Deposits*; Springer, Berlin, pp. 153–168
- Schneider, H.-J., Dulski, P., Luck, J., Möller, P. & Villalpando, A. (1978) – Correlation of trace element distribution in cassiterites and geotectonic position of their deposits in Bolivia; *Mineralium Deposita*, Vol. 13, pp. 119–122

- Schröcke, H. (1960) – Isomorphiebeziehungen in der Wolframitgruppe; Beiträge zur Mineralogie und Petrographie, Vol. 7, pp. 166-206
- Schwartz, M.O., Rajah, S.S., Askury, A.K., Putthapiban, P. & Djaswadi, S. (1995) – The Southeast Asian Tin Belt; Earth-Science Reviews, Vol. 38, pp. 95-293
- Schwarz-Schampera, U. (2000) – Indium-tin association in volcanogenic massive sulfide deposits: Evidences from active seafloor hydrothermal systems and ancient massive sulfide deposits on land; Ph.D. thesis, Freiberg University of Mining and Technology, 427 p.
- Schwarz-Schampera, U., Terblanche, H. & Oberthür, T. (2010) – Volcanic-hosted massive sulfide deposits in the Murchison greenstone belt, South Africa; Mineralium Deposita, Vol. 45, pp. 113-145
- Sears, J.W., George, G.M.S. & Winne, J.C. (2005) – Continental rift systems and anorogenic magmatism; Lithos, Vol. 80, pp. 147-154
- SEC (2010) – Dodd-Frank Wall Street Reform and Consumer Protection Act; United States Securities and Exchange Commission (SEC), H.R. 4173, Public Law 111-203, 111th Congress, 849 p.
- Secco, L., Nestola, F. & Dal Negro, A. (2008) – The wulfenite-stolzite series: centric or acentric structures?; Mineralogical Magazine, Vol. 72, pp. 987-990
- Seedorff, E., Dilles, J.H., Proffett, J.M., Einaudi, M.T., Zurcher, L., Stavast, W.J.A., Johnson, D.A. & Barton, M.D. (2005) – Porphyry deposits: characteristics and origin of hypogene features; in: Hedenquist, J.W., Thompson, J.F.H., Goldfarb, R.J. & Richards, J.P. (Eds.) – Economic Geology: 100th Anniversary Volume; Society of Economic Geologists, pp. 251-298
- Seifert, T. (1994) – Zur Metallogenie des Lagerstättendistriktes Marienberg (Ostteil des Mittelerzgebirgischen Antiklinalbreichs); Ph.D. thesis, Freiberg University of Mining and Technology, 174 p.
- Seifert, T., Schwarz-Schampera, U., Herzig, P.M., Hutchinson, R.W., Hennigh, Q. & Wagner, R. (1997) – Trace element characteristics of cassiterite in granite-related tin and tin-bearing VMS deposits; SEG Neves Corvo Field Conference, Abstracts and Program, Lisbon, p. 113
- Seifert, T. & Sandmann, D. (2006) – Mineralogy and geochemistry of indium-bearing polymetallic vein-type deposits: implications for host minerals from the Freiberg district, Eastern Erzgebirge, Germany; Ore Geology Reviews, Vol. 28, pp. 1-31
- Serranti, S., Ferrini, V., Masi, U. & Cabri, L.J. (2002) – Trace-element distribution in cassiterite and sulfides from rubané and massive ores of the Corvo deposit, Portugal; Canadian Mineralogist, Vol. 40, pp. 815-835
- Seward, T.M. & Barnes, H.L. (1997) – Metal transport by hydrothermal ore fluids; in: Barnes, H.L. (Ed.) – Geochemistry of hydrothermal ore deposits, 3rd edition, John Wiley & Sons, New York, pp. 435-486
- Shannon, R.D. (1976) – Revised effective ionic radii and systematic studies of interatomic distances in halides and chalcogenides; Acta Crystallographica Section A: Foundations of Crystallography, Vol. 32, pp. 751-767
- Shcherba, G.N. (1970a) – Greisens; International Geology Review, Vol. 12, Issue 2, pp. 114-150
- Shcherba, G.N. (1970b) – Greisens (Part 2); International Geology Review, Vol. 12, Issue 3, pp. 239-255
- Sheraton, J.W. & Black, L.P. (1973) – Geochemistry of mineralized granitic rocks of northeast Queensland; Journal of Geochemical Exploration, Vol. 2, pp. 331-348

- Sherman, D.M., Ragnarsdottir, K.V., Oelkers, E.H. & Collins, C.R. (2000) – Speciation of tin (Sn^{2+} and Sn^{4+}) in aqueous Cl solutions from 25°C to 350°C: an in situ EXAFS study; *Chemical Geology*, Vol. 167, pp. 169-176
- Shibue, Y. (1982) – Applications of thermodynamic data to the stability fields of ferberite, hübnerite, and ferric tungstate; *Neues Jahrbuch für Mineralogie – Monatshefte*, No. 3, pp. 125-132
- Sieber, K., Leiva, H., Kourtakis, K., Kershaw, R., Dwight, K. & Wold, A. (1983) – Preparation and properties of substituted iron tungstates; *Journal of Solid State Chemistry*, Vol. 47, pp. 361-367
- Sillitoe R.H., Halls, C. & Grant, J.N. (1975) – Porphyry tin deposit in Bolivia; *Economic Geology*, Vol. 70, pp. 913-927
- Silman J.F.B. (1954) – Native tin associated with pitchblende at Nesbitt LaBine uranium mines, Beaverlodge, Saskatchewan; *American Mineralogist*, Vol. 39, pp. 529-531
- Simmons, W.M.B. & Webber, K.L. (2008) – Pegmatite genesis: state of the art; *European Journal of Mineralogy*, Vol. 20, pp. 421-438
- Sinclair, W.D. (1996) – Vein-stockwork tin, tungsten; in: Eckstrand, O.R., Sinclair, W.D. & Thorpe, T.I. (Eds.) – *Geology of Canadian mineral deposit types*; *Geology of Canada* No 8, Geological Survey of Canada, Ottawa, pp. 409-420
- Singh Gaur, R.P. (2006) – Modern hydrometallurgical production methods for tungsten; *Journal of the Minerals, Metals and Materials Society*, Vol. 9, pp. 45-49
- Skaarup, P. (1974) – Strata-bound scheelite mineralization in skarns and gneisses from the Bindal area, Northern Norway; *Mineralium Deposita*, Vol. 99, pp. 299-308
- Sleight, A.W. (1972) – Accurate cell dimensions for ABO_4 molybdates and tungstates; *Acta Crystallographica Section B: Structural Science*, Vol. 28, pp. 2899-2902
- So, C.-S., Rye, D.M. & Shelton, K.L. (1983) – Carbon, hydrogen, oxygen, and sulphur isotope and fluid inclusion study of the Weolag tungsten-molybdenum deposits, Republic of Korea: fluid histories of metamorphic and ore-forming events; *Economic Geology*, Vol. 78, pp. 1551-1573
- Solomovich, L.I., Trifonov, B.A. & Sabelnikov, S.E. (2012) – Geology and mineralization of the Uchkoshkon tin deposit associated with a breccias pipe, Eastern Kyrgyzstan; *Ore Geology Reviews*, Vol. 44, pp. 59-69
- Somarin, A.K. & Ashley, P. (2004) – Hydrothermal alteration and mineralisation of the Glen Eden Mo-W-Sn deposit: a leucogranite-related hydrothermal system, Southern New England Orogen, NSW, Australia; *Mineralium Deposita*, Vol. 39, pp. 282-300
- Somarin, A.K. (2009) – Ore mineralogy and mineral chemistry of the Glen Eden Mo-W-Sn greisen-breccia system, eastern Australia; *Journal of Mineralogical and Petrological Sciences*, Vol. 104, pp. 339-355
- Souza, V.S., Pontes, R.M. & Moura, M.A. (2003) – Inclusões fluidas em topázio do Complexo Granítico Estanífero de Massangana (RO); *Revista escola de Minas, Ouro Preto*, Vol. 56, pp. 231-236
- Souza Neto, J.M., Legrand, J.M., Volfinger, M., Pascal, M.-L. & Sonnet, P. (2008) – W-Au skarns in the Neo-Proterozoic Seridó Mobile Belt, Barborema Province in northeastern Brazil: an overview with the emphasis on the Bonfim deposit; *Mineralium Deposita*, Vol. 43, pp. 185-205
- Speczik, S. & Wiszniewska, J. (1984) – Some comments about stratiform tin deposits in the Stara Kamienica chain (Southwestern Poland); *Mineralium Deposita*, Vol. 19, pp. 171-175
- Srivastava, P.K. & Sinha, A.K. (1997) – Geochemical characterization of tungsten-bearing granites from Rajasthan, India; *Journal of Geochemical Exploration*; Vol. 60, pp. 173-184

- Štemprok, M. (1990) – Solubility of tin, tungsten and molybdenum oxides in felsic magmas; *Mineralium Deposita*, Vol. 25, pp. 205-212
- Stevenson, B.G. & Taylor, R.G. (1973) – Trace element content of some cassiterites from Eastern Australia; *Proceedings of the Royal Society of Queensland*, Vol. 84, pp. 43-54
- Stilling, A., Černý, P. & Vanstone, P.J., (2006) – The Tanco pegmatite at Bernic Lake, Manitoba. XVI. Zonal and bulk compositions and their petrogenetic significance; *Canadian Mineralogist*, Vol. 44, pp. 599-623
- Stöcker, J. & Collongues, R. (1957) – Sur le système zircon-cassitérite; *Comptes rendus de l'académie des sciences Paris*, Vol. 244, pp. 83-85
- Strong, D.F. (1988) – A review and model for granite-related mineral deposits; in: Taylor, R.P. & Strong, D.F. (Eds.) – *Recent advances in the geology of granite-related mineral deposits*; The Canadian Institute of Mining and Metallurgy, Special Volume 39, Montreal, pp. 424-445
- Strunz, H. & Nickel, E.H. (2001) – *Strunz Mineralogical Tables, Chemical-Structural Mineral Classification System*; 9th edition, Schweizerbart, Stuttgart, 870 p.
- Sugaki, A., Kojima, S. & Shimada, N. (1988) – Fluid inclusion studies of the polymetallic hydrothermal ore deposits in Bolivia; *Mineralium Deposita*, Vol. 23, pp. 9-15
- Sugaki, A., Shimada, N., Ueno, H. & Kano, S. (2003) – K-Ar Ages of Tin-Polymetallic Mineralization in the Oruro Mining District, Central Bolivian Tin Belt; *Resource Geology*, Vol. 53, pp. 273-282
- Suk, N.I. (1997) – Behaviour of ore elements (W, Sn, Ti and Zr) in layered immiscible silicate-salt systems; *Petrology*, Vol. 5, pp. 20-27
- Sushchevskaya, T.M. & Bychkov, A.Y. (2010) – Physicochemical mechanisms of cassiterite and wolframite precipitation in the granite-related hydrothermal system: thermodynamic modelling; *Geochemistry International*, Vol. 48, pp. 1246-1253
- Suthakorn, P. (1992) – The distribution of tin and associated minerals in Thailand; *National Conference on Geologic Resources of Thailand: Potential for Future Development*, 17.-24. November 1992, Bangkok, Thailand, pp. 450-486
- Suwimonprecha, P., Černý, P. & Friedrich, G. (1995) – Rare metal mineralization related to granites and pegmatites, Phuket, Thailand; *Economic Geology*, Vol. 90, pp. 603-615
- Swinden, T.R. (1983) – An investigation of the variations in optical properties and chemical composition of cassiterite in Cornish tin lodes; Ph.D. thesis, Camborne School of Mines, 290 p.
- Sylvester, P.J. (2008) – Matrix effects in laser ablation-ICP-MS; in: Sylvester, P. (Ed.) – *Laser Ablation ICP-MS in the Earth Sciences: current practices and outstanding issues*; Short Course Series, Vol. 40, Mineralogical Association of Canada, Vancouver, pp. 67-78
- Tack, L., Wingate, M.T.D., De Waele, B., Meert, J., Belousova, E., Griffin, B., Tahon, A., Fernandez Alonso, M. (2010) – The 1375 Ma “Kibaran Event” in Central Africa: prominent emplacement of bimodal magmatism under extensional regime; *Precambrian Research*, Vol. 180, pp. 63-84
- Takahashi, M., Aramaki, S. & Ishihara, S. (1980) – Magnetite-series/Ilmenite-series vs. I-Type/S-type granitoids; in: Ishihara, S. & Takenouchi, S. (Eds.) – *Granitic magmatism and related mineralization*; Mining Geology Special Issue, Vol. 8, The Society of Mining Geologists of Japan, Tokyo, pp. 13-28
- Tanelli, G. & Lattanzi, P. (1985) – The cassiterite-polymetallic sulfide deposits of Dachang (Guangxi, People's Republic of China); *Mineralium Deposita*, Vol. 20, pp. 102-106

- Taylor, R.G. & Hosking, K.F.G. (1970) – Manganese-iron ratios in wolframite, South Crofty mine, Cornwall; *Economic Geology*, Vol. 65, pp. 47-53
- Taylor, R.G. & Steveson, B.G. (1972) – An analysis of metal distribution and zoning in the Herberton tinfield, North Queensland, Australia; *Economic Geology*, Vol. 67, pp. 1234-1240
- Taylor, R.G. (1979) – Geology of tin deposits; *Developments in Economic Geology*, Vol. 11, Elsevier, Amsterdam, 543 p.
- Taylor, R.P. (1992) – Petrological and geochemical characteristics of the Pleasant Ridge zinnwaldite-topaz granite, southern New Brunswick, and comparisons with other topaz-bearing felsic rock; *Canadian Mineralogist*, Vol. 30, pp. 895-921
- Taylor, J.R. & Wall, V.J. (1992) – The behavior of tin in granitoid magmas; *Economic Geology*, Vol. 87, pp. 403-420
- Taylor, J.R. & Wall, V.J. (1993) – Cassiterite solubility, tin speciation, and transport in a magmatic aqueous phase; *Economic Geology*, Vol. 88, pp. 437-460
- Thalhammer, O.A.R., Stumpfl, E.F. & Jahoda, R. (1989) – The Mittersill scheelite deposit, Austria; *Economic Geology*, Vol. 84, pp. 1153-1171
- Thermo (2005) – Finnigan™ ELEMENT 2 & Finnigan™ ELEMENT XR hardware manual; Thermo Electron Corporation, Waltham, 165 p.
- Theunissen, K.; Hanon, M. & Fernandez Alonso, M. (1991) – Carte Géologique du Rwanda; République Rwandaise, Ministère de l'Industrie et de l'Artisanat, Service Géologique, 1:250000
- Thomas, A.V. & Spooner, E.T.C. (1988) – Occurrence, petrology and fluid inclusion characteristics of tantalum mineralization in the Tanco granitic pegmatite, southeastern Manitoba; in: Taylor, R.P. & Strong, D.F. (Eds.) – Recent advances in the geology of granite-related mineral deposits; *The Canadian Institute of Mining and Metallurgy, Special Volume 39*, Montreal, pp. 208-222
- Thomas, R. & Webster, J.D. (2000) – Strong tin enrichment in a pegmatite-forming melt; *Mineralium Deposita*, Vol. 35, pp. 570-582
- Thompson, J.F.H., Sillitoe, R.H., Baker, T., Lang, J.R. & Mortensen, J.K. (1999) – Intrusion-related gold deposits associated with tungsten-tin provinces; *Mineralium Deposita*, Vol. 34, pp. 323-334
- Thorn, P.G. (1988) – Fluid inclusion and stable isotope studies at the Chicote tungsten deposit; Bolivia; *Economic Geology*, Vol. 83, pp. 62-68
- Timón Sánchez, S.M., Moro Benito, M. C. & Cembranos Pérez, M.L. (2009) – Mineralogical and physicochemical evolution of the Los Santos scheelite skarn, Salamanca, NW Spain; *Economic Geology*, Vol. 104, pp. 961-995
- Tindle, A.G. & Webb, P.C. (1989) Niobian wolframite from Glen Gairn in the Eastern highlands of Scotland: A microprobe investigation; *Geochimica et Cosmochimica Acta*, Vol. 53, pp. 1921-1935
- Tindle, A.G. & Breaks, F.W. (1998) – Oxide minerals of the Separation Rapids rare-element granitic pegmatite group, Northwestern Ontario; *Canadian Mineralogist*, Vol. 36, pp. 609-635
- Tischendorf, G. (1977) – Geochemical and petrographic characteristics of silicic rocks associated with rare-element mineralization; in: Štemprok, M., Tischendorf, G. & Burnil, L. (Eds.) – Metallization associated with acid magmatism; Vol. 2, *Czech Geological Survey, Prague*, pp. 41-96
- Tkachev, A.V. (2011) – Evolution of metallogeny of granitic pegmatites associated with orogens throughout geological time [including supplementary material]; in: Sial, A.N., Bettencourt, J.S., de Campos, C.P. & Ferreira, V.P. (Eds.) – Granite-related ore deposits; *The Geological Society, Special Publication*, Vol. 350, London, pp. 7-23

- Toplis, M.J. & Corgne, A. (2002) – An experimental study of element partitioning between magnetite, clinopyroxene and iron-bearing silicate liquids with particular emphasis on vanadium; *Contributions to Mineralogy and Petrology*; Vol. 144, pp. 22-37
- Tornos, F., Galindo, C., Crespo, J.L. & Spiro, B.F. (2008) – Geochemistry and origin of calcic tungsten-bearing skarns, Los Santos, Central Iberian Zone, Spain; *Canadian Mineralogist*, Vol. 46, pp. 87-109
- Triller, E. (1987) – Zur Geochemie und Spurenanalytik des Wolframs unter besonderer Berücksichtigung seines Verhaltens in einem südostnorwegischen Pegmatoid; Ph.D. thesis, Johann Wolfgang Goethe University Frankfurt/Main, *Frankfurter Geowissenschaftliche Arbeiten, Series C Mineralogy*, Vol. 7, 173 p.
- Turneure, F.S. (1971) – The Bolivian tin-silver province; *Economic Geology*, Vol. 66, pp. 215-225
- Uchida, E., Endo, S. & Makino, M. (2007) – Relationship between solidification depth of granitic rocks and formation of hydrothermal ore deposits; *Resource Geology*, Vol. 57, pp.47-56
- Uher, P., Černý, P. & Chapman, R. (2008) – Foordite-thoreaulite, $\text{Sn}^{2+}\text{Nb}_2\text{O}_6$ - $\text{Sn}^{2+}\text{Ta}_2\text{O}_6$: compositional variations and alteration products; *European Journal of Mineralogy*, Vol. 20, pp. 501-516
- United Nations (1999) – Geology and mineral resources of Mongolia; Atlas of mineral resources of the Economic and Social Commission for Asia and the Pacific (ESCAP), Vol. 14, 192 p.
- Urquidi-Barrau, F. (1989) – Tin and tungsten deposits of the Bolivian tin belt; in: Erickson, G.E., Cañas Pinochet, M.T. & Reinemund, J.A. (Eds.) – Geology of the Andes and its relation to hydrocarbon and mineral resources; *Circum-Pacific Council for Energy and Mineral Resources Earth Science Series*, Vol. 11, pp. 313-323
- Uspensky, E., Brugger, J. & Graeser, S. (1998) – REE geochemistry systematics of scheelite from the Alps using luminescence spectroscopy: From global regularities to local control; *Schweizerische mineralogische und petrographische Mitteilungen*, Vol. 78, pp. 31-54.
- Varlamoff, N. (1947) – Anthoinite, nouveau tungstate hydraté d'alumine; *Annales de la Société Géologie du Belgique*, Vol. 70, pp. 153-166
- Varlamoff, N. (1972) – Central and West African rare-metal granitic pegmatites, related aplites, quartz veins and mineral deposits; *Mineralium Deposita*, Vol. 7, pp. 202-216
- Veksler, I.V. (2005) – Element enrichment and fractionation by magmatic aqueous fluids: experimental constraints on melt-fluid immiscibility and element partitioning; in: Linnen, R.L. & Samson, I.M. (Eds.) – Rare-element geochemistry and mineral deposits; *Geological Association of Canada (GAC), Short Course Notes*, Vol. 17, pp. 69-85
- Vieira, R. & Lima, A. (2007) – Locality No. 2, Bajoca Mine, Almendra, Portugal; in: Lima, A. & Roda, E. (Eds.) – Granitic Pegmatites: the state of the art; *Field trip guide*, Universidade do Porto, Faculdade de Ciências, Departamento de Geologia, *Memórias*, Vol. 9, pp. 49-54
- Völkening, J., Köppe, M. & Heumann, K.G. (1991) – Tungsten isotope ratio determinations by negative thermal ionization mass spectrometry; *International Journal of Mass Spectrometry and Ion Processes*, Vol. 107, pp. 361-368
- Von Knorring, O. & Condliffe, E. (1987) – Mineralized pegmatites in Africa; *Geological Journal*, Vol. 22, pp. 253-270

- Voyevodin, V.N. (1981) – The relationship between chemical composition of wolframites and the geological conditions of their formation; *International Geology Review*, Vol. 25, pp. 561-570
- Wade, J., Wood, B.J. & Norris, C.A. (2013) – The oxidation state of tungsten in silicate melt at high pressures and temperatures; *Chemical Geology*, Vol. 335, pp. 189-193
- Wagener, G.F. (1989) – Systematic variation in the tin content of pegmatites in western central Namibia; *Journal of Geochemical Exploration*, Vol. 34, pp. 1-19
- Wagner, P.A. (1926) – Wood tin-gel replacement of cassiterite; *Economic Geology*, Vol. 21, pp. 727-731
- Wagner, T., Mlynarczyk, M.S., Williams-Jones, A.E. & Boyce, A.J. (2009) – Stable isotope constraints on ore formation at the San Rafael tin-copper deposit, Southeast Peru; *Economic Geology*, Vol. 104, pp. 223-248
- Walia, D.S. (1971) – Iron solubility in cassiterite (SnO₂); *The Compass*, Vol. 49, pp. 27-28
- Walker, R.J., Hanson, G.N. & Papike, J.J. (1989) – Trace element constraints on pegmatite genesis: Tin Mountain pegmatite, Black Hills, South Dakota; *Contributions to Mineralogy and Petrology*, Vol. 101, pp. 290-300
- Walraven, F., Armstrong, R. A., & Kruger, F. J. (1990) – A chronostratigraphic framework for the north-central Kaapvaal Craton, the Bushveld Complex and the Vredefort structure; *Tectonophysics*, Vol. 171, pp. 23-48.
- Walshe, J.L., Solomon, M., Whitford, D.J., Sun, S.-S. & Foden, J.D. (2011) – The role of the mantle in the genesis of tin deposits and tin provinces of Eastern Australia; *Economic Geology*, Vol. 106, pp. 297-305
- Wang, R.C., Xie, L., Chen, J., Yu, A., Wang, L., Lu, J. & Zhu, J. (2013) – Tin-carrier minerals in metaluminous granites of the western Nanling Range (southern China): Constraints on processes of tin mineralization in oxidized granites; *Journal of Asian Earth Sciences*; Vol. 74, pp. 361-372
- Ward, C.D., McArthur, J.M. & Walsh, J.N. (1992) – Rare earth element behaviour during evolution and alteration of the Dartmoor granite, SW England; *Journal of Petrology*, Vol. 33, pp. 785-815
- Webster, J.D., Thomas, R., Rhede, D., Förster, H.-J. & Seltmann, R. (1997) – Melt inclusions in quartz from an evolved peraluminous pegmatite: geochemical evidence for strong tin enrichment in fluorine-rich and phosphorus-rich residual liquids; *Geochimica et Cosmochimica Acta*, Vol. 61, pp. 2589-2604
- Wei, W., Hu, R., Bi, X., Peng, J., Su, W., Song, S. & Shi, S. (2012) – Infrared microthermometric and stable isotopic study of fluid inclusions in wolframite at the Xihuashan tungsten deposit, Jiangxi province, China; *Mineralium Deposita*, Vol. 47, pp. 589-605
- Werner, A.B.T., Sinclair, W.D. & Amey, E.B. (1998) – International Strategic Mineral Issues Summary Report: Tungsten; U.S. Geological Survey Circular 930-O, 71 p.
- Wesolowski, D., Drummond, S.E., Mesmer, R.E. & Ohmoto, H. (1984) – Hydrolysis equilibria of tungsten(VI) in aqueous sodium chloride solutions to 300 °C; *Inorganic Chemistry*, Vol. 23, pp. 1120-1132
- Whalen, J.B. & Currie, K.L. & Chappell, B.W. (1987) – A-type granites: geochemical characteristics, discrimination and petrogenesis; *Contributions to Mineralogy and Petrology*, Vol. 95, pp. 407-419
- White, W.M. (2009) – Geochemistry: an online text book; 701 p.
<http://www.imwa.info/white-geochemistry.html>
- White, A.J.R. & Chappell, B.W. (1977) Ultrametamorphism and granitoid genesis; *Tectonophysics*, Vol. 43, pp. 7-22

- Wiedenbeck, M., Bugoi, R., Duke, M.J.M., Dunai, T., Enzweiler, J., Horan, M., Jochum, K.P., Linge, K., Košler, J., Merchel, S., Morales, L.F.G., Nasdala, L., Stalder, R., Sylvester, P., Weis, U. & Zoubir, A. (2012) – GGR biennial critical review: analytical developments since 2010; *Geostandards and Geoanalytical Research*, Vol. 36, pp. 337-398
- Wiendl, U. (1968) – *Zur Geochemie und Lagerstättenkunde des Wolframs*; Ph.D. thesis, University of Technology Clausthal, 295 p.
- Wikarno, U., Suyatna, D.A.D. & Sukardi, S. (1988) – Granitoids of Sumatra and the Tin Islands; in: Hutchison, C.S. (Ed.) – *Geology of tin deposits in Asia and the Pacific: selected papers from the International Symposium on the Geology of Tin Deposits*, Nanning, China, October 26-30, 1984; Springer, Berlin, pp. 571-589
- Wilkinson, J.J. (2001) – Fluid inclusions in hydrothermal ore deposits; *Lithos*, Vol. 55, pp. 229-272
- Willbold, M., Elliott, T. & Moorbath, S. (2011) – The tungsten isotopic composition of the Earth's mantle before the terminal bombardment; *Nature*, Vol. 477, pp. 195-198
- Willgallis, A. (1982) – Zum Mischkristallverhältnis von Wolframiten; *Neues Jahrbuch für Mineralogie – Abhandlungen*, Vol. 145, pp. 308-326
- Williams-Jones, A.E. & Heinrich, C.A. (2005) – Vapor transport of metals and the formation of magmatic-hydrothermal ore deposits; *Economic Geology*, Vol. 100, pp. 1287-1312
- Williamson, B.J., Müller, A. & Shail, R.K. (2010) – Source and partitioning of B and Sn in the Cornubian batholith of southwest England; *Ore Geology Reviews* Vol. 38, pp. 1-8
- Willis-Richards, J. & Jackson, N.J. (1989) – Evolution of the Cornubian Ore Field, Southwest England: Part I. Batholith Modeling and Ore Distribution; *Economic Geology*, Vol. 84, pp. 1078-1100
- Wise, M.A. & Černý, P. (1996) – The crystal chemistry of the tapiolite series; *Canadian Mineralogist*, Vol. 34, pp. 631-647
- Wise, M.A. & Brown, C.D. (2011) – Chemical composition of coexisting columbite-group minerals and cassiterite from the Black Mountain pegmatite, Maine; *European Journal of Mineralogy*, Vol. 23, pp. 817-828
- Wiszniewska, J., Kozłowski, A. & Metz, P. (1998) – Significance of the composition of garnet to clarify the origin of tin mineralization in the Stara Kamienica schist belt, southwest Poland; in: Hagni, R.D. (Ed.) – *Proceedings of the Ninth Quadrennial IAGOD Symposium*, Beijing, China, August 12-18, 1994; Schweizerbart, Stuttgart, pp. 463-473
- Wolf, D. & Espozo, E. (1972) – Zur Geochemie bolivianischer Kassiterite; *Zeitschrift für angewandte Geologie*, Vol. 18, pp. 459-468
- Wood, S.A. & Vlassopoulos, D. (1989) – Experimental determination of the hydrothermal solubility and speciation of tungsten at 500 °C and 1 kbar; *Geochimica et Cosmochimica Acta*, Vol. 53, pp. 303-312
- Wood, S.A. (1992) – Experimental determination of the solubility of $WO_3(s)$ and the thermodynamic properties of $H_2WO_4(aq)$ in the range 300-600 °C at 1 kbar: Calculation of scheelite solubility; *Geochimica et Cosmochimica Acta*, Vol. 56, pp. 1827-1836
- Wood, S.A. & Samson, I.M. (1998) – Solubility of ore minerals and complexation of ore metals in hydrothermal solutions; in: Richards, J.P. & Larson, P.B. (Eds.) – *Techniques in hydrothermal ore deposits geology*; *Reviews in Economic Geology*, Vol. 10, Society of Economic Geologists, pp. 33-80
- Wood, S.A. & Samson, I.M. (2000) – The hydrothermal geochemistry of tungsten in granitoid environments: I. Relative solubilities of ferberite and scheelite as a function of T, P, pH, and m_{NaCl} ; *Economic Geology*, Vol. 95, pp. 143-182

- Wood, S.A. & Samson, I.M. (2006) – The aqueous geochemistry of gallium, germanium, indium and scandium; *Ore Geology Reviews*, Vol. 28, pp. 57-102
- Xie, L., Wang, R., Chen, J., Zhu, J., Zhang, W., Lu, J. & Zhang, R. (2013) – A tin-mineralized topaz rhyolite dike with coeval topaz granite enclaves at Qiguling in the Qitianling tin district, southern China; *Lithos*, Vol. 170-171, pp. 252-268
- Xu, K. & Zhu, J. (1988) – Time-space distribution of tin/tungsten deposits in south China and controlling factors of mineralization; in: Hutchison, C.S. (Ed.) – *Geology of tin deposits in Asia and the Pacific: selected papers from the International Symposium on the Geology of Tin Deposits*, Nanning, China, October 26-30, 1984; Springer, Berlin, pp. 265-277
- Yim, W.W.-S. (1994) – Particle size and trace element distribution characteristics of cassiterite as an aid to provenance study of stanniferous placers in northeastern Tasmania, Australia; *Journal of Southeast Asian Earth Sciences*; Vol. 10, pp. 131-142
- Zajacz, Z., Halter, W.E., Pettke, T. & Guillong, M. (2008) – Determination of fluid/melt partition coefficients by LA-ICPMS analysis of co-existing fluid and silicate melt inclusions: controls on element partitioning; *Geochimica et Cosmochimica Acta*, Vol. 72, pp. 2169-2197
- Zaw, K. & Singoyi, B. (2000) – Formation of magnetite-scheelite skarn mineralization at Kara, Northwestern Tasmania: evidence from mineral chemistry and stable isotopes; *Economic Geology*, Vol. 95, pp. 1215-1230
- Zhang, Y., Liu, Y., Gao, S. & He, Q. (1990) – REE geochemical characteristics of tungsten minerals as a discriminant indicator of genetic types of ore deposits; *Chinese Journal of Geochemistry*, Vol. 9, pp. 319-329
- Zhang, Z., Mao, J., Yang, J., Wang, Z. & Zhang, Z. (2003) – Geology and genesis of the Ta'ergou skarn – quartz vein tungsten deposit in the North Qilian Caledonian orogenic belt, Northwest China; *Resource Geology*, Vol. 53, pp. 101-114
- Zhao, K.-D., Jiang, S.-Y., Jiang, Y.-H. & Wang, R.-C. (2005) – Mineral chemistry of the Qitianling granitoid and the Furong tin ore deposit in Hunan Province, South China: implication for the genesis of granite and related tin mineralization; *European Journal of Mineralogy*, Vol. 17, pp. 635-648

Lebenslauf

Werdegang

- seit 04.10.2011 Wissenschaftlicher Mitarbeiter im Fachbereich „Geologie der mineralischen Rohstoffe“ (B1.2) an der Bundesanstalt für Geowissenschaften und Rohstoffe
- 01.11.2008 – 30.09.2011 Wissenschaftlicher Mitarbeiter am Institut für Mineralogie der Leibniz Universität Hannover; Hochschulvergabeprojekt zum Herkunftsnachweis von Zinn- und Wolframerzen
- Nov. 2007 – Sept. 2008 Diplomarbeit am Institut für Mineralogie der Leibniz Universität Hannover in Kooperation mit der Bundesanstalt für Geowissenschaften und Rohstoffe: „Mineralogical-Geochemical Characterization of Antimony-Gold-Mercury Deposits in the ‘Antimony Line’, Murchison Greenstone Belt, Republic of South Africa“; Abschlussnote: sehr gut (1,1)
- WS 2002/2003 – SS 2008 Studium der Geowissenschaften an der Leibniz Universität Hannover; Abschluss: Diplom mit der Note sehr gut (1,2)

Praktika & Nebentätigkeiten

- 04.09.2007 – 12.10.2007 Praktikum bei der Bundesanstalt für Geowissenschaften und Rohstoffe im Referat „Meeresgeologie und Tiefseebergbau“ (B 3.23)
- 02.05.2007 – 31.08.2007 Studentische Hilfskraft bei der AvJS Personal auf Zeit GmbH; eingesetzt bei der Bundesanstalt für Geowissenschaften und Rohstoffe im Referat „Lagerstättenforschung“ (B 4.23): Vorbereitung von Columbit-Tantalit-Proben für die Uran-Blei-Altersbestimmung
- 19.03.2007 – 13.04.2007 Praktikum bei der Bundesanstalt für Geowissenschaften und Rohstoffe im Referat „Lagerstättenforschung“ (B 4.23)